รายงานวิจัยฉบับสมบูรณ์

โครงการวิจัยการประยุกต์ใช้ตัวเร่งปฏิกิริยาและเครื่องปฏิกรณ์เคมี
สำหรับใช้ในอุตสาหกรรมปิโตรเคมี
(สัญญาเลขที่ RTA4780013)

โดย ศาสตราจารย์ ดร. ปิยะสาร ประเสริฐธรรม
จุฬาลงกรณ์มหาวิทยาลัย

กรกฎาคม 2550

บทคัดย่อ

รายงานฉบับนี้สรุปผลการดำเนินงานของโครงการวิจัยการประยุกต์ใช้ตัวเร่งปฏิกิริยาและเครื่องปฏิกรณ์เคมีสำหรับใช้ในอุตสาหกรรมปิโตรเคมี ซึ่งได้รับทุนส่งเสริมกลุ่มวิจัย จากสำนักงานกองทุนสนับสนุนการวิจัย โครงการนี้นอกจากมุ่งเน้นการสร้างองค์ความรู้ใหม่ที่มีความสำคัญต่อการพัฒนาอุตสาหกรรมปิโตรเคมีแล้ว ยังเน้นการเผยแพร่ผลงานวิจัยโดยการตีพิมพ์ผลงานในวารสารระดับนานาชาติที่มีการประเมินผลงานอย่างเข้มงวด การสร้างบุคลากรที่มีความสามารถทั้งในระดับปริญญาโทและปริญญาเอก การสร้างความร่วมมือระหว่างนักวิจัยในประเทศไทยและต่างประเทศ การพัฒนาห้องปฏิบัติการวิจัยในหน่วยงานเอกชน ตลอดจนการทำวิจัยร่วมกับภาคอุตสาหกรรม

ผลที่ได้จากการดำเนินงานสามารถสรุปได้ดังนี้ คือ สามารถตีพิมพ์ผลงานในวารสารระดับนานาชาติจำนวน 42 บทความ มากกว่าเป้าหมาย 75% สามารถผลิตมหาบัณฑิตได้ 48 คน มากกว่าเป้าหมาย 60% ผลิตดุษฎีบัณฑิตได้ 13 คน มากกว่าเป้าหมาย 44% ได้สร้างความร่วมมือทางด้านงานวิจัยกับบริษัท SCG Chemical Co. Ltd. โดยสร้างห้องปฏิบัติการวิจัยเพื่อทำงานวิจัยร่วมจำนวน 1 แห่ง นอกจากนี้ ยังได้ช่วยบริษัท TUNTEX PETROCHEMICALS (THAILAND) และบริษัทระยองโอเลฟินส์ในส่วนของการเลือกตัวเร่งปฏิกิริยาที่เหมาะสมอีกด้วย ผลสำเร็จที่ได้จากโครงการฯนี้นับเป็นประโยชน์อย่างมากต่อการพัฒนาอุตสาหกรรมปิโตรเคมีของประเทศไทย

คำสำคัญ: ตัวเร่งปฏิกิริยาเคมี คาตาไลซิส นาโนคาตาไลซิส เครื่องปฏิกรณ์เคมี ปิโตรเคมี

Abstract

This report summarizes the outputs from the project entitled “Application of Catalysts and Chemical Reactors for Petrochemical Industry” under the research promotion scholarship sponsored by the Thailand Research Fund. This project was aimed to explore new basic knowledge necessary for the development of petrochemical industry. In addition, it focused on publishing the acquired knowledge in peer-review international journals, producing talent and skillful master-degree and doctoral-degree graduates, developing and strengthening the collaborations with Thai researchers and foreign professors from famous universities, promoting the establishment of a private research laboratory and developing co-research with Thai industries.

The overall outputs from the project can be summarized as follows. There are 42 international publications which are 75% higher than the expected values. The numbers of master- and doctoral-graduates are 48 and 13, higher than the expected values by 60% and 44%, respectively. The research collaboration was strongly established between our center of excellence and SCG Chemical Co. Ltd., leading to one research lab founded. In addition, the project also supported two companies; i.e., TUNTEX PETROCHEMICALS (THAILAND) and Rayong Olefins Co. Ltd, on catalyst screening. It is noted that the success from this project was very beneficial to the development of Petrochemical Industry of Thailand.

Keywords: Catalyst; Catalysis; Nanocatalysis; Chemical reactor; Petrochemical

สัญญาเลขที่ RTA4780013

รายงานวิจัยฉบับสมบูรณ์

โครงการวิจัยการประยุกต์ใช้ตัวเร่งปฏิกิริยาและเครื่องปฏิกรณ์เคมี สำหรับใช้ในอุตสาหกรรมปิโตรเคมี

โดย ศาสตราจารย์ ดร. ปิยะสาร ประเสริฐธรรม
จุฬาลงกรณ์มหาวิทยาลัย

สนับสนุนโดยสำนักงานกองทุนสนับสนุนการวิจัย

สรุปผลการดำเนินการโครงการในรอบ 3 ปี

==========

ชื่อหัวหน้าโครงการ ศ.ดร. ปิยะสาร ประเสริฐธรรม

รายงานในช่วงเวลาตั้งแต่วันที่ 1 สิงหาคม พ.ศ. 2547 **ถึง** 31 กรกฎาคม พ.ศ. 2550

1. กิจกรรมที่ได้ดำเนินการ

1.1 ด้านการประสานงานระหว่างผู้ดำเนินการ

เนื่องจากคณะผู้วิจัยประกอบด้วยอาจารย์และนักวิจัยจากหลายสถาบัน การติดต่อประสานงานจึงดำเนินการด้วยวิธีดังนี้

1. รศ.ดร. ชาคริต ทองอุไร (มหาวิทยาลัยสงขลานครินทร์)
   การติดต่อทำโดยการโทรศัพท์
2. อ.ดร.ชูวงศ์ ชัยสุข (มหาวิทยาลัยศิลปากร)
   การติดต่อทำโดยการโทรศัพท์และเดินทางเข้ามาที่ภาควิชาวิศวกรรมเคมี คณะวิศวกรรมศาสตร์ จุฬาลงกรณ์มหาวิทยาลัย ประมาณสัปดาห์ละครั้ง
3. อ.ดร. โอกร เมฆาสุวรรณดำรง (มหาวิทยาลัยศิลปากร)
   การติดต่อทำโดยการโทรศัพท์และเดินทางเข้ามาที่ภาควิชาวิศวกรรมเคมี คณะวิศวกรรมศาสตร์ จุฬาลงกรณ์มหาวิทยาลัย ประมาณสัปดาห์ละครั้ง
4. ดร. นครินทร์ มงคลศิริ (บริษัทระยองโอเลฟินส์ จำกัด)
   การติดต่อทำโดยการโทรศัพท์และเดินทางเข้ามาที่ภาควิชาวิศวกรรมเคมี คณะวิศวกรรมศาสตร์ จุฬาลงกรณ์มหาวิทยาลัย ประมาณเดือนละครั้ง
   นอกจากนี้ ดร.จูงใจ ปั้นประณต เดินทางไปที่โรงงานประมาณ 3 เดือนครั้ง

2. ผลงาน

2.1 บทความวิจัยในวารสารระดับนานาชาติ

2.1.1 บทความที่ได้รับการตอบรับแล้ว จำนวน 42 ผลงาน

1. S. Sombatchaisak, P. P. Praserthdam, C. Chaisuk and J. Panpranot, “An Alternative Correlation Equation between Particle Size and Structure Stability of H-Y Zeolite under Hydrothermal Treatment Condition”, Ind. Eng. Chem. Res. 43 (2004) 4066-4072. (Impact factor 2004 = 1.424) (เอกสารแนบชุดที่ 1)
2. W. Sangtongkitcharoen, S. Assabumrungrat, V. Pavarajarn, N. Laosiripojana, and P. Praserthdam, “Comparison of Carbon Formation Boundary for Different Types of Solid Oxide Fuel Cells with Methane Feed”, J. Power Sources, 142 (1-2) , 75-80

(2005) (Impact factor 2005 = 2.770). (เอกสารแนบชุดที่ 2)

3. B. Jongsomjit, C. Sakdamnuson, and P. Praserthdam, “Dependence of crystalline phases in titania on catalytic properties during CO hydrogenation of Co/TiO_2 catalysts”, Materials Chemistry and Physics 89 (2005) 395-401. (Impact Factor 2005 = 1.136) (เอกสารแนบชุดที่ 3)
4. B. Jongsomjit, E. Chaichana and P. Praserthdam, “LLDPE/nano-silica composites synthesized via in situ polymerization of ethylene-1-hexene with MAO/metallocene catalyst” Journal of Materials Science 40 (8), 2043-2045 (2005) (Impact factor 2005 = 0.901). (เอกสารแนบชุดที่ 4)
5. B. Jongsomjit, T. Wongsalee and P. Praserthdam, “Study of Cobalt Dispersion on Titania Consisting Various Rutile Anatase Ratios” Materials Chemistry and Physics 92 (2-3), 572-577. (2005) (Impact factor 2005 = 1.136). (เอกสารแนบชุดที่ 5)
6. B. Jonsomjit**,** S. Ngamposri, and P. Praserthdam, “Catalytic activity during copolymerization of ethylene/1-hexene via mixed TiO_2/SiO_2-supported MAO with rac-Et$[Ind]_2ZrCl_2$ metallocene catalyst”, Molecules, (2005), 10, 603-609 (Impact factor 2005 = 1.113) (เอกสารแนบชุดที่ 6)
7. P. Praserthdam, C. Chaisuk, W. Kongsuebchart, S. Thongyai, S.K.N. Ayudhya, New concepts in material and energy utilization, Korean Journal of Chemical Engineering 22 (1) , 115-120 (2005) (Impact factor 2005 = 0.750) (เอกสารแนบชุดที่ 7)
8. B. Jongsomjit, S. Ngamposri, and P. Praserthdam, “Role of titania in TiO_2-SiO_2 mixed oxides-supported metallocene catalyst during ethylene/1-octene copolymerization”, Catalysis Letters, 100 (3-4) 139 – 146 (2005) (Impact factor 2005 = 2.088) (เอกสารแนบชุดที่ 8)
9. J. Panpranot, S. Kaewgun, and P. Praserthdam, “Metal-Support Interaction in Mesoporous Silica Supported Cobalt Fischer-Tropsch Catalysts”, Reaction Kinetics and Catalysis Letters, 85, (2005) 299-304. (Impact factor 2005 = 0.670) (เอกสารแนบชุดที่ 9)
10. P. Soisuwan, P. Praserthdam, Dean C. Chambers, David L. Trimm, O. Mekasuwandumrong, and J. Panpranot, “Characteristics and Catalytic Properties of Alumina-Zirconia Mixed Oxides Prepared by the Modified Pechini Method”, Catalysis Letters, 103 (2005) 63-68. (Impact factor 2005 = 2.088) (เอกสารแนบที่ชุดที่ 10)
11. B. Jongsomjit, A. Khotdee, and P. Praserthdam, “Behaviors of ethylene/norbornene

copolymerization with zirconocene catalysts", Iranian Polymer Journal, 14, 559 - 564 (2005). (Impact factor 2005 = 0.316) (เอกสารแนบชุดที่ 11)

12. S. Assabumrungrat, W. Sangtongkitcharoen, N. Laosiripojana, A. Arpornwichanop, Sumittra Charojrochkul and P. Praserthdam, "Effects of Electrolyte Type and Flow Pattern Mode on Performances of Methanol-Fueled Solid Oxide Fuel Cells" J. Power Sources 148 (2005) 18-23 (Impact factor 2005 = 2.770) (เอกสารแนบชุดที่ 12)
13. J. Panpranot, L. Nakkararuang, B. Ngamsom and P. Praserthdam, "Synthesis, Characterization, and Catalytic Properties of Pd and Pd-Ag Catalysts Supported on Nanocrystalline TiO_2 Prepared by the Solvothermal Method", Catalysis Letters, 103 (2005) 53-58. (Impact factor 2005 = 2.088) (เอกสารแนบที่ชุดที่ 13)
14. J. Panpranot, K. Pattamakomsan, and P. Praserthdam, "Deactivation of Silica Supported Pd Catalysts during Liquid-Phase Hydrogenation" Reaction Kinetics and Catalysis Letters, 86 (2005) 141-147. (Impact factor 2005 = 0.670) (เอกสารแนบชุดที่ 14)
15. J. Panpranot, **K.** Toophorm, and P. Praserthdam, "Effect of Particle Size on the Hydrothermal Stability and Catalytic Activity of Polycrystalline Beta Zeolite" Journal of Porous Materials, 12 (2005) 301-307 (Impact factor 2005 = 0.698) (เอกสารแนบชุดที่ 15)
16. J. Panpranot, N. Taochaiyaphum, and P. Praserthdam, "Glycothermal Synthesis of Nanocrystalline Zirconia and their Applications as Cobalt Catalyst Supports" Materials Chemistry and Physics, 94 (2005) 207-212 (Impact factor 2005 = 1.136) (เอกสารแนบชุดที่ 16)
17. B. Jongsomjit, S. Phoowakeereewiwat, S. Thongyai, T. Shiono, and P. Praserthdam, "Impact of diene addition on properties for ethylene-propylene copolymerization with rac-Et[Ind]$_2$$ZrCl_2$/MAO catalyst", Materials Letters, 59, 3771 – 3774 (2005) (Impact factor 2005 = 1.299) (เอกสารแนบชุดที่ 17)
18. B. Jongsomjit, T. Wongsalee, and P. Praserthdam, "Characteristics and catalytic properties of Co/TiO_2 for various rutile:anatase ratios", Catalysis Communications, 6, 705 – 710 (2005) (Impact factor 2005 = 2.098) (เอกสารแนบชุดที่ 18)
19. Joongjai Panpranot, Nuttakarn Taochaiyaphum, Bunjerd Jongsomjit, and Piyasan Praserthdam "Differences in Characteristics and Catalytic Properties of Co Catalysts Supported on Micron- and Nano-Sized Zirconia" Catalysis Communications 7 (2006) 192-197. (Impact factor 2005 = 2.098) (เอกสารแนบชุดที่

19)

20. J. Klongdee, W. Petchkroh, K. Phuempoonsathaporn, P. Prasertdam, A.S. Vangnai, and V. Pavarajarn, "Activity of Nanosized Titania Synthesized from Thermal Decomposition of Titanium (IV) n-Butoxide for the Photocatalytic Degradation of Diuron", Science and Technology of Advanced Materials, 6 (3-4 SPEC. ISS.), 290-295. (Impact factor 2005 = -) (เอกสารแนบชุดที่ 20)
21. B. Jongsomjit, T. Wongsalee, and P. Praserthdam, "Catalytic behaviors of mixed TiO_2-SiO_2-supported cobalt Fischer-Tropsch catalysts for carbon monoxide hydrogenation", Materials Chemistry and Physics 97 (2006) 343-350 (Impact factor 2005 = 1.136) (เอกสารแนบชุดที่ 21)
22. T. Wongsalee, B. Jongsomjit and P. Praserthdam, "Effect of Zirconia-Modified Titania Consisting of Different Phases on Characteristics and Catalytic Properties of Co/TiO_2 Catalysts", Catalysis Letters 108 (2006) 55-61 (Impact factor 2005 = 2.088) (เอกสารแนบชุดที่ 22)
23. Joongjai Panpranot, Nuttakarn Taochaiyaphum, and Piyasan Praserthdam "Effect of Si Addition on the Properties of Nanocrystalline ZrO_2-Supported Cobalt Catalysts" Reaction Kinetics and Catalysis Letters 87 (2006) 185-190. (Impact factor 2005 = 0.670) (เอกสารแนบชุดที่ 23)
24. Patta Soisuwan, Joongjai Panpranot, David L. Trimm and Piyasan Praserthdam "A Study of Alumina-Zirconia Mixed Oxides Prepared by the Modified Pechini Method as Co Catalyst Supports in CO Hydrogenation" Applied Catalysis A. General 303 (2006) 268-272. (Impact factor 2005 = 2.728) (เอกสารแนบชุดที่ 24)
25. Patta Soisuwan, Piyasan Praserthdam, Joongjai Panpranot, and David L. Trimm "Effects of Si- and Y-Modified Nanocrystalline Zirconia on the Properties of Co/ZrO_2 Catalysts" Catalysis Communications 7 (2006) 761-767 (Impact factor 2005 = 2.098) (เอกสารแนบชุดที่ 25)
26. Bunjerd Jongsomjit, Chitlada Sakdamnuson, Joongjai Panpranot, and Piyasan Praserthdam "Roles of ruthenium on reduction behaviors of ruthenium-promoted cobalt/titania Fischer-Tropsch catalyst", Reaction Kinetics and Catalysis Letters, 88 (2006), 65-71 (Impact factor 2005 = 0.670). (เอกสารแนบชุดที่ 26)
27. Bunjerd Jongsomjit, Tipnapa Wongsalee, and Piyasan Praserthdam "Elucidation of reduction behaviors for Co/TiO_2 catalysts with various rutile/anatase ratios", Studies

in Surface Science and Catalysis, 159 (2006), 285-288. (Impact factor 2005 = 0.307). (เอกสารแนบชุดที่ 27)

28. Watcharapong Khaodee, Bunjerd Jongsomjit, Suttichai Assabumrungrat, Piyasan Praserthdam, and Shigeo Goto, "Investigation of isosynthesis via CO hydrogenation over ZrO_2 and CeO_2 catalysts: effects of crystallite size, phase composition and acid-base sites" Catalysis communications 8 (2007) 548-556 (Impact factor 2005 = 2.098). (เอกสารแนบชุดที่ 28)
29. Joongjai Panpranot, Kunyaluck Kontapakdee, and Piyasan Praserthdam "Selective Hydrogenation of Acetylene in Excess Ethylene on Micron-Sized and Nanocrystalline TiO_2 Supported Pd Catalysts" *Applied Catalysis A: General* 314 (2006) 128-133 (Impact factor 2005 = 2.728). (เอกสารแนบชุดที่ 29)
30. Wilasinee Kongsuebchart, Piyasan Praserthdam, Joongjai Panpranot, Akawat Sirisuk, Piyawat Supphasrirongjaroen, and Chairit Satayaprasert "Effect of Crystallite Size on the Surface Defect of Nano-TiO_2 Prepared via Solvothermal Synthesis" *Journal of Crystal Growth* 297 (2006) 234-238 (Impact factor 2005 = 1.681). (เอกสารแนบชุดที่ 30)
31. Jongsomjit, B., Sakdamnuson, C., Panpranot, J., Praserthdam, P., "Role of ruthenium in the reduction behavior of ruthenium-promoted cobalt/titania Fischer-Tropsch catalysts", Reaction Kinetics and Catalysis Letters 88 (2006) 65-71 (Impact factor 2005 = 0.670). (เอกสารแนบชุดที่ 31)
32. Jongsomjit, B., Wongsalee, T., Praserthdam, P., "Elucidation of reduction behaviors for Co/TiO2 catalysts with various rutile/anatase ratios", Studies Surface Science and Catalysis 159 (2006) 285-288 (Impact factor 2005 = 0.307). (เอกสารแนบชุดที่ 32)
33. Chaichana, E., Jongsomjit, B., Praserthdam, P., "Effect of nano-SiO2 particle size on the formation of LLDPE/SiO2 nanocomposite synthesized via the in situ polymerization with metallocene catalyst", Chemical Engineering Science 62 (2006) 899-905 (Impact factor 2005 = 1.735). (เอกสารแนบชุดที่ 33)
34. Okorn Mekasuwandumrong, Varong Pavarajarn, Masashi Inoue and Piyasan Praserthdam, "Preparation and phase transformation behavior of χ-alumina via solvothermal synthesis", Materials Chemistry and Physics 100 (2006) 445-450 (Impact factor 2005 = 1.136). (เอกสารแนบชุดที่ 34)

35. Chalermpol Wonglert, Supakanok Thongyai, Piyasan Praserthdam, “Effect of Aging on Synthesis of Graft Copolymer of EPDM and Styrene”, J. Applied Polymer Science, **102 (5), pp. 4809-4813** (**Impact factor** 2005 = 1.072). **(เอกสารแนบชุดที่ 35)**
36. Satit Thanyaprueksanon, Supakanok Thongyai, Piyasan Praserthdam, “New synthesis method for polypropylene co ethylene-propylene rubber”, J. Applied Polymer Science, **103 (6), pp. 3609-3616** (**Impact factor** 2005 = 1.072). **(เอกสารแนบชุดที่ 36)**
37. Lerdlaksana Ubonnut, Supakanok Thongyai, Piyasan Praserthdam“ Interfacial adhesion enhancement of polyethylene-polypropylene mixture”, J. Applied Polymer Science, **104 (6), pp. 3766-3773** (**Impact factor** 2005 = 1.072). **(เอกสารแนบชุดที่ 37)**
38. Bunjerd Jongsomjit, Joongjai Panpranot, and Piyasan Praserthdam “Effect of nanoscale SiO_2 and ZrO_2 as the fillers on the microstructure of LLDPE nanocomposites synthesized via in situ polymerization with zirconocene”, Materials Letters, 61 (2007) 1376-1379 (Impact factor 2005 = 1.299). **(เอกสารแนบชุดที่ 38)**
39. Kamonchanok Pansanga, Okorn Mekasuwandumrong, Joongjai Panpranot, and Piyasan Praserthdam “Synthesis of Nanocrystalline Al_2O_3 by Thermal Decomposition of Aluminum Isopropoxide and its Application as Co Catalyst Support for Carbon Monoxide Hydrogenation” Korean Journal of Chemical Engineering, in press (**Impact factor** 2005 = 0.750).
40. Sujittra Kittiruangrayab, Tanuchnun Burakorn, Bunjerd Jongsomjit, and Piyasan Praserthdam, ”Characterization of cobalt dispersed on various micro- and nanoscale silica and zirconia supports”, Catalysis Letters, in press (**Impact factor** 2005 = 2.088).
41. **Parawee Tonto, Okorn Mekasuwandumrong, Suphot Phatanasri, Varong Pavarajarn and Piyasan Praserthdam, “Preparation of ZnO nanorod by solvothermal reaction of zinc acetate in various alcohols”, Ceramics International, in press (Impact factor 2005 = 0.702).**
42. **Kamonchanok Pansanga, Joongjai Panpranot, Okorn Mekasuwandumrong, Chairit Satayaprasert, and Piyasan Praserthdam “Effect of Mixed γ and χ Crystalline**

Phases in Nanocrystalline Al_2O_3 on the Dispersion of Cobalt on Al_2O_3" Catalysis Communications, accepted June 2007 (Impact factor 2005 = 2.098).

2.1.2 บทความที่อยู่ระหว่างการแก้ไข จำนวน 2 ผลงาน

1. Piyawat Supphasrirongjaroen, Piyasan Praserthdam, Joongjai Panpranot, and Duangkamol Na-Ranong "Effect of Quenching Medium on Photocatalytic Activity of Nano-Sized TiO_2 Prepared by Solvothermal Method" Chemical Engineering Journal, Submitted Revised Manuscript.
2. Kamonchanok Pansanga, Nattaporn Lohitharn, Andrew C. Y. Chien, Edgar Lotero, Joongjai Panpranot, Piyasan Praserthdam, and James G. Goodwin, Jr. "Copper-Modified Alumina as a Support for Iron Fischer Tropsch Synthesis Catalysts" *Applied Catalysis A. General*, June (2007). Submitted Revised Manuscript.

2.2 ผู้สำเร็จการศึกษาระดับปริญญาเอก จำนวน 5 คน

1. นายวรพล เกียรติกิตติพงษ์
2. น.ส.พัทธา สร้อยสุวรรณ
3. นายนวพร อินทรกำจร
4. น.ส.กมลชนก ปานสง่า
5. นายก้องเกียรติ สุริเย

หมายเหตุ นิสิตระดับปริญญาเอก อีกจำนวน 4 คน กำลังจะสำเร็จการศึกษา ดังรายชื่อต่อไปนี้

1. นายการุณย์ ธนรังสรรค์ จะสอบวิทยานิพนธ์ ในเดือนกันยายน 2550
2. น.ส.วิลาสินี คงสืบชาติ จะสอบวิทยานิพนธ์ ในเดือนกันยายน 2550
3. น.ส.วาสนา แจ่มศักดิ์ จะสอบวิทยานิพนธ์ ในเดือนมีนาคม 2551
4. น.ส.ศิรชญา กุญชร ณ อยุธยา จะสอบวิทยานิพนธ์ ในเดือนมีนาคม 2551
5. นายกิตติ ตั้งจิตเอื้อบุญ จะสอบวิทยานิพนธ์ ในเดือนมีนาคม 2551
6. นายฉัตรชัย มีโภคา (เต้) จะสอบวิทยานิพนธ์ ในเดือนมีนาคม 2551
7. นายสถาพร คำหอม (ยุ้ย) จะสอบวิทยานิพนธ์ ในเดือนมีนาคม 2551
8 นายปิยะวัฒน์ ศุภศรีรุ่งเจริญ จะสอบวิทยานิพนธ์ ในเดือนมีนาคม 2551

2.3 ผู้สำเร็จการศึกษาระดับปริญญาโท จำนวน 48 คน

1. นายสุทธิ งามโพธิศรี
2. น.ส.ศิริพร ไพศาลสิงห์
3. น.ส. จันทรา วิวัฒนพงษ์พันธ์
4. น.ส.ปารวี โทนโต๊ะ

5. น.ส.อรทัย ตั้งจิตวัฒนาการ
6. น.ส.ฤทัยรัตน์ ปรีชายุทธศิลป์
7. นายพิเชษฐ์ พหุพงศ์ทรัพย์
8. น.ส.อำไพพรรณ ศิวะวิชชกิจ
9. น.ส.รัชฎาภรณ์ นิลเพชร
10. นายจีรพงษ์ วัฒนาอรุณ
11. น.ส.อมรรัตน์ เหมือนภักตร์
12. น.ส.เกศสุดา ชัยรัตน์
13. น.ส.ลักขณา นครเรือง
14. น.ส.ณัฐกานต์ เต้าชัยภูมิ
15. นายอุกฤษ์ สหพัฒนสมบัติ
16. น.ส.คณิตา ธรรมะจริยวงศา
17. น.ส.ธนิษฐา ประสิทธิวุฒิศักดิ์
18. น.ส. ทิพย์นภา วงค์สลี
19. นายเอกราชันย์ ไชยชนะ
20. น.ส.สิรีธร ภูวคีรีวิวัฒน์
21. น.ส.อรกนก บุญธรรมติระวุฒิ
22. นายสนธิ ขำสว่าง
23. น.ส.ณฐินี ศรีเนตร
24. นายรุ่งโรจน์ ชาญชัยฤกษ์
25. น.ส.สุรีย์พร ศักดิ์ภาวุฒิ
26. นายสืบสกุล โพธิ์เกษม
27. นายทรงพล อังคพิพัฒนชัย
28. น.ส.ดรุณี สุขหอม
29. นายวัชรพงษ์ ขาวดี
30. นายวิบูลย์ แสงทองกิจเจริญ
31. น.ส.กรรณิการ์ แผ่นดินทอง
32. นายเอกวุฒิ ภูมิพิเชฐ
33. นายศุภวุฒิ ภู่ภัทรกุล
34. นายธนัชนันนท์ บูรกรณ์
35. นายขวัญพงศ์ เหมือนโพธิ์
36. นายพีรพล บัวแก้ว

37. น.ส.เลิศลักษณา อุบลนุช
38. นายเอกพล พรหมรส
39. น.ส.นิธิพร แสงเงิน
40. น.ส.รัตนวลี ศูนย์พลอย
41. นายประพัฒน์ ทนงคงสวัสดิ์
42. นายพิชิต ทิศทวีรัตน์
43. น.ส.เบญจพร เมืองสมบัติ
44. นายวรุณ วิมลสถิตย์
45. น.ส.ปวีณา เดือนฉาย
46. น.ส.กัลญาลักษณ์ คนธภักดี
47. น.ส.สุจิตรา กิตติเรืองระยับ
48. นายสาธิต ธัญญพฤกษานนท์

3. กิจกรรมอื่น ๆ ที่เกี่ยวข้อง

3.1 การนำเสนอผลงานในที่ประชุมระดับนานาชาติ

3.1.1 The 13th International Congress on Catalysis, July 11-15, (2004) Paris, France.

1. J. Panpranot, S. Kaewgun, and P. Praserthdam “Metal-Support Interaction in Mesoporous Silica Supported Cobalt Fischer-Tropsch Catalysts”.

3.1.2 Regional Symposium on Chemical Engineering (RSCE 2004), Bangkok, December 1 – 3, 2004

1. W. Sangtongkitcharoen, S. Assabumrungrat, V. Pavarajarn, N. Laosiripojana and P. Praserthdam “Prediction of Boundary of Carbon Formation for Different Types of Solid Oxide Fuel Cells with Methane Feed”.
2. N. Taochaiyapoom, J. Panpranot, and P. Praserthdam “Characteristics of Cobalt Catalysts Supported on Zirconia Nanoparticles Prepared by Glycothermal Method”.
3. O. Tungjitwattakarn, J. Panpranot, and P. Praserthdam “Liquid Phase Hydrogenation on Silica Supported Pd Catalysts: Effects of Pd Precursors and Reduction Temperature”.
4. L. Nakkararuang, J. Panpranot, B. Ngamsom, and P. Praserthdam "Selective hydrogenation of acetylene on Pd catalysts supported on solvothermal-derived TiO_2”.

5. S. Ngamposri S, B. Jongsomjit, and P. Praserthdam, “Ethylene/1-octene copolymerization using mixed titania/silica-supported MAO with zirconocene catalyst”.
6. E. Chaichana, B. Jongsomjit, and P. Praserthdam, “Synthesis of LLDPE/silica-nanocomposites by in situ polymerization with MAO/zirconocene catalyst”.
7. T. Wongsalee, B. Jongsomjit, and Praserthdam P., “Dependence of crystalline forms of titania on catalytic properties of Co/TiO_2 catalysts”.
8. C.Wonglert, S.Thongyai, P.Praserthdam, “Blend Properties and Synthesis of Graft-copolymer between Ethylene-Propylene-Diene Terpolymer and Styrene”.
9. E.Singnoo, S.Thongyai, P.Praserthdam, “Effects of Low Molar Mass Liquid Crystal and Lubricant Additive on the Crystallinity of Isotactic Polypropylene”.
10. A.Buasri, S.Thongyai, P.Praserthdam, “Effects of Low Molar Mass Liquid Crystal and Lubricant Additive on the Crystallinity of Syndiotactic Polystyrene”.
11. J.Klongdee, V.Pavarajarn, O.Mekasuwandumrong and P.Praserthdam, “Photocatalytic Degradation of Methylene Blue by TiO_2 Nanocrystals Synthesized via Thermal Decomposition of Titanium (IV) n-Butoxide in Organic Solvents”.
12. R.Precharyutasin, V.Pavarajarn and P.Praserthdam, “Effects of the Reaction Parameters on the Carbothermal Reduction and Nitridation of Rice Husk Ash for Silicon Nitride Synthesis”.

3.1.3 International Symposium on Nanotechnology in Environmental Protection and Pollution (ISNEPP 2005), Bangkok, January 12 – 14, 2005

1. J. Klongdee, W. Petchkroh, K. Phuempoonsathaporn, P. Prasertdam, A.S. Vangnai, and V. Pavarajarn, “Activity of Nanosized Titania Synthesized from Thermal Decomposition of Titanium (IV) n-Butoxide for the Photocatalytic Degradation of Diuron”

3.1.4 Regional Symposium on Chemical Engineering (RSCE 2005) Hanoi Horison Hotel, Hanoi, VIETNAM (November 30th –December 2nd, 2005)

1. Rungroj Chanchairoek , Piyasan Praserthdam , Pitt Supaphol ,and Varong Pavarajarna) “Effect of Synthesis and Calcination Parameters on Cristobalite Nanofibers by Combined Sol-Gel and Electrospinning Techniques”
2. Garun Tanarungsuna, Suttichai Assabumrungrata, ,Worapon Kiatkittipongb,

Piyasan Praserthdama, Hiroshi Yamadac *and* Tomohiko Tagawac “Direct hydroxylation of benzene to phenol with hydrogen peroxide catalyzed by Fe/TiO2”

3. Teerawut Ruangsanama, Okorn Mekasuwandumrongb, Piyasan Praserthdama and Varong Pavarajarna, “Physical and Optical Properties of Gallium-Doped Zinc Oxide Nanoparticles Synthesized via Glycothermal Method”
4. Kanyaluck Kontapakdee, Joongjai Panpranot, and Piyasan Praserthdam “Effect of Titania Polymorph on the Characteristics and Catalytic Properties of Pd/TiO2 in Selective Hydrogenation of Acetylene”
5. Kunnika Phandinthong, Joongjai Panpranot, Wandee Luesaiwong, and Piyasan Praserthdam, “A Comparative Study of Liquid Phase Hydrogenation on Pd/SiO2 in Organic Solvents and Under Pressurized Carbon Dioxide”

3.1.5 Technology and Innovation for Sustainable Development Conference (TISD 2006), 25-27 January 2006 Khon Kaen, Thailand

1. Songphol Angkapipattanachai, Thanapon Sangvanich, Pawin Boonyaporn, Joongjai Panpranot*, and Piyasan Praserthdam “Study of Acetylene Hydrogenation Catalysts: Role of Coke Deposits”

3.1.6 Regional Symposium on Chemical Engineering (RSCE 2006) Singapore, (December 3-5, 2006)

1. Terachai Sirikajorn* and Joongjai Panpranot “Synthesis and Catalytic Behavior of Pd supported on nanocrystalline $ZnAl_2O_4$ in Liquid-Phase Semihydrogenation”
2. Patcharaporn Weerachawanasak* and Joongjai Panpranot+ Characteristics and catalytic properties of micron- and nano-sized TiO_2 supported Pd catalysts in liquid-phase hydrogenation of phenylacetylene
3. Sirima Somboonthanakij[a,*], Joongjai Panpranot+, and Okorn Mekasuwandumrong[b] “Characteristics and Catalytic Properties of Nano-Pd/SiO_2 Catalysts Prepared by Flame Spray Pyrolysis”
4. Pimchanok Tupabut, Bunjerd Jongsomjit, and Piyasan Prasethdam, “Characterization of Co/SiO_2-B catalyst and catalytic properties during CO hydrogenation”.
5. Nithinart Chitpong, Bunjerd Jongsomjit, and Piyasan Praserthdam, “Effect of boron-modified zirconia-supported cobalt catalysts and their catalytic properties via CO hydrogenation”.

6. Thidarat Boosamsaiy, Bunjerd Jongsomjit and Piyasan Praserthdam, “Study of cobalt dispersion on the nanoscale Al_2O_3 and SiO_2 supports”.
7. Sirinlak Bunchongturakarn, Bunjerd Jongsomjit, and Piyasan Praserthdam, “Impact of MCM-41 pore structure on ethylene/1-octene copolymerization using MCM-41-supported dried MMAO with zirconocene catalyst”.
8. Chanathip Desharun, Bunjerd Jongsomjit, and Piyasan Praserthdam, “Synthesis of LLDPE-Al_2O_3 polymer nanocomposites via in situ polymerization with zirconocene catalyst”.
9. Supaluk Jiamwijitkul, Bunjerd Jongsomjit, and Piyasan Praserthdam, “Copolymerization behaviors of ethylene/1-octene via boron-modified MCM41-supported zirconocene catalyst”.
10. Chanintorn Ketloy, Bunjerd Jongsomjit, and Piyasan Praserthdam, “Supporting effect of [*t*-BuNSiMe_2Flu]TiMe_2 complex during ethylene/1-octene copolymerization”.
11. Akawat Sirisuk and Kulapong Boonyawes, “Improving efficiency of dye-sensitized solar cell by modification of TiO_2 electrode layer”.
12. Akawat Sirisuk and Sutthirut Charatsaengchirachot, “Synthesis of TiO_2 hollow spheres using spraying technique”.
13. Akawat Sirisuk and Sorathon Wattanamalachai, “Novel method for deposition of copper on zinc oxide by using supercritical carbon dioxide”.
14. Akawat Sirisuk, Prasert Pavasant, and Narakorn Chanprasert, “Photocatalytic degradation of organic dyes using TiO_2 in an air-lift reactor”.

3.1.7 The 4rd Asia-Pacific Congress on Catalysis (APCAT4), December 6-8, 2006, Singapore

1. Nitikon Wongwaranon, Joongjai Panpranot, and Piyasan Praserthdam “Effect of Ni-modified Al_2O_3 on the Properties of Pd/α-Al_2O_3 Catalysts in Selective Hydrogenation of Acetylene”
2. Akawat Sirisuk, Peerapon Buakaew, and Piyasan Praserthdam, “Photocatalytic oxidation of ethylene over gold-deposited titanium dioxide nanoparticles.

3.2 การเชื่อมโยงทางวิชาการกับอุตสาหกรรม

3.2.1 ความร่วมมือกับบริษัทบางกอกโพลีเอททิลีน จำกัด (มหาชน)

ตั้งแต่เริ่มโครงการวิจัยนี้ศูนย์เชี่ยวชาญฯ ได้มีการติดต่อประสานงานกับนักวิจัยของศูนย์วิจัยและพัฒนาของบริษัทฯ คือ ดร. จริยา แซ่จาว และคุณนุชนันท์ อุทัยรัตน์ ซึ่งเป็นหัวหน้าแผนกประกันคุณภาพ ฝ่ายผลิตและวิศวกรรม บริษัทบางกอกโพลีเอททีลีน โดยแผนงานที่ได้ดำเนินการไปแล้ว คือ การให้ความช่วยเหลือและความร่วมมือในการสังเคราะห์ตัวเร่งปฏิกิริยาเมทัลโลซีน (Metallocene catalysis) ที่เป็นสารประกอบเชิงซ้อนของโลหะไทเทเนียมซึ่งมีความว่องไวต่อปฏิกิริยาพอลิเมอร์ไรเซชันของพอลิโอเลฟิน การเตรียมตัวเร่งปฏิกิริยาชนิดนี้เป็นสิ่งที่ยากเนื่องจากสารมัธยันห์ (Intermediates) ที่เกิดขึ้นจะมีความว่องไวต่อสิ่งเจือปน (Impurity) ความชื้น และอากาศ อย่างไรก็ตามเนื่องจากทางศูนย์เชี่ยวชาญฯ เองก็ได้มีความร่วมมือกับผู้เชี่ยวชาญต่างประเทศอยู่แล้ว คือ Professor Takeshi Shiono ณ Hiroshima University ประเทศญี่ปุ่น ภายใต้โครงการการถ่ายทอดเทคโนโลยีไทย-ญี่ปุ่น (Thailand-Japan Technology Transfer Project) ทำให้ได้รับคำแนะนำและเทคนิคในการเตรียมที่ดี ทั้งนี้จากความร่วมมือดังกล่าวทางบริษัทฯ จำกัดได้ส่งนักวิจัยของบริษัทมาเรียนรู้และทำการสังเคราะห์ตัวเร่งปฏิกิริยาเมทัลโลซีนดังกล่าวที่ห้องปฏิบัติการของศูนย์ฯ ในปัจจุบันการเตรียมตัวเร่งปฏิกิริยาดังกล่าวได้บรรลุผลตามเป้าหมายที่วางไว้แล้ว

ในช่วงที่ระยะเวลาหกเดือนที่ผ่านมาศูนย์ฯ ได้ส่งนิสิตปริญญาโทซึ่งได้รับทุนการศึกษาในระดับมหาบัณฑิตจากบริษัทฯ คือ นายสนธยา ศรีจำนอง ไปทำวิจัยที่บริษัทในช่วงปิดเทอมที่ผ่านมา (ตุลาคม - พฤศจิกายน 2549) โดยนิสิตได้ทำการสังเคราะห์ตัวเร่งปฏิกิริยาเมทัลโลซีน คือ สารประกอบเชิงซ้อน Bis[*N*-(3-*tert*–butylsalicylidene)anilinato] zirconium(IV) dichloride ที่มีหมู่ลิแกนด์เป็นกลุ่มของ Phenoxy-Imine โดยมีตัวโลหะเซอร์โคเนียม (Zr) เป็นโลหะอะตอมกลางสำหรับกระบวนการ Ethylene Polymerization ซึ่งมีการตั้งชื่อเป็นกลุ่ม FI catalyst จากการศึกษาที่ผ่านมาพบว่ากลุ่ม FI catalyst นี้จะให้ค่า activity ของกระบวนการ Ethylene Polymerization ที่สูงและให้ผลิตภัณฑ์โพลีเอททีลีนที่มีลักษณะแปลกใหม่ เช่น มีน้ำหนักโมเลกุลที่ต่ำจนถึงสูงมาก ดังนั้นจึงมีความเป็นไปได้สูงที่จะนำตัวเร่งปฏิกิริยาชนิดนี้ไปใช้ในทางอุตสาหกรรมต่อไป ขั้นตอนในการเตรียมจะต้องทำการเตรียมลิแกนด์ก่อนแล้วจึงใส่อะตอมกลางลงไป จากนั้นจึงนำไปทดสอบในปฏิกิริยาพอลิเมอร์ไรเซชันของเอทิลีนต่อไป โดยสามารถสรุปขั้นตอนได้ตามรูปข้างล่างดังนี้

ขั้นตอนการสังเคราะห์ลิแกนด์

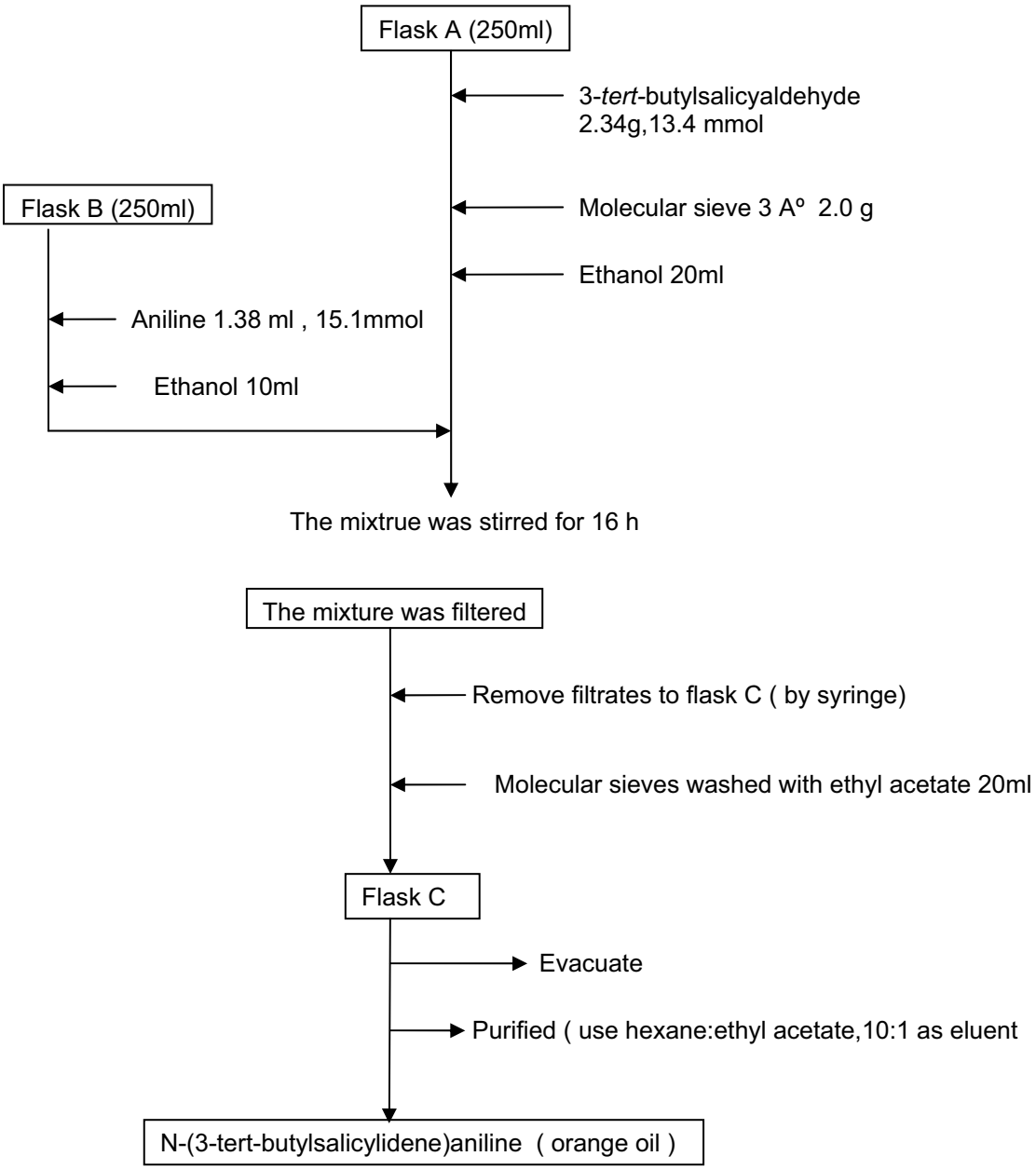

รูปที่ 1 การเตรียมลิแกนด์

ขั้นตอนการเตรียมตัวเร่งปฏิกิริยา

Complex Synthesis (Bis [N-(3-tert-butylsalicylidene) anilinatotitanium(IV)dichloride

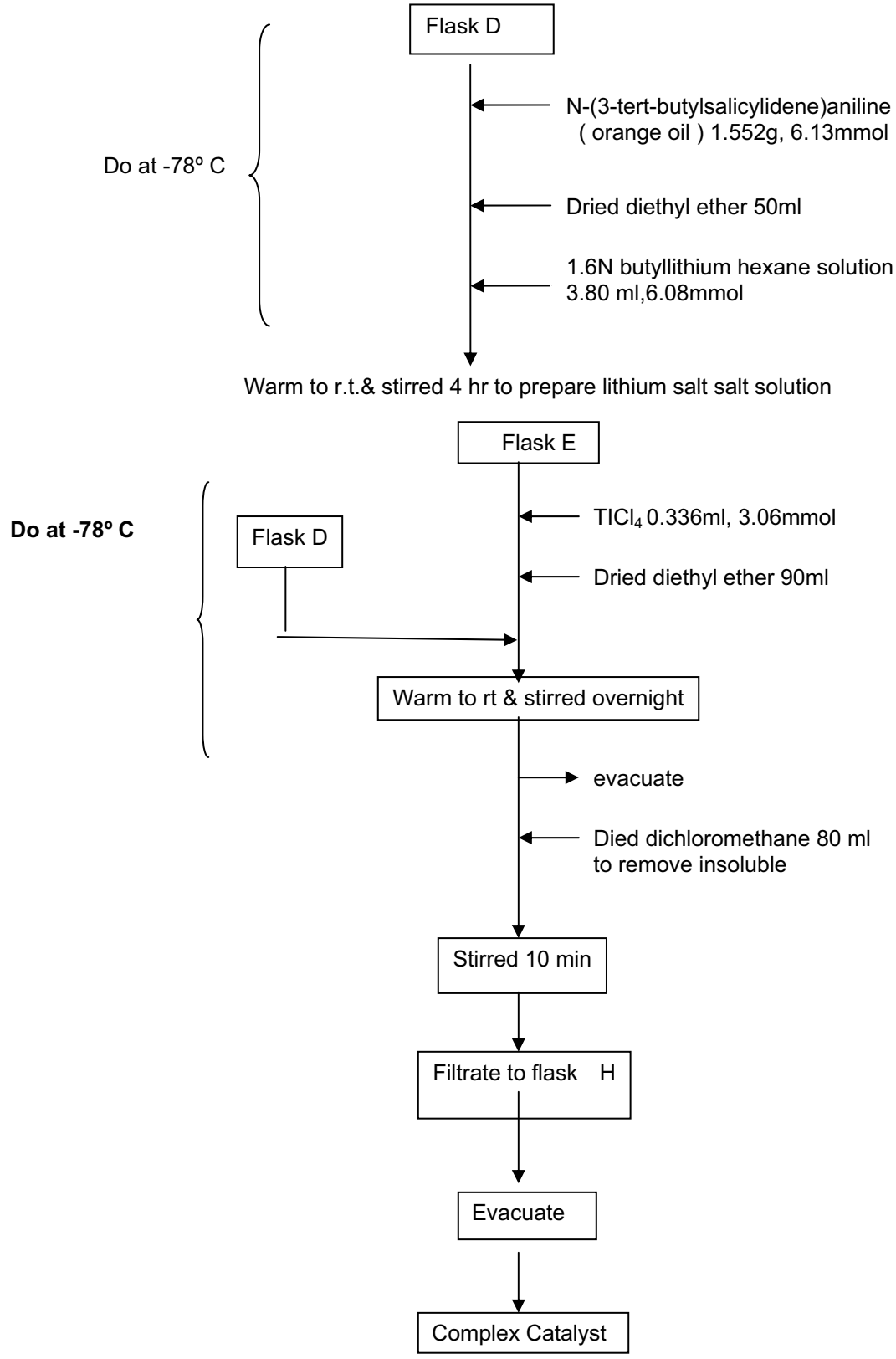

รูปที่ 2 แสดงการเตรียมตัวเร่งปฏิกิริยา

นอกจากการศึกษาสมบัติของตัวเร่งปฏิกิริยาในระบบเอกพันธ์แล้ว ในปัจจุบันยังได้มีการนำตัวเร่งปฏิกิริยาดังกล่าวไปใช้ในระบบวิวิธพันธ์ซึ่งมีตัวรองรับเป็นซิลิกา ไทเทเนีย และออกไซด์ผสมระหว่างซิลิกากับไทเทเนีย เพื่อศึกษาและเก็บข้อมูลต่อไป โดยคาดว่านิสิตจะนำผลวิจัยที่ได้ไปเขียนวิทยานิพนธ์และสำเร็จการศึกษาในระดับมหาบัณฑิตได้ภายในปีการศึกษานี้

3.2.2 ความร่วมมือกับบริษัทระยองโอเลฟินส์ จำกัด
โครงงานปี 2547-2549

โครงการวิจัยร่วมระหว่างศูนย์เชี่ยวชาญเฉพาะทางด้านคาตาไลซิสและวิศวกรรมปฏิกิริยาที่ใช้ตัวเร่งปฏิกิริยาและ บ.ระยองโอเลฟินส์ จำกัด มีวัตถุประสงค์ในการเพิ่มประสิทธิภาพของตัวเร่งปฏิกิริยาสำหรับปฏิกิริยาไฮโดรจิเนชันของอะเซทิลีนซึ่งเป็นขั้นตอนหนึ่งที่สำคัญในกระบวนการผลิตพอลิเอทิลีน โดยปฏิกิริยาไฮโดรจิเนชันของอะเซทิลีนเป็นการกำจัดก๊าซอะเซทิลีนที่ปนเปื้อนในสารตั้งต้น (เอทิลีน) ออกก่อนที่จะเข้าสู่การทำปฏิกิริยาพอลิมอไรเซชันไปเป็นพอลิเอทิลีนก๊าซอะเซทิลีนที่ปนเปื้อนนี้นอกจากจะไปทำให้ความว่องไวของตัวเร่งปฏิกิริยาที่ใช้ในปฏิกิริยาพอลิเมอไรเซชันมีค่าลดลงแล้วยังสามารถเกิดสารประกอบที่เป็นอันตราย เช่น เมทัลอะเซทิลิไดน์ ซึ่งทำให้เกิดการระเบิดได้อีกด้วย ดังนั้นการกำจัดอะเซทิลีนให้ลดลงเหลือปริมาณไม่เกิน 5 ppm จึงมีความจำเป็นอย่างยิ่ง ตัวเร่งปฏิกิริยาที่ใช้ในปฏิกิริยาไฮโดรจิเนชันของอะเซทิลีนที่ใช้อยู่ในปัจจุบันของ บ. ระยองโอเลฟินส์ ได้แก่ตัวเร่งปฏิกิริยาแพลเลเดียมบนอะลูมินาที่เสริมด้วยโลหะซิลเวอร์ ($Pd\text{-}Ag/Al_2O_3$)

งานวิจัยสามารถแบ่งเป็นหัวข้อต่างๆได้ดังนี้

1) การเพิ่มประสิทธิภาพของตัวเร่งปฏิกิริยาใหม่ (Fresh $Pd\text{-}Ag/Al_2O_3$ catalyst) โดยการใช้แก๊สไนตรัสในการทรีตท์เมนต์ตัวเร่งปฏิกิริยา $Pd\text{-}Ag/Al_2O_3$ ซึ่งจากการศึกษางานวิจัยที่เกี่ยวข้องพบว่าพบว่าแก๊สดังกล่าวจะไปขัดขวางการดูดซับของเอทิลีนบนพื้นผิวของตัวเร่งปฏิกิริยาทำให้ได้ผลิตภัณฑ์ที่มีค่าการเลือกเกิดของเอทิลีนสูงขึ้นและลดการเกิดอีเทนได้ โดยทำการหาสภาวะที่เหมาะสมในการทรีตท์เมนต์ พบว่าที่การใช้ปริมาณแก๊สไนตรัสระหว่าง 50-100 ไมโครลิตร ที่อุณหภูมิ 90-100°C ทำให้ได้ปริมาณอะเซทิลีนคอนเวอชันและผลิตภัณฑ์เอทิลีนสูงที่สุด

2) การศึกษาผลของโค้กต่อประสิทธิภาพของตัวเร่งปฏิกิริยาและศึกษาแนวทางในการปรับปรุงกระบวนการฟื้นฟูสภาพของตัวเร่งปฏิกิริยาภายหลังจากการใช้งานในปฏิกิริยาอะเซทิลีนไฮโดรจิเนชันพบว่าตัวเร่งปฏิกิริยาที่ผ่านการใช้งานและฟื้นฟูสภาพแล้วโดยทำการเก็บจากจุดต่างๆของเครื่องปฏิกรณ์ C2-Reactor ของโรงงาน ROC มีปริมาณโค้กหลงเหลืออยู่ทำให้ตัวเร่งปฏิกิริยามีประสิทธิภาพลดลง ในการหาสภาวะที่เหมาะสมในการฟื้นฟูสภาพของตัวเร่งปฏิกิริยาได้ศึกษาตัวแปรต่างๆคือ อุณหภูมิ ความเข้มข้นของออกซิเจนและค่า GHSV พบว่าที่อุณหภูมิ 500°C ขึ้นไปจึงจะทำให้เกิดการเผาไหม้โค้กที่สมบูรณ์ ปริมาณความเข้มข้นของออกซิเจนที่เหมาะสม 10-21% ค่า GHSV = 8000-17000 h^{-1} การใช้ออกซิเจนที่ความเข้มข้นต่ำเกินไปและค่า GHSV สูงเกินไปจะทำให้โค้กเผาไหม้ไม่หมดหรือต้องใช้เวลาในการเผาไหม้นานมาก

รูปแสดงตัวอย่างตัวเร่งปฏิกิริยาที่นำมาทดสอบการกำจัดโค้กที่สภาวะต่าง ๆ

3) การศึกษาความเป็นไปได้ในการนำตัวเร่งปฏิกิริยาที่ผ่านการใช้งานและฟื้นฟูสภาพแล้วมาทำการทรีตเมนต์ด้วยแก๊สไนตรัส พบว่าไม่สามารถทำได้ถึงแม้ว่าตัวเร่งปฏิกิริยาจะไม่มีโค้กหลงเหลืออยู่แล้วก็ตาม ได้ทำการทดสอบด้วยเครื่องมือวิเคราะห์ต่าง ๆอาทิ X-ray Diffraction และ X-ray photoelectron spectroscopy พบว่าเมื่อตัวเร่งปฏิกิริยาผ่านกระบวนการฟื้นฟูสภาพที่อุณหภูมิมากกว่า 500°C จะทำให้โลหะซิลเวอร์เกิดการเคลื่อนที่และมีขนาดเล็กลงทำให้สภาพพื้นผิวของตัวเร่งปฏิกิริยาเปลี่ยนไปและไม่สามารถทำการทรีตด้วยแก๊สไนตรัสได้อีก อย่างไรก็ตามถ้าทำการฟื้นฟูสภาพตัวเร่งปฏิกิริยา (ที่ไม่ได้ผ่านการใช้งาน) ที่อุณหภูมิ 300°C จะสามารถเพิ่มประสิทธิภาพโดยการทรีตเมนต์ด้วยแก๊สไนตรัสได้

ผลงานวิจัยบางส่วนได้มีการนำไปเสนอในที่ประชุมวิชาการระดับนานาชาติ Technology and Innovation for Sustainable Development Conference (TISD) 2006 จัดโดยมหาวิทยาลัยขอนแก่นร่วมกับวิศวกรรมสถานแห่งประเทศไทยในพระบรมราชูปถัมภ์ สถานจัดการและอนุรักษ์พลังงานมหาวิทยาลัยขอนแก่น ศูนย์วิจัยและพัฒนาโครงสร้างมูลฐานอย่างยั่งยืน ศูนย์วิจัยด้านการจัดการสิ่งแวดล้อมและสารอันตราย ระหว่างวันที่ 25-27 มกราคม 2549 ในหัวข้อ “Study of Acetylene Hydrogenation Catalysts: Role of Coke Deposits” โดย Songphol Aungkapipattanachai, Thanapon Sangvanich, Pawin Boonyaporn, Piyasan Praserthdam, and Joongjai Panpranot ณ โรงแรมโซฟิเทล จ.ขอนแก่น

โครงงานปี 2549-2550

การกำจัดสารปนเปื้อนอะโรเมติกส์ออกจากสารนอนอะโรเมติกส์ด้วยกระบวนการไฮโดรจิเนชันโดยใช้ตัวเร่งปฏิกิริยา

(Removal of Aromatics Contaminants from Non-Aromatics Stream by Catalytic Hydrogenation Reaction)

- **ความเป็นมาและความสำคัญของเรื่อง**

ตัวทำละลายอินทรีย์จำพวกนอนอะโรเมติกส์มีความสำคัญในอุตสาหกรรมต่าง ๆและมีการใช้งานในปริมาณสูง โครงการนี้ได้พัฒนาขึ้นเนื่องจากบริษัทระยองโอเลฟินส์ จำกัด มีความสนใจที่จะวิจัยและพัฒนาตัวทำละลายขึ้นใช้เองโดยพัฒนาจากผลิตภัณฑ์รองของบริษัท อย่างไรก็ตามในกระบวนการผลิตตัวทำละลายอินทรีย์มักมีสารปนเปื้อนที่เป็นสารอะโรเมติกส์ปนอยู่ปริมาณเล็กน้อยซึ่งสารอะโรเมติกส์นี้มีความเป็นพิษสูง ซึ่งมีความจำเป็นต้องกำจัดออกเพื่อความปลอดภัยในการใช้งานทั้งต่อคนและสิ่งแวดล้อม

โดยทั่วไปการกำจัดสารอะโรเมติกส์ออกจากสารนอนอะโรเมติกส์ทำได้โดยกระบวนการกลั่นแยกแต่วิธีดังกล่าวจำเป็นต้องใช้พลังงานสูงมาก จึงมีความพยายามที่จะหาเทคนิคหรือวิธีอื่นที่มีประสิทธิภาพมากขึ้นและใช้พลังงานน้อยลง จากการศึกษาในเบื้องต้นพบว่ากระบวนการไฮโดรจิเนชันโดยใช้ตัวเร่งปฏิกิริยาเป็นอีกวิธีหนึ่งที่น่าสนใจเนื่องจากมีประสิทธิภาพสูงและไม่จำเป็นต้องใช้พลังงานมาก อย่างไรก็ดี เพื่อเป็นการพัฒนาเทคโนโลยีขึ้นเองภายในประเทศ ลดภาระการพึ่งพาและค่าใช้จ่ายการในการซื้อเทคโนโลยีจากต่างประเทศ ทางบริษัท ระยองโอเลฟินส์ จึงสนใจที่จะทำวิจัยร่วมกับภาควิชาวิศวกรรมเคมี จุฬาลงกรณ์มหาวิทยาลัยในการพัฒนากระบวนการกำจัดสารปนเปื้อนอะโรเมติกส์ออกจากสารนอนอะโรเมติกส์ด้วยกระบวนการไฮโดรจิเนชัน โดยมุ่งเน้นให้ศึกษาปัจจัยต่าง ๆเช่น ชนิดและปริมาณของตัวเร่งปฏิกิริยา อุณหภูมิ และความดันในการเกิดปฏิกิริยา ซึ่งผลที่ได้จากการศึกษาครั้งนี้จะใช้เป็นแนวทางในการออกแบบเตาปฏิกรณ์และระบบควบคุมปฏิกิริยาไฮโดรจิเนชันสำหรับการกำจัดสารอะโรเมติกส์ออกจากสารนอนอะโรเมติกส์ต่อไปเพื่อให้ได้ประสิทธิภาพในการผลิตตัวทำละลายสำหรับใช้ในกระบวนการต่าง ๆที่เป็นมิตรต่อสิ่งแวดล้อมและใช้พลังงานน้อย

- **วัตถุประสงค์ของโครงงาน**

ศึกษาผลของตัวเร่งปฏิกิริยา อุณหภูมิ และความดันที่มีต่อการเกิดปฏิกิริยาไฮโดรจิเนชันเพื่อการกำจัดสารปนเปื้อนอะโรเมติกส์ออกจากสารนอนอะโรเมติกส์ในกระบวนการผลิตตัวทำละลาย

- **ผลที่คาดว่าจะได้รับ**

ก. สามารถพัฒนากระบวนการกำจัดสารปนเปื้อนอะโรเมติกส์ออกจากสารนอนอะโรเมติกส์แทนการกลั่นแยกเพื่อลดการใช้พลังงานและสามารถหาสภาวะการทำงานที่เหมาะสมเพื่อใช้ในการออกแบบเตาปฏิกรณ์และหน่วยแยกที่คุ้มค่าต่อการลงทุนมากที่สุด

ข. สามารถนำผลิตภัณฑ์รองของบริษัทไปพัฒนาเป็นผลิตภัณฑ์ที่มีมูลค่าเพิ่มสูงขึ้นและไม่เป็นพิษต่อสิ่งแวดล้อม

ค. เป็นกระบวนการต้นแบบสำหรับการศึกษาการกำจัดสารอะโรเมติกส์ออกจากตัวทำละลาย

ในอุตสาหกรรมอื่นๆ

- **แผนการทำงาน**

- ออกแบบอุปกรณ์การทดลองให้สามารถรองรับสภาวะการเกิดปฏิกิริยาที่ต้องการศึกษาได้ โดยอุปกรณ์จะต้องประกอบด้วย

ก.เตาปฏิกรณ์ขนาดทดลองและส่วนประกอบต่างๆที่เพียงพอสำหรับการบรรจุตัวเร่งปฏิกิริยาและควบคุมการการป้อนเข้าสารเพื่อทำปฏิกิริยาและสามารถเก็บตัวอย่างสารหลังทำปฏิกิริยามาวิเคราะห์ได้

ข.อุปกรณ์ให้ความร้อนที่สามารถควบคุมและเปลี่ยนระดับของอุณหภูมิในเตาปฏิกรณ์ตามต้องการได้

ค. อุปกรณ์ควบคุมและเปลี่ยนระดับของความดันในเตาปฏิกรณ์ตามต้องการได้

ง. อุปกรณ์วัดอุณหภูมิและความดันในเตาปฏิกรณ์

จ. อุปกรณ์วัดอัตราการไหล

ฉ. พารามิเตอร์ที่ใช้ในการควบคุมคุณภาพหรือประเมินประสิทธิภาพของการเกิดปฏิกิริยา

- ออกแบบการทดลองโดยการประยุกต์หลักการ DOE (Design of Experiment) มาใช้ ซึ่งจะเป็นการออกแบบการทดลองเพื่อการเก็บข้อมูลแบบสุ่มเพื่อตัดผลของตัวแปรที่ไม่ได้ควบคุมออกไปจากการทดลอง

- ทำการทดลองตามที่ออกแบบไว้เพื่อให้ได้ข้อมูลที่เพียงพอในการวิเคราะห์

ก. อิทธิพลของตัวเร่งปฏิกิริยา

ข. อิทธิพลของอุณหภูมิ

ค. อิทธิพลของความดัน

ง. อิทธิพลร่วมของตัวเร่งปฏิกิริยากับอุณหภูมิ

จ. อิทธิพลร่วมของตัวเร่งปฏิกิริยากับความดัน

ฉ. อิทธิพลร่วมของอุณหภูมิกับความดัน

ช. อิทธิพลร่วมของตัวเร่งปฏิกิริยา อุณหภูมิ และความดัน

- วิเคราะห์ผลการวิจัยและอภิปรายร่วมกับโรงงานเพื่อนำไปทดลองปฏิบัติจริง
- ติดตามผลการปฏิบัติ และประเมินผลสำเร็จ
- จัดทำรายงานสรุป

- **งานที่ได้ดำเนินการไปแล้ว**

- สร้างระบบทดสอบปฏิกิริยาไฮโดรจิเนชันในวัฏภาคของเหลวที่ความดันสูง
- ออกแบบการทดลองโดยใช้โปรแกรม MiniTab ตามหลักการของ DOE
- ทดสอบตัวเร่งปฏิกิริยาที่ใช้ทางการค้าจำนวน 3 ชนิด
- ทดสอบปฏิกิริยาที่สภาวะต่างๆตามที่ได้ออกแบบการทดลองไว้

- **ตัวอย่างผลการวิจัย**

อุปกรณ์สำหรับการทดสอบปฏิกิริยาไฮโดรจิเนชันในวัฏภาคของเหลวที่ความดันสูง

ตัวอย่างผลิตภัณฑ์

ผลการทดลองที่สภาวะต่าง ๆโดยใช้หลักการออกแบบการทดลองแบบ 2^5 factorial design

(benzene concentration; A, amount of catalyst; B, hydrogen pressure; C, reaction temperature; D, reaction time; E, and coded value; X.)

Run number	A (°C)	B (bar)	C (minutes)	D (%wt)	E (g)	Benzene Conversion (%)
1	1	5	30	100	30	5.4
2	10	15	30	150	120	20.7
3	10	15	30	100	30	42.0
4	1	15	10	100	30	28.2
5	10	5	30	150	30	5.3
6	1	15	30	150	30	41.6
7	1	5	10	150	30	25.0
8	6	10	20	125	75	23.0
9	6	10	20	125	75	27.6
10	1	15	30	100	120	38.8
11	1	5	30	150	120	100.0
12	1	15	10	150	120	17.2
13	1	5	10	100	120	26.7
14	10	5	10	100	30	5.6
15	10	15	10	100	120	32.3
16	6	10	20	125	75	21.1
17	10	5	10	150	120	20.8
18	10	5	30	100	120	14.8
19	10	15	10	150	30	37.8

ข้อมูลทางสถิติ

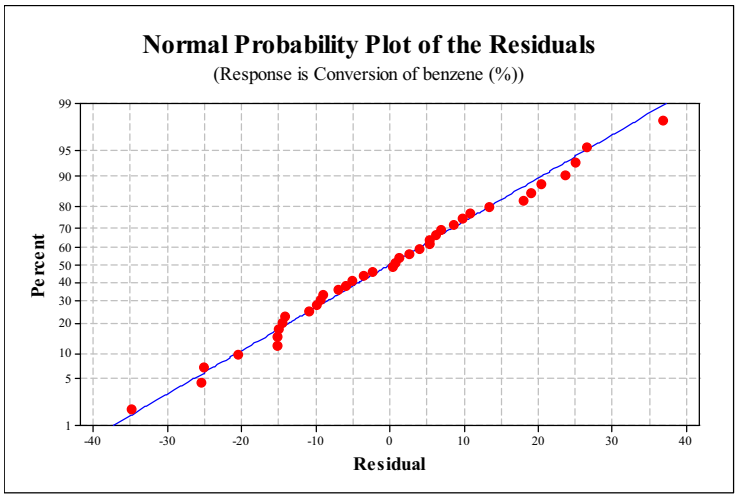
Normal Probability Plot of the Residuals
(Response is Conversion of benzene (%))
Percent
Residual

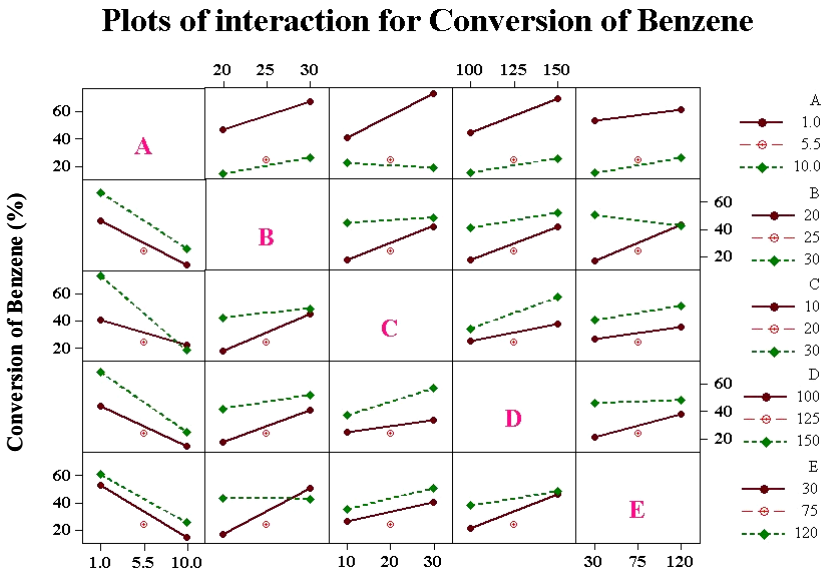
Plots of interaction for Conversion of Benzene
Conversion of Benzene (%)
A
B
C
D
E

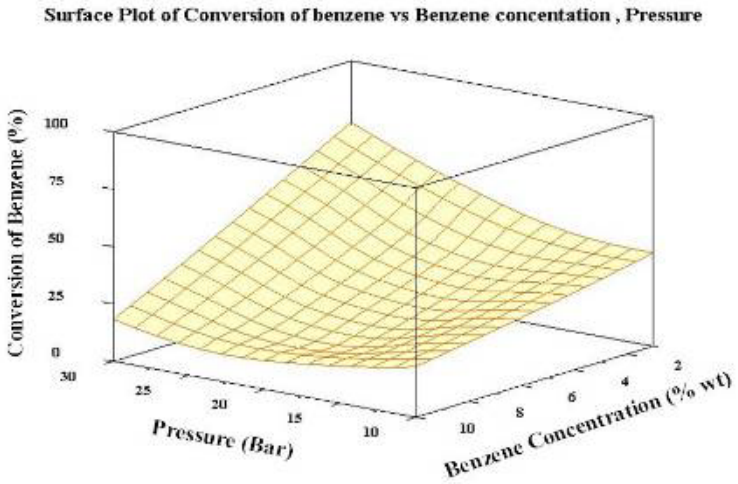
Surface Plot of Conversion of benzene vs Benzene concentation , Pressure
Conversion of Benzene (%)
Pressure (Bar)
Benzene Concentration (% wt)

- **ผลที่ได้รับจากการวิจัย**

ก. สามารถพัฒนากระบวนการกำจัดสารปนเปื้อนอะโรเมติกส์ออกจากสารนอนอะโรเมติกส์แทนการกลั่นแยกเพื่อลดการใช้พลังงานและสามารถหาสภาวะการทำงานที่เหมาะสมเพื่อใช้ในการออกแบบเตาปฏิกรณ์และหน่วยแยกที่คุ้มค่าต่อการลงทุนมากที่สุด

ข. สามารถนำผลิตภัณฑ์รองของบริษัทไปพัฒนาเป็นผลิตภัณฑ์ที่มีมูลค่าเพิ่มสูงขึ้นและไม่เป็นพิษต่อสิ่งแวดล้อม

ค. เป็นกระบวนการต้นแบบสำหรับการศึกษาการกำจัดสารอะโรเมติกส์ออกจากตัวทำละลายในอุตสาหกรรมอื่นๆ

4. การสร้างห้องปฏิบัติการวิจัยในบริษัทเอกชน

ได้ทำสัญญาความร่วมมือในการทำวิจัยกับบริษัท SCG Chemical CO. LTD. โดยมีการสร้างห้องปฏิบัติการวิจัยของบริษัทฯ ในพื้นที่ภายในมหาวิทยาลัย โดยโครงการความร่วมมือคิดเป็นงบประมาณทั้งสิ้น 39 ล้านบาท โดยเริ่มโครงการตั้งแต่วันที่ 9 เมษายน 2550

5. การจัดสัมมนาเพื่อเผยแพร่ผลงานวิจัย

ได้มีการจัดสัมมนาทางวิชาการเพื่อเผยแพร่ผลงานจากทุนส่งเสริมกลุ่มวิจัยในหัวข้อ “การประยุกต์ใช้ตัวเร่งปฏิกิริยาและเครื่องปฏิกรณ์เคมีสำหรับอุตสาหกรรมปิโตรเคมี” ในวันที่ 27 กรกฎาคม 2550 ณ ห้องประชุม ชั้น 2 ตึกเจริญวิศวกรรม อาคาร 4 คณะวิศวกรรมศาสตร์ จุฬาลงกรณ์มหาวิทยาลัย โดยมีผู้เข้าร่วมสัมมนาทั้งสิ้น 68 คน โดยมีรายละเอียดการสัมมนาดังแสดงในเอกสารแนบชุดที่ 39

6. สรุปผลงาน

ตารางที่ 1 สรุปผลงานตามข้อเสนอโครงการและผลงานในรอบ 3 ปี

รายการ	**ผลงานตามข้อเสนอโครงการ**	**ผลงานรวมที่ทำได้**
1. การสร้างห้องปฏิบัติการวิจัยในบริษัทเอกชน	1	1
2. การเลือกตัวเร่งปฏิกิริยาที่เหมาะสมสำหรับการใช้งานในทางการค้า	1	2[1]
3. ผลงานตีพิมพ์ในวารสารระดับนานาชาติ	24	42 + 2[2]

4. ผู้สำเร็จระดับปริญญาเอก	9	5 + 8[3]
5. ผู้สำเร็จระดับปริญญาโท	30	48
6. การจัดสัมมนาเผยแพร่ผลงานวิจัย	1	1

หมายเหตุ [1] วิเคราะห์ตัวอย่างให้บริษัท TUNTEX PETROCHEMICALS (THAILAND) PUBLIC COMPANY LIMITED 3 ตัวอย่าง และวิเคราะห์ตัวอย่างให้บริษัทระยองโอเลฟินส์ 8 ตัวอย่าง

[2] จำนวนบทความที่อยู่ระหว่างการแก้ไข

[3] จำนวนนิสิตปริญญาเอกที่จะสำเร็จการศึกษา

ลงนาม

(ศ.ดร. ปิยะสาร ประเสริฐธรรม)
หัวหน้าโครงการ

An Alternative Correlation Equation between Particle Size and Structure Stability of H−Y Zeolite under Hydrothermal Treatment Conditions

Somyod Sombatchaisak,[†] Piyasan Praserthdam,*[,†] Choowong Chaisuk,[‡] and Joongjai Panpranot[†]

Center of Excellence on Catalysis and Catalytic Reaction Engineering, Department of Chemical Engineering, Chulalongkorn University, Bangkok 10330, Thailand, and Department of Chemical Engineering, Faculty of Engineering and Industrial Technology, Silpakorn University, Nakon Pathom 73000, Thailand

The effect of particle size in the range of 0.16−2.01 μm on the hydrothermal stability of H−Y zeolite under hydrothermal treatment conditions similar to those used in FCC processes was investigated. The average particle size of 0.45 μm was found to be the optimum particle size of H−Y zeolite to retain a high percent crystallinity upon hydrothermal treatment. A new correlation was developed by plotting the relative crystallinity (C/C_0) against the reciprocal of the square root of the particle size (d_0) of Y zeolite. The correlation accurately predicts the hydrothermal stability of Y zeolite in small to medium particle sizes for a given temperature. For the larger particle sizes of Y zeolite (>0.45 μm), no exact correlation between particle size and hydrothermal stability was found, probably because of the presence of more structural defects in the zeolite, as shown by higher Brønsted/Lewis acid ratios.

1. Introduction

Fluid catalytic cracking (FCC) produces approximately one-third of the world's gasoline supply using faujasite-type zeolites. The commercial FCC catalysts consist of 1−2-μm Y zeolite embedded in a matrix of 40−80-μm spherical amorphous aluminosilicate particles. While circulating in an FCC unit, zeolites encounter severe hydrothermal conditions, resulting in physical and chemical changes that affect the surface area, pore volume, and catalytic cracking performance of the zeolites. Several factors influencing the hydrothermal stability of Y zeolite have been reported, including the Si/Al ratio,[1] the dealumination procedure,[2−6] and the hydrothermal aging conditions.[7,8] Zeolites with higher hydrothermal stability can be obtained by using higher Si/Al ratios or by incorporating rare earth or noble metals into the zeolite framework to help prevent dealumination upon hydrothermal treatment.[9−12]

Particle size has been found to affect the performance of zeolites for many catalytic reactions. For examples, Rajagopalan et al.[13] studied the effect of the particle size of NaY zeolite in the range of 0.06−0.65 μm on its activity and selectivity in FCC reaction. It was found that catalysts containing smaller-particle zeolites exhibited higher activities in the cracking of gasoil and higher selectivities to gasoline and light cycle oil than those containing larger-particle zeolites. Gianetto et al.[14] found similar results for ultrastable submicron Y (USSY) zeolites. Changes in the zeolite particle size significantly affect the amounts of total aromatics, benzene, C_4 olefins, and coke during FCC. Al Khattaf and de Lasa[15] reported that the cracking conversion of 1,3,5-triisopropylbenzene using 0.4-μm Y zeolite was higher than that obtained using 0.9-μm zeolite because of the constrained diffusional transport in the larger Y zeolite particles. However, smaller-particle zeolites have often been found to be less stable than larger-particle ones. The optimum size of the zeolite crystal is, therefore, required to achieve the desired performance.[16,17] In a previous study reported by our laboratory, Praserthdam et al.[18] investigated the effect of crystal size on the durability of Co/HZSM-5 in the selective reduction of NO. The Co/HZSM-5 with the smaller crystal size showed the greater durability. The critical diameter of the crystal size of Co/HZSM-5 for this reaction was determined to be 2 μm.

In this study, an alternative correlation between the particle size and structure stability of H−Y zeolite under hydrothermal treatment conditions is developed. The effects of particle size and hydrothermal conditions similar to those used in the FCC process on the structural changes of Y zeolite were investigated by means of X-ray diffraction (XRD), BET surface area measurements, nuclear magnetic resonance (NMR) spectroscopy, scanning electron microscopy (SEM), temperature-programmed desorption (TPD) of NH_3, and Fourier transform infrared (FTIR) spectroscopy of adsorbed pyridine.

2. Experimental Section

2.1. Preparation of H−Y Zeolite Catalysts. H−Y zeolite catalysts with different particle sizes in the range of 0.16−2.01 μm were prepared in our laboratory according to the method of Miyanohara et al.[19] The Si/Al ratio of 4.5 was used for all catalyst samples. The initial materials for the synthesis of zeolite Y are sodium silicate (Merck), sodium hydroxide (Merck), sodium aluminate (Fuka), and distilled water. The molar composition of the gel was 3.68 Na_2O/1 Al_2O_3/12 SiO_2/148 H_2O. The gel was aged at room temperature for various aging times (0.5, 2, 4.5, or 6.5 days). Then, it was heated to a specified temperature (363, 373, or 383 K) in an

* To whom correspondence should be addressed. Tel.: +662-218-6766; Fax: +662-218-6769 E-mail: piyasan.p@chula.ac.th.
[†] Chulalongkorn University.
[‡] Silpakorn University.

10.1021/ie049847k CCC: $27.50
Published on Web 06/11/2004

oven for 24 h. After being cooled to ambient temperature, the sample was washed thoroughly several times with deionized water until the pH was 7. The obtained samples were dried at 383 K overnight and calcined at 773 K in an air flow for 2 h. The hydrogen form of Y zeolite was then obtained by first exchanging Na^+ with NH_4^+ using an aqueous solution of NH_4NO_3 and subsequently decomposing the NH_4^+ by calcination in air at 773 K for 2 h.

2.2. Hydrothermal Treatment. Hydrothermal treatment of the catalysts was performed in a homemade system. Approximately 0.5 g of catalyst sample was placed in the reactor and was first heated in a nitrogen flow to the specified temperature (873, 973, 1073, 1173, or 1273 K) using a ramp rate of 10 K/min. The sample was kept at this temperature for a specified time period (0.5, 1, 2, 3, or 5 h) while steam at different partial pressures (0.05, 0.1, 0.2, 0.5, or 1.0) was added. Finally, the sample was cooled to room temperature in a nitrogen stream.

2.3. Catalyst Characterization. 2.3.1. Scanning Electron Microscopy (SEM). The average particle sizes and particle size distributions of the catalysts before and after hydrothermal treatment were determined visually from SEM micrographs obtained using a JEOL JSM-35 CF model scanning electron microscope.

2.3.2. BET Surface Area Analysis. The specific surface areas of the samples were calculated using the Brunauer–Emmett–Teller (BET) single-point method. Approximately 0.3–0.5 g of the catalyst sample was placed in the sample cell, heated to 473 K, and held at that temperature for 10 h under a 30% N_2/He flow. The catalyst sample was then cooled to room temperature and dipped into liquid nitrogen. After the adsorption of nitrogen reached equilibrium, the sample cell was then dipped into a water bath at room temperature. The amount of nitrogen desorbed was measured by a gas chromatograph (GOW-MAC).

2.3.3. X-ray Diffraction (XRD). X-ray diffraction patterns of the catalysts were obtained using a Seimens D5000 X-ray diffractometer with monochromatized Cu Kα radiation (10 kV, 20 mA). The relative crystallinity was estimated by comparing the peak intensities of the treated samples with those of fresh samples. The total intensities of the eight peaks assigned to the (331), (511), (440), (533), (642), (822), (555), and (664) reflections were used for comparison according to ASTM D3906 method.

2.3.4. Nuclear Magnetic Resonance (NMR) Spectroscopy. The chemical state of Al was measured by ^{27}Al MAS NMR spectroscopy using a Bruker DPX-300 NMR spectrometer operated at 78.2 MHz at the magic angle. The relative area of tetrahedral ^{27}Al was calculated from the area of tetrahedral aluminum per summation area of tetrahedral and octahedral aluminum.

2.3.5. NH_3 Temperature Program Desorption (NH_3 TPD). The amount of acidic sites on the catalysts was measured using the NH_3 temperature-programmed desorption (TPD) technique. Approximately 0.25 g of Y zeolite catalyst was placed in a U-shape quartz tube, incorporated in a temperature-controlled oven, and connected to a thermal conductivity detector (TCD). Prior to ammonia adsorption, the catalyst was first heated to 773 K at a ramp rate of 10 K/min in a nitrogen flow and held at this temperature for 1 h to remove any remaining water or other organic compounds. It was then cooled to 353 K before saturation of catalyst surface with ammonia using 10% NH_3/He (high purity grade, Thai Industrial Gas Co., Ltd.) at a flow rate of 60 mL/min.

The temperature-programmed desorption was performed with a constant heating rate of ca. 10 K/min from 363 to 973 K. The amount of NH_3 desorbed was measured by analyzing the effluent gas with a thermal conductivity detector.

2.3.6 Fourier Transform Infrared (FTIR) Spectroscopy. IR spectra of adsorbed pyridine were recorded to distinguish and measure the two types of acidic sites on the zeolite surface, i.e., Lewis and Brønsted acid sites. FTIR experiments are performed on a Nicolet model Impact 400 instrument with deuterated triglycine sulfate (DTGS) detector in the same manner as used by Linjie et al.[20] Approximately 0.06 g of catalyst powder was pressed into wafers (1 cm in diameter) and pretreated in a vacuum of 10^{-4} Torr at room temperature for 1 h. Then, pyridine was introduced into the IR cell by self-vaporizing in a vacuum and was circulated through the system by electromagnetic pump. After saturation, the adsorbed pyridine was evacuated at room temperature for 5 h or until no change in IR spectrum was observed. Then, FTIR measurement of the spectrum of the pyridine-adsorbed sample was started at room temperature.

Table 1. Effect of Preparation Conditions on the Average Particle Size of HY Zeolite

aging time (day)	reaction temperature (K)	average particle size (μm)[a]
0.5	363	1.19
	373	amorphous
	383	amorphous
2.0	363	0.82
	373	1.81
	383	2.01
4.5	363	0.31
	373	0.45
	383	0.40
6.5	363	0.16
	373	0.25
	383	0.45

[a] Average particle size was evaluated using SEM. Measurement error = ±5%.

3. Results and Discussion

3.1. Effect of Preparation Conditions on Particle Size of H–Y Zeolite. The Y zeolites with different particle sizes ranging from 0.16 to 0.21 μm used in this study were prepared by varying the aging time of nucleation and the gel reaction temperature. The average particle sizes of the Y zeolites obtained under various synthesis conditions are reported in Table 1. Reaction temperatures in the range 363–383 K were found to be optimum for producing Y zeolite.[21] The minimum time required to obtain a zeolite crystal structure was determined to be ca. 2 days; otherwise, amorphous materials were produced. It was found that lower reaction temperature (lower crystal growth rate) and longer aging time of nucleation resulted in smaller zeolite crystals. A similar result was reported by Zhdanov et al.[8] for the synthesis of Na–A zeolite. Typically, the particle size of zeolites depends on the relative rates of the two competing phenomena occurring during synthesis, namely, nucleation and crystal growth. Both rates decrease with decreasing temperature;[22] however,

Table 2. Characteristics of HY Zeolite before and after the Hydrothermal Treatment[a]

particle size[b] (μm)		BET surface area[c] (m^2/g)		
before	after	before	after	relative BET SA (%)
0.16	0.16	521	322	38
0.31	0.31	546	366	33
0.45	0.45	511	441	14
0.82	0.82	531	397	25
2.01	2.01	550	339	38

[a] Treatment conditions were 1073 K, 10 mol % steam, and 1 h. [b] Average particle size was evaluated using SEM. Measurement error = ±5%. [c] Measurement error = ±10%.

the impact of decreasing temperature is more pronounced on the crystal growth rate than on the nucleation rate, resulting in smaller particle size at lower temperature.[23] Another factor influencing the size of zeolite crystals is the aging time of nucleation. The longer the aging time of nucleation, the lower the uniformity of nucleus precursors in the reaction mixture, and consequently, the smaller the zeolite particles formed.[24]

3.2. Effect of Hydrothermal Treatment on the Physical Properties of H−Y Zeolite. The particle sizes and BET surface areas of Y zeolites before and after hydrothermal treatment are reported in Table 2. The Y zeolites prepared under different preparation conditions resulted in spherical particles with average particle sizes varying from 0.16 to 2.01 μm. The particle sizes and shape remained unaltered after the samples underwent hydrothermal treatment at 1073 K and 10 mol % steam for 1 h. It is known that the BET surface area of Y zeolite decreases upon hydrothermal treatment because of the collapse of the zeolite framework.[25] However, in this study, it was found that changes in BET surface areas were more pronounced for smaller- or larger-particle-size Y zeolites compared to the medium-particle-size samples (0.45 μm).

The crystallinity of Y zeolite was also affected during hydrothermal treatment as a result of aluminum extraction and dehydroxylation.[26] Figure 1a−c shows the effect of particle size on the crystallinity of Y zeolite when the aging parameters are varied as follows: (a) temperature (873−1273 K), (b) aging time (30−300 min), and (c) steam partial pressure (5−100%). The relationships between the percent crystallinity and the particle size of Y zeolite when the aging parameters are varied follow similar volcano trends. The percentages of crystallinity decreased significantly with increasing hydrothermal temperature, steam partial pressure, and aging time, which is typical hydrothermal behavior for zeolites in FCC catalysts.[2] In this study, the lowest percent crystallinity was observed for the most severe hydrothermal conditions (1273 K, 100% steam partial pressure, and 300 min).

The hydrothermal stability of the Y zeolites was also found to be strongly dependent on their particle size. For the particle sizes ranging from 0.16 to 0.45 μm, the percent crystallinity increased with increasing particle sizes, and the maximum percent crystallinity of ca. 80−90% was observed for the particle size of 0.45 μm. This trend is in agreement with the literature findings that smaller-crystallite zeolites are more active but less stable than those with larger crystallites.[27,28] The percent crystallinity of the Y zeolites, however, gradually decreased for particle sizes larger than 0.45 μm. The hydrothermal behavior of larger-particle Y zeolite

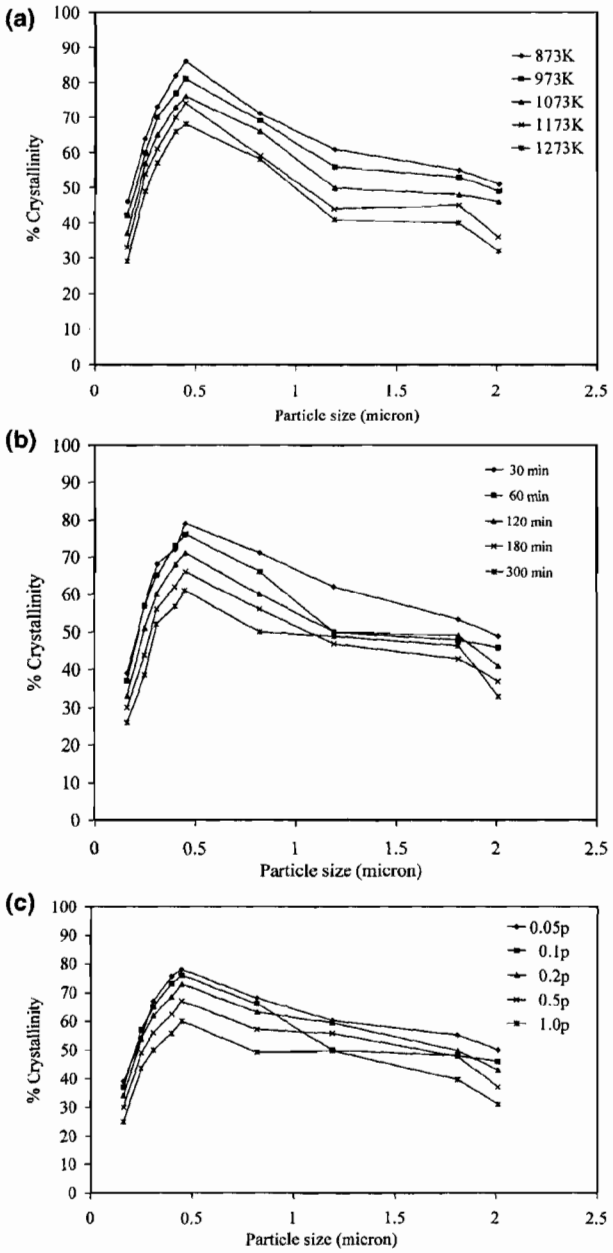

Figure 1. Relationship between percent crystallinity and particle size of Y zeolite after hydrothermal treatment with different treatment parameters: (a) 873−1273 K, 10 mol % steam, and 60 min; (b) 30−300 min, 10 mol % steam, and 1073 K; (c) 0.05−1 P/P_0, 60 min, and 1073 K. Measurement error was ±5%.

is still unclear; however, the decrease in percent crystallinity is probably due to a larger amount of defects in larger-particle-size Y zeolite. In addition, there might be an influence from the average distance between acidic and metallic sites[29] or the various pore sizes in large-particle shape-selective zeolite. In a previous study, Praserthdam et al.[18] reported that the larger-particle Co/HZSM-5 catalysts experienced significant losses of crystallinity and tetrahedral aluminum upon hydrothermal treatment whereas those characteristics for the smaller-particle catalysts remained unaffected.

3.3. Dealumination after Hydrothermal Treatment. ^{27}Al MAS NMR spectra for all of the catalyst samples in this study were collected. Figure 2a−c shows

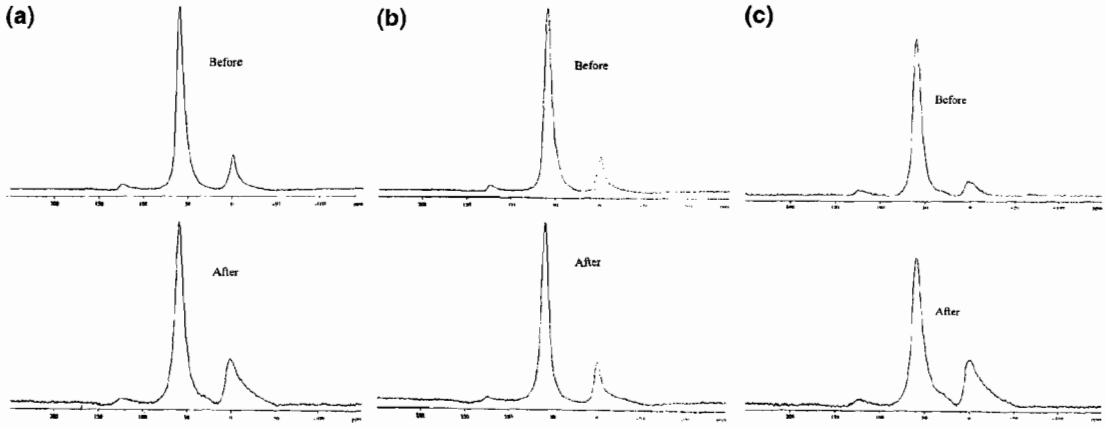

Figure 2. ^{27}Al MAS NMR spectra of Y zeolite fresh samples with the different average particle sizes (a) 0.16, (b) 0.45, and (c) 0.82 μm before and after hydrothermal treatment at 1073 K, 10 mol % steam, and 1 h.

Table 3. Relative Areas of ^{27}Al NMR Peaks and Acid Properties of HY Zeolite with Various Particle Sizes

particle size (μm)	relative area of tetrahedral ^{27}Al[a]		acid site[b]		ratio of B/L[c]
	before	after	Brønsted	Lewis	
0.16	83.69	69.14	62	201	0.31
0.31	85.06	77.99	86	245	0.35
0.45	84.52	83.63	79	243	0.33
0.82	90.64	78.97	120	259	0.46
2.01	94.63	71.35	189	284	0.67

[a] Relative area of tetrahedral ^{27}Al was calculated from the area of tetrahedral aluminum per summation area of tetrahedral and octahedral aluminum. Measurement error = ±10%. [b] Acid site was calculated using the area of the Brønsted band at 1540 cm^{-1} and the area of Lewis band at 1450 cm^{-1} from FTIR experiments. [c] Ratio of B/L was calculated from area of Brønsted sites per area of Lewis sites.

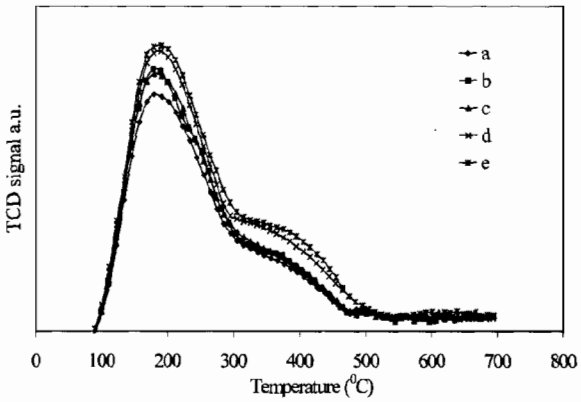

Figure 3. NH_3 TPD of fresh Y zeolite at various particle sizes: (a) 0.16, (b) 0.31, (c) 0.45, (d) 0.82, and (e) 2.01 μm.

the ^{27}Al MAS NMR spectra of Y zeolites with particle sizes of 0.16, 0.45, and 2.01 μm before and after hydrothermal aging. In the fresh samples, a strong signal at ca. 56 ppm and a weak signal at ca. 0 ppm were detected. These peaks correspond to tetrahedrally coordinated Al species (Al^{IV}) in the zeolitic framework and octahedrally coordinated extraframework Al (Al^{VI}), respectively.[30,31] After hydrothermal aging at 1073 K for 1 h, a decrease in tetrahedral aluminum and an increase in octahedral aluminum were observed for Y zeolites in all particle sizes used in this study except for the medium size (0.45 μm). The loss in crystallinity is due to framework dealumination of the zeolite.[18,31] For strongly dealuminated samples, another peak or a small shoulder is often visible between 30 and 50 ppm in the ^{27}Al MAS NMR spectra, which has been assigned to pentacoordinated aluminum atoms[32] or distorted tetrahedrally coordinated aluminum atoms in extraframework species.[33-34]

The relative areas of tetrahedral ^{27}Al before and after hydrothermal treatment are reported in Table 3. They were found to be in accordance with the percentages of crystallinity. Medium-particle-size Y zeolite (0.45 μm) exhibited the lowest amount of dealumination; subsequently, the highest percent crystallinity was obtained with these samples.

3.4. Characterization of Acidic Sites. The NH_3 temperature-programmed desorption (TPD) technique provides information on the amount and strength of acidic sites. The peak area of a TPD profile represents the amount of desorbed NH_3, whereas the peak position corresponds to the strength of acidity. The NH_3 TPD profiles of Y zeolites with various particle sizes are shown in Figure 3. All catalyst samples exhibited similar TPD profiles. The first desorption peak at ca. 473 K is assigned to the weak acid sites, whereas the second peak at ca. 653 K corresponds to strong acid sites.[35] The amount of weak acid sites was determined to be much higher than the amount of strong acid sites. Interestingly, higher amounts of strong acid sites were detected on larger-particle-size of Y zeolite.

Pyridine adsorption IR spectroscopy is another powerful technique for measuring and distinguishing the acidic sites on a zeolite surface. Figure 4 shows the pyridine adsorption behaviors of fresh Y zeolites with different particle sizes. The two bands at ca. 1450 and 1540 cm^{-1} are assigned to pyridine molecules adsorbed on Lewis acid sites and Brønsted acid sites, respectively. The integrated areas of the bands are proportional to the numbers of corresponding acid sites. The type of acid sites has been found to depend on the synthesis conditions. Kumar et al.[36] reported that fresh H−ZSM-5 catalysts synthesized at the longest aging time used in the study exhibited the highest number of Brønsted acid sites. The ratio of Brønsted to Lewis (B/L) acid sites, as well as the relative area of ^{27}Al obtained from ^{27}Al MAS

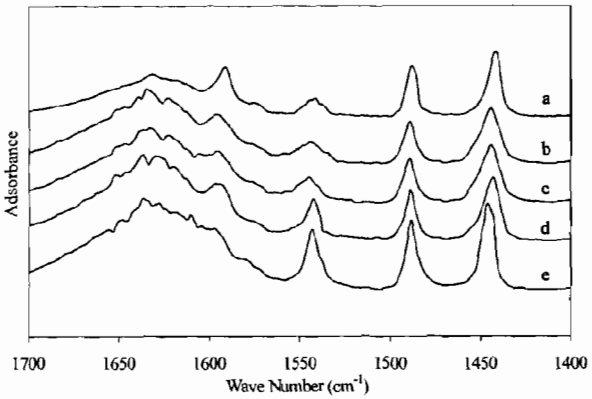

Figure 4. Pyridine adsorption at room temperature of fresh Y zeolite with various particle sizes: (a) 0.16, (b) 0.31, (c) 0.45, (d) 0.82, and (e) 2.01 μm.

NMR spectra, as functions of the particle size of Y zeolites are summarized in Table 3. All Y zeolite catalyst samples contained both Lewis and Brønsted acid sites with higher amounts of Lewis acid sites than Brønsted acid sites. It was found that the larger-particle-size Y zeolites exhibited higher Brønsted/Lewis acid site (B/L) ratios than the smaller-particle-size ones. The results from FTIR spectroscopy are in accordance with the NH_3 TPD results that higher amounts of strong acid sites were detected on larger-particle Y zeolites.

Because a significant loss of crystallinity and a high level of Bronsted acid sites were observed for larger particles, it is suggested that more defects in larger particles might result in the difference in acidity and play a role in crystallinity loss upon hydrothermal treatment. The higher amount of Bronsted acid sites has been ascribed to a higher density of hydroxyl groups.[37] A shorter distance between hydroxyl groups increases the probability of dehydroxylation and dealumination resulting in loss of crystallinity.

3.5. Correlation between Particle Size and Hydrothermal Stability of Y Zeolites. The hydrothermal stability of the Y zeolites was determined in terms of changes in crystallinity (C/C_0) where C_0 is the catalyst's initial crystallinity and C is the crystallinity observed after hydrothermal treatment. Figure 5a–c shows plots of C/C_0 vs $1/(d_0)^{1/2}$, where d_0 is the particle size of the Y zeolite, for different hydrothermal treatment conditions: (a) 0.1 steam partial pressure, 60 min, 873–1273 K; (b) 0.1 steam partial pressure, 1073 K, 30–300 min; and (c) 1073 K, 60 min, 0.1–1.0 steam partial pressure. It was found that all of the plots exhibit the same characteristics consisting of two parts. The first parts represent the correlation between hydrothermal stability and particle size for larger particles and have irregular shapes, whereas the second parts represent the correlation for the smaller particles and show fairly the same linear trend. The irregular shape in the first part of each figure was probably caused by structure defects as stated in a preceding paragraph.

However, the existence of the linear trend in the second part of Figure 5a provides new insight into the effect of particle size on the hydrothermal stability of Y zeolite. The hydrothermal stability of Y zeolite can be predicted from particle size and operating temperature using the following empirical correlation of observed changes in zeolite crystallinity as a function of particle

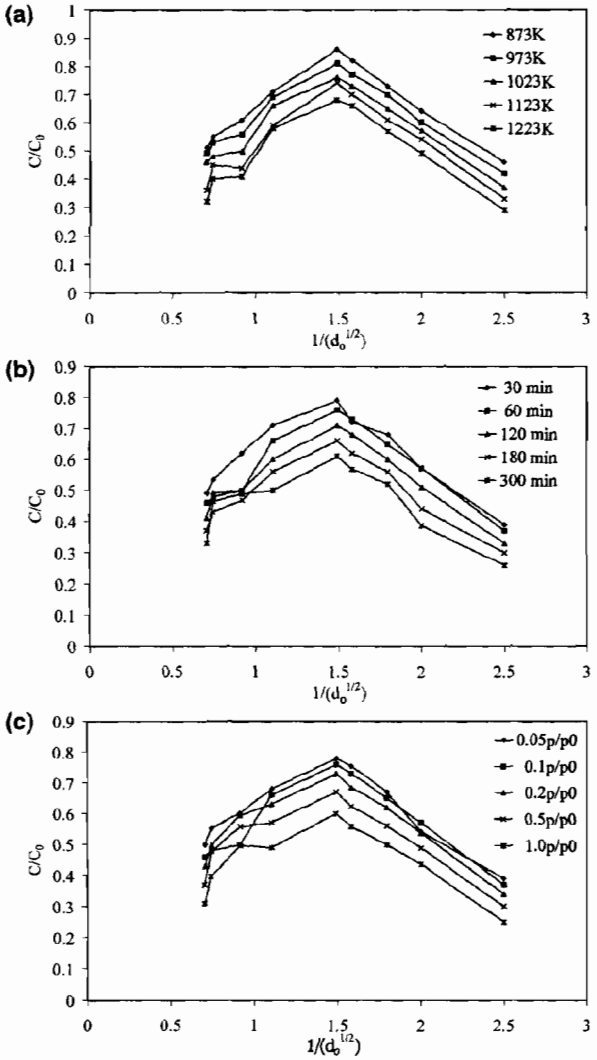

Figure 5. Correlation between C/C_0 and $1/(d_0)^{1/2}$ at different treatment parameters: (a) 873–1273 K, 10 mol % steam, and 60 min; (b) 30–300 min, 10 mol % steam, and 1073 K; (c) 0.05–1 P/P_0, 60 min, and 1073 K.

size and temperature

$$\frac{C}{C_0} = n\left(\frac{1}{\sqrt{d_0}}\right) + f(T) \qquad (1)$$

where C_0 is the catalyst's initial crystallinity, C is the crystallinity observed after hydrothermal treatment, d_0 is the particle size before treatment (μm), n is the slope of the graph, and T is treatment temperature (K). The value of n was determined by averaging the slopes of the graphs. The function of T, $f(T)$, was determined by plotting the intercept values of each plot versus temperature. Therefore, eq 1 can be written as

$$\frac{C}{C_0} = -0.3937\left(\frac{1}{\sqrt{d_0}}\right) + \frac{498}{T} + 0.881 \qquad (2)$$

This correlation was found to correctly predict the hydrothermal stability of Y zeolites of small to medium particle size (0.1–0.45 μm). The square root of the

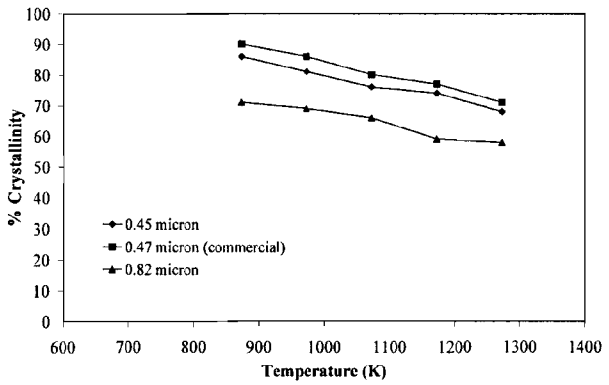

Figure 6. Comparison of the hydrothermal stability of a commercial HY zeolite and the synthesized catalysts (the treatment conditions were 873−1273 K, 10% mol steam, and 1 h).

particle size of the Y zeolite prior to hydrothermal treatment in our correlation probably includes the effects of the nucleus density in amorphous gel at the reaction temperature and/or the initial pseudo-cell concentration in the gel phase as these two factors have been determined to be proportional to the gel reaction temperature and the crystal size during the crystallization of zeolites.[38]

The validity of this correlation was tested by performing the hydrothermal treatment of a commercial Y zeolite catalyst obtained from Tosoh Corporation, Tokyo, Japan, with a particle size of 0.47. The results are shown in Figure 6. Similar profiles were observed for the catalysts prepared in our laboratory and the commercial one. However, for a similar particle size, a slightly higher hydrothermal stability was observed for the commercial catalyst, probably because of a higher Si/Al ratio. Therefore, the correlation proposed in this study might be limited to a Si/Al ratio of 4.5. The results, however, offer interesting possibilities for developing a more versatile correlation that can be applied to Y zeolites with different Si/Al ratios and/or that were prepared under different reaction conditions.

4. Conclusion

The hydrothermal stability of Y zeolite was found to strongly depend on the particle size. The maximum percent crystallinity after hydrothermal treatment was obtained for Y zeolite with a particle size 0.45 μm. By plotting the relative percent crystallinity (C/C_0) versus the particle size of Y zeolite (d_0, μm) in the form of $1/\sqrt{d_0}$ for a given treatment temperature (T, K), an alternative correlation was found

$$\frac{C}{C_0} = -0.3937\left(\frac{1}{\sqrt{d_0}}\right) + \frac{498}{T} + 0.881$$

This correlation can be applied for small to medium particle sizes ranging from 0.1 to 0.45 μm. For larger particle sizes, the defects in the Y zeolite structure, as indicated by higher Bronsted acid site contents, were probably responsible for a decrease in crystal stability upon hydrothermal treatment.

Acknowledgment

The financial support from the Thailand Research Fund (TRF) and TJTTP-JBIC is gratefully acknowledged.

Literature Cited

(1) Dashiti, H.; Albazaz, H. Comparative Study of the Hydrothermal Stability and Performance of Y-Zeolite Based FCC Catalyst Having Differrent Initial Si/Al Ratio. *Fuel Sci. Technol. Int.* **1995**, *13*, 451.

(2) Triantafillidis, C. S.; Vlessidis, A. G.; Evmiridis, N. P. Dealuminated H−Y Zeolites: Influence of the Degree and the Type of Dealumination Method on the Structural and Acidic Characteristics of H−Y Zeolites. *Ind. Eng. Chem. Res.* **2000**, *39*, 307.

(3) Niu, G.; Huang, Y.; Chen, X.; He, J.; Liu, Y.; He, A. Thermal and Hydrothermal Stability of Siliceous Y Zeolite and Its Application to High-Temperature Catalytic Combustion. *Appl. Catal. B* **1999**, *21*, 63.

(4) Gola, A.; Rebours, B.; Milazzo, E.; Lynch, J.; Benazzi, E.; Lacombe, S.; Delevoye L.; Fernandez C. Effect of Leaching Agent in the Dealumination of Stabilized Y Zeolites. *Microporous Mesoporous Mater.* **2000**, *40*, 73.

(5) Zi, G.; Yi, T.; Yugin, Z. Effect of Dealumination Defects on the Properties of Zeolite Y. *Appl. Catal.* **1989**, *56*, 83.

(6) Kugler E. L.; Gardner T. H.; Panpranot, J. Hydrothermal Deactivation Kinetics of FCC Catalysts Containing USY Zeolite. *Abstr. Pap. Am. Chem. Soc.* **1999**, *218*, 34.

(7) Zhdanov, S. P.; Feoktistova, N. N.; Vtjurina, L. M. Temperature Dependence of Nucleation of Zeolites in Alkaline Aluminosilicate Gels in Hydrothermal Crystallization Condition. *Catalysis and Adsorption by Zeolites*; Elsevier Science Publishers B.V.: Amsterdam, 1991; p 287.

(8) Tian, H. P.; Huang, C. J.; Fan, Z. B. Metals on a Novel USY Zeolite after Hydrothermal Aging. *Stud. Surf. Sci. Catal.* **2001**, *139*, 351.

(9) Gutierrez, L.; Boix, A.; Petunchi, J. Promoting Effect of Pt on Co/Zeolites upon the SCR of NO_x. *J. Catal.* **1998**, *179*, 179.

(10) Praserthdam. P.; Phatanasri. S.; Rungsimanop. J.; Kanchanawanichkun. P.; Effect of Pd on the Stability Improvement of Cu/H-MFI for NO Removal under Hydrothermal Pretreatment Condition. *J. Mol. Catal. A: Chem.* **2001**, *169*, 113.

(11) Dangsawai. T.; Praserthdam. P.; Kim. J. B.; Inui. T. Pd Modification of Cu/H−ZSM-5 Catalyst for NO Removal under Hydrothermal Pretreatment Conditions. *Adv. Environ. Res.* **2000**, *3*, 450.

(12) Yang, G.; Wang, Y.; Zhou, J. Q.; Liu, X. C.; Han, X. W.; Bao, X. H. On Configuration of Exchanged La^{3+} in ZSM-5: A Theoretical Approach to the Improvement in Hydrothermal Stability of La-Modified ZSM-5 Zeolite. *J. Chem. Phys.* **2003**, *18*, 9765.

(13) Rajagopalan, K.; Peters, A. W.; Edwards, G. C. Influence of Zeolite Particle size on Selectivity during Fluid Catalytic Cracking. *Appl. Catal.* **1986**, *23*, 69.

(14) Gianetto, A.; Farag, H. I.; Alberto, P. B.; de Lasa, H. I. Fuild Catalytic Cracking Catalyst for Reformulated Gasolines—Kinetic Modeling. *Ind. Eng. Chem. Res.* **1994**, *33*, 3053.

(15) Al-Khattaf, S.; de Lasa, H. The Role of Diffusion in Alkyl-Benzenes Catalytic Cracking. *Appl. Catal. A* **2002**, *226*, 139.

(16) Tatlier, M.; Erdem-Senatalar, A. Optimization of the Cycle Durations of Adsorption Heat Pumps Employing Zeolite Coatings Synthesized on Metal Supports. *Microporous Mesoporous Mater.* **2000**, *34*, 23.

(17) Bonetto, L.; Clamblor, M. A.; Corma, A.; Perez-Pariente, J. Optimization of Zeolite-β in Cracking Catalysts: Influence of Crystallite Size. *Appl. Catal. A.* **1992**, *82*, 37.

(18) Praserthdam, P.; Mongkolsiri, Nakarin.; Kanchanawanichkun, P. Effect of Crystal Size on the Durability of Co/HZSM-5 in Selective Catalytic Reduction of NO by Methane. *Catal Commun.* **2002**, *3*, 191.

(19) Miyanohara, I.; Hashimoto, S.; Miyazaki H. Process for Producing Y-Type Zeolite. U.S. Patent. 4,376,106, 1983.

(20) Linjie, H.; Guofu, X.; Lianglong, Q.; Can, L.; Qin, X.; Dadong, L.; The Effect of Chromium on Sulfur Resistance of Pd/HY−Al_2O_3 Catalysts for Aromatic Hydrogenation. *J. Catal.* **2001**, *202*, 220.

(21) Valtchev, V.; Mintova, S.; Dimov, V.; Toneva, A.; Radev, D. Tribochemical Activation of Seeds for Rapid Crystallization of Zeolite Y. *Zeolites* **1995**, *15*, 193.

(22) Mintova, S.; Valtchev, V.; Vultcheva, E.; Veleva, S. Crystallization Kinetics of Zeolite ZSM-5. *Zeolites* **1992**, *12*, 210.

(23) Cundy, C. S.; Lowe, B. M.; Sinclair, D. M. J. Crystallization of Zeolitic Molecular-Sieves—Direct Measurements of the Growth-Behavior of Single-Crystals as a Function of Synthesis Conditions. *Chem. Faraday Discuss.* **1993**, *95*, 235.

(24) Köroğlu, H. J.; Sarıoğlan, A.; Tather, M.; Şenatalar, A. E.; Savaşç, Ö.T. Effects of Low-Temperature Gel Aging on the Synthesis of Zeolite Y at Different Alkalinities. *J. Crystal Growth* **2002**, *241*, 481.

(25) Gutierrez, L.; Boix, A.; Petunchi, J. Promoting Effect of Pt on Co Zeolites upon the SCR of NO_x. *J. Catal.* **1998**, *179*, 179.

(26) Kubelkova, L.; Seidl, V.; Borbely, G., Beyer, H. K. Correlations between Wavenumbers of Skeletal Vibrations, Unit-Cell Size, and Molar Fraction of Aluminum of Y Zeolites. *J. Chem. Soc., Faraday Trans.* **1988**, *84*(5), 1447.

(27) Aguiar, E. F. S.; Murta Valle, M. L.; Silva, M. P.; Débora, F. S. Influence of External Surface Area of Rare-Earth Containing Y Zeolites on the Cracking of 1,3,5-Triisopropylbenzene. *Zeolites* **1995**, *15*, 620.

(28) Jacobs. P. A. Metal-zeolites: transetters in selective Fischer−Tropsch chemistry. In *Catalysis by zeolites*; Elsevier Science Publishers B.V.: Amsterdam, 1980; p 293.

(29) Di Renzo, F. Zeolites as Tailor-Made Catalysts: Control of the Large Crystal Size. *Catal Today* **1998**, *41*, 37.

(30) Thomas, J. M.; Klinowski, J. The Study of Aluminosilicate and Related Catalysts by High-Resolution Solid-State NMR. *Adv. Catal.* **1985**, *33*, 199.

(31) Budi, P.; Howe, R. F. Steam Deactivation of CoZSM-5 NO_x Reduction Catalysts. *Catal. Today* **1997**, *38*, 175.

(32) Sanz J.; Fornés, V.; Corma, A. Extraframework Aluminum in Steam- and $SiCl_4$-Dealuminated Y Zeolite. *J. Chem, Soc., Faraday Trans.* **1988**, *84*, 3113.

(33) Samoson, A.; Lippmaa, E.; Engelhardt, G.; Lohse, U.; Jerschkewitz, H. G. Quantitative High-Resolution ^{27}Al NMR: Tetrahedral Non-Framework Aluminium in Hydrothermally Treated Zeolites. *Chem. Phys. Lett.* **1987**, *134*, 589.

(34) Omegna, A.; Haouas, M.; Kogelbauer, A.; Prins, R. Realumination of Dealuminated HZSM-5 Zeolites by Acid Treatment: A Reexamination. *Microporous Mesoporous Mater.* **2001**, *46*, 177.

(35) Karge, H. G.; Jozefowicz, L. C. A Comparative Study of the Acidity of Various Zeolites using the Differential Heats of Ammonia Adsorption as Measured by High Vacuum Microcalorimetry. *Stud. Surf. Sci. Catal.* **1994**, *84A*, 685.

(36) Kumar, N.; Nieminen, V.; Dermirkan, K.; Salmi, T.; Murzin, D. Yu.; Laine, E. Effect of Synthesis Time and Mode of Stirring on Physico-Chemical and Catalytic Properties of ZSM-5 Zeolite Catalysts. *Appl. Catal. A* **2002**, *235*, 113.

(37) Satterfield, C. N. *Heterogeneous Catalysis in Industrial Practice*, 2nd ed.; McGraw-Hill: New York, 1991; Vol. 259, p 226.

(38) Falamaki, C.; Edrissi, M.; Sohrabi, M. Studies on the Crystallization Kinetics of Zeolite ZSM-5 with 1,6-Hexanediol as a Structure-Directing Agent. *Zeolites* **1997**, *19*, 362.

Received for review February 25, 2004
Revised manuscript received April 23, 2004
Accepted May 12, 2004

IE049847K

Available online at www.sciencedirect.com
SCIENCE DIRECT®
Journal of Power Sources 142 (2005) 75–80
JOURNAL OF POWER SOURCES
www.elsevier.com/locate/jpowsour

Short communication

Comparison of carbon formation boundary in different modes of solid oxide fuel cells fueled by methane

W. Sangtongkitcharoen[a], S. Assabumrungrat[a,*], V. Pavarajarn[a], N. Laosiripojana[b], P. Praserthdam[a]

[a] *Center of Excellence in Catalysis and Catalytic Reaction Engineering, Department of Chemical Engineering, Chulalongkorn University, Bangkok 10330, Thailand*
[b] *The Joint Graduate School of Energy and Environment, King Mongkut's University of Technology Thonburi, Bangkok 10140, Thailand*

Received 10 August 2004; accepted 20 October 2004
Available online 8 December 2004

Abstract

A detailed thermodynamic analysis is employed as a tool for prediction of carbon formation boundary for solid oxide fuel cells (SOFCs) fueled by methane. Three operating modes of SOFCs, i.e. external reforming (ER), indirect internal reforming (IIR) and direct internal reforming (DIR), are considered. The carbon formation boundary is determined by finding the value of inlet steam/methane (H_2O/CH_4) ratio whose equilibrium gas composition provides the value of carbon activity of one. It was found that the minimum H_2O/CH_4 ratio requirement for which the carbon formation is thermodynamically unfavorable decreases with increasing temperature. For SOFCs with the oxygen-conducting electrolyte, ER-SOFC and IIR-SOFC show the same values of H_2O/CH_4 ratio at the carbon formation boundary, independent of the extent of electrochemical reaction of hydrogen. In contrast, due to the presence of extra H_2O from the electrochemical reaction at the anode chamber, DIR-SOFC can be operated at lower values of the H_2O/CH_4 ratio compared to the other modes. The difference becomes more pronounced at higher values of the extent of electrochemical reaction.

For comparison purpose, SOFCs with the hydrogen-conducting electrolyte were also investigated. According to the study, they were observed to be impractical for use, regarding to the tendency of carbon formation. Higher values of the H_2O/CH_4 ratio are required for the hydrogen-conducting electrolyte, which is mainly due to the difference in location of water formed by the electrochemical reaction at the electrodes. In addition, with this type of electrolyte, the required H_2O/CH_4 ratio is independent on the SOFC operation modes. From the study, DIR-SOFC with the oxygen-conducting electrolyte seems to be the promising choice for operation.

Keywords: Solid oxide fuel cell; Carbon formation; Thermodynamics analysis; Methane

1. Introduction

Solid oxide fuel cell (SOFC) is an energy conversion unit that produces electrical energy and heat with greater energy efficiency and lower pollutant emission than the conventional heat engines, steam and gas turbines, and combined cycles. Due to its high operating temperature, SOFC offers the widest potential range of applications, flexibility of fuel choices and possibility for operation with an internal reformer. Recent developments on SOFCs seem to move towards to two main issues: intermediate temperature operation and use of other fuels instead of hydrogen. The uses of various alternative fuels, i.e. methane, methanol, ethanol, gasoline and other oil derivatives, in SOFCs have been widely investigated [1–3]. To date, methane is a promising fuel as it is an abundant component in natural gas and the methane steam reforming technology is relatively well established. As SOFC is operated at such a high temperature, methane can be reformed effectively by either catalytic steam reforming or partial oxi-

* Corresponding author. Tel.: +662 218 6868; fax: +662 218 6877.
E-mail address: suttichai.a@eng.chula.ac.th (S. Assabumrungrat).

0378-7753/$ – see front matter © 2004 Elsevier B.V. All rights reserved.
doi:10.1016/j.jpowsour.2004.10.009

Nomenclature

a	inlet moles of methane (mol)
b	inlet moles of steam (mol)
c	extent of the electrochemical reaction of hydrogen (mol)
K_1	equilibrium constant of reaction (25) (kPa^{-1})
K_2	equilibrium constant of reaction (26) (kPa)
K_3	equilibrium constant of reaction (27) (kPa^{-1})
n_i	number of moles of component i (mol)
p_i	partial pressure of component i (kPa)
x	converted moles associated with reaction (1) (mol)
y	converted moles associated with reaction (2) (mol)

Subscripts

R	reforming chamber
F	fuel cell chamber

Greek letter

α_c	carbon activity

dation to produce a H_2/CO rich gas, which is eventually used to generate the electrical energy and heat. However, several major problems remain to be solved before such SOFCs can be routinely operated on the direct feed of alternative fuels other than hydrogen. One of them is the problem of carbon deposition on the anode, causing loss of active site and cell performance as well as poor durability. The growth of carbon filaments attached to anode crystallites can generate massive forces within the electrode structure leading to its rapid breakdown [4].

A number of efforts have been carried out to alleviate this problem. One approach is to search for appropriate anode formulations and operating conditions. A number of additives were added to the anode in order to lower the rate of carbon formation. For example, the addition of molybdenum and ceria-based materials to Ni-based anode was reported to reduce carbon deposition, and in some cases, to increase the fuel conversion [5,6]. Addition of alkali, such as potassium, can accelerate the reaction of carbon with steam and also neutralize the acidity of the catalyst support, hence reducing carbon deposition [7].

For the steam reforming, addition of extra steam to the feed is a conventional approach to avoid carbon deposition. Selection of a suitable steam/hydrocarbon ratio becomes an important issue. Carbon formation can occur when the SOFC is operated at low steam/hydrocarbon ratio. However, use of high steam/hydrocarbon ratio is unattractive as it lowers the electrical efficiency of the SOFC by steam dilution of fuel and the system efficiency [6]. Consequently, it is necessary to optimize the suitable steam/hydrocarbon ratio at the carbon formation boundary whose value represents the minimum steam/hydrocarbon ratio required to operate the SOFC at carbon-free condition. Our previous works employed thermodynamic calculations to predict the required steam/alcohol ratio for direct internal reforming SOFCs fed by ethanol [8] and methanol [9]. It was found that the SOFCs with an oxygen-conducting electrolyte require less steam/alcohol ratio than that with a hydrogen-conducting electrolyte because extra steam generated from the electrochemical reaction is available for use in the anode chamber.

In this paper, a detailed thermodynamic analysis is carried out to predict the carbon formation boundary for SOFCs fueled by methane. Three operating modes of SOFCs, i.e. external reforming (ER), indirect internal reforming (IIR) and direct internal reforming (DIR), with two electrolyte types, i.e. oxygen- and hydrogen-conducting electrolytes, are investigated to compare the required steam/methane (H_2O/CH_4) ratios between different SOFC operating modes.

2. Theory

The main reactions involved in the production of hydrogen from methane and water are the methane steam reforming and water gas shift reactions as shown in Eqs. (1) and (2), respectively.

$$CH_4 + H_2O = 3H_2 + CO \quad (1)$$

$$CO + H_2O = H_2 + CO_2 \quad (2)$$

The former is strongly endothermic while the latter is mildly exothermic. Methane steam reforming is commercially operated at 1000–1100 K and 2.17–2.86 MPa over nickel based catalysts [10]. The feed contains steam in excess of the stoichiometric amount with H_2O/CH_4 molar ratios of 3–5 to prevent soot formation [11].

When SOFCs are operated with a fuel, such as hydrocarbon and alcohol, three modes of operation, i.e. external reforming SOFC (ER-SOFC), indirect internal reforming SOFC (IIR-SOFC) and direct internal reforming SOFC (DIR-SOFC) as shown in Fig. 1, are possible. For ER-SOFC operation, the endothermic steam reforming and the electrochemical reactions are operated separately in different units, and there is no direct heat transfer between both units. High energy supply to the outside reformer is required due to the high endothermic over this part. In contrast, for both IIR-SOFC and DIR-SOFC, the endothermic reaction from the steam reforming reaction and the exothermic reaction from the oxidation reaction are operated together in a single unit. Therefore, the requirement of a separate fuel reformer and energy supply to this unit can be eliminated. This configuration is expected to simplify the overall system design, making SOFC more attractive and efficient means of producing electrical power.

For IIR-SOFC, the reforming reaction occurs in the vicinity of the cell stack. This enables heat transfer from the fuel

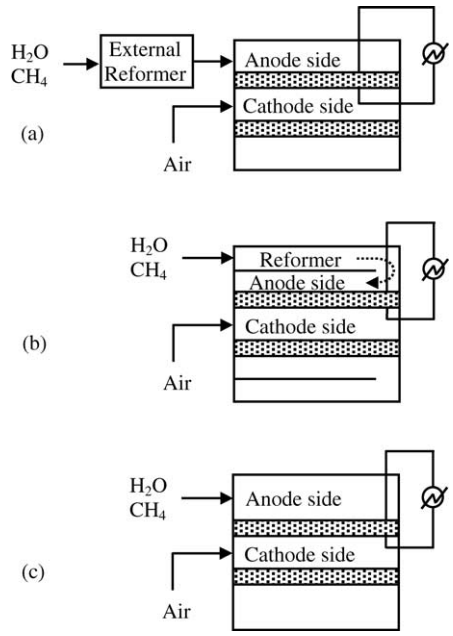

Fig. 1. Configurations of various SOFC modes. (a) ER-SOFC, (b) IIR-SOFC and (c) DIR-SOFC.

cell chamber to the reformer, which leads to energetic economy. However, part of heat may not be efficiently utilized due to its limited heat transfer rate. For DIR operation, the reforming reaction takes place at the anode of the fuel cell. Heat and steam released from the electrochemical reaction upon power generation is effectively used for the endothermic reforming reaction since both processes take place simultaneously at the anode. Therefore, in term of energy aspect, DIR-SOFC is more attractive than the others. It should be noted that state-of-the-art SOFC nickel cermet anodes can provide sufficient activity for the steam reforming and shift reactions without the need for additional catalysts [4,12].

Two types of solid electrolytes can be employed in the SOFC, i.e. oxygen- and hydrogen-conducting electrolytes. The reactions taking place in the anode and the cathode can be summarized as follows:

- Oxygen-conduction electrolyte:

$$\text{anode}: \quad H_2 + O^{2-} = H_2O + 2e^- \tag{3}$$

$$\text{cathode}: \quad O_2 + 4e^- = 2O^{2-} \tag{4}$$

- Hydrogen-conducting electrolyte:

$$\text{anode}: \quad H_2 = 2H^+ + 2e^- \tag{5}$$

$$\text{cathode}: \quad 2H^+ + \tfrac{1}{2}O_2 + 2e^- = H_2O \tag{6}$$

The difference between both electrolyte types is the location of the water produced. With the oxygen-conducting electrolyte, water is produced in the reaction mixture in the anode chamber. In the case of the hydrogen-conducting electrolyte, water appears on the cathode side. The number of moles of each component involved in different SOFC modes is discussed in the following sections.

2.1. ER-SOFC and IIR-SOFC

For ER-SOFC and IIR-SOFC, the methane steam reforming and water gas shift reaction take place initially at the reforming chamber. Then the exit gas from the reformer is fed to the fuel cell chamber where all the methane steam reforming, water gas shift reaction and electrochemical reactions occur. If required, additional water feed can be added to the reformer exit gas before being fed to the fuel cell chamber. The number of moles of each component is given by the following expressions:

- Reforming chamber

$$n_{CH_4} = a - x_R \tag{7}$$

$$n_{CO} = x_R - y_R \tag{8}$$

$$n_{CO_2} = y_R \tag{9}$$

$$n_{H_2} = 3x_R + y_R \tag{10}$$

$$n_{H_2O} = b_R - x_R - y_R \tag{11}$$

$$n_{total} = \sum_{i-1}^{5} n_i \tag{12}$$

where a and b_R represent the inlet moles of methane and water, respectively, and x_R and y_R are the converted moles in the reforming chamber associated to the reactions (1) and (2), respectively.

- Fuel cell chamber

$$n_{CH_4} = a - x_R - x_F \tag{13}$$

$$n_{CO} = x_R - y_R + x_F - y_F \tag{14}$$

$$n_{CO_2} = y_R + y_F \tag{15}$$

$$n_{H_2} = 3x_R + y_R + 3x_F + y_F - c \tag{16}$$

$$\begin{aligned} n_{H_2O} &= b_R - x_R - y_R + b_F - x_F - y_F \\ &\quad \text{(for hydrogen-conducting electrolyte)} \\ n_{H_2O} &= b_R - x_R - y_R + b_F - x_F - y_F + c \\ &\quad \text{(for oxygen-conducting electrolyte)} \end{aligned} \tag{17}$$

$$n_{total} = \sum_{i-1}^{5} n_i \tag{18}$$

where b_F is the additional mole of water fed to the fuel cell chamber, x_F and y_F the converted moles in the fuel cell chamber associated to the reactions (1) and (2), respectively and c is the extent of the electrochemical reaction of hydrogen. It should be noted that only hydrogen is assumed to react electrochemically with oxygen supplied from the cathode side. Then, the overall inlet H_2O/CH_4 ratio for these modes is equal to $(b_R + b_F)/a$.

2.2. DIR-SOFC

For DIR-SOFC, as described, there is no requirement of the separated reforming chamber in the system. All the reactions mentioned earlier take place simultaneously in the fuel cell chamber. The number of moles of each component is given by the following expressions:

$$n_{CH_4} = a - x_F \tag{19}$$

$$n_{CO} = x_F - y_F \tag{20}$$

$$n_{CO_2} = y_F \tag{21}$$

$$n_{H_2} = 3x_F + y_F - c \tag{22}$$

$$\begin{aligned} n_{H_2O} &= b_F - x_F - y_F + c \\ &\quad \text{(for oxygen-conducting electrolyte)} \\ n_{H_2O} &= b_F - x_F - y_F \\ &\quad \text{(for hydrogen-conducting electrolyte)} \end{aligned} \tag{23}$$

$$n_{total} = \sum_{i-1}^{5} n_i \tag{24}$$

Calculations of the thermodynamic equilibrium composition are accomplished by solving a system of non-linear equations relating the moles of each component to the equilibrium constants of the reactions.

The following reactions are the most probable reactions that lead to carbon formation in the reaction system [13]:

$$2CO = CO_2 + C \tag{25}$$

$$CH_4 = 2H_2 + C \tag{26}$$

$$CO + H_2 = H_2O + C \tag{27}$$

The Boudard reaction (Eq. (25)) and the decomposition of methane (Eq. (26)) are the major pathways for carbon formation at high operating temperature [14]. It should be noted that due to the exothermic nature of the water gas shift reaction (Eq. (2)), the amount of CO becomes significant at high temperature [15]. All reactions are employed to examine the thermodynamic possibility of carbon formation. The carbon activities, defined in Eqs. (28)–(30), are used to determine the possibility of carbon formation.

$$\alpha_{c,CO} = K_1 \frac{p_{CO}^2}{p_{CO_2}} \tag{28}$$

$$\alpha_{c,CH_4} = K_2 \frac{p_{CH_4}}{p_{H_2}{}^2} \tag{29}$$

$$\alpha_{c,CO-H_2} = K_3 \frac{p_{CO} p_{H_2}}{p_{H_2O}} \tag{30}$$

where K_1, K_2 and K_3 represent the equilibrium constants of the reactions (25), (26) and (27), respectively, and p_i is the partial pressure of component i. When $\alpha_c > 1$, the system is not in equilibrium and carbon formation is observed. The system is at equilibrium when $\alpha_c = 1$. It is noted that the carbon activity is only the indicator for the presence of carbon in the system. It does not give the information regarding the amount of carbon formed. Finally, when $\alpha_c < 1$, carbon formation is thermodynamically impossible.

In order to identify the range of SOFC operation, which does not suffer from the formation of carbon, the operating temperature and the extent of the electrochemical reaction of hydrogen are specified. Then the initial value of the H_2O/CH_4 ratio is varied and the corresponding values of α_c are calculated. The carbon formation boundary is defined as the value of H_2O/CH_4 whose value of $(1-\alpha_c)$ is approaching zero. This value represents the minimum inlet H_2O/CH_4 mole ratio at which carbon formation in the equilibrium mixture is thermodynamically impossible. For ER-SOFC and IIR-SOFC, the calculations for both reformer and fuel cell chambers are required. It should be noted that although recent investigators estimated the carbon concentration in the steam reforming reactions by the method of Gibbs energy minimization, the principle of equilibrated gas to predict the carbon formation in this study is still meaningful because the calculations are carried in order to determine the carbon formation boundary where the carbon starts forming on the surface. In addition, other possible factors such as mass and heat transfer or rate of reactions may also affect the prediction of the carbon formation boundary. Local compositions, which allow the local carbon formation, may exist although the carbon formation is unfavorable according to the calculation based on equilibrium bulk compositions. Moreover, other forms of carbonaceous compounds such as C_nH_m may be formed and result in comparable damages.

3. Results and discussion

The influence of inlet steam/methane (H_2O/CH_4) ratio on equilibrium composition of species at the reformer section was firstly carried out as illustrated in Fig. 2. The molar fractions of CO_2, H_2O and H_2 increased with increasing the inlet steam/methane ratio, whereas the decrease in CO production

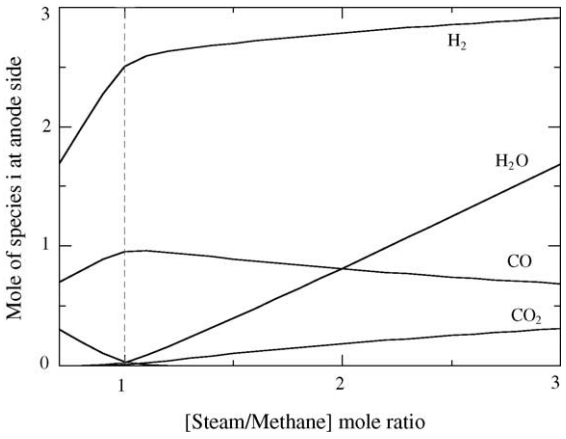

Fig. 2. Effect of inlet H_2O/CH_4 ratio on each component mole in the reformer (a = 1 mol, P = 101.3 kPa and T = 1173 K).

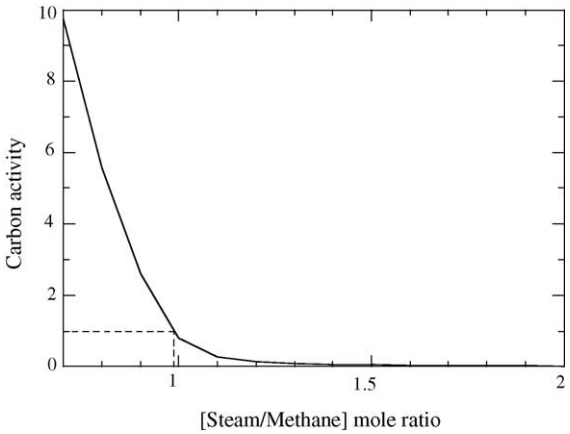

Fig. 3. Effect of inlet H_2O/CH_4 ratio on carbon activity in the reformer (a = 1 mol, P = 101.3 kPa and T = 1173 K).

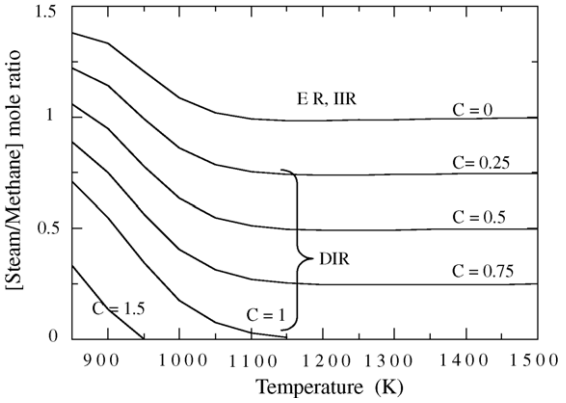

Fig. 4. Influence of the operation mode on the requirement of inlet H_2O/CH_4 ratio at different operating temperatures (oxygen-conducting electrolyte, a = 1 mol and P = 101.3 kPa).

is observed. Apparently, the increasing of inlet H_2O/CH_4 ratio moves both methane steam reforming (Eq. (1)) and water gas shift reaction (Eq. (2)) into the forward direction. The number of mole for methane is very small since it is the reactant of the endothermic reaction, which proceeds in great extent at high temperature. It should be noted that according to Eqs. (25)–(27), the presence of high molar fractions of CO_2, H_2 and H_2O is effective for preventing the carbon formation in the system.

Fig. 3 shows the influence of inlet H_2O/CH_4 ratio on the corresponding values of the carbon activity calculated from the equilibrium compositions. The initial high slope at the low H_2O/CH_4 ratio implies that the opportunity of the carbon formation is rapidly decreased with an addition of steam into the system. The carbon formation becomes thermodynamically unfavored, as the carbon activity is less than one, when the H_2O/CH_4 ratio is approximately greater than one. It is therefore indicated that the carbon formation is less likely as the H_2O/CH_4 ratio is increased. It should also be noted that the values of carbon activities calculated from Eqs. (28)–(30) are equal because the calculations are based on the gas phase compositions at equilibrium. This is also observed by other investigator [16].

Fig. 4 shows the H_2O/CH_4 ratio at the carbon formation boundary for typical SOFCs with the oxygen-conducting electrolyte for different operating modes and various extents of electrochemical reaction of hydrogen. It can be seen from the figure that the required inlet H_2O/CH_4 ratio for avoiding carbon formation decreases with increasing operating temperature and becomes constant at high temperature. This similar behavior was reported in our previous works with other types of fuel including ethanol [8] and methanol [9]. Therefore, raising the SOFC operating temperature is one possibility to prevent carbon formation at the anode, however, the cost of high temperature materials as well as the problem of cell sealing must also be considered. Comparison between different operating modes indicates that the required H_2O/CH_4 ratios for ER-SOFC and IIR-SOFC are the same, independent of the extent of electrochemical reaction of hydrogen. In contrast, for DIR-SOFC, hydrogen from the electrochemical reaction is converted to steam at the anode side, where the reforming reaction simultaneously takes place and, consequently reduces the requirement of H_2O/CH_4 ratio in the feed. It is particularly pronounced when DIR-SOFC is operated at high current density. Nevertheless, due to the fact that DIR-SOFC requires anode material with sufficient catalytic activity for both reforming and electrochemical reactions whereas ER-SOFC and IIR-SOFC can employ two separated materials readily available for each reaction, ER-SOFC and IIR-SOFC may be preferred at the moment. In case that either ER-SOFC or IIR-SOFC with the oxygen-conducting electrolyte is employed, it should be noted that the damage from carbon deposition in the fuel cell chamber would be less likely, comparing to that in the reformer. Water produced from the electrochemical reaction in the fuel cell chamber in addition to the amount of water in the inlet stream, which is already adjusted to avoid the formation of carbon in the reformer, further decreases the possibility of carbon deposition in the fuel cell chamber.

For comparison, the requirement of H_2O/CH_4 ratios to prevent the carbon formation for ER-SOFC, IIR-SOFC, and DIR-SOFC with the hydrogen-conducting electrolyte are also carried out as shown in Fig. 5. Independent of the operating modes, more inlet steam is required when the cell is operated at high extents of electrochemical reaction of hydrogen. It should be noted that the benefit of steam generation at the cathode by the electrochemical reaction is not recognized for this system. The disappearance of hydrogen from the anode side by electrochemical reaction favors the carbon formation and, consequently required higher steam in order to prevent the formation of carbon species.

From the above results, DIR-SOFC with the oxygen-conducting electrolyte seems to be a promising operation mode due to the good heat utilization within the system and the reduction of inlet H_2O/CH_4 ratio requirement. This summary is in contrast to one previous work, which reported that the SOFC with the hydrogen-conducting electrolyte provides higher electrical efficiency than that with the oxygen-

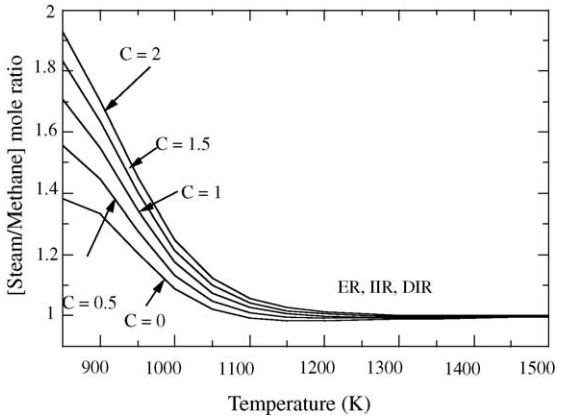

Fig. 5. Influence of operation mode on the requirement of inlet H_2O/CH_4 ratio at different operating temperatures (hydrogen-conducting electrolyte, $a = 1$ mol and $P = 101.3$ kPa).

conducting electrolyte because high partial of hydrogen is maintained at the anode side [17]. However, since the comparison in that work was based on the calculations using the same value of inlet H_2O/CH_4 ratio, the benefit from the reduced steam requirement was not taken into account. This subject will be discussed in more details in our next paper dealing with the efficiency of the overall SOFC system.

4. Conclusion

Theoretical thermodynamic analysis was performed to predict the carbon formation boundary for the SOFCs with different operating modes. It was observed that the required H_2O/CH_4 ratio to prevent the carbon formation mainly depended on the operating temperature, SOFC operation mode, and electrolyte type. In general, operation at high temperature reduces the required inlet H_2O/CH_4 ratio in all cases. The oxygen-conducting electrolyte is more attractive than the hydrogen-conducting electrolyte as the former system requires less steam. This is directly related to water generated from the electrochemical reaction of hydrogen at electrodes. The difference in steam requirement is particularly pronounced at high extent of the electrochemical reaction of hydrogen. The required H_2O/CH_4 ratio is independent of the SOFC operating modes for those with the hydrogen-conducting electrolyte. On the other hand, for the SOFC with the oxygen-conducting electrolyte, DIR-SOFC requires less steam than both ER-SOFC and IIR-SOFC. In summary, the DIR-SOFC with the oxygen-conducting electrolyte seems to be a favorable choice for SOFC operation in the point of view of the amount of steam required.

It should be noted that although the thermodynamic calculations can be used to predict the minimum inlet H_2O/CH_4 ratio for which carbon formation is not favored, the deactivation of anode is not solely the result from the deposition of carbon. Deposition of other forms of carbonaceous compounds such as polymeric coke (C_nH_m) may result in comparable damage. Therefore, the results obtained in this study should be considered only as crude guideline for operating condition of SOFC.

Acknowledgement

The supports from the Thailand Research Fund and the Chulalongkorn University Graduate Scholarship commemoratory the 7th Anniversary of H.M. King Rama IX, and suggestions from Professor Jaime Wisniak are gratefully acknowledged.

References

[1] S.L. Douvartzides, F.A. Coutelieris, K. Demin, P.E. Tsiakaras, AIChE J. 49 (2003) 248–257.
[2] L.F. Brown, Int. J. Hydrogen Energy 26 (2001) 381–397.
[3] G. Maggio, S. Freni, S. Cavallaro, J. Power Sources 74 (1998) 17–23.
[4] S.H. Clarke, A.L. Dicks, K. Pointon, T.A. Smith, A. Swann, Catal. Today 38 (1997) 411–423.
[5] C.M. Finnerty, R.M. Ormerod, J. Power Sources 86 (2000) 390–394.
[6] S. Park, R.J. Gorte, J.M. Vohs, Appl. Catal. A 200 (2000) 55–61.
[7] C.M. Finnerty, N.J. Coe, R.H. Cunningham, R.M. Ormerod, Catal. Today 46 (1998) 137–145.
[8] S. Assabumrungrat, V. Pavarajarn, S. Charojrochkul, N. Laosiripojana, Chem. Eng. Sci. 59 (2004) 6017–6022.
[9] S. Assabumrungrat, N. Laosiripojana, V. Pavarajarn, W. Sangtongkitcharoen, A. Tangjitmatee, P. Praserthdam, J. Power Sources 139 (2005) 55–60.
[10] T.A. Czuppon, S.A. Knez, D.A. Newsome, Hydrogen, in: J.L. Kroschwitz, M. Howe-Grant (Eds.), Kirk-Othmer, Encyclopedia of Chemical Technology, vol. 13, fourth ed., Wiley, New York, 1995, pp. 383–394, esp. 852–865.
[11] H.-J. Renner, F. Marschner, Catalytic reforming of natural gas and other hydrocarbon, in: B. Elvers, S. Hawkins, M. Ravenscroft, J.F. Rousaville, G. Schulz (Eds.), Ullmann's Encyclopedia of Industrial Chemistry, vol. A2, fifth ed., VCH Verlagsgesellschaft, Weinheim, Germany, 1985, pp. 143-242, esp. 186–204.
[12] A.L. Dicks, J. Power Sources 717 (1998) 111–122.
[13] P. Pietrogrande, M. Bezzeccheri, in: L.J.M.J. Blomen, M.N. Mugerwa (Eds.), Fuel Cell Systems, Plenum Press, New York, 1993, p. 142.
[14] J.N. Amor, Appl. Catal. A 176 (1999) 159–176.
[15] L.F. Brown, Int. J. Hydrogen Energy 26 (2001) 381–397.
[16] S. Nagata, A. Momma, T. Kato, Y. Kasuga, J. Power Sources 101 (2001) 60–71.
[17] A.K. Demin, P.E. Tsiakaras, V.A. Sobyanin, S.Y. Hramova, Solid State Ionics 152–153 (2002) 555–560.

Available online at www.sciencedirect.com
SCIENCE DIRECT®
Materials Chemistry and Physics 89 (2005) 395–401
MATERIALS CHEMISTRY AND PHYSICS
www.elsevier.com/locate/matchemphys

Dependence of crystalline phases in titania on catalytic properties during CO hydrogenation of Co/TiO_2 catalysts

Bunjerd Jongsomjit*, Chitlada Sakdamnuson, Piyasan Praserthdam

Department of Chemical Engineering, Faculty of Engineering, Center of Excellence on Catalysis and Catalytic Reaction Engineering, Chulalongkorn University, Bangkok 10330, Thailand

Received 20 July 2004; received in revised form 7 September 2004; accepted 20 September 2004

Abstract

The present research showed dependence of crystalline phases in titania on the catalytic properties of Co/TiO_2 catalysts during CO hydrogenation. A comparative study of anatase TiO_2- and rultile-anatase coupled TiO_2-supported Co catalysts was conducted. It was found that the presence of rutile phase (19 mol%) in titania resulted in a significant increase in the catalytic activity during CO hydrogenation. It was proposed that the role of rutile phase was to increase the stability of the support. The impact of water vapor produced during reduction on the formation of cobalt species strongly interacted with the support was probably inhibited by the presence of rutile phase in titania leading to a decrease in the reducibility loss during reduction.

Keywords: Supported catalyst; Cobalt catalyst; CO hydrogenation; Titania; Reducibility

1. Introduction

In Fischer–Tropsch (FT) catalysis, supported cobalt (Co) catalysts are preferred because of their high activities during FT synthesis based on natural gas [1], high selectivity to linear long chain hydrocarbons and also low activities for the competitive water–gas shift (WGS) reaction [2,3]. Many inorganic supports such as SiO_2 [4–8], Al_2O_3 [9–14], TiO_2 [15–17] and Zeolites [18] have been extensively studied for supported Co catalysts for years. It is known that in general, the catalytic properties depend on reaction conditions, catalyst compositions, metal dispersion, and types of inorganic supports used. Thus, changes the catalyst compositions and/or even though the compositions of supports used may lead to significantly enhance the catalytic properties as well.

During the past decade, titania-supported Co catalysts have been widely investigated by many authors, especially for the application of FT synthesis in a continuously stirred tank reactor (CSTR) [15–17]. However, it should be noted that titania itself has different crystalline phases such as anatase and rutile phases. The different crystalline phase compositions of titania could play an important role on the catalytic performance of titania-supported Co catalysts during CO hydrogenation as well. Thus, the main objective of this research was to investigate influences of different crystalline phases of titania supports on the catalytic properties during CO hydrogenation of Co/TiO_2 catalysts. In the present study, the Co/TiO_2 catalysts were prepared using different crystalline phase compositions of titania supports. The catalysts were pretreated, characterized and tested in order to evaluate the catalytic properties during CO hydrogenation.

2. Experimental

2.1. Catalyst preparation

A 20 wt.% of Co/TiO_2 was prepared by the incipient wetness impregnation. A designed amount of cobalt nitrate [$Co(NO_3)\cdot 6H_2O$] was dissolved in deionized water and then impregnated onto TiO_2 (contained 100 mol% of anatase phase calcined at 500 °C, obtained from Ishihara Sangyo, Japan) and onto TiO_2 (contained 81 mol% of anatase phase

* Corresponding author. Tel.: +66 2 2186869; fax: +66 2 2186877.
E-mail address: bunjerd.j@chula.ac.th (B. Jongsomjit).

0254-0584/$ – see front matter © 2004 Elsevier B.V. All rights reserved.
doi:10.1016/j.matchemphys.2004.09.019

and 19 mol% of rutile phase, also obtained from Ishihara Sangyo, Japan). The catalyst precursor was dried at 110 °C for 12 h and calcined in air at 500 °C for 4 h.

2.2. Catalyst pretreatments

2.2.1. Standard reduction

Standard reduction of the calcined catalyst was conducted in a fixed-bed flow reactor under differential conditions at 1 atm using a temperature ramp from ambient to 350 °C at 1 °C min^{-1} and holding at 350 °C for 10 h in a gas flow having a space velocity of 16,000 h^{-1} and consisting of H_2. The high space velocity of the H_2 flow was applied to insure that the partial pressure of water vapor in the catalyst bed produced by cobalt oxide reduction would be essentially zero. The reduced catalyst was then passivated at room temperature with air for 30 min prior to taking it out.

2.2.2. Hydrothermal treatment

In order to evaluate the stability of catalysts and impacts of water vapor during reduction, hydrothermal treatment was also conducted during standard reduction above. In addition, besides using pure H_2, mixtures of H_2 and water vapor (5–10 vol.%) were also applied separately at the same reduction condition as mentioned in Section 2.2.1.

2.3. Catalyst nomenclature

The nomenclature used for the catalyst samples in this study is as follows:

- Co/T1: titania (100 mol% of anatase phase)-supported Co catalyst;
- Co/T2: titania (81 mol% of anatase phase and 19 mol% of rutile phase)-supported Co catalyst;
- (C): calcined catalyst sample;
- (RW0), (RW5) and (RW10): reduced catalyst samples with no water vapor, 5 vol.% of water vapor, and 10 vol.% of water vapor, added during standard reduction, respectively.

2.4. Catalyst characterization

2.4.1. BET surface area

BET surface area of the samples after various pretreatments was performed to determine if the total surface area changes upon the various pretreatment conditions. It was determined using N_2 adsorption at 77 K in a Micromeritics ASAP 2010.

2.4.2. X-ray diffraction

XRD was performed to determine the bulk crystalline phases of catalyst following different pretreatment conditions. It was conducted using a SIEMENS D-5000 X-ray diffractometer with Cu Kα (λ = 1.54439 Å). The spectra were scanned at a rate of 2.4° min^{-1} in the range 2θ = 20–80°.

2.4.3. Scanning electron microscopy and energy dispersive X-ray spectroscopy

SEM and EDX were used to determine the catalyst morphologies and elemental distribution throughout the catalyst granules, respectively. The SEM of JEOL mode JSM-5800LV was applied. EDX was performed using Link Isis series 300 program.

2.4.4. Raman spectroscopy

The Raman spectra of the samples were collected by projecting a continuous wave laser of argon ion (Ar^+) green (514.532 nm) through the samples exposed to air at room temperature. A scanning range of 100 to 1000 cm^{-1} with a resolution of 2 cm^{-1} was applied. The data were analyzed using the Renishaw WiRE (Windows-based Raman Environment) software, which allows Raman spectra to be captured, calibrated, and analyzed using system 2000 functionality via Galactic GRAMS interface with global imaging capacity.

2.4.5. Temperature-programmed reduction

TPR was used to determine the reduction behaviors and reducibilities of the samples. It was carried out using 50 mg of a sample and a temperature ramp from 35 to 800 °C at 5 °C min^{-1}. The carrier gas was 5% H_2 in Ar. A cold trap was placed before the detector to remove water produced during the reaction. A thermal conductivity detector (TCD) was used to determine the amount of H_2 consumed during TPR. The H_2 consumption was calibrated using TPR of Ag_2O at the same conditions. The reduced samples were recalcined at the original calcination conditions prior to performing TPR. The calculation of reducibilities was described in elsewhere [9,19–22].

2.5. Reaction

CO hydrogenation (H_2/CO = 10/1) was performed to determine the overall activity of the catalyst samples reduced at various conditions. Hydrogenation of CO was carried out at 220 °C and 1 atm. A flow rate of H_2/CO/He = 20/2/8 cc min^{-1} in a fixed-bed flow reactor under differential conditions was used. A relatively high H_2/CO ratio was used to minimize deactivation due to carbon deposition during reaction. Typically, 20 mg of a catalyst sample was re-reduced in situ in flowing H_2 (30 cc min^{-1}) at 350 °C for 10 h prior to the reaction. Reactor effluent samples were taken at 1 h intervals and analyzed by GC. In all cases, steady-state was reached within 5 h.

3. Results and discussion

The present study was conducted in order to investigate the dependence of crystalline phases in titania on the catalytic properties during CO hydrogenation of Co/TiO_2 catalysts. As mentioned, in general titania used contains mainly two phases; anatase and rutile phases. Phase transfor-

mation of titania depends on the preparation of titania such as sol–gel or solvothermal methods and also calcination temperatures. However, it was proposed that the different phase compositions in titania could play an important role on the catalytic properties during CO hydrogenation of Co/TiO_2 catalysts. Section 3 is divided into two parts as follows:

3.1. Catalyst stability during reduction under hydrothermal treatments

It is known that Co metal rather than its oxide or carbide is the active form of supported Co catalysts during CO hydrogenation. Thus, reduction of Co oxide precursor is required in order to reduce it into Co metal form. Water vapor is a byproduct of reduction of metal oxide. It is also known that water vapor also has impacts on the reduction of alumina-supported Co oxide probably in two ways: (i) facilitation of the migration of Co ions into tetrahedral sites of alumina to form a non-reducible (at temperatures <900 °C) spinel; and (ii) inhibition of well-dispersed CoO interacting with the alumina support, posssibly by increasing the cobalt–alumina interaction [22]. Moreover, Co-Support compound formation (Co-SCF) can be formed during reduction, especially, when alumina [19] and silica [21] are used as the supports for Co catalysts. Thus, in order to evaluate the impacts of water vapor on the stability of Co/TiO_2 catalysts, hydrothermal treatments during reduction of the catalysts was also performed. After various pretreatments, the catalysts were characterized using different techniques. XRD patterns of samples are shown in Fig. 1. It can be observed that the T1 support contained pure anatase TiO_2, whereas the T2 support is composed of rutile (19 mol%) and anatase (81 mol%) forms. XRD patterns of T1 showed strong diffraction peaks at 26, 37, 48, 55, 62, 69, 71 and 75° indicating the TiO_2 in its anatase form. The additional diffraction peaks at 27, 36, 42 and 57° can been seen in XRD patterns of the T2 support indicating the presence of rutile phase in titania. The cobalt species on both supports exhibited the similar XRD patterns regardless of the pretreatment conditions. As expected, Co_3O_4 were detected at 36, 46 and 65° after calcination of samples. However, after reduction and passivation, only diffraction peaks at 37 and 63° corresponding to CoO were observed. Basically, after reduction of the calcined samples, Co_3O_4 species was reduced to Co^0 metal. However, after passivation with air, thin layer of CoO species was formed at the catalyst surface to prevent rapid oxidation by Co^0 metal when exposed to air as also reported [19,20]. As mentioned above, Co^0 metal was formed after reduction. However, Co^0 was present in a highly dispersed form, thus, invisible by XRD. The similar results were also reported [19,20]. Reduction process is conducted in order to transform Co-oxide species into the active Co^0 metal for catalyzing CO hydrogenation. Raman spectra of all pretreated samples are shown in Fig. 2. The similar trend in Raman spectroscopy was also observed as seen for XRD results. It was found that T1 support exhibited Raman bands

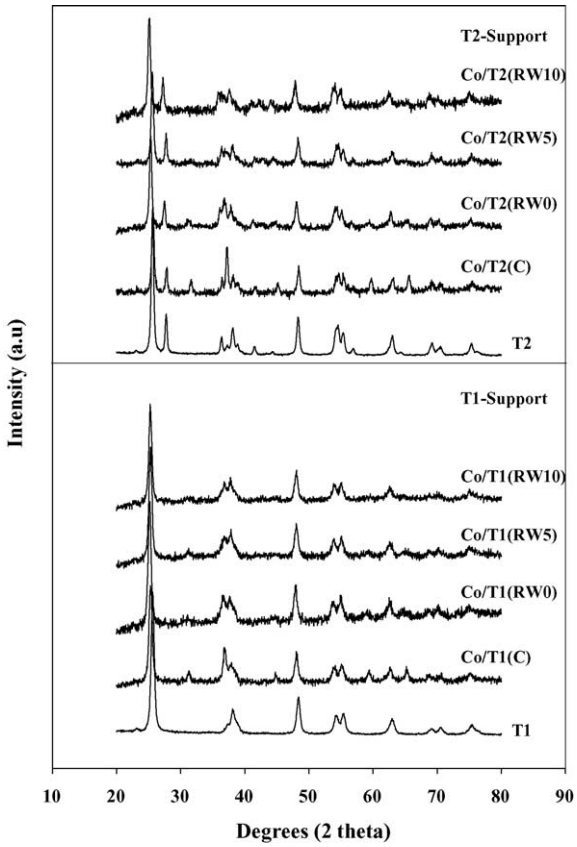

Fig. 1. XRD patterns of T1 and T2 supports, and catalyst samples pretreated under various conditions.

at 640, 514 and 397 cm^{-1} for TiO_2 in its anatase form. Besides the identical Raman bands as shown for the T1 support, the T2 support additionally exhibited a shoulder band around 445 cm^{-1} indicating TiO_2 in its rutile form. The Raman spectra for calcined samples in both T1 and T2 supports exhibited similar Raman bands at 640, 514 and 397 cm^{-1} as seen in those for T1 and T2 supports solely including two shoulders at 690 and 480 cm^{-1}, assigned to Co_3O_4 [9,19,20]. Raman spectra of all reduced samples showed the Raman bands of titania (T1 or T2) and the shoulders at 690 and 480 cm^{-1}. These can be assigned to Co_3O_4 present on catalyst surface rather than CoO (detected in the bulk by XRD) since Raman spectroscopy is more of surface technique [20]. SEM and EDX were also performed in order to study the morphologies and elemental distributions of catalyst after various pretreatments. However, no significant changes in morphologies and elemental distributions (not shown) were observed upon various pretreatment conditions used in this study. In summary, it should be noted that upon the various pretreatments even with or without hydrothermal treatments, the cobalt species on both T1 and T2 supports, essentially, exhibited the similar characteristics detected by XRD, Raman spectroscopy, and SEM/EDX. No surface compound species between Co and titania, if present, can be detected using those above techniques.

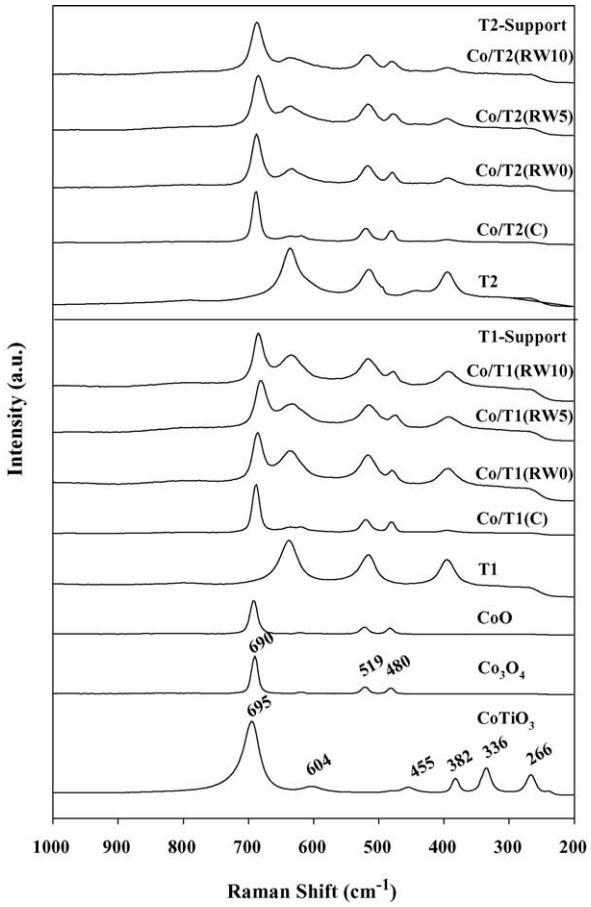

Fig. 2. Raman spectra of T1 and T2 supports, CoO, Co_3O_4, $CoTiO_3$, and catalyst samples pretreated under various conditions.

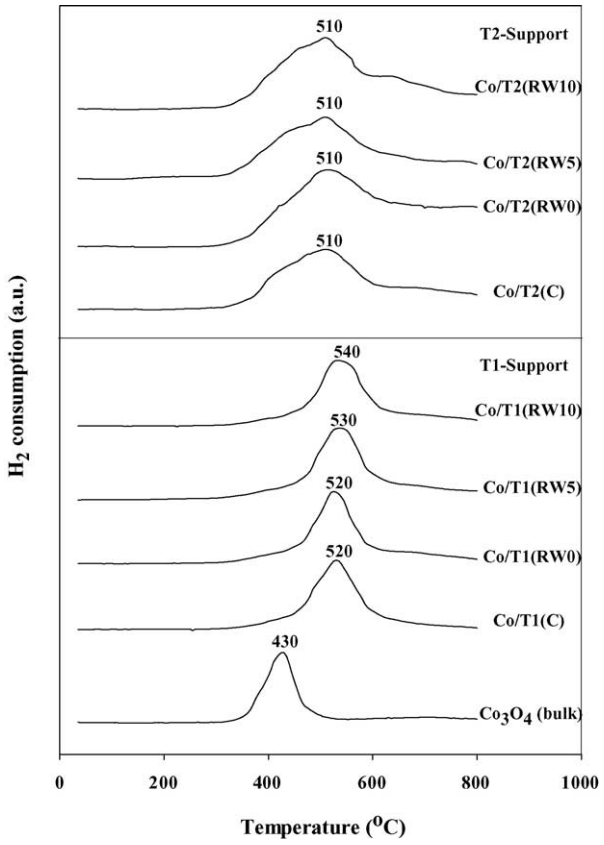

Fig. 3. TPR profiles of catalyst samples pretreated under various conditions.

TPR was performed to study reduction behaviors and to measure reducibility of catalysts. TPR profiles of all samples and Co_3O_4 are shown in Fig. 3. It was found that TPR profile of titania supports (not shown) for both T1 and T2 supports exhibited no reduction peak at this TPR condition. Only one strong reduction peak (max. at 430 °C) can be observed for bulk Co_3O_4 assigned to the overlap of two-step reduction of Co_3O_4 to CoO and then to Co^0 [22–24]. Upon the TPR conditions, the two-step reduction may or may not be observed. For T1 support, only one reduction peak located at ca. 370–620 °C (max. at 520 °C) can be observed for the calcined sample (Co/T1-C) indicated that no residual cobalt nitrates remain on the calcined samples upon calcination condition used in this study. TPR profiles for all reduced samples with T1 support were also similar exhibiting only one reduction peak located at ca. 400–620 °C. The maximum temperature at ca. 520 °C for Co/T1-RW0 was shifted about 10 and 20 °C when hydrothermal treatment was performed during reduction as seen for Co/T1-RW5 and Co/T1-RW10 samples, respectively. The shift of a reduction peak to a higher temperature (ca. 10–20 °C) indicates stronger interaction between cobalt and titania support. It is known that the amounts of Co species strongly interacted with the support are also proportional to the partial pressure of water vapor present during reduction [9,19–22]. For the T2 support, all pretreated samples also exhibited only one reduction peak (max. at 510 °C). However, it should be mentioned that there was no significant shift of the reduction temperatures upon the hydrothermal treatment during reduction indicating a lesser degree of cobalt-support interaction compared to what we have seen for the cobalt species on the T1 support. It was suggested that the presence of rutile phase (19 mol%) in T2 should result in an increase in stability of the titania support even though hydrothermal treatment was applied during reduction. An increase in stability of T2 support could be the cause for a difficulty of cobalt to interact with it.

Besides reduction behaviors obtained from TPR results, reducibilities of samples can be measured based on the peak areas below TPR curve (calibrated using Ag_2O), which are related to the amounts of hydrogen consumed during TPR [9,19–22]. The calculated reducibilities along with the BET surface areas of samples are shown in Table 1. There was no significant change in surface areas upon the pretreatment conditions used in this study. It was observed that for both T1 and T2 supports, the reducibilities decreased when the calcined samples were reduced and performed TPR indicating a loss in reducibility of cobalt oxide species after reduction [25]. The loss in reducibilities can be probably attributed to a non-reducible (at temperatures <800 °C) "Co-titanate" species

Table 1
Surface areas, reducibilities and reducibility loss after reduction of samples after various pretreatments

Samples	Surface area ($m^2\ g^{-1}$)	Reducibility during TPR at 35–800 °C (%)[a,b]	Reducibility loss after reduction (%)[c]
T1	70	0	–
T2	49	0	–
Co/T1 (C)	52	92	n/a
Co/T2 (C)	37	78	n/a
Co/T1 (RW0)	49	70	24
Co/T2 (RW0)	37	74	5
Co/T1 (RW5)	46	68	26
Co/T2 (RW5)	37	72	8
Co/T1 (RW10)	46	64	30
Co/T2 (RW10)	36	68	13

[a] The reduced samples were recalcined at the original calcination conditions prior to performing TPR. The reducibility was calculated based on the area below TPR curve, which was related to the amounts of H_2 consumed during TPR (calibrated using Ag_2O).
[b] Measurement error is ±5%.
[c] Reducibility loss (%) after reduction was calculated from [(reducibility of calcined sample − reducibility of reduced sample) × 100]/reducibility of calcined sample.

formed during standard reduction [25]. However, when considering the reducibility loss of the reduced samples without hydrothermal treatment (RW0 samples), it was found that the reducibility loss after reduction for Co/T2-RW0 sample was only 5%, whereas the 24% reducibility loss after reduction was observed for Co/T1-RW0 sample. A degree of reducibility loss also increased with the amounts of water vapor added during reduction for both T1 and T2 supports. In order to illustrate the reducibility loss upon the hydrothermal treatment during standard reduction for both T1 and T2 supports, Fig. 4 is also present. This is to provide a better idea how the presence of rutile phase leads to an increase in stability of the catalysts upon reduction and hydrothermal treatments in term of the reducibility loss after reduction under various conditions.

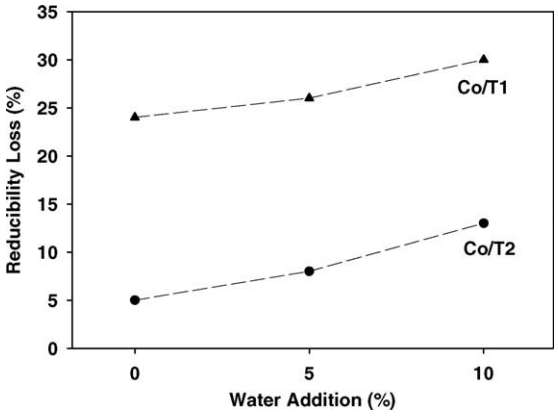

Fig. 4. A comparison of reducibility loss (%) during reduction with hydrothermal treatment for Co/T1 and Co/T2 catalyst samples.

3.2. Catalytic properties

In order to determine the effect of crystalline phases of titania on the catalytic properties of Co/TiO_2, CO hydrogenation was also conducted in a fixed-bed flow reactor under differential conditions. Results obtained from the reaction study are shown in Table 2. It was found that both initial and steady-state rates increased significantly upon the presence of rutile phase in titania as seen for catalysts on the T2 support. However, the increased activities for catalysts on the T1 support strongly depended on the pretreatment conditions used. For catalysts on the T1 support, it was shown that decreases in both initial and steady-state activities were proportional to the amounts of water vapors added during standard reduction. It should be also noted that decreases in activities were also related to the loss in reducibilities after standard reduction as well. Considering both initial and steady-state rates for catalysts on the T2 support, the phenomenon was essentially different from those for the T1 support. It was found that activities for catalysts on the T2 support exhibited much higher activities than those on the T1 support, especially, at the same hydrothermal treatment conditions. Moreover, the

Table 2
Reaction study during CO hydrogenation of catalyst samples pretreated under various conditions

Samples	CO conversion (%)[a]		Rate ($\times 10^2$ $gCH_2\ g_{cat}\ h^{-1}$)[b]		CH_4 selectivity (%)	
	Initial[c]	SS[d]	Initial	SS	Initial	SS
Co/T1 (C)	3.7	2.1	1.4	0.8	71	68
Co/T2 (C)	67.4	54.9	25	21	94	96
Co/T1 (RW0)	1.5	0.7	0.6	0.3	68	65
Co/T2 (RW0)	60.8	53.1	23	20	94	94
Co/T1 (RW5)	0.8	0.5	0.3	0.2	71	70
Co/T2 (RW5)	60.6	52.8	23	20	98	98
Co/T1 (RW10)	0.3	0.1	0.1	0.03	73	69
Co/T2 (RW10)	60.2	52.6	23	19	95	96

[a] CO hydrogenation was carried out at 220 °C, 1 atm and $H_2/CO/He = 20/2/8$ cc min^{-1}.
[b] Error ±5%. Rate of $-CH_2-$ formed as same as moles of CO converted represented the repeating unit of all hydrocarbon chains in product stream.
[c] After 5 min of reaction.
[d] After 5 h of reaction.

Table 3
Influence of surface area of TiO_2 on catalytic properties of supported cobalt catalysts during CO hydrogenation

Samples	Surface area ($m^2\ g^{-1}$)	CO conversion (%)[a]		Rate ($10^2\ gCH_2\ g_{cat}\ h^{-1}$)[b]	
		Initial[c]	SS[d]	Initial	SS
Co/T1 (C)	70	3.7	2.1	1.4	0.8
Co/T3 (C)[e]	145	42.7	9.4	16	4
Co/T4 (C)[f]	170	59.6	12.2	22	4
Co/T2 (C)	49	67.4	54.9	25	21

[a] CO hydrogenation was carried out at 220 °C, 1 atm and $H_2/CO/He = 20/2/8$ cc min^{-1}.
[b] Error ±5%.
[c] After 5 min of reaction.
[d] After 5 h of reaction.
[e] T3 is TiO_2 (pure anatase) which has surface area of 145 $m^2\ g^{-1}$.
[f] T4 is TiO_2 (pure anatase) which has surface area of 170 $m^2\ g^{-1}$.

initial activities of catalysts on the T2 support exhibited a lesser degree of decreased rates until they reached the steady-state rates compared to those on the T1 support. In addition, for catalysts on the T2 support, both initial and steady-state rates showed consistency in rates regardless of the pretreatment conditions used indicating high stability of catalysts. This is suggested that the hydrothermal treatment conditions used have no effect on the catalytic activities during CO hydrogenation of catalysts on the T2 support. This can be explained by the increased stability of T2 support due to the presence of rutile phase in titania resulting in an inhibition of Co-support compound formation (Co-SCF) [19,20] in the titania support [25].

Since the surface areas of the T1 (70 $m^2\ g^{-1}$) and T2 (49 $m^2\ g^{-1}$) supports were slightly different, one might think that a change in surface areas of the supports probably has the effect on rates as well. In order to elucidate this doubt, reaction study was also conducted using titania supports (anatase form only) with various surface areas. Results obtained from the reaction study are shown in Table 3. It was found that basically, both initial and steady-state activities increased with increasing surface areas from 70 to 170 $m^2\ g^{-1}$ for catalysts on pure anatase titania. This should be due to higher Co dispersion in larger surface areas of supports leading to an increase in the number of reduced surface Co metal atoms available for catalyzing the reaction. Thus, if one considered the dependence of rates based on the surface areas solely, catalysts on the T2 support, which had smaller surface areas would result in lower activities due to a decreased surface area. However, it is not true for what we have found in this present study. Essentially, even though the surface area of the T2 support was only 49 $m^2\ g^{-1}$, which was smaller than that for the pure anatase titania, activities of catalysts on the T2 support were still exceptional high with the presence of rutile phase in titania. This indicated that the presence of rutile phase in titania can result in an enhancement of catalytic activities of Co/TiO_2 catalyst during CO hydrogenation. Increases in activities were probably due to: (i) high stability to the hydrothermal treatment of the support used; and (ii) the presence of a higher number of reduced Co metal atoms resulted from the lesser amounts of Co-SCF.

Considering the selectivity of products during methanation, which is also shown in Table 2. It was found that catalysts on the T2 support exhibited higher selectivity to methane compared to those on the T1 support. This was suggested that catalysts on the T1 support produced more long chain hydrocarbons than those on the T2 support. This indicated that the presence of rutile phase on titania probably resulted in a lesser amounts of long chain hydrocarbons. In general, it has been known that catalytic activities of supported Co catalyst depend only on the number of surface reduced cobalt atoms available for catalyzing the reaction. Mostly, changes in catalytic activities do not alter the selectivity of products since only the number of active sites change, but the nature of active sites would be the same. However, in this case, we found a slight change in product selectivity. This indicated that the presence of rutile phase in titania affected not only on activities of Co/TiO_2 catalysts, but perhaps also on the selectivity of products as well. In order to give the best answer for how the presence of rutile phase affects the selectivity of products during CO hydrogenation, a rigorous study should be further investigated in more details. It is recommended that techniques such as steady-state isotropic transient kinetic analysis (SSITKA) or other surface analysis techniques must be applied in order to provide more details on the surface intermediates. Thus, this is not the main focus of our present study at this time. Besides, influences of rutile phase in titania on product distributions, an investigation of how the mole ratios of rutile per anatase phase affect the catalytic properties will be our main focus in the near future.

4. Conclusions

The present study has shown the dependence of crystalline phases in titania on the catalytic properties during CO hydrogenation of Co/TiO_2 catalysts. The presence of rutile phase (19 mol%) in titania resulted in significant increases in the catalytic activities during CO hydrogenation. This is mostly due to an increase in stability of the titania support with the presence of rutile phase. It was found that the presence of rutile phase enhanced the stability of the titania support and

also catalysts themselves leading to lesser degrees of a loss in reducibility after hydrothermal treatments during reduction of catalysts. It was proposed that the presence of rutile phase in titania stabilized the catalysts probably due to two reasons: (i) block the formation of Co species strongly interacted with the titania support or Co-SCF; and (ii) inhibition of the impact of water vapor produced during reduction.

Acknowledgements

We gratefully acknowledge the financial support by the National Research Council of Thailand (NRCT), the Thailand Research Fund (TRF) and Thailand-Japan Transfer Technology Project (TJTTP-JBIC). We would like to thank Prof. James G. Goodwin, Jr. at Clemson University for initiating this kind of project. We would like to extend our thanks to the National Metal and Materials Technology Center (MTECH) for Raman spectroscopy analysis.

References

[1] H.P. Wither Jr., K.F. Eliezer, J.W. Mechell, Ind. Eng. Chem. Res. 29 (1990) 1807.
[2] E. Iglesia, Appl. Catal. A 161 (1997) 59.
[3] R.C. Brady, R.J. Pettie, J. Am. Chem. Soc. 103 (1981) 1287.
[4] A. Martinez, C. Lopez, F. Marquez, I. Duaz, J. Catal. 220 (2003) 486.
[5] J. Panpranot, J.G. Goodwin Jr., A. Sayari, Catal. Today 77 (2002) 269.
[6] J. Panpranot, J.G. Goodwin Jr., A. Sayari, J. Catal. 211 (2002) 530.
[7] S.L. Sun, I. Isubaki, K. Fujimoto, Appl. Catal. A 202 (2000) 121.
[8] S. Ali, B. Chen, J.G. Goodwin Jr., J. Catal. 157 (1995) 35.
[9] B. Jongsomjit, J. Panpranot, J.G. Goodwin Jr., J. Catal. 215 (2003) 66.
[10] T. Das, G. Jacobs, P.M. Patterson, W.A. Conner, J.L. Li, B.H. Davis, Fuel 82 (2003) 805.
[11] G. Jacobs, P.M. Patterson, Y.Q. Zhang, T. Das, J.L. Li, B.H. Davis, Appl. Catal. A 233 (2002) 215.
[12] M. Rothaemel, K.F. Hanssen, E.A. Blekkan, D. Schanke, A. Holmen, Catal. Today 38 (1997) 79.
[13] V. Ragaini, R. Carli, C.L. Bianchi, D. Lorenzetti, G. Vergani, Appl. Catal. A 139 (1996) 17.
[14] V. Ragaini, R. Carli, C.L. Bianchi, D. Lorenzetti, G. Predieri, P. Moggi, Appl. Catal. A 139 (1996) 31.
[15] J.L. Li, G. Jacobs, T. Das, B.H. Davis, Appl. Catal. A 233 (2002) 255.
[16] G. Jacobs, T. Das, Y.Q. Zhang, J.L. Li, G. Racoillet, B.H. Davis, Appl. Catal. A 233 (2002) 263.
[17] J.L. Li, L.G. Xu, R. Keogh, B.H. Davis, Catal. Lett. 70 (2000) 127.
[18] X.H. Li, K. Asami, M.F. Luo, K. Michiki, N. Tsubaki, K. Fujimoto, Catal. Today 84 (2003) 59.
[19] B. Jongsomjit, J. Panpranot, J.G. Goodwin Jr., J. Catal. 204 (2001) 98.
[20] B. Jongsomjit, J.G. Goodwin Jr., Catal. Today 77 (2002) 191.
[21] A. Kogelbaue, J.C. Weber, J.G. Goodwin Jr., Catal. Lett. 34 (1995) 269.
[22] Y. Zhang, D. Wei, S. Hammache, J.G. Goodwin Jr., J. Catal. 188 (1999) 281.
[23] D. Schanke, S. Vada, E.A. Blekkan, A. Hilmen, A. Hoff, A. Holmen, J. Catal. 156 (1995) 85.
[24] B.A. Sexton, A.E. Hughes, T.W. Turney, J. Catal. 97 (1986) 390.
[25] B. Jongsomjit, C. Sakdamnuson, J.G. Goodwin Jr., P. Praserthdam, Catal. Lett. 94 (2004) 209.

LLDPE/nano-silica composites synthesized via *in situ* polymerization of ethylene/1-hexene with MAO/metallocene catalyst

BUNJERD JONGSOMJIT*, EKKRACHAN CHAICHANA, PIYASAN PRASERTHDAM
Center of Excellence on Catalysis and Catalytic Reaction Engineering, Department of Chemical Engineering, Faculty of Engineering, Chulalongkorn University, Bangkok 10330, Thailand
E-mail: bunjerd.j@chula.ac.th

It is known that the copolymerization of ethylene with higher 1-olefins is a commercial importance for productions of elastomer and linear low-density polyethylene (LLDPE). LLDPE (density 0.920 to 0.940) is one of the most widely used polyolefins in many applications, especially, for plastic films. However, in some cases, the use of polyolefins or LLDPE is limited by their drawbacks such as low mechanical strength, low thermal resistance, poor optical properties and so on. Thus, in order to improve the specific properties of these polymers, some additives need to be blended with them.

It has been reported that blending polymer with inorganic materials is considered as a powerful method to produce new materials called polymer composites or filled polymers. However, due to the significant development in nano-technologies in the recent years, nano-inorganic materials such as SiO_2, Al_2O_3 and TiO_2 have brought much attention to this research field. Therefore, the polymer composites filled with nano-inorganic materials are well recognized as polymer nano-composites. Essentially, addition of the nano-materials into polymers may lead to overcome the drawbacks and produce new materials, which are considered to be robust. Basically, there are three methods used to produce the filled polymer; (i) melt mixing, (ii) solution blending, and (iii) *in situ* polymerization. Due to the direct synthesis via polymerization along with the presence of nano-materials, the *in situ* polymerization is perhaps considered to be the most powerful techniques to produce polymer nano-composites with good dispersion of the nano-particles into polymer matrix. Although, many authors [1–6] have studied LLDPE composites only synthesized via melt mixing and solution blending, no further reports have been done on synthesizing polymer nano-composites via the *in situ* polymerization with metallocene catalysts.

In the present study, LLDPE/nano-SiO_2 composites synthesized via the *in situ* polymerization with MAO/metallocene catalyst was investigated for the first time. The nano-SiO_2 and nano-SiO_2 doped Al_2O_3 filled materials were synthesized using sol-gel method [7] to obtain the nano-SiO_2 with particle size of ca. 50 nm. The amounts of nano-materials filled were also varied. Yields, activities, and polymer morphologies were discussed.

The preparation of LLDPE/nano-composites via *in situ* polymerization was performed as follows; all chemicals [nano-SiO_2, nanoSiO_2 doped Al_2O_3, toluene, rac-ethylenebis (indenyl) zirconium dichloride [$Et(Ind)_2ZrCl_2$], methylaluminoxane (MAO), trimethylaluminum (TMA) and 1-hexene] were manipulated under an inert atmosphere using a vacuum glove box and/or Schelenk techniques. The nano-materials were heated under vacuum at 400 °C for 6 hr prior to impregnation with MAO. In order to impregnate MAO onto the nano-materials, the method was described as follows. One gram of the nano-materials was reacted with the desired amount of MAO at room temperature and stirred for 30 min. The solvent was then removed from the mixture. About 20 ml of toluene was added into the obtained precipitate, the mixture was stirred for 5 min, and then the solvent was removed. This procedure was done for five times to ensure the removal of impurities. Then, the solid part was dried under vacuum at room temperature to obtain white powder of nano-materials/ MAO.

Polymerization was conducted upon the methods as follows. The ethylene/1-hexene copolymerization reaction was carried out in a 100-ml semi-batch stainless steel autoclave reactor equipped with a magnetic stirrer. At first, 0.1, 0.2, and 0.3 g of the nano-materials/MAO ($[Al]_{MAO}/[Zr]$ = 1135, 2270, and 3405) and 0.018 mole of 1-hexene along with toluene (to make the total

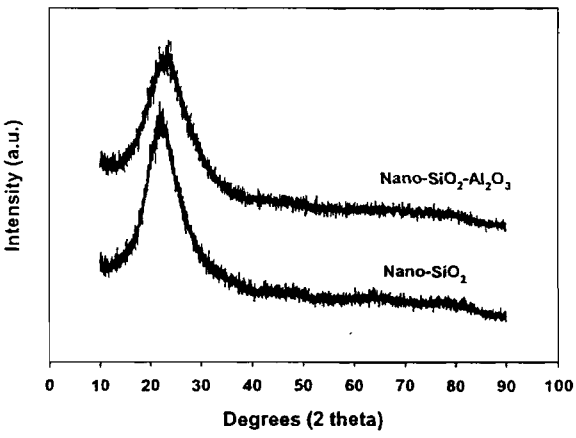

Figure 1 XRD patterns of nano-SiO_2 and nano-SiO_2-Al_2O_3.

*Author to whom all correspondence should be addressed.

0022–2461

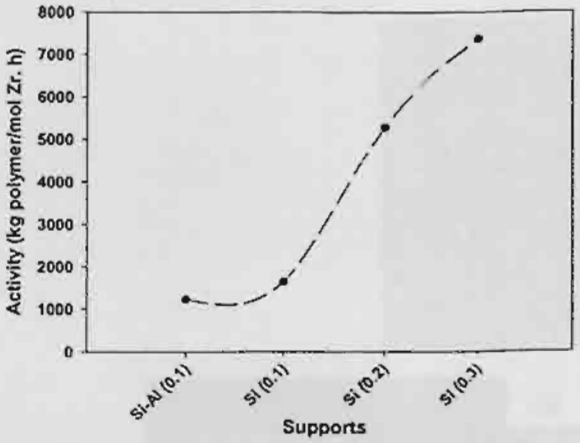

Figure 2 Activity profile with various amounts of support used.

volume of 30 ml) were put into the reactor. The desired amount of $Et(Ind)_2ZrCl_2$ (5×10^{-5} M) and TMA ($[Al]_{TMA}/[Zr] = 2500$) was mixed and stirred for 5-min aging at room temperature, separately, and then was injected into the reactor. The reactor was frozen in liquid nitrogen to stop reaction for 15 min and then the reactor was evacuated to remove argon. The reactor was heated up to polymerization temperature (70 °C). To start reaction, 0.018 mole of ethylene was fed into the reactor containing the comonomer and catalyst mixtures. After all ethylene was consumed, the reaction was terminated by addition of acidic methanol (0.1% HCl in methanol) and stirred for 30 min. After filtration, the obtained copolymer (white powder) was washed with methanol and dried at room temperature. The LLDPE/nano-SiO_2 composites obtained were characterized using scanning electron microscopy (SEM) and energy dispersive X-ray spectroscopy (EDX) to study morphologies and elemental distribution, respectively.

TABLE I Activity and yield of LLDPE/nano-composites via *in situ* polymerization with metallocene catalyst

Nano-filled	Amounts/Run (g)	Yield (g)	Time (s)	Activity (kg pol./mol. Zr.h)
SiO_2–Al_2O_3	0.1	0.2006	450	1234
SiO_2	0.1	0.2147	360	1652
SiO_2	0.2	0.6070	318	5288
SiO_2	0.3	0.8382	315	7369

XRD patterns of nano-SiO_2 and nano-SiO_2-Al_2O_3 are shown in Fig. 1. It was found that XRD patterns for both materials exhibited similar patterns assigning to amorphous silica. No XRD peaks of Al_2O_3 were detected indicating highly dispersed forms of it. After impregnation of MAO onto the nano-particles, copolymerization of ethylene/1-hexene was performed with various conditions based on changing types and/or amounts of the nano-particles used. Activities and yields of LLDPE/nono-composites are shown in Table I. It was observed that activities and yields dramatically increased with increasing the amounts of SiO_2 particles used due to increased MAO as a cocatalyst. However, at the same amount (0.1 g) of particles, the SiO_2-Al_2O_3 exhibited the lowest yield and activity of any other samples. A comparison of activities is also shown in Fig. 2. It should be noted that activities of LLDPE/nano-SiO_2 composites obtained in this present study were much lower (about three times) compared to the LLDPE/micron-SiO_2 composite as reported by our group [8]. This was probably due to more steric hindrance arising from the nano-particles. Morphologes of LLDPE/nano composites are shown in Fig. 3.

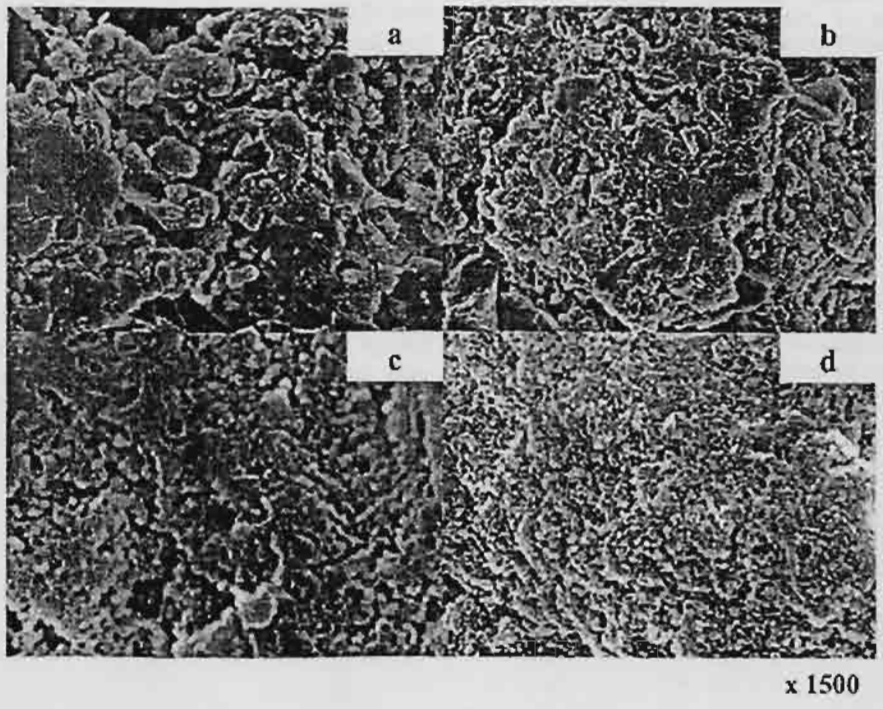

Figure 3 Morphologies of LLDPE/nano composites with: (a) SiO_2–Al_2O_3 (0.1 g), (b) SiO_2 (0.1 g), (c) SiO_2 (0.2 g), and (d) SiO_2 (0.3 g).

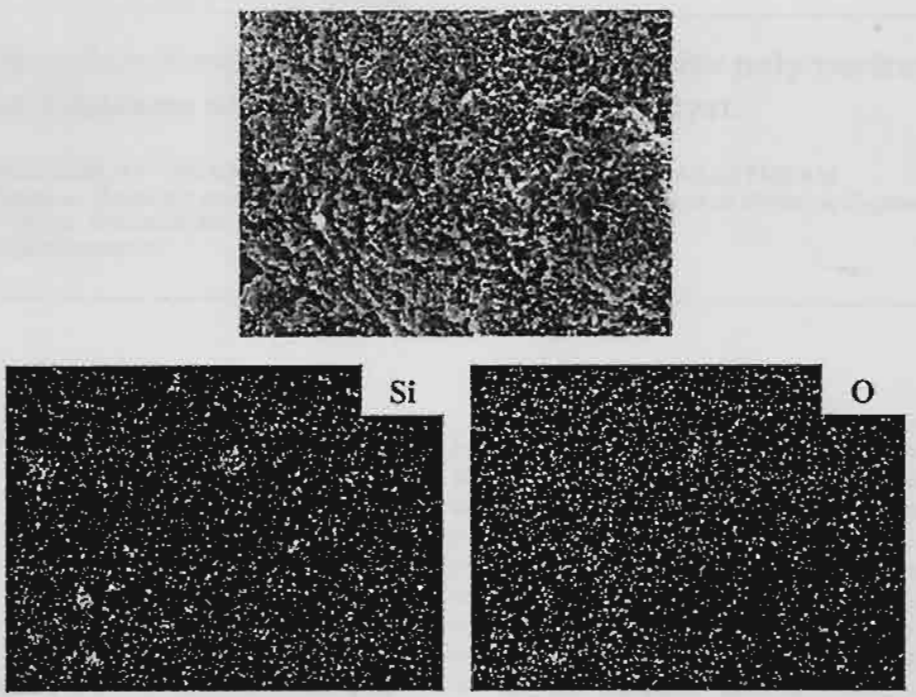

Figure 4 EDX mapping of LLDPE/nano-SiO_2 composite with SiO_2 (0.3 g) indicating distribution of Si and O.

It can be observed that with using SiO_2-Al_2O_3 (0.1 g), SiO_2 (0.1 g), and SiO_2 (0.2 g), morphologies [Fig. 3a–c] were found to be similar indicating only the polymer texture as seen in ref. [8]. However, with increasing the amount of nano-SiO_2 to 0.3 g, the morphology as shown in Fig. 3d was significantly changed indicating better combination between the silica and polymer textures. This was suggested that the LLDPE/nano-SiO_2 composite can be obtained at a certain amount of the nano-SiO_2 particles used. In order to identify the distribution of SiO_2 particles in the polymer matrix, EDX mapping was performed on the distribution of Si and O elements as shown in Fig. 4. It can be observed that Si and O elements exhibited good distribution all over the polymer matrix indicating good dispersion of nano-SiO_2 particles.

In summary, LLDPE/nano-SiO_2 composites can be obtained via the *in situ* polymerization with MAO/metallocene catalyst. It was found that silica particles were well dispersed in the polymer matrix at some certain amounts of them. However, activities and yields of polymerization were apparently low probably due to more steric hindrance arising from the nano-particles. Thus, polymerization conditions, catalysts used, and types of nano-particles need to be further investigated in order to increase productivity.

Acknowledgments

The authors would like to thank the Thailand Research Fund (TRF), National Research Council of Thailand (NRCT) and Thailand-Japan Transfer Technology Project (TJTTP-JBIC) for the financial support of this work. The authors would also like to thanks Prof. Takeshi Shiono at Hiroshima University, Japan, for his kind adviee throughout this project.

References

1. C. J. R. VERBEEK, *Mater. Lett.* 56 (2002) 226.
2. R. NAWANG, I. D. DANJAJI, U. S. ISHIAKU, H. ISMAIL and Z. A. MOHD ISHAK, *Polym. Testing.* 20 (2001) 167.
3. Y. HAUNG, S. JIANG, L. WU and Y. HUA, *ibid.* 23 (2004) 9.
4. Y. Q. HUANG, Y. Q. ZHANG and Y. Q. HUA, *J. Mater. Sci. Lett.* 22 (2003) 997.
5. I. D. DANJAJI, R. NAWANG, U. S. ISHIAKU, H. ISMAIL and Z. A. MOHD ISHAK, *Polym. Testing* 21 (2002) 75.
6. C. J. R. VERBEEK, *Mater. Lett.* 52 (2002) 453.
7. M. BUCKLEY and M. GREENBLATT, *J. Chem. Edu.* 71 (1994) 599.
8. B. JONGSOMJIT, P. PRASERTHDAM and P. KAEWKRAJANG, *Mater. Chem. Phys.* 86 (2004) 243.

Received 20 September
and accepted 7 October 2004

Available online at www.sciencedirect.com
SCIENCE DIRECT®
Materials Chemistry and Physics 92 (2005) 572–577
MATERIALS CHEMISTRY AND PHYSICS
www.elsevier.com/locate/matchemphys

Study of cobalt dispersion on titania consisting various rutile: anatase ratios

Bunjerd Jongsomjit*, Tipnapa Wongsalee, Piyasan Praserthdam

Center of Excellence on Catalysis and Catalytic Reaction Engineering, Department of Chemical Engineering, Faculty of Engineering, Chulalongkorn University, Bangkok 10330, Thailand

Received 29 October 2004; received in revised form 25 January 2005; accepted 16 February 2005

Abstract

The number of reduced cobalt metal surface atoms in Co/TiO_2 was found to increase with the presence of rutile phase. It was suggested that the increased number of reduced cobalt metal surface atoms be attributed to highly dispersed cobalt oxide species as seen by the transmission electron microscopy (TEM) technique. Besides the dispersion of cobalt oxide species, it should be noted that the presence of rutile phase in titania could facilitate the reduction of highly dispersed cobalt oxides species into the reduced cobalt metal surface atoms. It was concluded that both highly dispersed cobalt oxide species and the presence of rutile phase could result in the large number of reduced cobalt metal surface atoms.

Keywords: Titania; Cobalt; Catalyst; TEM; Chemisorption

1. Introduction

Inorganic materials such as silica (SiO_2), alumina (Al_2O_3), and titania (TiO_2) are commonly used as a carrier or support for catalytic materials due to their high surface areas, high thermal stability and high mechanical resistance. Thus, an active catalytic phase such as metal or metal oxide species can be highly dispersed on the high surface area supports. It is noted that high dispersion of the active catalytic phase may lead to great accessibility to utilize the active sites for surface reaction. Supported cobalt (Co) catalysts are preferred for Fischer–Tropsch synthesis (FTS) based on natural gas [1] due to their high activities for FTS, high selectivity for long chain hydrocarbons and low activities for the competitive water–gas shift (WGS) reaction [2,3]. Many inorganic supports such as silica [4–8], alumina [9–14], titania [15–17] and zeolites [18] have been extensively studied for supported Co catalysts for years. It is known that in general, the catalytic properties depend on reaction conditions, catalyst composition, type of inorganic support and the degree of metal dispersion as well.

It is reported that during the past decades, titania-supported Co catalysts have been investigated widely by many authors, especially for the application of FTS in a continuously stirred tank reactor (CSTR) [15–17]. However, it should be noted that titania itself has different crystalline phases such as anatase, brookite and rutile phase. Thus, the differences in compositions of crystalline phases could result in changes on physical and chemical properties of titania, then consequently for the dispersion of cobalt. In order to give a better understanding of those, the focus of this present study was to investigate the cobalt dispersion on titania consisting various ratios of rutile:anatase. The Co/TiO_2 was prepared and then characterized using different characterization techniques.

2. Experimental

2.1. Material preparation

2.1.1. Preparation of titania support consisting various rutile:anatase ratios

The various ratios of rutile:anatase in titania support were obtained by calcination of pure anatase titania (obtained from

* Corresponding author. Tel.: +66 2 2186869; fax: +66 2 2186766.
E-mail address: bunjerd.j@chula.ac.th (B. Jongsomjit).

0254-0584/$ – see front matter © 2005 Elsevier B.V. All rights reserved.
doi:10.1016/j.matchemphys.2005.02.016

Ishihara Sangyo, Japan) in air at temperatures between 800 and 1000 °C for 4 h. The high space velocity of air flow (16,000 h^{-1}) insured the gradual phase transformation to avoid rapid sintering of samples. The ratios of rutile:anatase were determined by XRD according to the method described by Jung et al. [19] as follows:

$$\%\text{Rutile} = \frac{1}{\left[\left(\frac{A}{R}\right)0.884 + 1\right]} \times 100$$

where, A and R are the peak area for major anatase ($2\theta = 25°$) and rutile phase ($2\theta = 28°$), respectively.

2.1.2. Preparation of Co/TiO_2 samples

A 20 wt.% of Co/TiO_2 was prepared by the incipient wetness impregnation. A designed amount of cobalt nitrate [$Co(NO_3)\cdot 6H_2O$] was dissolved in deionized water and then impregnated onto TiO_2 containing various ratios of rutile:anatase obtained from Section 2.1.1. The sample was dried at 110 °C for 12 h and calcined in air at 500 °C for 4 h.

2.2. Nomenclature

The nomenclature used for Co/TiO_2 samples in this study is following:

- Rn: titania support consisting *n*% of rutile phase (R);
- Co/Rn: titania support containing *n*% of rutile phase (R)-supported cobalt.

2.3. Characterization

2.3.1. BET surface area

BET surface area of the samples with various rutile:anatase ratios of titania was performed to determine if the total surface area changes. It was determined using N_2 adsorption at 77 K in a Micromeritics ASAP 2010.

2.3.2. X-ray diffraction

XRD was performed to determine the bulk crystalline phases of samples. It was conducted using a SIEMENS D-5000 X-ray diffractometer with Cu Kα (λ = 1.54439 Å). The spectra were scanned at a rate of 2.4° min^{-1} in the range $2\theta = 20$–80°.

2.3.3. Scanning electron microscopy and energy dispersive X-ray spectroscopy

SEM and EDX were used to determine the sample morphologies and elemental distribution throughout the sample granules, respectively. The SEM of JEOL model JSM-5800LV was applied. EDX was performed using Link Isis series 300 program.

2.3.4. Hydrogen chemisorption

Static H_2 chemisorption at 100 °C on the reduced samples was used to determine the number of reduced surface cobalt metal atoms. This is related to the overall activity of the samples during CO hydrogenation. Gas volumetric chemisorption at 100 °C was performed using the method described by Reuel and Bartholomew [20]. The experiment was performed in a Micromeritics ASAP 2010 using ASAP 2010C V3.00 software.

2.3.5. Transmission electron microscopy (TEM)

The dispersion of cobalt oxide species on the titania supports were determined using a JEOL-TEM 200CX transmission electron spectroscopy operated at 100 kV with 100 k magnification.

3. Results and discussion

The present study focused on investigation of cobalt dispersion on titania consisting various ratios of rutile:anatase. After calcination of the pure anatase titania under calcination temperatures ranged between 800 and 1000 °C for 4 h, the phase transformation from anatase to rutile phase in titania technically occurred. The amounts of rutile phase formed during calcination depend on temperatures used. The high space velocity of the air flow at 16,000 h^{-1} was applied during the calcination process in order to minimize the rapid sintering due to the phase transformation of titania. It was found that after calcination of the pure anatase sample, the amounts of rutile phase obtained ranged between 3 and 99%. The titania supports containing rutile phase of ca. 0, 3, 19, 40, 96, and 99% were named as R0, R3, R19, R40, R96, and R99, respectively. The surface areas of titania containing various rutile:anatase ratios essentially decreased from 70 $m^2\ g^{-1}$ for the R0 sample (pure anatase titania) to 49 $m^2\ g^{-1}$ for the R99 sample (99% rutile titania). XRD patterns of titania samples calcined at various temperatures between 800 and 1000 °C are shown in Fig. 1. For the pure anatase titania (R0), XRD peaks of the anatase phase of titania at 25° (major), 37°, 48°, 55°, 56°, 62°, 71°, and 75° were evident.

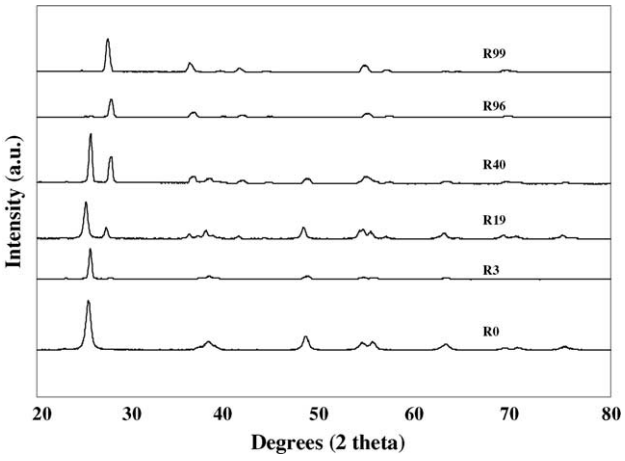

Fig. 1. XRD patterns of titania consisting various ratios of rutile:anatase phase.

After calcination of pure anatase titania sample, it was observed that besides the XRD peaks of pure anatase titania as shown above XRD peaks at 28° (major), 36°, 42°, and 57° were gradually seen. These peaks were assigned to the rutile phase essentially formed after calcination of the pure anatase titania. Apparently, the major peak at 28° of rutile phase gradually increased with increasing the calcination temperatures indicating higher content of rutile phase in titania was obtained. It was shown that the transformation from anatase to rutile phase (R99) was almost complete at temperature of ca. 1000 °C resulting in the disappearance of XRD peaks for the anatase phase of titania. After various titania supports were obtained, the preparation of Co/TiO_2 via various rutile:anatase ratios of titania was consequently conducted in order to investigate the effect of various ratios of rutile:anatase in titania supports on characteristics, especially the cobalt dispersion of Co/TiO_2.

A 20 wt.% of cobalt supported on titania consisting of various ratios of rutile:anatase phase was prepared by the conventional incipient wetness impregnation method. The XRD patterns for all calcined samples (Co/TiO_2) are shown in Fig. 2. After calcination, all calcined samples exhibited XRD peaks, which were identical with those for the corresponding titania supports. This indicated that there was no further phase transformation from anatase to rutile occurred after calcination (at temperature ca. 500 °C for 4 h) of the samples. Besides the XRD peaks of the corresponding titania supports detected, all calcined samples also exhibited weak XRD peaks at 31°, 36°, and 65°, which were assigned to the presence of Co_3O_4. However, at high content of rutile phase, the XRD peaks of Co_3O_4 were gradually diminished due to the hindrance of strong intensity of XRD peaks for the rutile phase of titania.

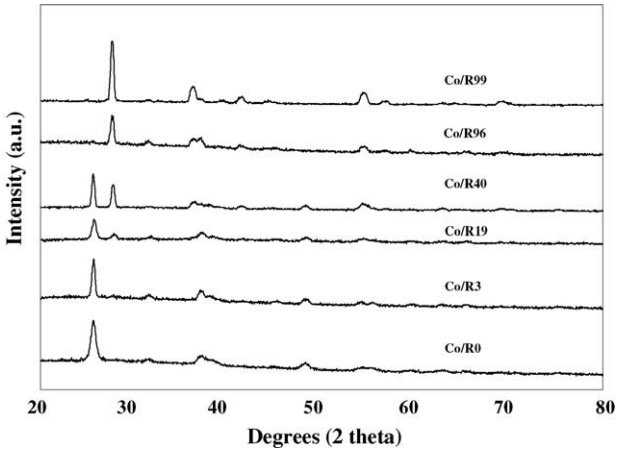

Fig. 2. XRD patterns of calcined Co/TiO_2 with various ratios of rutile:anatase phase.

Based on the XRD results, it was clear that Co_3O_4 species was definitely present in a highly dispersed form.

SEM and EDX were also conducted in order to study the morphologies and elemental distribution of the samples, respectively. Apparently, SEM micrographs and EDX mapping for all samples exhibited similar trends of morphologies and elemental (Co, Ti, and O) distributions. The typical SEM micrographs along with the EDX mapping (for Co, Ti, and O) for Co/R19 sample are illustrated in Fig. 3 indicating the external surface of the sample granule. It can be seen that the cobalt oxide species were well dispersed and distributed (shown on EDX mapping) all over the sample granule. Thus, SEM and EDX can not differentiate morphologies and elemental distributions of Co/TiO_2 consisting of various

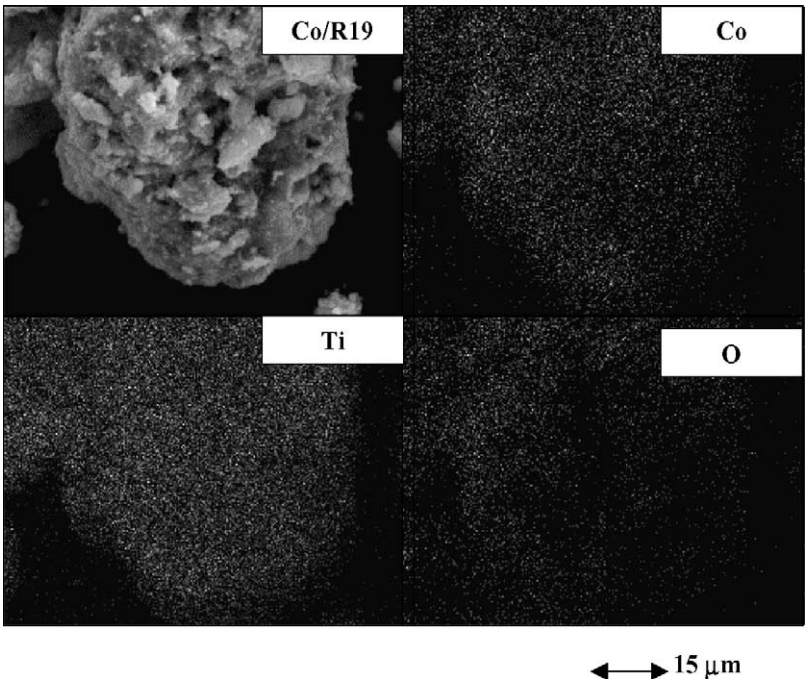

Fig. 3. SEM micrograph and EDX mapping of Co/R19 sample.

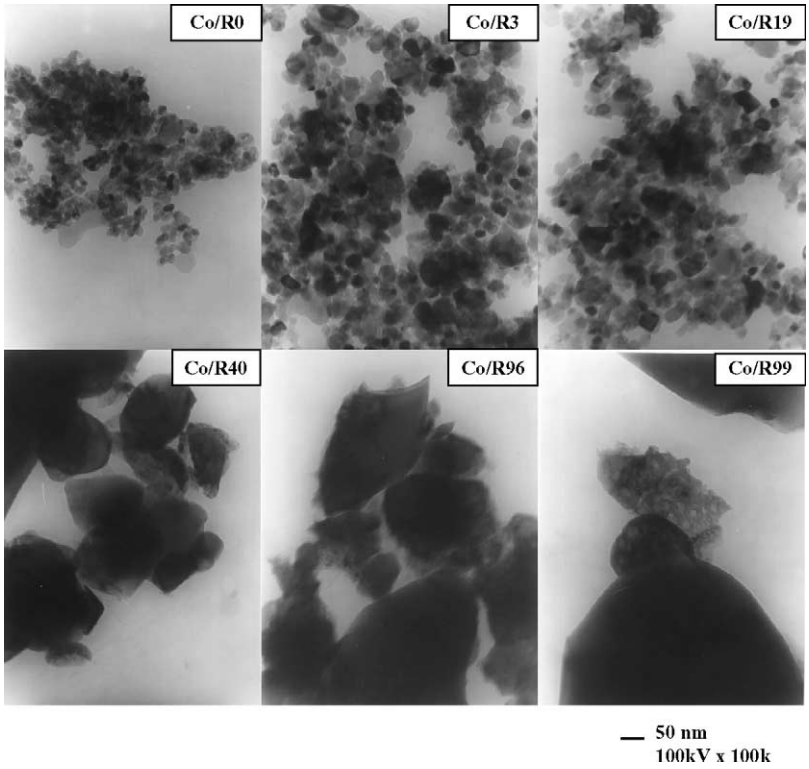

Fig. 4. TEM micrographs of Co/TiO_2 with various ratios of rutile:anatase phase.

ratios of rutile:anatase. In order to determine the dispersion of cobalt oxide species on titania, a more powerful technique such as TEM was applied to all samples. The TEM micrographs for all samples are shown in Fig. 4. The dark spots represented cobalt oxide species present after calcination of samples dispersing on titania consisting of various ratios of rutile:anatase. It can be observed that cobalt oxide species were highly dispersed on the titania supports for Co/R0, Co/R3, and Co/R19 samples resulting in an appearance of smaller cobalt oxide patches present. However, the degree of dispersion for cobalt oxide species essentially decreased with increasing the rutile phase in titania from 40 to 99% as seen for Co/R40, Co/R96, and Co/R99 samples resulting in the observation of larger cobalt oxide patches. It is suggested that the presence of the rutile phase in titania from 0 (pure anatase phase) to 19% exhibited the highly dispersed forms of cobalt oxide species for the calcined samples.

It is known that the active form of supported cobalt FTS catalysts is cobalt metal (Co^0). Thus, reduction of cobalt oxide species is essentially performed in order to transform cobalt oxide species obtained after calcination process into the active cobalt metal atoms for catalyzing the reaction. Therefore, the static H_2 chemisorption on the reduced cobalt samples was used to determine the number of reduced Co metal surface atoms. This is usually related to the overall activity of the catalyst during carbon monoxide (CO) hydrogenation. The resulted H_2 chemisorption for all samples is shown in Fig. 5. It was found that the number of the reduced cobalt metal surface atoms increased with the presence of rutile phase in titania up to a maximum at 19% of rutile phase (Co/R19) before decreasing with the greater amounts of rutile phase. Considering the number of cobalt metal atoms for Co/R0 (pure anatase titania), the number was apparently low even though highly dispersed cobalt oxides species. This was suggested that highly dispersed forms of cobalt oxide species be not only the factor that insures larger number of reduced cobalt metal surface atoms in Co/TiO_2. On the other hand, it can be observed that the number of reduced cobalt metal surface atoms for Co/R40 and Co/R96 (with the low degree of dispersion of cobalt oxide species as seen by TEM) was

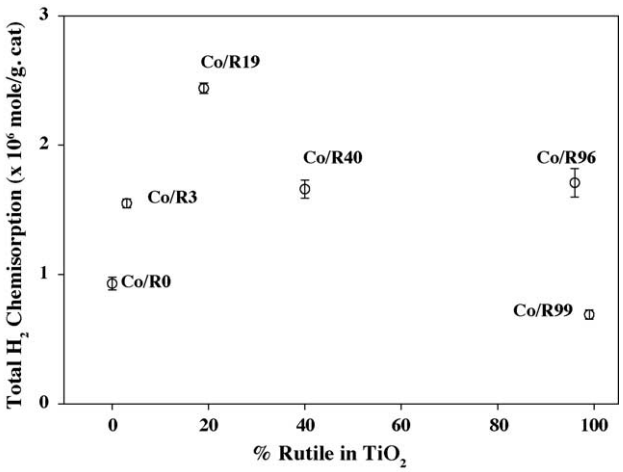

Fig. 5. A plot of the total H_2 chemisorption vs. % rutile in titania.

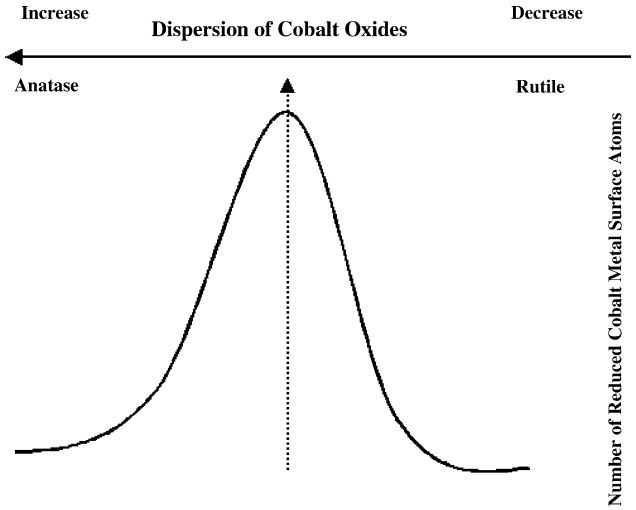

Fig. 6. A conceptual model on dependence of dispersion along with rutile phase on the number of reduced cobalt metal surface atoms for Co/TiO_2.

larger than that for Co/R0. This was due to the presence of rutile phase in Co/R40 and Co/R96. It should be mentioned that the largest number of reduced cobalt metal surface atoms for the Co/R19 sample was attributed to both highly dispersed cobalt oxide species and the presence of rutile phase in titania. In order to provide a better understanding for effects of both dispersion of cobalt oxide species and the presence of rutile phase in titania on the number of reduced cobalt metal surface atoms, a conceptual model of those is illustrated in Fig. 6. Thus, a large number of reduced cobalt metal surface atoms in Co/TiO_2 can be obtained with an optimum amount of rutile phase along with highly dispersed cobalt oxide species prior to reduction. It was suggested that the presence of rutile phase in titania can facilitate the reduction of cobalt oxide species as shown in Fig. 7. It was observed that the presence of rutile phase resulted in lowering the reduction temperature. However, the large amounts of rutile phase can result in a small number of reduced cobalt metal surface atoms. This is due to the low degree of dispersion for cobalt oxide species

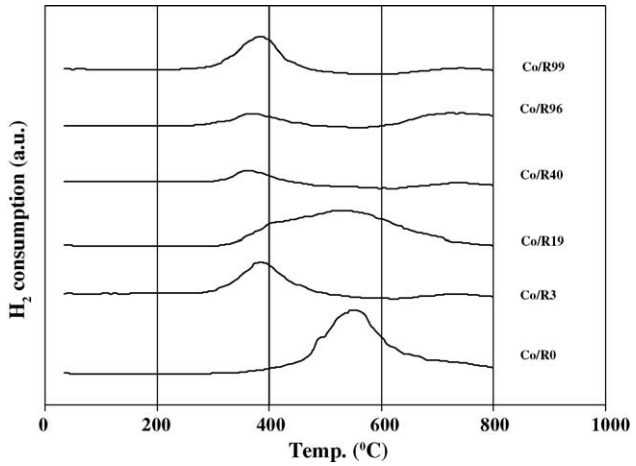

Fig. 7. TPR behaviors of Co/TiO_2 with various ratios of rutile:anatase phase.

with large amounts of rutile phase present. It should be also noted that part of the reason for the lower dispersion of Co is the lower BET surface area, especially for the rutile rich titania.

4. Conclusions

The present study showed dependence of both highly dispersed cobalt oxide species and the presence of rutile phase in titania on the number of reduced cobalt metal atoms in Co/TiO_2. It was found that the presence of rutile phase with optimum amounts in titania up to 19% resulted in highly dispersed cobalt oxide species as seen by TEM. Although with highly dispersed cobalt oxide species, Co/R0 (pure anatase titania) gave the low number of reduced cobalt metal surface atoms. On the other hand, Co/R40 and Co/R96 with a low degree of cobalt oxide dispersion apparently gave the higher number (compared to Co/Ro) of reduced cobalt metal surface atoms. Thus, both highly dispersed cobalt oxide species along with the presence of rutile phase in titania could play an important role on the number of reduced cobalt metal surface atoms for Co/TiO_2.

Acknowledgements

We gratefully acknowledge the financial support by the National Research Council of Thailand (NRCT), the Thailand Research Fund (TRF) and Thailand–Japan Technology Transfer Project (TJTTP-JBIC). We would like to thank Prof. James G. Goodwin Jr. at Clemson University for initiating this kind of project.

References

[1] H.P. Wither Jr., K.F. Eliezer, J.W. Mechell, Ind. Eng. Chem. Res. 29 (1990) 1807.
[2] E. Iglesia, Appl. Catal. A 161 (1997) 59.
[3] R.C. Brady, R.J. Pettie, J. Am. Chem. Soc. 103 (1981) 1287.
[4] A. Martinez, C. Lopez, F. Marquez, I. Duaz, J. Catal. 220 (2003) 486.
[5] J. Panpranot, J.G. Goodwin Jr., A. Sayari, Catal. Today 77 (2002) 269.
[6] J. Panpranot, J.G. Goodwin Jr., A. Sayari, J. Catal. 211 (2002) 530.
[7] S.L. Sun, I. Isubaki, K. Fujimoto, Appl. Catal. A 202 (2000) 121.
[8] S. Ali, B. Chen, J.G. Goodwin Jr., J. Catal. 157 (1995) 35.
[9] B. Jongsomjit, J. Panpranot, J.G. Goodwin Jr., J. Catal. 215 (2003) 66.
[10] T. Das, G. Jacobs, P.M. Patterson, W.A. Conner, J.L. Li, B.H. Davis, Fuel 82 (2003) 805.
[11] G. Jacobs, P.M. Patterson, Y.Q. Zhang, T. Das, J.L. Li, B.H. Davis, Appl. Catal. A 233 (2002) 215.
[12] M. Rothaemel, K.F. Hanssen, E.A. Blekkan, D. Schanke, A. Holmen, Catal. Today 38 (1997) 79.
[13] V. Ragaini, R. Carli, C.L. Bianchi, D. Lorenzetti, G. Vergani, Appl. Catal. A 139 (1996) 17.

[14] V. Ragaini, R. Carli, C.L. Bianchi, D. Lorenzetti, G. Predieri, P. Moggi, Appl. Catal. A 139 (1996) 31.
[15] J.L. Li, G. Jacobs, T. Das, B.H. Davis, Appl. Catal. A 233 (2002) 255.
[16] G. Jacobs, T. Das, Y.Q. Zhang, J.L. Li, G. Racoillet, B.H. Davis, Appl. Catal. A 233 (2002) 263.
[17] J.L. Li, L.G. Xu, R. Keogh, B.H. Davis, Catal. Lett. 70 (2000) 127.
[18] X.H. Li, K. Asami, M.F. Luo, K. Michiki, N. Tsubaki, K. Fujimoto, Catal. Today 84 (2003) 59.
[19] K.Y. Jung, S.B. Park, J. Photochem. Photobio. A: Chem. 127 (1999) 117.
[20] R.C. Reuel, C.H. Bartholomew, J. Catal. 85 (1984) 63.

Molecules **2005**, *10*, 672-678

molecules

ISSN 1420-3049
http://www.mdpi.org

Catalytic Activity During Copolymerization of Ethylene and 1-Hexene via Mixed TiO_2/SiO_2-Supported MAO with *rac*-$Et[Ind]_2ZrCl_2$ Metallocene Catalyst

Bunjerd Jongsomjit*, Sutti Ngamposri and Piyasan Praserthdam

Center of Excellence on Catalysis and Catalytic Reaction Engineering, Department of Chemical Engineering, Faculty of Engineering, Chulalongkorn University, Bangkok 10330 Thailand, Phone: (+66) 2-2186869, Fax: (+66) 2-2186766

*To whom all correspondence should be sent; e-mail: bunjerd.j@chula.ac.th

Received: 07 October 2004 / Accepted: 16 November 2004 / Published: 14 July 2005

Abstract: Activities during ethylene/1-hexene copolymerization were found to increase using the mixed titania/silica-supported MAO with *rac*-$Et[Ind]_2ZrCl_2$ metallocene catalyst. Energy Dispersive X-ray spectorcopy (EDX) indicated that the titania was apparently located on the outer surface of silica and acted as a spacer to anchor MAO to the silica surface. IR spectra revealed the Si-O-Ti stretching at 980 cm^{-1} with low content of titania. The presence of anchored titania resulted in less steric hindrance and less interaction due to supporting effect.

Keywords: Metallocene catalyst, titania, silica, supports, copolymerization

Introduction

Commercial interest in using metallocene catalysts for olefin polymerization has brought about an extensive effort towards utilizing metallocene catalysts more efficiently. It is known that the copolymerization of ethylene with higher 1-olefins is of commercial importance for production of elastomers and linear low-density polyethylene (LLDPE). Metallocene catalysts with MAO have been studied for such a copolymerization. In fact, zirconocene catalysts along with MAO have been reported to be potentially useful for polymerizing ethylene with 1-olefins [1-2].

However, it was found that homogeneous metallocene catalytic systems have two major disadvantages; the lack of morphology control of polymers produced and reactor fouling. Therefore, binding these metallocene catalysts onto inorganic supports can provide a promising way to overcome these drawbacks. Many inorganic supports such as SiO_2, Al_2O_3 and $MgCl_2$ have been extensively studied for this purpose [3-13]. Silica is perhaps the most widely used support for metallocene catalysts so far, but the properties of SiO_2 itself may not be completely satisfactory for all purposes based on activities and quality of polymer produced. For instance, it was found that the activity of the heterogeneous system was lower compared to the homogeneous one. Therefore, a modification of the support is required in order to maintain high activity. TiO_2-SiO_2 mixed oxide has been considered to be very attractive as combined catalyst and support, which have attracted much attention in recent years. It was reported that TiO_2-SiO_2 mixed materials have been used as catalysts and supports for various reactions [14]. This TiO_2-SiO_2 mixed oxide would lead to robust catalytic supports of metallocene catalysts for olefin polymerization.

In this present study, the ethylene/1-hexene copolymerization using TiO_2-SiO_2 mixed oxides supported-MAO with a zirconocene catalyst was investigated for the first time. The mixed oxide supports and catalyst precursors were prepared, characterized and tested for ethylene/1-hexene copolymerization.

Results and Discussion

The present study showed the influences of titania/silica mixed oxide supports on the catalytic activities in a heterogeneous metallocene catalytic system. The mixed oxide supports containing various amounts of titania and silica were characterized. It was found that at low concentrations (20 to 60 wt %) of titania, the latter was apparently located on the outer surface of silica. A typical EDX (Energy Dispersive X-ray spectroscopy) mapping for the cross sectional area of the mixed oxide support containing low concentrations of titania is shown in Figure 1, indicating the location of titania on the outer surface of silica. However, it can be observed that with high concentrations of titania, it started to segregate from silica probably due to its adsorption ability.

Figure 1. A typical EDX mapping of titania/silica mixed oxide support at low concentrations of titania.

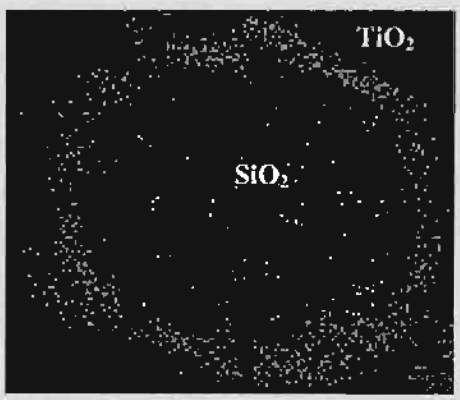

IR spectroscopy was also performed in order to identify chemical species and bonding of the mixed oxide supports. The IR spectra of samples are shown in Figure 2. It revealed that at low

concentrations of titania, the IR band at ca. 980 cm^{-1} assigning to Si-O-Ti connectivity was observed as also reported by Dutoit *et al.* [15]. This indicated that the Si-O-Ti bond was formed at the titania/silica ratios of 20/80 and 40/60 suggesting an anchor or a spacer effect. Strong IR bands were also seen at ca. 1100 cm^{-1} and assigned to asymmetric Si-O-Si stretching vibration.

Figure 2. IR spectra of titania/silica mixed oxide supports

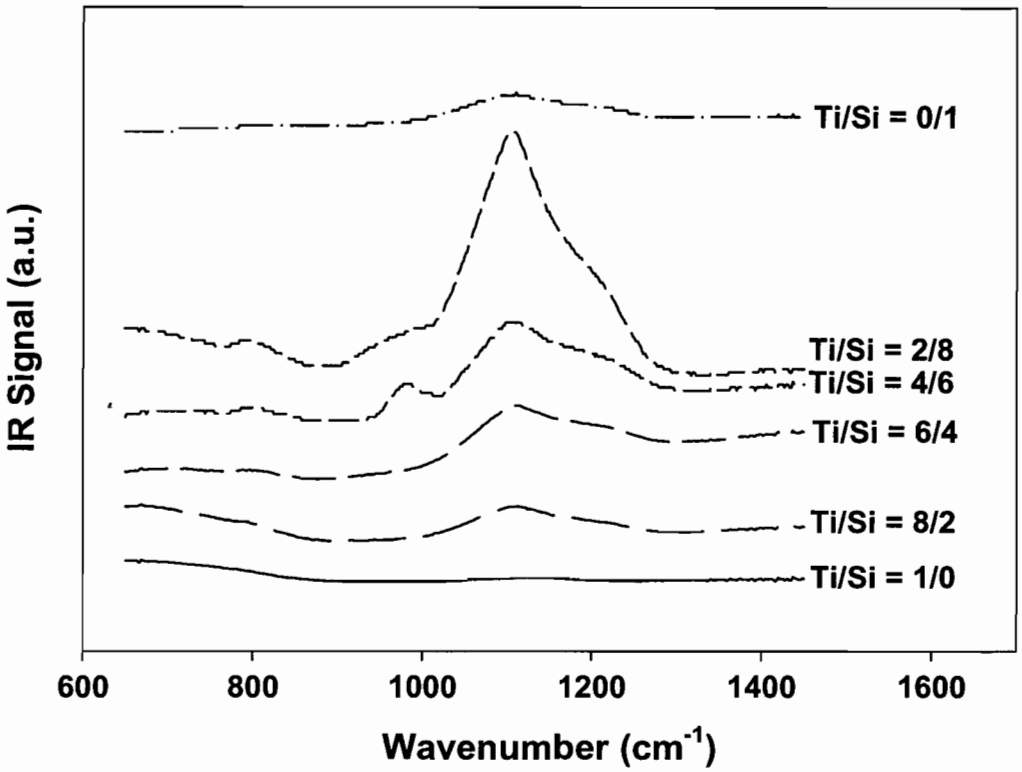

Copolymerization of ethylene/1-hexene via various titania/silica mixed oxides-supported MAO with a zirconocene catalyst was performed in order to determine the catalytic activities influenced by the various supports. The resulting reaction study is shown in Table 1 and Figure 3. The activities of the supported system were much lower than the homogeneous one, as expected. However, considering only the supported system, it was found that activities increased with increasing the amounts of titania up to 60% in the supports. The maximum activity can be obtained with the presence of 20% titania in the mixed support. However, increasing the amounts of titania more than 60% resulted in lower activities compared to the pure silica. It was also found that the activity for the pure titania is the lowest due to the strong support interaction between MAO and titania. Thus, due to the strong support interaction, it was more difficult for MAO to be released from the surface and reacted with the catalyst resulting in a low activity. Based on the resulted activities, the role of titania in titania/silica mixed oxide supports can be proposed.

Table 1: Catalytic activities during ethylene/1-hexene copolymerization via TiO_2-SiO_2 mixed oxides supported-MAO with zirconocene catalyst

TiO_2-SiO_2 Weight Ratios	wt% of TiO_2 in Mixed Support	Polymer Yield[a] (g)	Polymerization time (s)	Catalytic Activity[b] (x 10^{-4} kg polymer/mol Zr · h)
homogeneous	0	1.13	81	3.4
0/100	0	1.19	148	1.9
20/80	20	1.16	109	2.6
40/60	40	1.18	128	2.2
60/40	60	1.17	142	2.0
80/20	80	1.15	151	1.8
100/0	100	1.16	165	1.7

[a] The polymer yield was fixed [limited by ethylene fed and 1-hexene used (0.018 mole equally)]

[b] Activities were measured at polymerization temperature of 70°C, [ethylene] = 0.018 mole, [1-hexene] = 0.018 mole, $[Al]_{MAO}/[Zr]$ 1135, $[Al]_{TMA}/[Zr]$ = 2500, in toluene with total volume = 30 ml, and [Zr] = 5 x 10^{-5} M.

Figure 3. Activities of EH copolymerization via various mixed oxides-supported MAO and homogeneous system.

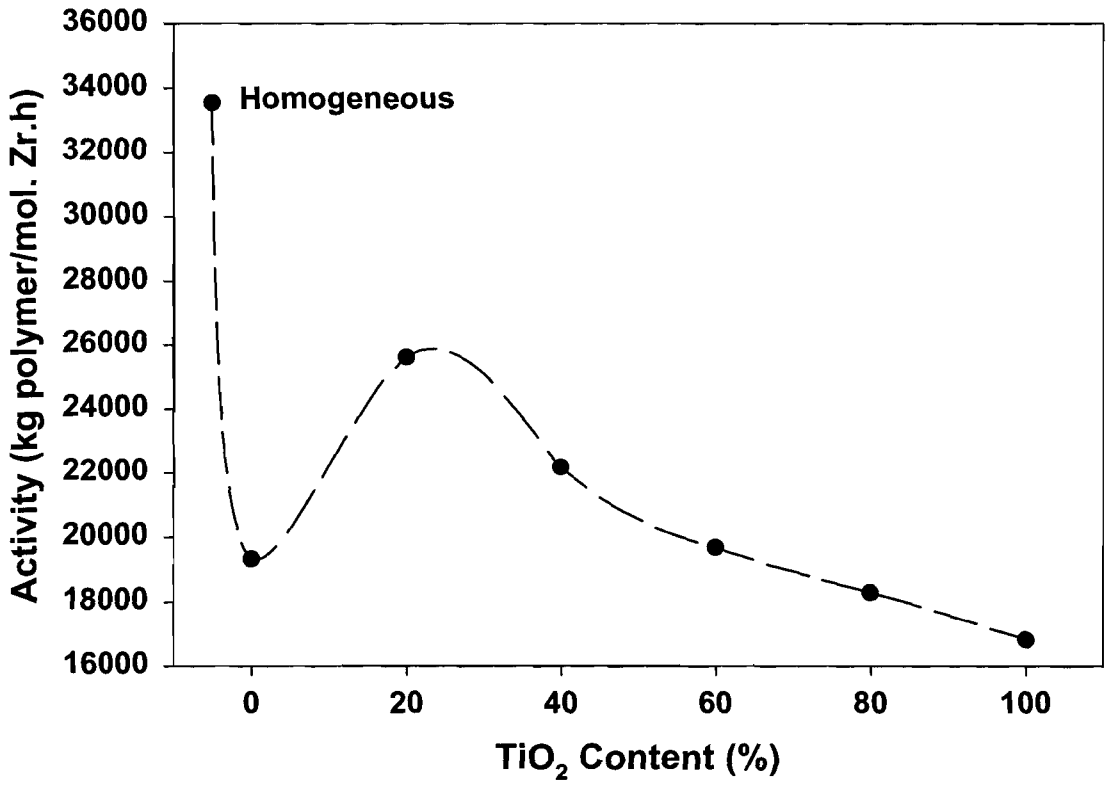

In order to give a better understanding for the role of titania, a conceptual model for titania effect is illustrated in Scheme 1.

Scheme 1 Suggested conceptual model as a spacer of titania

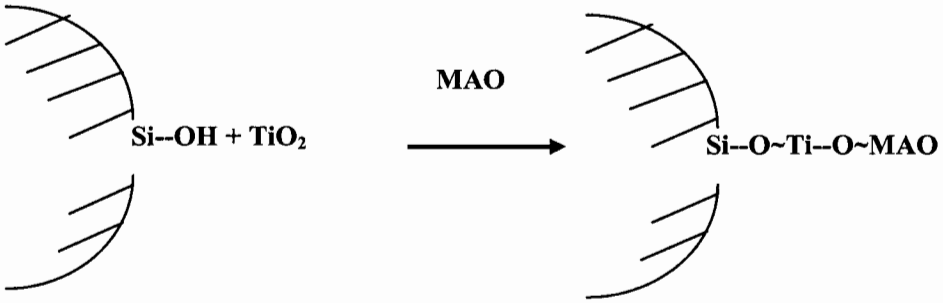

As known, when the supported system was conducted, activities decreased significantly compared to the homogeneous one. This should be due to a loss of active species by support interaction and/or the steric hindrance arising from the support. It can be observed that activities on the supported system can be divided into three levels; (i) moderate activity with the pure silica support, (ii) high activity with the certain amounts of titania present in the mixed oxide support, (iii) low activity with the pure titania support (due to strong support interaction). In Scheme 1, it showed that the presence of certain amounts (20 to 60 wt%) of titania enhanced activities. The contribution of titania can be drawn as MAO anchored on silica with titania as a spacer group. It can be also seen from SEM and EDX mapping that at low content, titania was decorated on silica surface and acted as a spacer to anchor MAO to the silica support. Thus, activities increased up to 30% with the presence of titania between 20 and 40 wt% in the mixed oxide supports. It should be mentioned that increased activities with the presence of titania as a spacer were observed because of less steric hindrance and less interaction on the support surface when a spacer was introduced. On the other hand, titania present would result in more homogeneous-like in terms of activities obtained. Investigation of a spacer such as silane in copolymerization of ethylene/1-olefins was also reported [16, 17]. However, when high amounts of titania were added, activities decreased because of the strong support interaction in titania compared to silica. Morphologies of polymers (not shown) produced via various supports were also investigated. It indicated that there was no significant change in polymer morphologies upon various mixed oxide supports used. Other characteristics of polymers produced need to be further investigated for future work.

Conclusions

The present study revealed influence of various titania/silica mixed oxides-supported MAO on the catalytic activities during copolymerization of ethylene/1-hexene with a zirconocene catalyst. It was found that with certain contents of titania ranged between 20 and 40 wt% in the mixed oxide supports, activities essentially increased up to 30% compared to one with the pure silica. It was proposed that titania added acted as a spacer to anchor MAO to the silica support resulting in less steric hindrance and less interaction on the support surface. On the other hand, titania present led to a more homogeneous-like catalytic system. However, larger amounts of titania resulted in lower activities due to the strong support interaction.

Acknowledgments

The authors would like to thank the Thailand Research Fund (TRF), National Research Council of Thailand (NRCT) and Thailand-Japan Transfer Technology Project (TJTTP-JBIC) for the financial support of this work.

Experimental

General

All chemicals [TiO_2 (anatase, Ishihara), SiO_2 (Cariact P-10), toluene, rac-ethylenebis(indenyl) zirconium dichloride [$Et(Ind)_2ZrCl_2$], methylaluminoxane (MAO), trimethylaluminum (TMA) and 1-hexene] were manipulated under an inert atmosphere using a vacuum glove box and/or Schelenk techniques.

Preparation of TiO_2-SiO_2 mixed oxides support

TiO_2-SiO_2 mixed oxide supports [surface areas of SiO_2 = 300 m^2/g and TiO_2 (anatase form) = 70 m^2/g] for MAO were prepared according to the method described by Conway *et al.* [18]. The TiO_2: SiO_2 ratios were varied from 0:1, 2:8, 4:6, 6:4, 8:2, and 1:0. The supports were heated under vacuum at 400°C for 6 h.

Preparation of TiO_2-SiO_2 mixed oxides-supported MAO

The TiO_2-SiO_2 mixed oxide support obtained above (1 g) was reacted with the desired amount of MAO at room temperature and stirred for 30 min. The solvent was then removed from the mixture. About 20 mL of toluene was added into the obtained precipitate, stirred the mixture for 5 min, and then removed the solvent. This procedure was done for 5 times to ensure the removal of impurities. Then, the solid part was dried under vacuum at room temperature to obtain white powder of TiO_2-SiO_2 mixed oxides-supported MAO.

Polymerization Reaction

The ethylene/1-hexene copolymerization reaction was carried out in a 100 mL semi-batch stainless steel autoclave reactor equipped with a magnetic stirrer. At first, the supported MAO (0.1 g, $[Al]_{MAO}/[Zr]$ = 1135) and 1-hexene (0.018 mole) along with toluene (to make the total volume of 30 mL) were put into the reactor. The desired amount of $Et(Ind)_2ZrCl_2$ (5×10^{-5}M) and TMA ($[Al]_{TMA}/[Zr]$ = 2500) was mixed and stirred for 5-min aging at room temperature, separately, then was injected into the reactor. The reactor was frozen in liquid nitrogen to stop reaction for 15 min and then the reactor was evacuated to remove argon. The reactor was heated up to polymerization temperature (70°C). To start the reaction, ethylene (0.018 mole) was fed into the reactor containing the comonomer and catalyst mixtures. After all ethylene was consumed, the reaction was terminated by addition of acidic

methanol (0.1% HCl in methanol) and stirred for 30 min. After filtration, the obtained copolymer (white powder) was washed with methanol and dried at room temperature.

Characterization of supports and catalyst precursors

Scanning Electron Microscopy and Energy Dispersive X-ray spectroscopy: SEM and EDX were used to determine the sample morphologies and elemental distribution throughout the sample granules, respectively. The JEOL model JSM-5800LV SEM was applied to determine morphologies of polymers. EDX was performed using Link Isis series 300 program. EDX is used to determine an elemental distribution as a density mapping of the specified element. Thus, it can reveal which elements are present and where they are located.

FTIR spectroscopy: FTIR was conducted on a Perkin-Elmer series 2000 instruments. The supports (1 mg) were mixed with 100 mg dried KBr. The sample cell was purged with oxygen. About 400 scans were accumulated for each spectrum in transmission with a resolution of 4 cm^{-1}. The spectrum of dried KBr was used as a background subtraction.

References

[1] Shan, C.L.P.; Soares, J.B.P.; Penlidis, A. *Polym. Chemistry* **2002**, *40*, 4426.
[2] Chu, K.J.; Shan, C.L.P.; Soares, J.B.P.; Penlidis, A. *Macromol. Chem. Phys.* **1999**, *200*, 2372.
[3] Uusitalo, A.M.; Pakkanen, T.T.; Iskola, E.I. *J. Mol. Catal. A: Chem.* **2002**, *177*, 179.
[4] Soga K.; Kaminaka, M. *Makromol. Chem.* **1993**, *194*, 1745.
[5] Ko, Y.S.; Han, T.K.; Park, J.W.; Woo, S.I. *Macromol. Rapid Commun.* **1996**, *17*, 749.
[6] Sugano T.; Yamamoto, K. *Eur. Pat. Appl.* 728773, **1996**.
[7] Margue M.; Conte, A. *J. Appl. Polm. Sci.* **2002**, *86*, 2054.
[8] Sensarma S.; Sivaram, S. *Polym Inter.* **2002**, *51*, 417.
[9] Belelli, P.G.; Ferreira M.L.; Damiani, D.E. *Appl.Catal. A: Gen.* **2002**, *228*, 189.
[10] Xu, J.T.; Zhu, Y.B.; Fan, Z.Q.; Feng, L.X. *J. Polym. Sci. Part A: Polym Chem.* **2001**, *39*, 3294.
[11] Korach L.; Czaja, K. *Polym. Bull.* **2001**, *46*, 67.
[12] Koppl A.; Alt, H.G. *J. Mol. Catal.A: Chem.* **2001**, *165*, 23.
[13] Jongsomjit, B.; Praserthdam, P.; Kaewkrajang, P. *Mater. Chem. Phys.* **2004**, *86*, 243.
[14] Gao X.; Wachs, I.E. *Catal. Today* **1999**, *51*, 233.
[15] Dutoit, D.C.M.; Schneider, M.; Baiker, A. *J. Catal.* **1995**, *153*, 165.
[16] Chao, C.; Pratchayawutthirat W.; Praserthdam, P.; Shiono T.; Rempel, G.L. *Macromol. Rapid Commun.* **2002**, *23*, 672.
[17] Jongsomjit, B.; Kaewkrajang, P.; Wanke, S.E.; Praserthdam, P. *Catal. Lett.* **2004**, *94*, 205.
[18] Conway, S.J.; Falconer, J.W.; Rochester, C.H. *J. Chem. Soc. Faraday Trans.* **1989**, *85*, 71.

Samples Availability: Available from the authors.

Korean J. Chem. Eng., 22(1), 115-120 (2005)

New Concepts in Material and Energy Utilization

Piyasan Praserthdam†, Choowong Chaisuk*, Wilasinee Kongsuebchart, Supakanok Thongyai and Sirachaya Kunjara Na Ayudhya

Center of Excellence on Catalysis and Catalytic Reaction Engineering,
Department of Chemical Engineering, Chulalongkorn University, Bangkok 10330, Thailand
*Department of Chemical Engineering, Silpakorn University,
Sanam Chandra Palace Campus, Nakorn Pathom 73000, Thailand
(*Received 13 July 2004 • accepted 15 October 2004*)

Abstract–New criteria in material and energy utilization are proposed. The potential index (Θ^*) is assigned to explain some natural processes in the world and to identify reasonably the preferable process instead of the efficiency. In addition, this term can first integrate the independent knowledge of the fields of mechanical, electrical and chemical engineering. It not only describes satisfactorily the transformation processes that are well-known in mechanical and electrical engineering, but also the increasing potential processes familiar in chemical engineering.

Key words: Material, Energy, Utilization, Potential, Potential Index

INTRODUCTION

In the beginning, chemical engineering originated by developing and applying the law of conservation of material, momentum and energy to explain simple phenomena in industrial processes. This was concerned with fundamentally designing equipment and operating processes well-known as "unit operations." Also, this knowledge was dramatically extended to a benign environmental approach, e.g. a waste treatment process. This can only minimize negative environmental impact in downstream, but it is not enough to optimize the usage of material and energy to acquire the highest gain or the lowest loss. Subsequently, a state-of-the-art method of cleaner technology was pronounced to be a promising way to manage the material and energy, since this procedure can determine an upstream route of processes. However, there is still some doubtfulness about this because most human beings tend to regard economic profits more than long-term planning. In addition, selecting the most suitable process is a difficult decision, especially in separation processes in chemical engineering, because there is not yet an indicator for analysis and interpretation. For example, which favorable process between distillation and solvent extraction is more worthy of the utilization of material and energy. On the contrary, most processes of energy transformation for mechanical and electrical engineering can be reliably altered by using the efficiency (η). Because of this we cannot point out the best direction of research and development in future. As mentioned above, we intend to propose a new approach to manage, utilize and optimize material and energy coincident with executive decision to select the preferable process in worldwide circumstances.

Usually in engineering work, we are familiar with the term efficiency, which is defined as the useful energy or work we want over the energy or work we have input. In addition, chemical engineers compare new process with conventional processes through the terms efficiency, conversion or recovery, which are usually defined the same as efficiency. The usage of efficiency, conversion and recovery is spread through many areas of chemical engineering such as packed bed columns [Han et al., 1985], combustion & conversion [Choi et al., 1985; Jung et al., 1988; Yun et al., 2001], distillation [Yoo et al., 1988; Kang et al., 1996], absorption [Park et al., 1990; Oh et al., 1999], fluidized beds [Kage et al., 1999; Jang, 2002] and membranes [Kang et al., 2002]. None of them can compare the processes that are different than their definition of efficiency, conversion and recovery. Most of them compared the new method in the same machine to the old process of the same machine and used it in the process design work only. That is the reason why we have proposed a new way of looking at efficiency, conversion or recovery and distributed these terms through many processes that we defined as the system and the surroundings. We have found many amazing results through the use of the potential index, as we will explain in detail as follows.

DETAILS

The basic idea of the law of conservation of mass, momentum and energy is mathematically expressed as follows [Smith et al. 2001; Jui, 1993; Van, 1959; Bird, 1960].

Rate of M.M.E. accumulation=Rate of M.M.E. generation
+Rate of M.M.E. Net I/P (1)

where M.M.E. refers to mass or momentum or energy and I/P refers to input minus output.

Eq. (1) can be applied to investigate simply mass minimization and energy preservation, but it still lacks a universal representative to evaluate and manipulate ineffective processes due to just a macroscopic approach. However, if the principle of energy interconversion and balance, which is the simplest expression of the first law of thermodynamics, is only considered, a measure of accomplishment of any processes may be definitely evaluated in terms of the efficiency (η) [Smith et al., 2001; Jui, 1993; Van, 1959] as defined:

†To whom correspondence should be addressed.
E-mail: piyasan.p@chula.ac.th

1. A process in which either material or energy is transformed is named as "Transformation Process".

2. A process in which either material or energy potentials in the system increase but no transformation is named as "Increasing Potential Process".

Mechanical and electrical engineers are interested in energy transformation processes, whereas chemical engineers have emphasized the increasing potential process, especially the separation process. Five examples of transformation of energy are shown as follows:

1. Thermal to mechanical energy.

- Carnot engine gives approximately 50% of the maximum thermal efficiency based on T_L=300 K and T_H=600 K [Smith et al., 2001; Jui, 1993; Van, 1959].
- Internal combustion engine [Heywood, 1988] shows maximum efficiency of spark ignition (SI) and direct injection (DI) as 0.30 and 0.45-0.53, respectively.

2. Mechanical to electrical energy or vice versa.

- Generator or motor has to be approximate values of efficiency in the range of 0.80-0.95 [Alexander et al., 1962; Sen, 1989].

3. Electrical to thermal energy.

- Heating element always shows 100% of the efficiency [Alexander et al., 1962; Sen, 1989].

4. Chemical to electrical energy.

- Fuel cell [Williams et al., 1966; EG & G. Services, 2002; Vielstich et al., 2003] can exhibit ideal or comparative thermal efficiency (ε_T) as defined in the following equation:

$$\varepsilon_T = \frac{\Delta G'}{\Delta H} = \varepsilon_G \cdot \frac{\Delta G}{\Delta H} \tag{10}$$

where $\varepsilon_G=\varepsilon_r$, ε_r=the free energy efficiency, ε_v=voltage efficiency and ε_c=current efficiency

Example: if the reaction is $H_2 + \frac{1}{2}O_2 \Leftrightarrow H_2O(l)$,

it will show ΔG^o=−56.69 kcal and ΔH^o=−68.32 kcal at 571 K.

It follows that a fuel cell with a free energy efficiency of 0.60 is as efficient as a device burning hydrogen at a thermal efficiency of

$$\varepsilon_T = 0.60 \times \left(\frac{-56.69}{-68.32}\right) = 0.50$$

5. Light to electrical energy.

- Solar cell shows average efficiency in the range of 7.5-30.5% [Green, 1998].

For all of transformations of one energy type to another, we have observed the same nature in such processes. When the input energy is transformed to the desired energy, the potential in the system relative to the input energy always decreases. The output reservoir shows lower temperature than the input one in a Carnot engine. The drop of voltage and the deceleration of angle velocity occur in motors or heaters and generators, respectively. To understand better the above idea, transformation of mass is also considered.

In every chemical reaction, the concentration of reactants is always reduced. Certainly, the decreasing potential behavior of material conversion is similar to that of energy transformation. As mentioned above, it is possible to imitate conversion as efficiency. However, the highest value of conversion will be limited by the thermodynamic equilibrium constant (K) [Octave, 1972] as defined in the following equation:

$$K = \frac{\text{concentration of products}}{\text{concentration of reactants}} \tag{11}$$

where K is dependent on reaction temperature.

The above observation leads to the following principle:

Principle 1 For the process in which material or energy is transformed into another form (transformation process), the material or energy potential in the system relative to the mass or energy input always decreases.

The first principle just explains the basic nature of all of processes, but it is not enough to indicate the explicit significance of the application to selecting exact useful processes. For processes concerned with energy conversion in mechanical and electrical engineering, it is well-known that the higher the efficiency, the better the process. For chemical reaction processes in chemical engineering, the promising process frequently shows higher conversion. Due to the familiar relationship of the efficiency, the mass conversion and the potential index, it can be implied that if the potential index of the system in whatever process is very high, such process can be preferable in practical operation. Recalling principle 1 and Eq. (7), it is clear that the drops of the material and energy potential are proportional to the increases of the potential index, and thus the preferable process exhibits much more decrease of the material or energy potential in the system. This statement is rewritten as follows:

Principle 2 For the process in which material or energy is transformed into another form (transformation process), the preferable process will show high potential index in the system relative to the mass or energy input.

The two principles are greater benefits to the field of mechanical and electrical engineering because most of the equipment in these fields involves energy transformation processes. However, in chemical engineering both principles can be powerfully useful in some situations. An example is the use of the second principle to understand better the second law of thermodynamics. This law affirms that every process proceeds in such a direction that the total entropy change associated with it is positive, the limiting value of zero being attained only by a reversible process. No process is possible for which the total entropy decreases. This can be expressed in the following mathematical statement [Cavaseno et al., 1979]:

$$\Delta S_{total} = \Delta S_{system} + \Delta S_{surroundings} \geq 0 \tag{12}$$

Attempts to relate the term of "potential index" with the entropy change (ΔS) are easily made. Considering the changes of thermal to mechanical energy in a reversible process with incompressible substances, the temperature (potential) of the reservoir is decreased from T_H to T_L. The entropy change of the system is expressed as follows [Cavaseno et al., 1979]:

$$\Delta S_{system} = \int \frac{\delta Q}{T} = \tilde{C}_P \int_{T_H}^{T_L} \frac{dT}{T} = \tilde{C}_P \ln \frac{T_L}{T_H} \tag{13}$$

where $\tilde{C}_P$=average heat capacity (J/K).

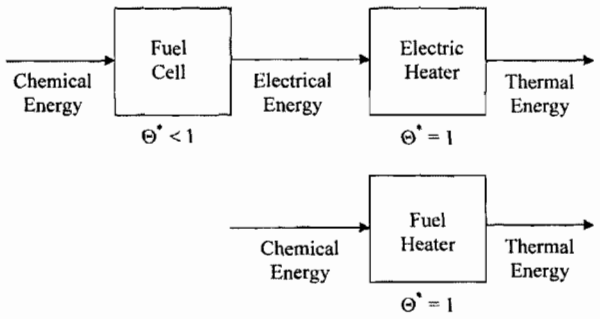

Fig. 1. Comparative process of electric and fuel heater.

From principle 2 and Eq. (13), it can be implied that a process will be great if there is much more entropy change of the system.

The two principles can briefly guide us to being careful in the operation of processes. If the potential index in the system of the transformation process is very low, such a process. Generators, motors and heaters are examples of preferable instruments because their potential indexes are normally unity. However, if there are many types of the instruments, we can select the preferable one as shown in the following example of the heater selection. At present, two main sources of heaters, electric and fuel heaters, are usually used. Both show a unity of the potential index. Nevertheless, if we focus on the same sources of the input energy, the relative difference can be obtained. This is schematically shown in Fig. 1.

Recalling principle 2, the electric heater should be avoided because there is a low potential index in the subsystem of the overall process.

Although the transformation process is very important, most of the processes in chemical engineering become the increasing potential processes, especially various separation processes. Two main examples are as follows:

1. Processes in which material potential in the system is increased.

As mentioned above, if we refer to material, the concentration will be considered as the potential and for all of these processes, the concentration increases. However, in some cases we may assign the mole fraction instead of the concentration. There are many examples in separation processes such as liquid-liquid extraction, solid-liquid extraction, crystallization, distillation, absorption, adsorption, evaporation, drying, filtration, membrane separation, centrifuge, thickener and electrochemical separation. To understand better, some of processes are investigated as follows:

• Liquid-liquid extraction (schematic diagram is shown in Fig. 2) [Herman et al., 1961; Carry, 1982; Warren et al., 1993; Seader et al., 1998; Alan, 1999; Piyasan, 1999].

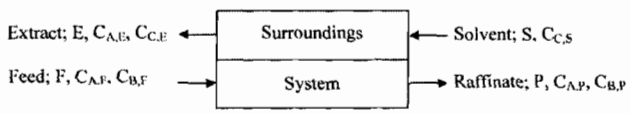

Fig. 2. Liquid-liquid extraction process: A and B=component in solute; C=solvent; F, P, S and E=volumetric flow rate (m^3s^{-1}) of feed, raffinate, solvent and extract, respectively; C_A, C_B and C_C=concentration of A, B and C (mole m^{-3}), respectively.

Basically, the process efficiency is given by recovery (R) as the following equation:

$$R = \frac{\text{A extracted}}{\text{A fed}} = \frac{FC_{A,F} - PC_{A,P}}{FC_{A,F}} \tag{14}$$

Let F=P

$$R = \frac{C_{A,F} - C_{A,P}}{C_{A,F}} = 1 - \frac{C_{A,P}}{C_{A,F}} \tag{15}$$

While

$$\Theta^*_{syst} = \frac{C_{B,P} - C_{B,F}}{C_{B,P}} = 1 - \frac{C_{B,F}}{C_{B,P}} \tag{16}$$

It is found that R and Θ^*_{syst} are quite different but still coincident. Additionally, if we just consider the surroundings, the potential index can be also expressed as follows:

$$\Theta^*_{surr} = \frac{C_{C,S} - C_{C,E}}{C_{C,S}} = 1 - \frac{C_{C,E}}{C_{C,S}} \tag{17}$$

where Θ^*_{syst}=the potential index of the system, Θ^*_{surr}=the potential index of the surroundings.

A remarkable observation is that for the extraction process if the concentration of one substance in the system is increased, the concentration of the other in the surroundings is always decreased. The "B" fraction out of the raffinate is increased, whereas the "C" fraction out of the extract is decreased.

• Binary distillation (schematic diagram is shown in Fig. 3) [Herman et al., 1961; Alan et al., 1980; Carry, 1982; Warren et al., 1993; Christie, 1993; Seader et al., 1998; Alan, 1999; Piyasan, 1999].

Again, the following recovery, potential index of the system and potential index of the surroundings are expressed:

$$R = \frac{\text{output (desired)}}{\text{Input}} = \frac{Dy_{A,D}}{Fz_{A,F}} \tag{18}$$

$$\Theta^*_{syst} = \frac{x_{C,B} - z_{C,F}}{x_{C,B}} \text{ or } \frac{y_{A,D} - z_{A,F}}{y_{A,D}} \tag{19}$$

$$\Theta^*_{surr} = \frac{T_H - T_L}{T_H} \tag{20}$$

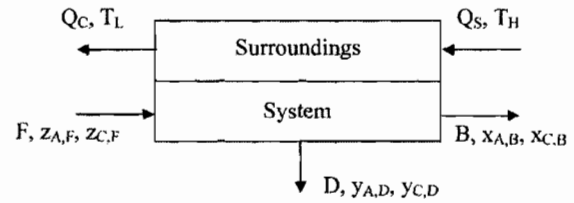

Fig. 3. Binary separation process: A and C=mixture component; F, B and D=molar flow rate (mole s^{-1}) of feed, bottom and top of distillation column, respectively; z, x and y=mole fraction in feed, bottom and top of distillation column, respectively; Q_S and Q_C=the heat flow (J s^{-1}) into reboiler and out of condenser, respectively; T_H and T_L=temperature (K) of reboiler and condenser, respectively.

The gain of potential in the system may be encountered in either the "A" component out of the top or the "C" component out of the bottom. It is clear that while "A" or "C" concentration is increased, the temperature of the bottom is higher than that of the top. This is consistent with the case of liquid-liquid extraction, but the decreasing potential term in the surroundings becomes the temperature instead of the solvent concentration.

In energy terms, potential index can be widely compared across the systems and processes similar to the term efficiency. These usually happen in case of mass terms; the potential index can be compared even with energy. In an instrument that performs similar actions such as distillation and liquid extraction, the surrounding potential index is defined as temperature in case of distillation, while the surrounding potential index is defined as concentration in the case of liquid extraction. However we can compare the potential index and select the better method according to previous or consequent processes that need to be performed in terms of potential index of the substance. The more purity of the substances, the more precious the materials.

Two examples of the processes in which material potential in the system is increased show the contradictory direction of the Θ^*_{syst} and the Θ^*_{surr}. To confirm this, we also focus on the processes in which energy potential in the system is increased.

2. Processes in which energy potential in the system is increased.

• Heat exchanger (schematic diagram is shown in Fig. 4) [Cavaseno et al., 1979; Smith et al., 2001].

A heat exchanger is a device in which energy is transferred from one fluid to another across a solid surface. The potential indexes of the system and the surroundings are shown in Eqs. (21) and (22), respectively.

$$\Theta^*_{syst} = \frac{T_H - T_L}{T_H} \tag{21}$$

$$\Theta^*_{surr} = \frac{T_{in} - T_{out}}{T_{in}} \tag{22}$$

• Pump or Compressor (schematic diagram is shown in Fig. 5)

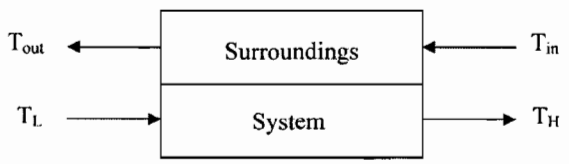

Fig. 4. Heat exchanger: T_L and T_{out}=low temperature (K), T_H and T_{in}=high temperature (K).

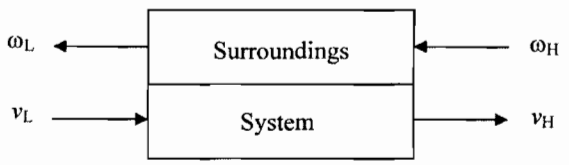

Fig. 5. Pump or compressor: v_L and v_H=liquid or gas velocity (m s^{-1}), ω_L and ω_H=angle velocity of the pump core (rpm).

[Cavaseno et al., 1979; Smith et al., 2001].

A pump is a device for moving a liquid or gas from one place to another. The potential indexes of the system and the surroundings are shown in Eqs. (23) and (24), respectively.

$$\Theta^*_{syst} = \frac{v_H - v_L}{v_H} \tag{23}$$

$$\Theta^*_{surr} = \frac{\omega_H - \omega_L}{\omega_H} \tag{24}$$

From the two examples, there is agreement with the explanation of the processes in which material potential in the systems is increased. For the heat exchanger, the temperature of the cold stream into the system is increased, whereas the temperature of the hot stream into the surroundings is decreased. For the pump or compressor, the fluid velocity into the system is increased while the angle velocity of the pump core of the surroundings is decreased. Hence, the following principle can be expressed:

Principle 3 For the process in which either material or energy potential in the system increases (increasing potential process), the material or energy potential in the surroundings always decreases.

Principle 3 is related to the second law of thermodynamics as well. From Eq. (13), the potential difference is proportional to the entropy change, and therefore the potential index can be referred to instead of the entropy change. Hence, the contradiction of ΔS_{system} and $\Delta S_{surroundings}$ in Eq, (12) implies the increases of Θ^*_{syst} coincident with the decreases of Θ^*_{surr}.

Considering some examples such as heat exchangers, a suitable heat exchanger is the one that possesses minimum mass flow rate of the substance according to economic reasons. Hence, the temperature difference, referred to as potential difference of its surroundings, is maximum. Another good example is liquid-liquid extraction. If the extract or solvent phase flow rate should be minimized, its concentration difference between input and output should consequently be high. Therefore, another principle is introduced to explain a general concept as in the above examples.

Principle 4 For the process in which either material or energy potential in the system increases (increasing potential process), if the increases of potential in the specific systems are the same, the process which shows the highest potential index in the surroundings will be preferable.

From principle 4, the calculations of liquid-liquid extraction, binary distillation and the other processes can be summarized as follows:

- Liquid-liquid extraction [Herman et al., 1961; Alan et al., 1980; Warren et al., 1993]: Θ^*_{syst} in the range of 0.080-0.530 and Θ^*_{surr} in the range of 0.120-0.595
- Binary distillation [Carry, 1982; Warren et al., 1993; Seader et al., 1998; Piyasan, 1999]: Θ^*_{syst} in the range of 0.430-0.583 and Θ^*_{surr} in the range of 0.180-0.308
- Stripping [Carry, 1982; Warren et al., 1993; Seader et al., 1998; Piyasan, 1999]: Θ^*_{syst} in the range of 0.00035-0.166 and Θ^*_{surr} in the range of 0.021-0.593
- Absorption [Alan et al., 1980; Warren et al., 1993; Shuzo, 1993;

Christie, 1993, 2003]: Θ^*_{syst} in the range of 0.012-0.196 and Θ^*_{surr} in the range of 0.0003-0.005

It is clear that if the Θ^*_{syst} of liquid-liquid extraction and binary distillation are the same, the preferable process is liquid-liquid extraction. Another observation is that if the Θ^*_{syst} of liquid-liquid extraction, stripping and absorption are the same, the preferable process becomes stripping.

The important suggestion is that whatever processes containing low potential index steps should be avoidable in operations. These are, for example, the processes involving biodiesel, gasohol, or hydrogen fuel cells. Biodiesel is produced from vegetable oil, whereas gasohol comes from ethanol. It is not worth increasing the purity of ethanol from 99.5% to 99.9% to make gasohol. Similarly, hydrogen used for fuel cells in cars is not an attractive way. These example processes are all comprised of systems of low potential index. If they are compared to other processes of fuel production such as petroleum distillation, which shows higher potential index, the latter may be more. Hence, an increase of potential index in the process is one of ways to achieve better production.

REFERENCES

Alan, J. H., *Extraction Methods in Organic Analysis*, Sheffield, England: Sheffield Academic Press, Boca Raton, FL: CRC Press (1999).

Alan, S. F., Leonard, A. W., Curtis, W. C., Louis, M. and Andersen, L. Bryce, *Principles of Unit Operations*, 2nd edition, John Wiley & Sons, Inc. (1980).

Alexander, G. and Wallace, G. A., *Principles and Practice of Electrical Engineering*, 8th edition, McGraw-Hill Book company (1962).

Atkins, P., *The Elements of Physical Chemistry*, 3rd, Oxford press (2001).

Bird, R. B., Warren, E. S. and Edwin, N. L., *Transport Phenomena*, John Wiley & Sons, INC. (1960).

Cary, J. K., *Separation Processes*, 2nd edition, New Delhi: Tata McGraw-Hill (1982).

Cavaseno, V. and the Stall of Chemical Engineering, *Process Heat Exchange*, Chemical Engineering McGraw-Hill Pub. Co. (1979).

Choi, J. H., Park, Y. S., Park, Y. O., Park, W. H. and Son, J. E., "Effect of Entrainment on Combustion Efficiency High Ash Anthracites in Fluidized Bed Combustors," *Korean J. Chem. Eng.*, **2**, 111 (1985).

Christie, J. G., *Transport Processes and Unit Operations*, 5th edition, Prentice-Hall International, Inc. (1993).

Christie, J. G., *Transport Processes and Separation Process Principles*, 4th edition, Pearson Education, Inc. (2003).

EG & G. Services, *Fuel Cell Handbook*, 5th edition, Parsons, Inc. Science Applications International Corporation (2002).

Green, M. A., "Progress in Photovoltaics, Research and Applications," **6**(1) (1998).

Han, M. W., Choi, D. K. and Lee, W. K., "Effect of Shape and Wettability of Packing Materials on the Efficiency of Packed Column," *Korean J. Chem. Eng.*, **2**, 25 (1985).

Herman, J. A., et al., *Separation Methods in Analytical Chemistry*, New York: Interscience Pub. (1961).

Heywood, J. B., *Internal Combustion Engine Fundamental*, McGraw-Hill Book Company (1988).

Jang, J. G., Kim, M. R., Lee, K. H. and Lee, J. K., "Enhancement of Combustion Efficiency with Mixing Ratio during Fluidized Bed Combustion of Anthracite and Bituminous Blended Coal," *Korean J. Chem. Eng.*, **19**, 1059 (2002).

Jui, S. H., *Engineering Thermodynamics*, Prentice-Hall, Inc. (1993).

Jung, Y. and Park, D., "Fluidized Bed Combustion of High Ash Anthracite: Analysis of Combustion Efficiency and Particle Size Distribution," *Korean J. Chem. Eng.*, **5**, 109 (1988).

Kage, H., Dohzaki, M., Ogura, H. and Matsuno, Y., "Powder Coating Efficiency of Small Particles and Their Agglomeration in Circulating Fluidized Bed," *Korean J. Chem. Eng.*, **16**, 630 (1999).

Kang, M. S., Kim, I. W. and Park, S., "Stage Efficiency Estimation by Modified MIMT Using NLP," *Korean J. Chem. Eng.*, **13**, 159 (1996).

Kang, M. S., Tanioka, A. and Moon, S. H., "Effects of Interface Hydrophilicity and Metallic Compounds on Water-Splitting Efficiency in Bipolar Membranes," *Korean J. Chem. Eng.*, **19**, 99 (2002).

Noel, D. N., *Physical and Chemical Equilibrium for Chemical Engineers*, John Wiley & Sons, Inc. (2002).

Octave, L., *Chemical Reaction Engineering*, 2nd edition, John Wiley & Sons, Inc. (1972).

Oh, E. K., Jung, G. H., Kim, S. G., Lee, H. K. and Kim, I. W., "Effect of Initial Droplet Size Distribution on Sulfur Removal Efficiency in FGD/SDA," *Korean J. Chem. Eng.*, **16**, 292 (1999).

Park, C. Y., Lee, Y. C., Chung, S. H. and Sohn, E. S., "Effect of Pore Structure on SO_2 Adsorption Efficiency," *Korean J. Chem. Eng.*, **7**, 296 (1990).

Piyasan, P., *Principles of Design Instrument for Separation*, 3th edition, cubook, Bangkok (1999).

Seader, J. D. and Ernest, J. H., *Separation Process Principles*, New York: Wiley (1998).

Sen, P. C., *Principles of Electric Machines and Power Electronics*, John Wiley & Sons, Inc. (1989).

Shuzo, O., "Distillation Engineering," Translated by Technology Promotion association (Thailand Japan), Bangkok (1993).

Smith, J. M., Van ness, Abbott, M. M., *Introduction to Chemical Engineering Thermodynamic*, 6th edition, McGraw-Hill (2001).

Van Wylen, G. J., *Thermadynamics*, John Wiley & Sons, Inc. (1959).

Vielstich, W., Lamm, A. and Gasteiger, H. A., *Handbook of Fuel Cells Fundamentals Technology and Applications*, Volume 4, John Wiley & Sons Inc., USA (2003).

Warren, L. M., Julian, C. S. and Peter Harriott, *Unit Operations of Chemical Engineering*, 4th edition, McGraw-Hill, Inc. (1993).

Williams, K. R., *An Introduction to Fuel Cells*, Elsevier publishing Company (1966).

Yoo, K. P., Lee, K. S., Lee, W. H. and Park, H. S., "Diagnosis of Thermodynamic Efficiency in Heat Integrated Distillation," *Korean J. Chem. Eng.*, **5**, 123 (1988).

Yun, Y. and Yoo, Y. D., "Performance of a Pilot-Scale Gasifier for Indonesian Baiduri Coal," *Korean J. Chem. Eng.*, **18**, 679 (2001).

Catalysis Letters Vol. 100, Nos. 3–4, April 2005 (© 2005)
DOI: 10.1007/s10562-004-3445-6

Role of titania in TiO_2–SiO_2 mixed oxides-supported metallocene catalyst during ethylene/1-octene copolymerization

Bunjerd Jongsomjit*, Sutti Ngamposri, and Piyasan Praserthdam

Department of Chemical Engineering, Faculty of Engineering, Center of Excellence on Catalysis and Catalytic Reaction Engineering, Chulalongkorn University, Bangkok, 10330, Thailand

Received 29 September 2004; accepted 11 December 2004

The present study showed enhanced activities of ethylene/1-octene copolymerization via TiO_2–SiO_2 mixed oxides-supported MAO with a zirconocene catalyst. It was proposed that titania was decorated on silica surface and acted as a spacer to anchor MAO to the silica support resulting in less steric hindrance and less interaction on the support surface.

KEY WORDS: mixed oxides; silica; supported catalyst; titania; zirconocene catalyst.

1. Introduction

Because of the commercial interest of using metallocene catalysts for olefin polymerization, it has led to an extensive effort for utilizing metallocene catalysts more efficiently. It is known that the copolymerization of ethylene with higher 1-olefins is a commercial importance for productions of elastomer and linear low-density polyethylene (LLDPE). Metallocene catalysts with MAO have been studied for such a copolymerization. In fact, zirconocene catalysts along with MAO have been reported for a potential use to polymerize ethylene with 1-olefins [1–2].

However, it was found that homogeneous metallocene catalytic system has two major disadvantages; the lack of morphology control of polymers produced and reactor fouling. Therefore, binding these metallocene catalysts onto inorganic supports can provide a promising way to overcome these drawbacks. It has been reported that many inorganic supports such as SiO_2, Al_2O_3, and $MgCl_2$ have been extensively studied [3–13]. It has been mentioned that silica is perhaps the most widely used support for metallocene catalysts so far. Unfortunately, due to the support effect, it is found that the catalytic activity of catalysts in heterogeneous system is usually lower than the homogeneous one. Therefore, a modification of the support properties is required in order to maintain high activity as in the homogeneous system or even closer. TiO_2–SiO_2 mixed oxide has been considered to be very attractive as catalysts and supports, which have brought much attention in recent years. It was reported that TiO_2–SiO_2mixed materials have been used as catalysts and supports for various reactions [14]. This TiO_2–SiO_2 mixed oxide would lead to robust catalytic supports of metallocene catalysts for olefin polymerization.

In this present study, the ethylene/1-octene copolymerization using TiO_2–SiO_2 mixed oxides supported-MAO with a zirconocene catalyst was investigated for the first time. The ratios of TiO_2/SiO_2 used were varied. The mixed oxide supports and catalyst precursors were prepared, characterized and tested for ethylene/1-octene copolymerization. The role of TiO_2 in the mixed oxide supports was also further discussed.

* To whom correspondence should be addressed.
E-mail: bunjerd.j@chula.ac.th

2. Experimental

All chemicals [TiO_2 (anatase, Ishihara), SiO_2 (Cariact P-10), toluene, rac-ethylenebis (indenyl) zirconium dichloride [$Et(Ind)_2ZrCl_2$], methylaluminoxane (MAO), trimethylaluminum (TMA) and 1-octene] were manipulated under an inert atmosphere using a vacuum glove box and/or Schelenk techniques.

2.1. Materials

2.1.1. Preparation of TiO_2–SiO_2 mixed oxides support

TiO_2–SiO_2 mixed oxide supports [surface areas of SiO_2 = 300 $m^2\ g^{-1}$ and TiO_2 (anatase form) = 70 $m^2\ g^{-1}$] for MAO were prepared according to the method described by Conway *et al.* [15]. The TiO_2:SiO_2 ratios were varied from 0:1, 2:8, 4:6, 6:4, 8:2, and 1:0. The supports were heated under vacuum at 400 °C for 6 h.

2.2. Preparation of TiO_2–SiO_2 mixed oxides-supported MAO

One gram of the TiO_2–SiO_2 mixed oxide support obtained from 2.1.1 was reacted with the desired amount of MAO at room temperature and stirred for

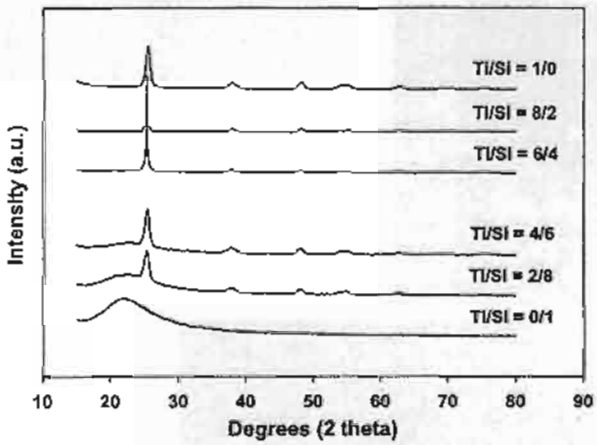

Figure 1. XRD patterns of various TiO_2–SiO_2 mixed oxide supports before MAO impregnation.

30 min. The solvent was then removed from the mixture. About 20 mL of toluene was added into the obtained precipitate, stirred the mixture for 5 min, and then removed the solvent. This procedure was done for 5 times to ensure the removal of impurities. Then, the solid part was dried under vacuum at room temperature to obtain white powder of TiO_2–SiO_2 mixed oxides-supported MAO.

2.3. Polymerization

The ethylene/1-octene copolymerization reaction was carried out in a 100 mL semi-batch stainless steel autoclave reactor equipped with a magnetic stirrer. At first, 0.1 g of the supported MAO ($[Al]_{MAO}/[Zr]$ = 1135) and 0.018 mol of 1-octene along with toluene (to make the total volume of 30 mL) were put into the reactor. The desired amount of $Et(Ind)_2ZrCl_2$ (5×10^{-5} M) and TMA ($[Al]_{TMA}/[Zr]$ = 2500) was mixed and stirred for 5-min aging at room temperature, separately, then was injected into the reactor. The reactor was frozen in liquid nitrogen to stop reaction for 15 min and then the reactor was evacuated to remove argon. The reactor was heated up to polymerization temperature (70 °C). By feeding the fixed amount of ethylene (0.018 mol ~6 psi) into the reaction mixtures, the ethylene consumption can be observed corresponding to the ethylene pressure drop. The polymerization reaction was stopped and the reaction time used was recorded when all ethylene

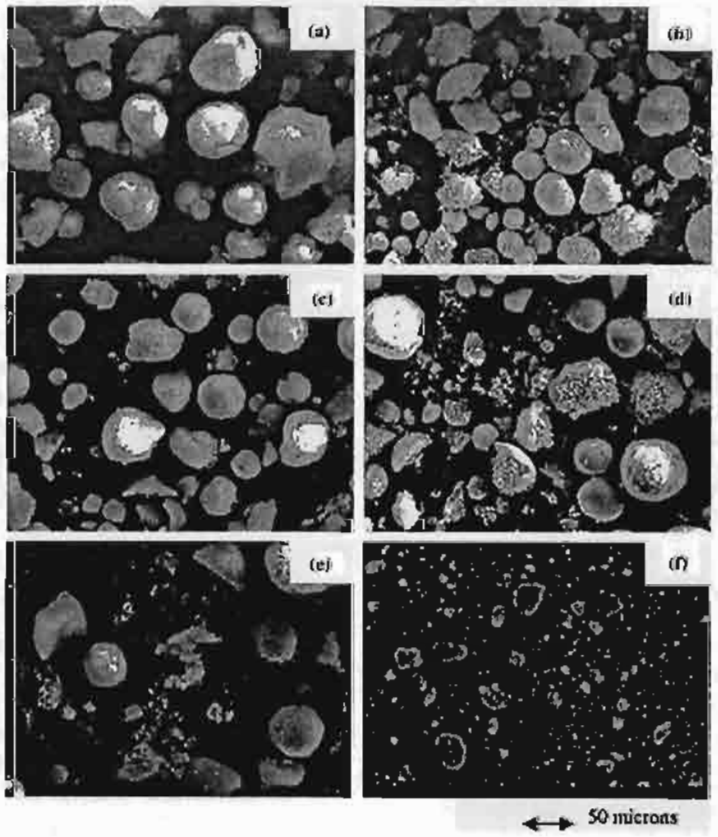

Figure 2. SEM micrographs of various TiO_2–SiO_2 mixed oxide supports before MAO impregnation: (a) Ti/Si = 0/1, (b) Ti/Si = 2/8, (c) Ti/Si = 4/6, (d) Ti/Si = 6/4, (e) Ti/Si = 8/2, (f) Ti/Si = 1/0.

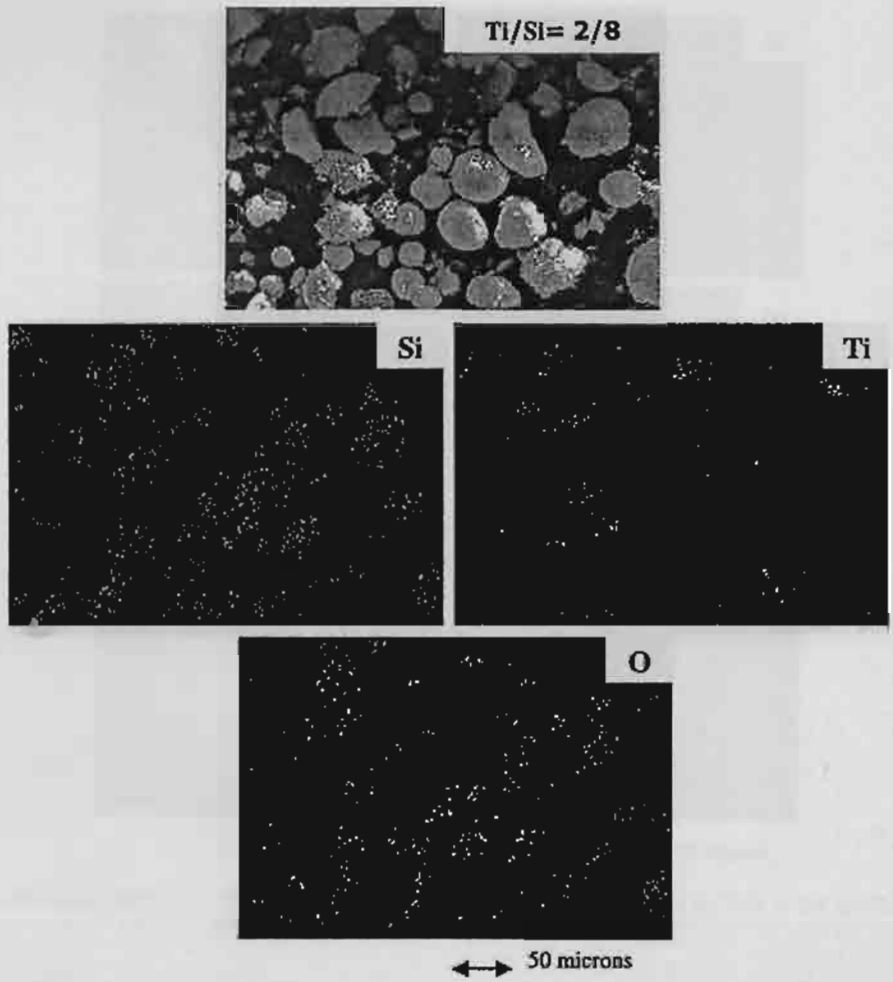

Figure 3. EDX mapping of a typical TiO_2–SiO_2 mixed oxide supports before MAO impregnation.

(0.018 mol) was totally consumed. To start reaction, 0.018 mol of ethylene was fed into the reactor containing the comonomer and catalyst mixtures. After all ethylene was consumed, the reaction was terminated by addition of acidic methanol (0.1% HCl in methanol) and stirred for 30 min. After filtration, the obtained copolymer (white powder) was washed with methanol and dried at room temperature.

2.4. Characterization

2.4.1. Characterization of supports and catalyst precursors

X-ray diffraction: XRD was performed to determine the bulk crystalline phases of samples. It was conducted using a SIEMENS D-5000 X-ray diffractometer with CuK_α(λ = 1.54439 Å). The spectra were scanned at a rate of 2.4° min^{-1} in the range 2θ = 20–80°.

Scanning electron microscopy and energy dispersive X-ray spectroscopy: SEM and EDX were used to determine the sample morphologies and elemental distribution throughout the sample granules, respectively. The SEM of JEOL mode JSM-5800LV was

Table 1
Catalytic activities during ethylene/1-octene copolymerization via TiO_2–SiO_2 mixed oxides supported-MAO with zirconocene catalyst

TiO_2–SiO_2 Weight ratios	wt% of TiO_2 in mixed support	Polymer yield (g)	Polymerization time (s)	Catalytic activity[a] ($\times 10^{-4}$ kg polymer mol^{-1} Zr. h)
Homogeneous	0	1.13	87	3.1
0/100	0	1.19	152	1.9
20/80	20	1.14	116	2.4
40/60	40	1.19	132	2.2
60/40	60	1.18	149	1.9
80/20	80	1.17	157	1.8
100/0	100	1.13	161	1.7

[a]Activities were measured at polymerization temperature of 70 °C, [ethylene] = 0.018 mol, [1-octene] = 0.018 mol, $[Al]_{MAO}/[Zr]$ 1135, $[Al]_{TMA}/[Zr]$ = 2500, in toluene with total volume = 30 mL, and [Zr] = 5×10^{-5} M.

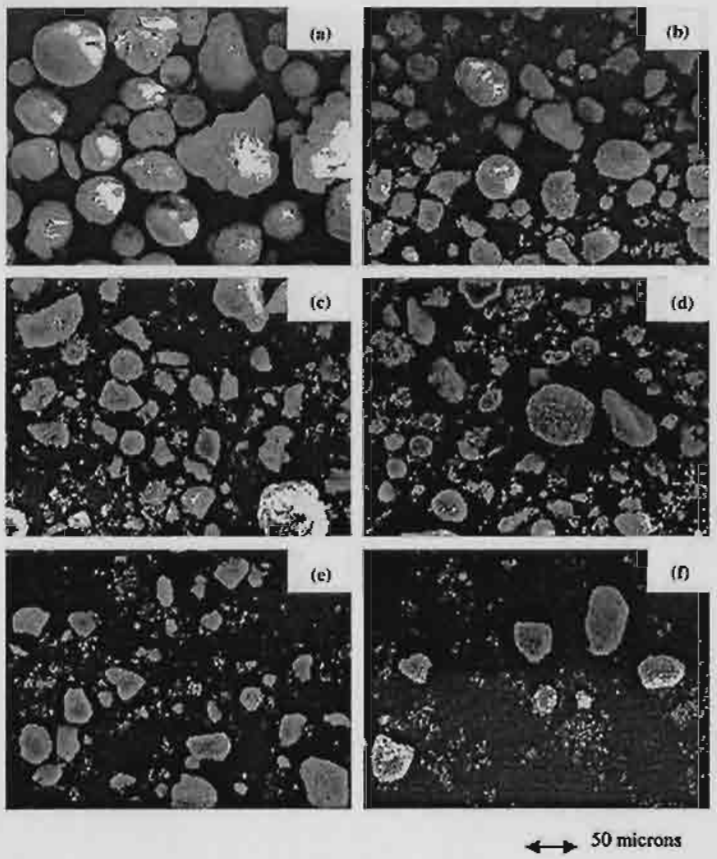

Figure 4. SEM micrographs of various TiO_2–SiO_2 mixed oxide supports after MAO impregnation; (a) Ti/Si = 0/1, (b) Ti/Si = 2/8, (c) Ti/Si = 4/6, (d) Ti/Si = 6/4, (e) Ti/Si = 8/2, (f) Ti/Si = 1/0.

applied. EDX was performed using Link Isis series 300 program.

FTIR spectroscopy: FTIR was conducted on a Perkin-Eelmer series 2000 instruments. The supports (1 mg) were mixed with 100 mg dried KBr. The sample cell was purged with oxygen. About 400 scans were accumulated for each spectrum in transmission with a resolution of 4 cm^{-1}. The spectrum of dried KBr was used as a background subtraction.

2.4.2. Characterization of polymer

Scanning electron microscopy: SEM was performed to study morphologies of polymers produced. The same equipment as mentioned above was employed.

Gel permeation chromatography (GPC): A high temperature GPC (Waters 150-C) equipped with a viscometric detector, differential optical refractometer and four Styragel HT type columns (HT3, HT4, HT5, and HT6) with a 1×10^7 exclusion limit for polysyrene was used to determined the molecular weight and molecular weight distributions of the copolymers produced. The analyses were performed at 135 °C using 1,2,4-trichlorobenzene as the solvent. The columns were calibrated with standard narrow molecular weight distribution polystyrene and LLDPE.

3. Results and discussion

The present study showed influences of TiO_2–SiO_2 mixed oxide supports on catalytic activities in heterogeneous metallocene catalytic system. The mixed oxide supports containing various amounts of titania and silica were characterized before and after impregnation with MAO. XRD patterns of the supports before impregnation with MAO are shown in figure 1. It was observed that the pure silica exhibited a broad XRD peak assigning to the conventional amorphous silica. Similar to the pure silica, the XRD patterns of the pure titania indicated only the characteristic peaks of anatase titania at 25° (major), 37°, 48°, 55°, 56°, 62°, 71°, and 75°. XRD patterns of the mixed oxide supports containing various amounts of titania and silica revealed the combination of titania and silica supports based on their content. It can be seen that the intensity of XRD characteristic peaks for both supports was changed based on the ratios of TiO_2/SiO_2. After impregnation with MAO, the mixed oxide supports were again identified using

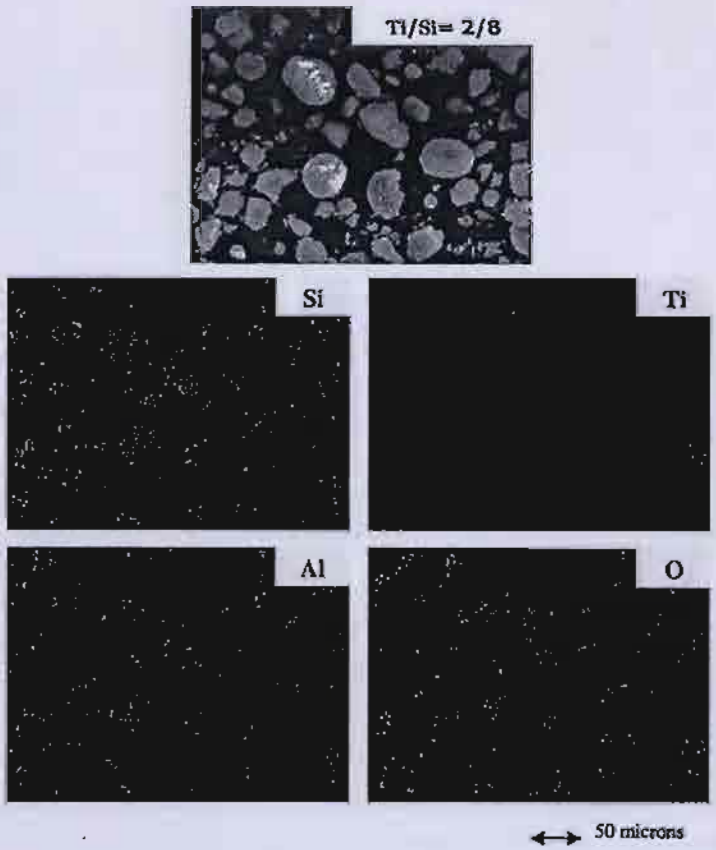

Figure 5. EDX mapping of a typical TiO_2–SiO_2 mixed oxide supports after MAO impregnation.

XRD. It was found that XRD patterns for the supports after impregnation with MAO were identical with those before impregnation with MAO indicating highly dispersed MAO species. In order to determine the morphologies and elemental distributions of the supports before and after impregnation, SEM and EDX were performed, respectively. The SEM micrographs of the supports before impregnation with MAO were shown in figure 2. It showed that silica was appeared in larger particles than titania. It also indicated that at the low content of titania ranged between 20 and 60%, titania was found to decorate on the silica surface as seen in the SEM micrographs. However, at high content of titania, it revealed that titania, essentially isolated from the silica surface. This was probably because the adsorption ability of silica surface with titania was limited by the titania contents in the mixed oxide supports. The distribution of all elements (Si, Ti, and O) obtained from EDX was similar in all samples. The typical EDX mapping images for the mixed oxide support are shown in figure 3 indicating titania located on the silica outer surface. After impregnation with MAO, SEM and EDX of the supports were also conducted. The SEM micrographs of the supports after impregnation with MAO are shown in figure 4 indicating similar results as seen in figure 2. The EDX mapping images of the supports can provide more information about the distribution of MAO as seen for Al distribution mapping on each support. It was found that MAO was well distributed all over the support granules. The typical EDX mapping images for the mixed oxide supports after impregnation with MAO are shown in figure 5. Figure 6 apparently shows SEM and EDX mapping of titania located on the outer surface of silica support. IR spectroscopy was also performed in order to identify chemical species and bonding of the mixed oxide supports. The IR spectra of samples are shown in figure 7. It revealed that at low concentrations of titania, the IR band at ca. 980 cm^{-1} assigning to Si–O–Ti connectivity was observed as also reported by Dutoit *et al.* [16]. The strong IR bands were also seen at ca. 1100 cm^{-1} assigning to asymetric Si–O–Si stretching vibration. Then, the various TiO_2–SiO_2 mixed oxide supports after impregnation with MAO were used and investigated for catalytic activities. Copolymerization of ethylene/1-octene via various TiO_2–SiO_2 mixed oxides-supported MAO with zirconocene catalyst was performed in order to determine the catalytic activities influenced by the various supports. The resulted reaction study is shown in table 1 and figure 8. The activities of the supported system were much

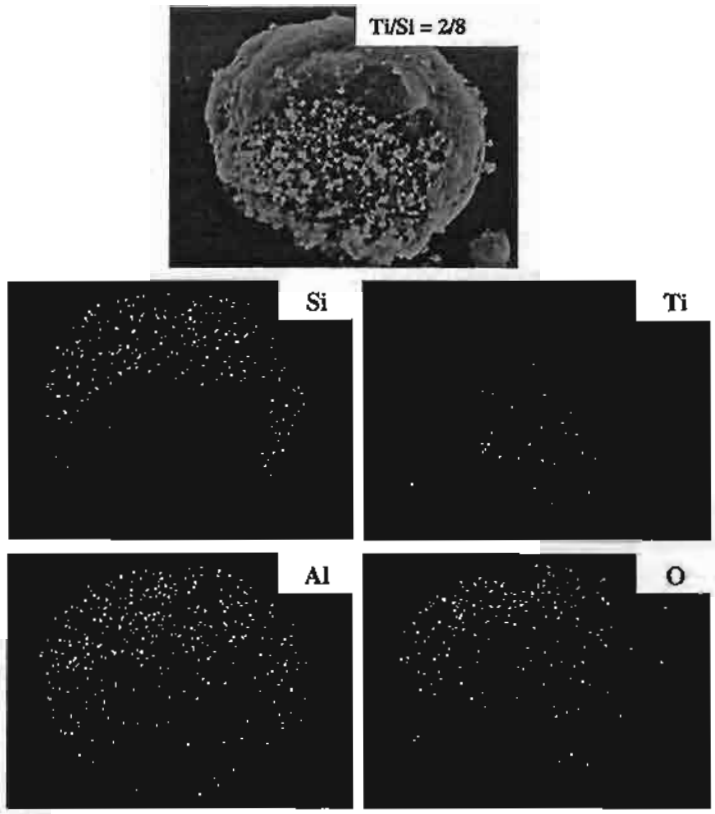

Figure 6. SEM and EDX mapping of titania located on the mixed support granule.

lower than the homogeneous one as expected. However, considering only the supported system, it was found that activities dramatically increased with increasing the amounts of titania up to 60% in the supports compared with those for the pure silica support. The maximum activity can be obtained with the presence of 20% titania in the mixed support. However, with increasing the amounts of titania more than 60% resulted in lower activities compared to the pure silica. It was also found that the activity for the pure titania is the lowest because the strong support interaction [17] between MAO and titania was more pronounced. Based on the resulted activities, the role of titania in TiO_2–SiO_2 mixed oxide supports can be proposed. In order to give a better understanding for the role of titania, a conceptual model for titania effect is illustrated in Scheme 1. As known,

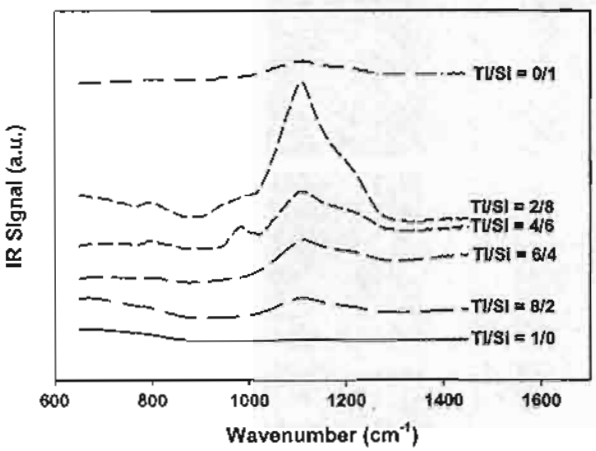

Figure 7. IR spectra of various mixed oxide supports.

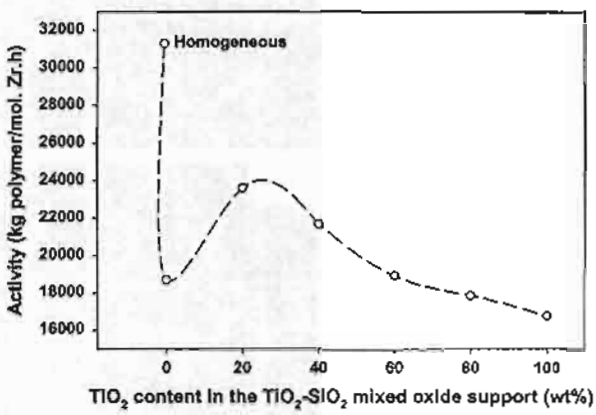

Figure 8. Activities of ethylene/1-octene copolymerization via various TiO_2–SiO_2 mixed oxides-supported MAO with a zirconocene catalyst.

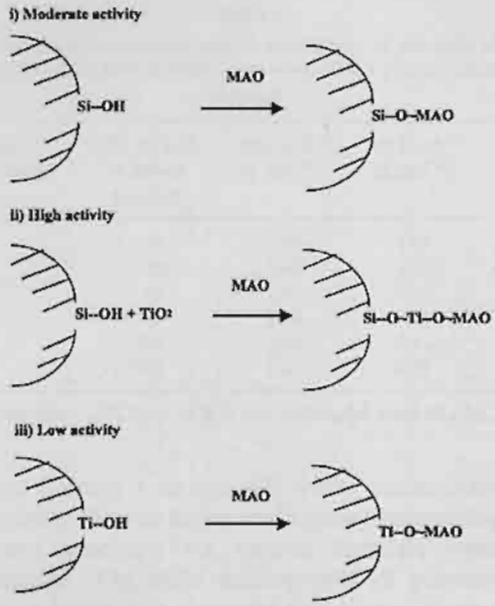

Scheme 1. A conceptual model for evaluation of activities via various TiO_2–SiO_2 mixed oxide supports.

when the heterogeneous system was conducted, activities decreased significantly compared to the homogeneous one as also seen in figure 8. This should be due to a loss of active species by support interaction and/or the steric hindrance arising from the support. Considering Scheme 1, activities on the heterogeneous system can be divided into three levels; (i) moderate activity with the conventional pure silica support, (ii) high activity with the certain amounts of titania present in the mixed oxide support, (iii) low activity with the pure titania support (due to strong support interaction [17]). In Scheme 1 (ii), it showed that the presence of certain amounts (20–60 wt%) of titania dramatically enhanced activities. The contribution of titania can be drawn as MAO anchored on silica with titania as a spacer group. It can be also seen from SEM and EDX that at low content of titania, it was apparently decorated on silica surface and acted as a spacer to anchor MAO to the silica support. Thus, activities increased about 15–25% with the presence of titania between 20 and 40% in the mixed oxide supports. It should be mentioned that increased activities with the presence of titania as a spacer were observed because of less steric hindrance and less interaction on the support surface when a spacer was introduced. Thus, this was suggested to be more homogeneous-like system. Investigation of a spacer such as silane in copolymerization of ethylene/1-olefins was also reported [18,19]. However, when high amounts of titania were added, activities decreased because the strong support interaction as seen in Scheme 1 (iii) can occurred resulting in a combination

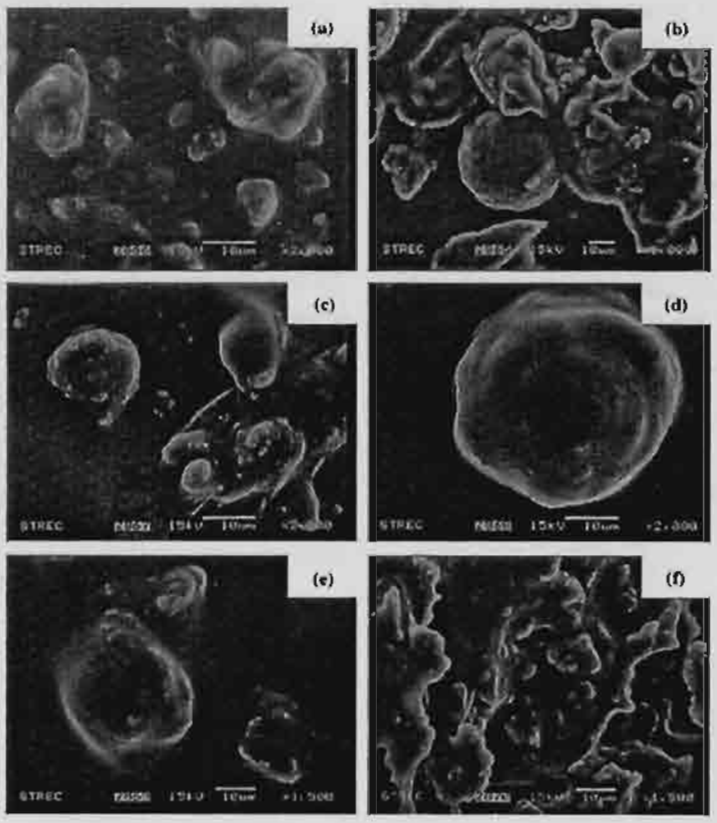

Figure 9. SEM micrographs of polymers obtained with various TiO_2–SiO_2 mixed oxide supports; (a) Ti/Si = 0/1, (b) Ti/Si = 2/8, (c) Ti/Si = 4/6, (d) Ti/Si = 6/4, (e) Ti/Si = 8/2, (f) Ti/Si = 1/0.

Table 2
Molar weight and molecular weight distribution of polymers obtained via TiO_2–SiO_2 mixed oxides supported-MAO with zirconocene catalyst

TiO_2–SiO_2 weight ratios	wt% of TiO_2 in mixed support	M_w^a($\times 10^{-4}$ g mol^{-1})	M_n^a($\times 10^{-4}$ g mol^{-1})	MWD[a]
0/100	0	3.61	1.06	3.4
20/80	20	3.42	1.08	3.2
40/60	40	2.91	1.13	2.6
60/40	60	2.60	0.96	2.7
80/20	80	2.65	0.93	2.8
100/0	100	2.41	0.59	4.1

[a]Obtained from GPC and MWD was calculated from M_w/M_n.

between Scheme 1 (i) and (iii) where titania started to isolate from silica as segregated titania. Morphologies of polymers produced via various supports were also investigated. The SEM micrographs of polymers are shown in figure 9. It indicated that there was no significant change in polymer morphologies upon various mixed oxide supports used. The molecular weight based on weight average (M_w) and based on number average (M_n), and molecular weight distribution (MWD) of polymers obtained are shown in table 2. It indicated that the addition of TiO_2 resulted in decreased molecular weights of polymers compared to those of pure SiO_2. However, the narrower molecular weight distribution was observed with the addition of TiO_2 except for the one with pure TiO_2.

4. Conclusions

The present study revealed influence of various TiO_2–SiO_2 mixed oxides supported-MAO on the catalytic activities during copolymerization of ethylene/1-octene. It was found that at certain contents of titania ranged between 20 and 60 wt% in the mixed oxide support, activities dramatically increased by 15–25% compared to those with the conventional pure silica support. It was proposed that titania added acted as a spacer to anchor MAO to the silica support resulting in less steric hindrance and less interaction on the support surface. However, larger amounts of titania resulted in lower activities because the strong support interaction between titania and MAO was more pronounced. The molecular weights of polymers were found to decrease with the addition of TiO_2 whereas narrower molecular weight distribution can be observed in the mixed TiO_2–SiO_2 supports.

Acknowledgments

The authors would like to thank the Thailand Research Fund (TRF), the National Research Council of Thailand (NRCT) and Thailand–Japan Transfer Technology Project (TJTTP-JBIC) for the financial support of this work. We would like to extend our thankful to Professor Takeshi Shiono at Hiroshima University, Japan for his kind advice of this project.

References

[1] C.L.P Shan, J.B.P Soares and A Penlidis, Polym. Chem. 40 (2002) 4426.
[2] K.J Chu, C.L.P Shan, A Soares and J.B.P Penlidis, Macromol. Chem. Phys. 200 (1999) 2372.
[3] A.M Uusitalo, T.T Pakkanen and E.I Iskola, J. Mol. Catal. A: Chem. 177 (2002) 179.
[4] K Soga and M Kaminaka, Makromol. Chem. 194 (1993) 1745.
[5] Y.S Ko, T.K Han, J.W Park and S.I Woo, Macromol. Rapid Commun. 17 (1996) 749.
[6] T. Sugano and K. Yamamoto *Eur. Pat. Appl.* 728773 (1996).
[7] M Margue and A Conte, J. Appl. Polm. Sci. 86 (2002) 2054.
[8] S Sensarma and S Sivaram, Polym. Inter. 51 (2002) 417.
[9] P.G Belelli, M.L Ferreira and D.E Damiani, Appl.Catal. A: Gen. 228 (2002) 189.
[10] J.T Xu, Y.B Zhu, Z.Q Fan and L.X Feng, J. Polym. Sci. Part A: Polym. Chem. 39 (2001) 3294.
[11] L Korach and K Czaja, Polym. Bull. 46 (2001) 67.
[12] A Koppl and H.G Alt, J. Mol. Catal. A: Chem. 165 (2001) 23.
[13] B Jongsomjit, P Praserthdam and P Kaewkrajang, Mater. Chem. Phys. 86 (2004) 243.
[14] X Gao and I.E Wachs, Catal. Today 51 (1999) 233.
[15] S.J Conway, J.W Falconer and C.H Rochester, J. Chem. Soc. Faraday Trans. 185 (1989) 71.
[16] D.C.M Dutoit, M Schneider and J Baiker A., J. Catal. 153 (1995) 165.
[17] R Riva, H Miessuer, R Vitali and G Del Piero, Appl. Catal. A 196 (2000) 111.
[18] C Chao, W Pratchayawutthirat, P Praserthdam Shiono and T Rempel, Macromol. Rapid Commun. 23 (2002) 672.
[19] B Jongsomjit, P Kaewkrajang, S.E Wanke and P Praserthdam Catal. Lett. 94 (2004) 205.

Jointly published by
Akadémiai Kiadó, Budapest
and Springer, Dordrecht

React.Kinet.Catal.Lett.
Vol. 85, No. 2, 299-304
(2005)

RKCL4652

METAL-SUPPORT INTERACTION IN MESOPOROUS SILICA SUPPORTED COBALT FISCHER-TROPSCH CATALYSTS

Joongjai Panpranot*, Sujaree Kaewgun and Piyasan Praserthdam
Center of Excellence on Catalysis and Catalytic Reaction Engineering,
Department of Chemical Engineering, Chulalongkorn University, Bangkok, Thailand

Received September 14, 2004
In revised form December 14, 2004
Accepted December 16, 2004

Abstract

The pore structure of silica supports (SiO_2 or MCM-41) has little influence on the metal-support interaction in silica supported cobalt catalysts. Cobalt dispersion, reduction behavior, and catalytic properties for the Fischer-Tropsch synthesis were primarily affected by the metal particle size.

Keywords: Cobalt catalyst, metal-support interaction, mesoporous silica, CO hydrogenation

INTRODUCTION

Cobalt-based catalysts are widely used in CO hydrogenation or Fischer-Tropsch synthesis (FTS) especially when high molecular weight paraffins are preferred [1-2]. To increase their activity, cobalt is usually deposited on a high surface area oxide support to obtain a high metal dispersion. Recently, the use of high surface area ordered mesoporous materials such as MCM-41 and SBA-15 for preparing Co-based Fischer-Tropsch catalysts has been explored [3-7]. Compared to amorphous silica-supported catalysts with similar Co loading, Co supported on these mesoporous materials have shown higher FTS activity due to a better dispersion of cobalt in mesoporous structure [8]. However, stronger interaction of cobalt species and the support in these catalysts were often found, resulted in catalysts with lower reducibilities. In this study, the effects of pore structure (SiO_2 and MCM-41) and the metal particle size on the metal-support interaction in supported Co F-T catalysts were investigated.

*Corresponding author. Tel: (66)-2-218-6859; Fax: (66)-2-218-6877
E-mail: joongjai.p@eng.chula.ac.th

0133-1736/2005/US$ 20.00.

EXPERIMENTAL

Catalyst preparation

Pure silica MCM-41 was prepared in the same manner as that of Kruk *et al.* [9] using the following gel composition: (1.0 SiO_2): (0.317 TMAOH): (0.45 CTMABr): (66.7 H_2O), where TMAOH denotes tetramethylammonium hydroxide and CTMABr denotes cetyltrimethyl ammonium bromide. High surface area SiO_2 with similar pore size to MCM-41 were obtained from Grace Davison Company. The series of supported Co catalysts (MCM-41 and SiO_2-supported) were prepared by the incipient wetness impregnation of the supports with an aqueous solution containing the desired amount of different cobalt precursors such as cobalt nitrate (Aldrich), cobalt acetate (APS), cobalt acetylacetonate (Aldrich), and cobalt chloride (Fluka). The catalysts were dried overnight in an oven at 110°C and then were calcined at 500°C in an air flow for 2 h. Elemental analysis was carried out for all the catalysts after calcination. The cobalt loading was determined to be approximately 7-8 wt.%.

Catalyst characterization

The BET surface area, pore volume, average pore diameter, and pore size distribution of the catalysts were determined by N_2 physisorption using a Micromeritics ASAP 2000 automated system. Each sample was degassed in the Micromeritics ASAP 2000 at 150°C for 4 h prior to N_2 physisorption. The XRD spectra of the catalysts were measured using a SIEMENS D5000 X-ray diffractometer, using Cu Kα radiation with a Ni filter in the 2-8° or 10-80°2θ angular regions. Temperature programmed reduction was performed using an in-house system and a temperature ramp of 5°C/min from 30 to 300°C in a flow of 5% H_2 in argon. Approximately 0.20 g of a calcined catalyst was placed in a quartz tube in a temperature-controlled oven and connected to a thermal conductivity detector. The H_2 consumption was measured by analyzing the effluent gas with a TCD.

Reaction study

CO hydrogenation was carried out at 220°C and 1 atm total pressure in a fixed-bed stainless steel reactor under differential conversion conditions. A flow rate of H_2/CO/Ar = 20/2/8 cm^3/min was used. Typically, 0.2 g of the catalyst samples was reduced *in situ* in flowing H_2 (50 cc/min) at 350°C for 10 h prior to reaction. The product samples were taken at 1-h intervals and

analyzed by gas chromatography. Steady state was reached after 6 h time-on-stream in all cases.

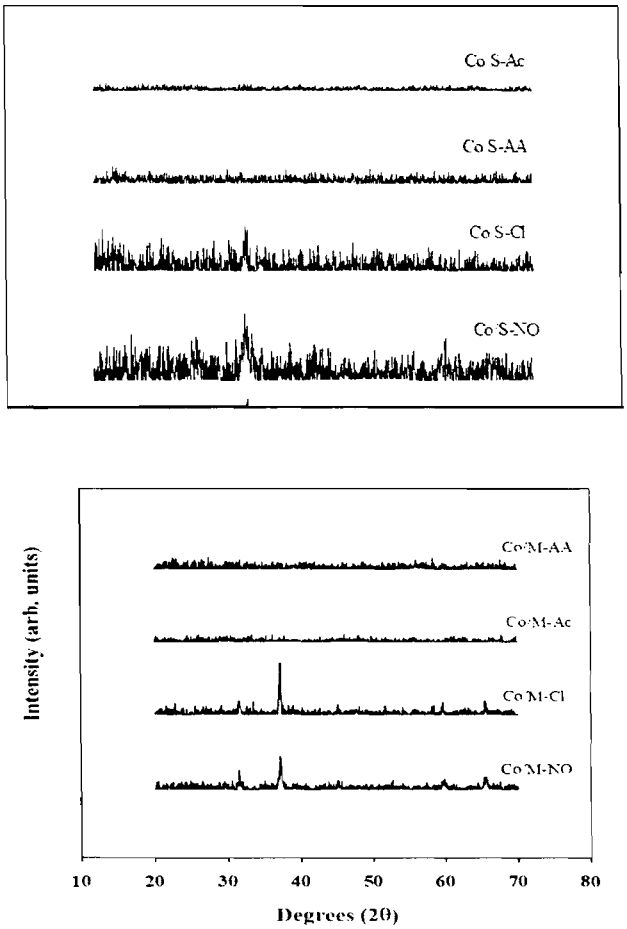

Fig. 1. XRD patterns of different SiO_2 and MCM-41-supported Co catalysts

RESULTS AND DISCUSSION

Two types of silica supported Co catalysts (Co/SiO_2 and Co/MCM-41) have been prepared using the incipient wetness impregnation method in order to study the effect of pore size and pore structure of the supports on cobalt dispersion, reduction behavior, and catalytic properties for the Fischer-Tropsch synthesis (FTS). The BET surface areas, pore volumes, and average pore

diameters of the original supports and the catalysts are given in Table 1. The significant decrease in surface area of the original support material suggests that cobalt was deposited in some of the pores of the supports. The XRD patterns of SiO_2 and MCM-41 supported Co catalysts after calcination in air at

Table 1

Characteristics of SiO_2 and MCM-41 supported Co catalysts

Catalyst	Co (wt%)[a]	BET S.A.[b] (m^2/g)	d_P[c] Co_3O_4 (nm)
SiO_2	-	717	-
Co/S-Ac	7.9	562	n/a
Co/S-AA	7.7	595	n/a
Co/S-Cl	7.1	517	17.6
Co/S-NO	8.4	571	16.4
MCM-41	-	1234	-
Co/M-Ac	8.3	756	n/a
Co/M-AA	7.8	675	n/a
Co/M-Cl	7.1	646	15.0
Co/M-NO	8.1	747	6.3

[a] Based on atomic absorption spectroscopy of the calcined catalysts.
[b] Based on the calcined catalysts. Error of measurement = ± 10%.
[c] Based on XRD line broadening of the calcined catalysts

500°C for 2 h are shown in Fig. 1. The catalysts prepared from cobalt nitrate and cobalt chloride exhibited the diffraction peaks of at 2θ of *ca.* 31.3°, 36.8°, 45.1°, 59.4°, and 65.4°, indicating the presence of Co_3O_4. The catalysts prepared from organic precursors (cobalt acetate and cobalt acetyl acetonate did not exhibit any distinct XRD patterns. This suggests that the crystallite sizes of Co_3O_4 prepared from organic precursors were much smaller than those prepared form inorganic ones [10].

Temperature-programmed reduction (TPR) profiles of SiO_2- and MCM-41-supported Co catalysts are shown in Fig. 2. In general, the reduction of Co_3O_4 composes of the two-step reduction of Co_3O_4 to CoO and then to Co^0 [11,12]. TPR profiles for supported Co catalysts, however, are more complex than for bulk Co_3O_4 due to various causes such as variation in metal particle size, metal-support interaction, and support porous structure resulting in differently reducible cobalt species on the support [13-14]. The TPR profiles of silica supported Co catalysts used in this study were found to be dependent on the type of cobalt precursors. Using organic cobalt precursors such as cobalt

acetate and cobalt acetylacetonate which could result in very small cobalt particles and stronger metal-support interaction showed a large portion of Co species that was reduced at higher reduction temperature. Any Co not reducible during the H_2 reduction up to 800°C is identified as "non-reducible" Co silicate [15,16]. However, for a given Co precursor, Co/SiO_2 and Co/MCM-41 exhibited similar TPR profiles. The results suggest that pore structure of the supports (SiO_2 or MCM-41) has little influence on the metal-support interaction on silica supported Co catalysts.

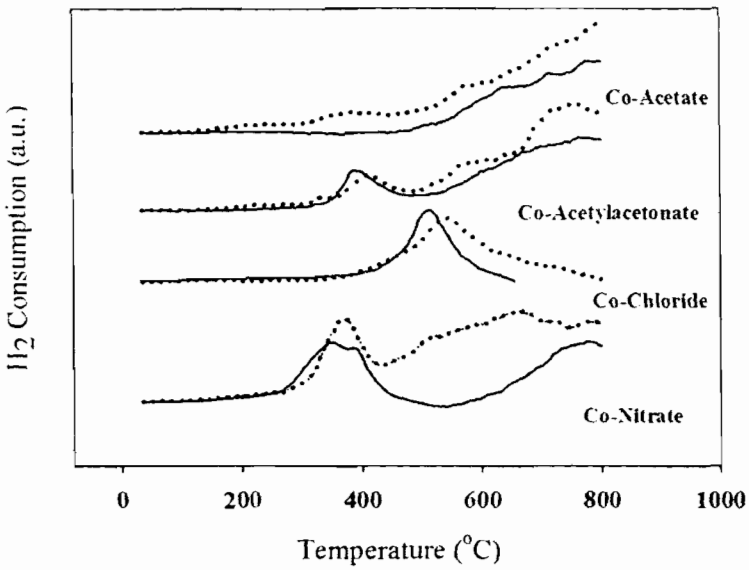

Fig. 2. Temperature program reduction (TPR) profiles of Co/MCM-41 (·····) and Co/SiO_2 (———).

The results of CO hydrogenation reaction test are reported in Table 2. It was found that Co-/M-NO exhibited the highest CO hydrogenation rate than all other catalysts in this study. The higher activity of such catalyst reflects the relatively high dispersion of cobalt on the catalysts. The catalysts prepared from cobalt chloride showed very low activities due to their low Co dispersion and maybe residual Cl^- blocking Co active sites [10]. The low activities of the ones prepared from cobalt acetate and cobalt acetyl acetonate were due probably to the unstable small Co particles forming Co silicates during reduction in H_2 and reaction.

Table 2

Results for CO hydrogenation[a]

Catalyst	Rate (gCH_2/ gcat./h)		CO Conversion (%)		Selectivity (%)		
	Initial	Steady-state	Initial	Steady-state	CH_4	C_2	C_3
Co/S-Ac	0.012	0.010	2.1	1.4	95	4.5	0.5
Co/S-AA	0.013	0.012	1.7	1.6	96	3.5	0.5
Co/S-Cl	0.007	0.006	0.9	0.8	84	13.0	3.0
Co/S-NO	0.176	0.167	23.4	22.7	95	5.0	-
Co/M-Ac	0.025	0.018	3.2	2.4	91	7.0	2.0
Co/M-AA	0.013	0.013	1.8	1.7	96	3.4	0.6
Co/M-Cl	0.024	0.018	3.3	2.4	97	2.5	0.5
Co/M-NO	0.449	0.323	59.8	47.6	82	6.0	2.0

[a] Reaction conditions are 220°C, 1 atm, and $H_2/CO = 10$

Acknowledgements. The financial supports from the Thailand Japan Technology Transfer Prject (TJTTP-JBIC) and the Thailand Research Fund (TRF) are gratefully acknowledged.

REFERENCES

1. R.B. Anderson: *The Fischer-Tropsch Synthesis*, Academic Press, San Diego 1984.
2. J.G. Goodwin, Jr.: *Prep. ACS. Div. Petr. Chem.*, **36**, 156 (1991).
3. D. Yin, W. Li, W. Yang, H. Xiang, Y. Sun, B. Zhong, S. Peng: *Micropor. Mesopor. Mater.*, **47**, 15 (2001).
4. J. Panpranot, J.G. Goodwin, Jr., A. Sayari: *Catal. Today*, **77**, 269 (2002).
5. Y. Wang, M. Noguchi, Y. Takahashi, Y. Ohtsuka: *Catal. Today*, **68**, 3 (2001).
6. A.Y. Khodakov, A. Griboval-Constant, R. Bechara, V.L. Zholobenko: *J. Catal.*, **206**, 230 (2002).
7. A. Martinez, C. Lopez, F. Marquez, I. Diaz: *J. Catal.*, **220**, 486 (2003).
8. J. Panpranot, J.G. Goodwin, Jr., A. Sayari: *J. Catal.*, **211**, 530 (2002).
9. M. Kruk, M. Jaronice, A. Sayari: *Micropor. Mesopor. Mater.*, **35-36**, 545 (2000).
10. J. Panpranot, S. Kaewgun, P. Praserthdam, J.G. Goodwin, Jr.: *Catal. Lett.*, **91**, 95 (2003).
11. A.M. Hilmen, D. Schanke, A. Holmen: *Catal. Lett.*, **38**, 143 (1996).
12. Y. Zhang, D. Wei, S. Hammache, J.G. Goodwin, Jr.: *J. Catal.*, **188**, 281 (1999).
13. R.C. Reuel, C.H. Bartholomew: *J. Catal.*, **85**, 63 (1984).
14. B. Ernst, S. Libs, P. Chaumette, A. Kiennemann, *Appl. Catal. A*, **186**, 145 (1999).
15. A. Kogelbauer, J.C. Weber, J.G. Goodwin, Jr.: *Catal. Lett.*, **34**, 259 (1995).
16. J.M. Jablonski, M. Wolcyrz, L. Krajczyk: *J. Catal.*, **173**, 530 (1998).

Catalysis Letters Vol. 103, Nos. 1–2, September 2005 (© 2005)
DOI: 10.1007/s10562-005-6504-8

Characteristics and catalytic properties of alumina–zirconia mixed oxides prepared by a modified Pechini method

Patta Soisuwan[a,b], Dean C. Chambers[c], David L. Trimm[b,c], Okorn Mekasuwandumrong[d], Joongjai Panpranot[a], and Piyasan Praserthdam[a,*]

[a]*Centre of Excellence on Catalysis and Catalytic Reaction Engineering, Department of Chemical Engineering, Faculty of Engineering, Chulalongkorn University, Bangkok, 10330 Thailand*
[b]*School of Chemical Engineering and Industrial Chemistry, University of New South Wales, Sydney, NSW, 2052 Australia*
[c]*CSIRO Petroleum, Private Bag 10, Clayton South, VIC, 3169 Australia*
[d]*Department of Chemical Engineering, Faculty of Engineering and Industrial Technology, Silpakorn University, Nakon Pathom, 73000 Thailand*

Received 22 November 2004; accepted 5 May 2005

A modified Pechini method was used to prepare alumina–zirconia mixed oxides at three different molar ratios. For comparison, pure alumina and pure zirconia were prepared using the same method. The mixed oxides were characterised by the BET method for surface area, X-ray diffraction, CO_2 and NH_3 temperature-programmed desorption. Elimination of 2-propanol was used as a probe reaction to characterise the surface of the mixed oxides. The modified Pechini preparation resulted in a poor acid–base strength of alumina surface resulting in high acetone selectivity where imperfect crystal structure of the tetragonal zirconia favoured high propylene production in 2-propanol elimination at 200 °C.

KEY WORDS: alumina; zirconia; mixed oxide; Pechini method; 2-propanol.

1. Introduction

The sol–gel technique is widely used for preparation of ceramic materials, especially mixed oxides, because lower temperatures are required compared to conventional ceramic mixing processes and it improves dispersion and homogeneity [1]. Different precursors have been used to prepare sol–gel materials, particularly metal alkoxides [2–10] and citric acid (CA) complexes [11–13]. The materials obtained from both processes are quite similar but gel formation is approached under different conditions. Zirconia prepared by the sol–gel method, however, usually possesses low surface area. Recently, it has been reported that solid powders were successfully prepared by the modified Pechini method [14,15], in which CA and ethylene glycol are polymerised around metal ions. In 1963, Pechini *et al.* discovered a preparation method of mixed oxides, which can be applied for ceramic and dielectric materials. Because of homogeneous starting solution producing resin intermediate and then resulting in oxide by ignition, this technique leads to closer combination of mixed oxides, which may enhance strong interaction between metal ions. Moreover, high surface area of solid powders is usually obtained by this method, which could bring about high dispersion of metal loading and consequently high active sites for catalytic reactions [15]. In this study, a modified Pechini method was used to prepare alumina, zirconia and alumina–zirconia mixed oxides. Zirconia toughened alumina is generally employed in ceramic application because of its well-known mechanical property, moreover, recently mixed oxide of zirconia and alumina has been introduced in medical application as a biocompatible nano-composite [16]. In catalytic reaction, zirconia alumina has been used as catalyst and/or support because of its surface property, stability and mechanical property. Modification of the mixed oxide by sulfate is well known and showed very good activity of isomerisation [17]. Zirconia alumina at different ratios was prepared to improve surface properties by well-dispersed sol gel preparation. The effect of Al/Zr ratio on the characteristics and catalytic properties of the alumina–zirconia mixed oxides was investigated by means of nitrogen physisorption (BET), X-ray diffraction (XRD) and CO_2 and NH_3 temperature-programmed desorption (TPD). Elimination reactions of 2-propanol were used to determine the catalytic activity of the oxides.

* To whom correspondence should be addressed.
E-mail: piyasan.p@chula.ac.th

2. Experimental

2.1. Preparation of alumina–zirconia mixed oxides

Alumina–zirconia mixed oxides were prepared using a modified Pechini method in the same manner as that of [14,15] with Al/Zr molar ratios of 1:3, 2:3, 1:1, and 3:1. For comparison, pure alumina and zirconia were prepared by the same method. Aluminium nitrate [$Al(NO_3)_3 \cdot 9H_2O$] and zirconyl nitrate [$ZrO(NO_3)_2 \cdot xH_2O$] were used as precursors. The nitrate salts

were dissolved in separately water. Aqueous CA solution was prepared and its pH was adjusted to ca. 1 by addition of 35% nitric acid. CA solution was added to the zirconyl nitrate solution at a molar ratio of [Al+Zr:CA]=3:7. Aluminium nitrate solution was added to the zirconyl citrate complex and finally ethylene glycol was added. The pH of the solution was adjusted to 7, by addition of 35% ammonium hydroxide, to form an alumina gel [18]. The resulting solution was heated under vacuum in a rotary evaporator at 90–100 °C until it became viscous and yellow. After the vacuum was removed, the solution became black and gel-like. This material was removed from the system, dried at 100 °C overnight and calcined in flowing air, with a heating rate of 1 °C/min and final temperature of 500 °C held for 6 h. In the case of pure zirconia, the gel-like material did not appear during the rotary evaporation step, even after many hours, but appeared after the vacuum was removed.

2.2. Characterisation

Characterisation of the samples using various analysis techniques was carried out on the calcined samples. The surface area was measured by nitrogen physisorption at 77 K after outgassing at 300 °C. Surface areas were determined by the BET method and pore-size distribution by the BJH method. The crystal structures were characterised by XRD (Siemens D5000) using nickel filtered CuK_α radiation. TPD of CO_2 was used to characterise the basic sites of the oxides. Samples were pre-treated at 400 °C for 1 h in He, then saturated with CO_2 (99.99%) at 35 °C for 3 h. Desorption of CO_2, by heating at 10 °C/min to 400 °C, was measured using a GOW-MAC thermal conductivity detector (TCD). TPD of NH_3 (Micromeritics Autochem 2910) was used to characterise the acid sites. Samples were pre-treated in He at 400 °C for 1 h and saturated with 10%NH_3/He at 100 °C for 2 h. Adsorbed NH_3 was removed by flowing He (10 mL/min) while heating at 10 °C/min to 400 °C and detected by TCD.

2.3. Catalytic activity

Catalyst testing was carried out at atmospheric pressure in a quartz fixed-bed reactor. The catalyst sample was treated in air at 400 °C for 1 h prior to the reaction to remove adsorbed H_2O and CO_2. Elimination of 2-propanol was carried out at 150, 200 and 250 °C as in [19,20]. Helium (~12 mL/min) was bubbled through 2-propanol at fixed temperature (~50 °C) to give a concentration of 12-mol% 2-propanol in He flowing through 100 mg of catalyst. Typical space velocities (WHSV) were in the range of 20–200 h^{-1} as in [20]. Reaction products were analysed using a Shimadzu GC-14A gas chromatograph with a flame ionisation detector and a column containing 15%-Carbowax 1000 supported on Chromosorb W. Measurements were taken every 20 min until a steady state was reached, typically after about 2 h. The reaction products were propylene, acetone and diisopropyl ether.

3. Results

3.1. N_2 adsorption

The BET surface areas and BJH pore size distributions of the mixed oxides solid powders after calcination for 6 h at 500 °C are given in table 1. The surface areas increased with alumina content. For pure zirconia, most of the pores were macro-sized (>50 nm), while the mixed oxides had pore volumes more evenly distributed between micro-, meso- and macropores. Pure alumina had most of its pore volume in the meso and macro range.

3.2. XRD analysis

Crystal phases of the mixed oxides were identified by XRD. Figure 1 shows the XRD patterns of pure zirconia, $Al_{40}Zr_{60}$ and pure alumina after calcination at 1000 °C. The identified crystal structures and crystallite sizes after ignition at 500 °C and calcinations at 800 and 1000 °C calculated using Scherrer's equation are shown in table 2.Calcination of zirconia at 500 °C and above gave mostly tetragonal phase, with the monoclinic phase becoming dominant at 1000 °C. Alumina was amorphous after calcination at 500 °C and changed from θ to α between 800 and 1000 °C. In the mixed oxide sample, no alumina XRD peaks could be detected at any temperature. The sample calcined at 500 °C was completely amorphous while only tetragonal zirconia peaks were detected even at 1000 °C. In all cases, the crystallite sizes increased with increasing calcinations temperature.

Table 1
Surface area and pore size distribution of zirconia, alumina and mixed oxides

Composition (mol%)	BET surface area (g/m^2)	BJH pore size distribution (%)		
		Micro <2 nm	Meso 2–50 nm	Macro >50 nm
Zirconia	56	6.2	24.1	69.7
$Al_{25}Zr_{75}$	70	26.4	43.8	29.7
$Al_{40}Zr_{60}$	182	24.5	33.9	41.7
$Al_{75}Zr_{25}$	228	34.2	30.5	35.4
Alumina	319	13.6	44.7	41.7

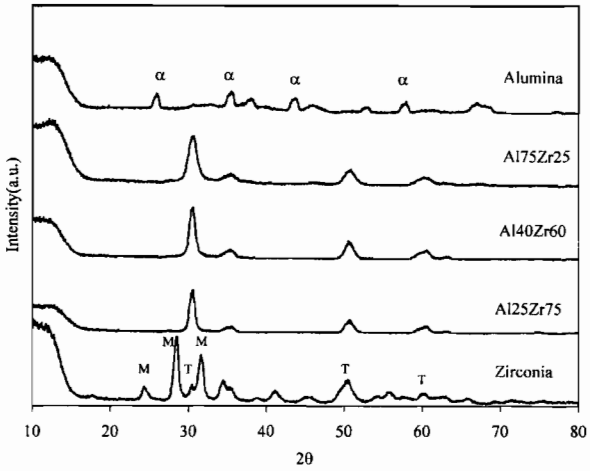

Figure 1. XRD diffraction pattern of zirconia, alumina and zirconia alumina mixed oxide calcined at 1000 °C.

Table 2
Crystal structure and size of zirconia crystals in zirconia, alumina and mixed oxides

Sample	Crystal structure (crystal size, nm)		
	Calcination temperature		
	500 °C	800 °C	1000 °C
Zirconia	T(13)	T(26)	M(31),T
$Al_{25}Zr_{75}$	A	T(13)	T(28)
$Al_{40}Zr_{60}$	A	T(14)	T(19)
$Al_{75}Zr_{25}$	A	A	T(13)
Alumina	A	θ	α

Symbols A, M and T indicate amorphous, monoclinic and tetragonal phases of zirconia (or pure alumina) respectively.
Symbols θ and α indicate theta and alpha phases of alumina respectively.

3.3. CO_2 temperature programmed desorption

Basicity of the catalysts was measured by CO_2 temperature programmed desorption up to 400 °C. Figure 2 shows the CO_2 TPD profiles of all the catalyst samples. In all cases, a single desorption peak was observed around 100–115 °C. The CO_2 desorption temperature of pure zirconia and pure alumina were found to be slightly lower than that of the mixed oxides. The amounts of CO_2 desorbed from the mixed oxides, pure alumina and pure zirconia were calculated by integrating the areas of CO_2 TPD profiles and are reported in table 3.

3.4. NH_3 temperature programmed desorption

Acidity of the catalysts was measured by NH_3-TPD. The NH_3 TPD profiles for all the catalysts are shown in figure 3. None of the materials tested showed distinct NH_3 desorption peaks up to 400 °C. The broad desorption peaks below 200 °C occurred at slightly higher temperature for two of the mixed oxides than for pure alumina or zirconia. This suggests that the acid strength of those mixed oxides is slightly greater than the pure oxides. Table 3 also shows the amounts of NH_3 desorbed from each sample.

3.5. Reaction test

The catalytic activities of the mixed oxide were tested in the elimination reactions of 2-propanol at 150, 200, and 250 °C. The results are given in table 4. At 150 °C,

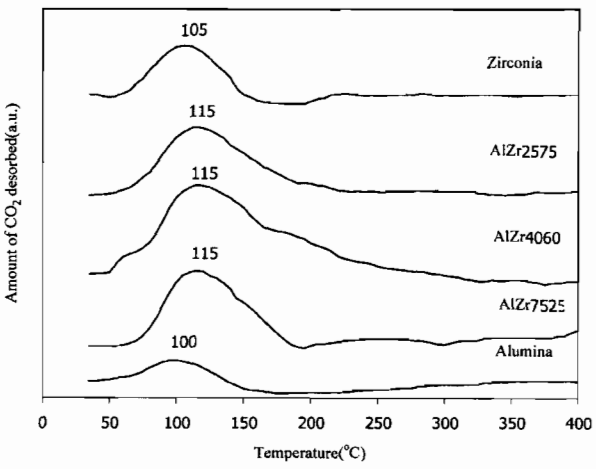

Figure 2. Temperature programmed desorption of CO_2 on mixed oxide, pure zirconia and pure alumina.

the elimination product was almost entirely acetone for all catalysts. At 200 °C, the product distribution depended on the catalyst composition. Catalysts high in alumina content produced mainly acetone, while those high in zirconia produced large amounts of propylene. Traces of diisopropyl ether appeared at this temperature. At higher temperature (250 °C) the product distribution changed again, to favour propylene production over all materials. Catalysts high in alumina also produced significant amounts of diisopropyl ether at this temperature. It should be noted that alumina activated in oxygen can exhibit dehydrogenation activity that may exceed considerably the dehydration selectivity [21]. However, the effect of oxygen pretreatment was not observed in this study (no oxidation reaction) since one would expect changes in selectivity of acetone with increasing reaction time due to consumption of oxygen covering the catalyst surface.

Table 3
Quantities of $CO_2$and NH_3 desorbed from zirconia, alumina and mixed oxides

Sample	CO_2 desorbed (μmol/g)	NH_3 desorbed (μmol/g)
Zirconia	172	202
$Al_{25}Zr_{75}$	279	478
$Al_{40}Zr_{60}$	632	752
$Al_{75}Zr_{25}$	485	830
Alumina	146	69

4. Discussion

The macropore system may occur after removal of organic material polymerised from CA and ethylene glycol in fresh gel. It is suggested that under these preparation conditions, well dispersed alumina and zirconia influencing orientation of alumina and zirconia crystal structure of the mixed oxide. Using this method, tetragonal phase of pure zirconia were obtained after calcination at 500 °C. The tetragonal phase zirconia is thermodynamically stable at a temperature above 1170 °C [22]. However, removal of combustible organic materials at 500 °C during preparation could result in sufficient energy to arrange the zirconia structure in tetragonal form.

Surface properties of pure zirconia, pure alumina and the mixed oxides might be classified into two types by probe molecule adsorption; CO_2 and NH_3 probe molecules. The interaction between CO_2 probe molecule and zirconia or mixed oxides surfaces might be physical adsorption in accordance with a result of Li *et al.* [23] showing desorption of CO_2 physical bonding on zirconia surface is around 100 °C. Desorption temperatures might be improved to be higher after atomically mixing zirconia with alumina. This is probably due to the interaction between aluminium, oxygen and zirconium ions in the mixed oxide increasing the physical strength between surface oxygen and CO_2 probe molecule.

It is known that the reaction pathways of 2-propanol elimination forming dehydration and dehydrogenation products occur on different nature and strength of acid–base sites [20]. Different mechanisms have been derived

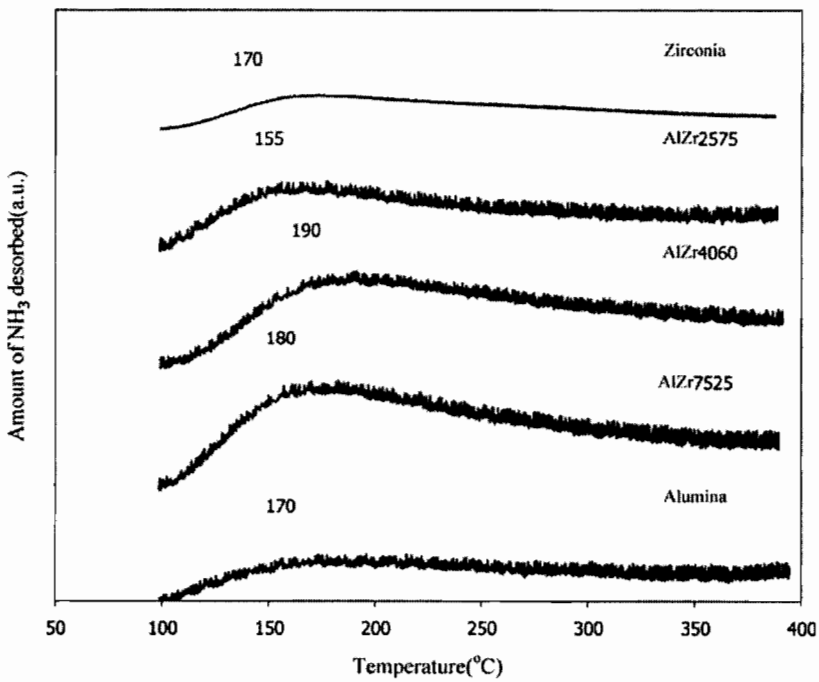

Figure 3. Temperature programmed desorption of NH_3 on mixed oxide, pure zirconia and pure alumina.

Table 4
Catalyst activity and selectivity during elimination of 2-propanol

Sample	T = 150 °C				T = 200 °C				T = 250 °C			
	% Conversion	S_P	S_A (%)	S_{DIP}	% Conversion	S_P	S_A (%)	S_{DIP}	% Conversion	S_P	S_A(%)	S_{DIP}
Alumina	3.5	2.0	98.0	0.0	9.8	1.6	98.1	0.3	36.6	66.3	24.1	9.5
$Al_{75}Zr_{25}$	5.5	1.3	98.7	0.0	2.5	6.3	92.6	1.1	6.9	66.6	28.7	4.6
$Al_{40}Zr_{60}$	0.3	10.2	89.8	0.0	1.0	7.7	92.3	0.0	10.7	48.3	48.8	2.9
$Al_{25}Zr_{75}$	2.2	2.0	98.0	0.0	1.3	27.5	71.7	0.8	7.5	64.3	34.5	1.2
Zirconia	1.0	8.9	91.1	0.0	4.4	89.2	10.2	0.6	7.5	75.2	24.5	0.3

based on individual transition states including E_1, E_2, and E_{1cB} [20,25]. E_1 mechanism requires strong acidic catalysts to form carbenium ions by abstraction of OH-group. The carbenium ions are rearranged via isomerisation and abstracted hydrogen resulting in different kind of alkenes [25].

In this study, the NH_3 temperature programmed desorption results exhibited a single peak below 200 °C suggesting that the acidic strength was probably unable to abstract OH groups. The E_1 mechanism then can be excluded. For E_2 mechanism, reaction occurs on dual acid–base sites to simultaneously eliminate a proton and hydroxyl group producing the main product alkene whereas for E_{1cB} mechanism, strong basic sites are required in order to firstly detach β hydrogen and then eliminate hydroxyl group [25].

Recently, Díez *et al.* [20,26] propose a mechanism slightly different from E_{1cB} mechanism in which reaction takes place via acid–base sites of imbalanced strength. Adsorption of OH group occurs on weak acid–base sites to form a surface propoxide intermediate. The most acidic hydrogen of alcohol is attacked by strong base site (the surface oxygen), in contrast, the Lewis acid site (the surface cation) attacks the oxygen of alcohol resulting in rupture of hydroxyl groups. Two pathways were proposed after forming propoxide on the surface: (a) dehydration of 2-propanol where acetone is a result of abstraction α-hydrogen and (b) dehydrogenation of 2-propanol producing propylene by detaching β-hydrogen. The products of the E_{1cB} mechanism could be either propylene or acetone or both depending on the strength of base site. However, the base site detaching β-hydrogen is stronger than the one detaching α-hydrogen. Waugh *et al.* [26,27] found that the activation energy of α-hydrogen abstraction is lower than the activation energy of β-hydrogen abstraction.

Generally, elimination of 2-propanol on alumina produces propylene as the main product via E_2 mechanism due to amphoteric properties of alumina [19, 28]. Dominuguez *et al.* [19] showed that γ-alumina gave propylene selectivity more than 80% in a range of reaction temperature 180–240 °C. However, in this study we observed that most of the propanol elimination products over the Pechini alumina were more than 90% acetone. Disordered structure of the Pechini amorphous alumina could result in an imbalanced strength of acid–base sites and the reaction pathway might occur via E_{1cB} proposed by Díez *et al.* The weak physically adsorbing CO_2 site of alumina as shown by the low temperature CO_2 desorption peak in figure 2 could bring about abstraction of α-hydrogen mostly resulting in acetone formation. This might be representative of very poor basicity of alumina surface.

Similar to the pure alumina, the Pechini alumina–zirconia mixed oxides converted to propanol towards acetone with more than 70% selectivity at 150 and 200 °C. Increasing zirconia content in the mixed oxides resulted in a slight decrease in acetone and increase in propylene selectivity at 200 °C. The propylene formation may be ascribed to zirconia. The E_{1cB} mechanism appeared to dominate over the alumina–zirconia mixed oxides. Although the CO_2 desorption peaks of the mixed oxides shifted towards 115 °C, the strength of basicity would not be very effective to abstract β-hydrogen. Increasing propylene selectivity over the alumina–zirconia mixed oxides was probably affected by dual acid–base property of zirconia via the E_2 mechanism. This is in a good agreement with the work reported by Tanabe [29], in which 2-propanol elimination on zirconia catalysts proceed by acid–base site bifunctional catalysis. The orientation of these sites plays an importance role in governing the reaction [30]. However, the orientation of alumina–zirconia mixed oxides structure would be undisciplined resulting in a decrease in acid–base bifunctional property. Therefore, the E_2 mechanism would not dominate over the alumina–zirconia mixed oxides.

Conversion of propanol towards propylene over tetragonal zirconia was observed with more than 80% selectivity at 200 °C. The well-ordered structure of tetragonal zirconia exhibited high selectivity of propylene via the dominant E_2 mechanism. In contrast, partly imperfect crystal of tetragonal zirconia could result in imbalanced acid–base site leading to acetone formation via the E_{1cB} mechanism.

5. Conclusions

The alumina–zirconia mixed oxides produced by the modified Pechini method resulted in combination of aluminium and zirconium atoms. Due to good

dispersion of aluminium and zirconium ions, the mixed oxides present only amorphous form. Apparently, the interaction between Al, Zr, and O in the mixed oxides resulted in higher physical strength of CO_2 adsorption. The modified acidity was, however, ambiguous because all the catalyst samples exhibited low acidity. The imbalance strength of acid–base site due to the imperfect crystal structure of all the catalysts resulted in higher acetone formation via E_{1cB} mechanism. However, 90% propylene selectivity was obtained on pure zirconia prepared by the modified Pechini method and 200 °C reaction temperature.

Acknowledgments

The authors would like to thank the Cooperative Research Network, Thai Ministry of Education, the Thailand Research Fund, the University of New South Wales and CSIRO for financial support. The authors also thank Mr Praharso, Ms Sarah Watson, Mr Richard Burgess and Mr John Starling and Dr Manh Hoang for their support.

References

[1] G. Ertl, H. Knözinger and J. Weitkamp, *Handbook of Heterogeneous Catalysis* (Wiley-VCH, City, 1997).
[2] J.C. Debsikdar, J. Non-Cryst. Solids 86 (1986) 231.
[3] R. Guinebretière, A. Dauger, A. Lecomte and H. Vesteghem, J. Non-Cryst. Solids 147&148 (1992) 542.
[4] J. Livage, F. Beteille, C. Roux, M. Chatry and P. Davidson, Acta mater. 46 (1998) 743.
[5] C. Stöcker and J. Baiker A., Non-Cryst. Solids 223 (1998) 165.
[6] M.M. Pineda, S. Castillo, T. López, R. Gómez, Cordero-Borboa and O. Novaro, Appl. Catal. B: Environ. 21 (1999) 79.
[7] J.L. Lakshmi, T.R.B. Jones, M. Gurgi and J.M. Miller, J. Mol. Catal. A: Chem. 152 (2000) 99.
[8] D.D. Jayaseelan, D.A. Rani, T. Nishikawa, H. Awaji and F.D. Gnanam, J. Euro. Ceram. Soc. 20 (2000) 267.
[9] A.C. Geiculescu and H.J. Rack, J. Non-Crytal. Solids 289 (2001) 53.
[10] Y. Hao, J. Li, X. Yang, X. Wang and L. Lu, Mat. Sci. Eng. A 367 (2004) 243.
[11] M. Ishii, M. Kakihana, K. Ishii, Y. Ikuma and M. Yoshimura, J. Mat. Res. Soc. 11(6) (1996) 1410.
[12] M. Kakihana, S. Kato, M. Yashima and M. Yoshimura, J. Alloys Comp. 280 (1998) 125.
[13] E.N.S. Muccillo, E.C.C. Souza and R. Muccillo, J. Alloys Comp. 344 (2002) 175.
[14] M.P. Pechini, Patent, 11 July (1967) 3,330,697.
[15] C.L. Robert, F. Ansart, C. Deloget, M. Gaudon and A. Rousset, Ceram. Int. 29 (2003) 151.
[16] Y.M. Kong, C.J. Bae, S.H. Lee, H.W. Kim and H.E. Kim, Biomaterials 26 (2005) 509.
[17] I.I. Abu, D.D. Das, H.K. Mishra and A.K. Dalai, J. Colloid Interface Sci. 267 (2003) 382.
[18] R. Mezei and K. Sinkó, Colloid Polym. Sci. 274 (1996) 1054.
[19] J.M. Dominguez, J.L. Hernandez and G. Sandoval, Appl. Cata. A: Gen. 197 (2000) 119.
[20] V.K. Díez, C.R. Apesteguía and J.I. Di Cosimo, J. Catal. 215 (2003) 220.
[21] B.H. Davis, J. Catal. 26 (1972) 348.
[23] P.D.L. Mercera, J.G. van Ommen, E.B.M. Doesburg, A.J. Burggraaf and J.R.H. Ross, Appl. Catal. 71 (1991) 363.
[23] Y. Li, D. He, Z. Cheng, C. Zu, J. Le and Q. Zhu, J. Mol. Catal. A: Chem. 175 (2001) 267.
[24] A. Davydov, *Molecular Spectroscopy of Oxide Catalyst Surfaces* (John Wiley & Sons, England, 2003).
[25] K. Tanabe, M. Misono, Y. Ono and H. Hattari, *New Solid Acids and Bases Their Catalyst Properties* (Kodansha, Tokyo, 1989).
[26] V.K. Díez, C.R. Apesteguía and J.I. Di Cosimo, Catal. Today 63 (2000) 53.
[27] K.C. Waugh, M. Bowker, R.W. Petts, H.D. Vanderwell and J. O'Malley, Appl. Catal. 25 (1986) 121.
[28] A. Gervasini, J. Fenyvesi and A. Auroux, Catal. Lett. 43 (1997) 219.
[29] K. Tanabe, Mat. Chem. Phys. 13 (1985) 347.
[30] S. Chokkaram and B.H. Davis, J. Mol. Catal. A: Chem. 118 (1997) 89.

Catalysis Letters Vol. 103, Nos. 1–2, September 2005 (© 2005)
DOI: 10.1007/s10562-005-6504-8

Characteristics and catalytic properties of alumina–zirconia mixed oxides prepared by a modified Pechini method

Patta Soisuwan[a,b], Dean C. Chambers[c], David L. Trimm[b,c], Okorn Mekasuwandumrong[d], Joongjai Panpranot[a], and Piyasan Praserthdam[a,*]

[a]*Centre of Excellence on Catalysis and Catalytic Reaction Engineering, Department of Chemical Engineering, Faculty of Engineering, Chulalongkorn University, Bangkok, 10330 Thailand*
[b]*School of Chemical Engineering and Industrial Chemistry, University of New South Wales, Sydney, NSW, 2052 Australia*
[c]*CSIRO Petroleum, Private Bag 10, Clayton South, VIC, 3169 Australia*
[d]*Department of Chemical Engineering, Faculty of Engineering and Industrial Technology, Silpakorn University, Nakon Pathom, 73000 Thailand*

Received 22 November 2004; accepted 5 May 2005

A modified Pechini method was used to prepare alumina–zirconia mixed oxides at three different molar ratios. For comparison, pure alumina and pure zirconia were prepared using the same method. The mixed oxides were characterised by the BET method for surface area, X-ray diffraction, CO_2 and NH_3 temperature-programmed desorption. Elimination of 2-propanol was used as a probe reaction to characterise the surface of the mixed oxides. The modified Pechini preparation resulted in a poor acid–base strength of alumina surface resulting in high acetone selectivity where imperfect crystal structure of the tetragonal zirconia favoured high propylene production in 2-propanol elimination at 200 °C.

KEY WORDS: alumina; zirconia; mixed oxide; Pechini method; 2-propanol.

1. Introduction

The sol–gel technique is widely used for preparation of ceramic materials, especially mixed oxides, because lower temperatures are required compared to conventional ceramic mixing processes and it improves dispersion and homogeneity [1]. Different precursors have been used to prepare sol–gel materials, particularly metal alkoxides [2–10] and citric acid (CA) complexes [11–13]. The materials obtained from both processes are quite similar but gel formation is approached under different conditions. Zirconia prepared by the sol–gel method, however, usually possesses low surface area. Recently, it has been reported that solid powders were successfully prepared by the modified Pechini method [14,15], in which CA and ethylene glycol are polymerised around metal ions. In 1963, Pechini *et al.* discovered a preparation method of mixed oxides, which can be applied for ceramic and dielectric materials. Because of homogeneous starting solution producing resin intermediate and then resulting in oxide by ignition, this technique leads to closer combination of mixed oxides, which may enhance strong interaction between metal ions. Moreover, high surface area of solid powders is usually obtained by this method, which could bring about high dispersion of metal loading and consequently high active sites for catalytic reactions [15]. In this study, a modified Pechini method was used to prepare alumina, zirconia and alumina–zirconia mixed oxides. Zirconia toughened alumina is generally employed in ceramic application because of its well-known mechanical property, moreover, recently mixed oxide of zirconia and alumina has been introduced in medical application as a biocompatible nano-composite [16]. In catalytic reaction, zirconia alumina has been used as catalyst and/or support because of its surface property, stability and mechanical property. Modification of the mixed oxide by sulfate is well known and showed very good activity of isomerisation [17]. Zirconia alumina at different ratios was prepared to improve surface properties by well-dispersed sol gel preparation. The effect of Al/Zr ratio on the characteristics and catalytic properties of the alumina–zirconia mixed oxides was investigated by means of nitrogen physisorption (BET), X-ray diffraction (XRD) and CO_2 and NH_3 temperature-programmed desorption (TPD). Elimination reactions of 2-propanol were used to determine the catalytic activity of the oxides.

* To whom correspondence should be addressed.
E-mail: piyasan.p@chula.ac.th

2. Experimental

2.1. Preparation of alumina–zirconia mixed oxides

Alumina–zirconia mixed oxides were prepared using a modified Pechini method in the same manner as that of [14,15] with Al/Zr molar ratios of 1:3, 2:3, 1:1, and 3:1. For comparison, pure alumina and zirconia were prepared by the same method. Aluminium nitrate [$Al(NO_3)_3 \cdot 9H_2O$] and zirconyl nitrate [$ZrO(NO_3)_2 \cdot xH_2O$] were used as precursors. The nitrate salts

were dissolved in separately water. Aqueous CA solution was prepared and its pH was adjusted to ca. 1 by addition of 35% nitric acid. CA solution was added to the zirconyl nitrate solution at a molar ratio of [Al+Zr:CA]=3:7. Aluminium nitrate solution was added to the zirconyl citrate complex and finally ethylene glycol was added. The pH of the solution was adjusted to 7, by addition of 35% ammonium hydroxide, to form an alumina gel [18]. The resulting solution was heated under vacuum in a rotary evaporator at 90–100 °C until it became viscous and yellow. After the vacuum was removed, the solution became black and gel-like. This material was removed from the system, dried at 100 °C overnight and calcined in flowing air, with a heating rate of 1 °C/min and final temperature of 500 °C held for 6 h. In the case of pure zirconia, the gel-like material did not appear during the rotary evaporation step, even after many hours, but appeared after the vacuum was removed.

2.2. Characterisation

Characterisation of the samples using various analysis techniques was carried out on the calcined samples. The surface area was measured by nitrogen physisorption at 77 K after outgassing at 300 °C. Surface areas were determined by the BET method and pore-size distribution by the BJH method. The crystal structures were characterised by XRD (Siemens D5000) using nickel filtered CuK_α radiation. TPD of CO_2 was used to characterise the basic sites of the oxides. Samples were pre-treated at 400 °C for 1 h in He, then saturated with CO_2 (99.99%) at 35 °C for 3 h. Desorption of CO_2, by heating at 10 °C/min to 400 °C, was measured using a GOW-MAC thermal conductivity detector (TCD). TPD of NH_3 (Micromeritics Autochem 2910) was used to characterise the acid sites. Samples were pre-treated in He at 400 °C for 1 h and saturated with 10%NH_3/He at 100 °C for 2 h. Adsorbed NH_3 was removed by flowing He (10 mL/min) while heating at 10 °C/min to 400 °C and detected by TCD.

2.3. Catalytic activity

Catalyst testing was carried out at atmospheric pressure in a quartz fixed-bed reactor. The catalyst sample was treated in air at 400 °C for 1 h prior to the reaction to remove adsorbed H_2O and CO_2. Elimination of 2-propanol was carried out at 150, 200 and 250 °C as in [19,20]. Helium (~12 mL/min) was bubbled through 2-propanol at fixed temperature (~50 °C) to give a concentration of 12-mol% 2-propanol in He flowing through 100 mg of catalyst. Typical space velocities (WHSV) were in the range of 20–200 h^{-1} as in [20]. Reaction products were analysed using a Shimadzu GC-14A gas chromatograph with a flame ionisation detector and a column containing 15%-Carbowax 1000 supported on Chromosorb W. Measurements were taken every 20 min until a steady state was reached, typically after about 2 h. The reaction products were propylene, acetone and diisopropyl ether.

3. Results

3.1. N_2 adsorption

The BET surface areas and BJH pore size distributions of the mixed oxides solid powders after calcination for 6 h at 500 °C are given in table 1. The surface areas increased with alumina content. For pure zirconia, most of the pores were macro-sized (>50 nm), while the mixed oxides had pore volumes more evenly distributed between micro-, meso- and macropores. Pure alumina had most of its pore volume in the meso and macro range.

3.2. XRD analysis

Crystal phases of the mixed oxides were identified by XRD. Figure 1 shows the XRD patterns of pure zirconia, $Al_{40}Zr_{60}$ and pure alumina after calcination at 1000 °C. The identified crystal structures and crystallite sizes after ignition at 500 °C and calcinations at 800 and 1000 °C calculated using Scherrer's equation are shown in table 2.Calcination of zirconia at 500 °C and above gave mostly tetragonal phase, with the monoclinic phase becoming dominant at 1000 °C. Alumina was amorphous after calcination at 500 °C and changed from θ to α between 800 and 1000 °C. In the mixed oxide sample, no alumina XRD peaks could be detected at any temperature. The sample calcined at 500 °C was completely amorphous while only tetragonal zirconia peaks were detected even at 1000 °C. In all cases, the crystallite sizes increased with increasing calcinations temperature.

Table 1
Surface area and pore size distribution of zirconia, alumina and mixed oxides

Composition (mol%)	BET surface area (g/m^2)	BJH pore size distribution (%)		
		Micro <2 nm	Meso 2–50 nm	Macro >50 nm
Zirconia	56	6.2	24.1	69.7
$Al_{25}Zr_{75}$	70	26.4	43.8	29.7
$Al_{40}Zr_{60}$	182	24.5	33.9	41.7
$Al_{75}Zr_{25}$	228	34.2	30.5	35.4
Alumina	319	13.6	44.7	41.7

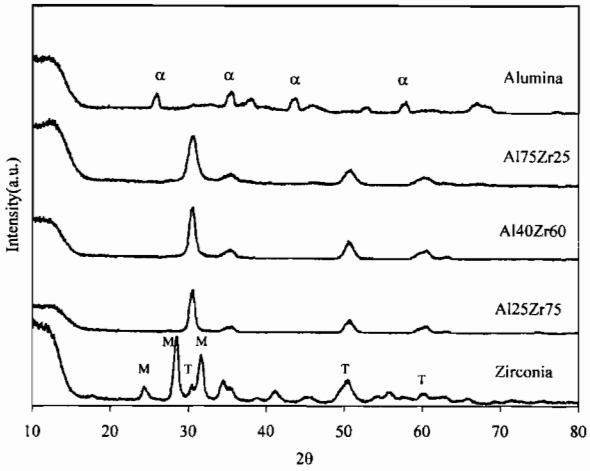

Figure 1. XRD diffraction pattern of zirconia, alumina and zirconia alumina mixed oxide calcined at 1000 °C.

Table 2
Crystal structure and size of zirconia crystals in zirconia, alumina and mixed oxides

Sample	Crystal structure (crystal size, nm)		
	Calcination temperature		
	500 °C	800 °C	1000 °C
Zirconia	T(13)	T(26)	M(31),T
$Al_{25}Zr_{75}$	A	T(13)	T(28)
$Al_{40}Zr_{60}$	A	T(14)	T(19)
$Al_{75}Zr_{25}$	A	A	T(13)
Alumina	A	θ	α

Symbols A, M and T indicate amorphous, monoclinic and tetragonal phases of zirconia (or pure alumina) respectively.
Symbols θ and α indicate theta and alpha phases of alumina respectively.

3.3. CO_2 temperature programmed desorption

Basicity of the catalysts was measured by CO_2 temperature programmed desorption up to 400 °C. Figure 2 shows the CO_2 TPD profiles of all the catalyst samples. In all cases, a single desorption peak was observed around 100–115 °C. The CO_2 desorption temperature of pure zirconia and pure alumina were found to be slightly lower than that of the mixed oxides. The amounts of CO_2 desorbed from the mixed oxides, pure alumina and pure zirconia were calculated by integrating the areas of CO_2 TPD profiles and are reported in table 3.

3.4. NH_3 temperature programmed desorption

Acidity of the catalysts was measured by NH_3-TPD. The NH_3 TPD profiles for all the catalysts are shown in figure 3. None of the materials tested showed distinct NH_3 desorption peaks up to 400 °C. The broad desorption peaks below 200 °C occurred at slightly higher temperature for two of the mixed oxides than for pure alumina or zirconia. This suggests that the acid strength of those mixed oxides is slightly greater than the pure oxides. Table 3 also shows the amounts of NH_3 desorbed from each sample.

3.5. Reaction test

The catalytic activities of the mixed oxide were tested in the elimination reactions of 2-propanol at 150, 200, and 250 °C. The results are given in table 4. At 150 °C,

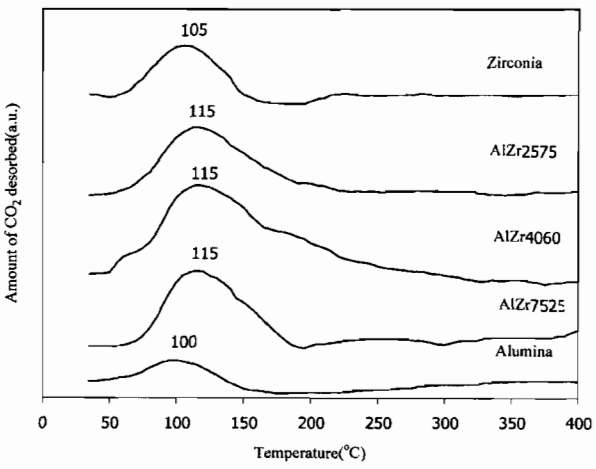

Figure 2. Temperature programmed desorption of CO_2 on mixed oxide, pure zirconia and pure alumina.

the elimination product was almost entirely acetone for all catalysts. At 200 °C, the product distribution depended on the catalyst composition. Catalysts high in alumina content produced mainly acetone, while those high in zirconia produced large amounts of propylene. Traces of diisopropyl ether appeared at this temperature. At higher temperature (250 °C) the product distribution changed again, to favour propylene production over all materials. Catalysts high in alumina also produced significant amounts of diisopropyl ether at this temperature. It should be noted that alumina activated in oxygen can exhibit dehydrogenation activity that may exceed considerably the dehydration selectivity [21]. However, the effect of oxygen pretreatment was not observed in this study (no oxidation reaction) since one would expect changes in selectivity of acetone with increasing reaction time due to consumption of oxygen covering the catalyst surface.

Table 3
Quantities of $CO_2$and NH_3 desorbed from zirconia, alumina and mixed oxides

Sample	CO_2 desorbed (μmol/g)	NH_3 desorbed (μmol/g)
Zirconia	172	202
$Al_{25}Zr_{75}$	279	478
$Al_{40}Zr_{60}$	632	752
$Al_{75}Zr_{25}$	485	830
Alumina	146	69

4. Discussion

The macropore system may occur after removal of organic material polymerised from CA and ethylene glycol in fresh gel. It is suggested that under these preparation conditions, well dispersed alumina and zirconia influencing orientation of alumina and zirconia crystal structure of the mixed oxide. Using this method, tetragonal phase of pure zirconia were obtained after calcination at 500 °C. The tetragonal phase zirconia is thermodynamically stable at a temperature above 1170 °C [22]. However, removal of combustible organic materials at 500 °C during preparation could result in sufficient energy to arrange the zirconia structure in tetragonal form.

Surface properties of pure zirconia, pure alumina and the mixed oxides might be classified into two types by probe molecule adsorption; CO_2 and NH_3 probe molecules. The interaction between CO_2 probe molecule and zirconia or mixed oxides surfaces might be physical adsorption in accordance with a result of Li *et al.* [23] showing desorption of CO_2 physical bonding on zirconia surface is around 100 °C. Desorption temperatures might be improved to be higher after atomically mixing zirconia with alumina. This is probably due to the interaction between aluminium, oxygen and zirconium ions in the mixed oxide increasing the physical strength between surface oxygen and CO_2 probe molecule.

It is known that the reaction pathways of 2-propanol elimination forming dehydration and dehydrogenation products occur on different nature and strength of acid–base sites [20]. Different mechanisms have been derived

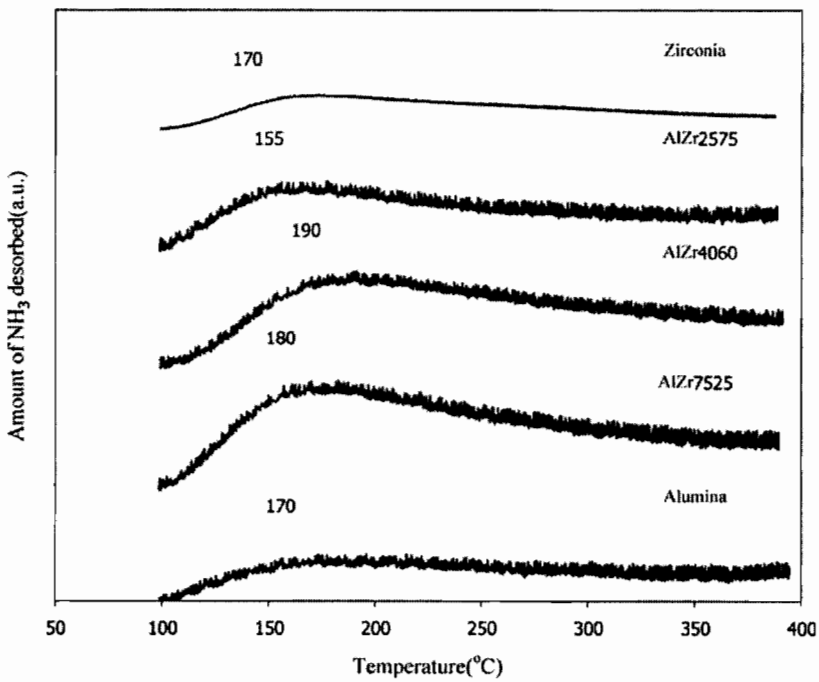

Figure 3. Temperature programmed desorption of NH_3 on mixed oxide, pure zirconia and pure alumina.

Table 4
Catalyst activity and selectivity during elimination of 2-propanol

Sample	T = 150 °C				T = 200 °C				T = 250 °C			
	% Conversion	S_P	S_A (%)	S_{DIP}	% Conversion	S_P	S_A (%)	S_{DIP}	% Conversion	S_P	S_A(%)	S_{DIP}
Alumina	3.5	2.0	98.0	0.0	9.8	1.6	98.1	0.3	36.6	66.3	24.1	9.5
$Al_{75}Zr_{25}$	5.5	1.3	98.7	0.0	2.5	6.3	92.6	1.1	6.9	66.6	28.7	4.6
$Al_{40}Zr_{60}$	0.3	10.2	89.8	0.0	1.0	7.7	92.3	0.0	10.7	48.3	48.8	2.9
$Al_{25}Zr_{75}$	2.2	2.0	98.0	0.0	1.3	27.5	71.7	0.8	7.5	64.3	34.5	1.2
Zirconia	1.0	8.9	91.1	0.0	4.4	89.2	10.2	0.6	7.5	75.2	24.5	0.3

based on individual transition states including E_1, E_2, and E_{1cB} [20,25]. E_1 mechanism requires strong acidic catalysts to form carbenium ions by abstraction of OH-group. The carbenium ions are rearranged via isomerisation and abstracted hydrogen resulting in different kind of alkenes [25].

In this study, the NH_3 temperature programmed desorption results exhibited a single peak below 200 °C suggesting that the acidic strength was probably unable to abstract OH groups. The E_1 mechanism then can be excluded. For E_2 mechanism, reaction occurs on dual acid–base sites to simultaneously eliminate a proton and hydroxyl group producing the main product alkene whereas for E_{1cB} mechanism, strong basic sites are required in order to firstly detach β hydrogen and then eliminate hydroxyl group [25].

Recently, Díez *et al.* [20,26] propose a mechanism slightly different from E_{1cB} mechanism in which reaction takes place via acid–base sites of imbalanced strength. Adsorption of OH group occurs on weak acid–base sites to form a surface propoxide intermediate. The most acidic hydrogen of alcohol is attacked by strong base site (the surface oxygen), in contrast, the Lewis acid site (the surface cation) attacks the oxygen of alcohol resulting in rupture of hydroxyl groups. Two pathways were proposed after forming propoxide on the surface: (a) dehydration of 2-propanol where acetone is a result of abstraction α-hydrogen and (b) dehydrogenation of 2-propanol producing propylene by detaching β-hydrogen. The products of the E_{1cB} mechanism could be either propylene or acetone or both depending on the strength of base site. However, the base site detaching β-hydrogen is stronger than the one detaching α-hydrogen. Waugh *et al.* [26,27] found that the activation energy of α-hydrogen abstraction is lower than the activation energy of β-hydrogen abstraction.

Generally, elimination of 2-propanol on alumina produces propylene as the main product via E_2 mechanism due to amphoteric properties of alumina [19, 28]. Dominuguez *et al.* [19] showed that γ-alumina gave propylene selectivity more than 80% in a range of reaction temperature 180–240 °C. However, in this study we observed that most of the propanol elimination products over the Pechini alumina were more than 90% acetone. Disordered structure of the Pechini amorphous alumina could result in an imbalanced strength of acid–base sites and the reaction pathway might occur via E_{1cB} proposed by Díez *et al.* The weak physically adsorbing CO_2 site of alumina as shown by the low temperature CO_2 desorption peak in figure 2 could bring about abstraction of α-hydrogen mostly resulting in acetone formation. This might be representative of very poor basicity of alumina surface.

Similar to the pure alumina, the Pechini alumina–zirconia mixed oxides converted to propanol towards acetone with more than 70% selectivity at 150 and 200 °C. Increasing zirconia content in the mixed oxides resulted in a slight decrease in acetone and increase in propylene selectivity at 200 °C. The propylene formation may be ascribed to zirconia. The E_{1cB} mechanism appeared to dominate over the alumina–zirconia mixed oxides. Although the CO_2 desorption peaks of the mixed oxides shifted towards 115 °C, the strength of basicity would not be very effective to abstract β-hydrogen. Increasing propylene selectivity over the alumina–zirconia mixed oxides was probably affected by dual acid–base property of zirconia via the E_2 mechanism. This is in a good agreement with the work reported by Tanabe [29], in which 2-propanol elimination on zirconia catalysts proceed by acid–base site bifunctional catalysis. The orientation of these sites plays an importance role in governing the reaction [30]. However, the orientation of alumina–zirconia mixed oxides structure would be undisciplined resulting in a decrease in acid–base bifunctional property. Therefore, the E_2 mechanism would not dominate over the alumina–zirconia mixed oxides.

Conversion of propanol towards propylene over tetragonal zirconia was observed with more than 80% selectivity at 200 °C. The well-ordered structure of tetragonal zirconia exhibited high selectivity of propylene via the dominant E_2 mechanism. In contrast, partly imperfect crystal of tetragonal zirconia could result in imbalanced acid–base site leading to acetone formation via the E_{1cB} mechanism.

5. Conclusions

The alumina–zirconia mixed oxides produced by the modified Pechini method resulted in combination of aluminium and zirconium atoms. Due to good

dispersion of aluminium and zirconium ions, the mixed oxides present only amorphous form. Apparently, the interaction between Al, Zr, and O in the mixed oxides resulted in higher physical strength of CO_2 adsorption. The modified acidity was, however, ambiguous because all the catalyst samples exhibited low acidity. The imbalance strength of acid–base site due to the imperfect crystal structure of all the catalysts resulted in higher acetone formation via E_{1cB} mechanism. However, 90% propylene selectivity was obtained on pure zirconia prepared by the modified Pechini method and 200 °C reaction temperature.

Acknowledgments

The authors would like to thank the Cooperative Research Network, Thai Ministry of Education, the Thailand Research Fund, the University of New South Wales and CSIRO for financial support. The authors also thank Mr Praharso, Ms Sarah Watson, Mr Richard Burgess and Mr John Starling and Dr Manh Hoang for their support.

References

[1] G. Ertl, H. Knözinger and J. Weitkamp, *Handbook of Heterogeneous Catalysis* (Wiley-VCH, City, 1997).
[2] J.C. Debsikdar, J. Non-Cryst. Solids 86 (1986) 231.
[3] R. Guinebretière, A. Dauger, A. Lecomte and H. Vesteghem, J. Non-Cryst. Solids 147&148 (1992) 542.
[4] J. Livage, F. Beteille, C. Roux, M. Chatry and P. Davidson, Acta mater. 46 (1998) 743.
[5] C. Stöcker and J. Baiker A., Non-Cryst. Solids 223 (1998) 165.
[6] M.M. Pineda, S. Castillo, T. López, R. Gómez, Cordero-Borboa and O. Novaro, Appl. Catal. B: Environ. 21 (1999) 79.
[7] J.L. Lakshmi, T.R.B. Jones, M. Gurgi and J.M. Miller, J. Mol. Catal. A: Chem. 152 (2000) 99.
[8] D.D. Jayaseelan, D.A. Rani, T. Nishikawa, H. Awaji and F.D. Gnanam, J. Euro. Ceram. Soc. 20 (2000) 267.
[9] A.C. Geiculescu and H.J. Rack, J. Non-Crytal. Solids 289 (2001) 53.
[10] Y. Hao, J. Li, X. Yang, X. Wang and L. Lu, Mat. Sci. Eng. A 367 (2004) 243.
[11] M. Ishii, M. Kakihana, K. Ishii, Y. Ikuma and M. Yoshimura, J. Mat. Res. Soc. 11(6) (1996) 1410.
[12] M. Kakihana, S. Kato, M. Yashima and M. Yoshimura, J. Alloys Comp. 280 (1998) 125.
[13] E.N.S. Muccillo, E.C.C. Souza and R. Muccillo, J. Alloys Comp. 344 (2002) 175.
[14] M.P. Pechini, Patent, 11 July (1967) 3,330,697.
[15] C.L. Robert, F. Ansart, C. Deloget, M. Gaudon and A. Rousset, Ceram. Int. 29 (2003) 151.
[16] Y.M. Kong, C.J. Bae, S.H. Lee, H.W. Kim and H.E. Kim, Biomaterials 26 (2005) 509.
[17] I.I. Abu, D.D. Das, H.K. Mishra and A.K. Dalai, J. Colloid Interface Sci. 267 (2003) 382.
[18] R. Mezei and K. Sinkó, Colloid Polym. Sci. 274 (1996) 1054.
[19] J.M. Dominguez, J.L. Hernandez and G. Sandoval, Appl. Cata. A: Gen. 197 (2000) 119.
[20] V.K. Díez, C.R. Apesteguía and J.I. Di Cosimo, J. Catal. 215 (2003) 220.
[21] B.H. Davis, J. Catal. 26 (1972) 348.
[23] P.D.L. Mercera, J.G. van Ommen, E.B.M. Doesburg, A.J. Burggraaf and J.R.H. Ross, Appl. Catal. 71 (1991) 363.
[23] Y. Li, D. He, Z. Cheng, C. Zu, J. Le and Q. Zhu, J. Mol. Catal. A: Chem. 175 (2001) 267.
[24] A. Davydov, *Molecular Spectroscopy of Oxide Catalyst Surfaces* (John Wiley & Sons, England, 2003).
[25] K. Tanabe, M. Misono, Y. Ono and H. Hattari, *New Solid Acids and Bases Their Catalyst Properties* (Kodansha, Tokyo, 1989).
[26] V.K. Díez, C.R. Apesteguía and J.I. Di Cosimo, Catal. Today 63 (2000) 53.
[27] K.C. Waugh, M. Bowker, R.W. Petts, H.D. Vanderwell and J. O'Malley, Appl. Catal. 25 (1986) 121.
[28] A. Gervasini, J. Fenyvesi and A. Auroux, Catal. Lett. 43 (1997) 219.
[29] K. Tanabe, Mat. Chem. Phys. 13 (1985) 347.
[30] S. Chokkaram and B.H. Davis, J. Mol. Catal. A: Chem. 118 (1997) 89.

Available online at www.sciencedirect.com
SCIENCE DIRECT®
Journal of Power Sources 148 (2005) 18–23
JOURNAL OF POWER SOURCES
www.elsevier.com/locate/jpowsour

Short communication

Effects of electrolyte type and flow pattern on performance of methanol-fuelled solid oxide fuel cells

S. Assabumrungrat [a,*], W. Sangtongkitcharoen [a], N. Laosiripojana [b], A. Arpornwichanop [c], S. Charojrochkul [d], P. Praserthdam [a]

[a] *Center of Excellence in Catalysis and Catalytic Reaction Engineering, Department of Chemical Engineering, Faculty of Engineering, Chulalongkorn University, Bangkok 10330, Thailand*
[b] *The Joint Graduate School of Energy and Environment, King Mongkut's University of Technology Thonburi, Bangkok 10140, Thailand*
[c] *Control and Systems Engineering, Department of Chemical Engineering, Faculty of Engineering, Chulalongkorn University, Bangkok 10330, Thailand*
[d] *National Metal and Materials Technology Center (MTEC), Pathumthani, Thailand*

Received 1 November 2004; received in revised form 20 January 2005; accepted 25 January 2005
Available online 2 April 2005

Abstract

A comparison is made of the performances of methanol-fuelled solid oxide fuel cells (SOFCs) with different types of electrolyte (i.e., oxygen ion- and proton-conducting electrolytes) and flow patterns (i.e., plug flow (PF) and mixed flow (MF)). Although it was demonstrated earlier that, under the same inlet steam:methane ratio, an SOFC with a proton-conducting electrolyte (SOFC-H^+) thermodynamically offers higher efficiency than one with an oxygen ion-conducting electrolyte (SOFC-O^{2-}), the benefit of a lower steam requirement for the SOFC-O^{2-} was not taken into account. Therefore, this study attempts to consider the benefit of differences in the steam requirement on the performance of SOFCs operated with different electrolytes and flow patterns. The efficiencies under the best conditions are compared in the temperature range of 900–1300 K. It is found that the maximum efficiencies decrease with increasing temperature and follow the sequence: SOFC-H^+ (PF) > SOFC-O^{2-} (PF) > SOFC-H^+ (MF) > SOFC-O^{2-} (MF). The corresponding inlet H_2O:MeOH ratios are at the carbon formation boundary for the SOFC-O^{2-} electrolyte, but are about 1.3–1.5 times the stoichiometric ratio for the SOFC-H^+. It is clearly demonstrated that the PF mode is superior to the MF mode and that, although the benefit from the lower steam requirement is realized for the SOFC-O^{2-}, the use of the proton-conducting electrolyte in the SOFCs is more promising.

Keywords: Solid oxide fuel cell; Electrolyte; Efficiency; Methanol; Flow pattern; Steam requirement

1. Introduction

The solid oxide fuel cell (SOFC) is a promising technology for electrochemical power generation. Due to its high operating temperature, the SOFC offers the prospect of a wide range of applications, flexibility of fuel choices and the possibility of operation with an internal reformer. Among the various possible fuels, i.e., methane, methanol, ethanol and gasoline, both ethanol and methanol have been reported [1] to offer high electromotive force output and efficiency. Methanol is preferable given its availability, high energy density and ready storage and distribution [2,3], as well as the claim [4] that methanol can be injected directly onto anodes without serious carbon blockage [4]. In operation, the SOFC can use either an oxygen ion-conducting electrolyte or a proton-conducting electrolyte. Most current research efforts have been focusing on the SOFC with the oxygen ion-conducting electrolyte (SOFC-O^{2-}) rather than with the proton-conducting electrolyte (SOFC-H^+). A number of recent studies on advanced SOFC operations, such as development of intermediate temperature-SOFCs [5] and the integration of SOFCs with intercool gas turbines [6], are still based mainly on the use of the oxygen ion-conducting electrolyte.

* Corresponding author. Tel.: +662 218 6868; fax: +662 218 6877.
E-mail address: Suttichai.A@chula.ac.th (S. Assabumrungrat).

0378-7753/$ – see front matter © 2005 Elsevier B.V. All rights reserved.
doi:10.1016/j.jpowsour.2005.01.034

Nomenclature

E	electromotive force of a cell (V)
F	Faraday constant (C mol^{-1})
ΔH^0	lower heating value of methanol (J s^{-1})
K	equilibrium constant of the hydrogen oxidation reaction (kPa$^{-0.5}$)
p_i	partial pressure of component i (kPa)
q	electrical charge (A)
R	gas constant (J mol^{-1} K^{-1})
T	temperature (K)
U_f	fuel utilization (%)
W	electrical work (W)

Greek letters

φ	potential (V)
η	system efficiency (%)

Subscripts

a	anode
c	cathode

Some research efforts have been carried out to compare the performances of SOFCs with different electrolytes. Thermodynamic analysis reveals that the SOFC-H^+ shows higher efficiency for the conversion of chemical energy to electrical power than the SOFC-O^{2-} for systems fed by hydrogen [7]. The same conclusion has also been reached for methane-fuelled SOFCs [8]. The comparisons were, however, performed under the same inlet steam:methane ratio [8]. Our previous work employed thermodynamic analysis to determine the carbon formation boundary for a direct internal-reforming (DIR) SOFC fed by methanol [9] and found that the SOFC-O^{2-} is more attractive than the SOFC-H^+ in terms of a lower steam requirement at the feed to the anode due to the simultaneous formation of steam by the electrochemical reaction of H_2 and O^{2-}.

The difference in the steam requirement among both types of SOFC is particularly pronounced at high values of the extent of the electrochemical reaction. The effect of the SOFC operation modes (i.e., external reforming (ER), indirect internal-reforming (IIR) and direct internal-reforming (DIR)) on the steam requirement at the carbon formation boundary has been investigated for SOFCs fed by methane [10]. It was found that when using the SOFC-O^{2-}, the ER-SOFC and the IIR-SOFC show the same values of the steam:methane ratio at the carbon formation boundary, independent of the extent of electrochemical reaction. By contrast, due to the presence of extra steam from the electrochemical reaction at the anode chamber, the DIR-SOFC can be operated at lower values of the steam:methane ratio compared with the other modes. For the SOFC-H^+, the required steam:methane ratios are higher than those for the SOFC-O^{2-}, but they are independent of the SOFC operation modes. In the performance comparisons among the SOFCs with different types of electrolyte, the differences in the steam requirement should be taken into account as it is generally known that extra steam can act as a diluent and lower the SOFC efficiency. Therefore, it remains unclear whether the SOFC-H^+ is superior to the SOFC-O^{2-}.

It is the objective of this study to compare the performances of DIR-SOFCs with different electrolytes (i.e., oxygen ion- and proton-conducting electrolytes) and flow patterns (i.e., plug flow (PF) and mixed flow (MF)) by taking into account the benefit from the differences in their steam requirement. The flow pattern should be considered because it affects both the steam requirement of the system, particularly for the SOFC-O^{2-}, and the cell performance. The information obtained from this work is important for determining whether research into fuel cell development should be directed towards the system using the proton-conducting electrolyte.

2. Theory

The reactions involved in the production of hydrogen from methanol steam-reforming can be represented by Eqs. (1)–(3) [11,12], i.e.,

$$CH_3OH = 2H_2 + CO \text{ (methanol decomposition)} \quad (1)$$

$$CO + H_2O = H_2 + CO_2 \text{ (water gas shift reaction)} \quad (2)$$

$$CO + 3H_2 = CH_4 + H_2O \text{ (methanation)} \quad (3)$$

The reactions taking place at the anode and the cathode for the two types of electrolyte can be summarized as follows:

SOFC-O^{2-}:

$$\text{anode} : H_2 + O^{2-} = H_2O + 2e^- \quad (4)$$

$$\text{cathode} : O_2 + 4e^- = 2O^{2-} \quad (5)$$

SOFC-H^+:

$$\text{anode} : H_2 = 2H^+ + 2e^- \quad (6)$$

$$\text{Cathode} : 2H^+ + \tfrac{1}{2}O_2 + 2e^- = H_2O \quad (7)$$

As seen from the above equations, it should be noted that water is produced in the anode chamber for the SOFC-O^{2-}, but in the cathode chamber for the SOFC-H^+.

The electromotive force (E) of a cell is the difference in the potential of the two electrodes. Thus, the electromotive force can be represented as follows:

$$E = |\varphi_c - \varphi_a| \quad (8)$$

where φ_c and φ_a are the potentials of the cathode and the anode, respectively. The electrode potential can be calculated from Nernst equation. Because the electrochemical reactions at the electrodes are different, depending on the electrolyte

type, the potential can be expressed as follows:

$$\text{SOFC-O}^{2-}: \quad \varphi = \left(\frac{RT}{4F}\right) \ln\, p_{O_2} \tag{9}$$

$$\text{SOFC-H}^{+}: \quad \varphi = \left(\frac{RT}{2F}\right) \ln\, p_{H_2} \tag{10}$$

where p_i is the partial pressure of component i, R the universal gas constant, T the absolute temperature and F is the Faraday constant.

For SOFC-O^{2-}, the partial pressure of oxygen in the cathode chamber is calculated from its mole fraction, while the following equation is used to determine the partial pressure of oxygen in the anode chamber.

$$p_{O_2} = \left(\frac{p_{H_2O}}{K p_{H_2}}\right)^2 \tag{11}$$

For the SOFC-H^{+}, the partial pressure of hydrogen in the anode chamber is calculated from its mole fraction, while the partial pressure of hydrogen in the cathode is given by:

$$p_{H_2} = \frac{p_{H_2O}}{K p_{O_2}^{1/2}} \tag{12}$$

In Eqs. (11) and (12), K is the equilibrium constant of the hydrogen oxidation reaction.

Regarding the possible SOFC configurations, gas flow within the flow channels of the SOFC stack can be classified broadly into two ideal flow patterns, i.e., plug flow and mixed flow. The former is characterized by the fact that the gas mixture moves orderly through the channel with no element of the gas mixing with any other element ahead or behind, whereas with mixed flow the contents are well-mixed and uniform throughout. Although most typical SOFCs are operated under a condition close to the PF mode, the MF mode can be realized by using a high recycle rate.

In the PF mode, the electromotive force (E) changes along the SOFC stack due to the distribution of gas compositions along the flow channels in both the anode and the cathode sections. The average electromotive force ($\bar{E}$) can be obtained from numerical integration of the gas distribution along the stack. To simplify the calculation, the gas compositions at the anode are assumed to reach their equilibrium compositions along the stack. The calculation procedures of the equilibrium compositions in SOFCs have been described in our previous work [9].

When current is drawn from the SOFC cell, the maximum electrical work (W) produced by the SOFC and the system efficiency (η) defined as the ratio of the maximum conversion of the chemical energy of the fuel fed in the SOFC system to electrical work, are calculated from Eqs. (13) and (14), respectively.

$$W = q\bar{E} \tag{13}$$

$$\eta = \frac{q\bar{E}}{-\Delta H^0} \times 100\% \tag{14}$$

where q is the electrical charge passing through the electrolyte and ΔH^0 is the lower heating value (LHV) of methanol at the standard condition.

It should be noted that the assumption of the equilibrium state of gas compositions along the flow channel may be reasonable because the rates of methanol steam-reforming and the water gas shift reaction are fast, particularly at high temperature [13–16]. Several researchers reported that the conversion of methanol from the methanol steam-reforming always close to 100% when the operating temperature above 573 K is applied [13–15]. Moreover, at 1173 K, methanol steam-reforming has been reported [16] to occur homogenously and reach equilibrium. Deviation from this equilibrium condition would result in lower values of the electromotive force and the efficiency of SOFCs as less hydrogen would be generated in the anode chamber to compensate for the hydrogen consumed by the electrochemical reaction. Therefore, the results shown in this work represent the best performances for all SOFC cases.

3. Results and discussion

The efficiency and electromotive force at different fuel utilizations for methanol-fuelled SOFCs with different electrolyte types and flow patterns are shown in Fig. 1. The inlet steam:methanol (H_2O:MeOH) ratio is at the stoichiometric value of 1 for all SOFCs. The fuel utilization, U_f, is defined as the moles of hydrogen consumed by the electrochemical reaction divided by the maximum moles of hydrogen produced from the methanol steam-reforming (3 mol of hydrogen per 1 mol of methanol). As can be seen from Fig. 1(a), efficiencies increase with increasing fuel utilization for all SOFCs because more hydrogen is utilized for electrical power production. At high fuel utilization, however, the efficiencies of the SOFCs with the MF mode decrease, which corresponds to a sharp drop in the electromotive force observed in the MF mode (Fig. 1(b)). Although it is typical that the electromotive force decreases with increasing fuel utilization as the hydrogen partial pressure becomes smaller at higher fuel utilization, the flow characteristics of the PF mode allow the electromotive force to decrease gradually along the flow channel. Consequently, the PF mode provides a higher average electromotive force than the MF mode in which the electromotive force is at its minimum value over the entire cell area. It should be noted that although both ideal flow modes are not achieved in real operations, experimental SOFCs using tubular and planar cells show behaviour close to the PF and MF modes, respectively.

At present, most experimental studies related to the investigation of SOFC performance are based on systems that use an oxygen ion-conducting electrolyte, and experimental comparison of SOFC performance for the two flow patterns at the same operating condition is not available in the literature. According to Veyo and Forbes [17], an efficiency of 66–70% was achieved at 85% fuel utilization when pure hy-

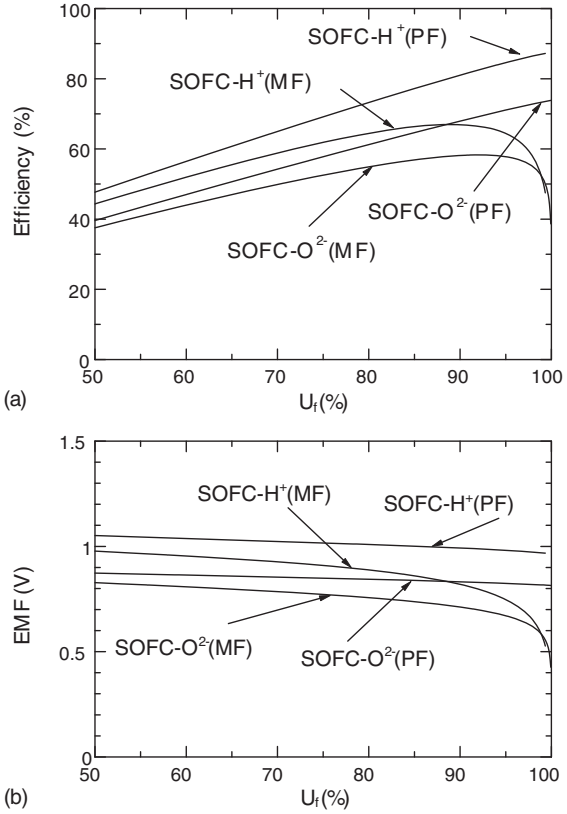

Fig. 1. Performance of SOFC-O^{2-} and SOFC-H^{+} operated under plug flow (PF) and mixed flow (MF): (a) efficiency; (b) electromotive force (inlet H_2O:MeOH = 1, T = 1300 K, P = 101.3 kPa).

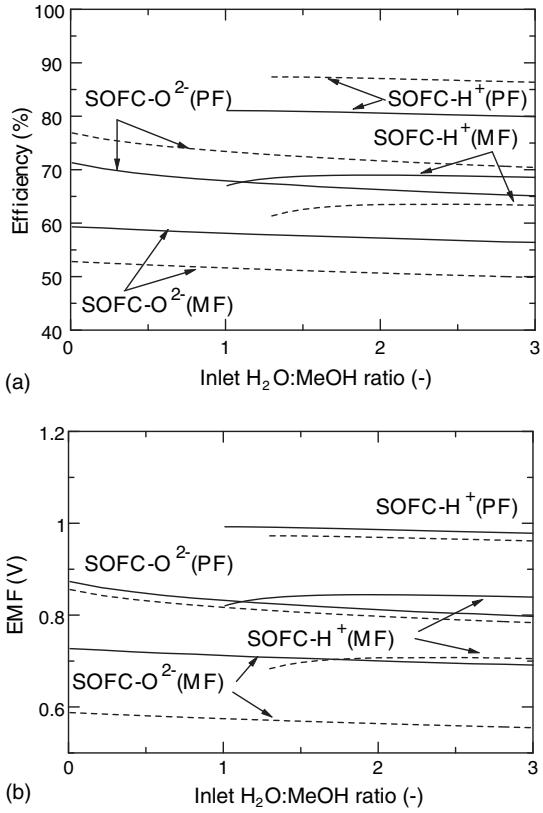

Fig. 2. Influence of inlet H_2O:MeOH ratio on SOFC performance at fuel utilization of 90% (solid line) and 99% (dashed line): (a) efficiency; (b) electromotive force (T = 1300 K, P = 101.3 kPa).

drogen was used as a fuel in a tubular SOFC. At the same level of utilization, the data in Fig. 1(a) show that the efficiency is reduced to 65% if methanol is fed to the system and a SOFC-O^{2-} (PF) combination is used. The information obtained has strengthened the fact that operation with pure hydrogen fuel yields higher efficiency than using any fuel of an equivalent amount. In addition, when methane was fed to a planar SOFC, at a methane utilization of 86% an efficiency of 53.6% was obtained [18], which is close to the value of 55% if methanol is applied in place of methane in our study (SOFC-O^{2-} (MF)).

The results in Fig. 1 also show that the SOFC-H^{+} offers higher efficiency than the SOFC-O^{2-} for both flow pattern modes. This is in good agreement with previous results obtained for SOFCs fuelled by hydrogen [7] and methane [8]. The electrolyte type plays an important role on the value of the hydrogen partial pressure in the anode side and, therefore, on the electromotive force and efficiency of the SOFC. The partial pressure of hydrogen for the SOFC-H^{+} is relatively higher than that for the SOFC-O^{2-} because the water generated from the electrochemical reaction is present and acts as an inert gas at the anode side for the SOFC-O^{2-}, whereas it appears at the cathode side for the SOFC-H^{+}. It is noted that when pure hydrogen is fed to the anode, the mole fraction of hydrogen in the anode chamber is always unity along the cell length for the SOFC-H^{+}.

According to the above analysis for SOFCs with different electrolyte types and flow patterns under the same inlet H_2O:MeOH ratio, it is demonstrated that the SOFC with the proton-conducting electrolyte operated under the PF mode (SOFC-H^{+} (PF)) is the most favourable choice. Our previous work [9] has shown, however, that the steam requirement to operate the SOFC without carbon formation for the SOFC-O^{2-} is lower than that of the SOFC-H^{+}. Thus, it is important to take into account this benefit in efficiency comparisons between different SOFCs. The effect of the inlet H_2O:MeOH ratio on the efficiency and electromotive force of the SOFC at the fuel utilizations of 90% (solid lines) and 99% (dashed lines) is presented in Fig. 2. The minimum inlet H_2O:MeOH ratios represent values at the carbon formation boundary. Details of the calculations for the carbon formation boundary in each operating mode have been described in our earlier work [9]. It was found that the SOFC-O^{2-} can be operated at the carbon-free condition without a requirement for extra steam in the methanol feed, and both the efficiency and electromotive force decrease with an increase in the inlet H_2O:MeOH ratio. Therefore, an addition of steam in the feed lowers the performance of the SOFC-O^{2-}. For the SOFC-H^{+}, the inlet H_2O:MeOH ratios at the carbon formation boundary are higher than those for the SOFC-O^{2-}, particularly at high fuel utilization, and the effect of the inlet H_2O:MeOH ratio on the SOFC performance is less pronounced. As the water from

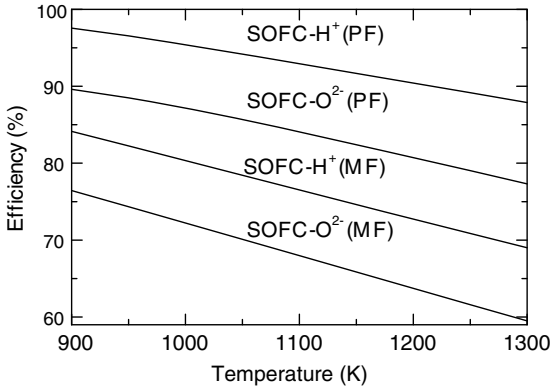

Fig. 3. Maximum efficiency of different SOFCs at different operating temperatures ($P = 101.3$ kPa).

the electrochemical reaction is generated at the cathode side, additional steam is required in the methanol feed at the anode side to promote hydrogen production. On the other hand, excessive steam will reduce the hydrogen concentration of the gas mixture at the anode side.

As it has been found that the SOFC performance is dependent on fuel utilization and inlet H_2O:MeOH ratio, it is possible to determine the maximum efficiency and the corresponding conditions for all SOFC cases at a specified temperature by performing calculations at various values of the inlet H_2O:MeOH ratio and the fuel utilization. The results for a temperature range of 900–1300 K are shown in Figs. 3 and 4. The maximum efficiencies follow the sequence: SOFC-H^+ (PF) > SOFC-O^{2-} (PF) > SOFC-H^+ (MF) > SOFC-O^{2-} (MF). The corresponding inlet H_2O:MeOH ratios are at the carbon formation boundary for both the SOFC-O^{2-} (PF) and SOFC-O^{2-} (MF), but are about 1.3 and 1.5 times the stoichiometric ratio for the SOFC-H^+ (MF) and the SOFC-H^+ (PF), respectively. The values of fuel utilization at the maximum efficiency are mainly governed by the flow pattern. For SOFCs operated under the PF mode, the utilization is constant at approximately 99%, but decreases slightly from 96.1 to 92.3% and from 95.5 to 92.0% for the SOFC-H^+ (MF) and the SOFC-O^{2-} (MF), respectively, when the temperature is increased from 900 to 1300 K. From these results, it is obvious that the proton-conducting electrolyte is more preferable for use in SOFCs. In addition, the PF mode is better than the MF mode. The SOFC-H^+ provides approximately 7.7–10.6% higher efficiency than the SOFC-O^{2-} with the same flow pattern mode in the range of temperature studied. The maximum efficiency for all cases decreases with increasing temperature. This is in good agreement with the decrease in electromotive force due to the thermodynamic Gibb's free energy.

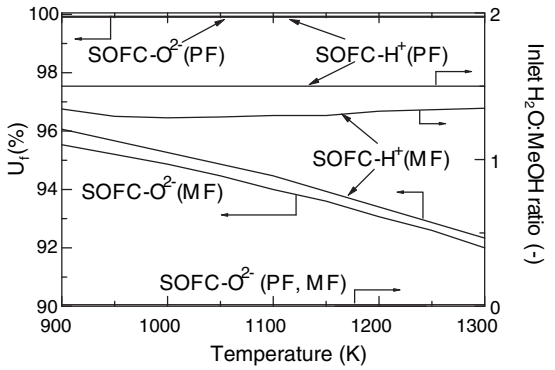

Fig. 4. Operating conditions corresponding to those in Fig. 3, at maximum efficiency ($P = 101.3$ kPa).

From the above studies, it is found that although the benefit of lower steam requirement is taken into account in the calculations for the SOFC-O^{2-}, the SOFC-H^+ still shows higher efficiency than the SOFC-O^{2-} for both the PF and the MF modes. This implies that the development of SOFCs should be directed towards the use of the proton-conducting electrolyte. It should also be noted, however, that this study has not taken into account all the losses presented in real SOFC operation and, therefore, it will be the aim of our next investigation to consider these losses when undertaking efficiency comparisons. The SOFC-H^+ allows the cell to reach easily a high hydrogen utilization without an additional effort to separate steam from the anode gas and circulate it back to the cell as required for the SOFC-O^{2-}.

4. Conclusions

The performance of methanol-fuelled SOFCs using proton- and oxygen ion-conducting electrolytes and operating under plug flow and mixed flow modes is investigated. The electromotive force and efficiency are dependent on fuel utilization, inlet H_2O:MeOH ratio, operating temperature, operation mode and electrolyte type. The benefit of less steam requirement for the SOFC-O^{2-} is taken into account in comparisons of SOFC performance. It is demonstrated that the plug flow is superior to the mixed flow and that the use of the proton-conducting electrolyte is more preferable. These findings indicate that SOFC development should be directed towards a system that was the proton-conducting electrolyte.

Acknowledgements

Support from the Thailand Research Fund and Chulalongkorn University Graduate Scholarship commemorating the 72nd Anniversary of H.M. King RAMA IX is gratefully acknowledged.

References

[1] S.L. Douvartzides, F.A. Coutelieris, K. Demin, P.E. Tsiakaras, AIChE J. 49 (2003) 248–257.
[2] B. Emonts, J.B. Hansen, S.L. Jorgensen, B. Hohlein, R. Peters, J. Power Sources 71 (1998) 288.

[3] K. Ledjeff-Hey, V. Formanski, T. Kalk, J. Roes, J. Power Sources 71 (1998) 199–207.
[4] G.J. Saunders, J. Preece, K. Kendal, J. Power Sources 131 (1–2) (2004) 23–26.
[5] P. Aguiar, C.S. Adjiman, N.P. Brandon, J. Power Sources 138 (2004) 120–136.
[6] Y. Yi, A.D. Rao, J. Brouwer, G.S. Samuelsen, J. Power Sources 132 (2004) 77–85.
[7] A.K. Demin, P.E. Tsiakaras, Int. J. Hydrogen Energy 26 (2001) 1103–1108.
[8] A.K. Demin, P.E. Tsiakaras, V.A. Sobyanin, S.Y. Hramova, Solid State Ionics 152–153 (2002) 555–560.
[9] S. Assabumrungrat, N. Laosiripojana, V. Pavarajarn, W. Sangtongkitcharoen, A. Tangjitmatee, P. Praserthdam, J. Power Sources 139 (2005) 55–60.
[10] W. Sangtongkitcharoen, S. Assabumrungrat, V. Pavarajarn, N. Laosiripojana, P. Praserthdam, J. Power Sources 142 (2005) 75–80.
[11] J.C. Amphlett, M.J. Evans, R.A. Jones, R.F. Mann, R.D. Weir, Can. J. Chem. Eng. 59 (1981) 720.
[12] Y. Lwin, W.R.W. Daud, A.B. Mohamad, Z. Yaakob, Int. J. Hydrogen Energy 25 (1) (2000) 47–53.
[13] P.J. de Wild, M.J.F.M. Verhaak, Catal. Today 60 (2000) 3–10.
[14] X. Zhang, P. Shi, J. Mol. Catal. A-Chem. 194 (2003) 99–105.
[15] P. Chantaravitoon, S. Chavadej, J. Schwank, Chem. Eng. J. 97 (2004) 161–171.
[16] N. Laosiripojana, Reaction engineering of indirect internal steam reforming of methane for application in solid oxide fuel cells, Ph.D. Thesis, University of London, UK, 2003.
[17] S.E. Veyo, C.A. Forbes, in: P. Stevens (Ed.), Proceedings of Third European Solid Oxide Fuel Cell Forum, Nantes, France, 1998, pp. 79–86.
[18] Y. Matsuzaki, Y. Baba, T. Ogiwara, H. Yakabe, in: J. Huijsmans (Ed.), Proceedings of Fifth European Solid Oxide Fuel Cell Forum, Lucerne, Switzerland, 2002, pp. 776–783.

Catalysis Letters Vol. 103, Nos. 1–2, September 2005 (© 2005)
DOI: 10.1007/s10562-005-6502-x

Synthesis, characterization, and catalytic properties of Pd and Pd–Ag catalysts supported on nanocrystalline TiO_2 prepared by the solvothermal method

Joongjai Panpranot[a,*], Lakkana Nakkararuang[a], Bongkot Ngamsom[b], and Piyasan Praserthdam[a]

[a]*Department of Chemical Engineering, Center of Excellence on Catalysis and Catalytic Reaction Engineering, Chulalongkorn University, Bangkok, 10330, Thailand*

[b]*Department of Chemical Engineering, King Mongkut Institute of Technology, Ladkrabang, Bangkok, Thailand*

Received 25 February 2005; accepted 5 May 2005

Nanocrystalline titania have been prepared by thermal decomposition of titanium (IV) *n*-butoxide in two different solvents (toluene and 1,4-butanediol) at 320 °C and employed as supports for Pd and Pd–Ag catalysts for selective acetylene hydrogenation for the first time. The titania products obtained from both solvents were pure anatase phase with relatively the same crystallite sizes and BET surface areas. However, due to different crystallization pathways, the number of Ti^{3+} defective sites as shown by ESR results of the titania prepared in toluene was much higher than the ones prepared in 1,4-butanediol. It was found that the use of anatase titania with higher defective sites as a support for Pd catalysts resulted in lower activity and selectivity in selective acetylene hydrogenation. However, this effect was suppressed by Ag promotion.

KEY WORDS: nanocrystalline titania; solvothermal method; acetylene hydrogenation; supported Pd catalysts.

1. Introduction

The solvothermal method has been used to successfully synthesize various types of nanosized metal oxides with large surface area, high crystallinity, and high thermal stability [1–7]. For example, thermal decomposition of titanium (IV) *n*-butoxide in organic solvents yields nano-sized pure anatase titania without bothersome procedures such as purification of the reactants or handling in an inert atmosphere. These nanocrystalline titanias have been shown to exhibit high photocatalytic activities [8, 9]. However, the thermal stability as well as photocatalytic activity of the solvothermal-derived titania were found to be strongly dependent on the organic solvent used as the reaction medium during crystallization [7]. The titania products synthesized in toluene showed lower thermal stability and lower photocatalytic activities than the ones synthesized in 1,4-butanediol. The authors suggested that the amount of defect structures in the titania prepared by this method was different depending on the solvent used due to the different crystallization pathways.

Due to their unique properties, it is interesting to investigate the characteristics and catalytic properties of the solvothermal-derived nanocrystalline titania supported noble metal as another exploitation of such materials. It is well known that metal catalyst supported on titania exhibits 'the strong metal-support interaction' (SMSI) phenomenon after reduction at high temperatures due to the decoration of the metal surface by partially reducible metal oxides [10, 11] or by an electron transfer between the support and the metals [12, 13]. In selective hydrogenation of acetylene to ethylene on Pd/TiO_2 catalysts, the charge transfer from Ti species to Pd weakened the adsorption strength of ethylene on the Pd surface hence higher ethylene selectivity was obtained [14].

In this study, nanocrystalline titanias were synthesized by the solvothermal method in two different solvents (1,4-butanediol and toluene) and employed as supports for Pd and Pd–Ag catalysts for selective hydrogenation of acetylene for the first time. The physicochemical properties of the titania and the titania supported catalysts were analyzed by means of X-ray diffraction (XRD), N_2 physisorption, scanning electron microscopy (SEM), electron spin resonance (ESR), and CO chemisorption. Moreover, the effect of defective structures in titania on the catalytic performance of the titania supported Pd and Pd–Ag catalysts in acetylene hydrogenation was investigated.

2. Experimental

2.1. Preparation of TiO_2 by the solvothermal method

TiO_2 was prepared according to the method described in Payakgul *et al.* [7] using 25 g of titanium(IV) *n*-butoxide (TNB) 97% from Aldrich. The starting material was suspended in 100 ml of solvent

* To whom correspondence should be addressed.
E-mail: joongjai.p@eng.chula.ac.th

1011-372X/05/0900-0053/0 © 2005 Springer Science+Business Media, Inc.

(1,4-butanediol or toluene) in a test tube and then set up in an autoclave. In the gap between the test tube and autoclave wall, 30 ml of solvent was added. After the autoclave was completely purged with nitrogen, the autoclave was heated to 320 °C at 2.5 °C/min and held at that temperature for 6 h. Autogenous pressure during the reaction gradually increased as the temperature was raised. After the reaction, the autoclave was cooled to room temperature. The resulting powders were collected after repeated washing with methanol by centrifugation. They were then air-dried at room temperature.

2.2. Preparation of TiO_2 supported Pd and Pd–Ag catalysts

1%Pd/TiO_2 were prepared by the incipient wetness impregnation technique using an aqueous solution of the desired amount of $Pd(NO_3)_2$ (Wako). The catalysts were dried overnight at 110 °C and then calcined in N_2 flow 60 cc/min with a heating rate of 10 °C/min until the temperature reached 500 °C and then in air flow 100 cc/min at 500 °C for 2 h. 1%Pd–3%Ag/TiO_2 catalysts were prepared by sequential impregnation of the 1%Pd/TiO_2 with an aqueous solution of $Ag(NO_3)$ (Aldrich) and were calcined using the same calcination procedure as for 1%Pd/TiO_2.

2.3. Catalyst characterization

The BET surface areas of the samples were determined by N_2 physisorption using a Micromeritics ASAP 2000 automated system. Each sample was degassed under vacuum at $< 10\mu$m Hg in the Micromeritics ASAP 2000 at 150 °C for 4 h prior to N_2 physisorption. The XRD spectra of the catalyst samples were measured from 20–80° 2θ using a SIEMENS D5000 X-ray diffractometer and CuK_α radiation with a Ni filter. Electron spin resonance (ESR) spectra were taken at −150 °C using a JEOL JES-RE2X spectrometer. Relative percentages of palladium dispersion were determined by pulsing carbon monoxide over the reduced catalyst. Approximately 0.2 g of catalyst was placed in a quartz tube in a temperature-controlled oven. CO adsorption was determined by a thermal conductivity detector (TCD) at the exit. Prior to chemisorption, the catalyst was reduced in a flow of hydrogen (50 cc/min) at room temperature for 2 h. Then the sample was purged at this temperature with helium for 1 h. Carbon monoxide was pulsed at room temperature over the reduced catalyst until the TCD signal from a pulse was constant.

The ethylene-TPD profiles of supported palladium catalysts were obtained by temperature programmed desorption from 35 to 800 °C. Approximately 0.05 g of a calcined catalyst was placed in a quartz tube in a temperature-controlled oven and connected to a thermal conductivity detector (TCD). The catalyst was first reduced in H_2 flow 100 cc/min for 1 h at 500 °C (using a ramp rate of 10 °C/min) and cooled down to room temperature before ramping up again to 70 °C in helium flow. The catalyst surface was saturated with ethylene by applying a high purity grade ethylene from the Thai Industrial Gas, Co., Ltd. at 60 ml/min for 3 h. Then the samples were flushed with helium while cooling down to room temperature for about 1 h. The temperature-programmed desorption was performed with a constant heating rate of ca. 10 °C/min from 35 to 800 °C. The amount of desorbed ethylene was measured by analyzing the effluent gas with a thermal conductivity detector.

2.4. Selective hydrogenation of acetylene

Approximately 0.2 g of catalyst was packed in a quartz tubular reactor in a temperature-controlled furnace. Prior to reaction, the catalyst was reduced in H_2 at 500 °C for 2 h. The reactor was then cooled down to 40 °C and the reactant gas composed of $C_2H_2/H_2 = 1{:}2$ (2/4 cc) balance with N_2 total flow of 200 ml/min was fed to the reactor to start the reaction. The product samples were taken at 30 min intervals and analyzed by GC.

3. Results and discussion

3.1. Physicochemical properties of the solvothermal-derived TiO_2

Figure 1 shows the XRD patterns of the TiO_2 particles prepared by thermal decomposition of titanium *n*-butoxide in organic solvents. It was found that nano-sized anatase titania was produced without any contamination of other phases. The crystallite sizes (d) and BET surface areas of the TiO_2 products synthesized in 1,4-butanediol and toluene were found to be essentially the same ($d = 9$–10 nm and BET S.A. 65 m^2/g). However, the morphology of the TiO_2 particles was different as shown by SEM micrographs (figure 2). The products synthesized in toluene agglomerated into spherical micron-sized particles whereas irregular aggregates of nanometer particles were observed for the ones prepared in 1,4-butanediol. The effect of reaction medium on the synthesis of TiO_2 nanocrystals by solvothermal method has recently been reported by Praserthdam *et al.* [7]. It was suggested that anatase titania synthesized in 1,4-butanediol was the result from direct crystallization while titania synthesized in toluene was transformed from precipitated amorphous intermediate.

Due to the different crystallization pathways, degree of crystallinity of the TiO_2 synthesized in 1,4-butanediol and toluene may be different. In this study, the number of defective sites of TiO_2 was determined using electron spin resonance spectroscopy technique and the results are shown in figure 3. ESR has been shown to be a powerful tool to detect Ti^{3+} species in TiO_2 particles. Such Ti^{3+} species are produced by trapping of electrons at defective sites of TiO_2 and the amount of

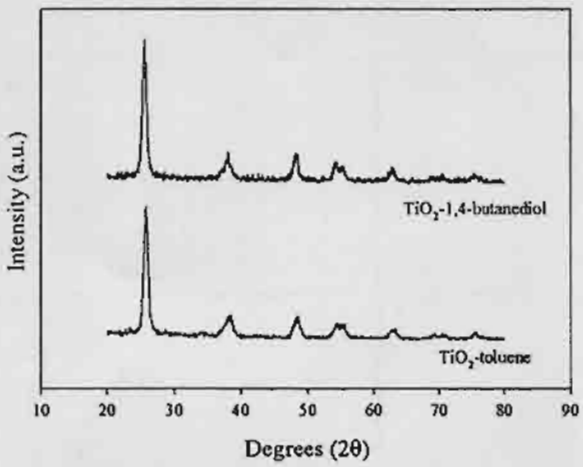

Figure 1. XRD patterns of the solvothermal-derived TiO_2 prepared in two different solvents.

accumulated electrons may therefore reflect the number of defective sites [15]. The signal of g value less than 2 was assigned to Ti^{3+} ($3d^1$) [16]. Both TiO_2-1,4-butanediol and TiO_2-toluene show Ti^{3+} ESR signal at $g = 1.9979–1.9980$ with TiO_2-toluene exhibited much higher intensity. The results clearly show that TiO_2-toluene possessed more Ti^{3+} defective sites than TiO_2-1,4-butanediol.

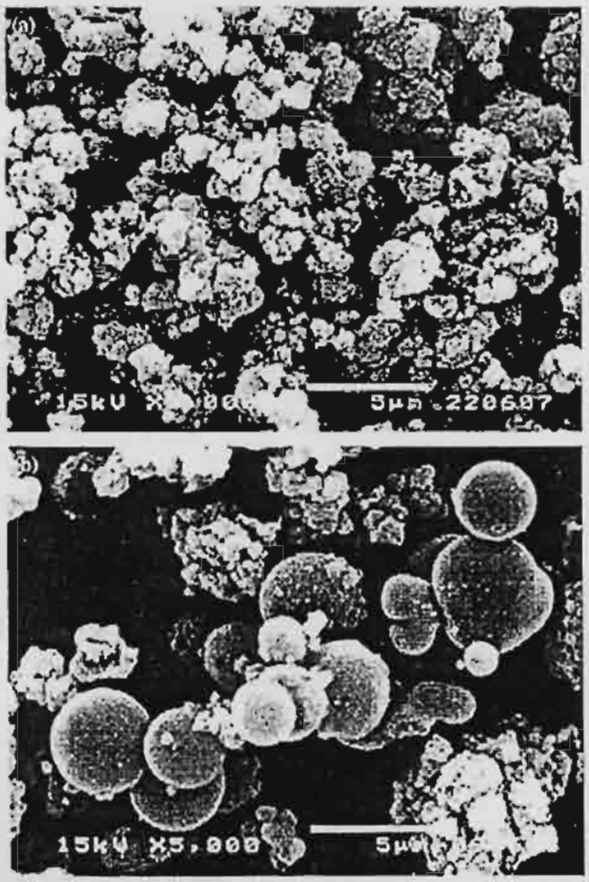

Figure 2. SEM micrographs of (a) TiO_2-1,4-butanediol and (b) TiO_2-toluene.

3.2. *Characteristics of Pd/TiO_2 and Pd–Ag/TiO_2 catalysts*

Table 1 shows the physicochemical properties of the Pd/TiO_2 and Pd–Ag/TiO_2 catalysts. It was found that BET surface areas of the TiO_2 were slightly decreased after impregnation Pd and Pd–Ag suggesting that the metals were deposited in some of the pores of TiO_2. The pulse CO chemisorption technique was based on the assumption that one carbon monoxide molecule adsorbs on one palladium site [17–19]. It was found that Pd/TiO_2-1,4-butanediol exhibited higher amount of CO chemisorption than Pd/TiO_2-toluene. Since both TiO_2 supports possess similar BET surface areas and crystallite sizes, the differences in the amount of active surface Pd were probably induced by the different degrees of crystallinity of the TiO_2 particles.

Addition of Ag to Pd/TiO_2 catalysts resulted in lower amount of active surface Pd. The bimetallic Pd–Ag catalyst has been reported to show many beneficial effects in selective hydrogenation of acetylene to ethylene, for examples, suppression of oligomers formation and improvement of ethylene selectivity [20]. These beneficial effects are due to the altered surface arrangement of Ag atoms on the Pd surface. Roder *et al.* [21] suggested that Ag atoms are likely to stay at the surface in segregated form with Pd rather than forming an alloy.

3.3. *Catalytic performance in selective acetylene hydrogenation*

The conversion and selectivity of Pd and Pd–Ag catalysts supported on TiO_2-1,4-butanediol and TiO_2-toluene in selective acetylene hydrogenation as a function

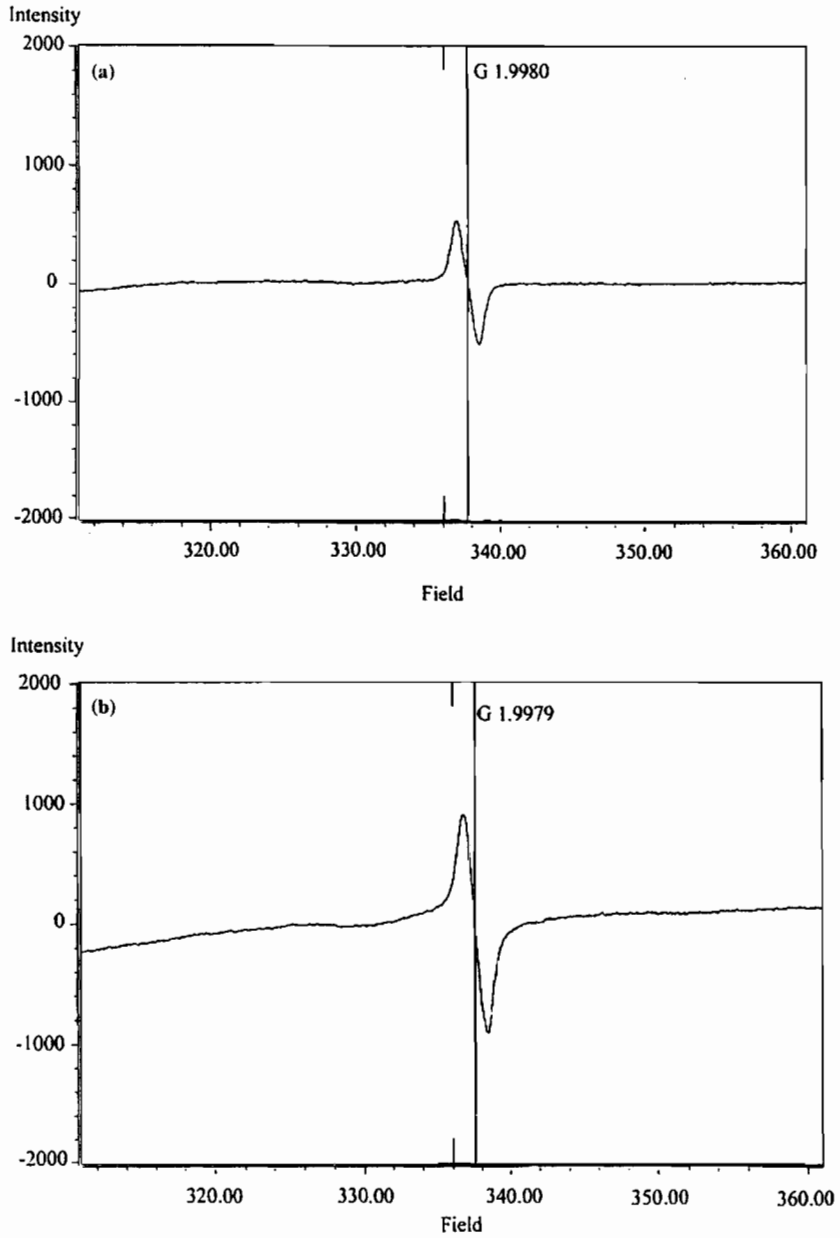

Figure 3. ESR results of (a) TiO_2-1,4-butanediol and (b) TiO_2-toluene.

Table 1
Characteristics of Pd and Pd–Ag catalysts supported on solvothermal-derived TiO_2 prepared in different solvents

Catalyst	BET S.A.[a] (m^2/g)	CO chemisorption[b] (molecule CO $\times 10^{18}$/g catalysis)	Pd dispersion (%)	d_p, Pd^0 (nm)[c]
1%Pd/TiO_2 (1,4-butanediol)	52	5.65	10.0	11.2
1%Pd/TiO_2 (toluene)	60	4.69	8.3	13.5
1%Pd–3%Ag/TiO_2 (1,4-butanediol)	42	2.18	3.8	29.1
1%Pd–3%Ag/TiO_2 (toluene)	47	2.05	3.6	30.9

[a]Error of measurement = ± 10 %.
[b]Error of measurement = ± 5 %.
[c]Based on $d = 1.12/D$ (nm), where D = fractional metal dispersion [17].

of reaction temperature are shown in figures 4 and 5, respectively. The use of TiO_2-1,4-butanediol as the supports for Pd or Pd–Ag catalysts resulted in higher acetylene conversions than the ones supported on TiO_2-toluene. Acetylene conversion of the single metal catalysts reached 100% at ca. 70 °C while those for the bimetallic catalysts showed only 40% (for Pd–Ag/TiO_2-toluene) and 80% (for Pd–Ag/TiO_2-1,4-butanediol) conversions at 90 °C. The ethylene selectivity for all the catalysts at the temperature ranges 40–50 °C were not significantly difference and were found to be ca. 80–90%. However, at 60–70 °C, ethylene selectivity of Pd/TiO_2-1,4-butanediol was much higher than those of Pd/TiO_2-toluene. Ethylene selectivity for the Ag-promoted catalysts were similar for all the reaction temperature used in this study and were higher than those of the non-promoted ones. It was reported that SMSI effect occurs for Pd/TiO_2 catalysts after reduction at high temperature lowering the adsorption strength of ethylene on catalyst surface thus high ethylene selectivity is obtained [10]. Recently, Fan *et al.* [22] reported that diffusion of Ti^{3+} from the lattice of anatase TiO_2 to surface Pd particle can lower the temperature to induce SMSI. However, in this study we have found that use of TiO_2 with higher concentration of Ti^{3+} as a support for Pd catalyst resulted in lower acetylene conversion and selectivity for ethylene after reduction at 500 °C. The turnover frequencies were calculated to be ca. 0.50–0.95 s^{-1} based on the reaction rates at 50 °C. Since the TOFs for all the catalysts were quite similar, it would appear that there was no support effect on the specific activity.

The characteristics of the surface active sites of the catalysts were studied by means of the temperature programmed desorption of ethylene from 30–800 °C. The results are shown in figure 6. The TiO_2-toluene support was found to exhibit two main desorption peaks at ca. 460–680 °C while the TiO_2-1,4-butanediol showed only one desorption peak at 680°C. The results suggest that there were two different active sites on the TiO_2-toluene support, probably Ti^{3+} and Ti^{4+} sites. The high temperature peak for both TiO_2 supports disappeared after Pd loading as shown in the profiles of the Pd catalysts. However, desorption peak at ca. 460 °C was still apparent for Pd/TiO_2-toluene. Since lower ethylene

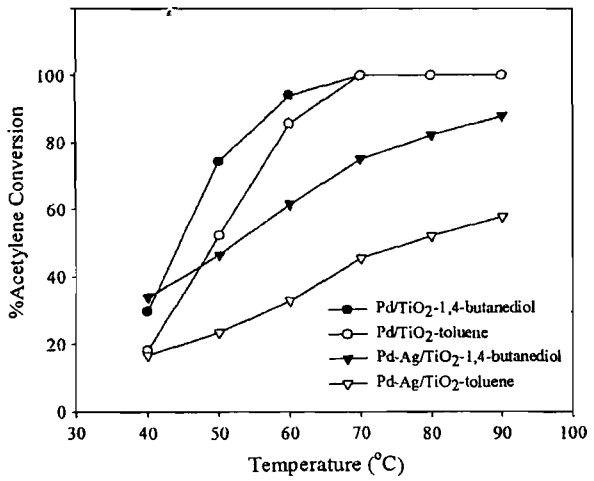

Figure 4. Acetylene conversion as a function of temperature for various TiO_2 supported catalysts.

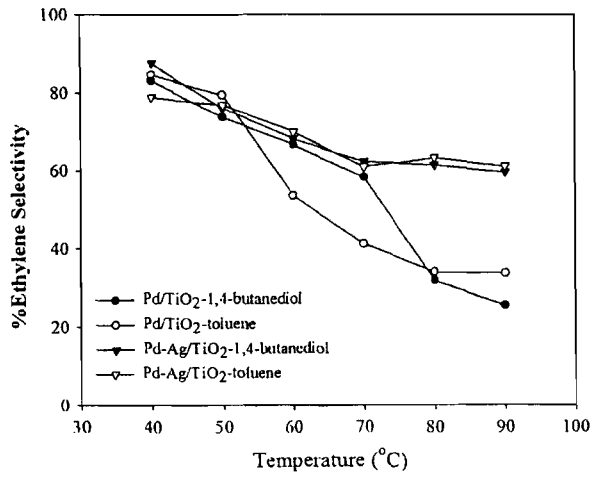

Figure 5. Ethylene selectivity as a function of temperature for various TiO_2 supported catalysts.

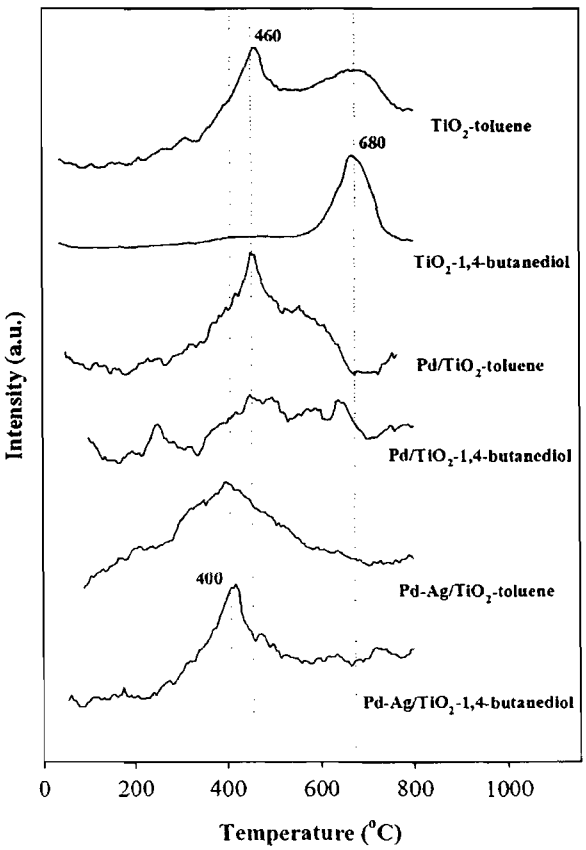

Figure 6. Ethylene-TPD results.

selectivity was found for Pd/TiO_2-toluene than Pd/TiO_2-1,4-butanediol for similar acetylene conversion, this peak can be assigned to the sites for ethylene hydrogenation to ethane. Ethylene hydrogenation is usually believed to take place on the support by means of a hydrogen transfer mechanism [23]. Since only Ti^{3+} species that were in contact with palladium surface promoted SMSI effect [22], ethylene hydrogenation could take place on the Ti^{3+} defective sites that were not in contact with palladium resulting in lower acetylene conversion and selectivity for ethylene as observed in the case of Pd/TiO_2-toluene in this study. The Ag-promoted Pd catalysts exhibited only one ethylene desorption peak at ca. 400 °C suggesting that the Pd catalyst surface on both TiO_2 supports was modified by Ag atoms. The presence of Ag probably blocked the sites for ethylene hydrogenation to ethane for both catalysts thus a significant improvement in ethylene selectivity was observed especially for high acetylene conversion at high temperature. Further study on the titanium defective sites using more sophisticated characterization techniques such as XPS and SIMS is recommended in order to obtain more information on other titanium oxidation states that might be involved in the defective sites, oxygen to titanium ratio, etc. However, in term of catalyst deactivation, we did not observe a decrease in activity or ethylene selectivity for all the catalyst after 12 h on stream. Therefore, there was no effect of carbonaceous deposits involved in the mechanism of acetylene hydrogenation in this study.

4. Conclusions

Nanocrystalline anatase titania prepared by the solvothermal method were successfully used as supports for Pd and Pd–Ag catalysts for selective hydrogenation of acetylene to ethylene. However, Pd supported on titania synthesized in toluene (higher defective sites) exhibited lower activity and selectivity for selective acetylene hydrogenation than the ones supported on titania synthesized in 1,4-butanediol (lower defective sites). Ethylene hydrogenation probably took place on the Ti^{3+} defective sites that were not in contact with palladium surface. These sites were blocked by promotion of Pd/TiO_2 with Ag metal.

Acknowledgments

The financial supports from the Thailand Japan Technology Transfer Project (TJTTP-JBIC), the Thailand Research Fund (TRF), and the Graduate School of Chulalongkorn University are gratefully acknowledged.

References

[1] M. Inoue, Y. Kondo and T. Inui, Inorg. Chem. 27 (1988) 215.
[2] M. Inoue, H. Kominami and T. Inui, J. Am. Ceram. Soc. 75 (1992) 2597.
[3] M. Inoue, H. Kominami and T. Inui, Appl. Catal. A 97 (1993) 125.
[4] H. Kominami, J.-I. Kato, S.-Y. Murakami, Y. Kera, M. Inoue T. Inui and B. Ohtani, J. Mol. Catal. A 144 (1999) 165.
[5] S. Kongwudthiti, P. Praserthdam, P.L. Silveston and M. Inoue, Ceram. Int. 29 (2003) 807.
[6] O. Mekasuwandumrong, P.L. Silveston, P. Praserthdam, M. Inoue, V. Pavarajarn and W. Tanakulrungsank, Inorg. Chem. Commun. 6 (2003) 930.
[7] W. Payakgul, O. Mekasuwandumrong, V. Pavarajarn and P. Praserthdam, Ceram. Int. (2004) in press.
[8] H. Kominami, S.-Y. Murakami, M. Kohno, Y. Kera, K. Okada and B. Ohtani, Phys. Chem. Chem. Phys. 3 (2001) 4102.
[9] B. Ohtani, K. Tennon, S.-I. Nishimoto and T. Inui, J. Photosci. 2 (1995) 7.
[10] J. Santos, J. Phillips and J.A. Dumesic, J. Catal. 81 (1983) 147.
[11] G.B. Raupp and J.A. Dumesic, J. Catal. 95 (1985) 587.
[12] M.J. Herrmann, M. Gravelle-Rumeau-Maillot and P.C. Gravelle, J. Catal. 104 (1987) 136.
[13] P. Chou and M.A. Vannice, J. Catal. 104 (1987) 1.
[14] J.H. Kang, E.W. Shin, W.J. Kim, J.D. Park and S.H. Moon, J. Catal. 208 (2002) 310.
[15] S. Ikeda, N. Sugiyama, S. Murakami, H. Kominami, Y. Kera, H. Noguchi, K. Uosaki, T. Torimoto and B. Ohtani, Phys. Chem. Chem. Phys. 5 (2003) 778.
[16] T.M. Salama, H. Hattori, H. Kita, K. Ebitani and T. Tanaka, J. Chem. Soc. Faraday Trans. 89 (1993) 2067.
[17] N. Mahata and V. Vishwanathan, J. Catal. 196 (2000) 262.
[18] S.H. Ali and J.G. Goodwin Jr., J. Catal. 176 (1998) 3.
[19] E.A. Sales, G. Bugli, A. Ensuque, M.J. Mendes and F. Bozon-Verduraz, Phys. Chem. Chem. Phys. 1 (1999) 491.
[20] D.C. Huang, K.H. Chang, W.F. Pong, P.K. Tseng, K.J. Hung and W.F. Huang, Catal. Lett. 53 (1998) 155.
[21] H. Roder, R. Schuster, H. Brune and K. Kern, Phys. Rev. Lett. 71 (1993) 2086.
[22] Y. Li, B. Xu, Y. Fan, N. Feng, A. Qiu, J. Miao, J. He, H. Yang and Y. Chen, J. Mol. Catal. A 216 (2004) 107.
[23] S. Aplund, J. Catal. 158 (1996) 267.

Jointly published by
Akadémiai Kiadó, Budapest
and Springer, Dordrecht

React.Kinet.Catal.Lett.
Vol. 86, No. 1, 141-147
(2005)

RKCL4581

DEACTIVATION OF SILICA SUPPORTED Pd CATALYSTS DURING LIQUID-PHASE HYDROGENATION

Joongjai Panpranot*, Kanda Pattamakomsan and Piyasan Praserthdam

Center of Excellence on Catalysis and Catalytic Reaction Engineering
Department of Chemical Engineering, Faculty of Engineering
Chulalongkorn University, Bangkok, 10330, Thailand

Received May 28, 2004
In revised form March 16, 2005
Accepted March 24, 2005

Abstract

Large pore MCM-41 was found to provide a better stabilization of Pd particles than amorphous SiO_2 during liquid phase hydrogenation. Pd/large pore MCM-41 exhibited higher hydrogenation activities as well as lower amount of metal loss by Pd leaching.

Keywords: Liquid-phase hydrogenation, Pd/MCM-41, Pd/SiO_2, 1-hexene hydrogenation

INTRODUCTION

Supported Pd catalysts are widely used in liquid-phase hydrogenation for many important organic transformations [1]. The nature of support affects catalyst activity, selectivity, recycling, refining, materials handling, and reproducibility. For examples, Pinna *et al.* [2] compared Pd on activated carbon, silica, and alumina in the selective hydrogenation of benzaldehyde to benzyl alcohol. Pd/Al_2O_3 was found to exhibit strong metal-support interaction while Pd/C showed the highest activity for benzaldehyde hydrogenation. Choudary *et al.* [3] reported that Pd/MCM-41 is more active in partial-hydrogenation of acetylenic compounds than Pd/Y-zeolite or Pd/K-10 clay.

* Corresponding author. Phone: +66 (02)-218-6859; Fax: +66 (02)-218-6877
E-mail: joongjai.p@eng.chula.ac.th

0133-1736/2005/US$ 20.00

However, the effects of pore size and pore structure of the same material in liquid phase hydrogenation on activity and catalyst deactivation remain unclear. In this study, the effects of silica-structure and pore size of the silica supports were investigated in terms of metal dispersion, catalytic activity in liquid-phase hydrogenation, and catalyst deactivation due to leaching and/or sintering of metal.

EXPERIMENTAL

Preparation of supported Pd catalysts

Pure silica MCM-41 with 3 nm pore diameter was prepared in the same manner as that of Cho *et al.* [4] using the gel composition of CTAB: 0.3 NH_3: 4 SiO_2: Na_2O: 200 H_2O, where CTAB denotes cetyltrimethyl ammonium bromide. The larger pore (d_{pore}= 7 nm) MCM-41 was prepared by treating the MCM-41-small pore in an emulsion containing *N,N*-dimethyldecylamine (0.625 g in 37.5 g of water for each gram of MCM-41) for 3 days at 120°C. The MCM-41 materials were calcined at 550°C (ramp rate 1-2 °C/min) in flowing nitrogen, and then in air at the same temperature for 5 h. The amorphous SiO_2-small pore with average pore diameter of 3 nm and SiO_2-large pore were obtained commercially from Grace Davison and Strem chemicals, respectively.

Supported Pd catalysts were prepared by the incipient wetness impregnation of the supports with an aqueous solution containing the desired amount of Pd nitrate dehydrate to yield a final loading of approximately 0.5 wt.% Pd. The catalysts were dried overnight at 110°C and then calcined in air at 500°C for 2 h.

Catalyst characterization

The bulk composition of palladium was determined using a Varian Spectra A800 atomic absorption spectrometer. The BET surface areas of the catalysts were determined by N_2 physisorption using a Micromeritics ASAP 2000 automated system. Each sample was degassed in the Micromeritics ASAP 2000 at 150°C for 4 h prior to N_2 physisorption. The XRD spectra of the catalysts were measured using a SIEMENS D5000 X-ray diffractometer and Cu Kα radiation with a Ni filter in the 2-10° or 20-80°2θ angular regions.

The palladium oxide particle size and distribution of palladium was observed using a JEOL-TEM 200CX transmission electron microscope operated at 100 kv. The catalyst sample was first suspended in ethanol using ultrasonic agitation for 10 min. The suspension was dropped onto a thin Formvar film supported on a copper grid and dried at room temperature before TEM

observation. Relative percentages of palladium dispersion were determined by pulsing carbon monoxide over the reduced catalyst. Approximately 0.2 g of catalyst was placed in a quartz tube, incorporated in a temperature-controlled oven and connected to a thermal conductivity detector (TCD). Prior to chemisorption, the catalyst was reduced in a flow of hydrogen (50 cm^3) at room temperature for 2 h. Then the sample was purged with helium for 1 h. Carbon monoxide was pulsed at room temperature over the reduced catalyst until the TCD signal from the pulse was constant.

Liquid-phase hydrogenation

Liquid-phase hydrogenation reactions were carried out at 25°C and 1 atm in a stainless steel Parr autoclave. Approximately 1 g of supported Pd catalyst was placed into the autoclave. The system was purged with nitrogen to remove remaining air. The supported Pd catalyst was reduced with hydrogen at room temperature for 2 h. The reaction mixture composed of 15 mL of 1-hexene and 400 ethanol was first kept in a 600 mL feed column. The reaction mixture was introduced into the reactor with nitrogen to start the reaction. The stirring rate used in this study was 1,400 rpm. It was ensured that the reaction rate does not depend on the stirring rate. The content of hydrogen consumption was monitored every five minutes by noting the change in pressure of hydrogen.

RESULTS AND DISCUSSION

Catalyst activities

Liquid-phase hydrogenation of 1-hexene was carried out as a model reaction to compare the hydrogenation activity of the MCM-41- and SiO_2-supported Pd catalysts. The kinetics study of liquid phase hydrogenation using rate of hydrogen consumption has been reported in other research investigations [3,5]. The slope of the line at the origin represents the initial rate of the reactions and the rate constant assuming zero order dependence of reaction on hydrogen [3,6]. The rate constant of the different supported Pd catalysts in liquid phase hydrogenation of 1-hexene at 25°C and the TOFs are reported in Table 1. The activity of the catalysts were found to be in the order of Pd/MCM-41-large pore > Pd/MCM-41-small pore ≈ Pd/SiO_2-large pore > Pd/SiO_2-small pore. The turnover frequencies (TOFs) were calculated based on the CO chemisorption data and are given in Table 1. Given that in all cases the support was silica, albeit in slightly different forms, it is not surprising that specific activities in the form of TOFs were so similar. Since the TOFs were similar but Pd particle

locations so disparate, it would appear that there were no pore diffusion effects on reaction rate. However, there might have been some limitations in the mass transfer of hydrogen from the gas phase to the liquid phase, given that hydrogenation is such a fast reaction on noble metals. However, we did not detect any mass transfer limitations due to pore diffusion.

Table 1

Liquid phase hydrogenation activities of various Pd catalysts[a]

Catalyst	Rate constant $x10^3$ (mol/min g cat.)	TOF (s^{-1})
Pd/SiO_2-small pore	2.45	19
Pd/SiO_2-large pore	3.40	29
Pd/MCM-41-small pore	3.41	28
Pd/MCM-41-large pore	4.75	23

[a]After 5 h batch hydrogenation of 1-hexene at 25°C and 1 atm and re-calcination at 500°C for 2 h

Catalyst deactivation due to metal sintering

The particle sizes of palladium particles before and after reaction were determined by XRD, TEM, and CO pulse chemisorption and are reported in Table 2. The fresh catalysts are referred to the catalysts after calcination in air at 500°C for 2 h. The spent catalysts were collected after one 5 h batch reaction. In order to avoid the influence of carbon deposits on the pore structure and the contrast of TEM images of the used catalysts, the spent catalysts were re-calcined in air at 500°C for 2 h before characterization to remove any carbon deposits.

Table 2

PdO and Pd^0 particle sizes before and after reaction

Catalyst	Particle size (nm)					
	XRD[a]		TEM		CO chemisorption[b]	
	Fresh	Spent	Fresh	Spent	Fresh	Spent
Pd/SiO_2-small pore	7.8	13.8	8.0	13.0	17.2	29.2
Pd/SiO_2-large pore	10.8	21.9	10.0	23.0	15.3	30.1
Pd/MCM-41-small pore	14.2	16.1	12.8	14.3	24.9	45.3
Pd/MCM-41-large pore	9.1	18.0	6.7	14.7	9.4	14.7

[a] Based on $d = (1.12/D)$ nm [9].
[b] Error of measurement = +/- 5%.

The PdO particle sizes were calculated by X-ray line broadening using the Scherrer's equation [7]. The PdO particles/clusters of the fresh catalysts were found to be ca. 8-14 nm in the order of Pd/MCM-41-small pore > Pd/SiO_2-large pore > Pd/MCM-41-large pore ≈ Pd/SiO_2-small pore. After reaction and re-calcination, it was found that the PdO particle sizes for all catalyst samples became larger, suggesting sintering of palladium metal particles [8]. Use of large pore supports resulted in the greatest amount of Pd sintering. This is probably due to the lower surface area of the supports resulting in higher probability of a metal particle to be closed to other ones and therefore the sintering probability was higher. TEM micrographs were taken in order to physically measure the size of the palladium oxide particles and/or palladium clusters. The particle sizes of PdO particles measured from TEM images before and after reaction were found to be in accordance with the results from XRD.

Pulse CO chemisorption experiments have been performed on both fresh and spent catalysts in order to determine the Pd metal particle sizes. The pulse CO chemisorption technique was based on the assumption that one carbon monoxide molecule adsorbs on one palladium site [9-12]. Average particle size

for reduced Pd^0 was calculated to be in the range of 9.4-24.9 nm before reaction and 14.7-45.3 nm after reaction. These average Pd metal particle sizes calculated based on CO chemisorption are not identical of course to the PdO particle sizes obtained by XRD and TEM.

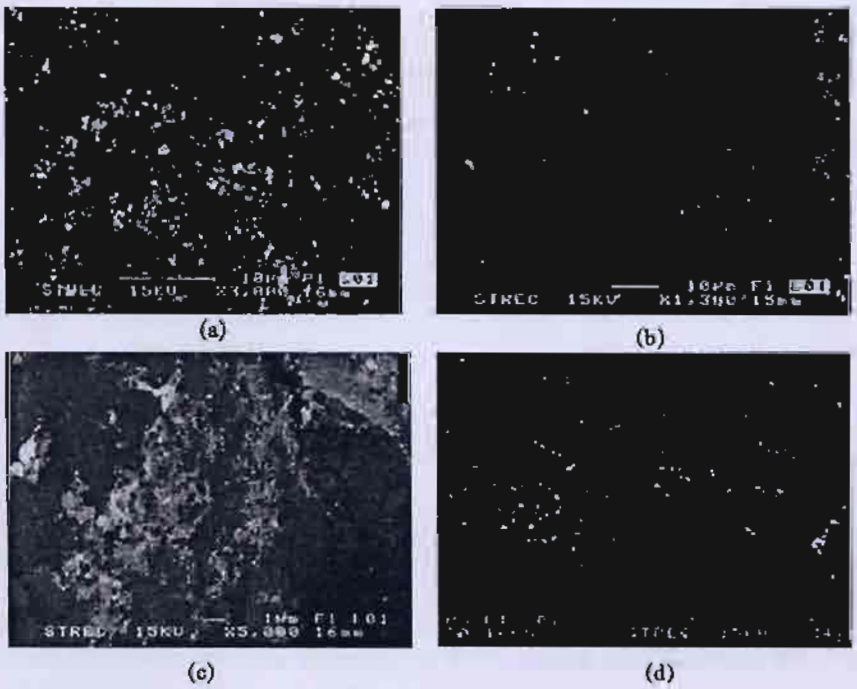

Fig. 1. SEM micrographs under back scattering mode of various silica supported Pd catalysts before and after liquid phase hydrogenation reaction (a) fresh Pd/SiO_2-small pore (b) spent Pd/SiO_2-small pore (c) fresh Pd/MCM-41-large pore (d) spent Pd/MCM-41-large pore

Catalyst deactivation due to metal leaching

SEM images in the back scattering mode shown in Fig. 1 have revealed that Pd leaching occurred during 5 h liquid phase reaction on various silica supported Pd catalysts. The actual amounts of palladium loading before and after reaction were determined by atomic adsorption spectroscopy and are given in Table 3. Before reaction, palladium loading on the catalyst samples was approximately 0.29-0.48 wt%. After one 5 h batch hydrogenation reactions of 1-hexene, palladium loading had decreased to 0.15-0.32 wt.%. The order of percentages of the amount of palladium leaching was found to be Pd/SiO_2-small

pore > Pd/SiO_2-large pore > Pd/MCM-41-small pore >> Pd/MCM-41-large pore. Pd/MCM-41-large pore showed almost no leaching of palladium into the reaction media within experimental error. The results suggest that large pore MCM-41 provided a better stabilization of small Pd particles than amorphous SiO_2 during liquid phase hydrogenation.

Table 3

Results from atomic absorption spectroscopy (AAS)

Catalyst	wt.% Pd[a]	
	Fresh	Spent
Pd/SiO_2-small pore	0.35	0.15
Pd/SiO_2-large pore	0.29	0.18
Pd/MCM-41-small pore	0.41	0.32
Pd/MCM-41-large pore	0.33	0.31

[a] Error of measurement = +/- 5%

Acknowledgement. Financial support by the Thailand Research Fund (TRF) and TJTTP-JBIC is gratefully acknowledged. The authors also thank Professor Abdel Sayari, University of Ottawa, Canada and Dr. Aticha Chaisuwan, Chulalongkorn University, Thailand for the assistance with MCM-41 preparation. We are also thankful to Prof. James G. Goodwin, Jr., Clemson University, USA, for discussion.

REFERENCES

1. P.N. Rylander: *Hydrogenation Methods*, Academic Press, New York 1985.
2. F. Pinna, F. Menegazzo, M. Signoretto, P. Canton, G. Fagherazzi, N. Pernicone: *Appl. Catal. A*, **219**, 195 (2001).
3. B.M. Choudary, M.L. Kantam, N.M. Reddy, K.K. Rao, Y. Haritha, V. Bhaskar, F. Figueras, A. Tuel: *Appl. Catal. A.* **181**, 139 (1999).
4. D.H. Cho, T.S. Chang, S.K. Ryu, Y.K. Lee: *Catal. Lett.*, **64**, 227 (2000).
5. M.K. Dalal, R.N. Ram: *Eur. Polym. J.*, **33**, 1495 (1997).
6. E.A. Sales, M. D. Mendes, F. Bozon-Verduraz: *J. Catal.*, **195**, 96 (2000).
7. H.P. Klug, L.E. Alexander: *X-Ray Diffraction Procedures for Polycrystalline Amorphous Materials*, 2nd ed., Wiley, New York 1974.
8. O. Dominguez-Quintero, S. Martinez, Y. Henriquez, L. D'Ornelas, H. Krentzien, J. Osuna: *J. Mol. Catal. A*: **197**, 185 (2003).
9. N. Mahata, V. Vishwanathan: *J. Catal.*, **196**, 262 (2000).
10. S. H. Ali, J.G. Goodwin, Jr.: *J. Catal.*, **176**, 3 (1998).
11. E.A. Sales, G. Bugli, A. Ensuque, M. J. Mendes, F. Bozon-Verduraz: *Phys. Chem. Chem. Phys.*, **1**, 491 (1999).
12. A. Sárkány, Z. Zsoldos, B. Furlong, J.W. Hightower, L. Guczi: *J. Catal.*, **141**, 566 (1993).

Journal of Porous Materials 12: 293–299, 2005

Effect of Particle Size on the Hydrothermal Stability and Catalytic Activity of Polycrystalline Beta Zeolite

JOONGJAI PANPRANOT*, USNEE TOOPHORM AND PIYASAN PRASERTHDAM
Center of Excellence on Catalysis and Catalytic Reaction Engineering, Department of Chemical Engineering, Chulalongkorn University, Bangkok 10330, Thailand
Joongjai.P@eng.chula.ac.th

Received January 5, 2005; Revised March 21, 2005

Abstract. The effect of particle size in the range of 0.2–0.9 μm on the hydrothermal stability of polycrystalline beta zeolites was investigated in terms of changes in BET surface areas, percent crystallinity, and framework aluminum atoms. It was found that the hydrothermal stability of beta zeolite increased with increasing particle size while the catalytic activities decreased. However, the XRD results have revealed that percent crystallinity of the hydrothermally treated beta zeolite remained relatively high (>95%) although dealumination occurred in most cases. This high stability is due probably to small amount of Al atoms present in the unit cell of this zeolite.

Keywords: beta zeolite, particle size effect, hydrothermal stability, methanol conversion

1. Introduction

Beta zeolite first synthesized by the Mobil Oil researchers [1] possesses a three dimensional large pore system of a 12-membered ring with two different types of channels, which are 0.7 and 0.5 nm wide. Beta zeolite has been studied in many catalytic reactions such as alkane isomerization [2], aromatic alkylation [3], aromatic acylation [4], aromatic nitration [5], aliphatic alkylation [6], and indole synthesis [7]. The commercial beta zeolite is generally synthesized with particle size less than 1 μm. Although smaller particles of zeolites were often found to be more active due to less diffusion constraint of the reactants and products, they were less stable than larger ones. Praserthdam et al. [8] have investigated the effect of crystal size on the durability of Co/HZSM-5 in selective reduction of NO. The smaller crystal size Co/HZSM-5 showed the greater durability. The role of particle size in the catalytic activity of beta zeolite has been reported by a number of groups [2, 9–11]. Bonetto et al. [9] studied the catalytic performances of beta zeolite with three different particle sizes (0.17, 0.40, and 0.70 μm) in gasoil cracking. The beta zeolite with the particle size of 0.40 μm was found to produce the highest liquefied petroleum gas and iso-butane yield. Arribus and Martinez [2] showed that the catalytic performance of Pt/Beta zeolite catalysts in simultaneous isomerization of *n*-heptane and saturation of benzene could be improved by decreasing the zeolite crystal size.

Thus, in previous studies, the effects of crystal or particle size on the catalytic performance of zeolites have been studied and compared. However, the effect of particle size on the structural stability under hydrothermal conditions of polycrystalline beta zeolite has not been studied to a great extent. In this study, a correlation between particle size and hydrothermal stability of polycrystalline beta zeolites was investigated by means of various characterization techniques such as X-ray diffraction, N_2 physisorption, nuclear magnetic resonance (NMR), and scanning electron microscopy. The catalytic activities of beta zeolites were also tested in methanol conversion.

*To whom correspondence should be addressed.

2. Experimental

2.1. *Synthesis of H-Beta Zeolite*

The hydrogen form of beta zeolite with different particle sizes was prepared as reported elsewhere [12] using hydrothermal method and the following gel composition: K_2O:2Na_2O:12.5TEAOH: 1/2Al_2O_3:30SiO_2:700H_2O, where TEAOH denotes tetraethylammonium hydroxide. The mixture of synthesis reagents was stirred under vigorous magnetic stirring before transferring into a stainless steel autoclave. Then it was heated from room temperature to 135°C in 1 h under a pressure of nitrogen at 3 kg/cm^2 and maintained at this condition for 40 h. The obtained solid material was filtered, washed with deionized water until pH = 9, and dried overnight in an oven at 110°C. The sample was then calcined in air at 540°C (8.5°C/min) for 3.5 h. The hydrogen form of beta zeolite was obtained by first exchanging Na^+ with NH^{4+} using an aqueous solution of NH_4NO_3 and subsequently decomposing the NH^{4+} by calcination in air at 500°C for 2 h.

2.2. *Hydrothermal Treatment*

Hydrothermal treatment of the catalysts was performed in a home-made system. Approximately 0.5 g of catalyst sample was placed in the reactor and was first heated in a He flow to 600°C using a ramp rate of 10°C/min then from 600–800°C using a ramp rate of 1.7 °C/min. It was kept at this final temperature for 30 min under 10 mol% water vapor. Finally, it was cooled down to room temperature in a He stream.

2.3. *Catalyst Characterization*

Average particle size and particle size distribution of the catalysts before and after hydrothermal treatment were determined visually from SEM micrographs obtained from a JEOL JSM-35 CF model scanning electron microscope. The crystallinity of the zeolite was determined using X-ray diffractometer (SIEMENS D5000) with monochromatized Cu K_α radiation (10 kV, 20 mA). Percent crystallinity was calculated based on the area of the main peak compared with that of fresh beta zeolite as a reference. Specific surface areas of the zeolite were calculated using a BET single point method from the measured amount of N_2 uptake at liquid nitrogen boiling point temperature using a GOW-MAC gas chromatograph. Quantities of Si and Al in the sample were determined using a FISONS ARL8410 XRF analyzer. The chemical state of Al was measured by ^{27}Al MAS-NMR using a BRUKER DPX-300 NMR spectrometer operated at 78.2 MHz at the magic angle. The relative area of tetrahedral ^{27}Al was calculated from the area of tetrahedral aluminum per summation area of tetrahedral and octahedral aluminum.

2.4. *Reaction Study*

Methanol conversion was performed in a down-flow differential fixed-bed quartz tubular reactor. A GHSV of ca. 4,000 h^{-1} and a 20 mol% methanol were used. Approximately 0.2 g catalyst was held in the middle of the reactor using quartz wool. It was first heated in a 50 cc/min N_2 flow to 450°C, using a ramp rate of 10°C/min and held at this temperature for 30 min prior to reaction. The reaction was initiated by allowing the N_2 flow to pass through the reactants inside the saturator in the water bath. After the start-up for 1 h, samples were taken and analyzed by a GC (Shimadzu GU-14A). The catalytic activity was evaluated based on the conversion of methanol to hydrocarbons.

3. Results and Discussion

Scanning electron micrographs of beta zeolite samples with various crystallite sizes are shown in Fig. 1. Typically a spherical shape was formed for all crystallite sizes of beta zeolites. The average crystal sizes of the samples were measured from scanning electron micrographs by averaging the diameters of a hundred primary particles. The effect of particle size on the

Table 1. The effect of particle size on the percent decrease in specific surface areas of beta zeolite after hydrothermal treatment.[a]

Particle size (μm)	Specific surface area (m^2/g)		% decrease of S.A.
	Fresh	Treated	
0.2	612	490	19.9
0.3	579	481	16.9
0.4	500	459	8.2
0.5	464	446	3.9
0.7	382	364	4.7
0.9	374	355	5.1

[a]Hydrothermal treatment conditions were 800°C, 10 mol% water vapor, and 30 min.

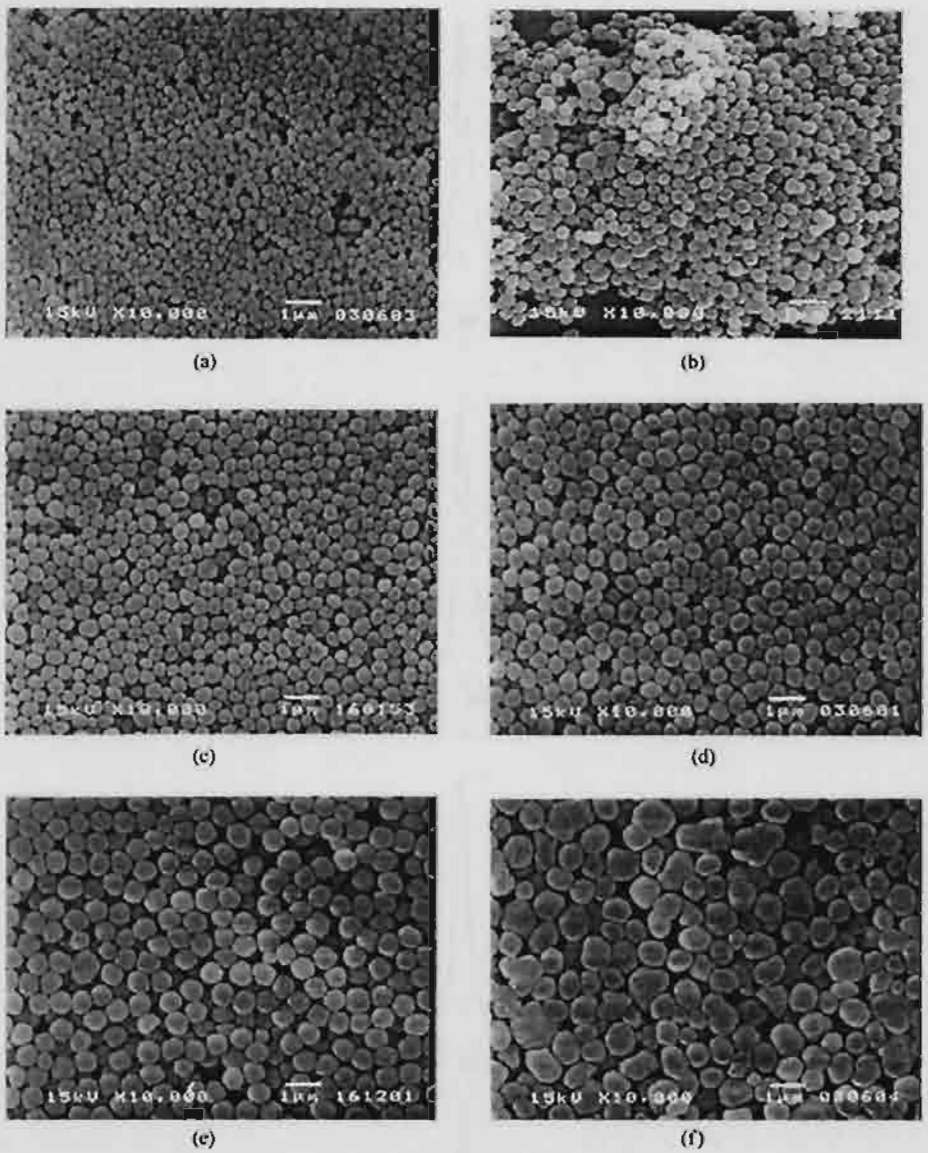

Figure 1. SEM micrographs of beta zeolites with various particle sizes (a) 0.2 μm, (b) 0.3 μm, (c) 0.4 μm, (d) 0.5 μm, (e) 0.7 μm and (f) 0.9 μm.

percent decrease of surface areas of beta zeolites after hydrothermal treatment at 800°C with 10 mol% water vapor for 30 min is shown in Table 1. It was found that the surface areas of beta zeolite samples with the crystallite sizes in the range of 0.2–0.4 μm decreased significantly after hydrothermal treatment with the particle size of 0.2 μm showed the highest loss of surface area (ca. 20%). The beta zeolites with larger particle sizes ranging from 0.5–0.9 μm showed only 4–5% decrease in surface areas. A loss of surface area upon hydrothermal treatment suggests a partial collapse of zeolite framework [10–14].

The environment of the aluminum atoms in the zeolite samples was studied using ^{27}Al MAS NMR spectroscopy. Figure 2 presents the ^{27}Al MAS NMR spectra of H-beta zeolite with particle sizes of 0.3 and 0.9 μm before and after hydrothermal treatment. The tetrahedral Al presented in the zeolite framework ($Al(OSi)_4$)

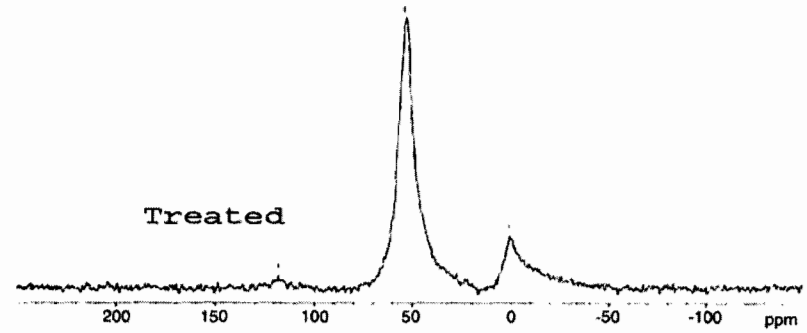

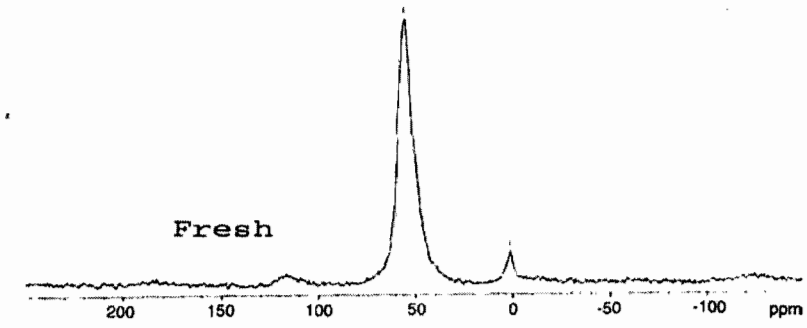

(a)

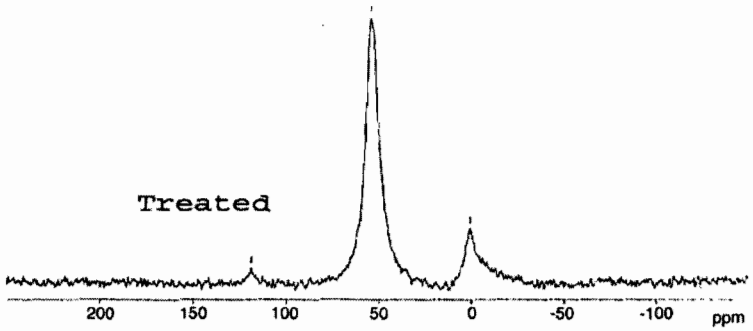

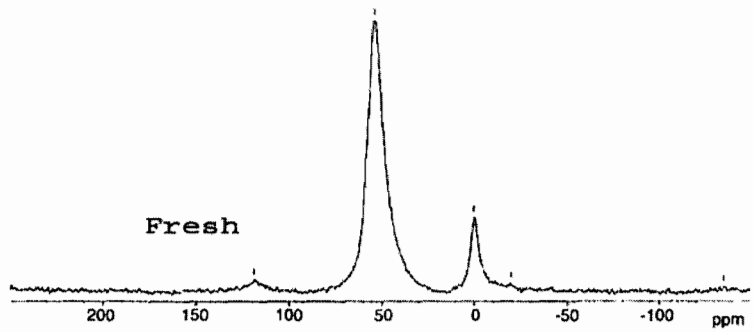

(b)

ure 2. (a) NMR spectra of beta zeolites with particle size of 0.3 μm before and after hydrothermal treatment. (b) NMR spectra of beta. olites with particle size of 0.9 μm before and after hydrothermal treatment.

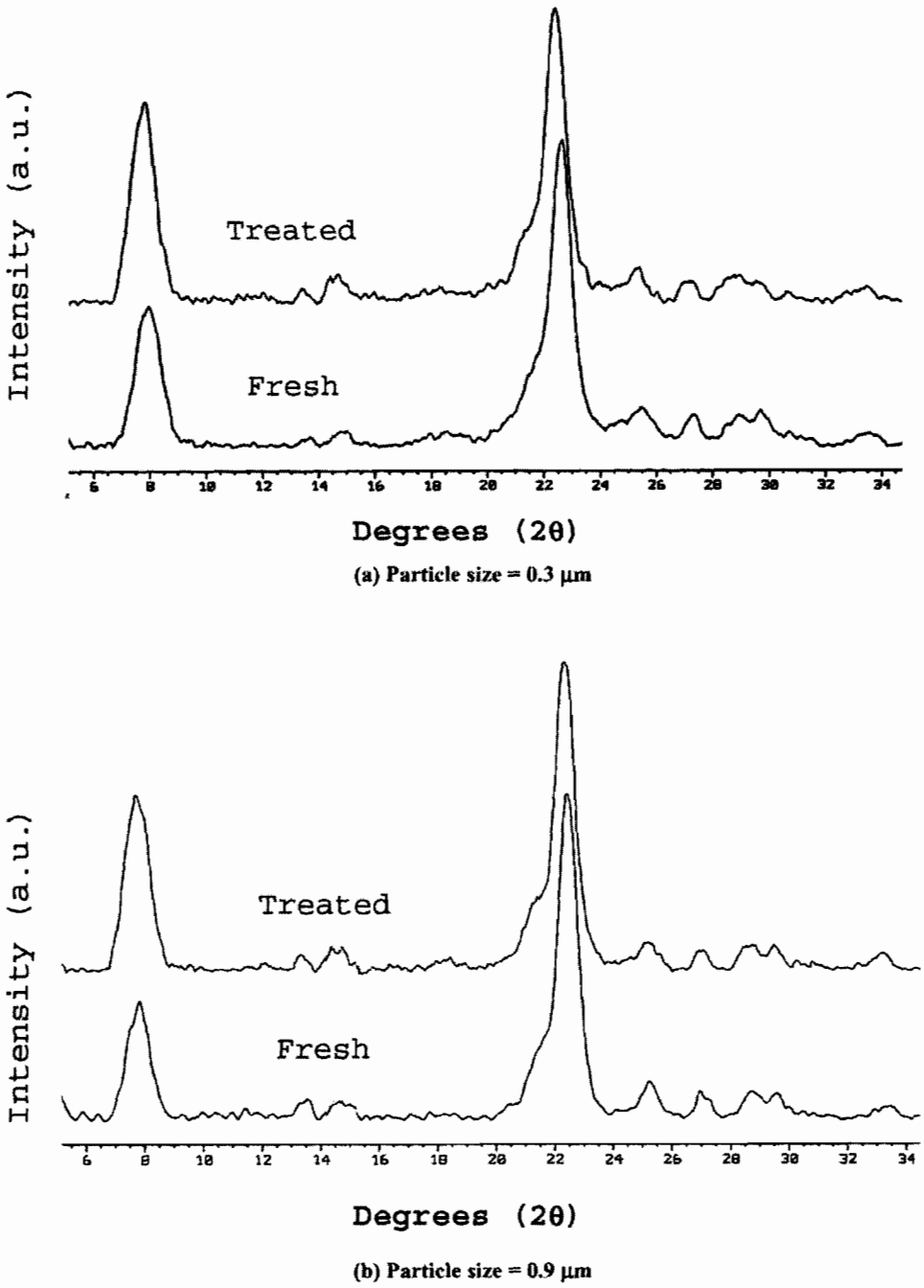

Figure 3. XRD patterns of beta zeolites with different particle sizes.

is shown by NMR signal at ca. 52 ppm while extra-framework aluminum (EFAl) species which are usually octahedrally coordinated is shown at a chemical shift of ca. 0 ppm [13, 14]. A strong peak of tetrahedrally coordinated framework Al and a very weak signal of octahedral EFAl were found in all samples. The EFAl species in the fresh samples were probably formed during the calcinations in the preparation

Table 2. The effect of particle size on the percent decrease of tetrahedral ^{27}Al and % crystallinity after hydrothermal treatment.[a]

Particle size (μm)	The relative areas of tetrahedral ^{27}Al (%)		% decrease of tetrahedral ^{27}Al	% crystallinity after hydrothermal treatment
	Fresh	Treated		
0.2	94	77	18.1	95
0.3	95	78	17.9	95
0.4	93	79	15.1	96
0.5	88	78	11.4	97
0.7	89	81	9.0	96
0.9	94	78	17.0	95

[a]Hydrothermal treatment conditions were 800°C, 10 mol% water vapor, and 30 min.

procedure to transform as-synthesized to H-form beta zeolites [15]. After hydrothermal treatment, a decrease in tetrahedral aluminum and an increase in octahedral aluminum were observed for all particle sizes of beta zeolites used in this study, suggesting that dealumination occurred upon hydrothermal treatment. The relative areas of tetrahedral ^{27}Al were calculated from the area of tetrahedral aluminum per summation area of tetrahedral and octahedral aluminum and are given in Table 2. The beta zeolite with particle size of 0.7 μm was found to exhibit the lowest extent of dealumination. It should be noted that upon hydrothermal treatment of beta zeolite besides dealumination, formation of mesoporosity has also been observed [16–18].

The XRD patterns of beta zeolite before and afte hydrothermal treatment for different crystallite size are shown in Fig. 3. The two characteristic peaks o H-beta zeolite at 2θ 7.8° and 22.4° were detected. Th percent crystallinity of the samples was calculated b comparing the peak intensities of the treated sample with the fresh samples. The 22.4° peak was chosen fo comparison since it was found to be a major character istic peak of H-beta zeolite [19–21]. It was found tha the relative % crystallinity of the samples remaine as high as 95–97% after hydrothermal treatment. Du probably to the presence of only 3–4 Al atoms in th unit cell, the crystallinity of the zeolite does not signif icantly change although all the Al atoms are remove from the framework [11, 12, 22]. Similar result was als

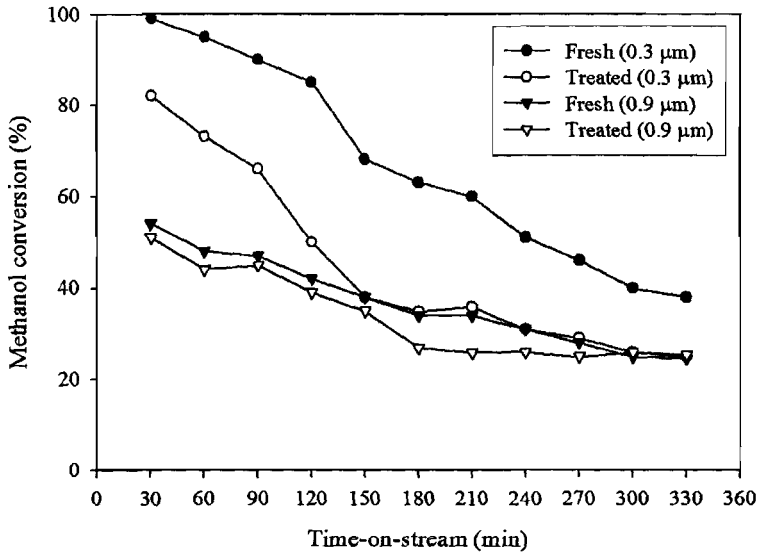

Figure 4. Methanol conversion over fresh and hydrothermally treated beta zeolite with different particle sizes.

found for dealumination of ZSM-5 zeolite as reported by Traintafillidis et al. [23].

Samples of fresh and hydrothermally treated beta zeolites with different particle sizes have been tested for catalytic activities in methanol conversion. The results of methanol conversions as a function of time-on-stream are shown in Fig. 4. It was found that smaller particle size of beta zeolites exhibited higher activities in methanol conversion than the larger ones. And for a given particle size, the activities of untreated catalysts were higher than the hydrothermal treated ones in all ranges of time-on-stream. The activities of the beta zeolite with smaller particle size, however, decreased significantly with time-on-stream while for larger particle size the initial activities and after 330 min on stream were not significantly different. The results were found to be in agreement with the well-established trends in the literature that smaller particle zeolites were more active than those of larger particle ones. However, it should be emphasized that our results support the need for a balance between hydrothermal stability and high catalytic activity. Thus, an appropriate particle size of beta zeolite must be carefully chosen, especially when the reaction is carried out under severe hydrothermal conditions.

4. Conclusions

The hydrothermal stability and catalytic activity of beta zeolite were found to be dependent on the particle size. While the hydrothermal stability increased with increasing particle size, the catalytic activity in methanol conversion changed in the opposite direction. The hydrothermal treatment caused dealumination of the zeolite framework, decreased BET surface areas, and lowered catalytic activities. However, hydrothermal treatment did not alter the relative crystallinity of beta zeolite due probably to the small amount of Al atoms presented in the unit cell.

Acknowledgment

The financial supports from the Thailand Research Fund (TRF) and TJTTP-JBIC are gratefully acknowledged.

References

1. R.L. Wadlinger, G.T. Kerr, and E.J. Rosinski, US Patent N(3,308,069, Mobil oil Corp. (1967).
2. M.A. Arribas and A. Martinez, Catal. Today **65**, 117 (2001).
3. G. Bellusi, G. Pazzuconi, C. Perego, G. Girotti, and G. Terzon J. Catal. **157**, 227 (1995).
4. A.J. Hoefinagel and H. van Bekkum, Appl. Catal. A **97**, 8 (1993).
5. K. Smith, A. Musson, and G.A. DeBoos, J. Chem. Soc. Chen Commun. **469** (1996).
6. K.P. de Jong, C.M.A.M. Mesters, D.G.R. Peferoen, P.T.M van Brugge, and C. de Groot, Chem. Eng. Sci. **51**, 205 (1996).
7. M.S. Rigutto, H.J.A. de Vries, S.R. Magill, A.J. Hoefi nagel, and H. van Bekkum, Stud. Surf. Sci. Catal. **78**, 66 (1993).
8. P. Praserthdam, N. Mongkolsiri, and P. Kanchanawanichkun Catal. Commun. **3**, 191 (2002).
9. L. Bonetto, M.A. Camblor, and A. Corma, Appl. Catal. A **82** 37 (1992).
10. F. Vaudry, F. Di renzo, F. Fajula, and P. Schulz, J. Chem, Soc. Faraday Trans. **94**, 617 (1998).
11. P. Sharma, Y. Igushi, Y. Sekine, E. Kikuchi, and M. Matsukata Stud. Surf. Sci. Catal. **145**, 219 (2003).
12. J. Perez-Pariente, J.A. Martens, and P.A. Jacobs, Zeolites **8**, 4((1988).
13. J. Sanz, V. Fornés, and A. Corma, J. Chem, Soc., Faraday Trans **84**, 3113 (1988).
14. J.P. Jilson, G.C. Edwards, A.W. Peters, K. Rajagopalan, R.F Wormsbecher, T.G. Roberie, and M.P. Shatlock, J. Chem. Soc. Chem. Commun. **91** (1987).
15. B.B. Ramesh and P.A. Clearfield, J. Phys. Chem. **96**, 672((1992).
16. S. Bernasconi, J.A. van Bokhoven, F. Krumeich, G.D. Pirngru ber, and R. Prins, Microporous and Mesoporous Mater. **66**, 2 (2003).
17. M.V. Landau, D. Taylor, O. Regev, M.L. Kaliya, M. Herskowitz V. Valtchev, and S. Mintova, Chem. Mater. **11**, 203((1999).
18. M.A. Camblor, A. Corma, A. Mifsud, J. Perez-Pariente S. Valencia, Stud. Surf. Sci. Catal. **105A**, 341 (1997).
19. A.M. Camiloti, S.L. Jahn, N.D. Velasco, L.F. Moura, and D Cardoso, Appl. Catal. A **182**, 107 (1999).
20. P.J. Kunkeler, B.J. Zurdeeg, J.C. van der Waal, J.A. vai Bokhoven, D.C. Koningsberge, and H. van Bekkun, J. Catal **180**, 234 (1998).
21. R. Szoztak, *Molecular Sieve Principles of Synthesis an Identification* (van Nostrand Reingold, New York, 1989) pp. 1–50.
22. C.T. Costa, G.V. Athanasios, L. Nalbandian, and P.E. Nicholas Microporous and Mesoporous Mater. **47**, 369 (2001).
23. C.S. Triantafillidis, A.G. Vlessidis, and N.P. Evmiridis, Ind. Eng Chem. Res. **39**, 307 (2000).

Available online at www.sciencedirect.com
SCIENCE DIRECT
Materials Chemistry and Physics 94 (2005) 207–212
MATERIALS CHEMISTRY AND PHYSICS
www.elsevier.com/locate/matchemphys

Glycothermal synthesis of nanocrystalline zirconia and their applications as cobalt catalyst supports

Joongjai Panpranot*, Nuttakarn Taochaiyaphum, Piyasan Praserthdam

Center of Excellence on Catalysis and Catalytic Reaction Engineering, Department of Chemical Engineering, Chulalongkorn University, Bangkok 10330, Thailand

Received 8 December 2004; received in revised form 3 March 2005; accepted 19 April 2005

Abstract

Nanocrystalline zirconia have been prepared by the glycothermal method with two different glycols (1,4-butanediol and 1,5-pentanediol) and employed as the support for cobalt catalysts. Commercial zirconia supported cobalt catalyst was also prepared and used as a reference material. The glycothermal-derived zirconia possesses large surface areas with crystallite sizes of 3–4 nm. The catalytic activities for CO hydrogenation of the glycothermal-derived zirconia supported cobalt catalysts were found to be much higher than that of the commercial zirconia supported one. However, the cobalt catalysts supported on zirconia prepared in 1,4-butanediol with lower amount of Zr content in the starting solution exhibited higher activities than the ones supported on zirconia prepared in 1,5-pentanediol. The results suggest that the different crystallization mechanism occurred in the two glycols may affect the amount of crystal defects produced in the corresponding zirconia. As shown by TPR profiles, lower metal-support interaction was observed for the catalysts supported on the zirconia formed via solid-state reaction in 1,4-butanediol (more defects). Consequently, higher active surface cobalt was available for H_2 chemisorption and CO hydrogenation reaction.

Keywords: A. Nanocrystalline zirconia; B. Glycothermal method; Zirconia supported cobalt

1. Introduction

Zirconia powder has been effectively used in different areas of chemistry such as in ceramics and catalysis. It has been found that zirconia has high catalytic activities for isomerization of olefins [1] and epoxides [2]. Commercially available zirconia, however, usually possesses low BET surface area (<50 $m^2\,g^{-1}$) thus may have limited their uses as catalyst supports where a high dispersion of metal is required in order to have high catalytic activity. Recently, synthesis of a high surface area nanocrystalline zirconia has been developed by Inoue et al. [3,4] and is so-called the glycothermal or solvothermal method depending on the solvent used. By thermal decomposition of zirconium alkoxide in organic solvents, large surface area zirconia can be obtained directly without bothersome procedures such as purification of the reactants or handling in an inert atmosphere. Nanocrystals were formed when the starting materials were completely dissolved into the solvent. However, apparently polycrystalline outlines can be observed due to rapid crystal growth [5]. Processing variables such as pH, concentration, temperature, reaction medium, and crystallization time have influences on the crystal structure of zirconia [6–9].

In this study, nanocrystalline zirconia were prepared by the glycothermal method in two different glycols and used as supports for cobalt catalysts. The influences of the glycol source and the Zr concentration in the starting materials on the physicochemical properties of the zirconia were investigated by means of N_2 physisorption, XRD, and SEM. The corresponding glycothermal-derived zirconia supported cobalt catalysts were further characterized by H_2 chemisorption, temperature programmed reduction, and were tested for catalytic activities in CO hydrogenation reaction.

* Corresponding author. Tel.: +66 2 218 6859; fax: +66 2 218 6877.
E-mail address: joongjai.p@eng.chula.ac.th (J. Panpranot).

0254-0584/$ – see front matter © 2005 Elsevier B.V. All rights reserved.
doi:10.1016/j.matchemphys.2005.04.035

2. Experimental

2.1. Preparation of zirconia

Nanocrystalline zirconia was prepared by the glycothermal method according to the procedure described in Ref. [9]. Approximately 15 g of zirconium tetra *n*-propoxide, $Zr(OC_3H_7)_4$ (ZNP) with 20.5% Zr from Strem Chemicals or ZNP with 29.5% Zr from Mitsuwa Pure Chemicals was added to 100 ml of a glycol (1,4-butanediol (Aldrich) or 1,5-butanediol (Merck). This mixture was placed in a 300 ml-autoclave. After the atmosphere inside the autoclave was replaced with nitrogen, the mixture was heated to 300 °C at a heating rate of 2.5 °C min^{-1} and was kept at that temperature for 2 h. After cooling to room temperature, the resulting powders were collected after repeated washing with methanol. The products were then air-dried and were used without further calcinations. For comparison purposes, commercial zirconium dioxide was obtained from Aldrich.

2.2. Catalyst preparation

The zirconia supported cobalt catalysts were prepared by incipient wetness impregnation method using Co(II) nitrate hexahydrate (Aldrich). The catalysts were dried overnight at 110 °C and then calcined in air at 300 °C for 2 h. The final cobalt loading of the calcined catalysts were determined using atomic absorption spectroscopy (Varian Spectra A800) to be ca. 8 wt%.

2.3. Catalyst nomenclature

The different glycothermal-derived zirconia are designated as ZrO_2–BG-20, ZrO_2–BG-30, ZrO_2–PeG-20, and ZrO_2–PeG-30 in which BG and PeG refer to the glycol used (BG = 1,4-butanediol, PeG = 1,5-pentanediol) and the number 20 and 30 refer to the concentration of Zr in the ZNP solution used. Commercial zirconia was designated as ZrO_2-com. Cobalt catalysts supported on different zirconia are designated as Co/ZrO_2–BG-20 for Co supported on ZrO_2–BG-20 and so on.

2.4. Catalyst characterization

The BET surface areas were determined by N_2 physisorption using a Quantachrome Nova 1000 automated system. Each sample was degassed in the system at 150 °C for 2 h prior to N_2 physisorption. The XRD spectra of the sample powders were measured using a SIEMENS D5000 X-ray diffractometer using Cu Kα radiation with a Ni filter in the 10–80° 2θ angular regions. The particle morphology was obtained using a JEOL JSM-35CF scanning electron microscope (SEM) operated at 20 kV. H_2 chemisorption was carried out following the procedure described by Reuel and Bartholomew [10] using a Micromeritics Pulse Chemisorb 2700 system. Prior to chemisorption, the catalysts were reduced at 350 °C for 10 h after ramping at a rate of 1 °C min^{-1}. Static H_2 chemisorption was performed at 100 °C. The TPR profiles of supported cobalt catalysts were obtained by temperature programmed reduction using an in-house system and a temperature ramp of 5 °C min^{-1} from 30 to 500 °C in a flow of 5% H_2 in argon. Approximately 0.20 g of a calcined catalyst was placed in a quartz tube in a temperature-controlled oven and connected to a thermal conductivity detector (TCD). The H_2 consumption was measured by analyzing the effluent gas with a thermal conductivity detector.

2.5. CO hydrogenation reaction

CO hydrogenation was carried out at 220 °C and 1 atm total pressure in a fixed-bed stainless steel reactor under differential conversion conditions. A flow rate of H_2/CO/Ar = 20/2/8 cm^3 min^{-1} was used. Typically, 0.2 g of the catalyst samples was reduced in situ in flowing H2 (50 cm^3 min^{-1}) at 350 °C for 10 h prior to reaction. The product samples were taken at 1 h intervals and analyzed by gas chromatography. Steady state was reached after 6 h time-on-stream in all cases. The percentages of CO conversion and reaction rates were defined as

$$\%\text{CO conversion} = \frac{\text{mole of CO in feed} - \text{mole of CO in products}}{\text{mole of CO in feed}} \times 100$$

$$\text{reaction rate (g CH}_2\text{ g cat.}^{-1}\text{ h}^{-1}) = \frac{\%\text{CO conversion} \times \text{flowrate of CO in feed(cm}^3\text{ min}^{-1}) \times 60\text{ min h}^{-1} \times \text{mol.wt. of CH}_2\text{(g mol}^{-1})}{\text{catalyst weight(g)} \times 22400\text{ cm}^3\text{ mol}^{-1}}$$

3. Results and discussion

The X-ray diffraction patterns of the zirconia powders prepared by the glycothermal method in two different glycols with various Zr contents in the ZNP solutions and the commercial zirconia are shown in Fig. 1. All the glycothermal-derived zirconia samples exhibited tetragonal crystalline zirconia phase. No other crystal structures were observed. The crystal structure of the commercial zirconia as observed from XRD shows a mixture of tetragonal and monoclinic phases, typical for a commercial one. The average crystallite sizes calculated from the XRD line broadening using the Scherrer's equation [11] and the BET surface areas of the zirconia are reported in Table 1. The average crystallite sizes of the glycothermal-derived zirconia were approximately 3–4 nm while that of the commercial zirconia were found to be ca. 10.5 nm. The BET surface areas of the glycothermal-derived zirconia were found to be much higher (195–220 m^2 g^{-1}) than that of a commercial

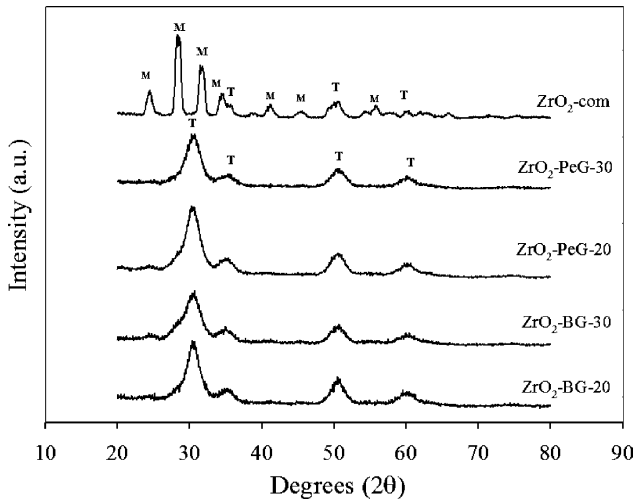

Fig. 1. X-ray diffraction patterns of the zirconia (T = tetragonal, M = monoclinic).

zirconia (50 $m^2\ g^{-1}$). Within experimental error, there was no significant difference in BET surface areas and the crystallite sizes of the zirconia prepared in different glycols or prepared with different amounts of Zr content in the ZNP solution.

Typical SEM micrographs of zirconia samples prepared in 1,4-butanediol and 1,5-pentanediol with different Zr contents are shown in Fig. 2. It was reported that when the starting material were completely dissolved into the glycol, nanocrystals were formed [5]. Each particle was, therefore, a single crystal grown from a nucleus. It was found that the samples prepared in 1,4-butanediol have a spherical shape and a dense mass while in 1,5-pentanediol the samples did not form separate spherical particles. The secondary particles which appeared as separate spherical particles when prepared in 1,4-butanediol seem to be formed by aggregation of primary particles. The results were found to be in agreement with the work previously reported by our group on the effect of solvent on the preparation of zirconia by glycothermal method [9]. It has been proposed by Praserthdam et al. [9] that the mechanisms during crystallization of zirconia in the two glycols were completely different. While the synthesis in 1,5-pentanediol, a homogeneous solution (i.e., glycoxide) was formed after the mixture was heated to 250 °C and cooled down, the synthesis in 1,4-butanediol yielded a solid precipitate. The authors suggested that crystal growth of zirconia in 1,5-pentanediol proceeded by precipication and crystallization of the glycoxide while zirconia particles crystallized from solid-state transformation in 1,4-butanediol.

Table 1
The characteristics of the zirconia samples

Sample	Average crystallite size[a] (nm)	Crystal structure[b]	BET surface area[c] ($m^2\ g^{-1}$)
ZrO_2–BG-20	4.0	T	206
ZrO_2–BG-30	3.0	T	195
ZrO_2–PeG-20	3.7	T	220
ZrO_2–PeG-30	3.6	T	207
ZrO_2-com	10.5	T, M	50

[a] Based on XRD line broadening.
[b] T = tetragonal, M = monoclinic.
[c] Error of measurement = ±10%.

The characteristics and catalytic activities for CO hydrogenation of various zirconia supported cobalt catalysts are shown in Table 2. In this study, cobalt loading on the catalyst samples was approximately 8 wt% in order to make it close to that required for a commercial cobalt catalyst used in the Fischer–Tropsch synthesis. The BET surface areas of the zirconia supported cobalt catalysts were slightly less than that of the original zirconia supports suggesting that cobalt was deposited in some of the pores of zirconia. It would appear that the particle size and shape of the catalyst particles were not affected by impregnation of cobalt since no physical changes were observed. The X-ray diffraction patterns of the zirconia-supported cobalt catalysts are shown in Fig. 3. The XRD diffraction peaks for cobalt oxide (Co_3O_4) at ca. 31.3°, 36.8°, 45.1°, 59.4°, and 65.4° 2θ were not clearly seen for all the catalyst samples except for the Co/ZrO_2-com where a small peak at ca. 36.8° 2θ was apparent. The results suggest that the crystallite sizes of cobalt oxide on the glycothermal-derived zirconia were probably smaller than the lower limit of XRD detectability (3–5 nm). It is also possible that on glycothermal-derived zirconia, cobalt did not form Co_3O_4 crystallites but may have formed an amorphous cobalt oxide [12]. The non-appearance of the XRD characteristic peaks for cobalt oxides was similar to the results obtained from cobalt supported on other metal oxides prepared by sol–gel technique that usually possesses very small cobalt particles [13–18].

The relative amounts of active cobalt metals on the catalyst samples were calculated from H_2 chemisorption experiments at 100 °C according to Reuel and Bartholomew [10]. It is known that only surface cobalt metal atoms are active for CO hydrogenation not its oxide or carbide [19]. It was found that our glycothermal-derived zirconia supported cobalt catalysts exhibited much higher H_2 chemisorption and CO hydrogenation activities than the commercial zirconia supported one with Co/ZrO_2–BG-20 exhibited the highest amount of H_2 chemisorption and CO hydrogenation activity. It should be noted that differences in the amount of H_2 chemisorption and the catalytic activities among the glycothermal-derived zirconia supported catalysts were not due to difference in the BET surfaces areas or the crystallite sizes of zirconia because within experimental error the BET surface areas for all the glycothermal-derived zirconia supported cobalt catalysts and the crystal sizes of zirconia were quite similar. However, the crystallization mechanism in the two glycols probably yielded the final zirconia particles with different amount of crystal defects. Since crystal defects were frequently created especially when crystal growth proceeded rapidly, zirconia prepared in 1,4-butanediol which was found to form via solid-state reaction would contain more crystal defects compared to the ones prepared in 1,5-pentanediol which crystallized via precipitation of alkoxide solution. These defects in the zirco-

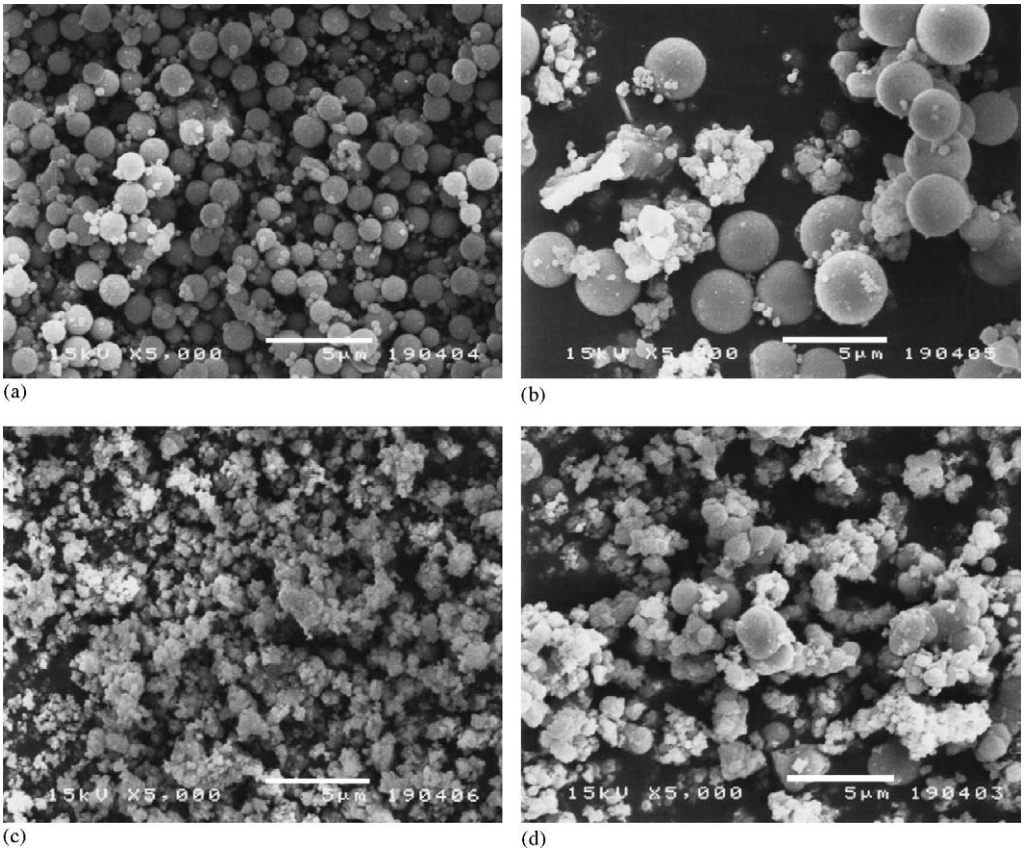

Fig. 2. SEM micrographs of (a) ZrO_2–BG-20 (b) ZrO_2–BG-30 (c) ZrO_2–PeG-20 and (d) ZrO_2–PeG-30.

nia particles may play a role in cobalt-support interaction in supported cobalt catalysts.

Fig. 4 shows the temperature program reduction (TPR) profiles of various zirconia supported cobalt catalysts. TPR is a powerful tool to study the reduction behavior of the catalysts. Reduction of cobalt in the oxide form, Co_3O_4 or Co_2O_3, to Co^0 involves a two-step reduction: first reduction of Co_3O_4 to CoO and then the subsequent reduction of CoO to Co^0 [20,21]. The two reduction steps may not always be observed as separate peaks in TPR profile, as seen in Fig. 4 for the reduction of bulk Co_3O_4 powder [22]. However, a separation of the two reduction steps has often been found for supported cobalt catalysts due to interactions between cobalt and support materials [23,24]. A wide range of variables such as metal particle size and metal-support interaction have an influence on the reduction behavior of cobalt catalysts resulting in the observation of different locations of the TPR peaks. Since the catalysts were pre-calcined at 300 °C, the nitrate precursor has been completely thermally decomposed below 300 °C [25]. Therefore, the hydrogen consumption observed during TPR study cannot be ascribed to residual nitrates. The TPR profiles of the glycothermal-derived zirconia supported cobalt catalysts were different from that of the commercial zirconia supported one in which the reduction

Table 2
The characteristics and catalytic activities of the zirconia supported Co catalysts for CO hydrogenation reaction

Catalyst	BET S.A.[a] ($m^2\ g^{-1}$)	H_2 chemisorption[b] ($\times 10^{18}$ mol g cat^{-1})	Reaction rate[c] (g CH_2 g cat^{-1} h^{-1})	Product selectivity (%)		
				CH_4	C_2–C_3	C_{4+}
Co/ZrO_2–BG-20	170	12.9	14.5	29.5	11.4	59.1
Co/ZrO_2–BG-30	160	6.7	12.0	53.6	11.7	34.8
Co/ZrO_2–PeG-20	173	5.9	7.7	70.7	4.2	25.1
Co/ZrO_2–PeG-30	180	5.8	6.4	73.4	7.5	19.1
Co/ZrO_2-com	46	3.1	3.8	77.8	8.6	13.5

[a] Error of measurement = ±10%.
[b] Error of Measurement = ±5%.
[c] Reaction conditions were 220 °C, 1 atm, and H_2/CO ratio = 10.

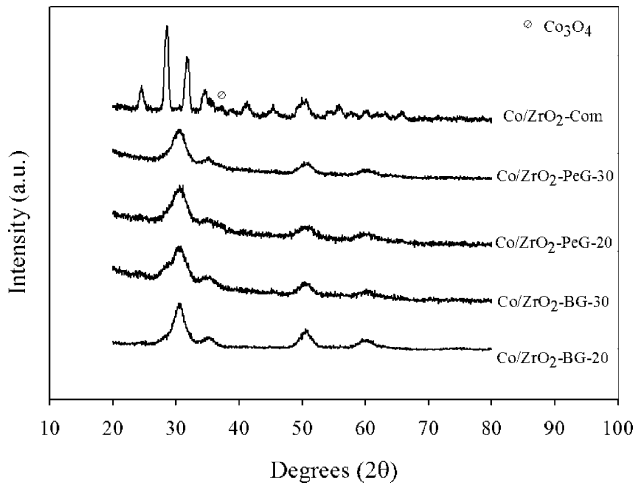

Fig. 3. X-ray diffraction patterns of various zirconia supported cobalt catalysts.

peaks tend to shift to lower temperatures. However, cobalt species supported on zirconia prepared in 1,5-pentanediol were found to be more difficult to reduce than the ones supported on zirconia prepared in 1,4-butanediol indicating a stronger metal-support interaction. The dotted line in the graph represents the standard reduction temperature used to reduce the catalysts prior to reaction (350 °C), it was found that on the zirconia prepared in 1,5-pentanediol and the commercial zirconia, a portion of cobalt oxide species could not be reduced at this temperature hence lower amount of active cobalt metals were available for H_2 chemisorption and CO hydrogenation reaction. Moreover, the selectivities for long chain hydrocarbons (C_{4+}) were found to be in the order: Co/ZrO_2–BG-20 > Co/ZrO_2–BG-30 > Co/ZrO_2–PeG-20 > Co/ZrO_2–PeG-30 > Co/ZrO_2-com. The unique properties of such glycothermal-derived zirconia supported cobalt catalysts offer interesting possibilities for catalyst design and applications.

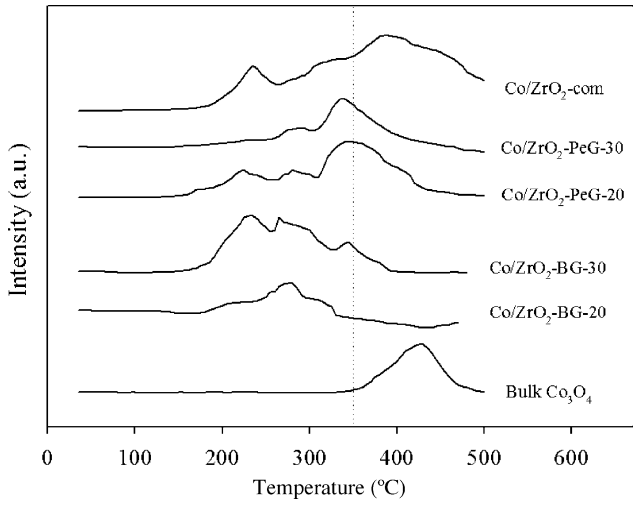

Fig. 4. Temperature programmed reduction (TPR) profiles of various zirconia supported cobalt catalysts.

4. Conclusions

Nanocrystalline zirconia prepared by the glycothermal method in two different glycols with various Zr content in the starting materials showed similar crystallite sizes of ca. 3–4 nm and large BET surface areas. Compared to commercial zirconia supported cobalt catalyst, the glycothermal-derived zirconia supported ones exhibited superior activities for CO hydrogenation with the use of zirconia prepared in 1,4-butanediol with lower amount of Zr content as the support resulted in the highest H_2 chemisorption and CO hydrogenation activities. The lower activities of cobalt catalysts supported on the zirconia prepared in 1,5-pentanediol were due to stronger interaction of cobalt and the zirconia supports as shown by higher reduction temperature peaks in the TPR profiles. The type of glycol used for preparation of the glycothermal-derived zirconia may affect the amount of crystal defects in the zirconia particles resulting in the difference in metal-support interaction behavior.

Acknowledgements

Financial supports by the Thailand Research Fund (TRF), TJTTP-JBIC, and the National Research Council of Thailand are gratefully acknowledged. The authors thank Dr. Nobuhiro Iwasa of the Graduate School of Engineering, Hokkaido University for BET measurements of the catalysts.

References

[1] Y. Nakano, T. Iizuka, H. Hattori, K. Tanabe, H. Hideshi, T. Kozo, J. Catal. 157 (1979) 1.
[2] K. Arata, K. Kato, K. Tanabe, Bull. Chem. Soc. Jpn. 49 (1976) 563.
[3] M. Inoue, H. Kominami, T. Inui, Appl. Catal. 97 (1993) 125.
[4] M. Inoue, H. Kominami, T. Inui, Catal. Lett. 65 (2000) 79.
[5] M. Inoue, Adv. Sci. Technol. 29 (2000) 855.
[6] E. Tani, M. Yoshimura, S. Somiya, J. Am. Ceram. Soc. 64 (1981) C-181.
[7] H. Nishisawa, N. Yamasaki, K. Matsuoka, J. Am. Ceram. Soc. 65 (1982) 343.
[8] G. Stefanic, S. Popovic, S. Music, Thermochim. Acta 303 (1997) 31.
[9] S. Kongwudthiti, P. Praserthdam, P.L. Silveston, M. Inoue, Ceram. Int. 29 (2003) 807.
[10] R.C. Reuel, C.H. Bartholomew, J. Catal. 85 (1984) 78.
[11] H.P. Klug, L.E. Alexander, X-ray Diffraction Procedures for Polycrystalline Amorphous Materials, 2nd ed., Wiley, New York, 1974.
[12] M. Kraum, M. Baerns, Appl. Catal. 186 (1999) 189.
[13] Y. Minato, K. Aoki, M. Shirai, M. Arai, Appl. Catal. A 209 (2001) 79.
[14] L. Ji, S. Tang, H.C. Zeng, J. Lin, K.L. Tan, Appl. Catal. A 207 (2001) 247.
[15] L. Guczi, Z. Schay, G. Stefler, F. Mizukami, J. Mol. Catal. A 141 (1999) 177.
[16] L. Guczi, L. Borko, Z. Schay, D. Basin, F. Mizukami, Catal. Today 65 (2001) 51.
[17] L. Guczi, G. Stefler, L. Borko, Z. Koppany, F. Mizukami, M. Toba, S. Niwa, Appl. Catal. A 246 (2003) 79.

[18] K. Okabe, X. Li, M. Wei, H. Arakwa, Catal. Today 89 (2004) 431.
[19] R.B. Anderson, The Fischer–Tropsch Synthesis, Academic Press, San Diego, 1984.
[20] D. Schanke, S. Vada, E.A. Blekkan, A. Hilmen, A. Hoff, A. Holmen, J. Catal. 156 (1995) 85.
[21] Y. Zhang, D. Wei, S. Hammache, J.G. Goodwin Jr., J. Catal. 188 (1999) 281.
[22] A. Lapidus, A. Krylova, V. Kazanskii, Z. Borovkov, J. Ratnousky, A. Zukal, M.C. Jan, Appl. Catal. A 186 (1999) 145.
[23] J. Panpranot, J.G. Goodwin Jr., A. Sayari, Catal. Today 77 (2002) 269.
[24] A.M. Hilmen, D. Schanke, A. Holmen, Catal. Lett. 38 (1996) 143.
[25] A. Lapidus, A. Krylova, V. Kazanskii, Z. Borovkov, A. Zaitsev, Appl. Catal. A 73 (1991) 65.

Available online at www.sciencedirect.com

SCIENCE DIRECT

Materials Letters 59 (2005) 3771 – 3774

materials letters

www.elsevier.com/locate/matlet

Impact of diene addition on properties for ethylene–propylene copolymerization with *rac*-Et[Ind]$_2$ZrCl$_2$/MAO catalyst

Bunjerd Jongsomjit [a,*], Sireethorn Phoowakeereewiwat [a], Supakanok Thongyai [a], Takeshi Shiono [b], Piyasan Praserthdam [a]

[a] *Center of Excellence on Catalysis and Catalytic Reaction Engineering, Department of Chemical Engineering, Faculty of Engineering, Chulalongkorn University, Bangkok 10330, Thailand*

[b] *Department of Applied Chemistry, Faculty of Engineering, Hiroshima University, Higashi-Hiroshima 739-8527, Japan*

Received 20 May 2005; accepted 7 July 2005
Available online 28 July 2005

Abstract

In the present study, the impact of diene addition during copolymerization of ethylene and propylene using a metallocene/MAO catalyst was investigated. It showed that with a small amount of diene added, the dienes (except for ENB) did not incorporate in the polymer backbone pronouncedly. However, the addition of dienes can alter the incorporation of ethylene and propylene in the polymer backbone according to different types of dienes used. The catalytic behaviors and yields were not significant changes with the addition of dienes. The characteristics of polymer obtained using ^{13}C NMR, SEM, and DSC were also further discussed in more detail.

Keywords: Polymerization; Metallocene; Catalyst; Elastomers; Methylaluminoxane

1. Introduction

It is known that the copolymerization of ethylene (E) and propylene (P) can result in a production of rubbery materials called EP elastomers [1–3]. Because there are no double bonds in the backbone of polymer chain, they are usually insensitive to oxygen, ozone, acids, and alkaline. It was found that addition of the third monomer such as dienes could be applied in order to escalate the properties of EP elastomers, the so-called EPDM elastomers. As known, EPDM can be widely used in many applications so far [4–6]. Currently, EPDM is synthesized using vanadium-based catalysts. With the presence of dienes, it was found that the vanadium-based catalysts exhibited low activities along with toxicity concerns due to the residual vanadium remains in the polymer [7]. Thus, in order to overcome those problems, an alternative way of using the homogeneous metallocene catalysts has been substantially investigated by many authors [8–10]. Nevertheless, the production of EPDM is considered to be an important matter, the approach of our present study was apparently different from the

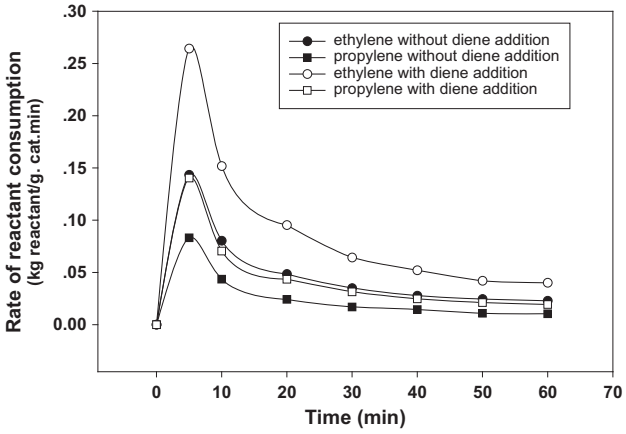

Fig. 1. Activity profiles based on ethylene (E) and propylene (P) consumption with and without diene addition.

* Corresponding author. Tel.: +66 662 2186869; fax: +66 662 2186877.
E-mail address: bunjerd.j@chula.ac.th (B. Jongsomjit).

0167-577X/$ - see front matter © 2005 Elsevier B.V. All rights reserved.
doi:10.1016/j.matlet.2005.07.014

Table 1
Yields and activities of EP elastomers produced from *rac*-Et[Ind]$_2$ZrCl$_2$/MAO catalyst; [Zr]=30 μM in toluene, [Al]/[Zr]=2000, [diene]=0.1 M, E/P molar ratio=75/25, polymerization temperature=40 °C, and polymerization time=1 h

Sample	Types of diene	Polymer yield (g)	Activity (kg polymer/mol Zr h)
EP (0)	None added	2.88	3198
EP(1)	ENB	2.40	2671
EP(2)	VCH	2.60	2887
EP(3)	HD	2.54	2824

others. Hereby, only a small amount of various dienes was introduced into the system during EP copolymerization, not for the purpose of synthesizing the EPDM as in general, but specifically for altering the behaviors of EP copolymerization. Thus, in our present study, the small amount of various dienes added did not incorporate into the polymer backbone, which can be determined using ^{13}C NMR measurement.

2. Experimental

In this study, EP copolymerization was performed using *rac*-Et[Ind]$_2$ZrCl$_2$ catalyst. All chemicals were manipulated under purified argon using a vacuum atmosphere glove boxes and/or Schlenk techniques. Polymerization was carried out in 100-ml stainless steel reactor with magnetic stirrer. First, 30 ml of toluene used as a solvent was added to the reactor. Then, methylaluminoxane (MAO) solution was added according to the specified ratio to the catalyst concentration ([Al]/[Zr]=2000) followed by the addition of 0.1 M of a selected diene [dienes used were 5-ethylidene-2-norbonene (ENB);(1), 4-vinylcyclohexene (VCH);(2), and 1,4-hexadiene (HD);(3)]. Then, the catalyst was injected into the system. The reactor was immediately put into liquid nitrogen to stop the reaction between the catalyst and cocatalyst (MAO). After the reaction mixture was frozen

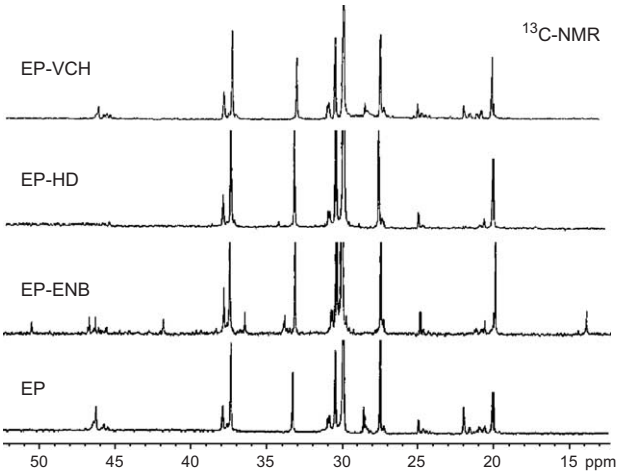

Fig. 2. ^{13}C NMR spectra of various EP elastomers with and without diene addition.

Table 2
Triad distribution obtained by ^{13}C NMR measurement of ethylene (E) and propylene (P) in polymers produced

Sample	Types of diene	EEE	PEE+EEP	PEP	EPE	EPP+PPE	PPP
EP (0)	None added	0.502	0.187	0.045	0.122	0.032	0.112
EP (1)	ENB	0.604	0.191	0.023	0.107	0.024	0.051
EP (2)	VCH	0.505	0.205	0.056	0.114	0.088	0.032
EP (3)	HD	0.609	0.210	0.032	0.118	0.031	–

for 15 min, the reactor was evacuated for 3 min to remove argon then filled with the gaseous monomers (ethylene/propylene with a molar ratio of 75/25) while the reactor was still frozen in liquid nitrogen. Then, the reactor was taken out of liquid nitrogen and heated up to polymerization temperature (40 °C) to start the polymerization reaction. The polymerization time was kept for 1 h. In order to stop the reaction, the gaseous monomers were released and the reaction mixture was washed with acidic methanol. The polymer (white rubbery powder) obtained was filtered and dried overnight at ambient condition. Technically, for each diene, the polymerization was run at least three times to ensure the results obtained. The average values were reported. Characterization of the polymer obtained was performed using the ^{13}carbon nuclear magnetic resonance, ^{13}C NMR (JEOL JMR-A500 operating at 125 MHz), differential scanning calorimetry, DSC (Perkin-Elmer DSC 7), and scanning electron microscopy, SEM (JSM-5800 LV).

3. Results and discussion

The present research indicated that a small amount of dienes (ENB, VCH, and HD) added could have impact on behaviors of ethylene–propylene (EP) copolymerization with a metallocene/MAO catalyst. In fact, a large amount of diene addition could result in a decreased activity of polymerization as reported by Malmberg et al. [5]. However, it should be noted that the large amounts (~10–16 mol%) of diene were technically required in order to produce the terpolymer of EPDM. In particular, only a small amount (~3.6 mol%) of each diene was added during EP copolymerization in this study in order to maintain high activity of polymerization at this specified condition.

The rates of consumption for E and P with and without the diene addition are shown in Fig. 1. It was found that the

Table 3
Incorporation of ethylene (E), propylene (P) and reactivity ratios of ethylene (r_E) and propylene (r_P) calculated from ^{13}C NMR measurement

Sample	Types of diene	Incorporation (%)		Reactivity ratios		
		E	P	r_E	r_P	$r_E r_P$
EP (0)	None added	73	27	5.3	1.9	10.1
EP (1)	ENB[a]	80	18	6.9	1.5	10.4
EP (2)	VCH	76	24	4.8	1.5	7.2
EP (3)	HD	85	15	6.2	1.1	6.8

[a] ENB incorporation ca. 2%.

Table 4
Thermal properties of polymers obtained from DSC measurement

Sample	Types of diene	T_c (°C)	T_m (°C)	ΔH_m (J/g)	% Crystallinity (% χ)
EP (0)	None added	59.3	73.6	30.6	10.6
EP (1)	ENB	57.2	73.8	23.8	8.2
EP (2)	VCH	65.2	80.5	36.3	12.5
EP (3)	HD	70.0	88.2	49.1	17.0

induction period of the catalyst was also observed at the beginning of polymerization. The consumption rate went to a maximum after 6–7 min, then decreased due to catalyst deactivation. With the diene addition, similar activity profiles can still be observed as also shown in Fig. 1. It was suggested that the addition of dienes would have no effect on the catalyst performance at all indicating the similar rate profiles. Yields and activities of various EP elastomers are shown in Table 1. It indicated that the addition of dienes could result in only slightly decreased activities regardless of the dienes used. The polymers obtained were then further characterized using ^{13}C NMR, SEM, and DSC as mentioned. As known, ^{13}C NMR is one of the most powerful techniques used to identify the microstructure of a polymer. The ^{13}C NMR spectra for all polymer samples are shown in Fig. 2. It can be observed that the ^{13}C NMR spectra of EP, EP-VCH, and EP-HD samples exhibited similar patterns corresponding with those as reported by Randall [11]. These revealed that there was no incorporation of HD and VCH in the polymer backbone. The ^{13}C NMR spectrum of EP-ENB sample is also shown in Fig. 2, which apparently exhibited the slightly different patterns compared with other samples as mentioned before. Besides the characteristic peaks of EP copolymer, the incorporation of ENB can be additionally observed at δ=14, 36.5 and 42 ppm. This indicated that only ENB was able to incorporate into the polymer backbone at this specified condition. The triad distribution, % incorporation, and the reactivity ratios of E and P can be also calculated based on the method described by Randall [11]. The triad distribution of E and P for all samples is shown in Table 2. It indicated that the similar triad distribution was observed, except no block PPP in EP (3) sample. However, % incorporation of E and P along with the reactivity ratios (r_E and r_P) are shown in Table 3. It revealed that upon the addition of a small amount of dienes during copolymerization of EP, the incorporation of ethylene in the polymer apparently increased, especially for the ENB and HD. Since the reactivity ratio of $r_E r_P > 1$, the blocky incorporation of comonomer was obtained, which was different from the behaviors for copolymerization of ethylene and higher 1-olefins such as 1-hexene, 1-octene, and 1-decene [9,10]. The thermal properties such as T_c and T_m obtained from DSC measurement along with % crystallinity [12] are also summarized in Table 4. It was found that T_m, T_c and % crystallinity of EP tended to increase with the addition of dienes. In addition, the various dienes gave different impacts on % crystallinity of EP. It showed that using HD would result in the largest number of T_m, T_c and % crystallinity. The SEM micrographs of various EP produced are shown in Fig. 3. It can be observed that there were some differences in morphologies of the various EP produced. Apparently, the EP produced with the addition of dienes appeared in a larger air gap in the texture compared to those without diene addition. It should be noted that the impact of diene on the different ratios of E/P would be interesting to

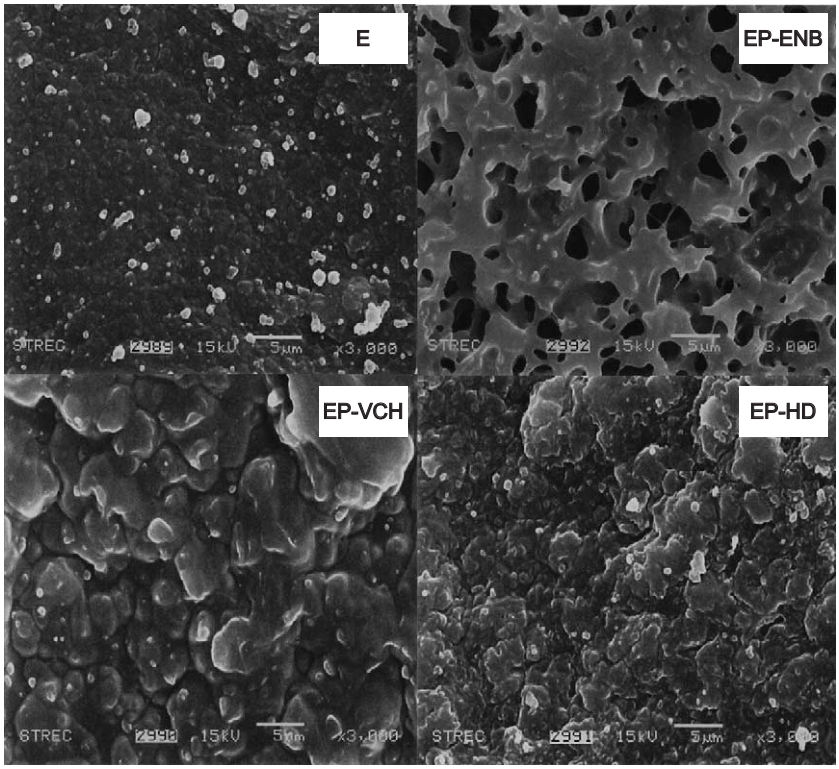

Fig. 3. SEM micrographs of various EP elastomers.

further investigate for our future work. In particular, the various ratios of E/P in the polymer backbone are considered to be the key role to obtain different properties for EP rubbers.

According to our experimental data, the mechanism of this copolymerization of ethylene and propylene could be drawn based on changes in the incorporation of ethylene and propylene upon the diene addition. As seen in Table 3, it can be observed that the insertion of propylene apparently decreased with the diene addition. Therefore, it can be proposed that the addition of diene probably inhibited the propylene insertion catalytic site and/or somehow promoted the catalytic site of ethylene insertion. Those phenomena resulted in a decreased propylene insertion. However, in order to provide a better understanding of the rigorous mechanism inside, we believe that a more powerful technique such as the steady-state isotopic transient kinetic analysis (SSITKA) [13–15], where the reaction intermediates can be identified would be helpful. This technique requires an additional instrument such as a mass spectrometer along with the isotopes (^{13}C) of the corresponding reactants.

4. Conclusions

In summary, our present study revealed, for the first time, that the addition of only a small amount of dienes under the specified condition could alter the copolymerization behaviors of ethylene and propylene instead of making the EPDM as in general. At the specified condition, dienes (except for ENB) did not incorporate into the polymer backbone as proved by ^{13}C NMR. Upon the various dienes used, % incorporation, T_m, T_c, and % crystallinity can be changed dramatically. However, in order to provide a better understanding, the roles of dienes should be further investigated in more detail, especially when the ratios of E/P are varied.

Acknowledgements

The authors thank the Thailand Research Fund (TRF), the National Research Council of Thailand (NRCT), the National Science and Technology Development Agency (NSTDA) and Thailand–Japan Technology Transfer Project (TJTTP-JBIC) for the financial support of this work.

References

[1] W. Kaminsky, M. Miri, J. Polym. Sci., Polym. Chem. 23 (1985) 2151.
[2] R.D. Allen, J. Elastomers Plast. 15 (1983) 19.
[3] E.L. Borg, in: M. Morton (Ed.), Rubber Technology, Krieger, Malabar, FL, 1981, p. 220.
[4] G.V. Strate, in: H.F. Mark, N.M. Bikales, C.G. Overberger, J.J Koschwitz (Eds.), Encyclopedia of Polymer Science and Engineering, J. Wiley & Sons, New York, 1973, p. 522.
[5] A. Malmberg, B. Lofgren, J. Appl. Polym. Sci. 66 (1997) 35.
[6] A. Deffieux, M. Dolakthani, H. Cramail, Macromol. Chem. Phys. 197 (1996) 289.
[7] K.L. Walton, M.M. Hughes, D.R. Parikh, Rubber Chem. Technol. 74 (2001) 688.
[8] W. Kaminsky, A. Laban, Appl. Catal., A Gen. 222 (2001) 47.
[9] B. Jongsomjit, P. Praserthdam, P. Kaewkrajang, Mater. Chem. Phys. 86 (2004) 243.
[10] B. Jongsomjit, P. Kaewkrajang, S.E. Wanke, P. Praserthdam, Catal. Lett. 94 (2004) 205.
[11] C. Randall, Macromol. Chem. Phys. 29 (1989) 201.
[12] S. Ottani, R.S. Porter, J. Polym. Sci., Part B, Polym. Phys. 29 (1991) 1179.
[13] A.R. Belambe, R. Oukaci, J.G. Goodwin Jr., J. Catal. 166 (1997) 8.
[14] S.L. Shannon, J.G. Goodwin Jr., Chem. Rev. 95 (1995) 677.
[15] B. Jongsomjit, J. Panpranot, J.G. Goodwin Jr., J. Catal. 215 (2003) 66.

Available online at www.sciencedirect.com
SCIENCE DIRECT®
Catalysis Communications 6 (2005) 705–710
CATALYSIS COMMUNICATIONS
www.elsevier.com/locate/catcom

Characteristics and catalytic properties of Co/TiO_2 for various rutile:anatase ratios

Bunjerd Jongsomjit *, Tipnapa Wongsalee, Piyasan Praserthdam

Center of Excellence on Catalysis and Catalytic Reaction Engineering, Department of Chemical Engineering, Faculty of Engineering, Chulalongkorn University, Bangkok 10330, Thailand

Received 21 March 2005; received in revised form 5 July 2005; accepted 5 July 2005
Available online 1 September 2005

Abstract

This present study revealed a dependence of rutile:anatase ratios in titania on the characteristics and catalytic properties of Co/TiO_2 catalysts during CO hydrogenation. In this study, Co/TiO_2 catalysts were prepared using various titania supports consisting of various rutile:anatase ratios of titania. In order to identify the characteristics, all catalyst materials were characterized using XRD, SEM/EDX, TPR, and hydrogen chemisorption. CO hydrogenation ($H_2/CO = 10/1$) was also performed to determine the overall activity and selectivity. It was found that both activity and selectivity were altered by changing the rutile:anatase ratios in the titania support.

Keywords: Cobalt catalyst; Titania; Chemisorption; CO; hydrogenation; Titania phase

1. Introduction

It has been known that supported cobalt (Co) catalysts are used for carbon monoxide (CO) hydrogenation because of their high activities based on natural gas [1], high selectivity to linear long chain hydrocarbons and also low activities for the competitive water–gas shift (WGS) reaction [2,3]. Many inorganic supports such as SiO_2 [4–8], Al_2O_3 [9–14], TiO_2 [15–17] and zeolites [18] have been extensively studied for supported Co catalysts for years. It is known that in general, the catalytic properties depend on reaction conditions, catalyst compositions, metal dispersion, and types of inorganic supports used. Thus, changes in the catalyst composition and/or even though the compositions of supports used may lead to significant enhanced catalytic properties as well.

During the past decades, titania-supported Co catalysts have been widely investigated by many authors, especially for the application of FT synthesis in a continuously stirred tank reactor (CSTR) [15–17]. However, it should be noted that titania itself has different crystalline phases such as anatase, brookite and rutile phase. Differences in crystalline phases may result in changes in physical and chemical properties of titania. Thus, different crystalline phase compositions of titania could play an important role on the catalytic performance of titania-supported Co catalysts during CO hydrogenation as well.

Therefore, the main objective of this present research was to investigate influences of various rutile:anatase ratios in titania support on the characteristics and catalytic properties during CO hydrogenation of Co/TiO_2 catalysts. In the present study, the Co/TiO_2 catalysts were prepared using various titania supports containing different ratios of rutile:anatase phase. The catalysts

* Corresponding author. Tel.: +662 218 6869; fax: +662 218 6766/6877.
E-mail address: bunjerd.j@chula.ac.th (B. Jongsomjit).

1566-7367/$ - see front matter © 2005 Elsevier B.V. All rights reserved.
doi:10.1016/j.catcom.2005.07.002

were characterized using various characterization techniques and tested in order to evaluate the catalytic properties during CO hydrogenation.

2. Experimental

2.1. Material preparation

2.1.1. Preparation of titania support

The various ratios of rutile:anatase in titania support were obtained by calcination of pure anatase titania (obtained from Ishihara Sangyo, Japan) in air at temperatures between 800 and 1000 °C for 4 h. The high space velocity of air flow (16,000 h^{-1}) insured the gradual phase transformation to avoid rapid sintering of samples. The ratios of rutile:anatase were determined by XRD according to the method described by Jung and Park [19] as follows:

$$\%\ \text{Rutile} = \frac{1}{[(A/R)0.884 + 1]} \times 100,$$

where A and R are the peak area for major anatase ($2\theta = 25°$) and rutile phase ($2\theta = 28°$), respectively.

2.1.2. Preparation of catalyst samples

A 20 wt% of Co/TiO_2 was prepared by the incipient wetness impregnation. A designed amount of cobalt nitrate [$Co(NO_3)\cdot 6H_2O$] was dissolved in deionized water and then impregnated onto TiO_2 containing various ratios of rutile:anatase obtained from Section 2.1.1. The catalyst precursor was dried at 110 °C for 12 h and calcined in air at 500 °C for 4 h.

2.2. Catalyst nomenclature

The nomenclature used for the catalyst samples in this study is following:

- *Rn:* titania support containing *n%* of rutile phase (R).
- *Co/Rn:* titania support containing *n%* of rutile phase (R)-supported cobalt.

2.3. Catalyst characterization

2.3.1. BET surface area

BET surface area of the samples with various rutile:anatase ratios of TiO_2 was performed to determine if the total surface area changes. It was determined using N_2 adsorption at 77 K in a Micromeritics ASAP 2010.

2.3.2. X-ray diffraction

XRD was performed to determine the bulk crystalline phases of catalyst. It was conducted using a SIEMENS D-5000 X-ray diffractometer with Cu $K\alpha(\lambda = 1.54439$ Å). The spectra were scanned at a rate of 2.4 deg/min in the range $2\theta = 20$–80°.

2.3.3. Scanning electron microscopy and energy dispersive X-ray spectroscopy

SEM and EDX were used to determine the catalyst morphologies and elemental distribution throughout the catalyst granules, respectively. SEM was carried out using a JEOL model JSM-5800LV. EDX was performed using Link Isis series 300 program.

2.3.4. Hydrogen chemisorption

Static H_2 chemisorption at 100 °C on the reduced cobalt catalysts was used to determine the number of reduced surface cobalt metal atoms. Prior to H_2 chemisorption, the catalyst sample was reduced in H_2 at 350 °C for 10 h. The resulting H_2 chemisorption is related to the overall activity of the catalysts during CO hydrogenation. Gas volumetric chemisorption at 100 °C was performed using the method described by Reuel and Bartholomew [20]. The experiment was performed in a Micromeritics ASAP 2010 using ASAP 2010C V3.00 software.

2.3.5. Temperature-programmed reduction

TPR was used to determine the reduction behaviors and reducibilities of the samples. It was carried out using 50 mg of a sample and a temperature ramp from 35 to 800 °C at 5 °C/min. The carrier gas was 5% H_2 in Ar. A cold trap was placed before the detector to remove water produced during the reaction. A thermal conductivity detector (TCD) was used to determine the amount of H_2 consumed during TPR. The H_2 consumption was calibrated using TPR of Ag_2O at the same conditions. The calculation of reducibilities was as described elsewhere [9,21–24].

2.4. Reaction

CO hydrogenation ($H_2/CO = 10/1$) was performed to determine the overall activity of the catalyst samples. Hydrogenation of CO was carried out at 220 °C and 1 atm. A flow rate of $H_2/CO/He = 20/2/8$ cm^3/min in a fixed-bed flow reactor under differential conditions was used. A relatively high H_2/CO ratio was used to minimize deactivation due to carbon deposition during reaction. Typically, 20 mg of a catalyst sample was reduced in situ in flowing H_2 (30 cm^3/min) at 350 °C for 10 h prior to the reaction. Reactor effluent samples were taken at 1 h intervals and analyzed by GC. In all cases, steady state was reached within 5 h.

3. Results and discussion

The present study showed the dependence of rutile: anatase ratios in titania on the catalytic properties during

CO hydrogenation of Co/TiO_2 catalysts. As mentioned, in general titania used contains mainly two phases; anatase and rutile phases. Phase transformation of titania depends on the preparation of titania such as sol–gel or solvothermal methods and also calcination temperatures. However, it was proposed that the different phase compositions in titania could play an important role on the catalytic properties during CO hydrogenation of Co/TiO_2 catalysts. Results and discussion are divided into two parts as follows.

3.1. Crystalline phases of titania

After calcination of the pure anatase titania under calcination temperatures ranging between 800 and 1000 °C for 4 h, the phase transformation from anatase to rutile phase should technically occur. The amounts of rutile phase formed during calcination depended on the temperature used. The high space velocity of the air flow at 16,000 h^{-1} was applied during the calcination process in order to minimize the rapid sintering due to the phase transformation of titania. It was found that after calcination of the pure anatase sample, the amounts of rutile phase obtained ranged between 3% and 99%. The titania supports containing rutile phase of ca. 0%, 3%, 19%, 40%, 96%, and 99% were named as R0, R3, R19, R40, R96, and R99, respectively. The surface areas of titania containing various rutile:anatase rations essentially decreased from 70 m^2/g for the R0 sample (pure anatase titania) to 49 m^2/g for the R99 sample (99% rutile titania). XRD patterns of titania samples calcined at various temperatures between 800 and 1000 °C are shown in Fig. 1. For the pure anatase titania (R0), XRD peaks of the anatase phase of titania at 25° (major), 37°, 48°, 55°, 56°, 62°, 71°, and 75° were evident. After calcination of the pure anatase titania sample, it was observed that besides the XRD peaks of pure anatase titania as shown above XRD peaks at 28° (major), 36°, 42°, and 57° were gradually seen. These peaks were assigned to the rutile phase essentially formed after calcination of the pure anatase titania. Apparently, the major peak at 28° of the rutile phase gradually increased with increasing the calcination temperatures indicating a higher content of rutile phase in the titania. It was shown that the transformation from anatase to rutile phase (R99) was almost complete at a temperature of ca. 1000 °C, resulting in the disappearance of XRD peaks for the anatase phase of titania. After various titania supports were obtained, the preparation of Co/TiO_2 with various rutile:anatase ratios of titania was consequently conducted in order to investigate the effect of the rutile:anatase ratio on characteristics and catalytic properties of the Co/TiO_2 catalysts during CO hydrogenation.

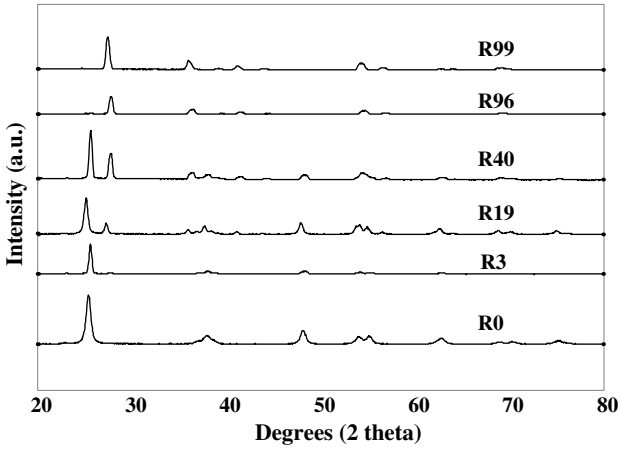

Fig. 1. XRD patterns for various ratios of rutile:anatase in titania supports.

3.2. Characteristics of Co/TiO_2

A 20 wt% of cobalt on titania supports containing various ratios of rutile:anatase phase was prepared by the conventional incipient wetness impregnation method. The XRD patterns for all calcined catalyst samples (Co/TiO_2) exhibited similar patterns as seen in Fig. 1. After calcination, all calcined samples exhibited XRD peaks, which were identical with those for the corresponding titania supports. This indicated that no further phase transformation from anatase to rutile occurred after calcination (at temperature ca. 500 °C for 4 h) of the catalyst samples. Besides the XRD peaks of the titania, all calcined samples also exhibited weak XRD peaks at 31°, 36°, and 65°, which were assigned to the presence of Co_3O_4. However, at high content of the rutile phase, the XRD peaks of Co_3O_4 were less apparent due to the strong intensity of XRD peaks for the rutile phase of titania. Based on the XRD results, it was clear that Co_3O_4 species were definitely present in a highly dispersed form.

SEM and EDX were also conducted in order to study the morphologies and elemental distribution of the catalyst samples, respectively. The typical SEM micrograph along with the EDX mapping (for Co, Ti, and O) are illustrated in Fig. 2 for the Co/R40 sample. The external surface of catalyst granule is shown in all figures and the light or white patches on the catalyst granule surface represent high concentration of cobalt oxides species on the surface. It can be seen that the cobalt oxide species were well dispersed and distributed (shown on mapping) all over the catalyst granule in all samples regardless of the ratio of rutile:anatase in the titania.

TPR was performed in order to identify the reduction behaviors and reducibility of catalysts. TPR profiles for all samples are shown in Fig. 3. TPR of the titania support samples used was also conducted at the same TPR conditions used for the catalyst samples (not shown) and no hydrogen consumption was detected.

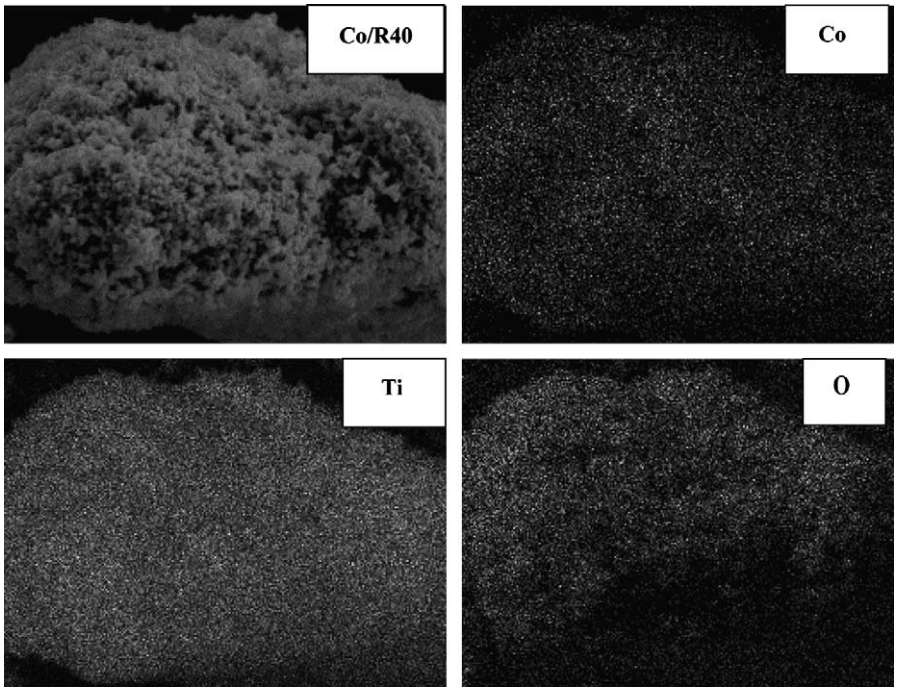

Fig. 2. A typical SEM micrograph for Co/R40 granule and EDX for Co, Ti, and O mapping.

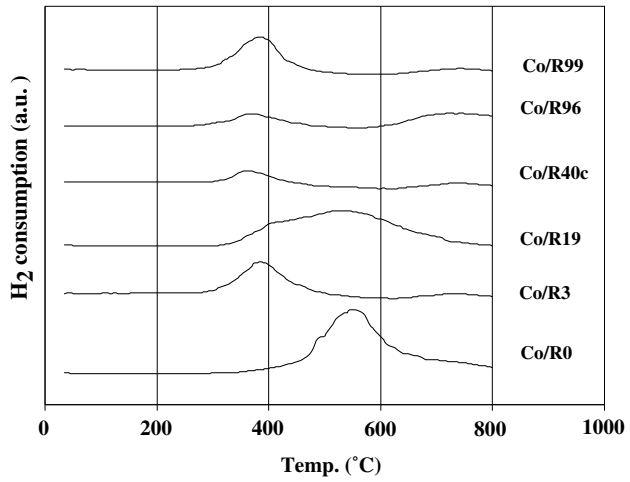

Fig. 3. TPR profiles for Co/TiO_2 catalysts with various ratios of rutile:anatase in titania supports used.

This indicated that the titania supports used themselves were not reducible at these TPR conditions. Apparently, TPR profiles of all calcined samples were similar exhibiting only one strong reduction peak as shown in Fig. 3. This peak can be assigned to the overlap of two-step reduction of Co_3O_4 to CoO and then to Co^0 [25]. Under TPR conditions, the two reduction peaks based on the two-step reduction may or may not be observed. The presence of only one reduction peak during TPR for all catalyst samples indicated that no residual cobalt nitrates precursor remained on the samples under the calcination condition used in this study. It was found that a TPR peak located at ca. 380–700 °C (max. at 520 °C) was observed for the Co/R0 sample. However, this reduction peak was dramatically shifted about 50–80 °C lower when ca. 3–99% of rutile phase (Co/R3 to Co/R99) was present in the titania supports used. This suggests that the presence of rutile phase in titania can facilitate the reduction process of cobalt oxide species on the titania support leading to reduction at a lower temperature. Since TPR is more of a bulk technique, it should be noted that the number of reduced Co metal obtained from the TPR measurement might not be well representative of the number of reduced Co metal surface atoms available for catalyzing CO hydrogenation. Therefore, static H_2 chemisorption on the reduced cobalt catalyst samples was used to determine the number of reduced Co metal surface atoms. This is usually related to the overall activity of the catalyst during CO hydrogenation.

The resulting H_2 chemisorption results for all catalyst samples are shown in Fig. 4. It was found that the amounts of H_2 adsorbed increased with the presence of rutile phase in titania up to a maximum at 19% of rutile phase (Co/R19) before decreasing when greater amounts of the rultile phase were present. Since H_2 chemisorption is a surface technique that the reduced Co metal surface atoms can be measured directly. The amounts of H_2 adsorbed on Co/TiO_2 obtained were lower compared to those for Co/Al_2O_3 and Co/SiO_2 at similar loading [5,6,21,22]. However, based on the H_2 chemisorption results in this present study, different ratios of rutile: anatase phase in titania exhibited different amounts of H_2 chemisorbed on the catalyst samples.

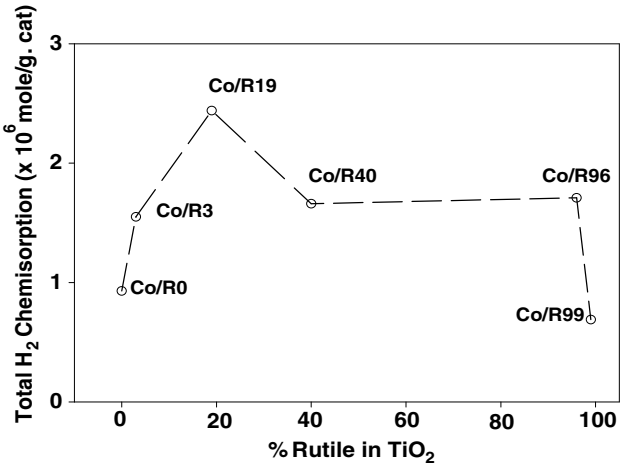

Fig. 4. H_2 chemisorption for Co/TiO_2 catalysts with various ratios of rutile:anatase in titania supports used.

3.3. Reactivity

In order to measure the catalytic properties of the catalyst samples with various ratios of rutile:anatase in titania, CO hydrogenation was performed in a fixed-bed flow reactor under differential condition. The results are shown in Fig. 5 and Table 1. It indicated that the reaction rate ranged between 0.3 and 6.6 μmole/g. cat. s (initial) and between 0.2 and 5.2 μmole/g cat s (steady state). This also showed that activities of the samples increased with the presence of rutile phase in titania up to a maximum at 19% of rutile phase (Co/R19) before decreasing when greater amounts of rutile phase were present, similar to the results obtained from H_2 chemisorption. Considering selectivity to methane, it was found that the presence of rutile phase in titania resulted in an increased selectivity to methane. After reaction, XRD of the spent catalyst samples was also

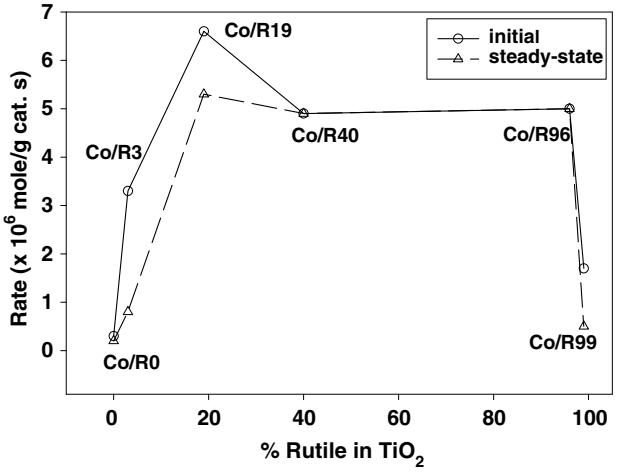

Fig. 5. Reaction rate during CO hydrogenation for Co/TiO_2 catalysts with various ratios of rutile:anatase in titania supports used.

Table 1
Activities and selectivity during CO hydrogenation of Co/TiO_2 via various rutile:anatase ratios of titania support

Catalyst samples	Rate (μmol/g cat s)[a]		Selectivity to CH_4(%)	
	Initial[b]	Steady state[c]	Initial[b]	Steady state[c]
Co/R0	0.3	0.2	71	68
Co/R3	3.3	0.8	99	99
Co/R19	6.6	5.3	98	98
Co/R40	4.9	4.9	97	96
Co/R96	5.0	5.0	99	99
Co/R99	1.7	0.5	94	94

[a] CO hydrogenation was carried out at 220 °C, 1 atm, and H_2/CO/He = 20/2/8.
[b] After 5 min of reaction.
[c] After 5 h of reaction.

performed in order to identify the bulk crystalline phases of the spent catalyst samples. It showed that the XRD patterns of all spent catalyst samples were identical with those of the corresponding fresh ones suggesting no phase changes occurred during the reaction condition used.

Based on the reaction study, it can be concluded that the catalytic properties of Co/TiO_2 depend on the ratio of rutile/anatase. The results revealed that the presence of rutile phase of an optimum of the rutile phase (i.e., Co/R19) result in an increased catalytic activity during CO hydrogenation. It is proposed that the presence of rutile phase in titania can facilitate the reduction process of cobalt oxides species resulting in lower reduction temperatures. The presence of some rutile phase also resulted in an increased number of reduced cobalt metal surface atoms available for catalyzing the reaction. However, higher ratios (more than 19%) of rutile:anatase in titania decreased the catalyst activities. It should be mentioned that besides the ratios of rutile:anatase in titania, there are also other factors such as preparation methods, titania precursors, particle sizes, modes and types of reactions that would affect the characteristics and catalytic properties of titania used both as a catalyst support or a catalyst itself.

4. Conclusion

The present research showed a dependence of the characteristics and catalytic properties during CO hydrogenation on the ratio of rutile/anatase in titania for Co. The study revealed that the presence of 19% rutile phase in titania for Co/TiO_2 (Co/R19) exhibited the highest activity during CO hydrogenation. It appeared that the increase in activity was due to two reasons;(i) the presence of rutile phase in titania can facilitrate the reduction process of cobalt oxide species into reduced cobalt metal and (ii) the presence of some rutile phase resulted in a larger number of reduced cobalt metal surface atoms, which is related to the activity during CO hydrogenation.

However, if the ratio of rutile:anatase was over 19%, the activity dramatically decreased. No further phase transformation of the supports occurred during calcination of the catalyst samples and reaction.

Acknowledgements

We gratefully acknowledge the financial support by the National Research Council of Thailand (NRCT), the Thailand Research Fund (TRF) and Thailand–Japan Technology Transfer Project (TJTTP-JBIC). We thank Prof. James G. Goodwin, Jr. at Clemson University for initiating this kind of project.

References

[1] A.P. Steynberg, M.E. Dry, B.H. Davis, B.B. Breman, in: Fischer-Tropsch Technology Study, Surface Science and Catalysis 152 (2004) 64.
[2] E. Iglesia, Appl. Catal. 161 (1997) 59.
[3] R.C. Brady, R.J. Pettie, J. Am. Chem. Soc. 103 (1981) 1287.
[4] A. Martinez, C. Lopez, F. Marquez, I. Duaz, J. Catal. 220 (2003) 486.
[5] J. Panpranot, J.G. Goodwin Jr., A. Sayari, Catal. Today 77 (2002) 269.
[6] J. Panpranot, J.G. Goodwin Jr., A. Sayari, J. Catal. 211 (2002) 530.
[7] S.L. Sun, I. Isubaki, K. Fujimoto, Appl. Catal. 202 (2000) 121.
[8] S. Ali, B. Chen, J.G. Goodwin Jr., J. Catal. 157 (1995) 35.
[9] B. Jongsomjit, J. Panpranot, J.G. Goodwin Jr., J. Catal. 215 (2003) 66.
[10] T. Das, G. Jacobs, P.M. Patterson, W.A. Conner, J.L. Li, B.H. Davis, Fuel 82 (2003) 805.
[11] G. Jacobs, P.M. Patterson, Y.Q. Zhang, T. Das, J.L. Li, B.H. Davis, Appl. Catal. 233 (2002) 215.
[12] M. Rothaemel, K.F. Hanssen, E.A. Blekkan, D. Schanke, A. Holmen, Catal. Today 38 (1997) 79.
[13] V. Ragaini, R. Carli, C.L. Bianchi, D. Lorenzetti, G. Vergani, Appl. Catal. 139 (1996) 17.
[14] V. Ragaini, R. Carli, C.L. Bianchi, D. Lorenzetti, G. Predieri, P. Moggi, Appl. Catal. 139 (1996) 31.
[15] J.L. Li, G. Jacobs, T. Das, B.H. Davis, Appl. Catal. 233 (2002) 255.
[16] G. Jacobs, T. Das, Y.Q. Zhang, J.L. Li, G. Racoillet, B.H. Davis., Appl. Catal. 233 (2002) 263.
[17] J.L. Li, L.G. Xu, R. Keogh, B.H. Davis, Catal. Lett. 70 (2000) 127.
[18] X.H. Li, K. Asami, M.F. Luo, K. Michiki, N. Tsubaki, K. Fujimoto, Catal. Today 84 (2003) 59.
[19] K.Y. Jung, S.B. Park, J. Photochem. Photobiol. A. 127 (1999) 117.
[20] R.C. Reuel, C.H. Bartholomew, J. Catal. 85 (1984) 63.
[21] B. Jongsomjit, J. Panpranot, J.G. Goodwin Jr., J. Catal. 204 (2001) 98.
[22] B. Jongsomjit, J.G. Goodwin Jr., Catal. Today 77 (2002) 191.
[23] A. Kogelbauer, J.C. Weber, J.G. Goodwin Jr., Catal. Lett. 34 (1995) 269.
[24] Y. Zhang, D. Wei, S. Hammache, J.G. Goodwin Jr., J. Catal. 188 (1999) 281.
[25] B. Jongsomjit, C. Sakdamnuson, J.G. Goodwin Jr., P. Praserthdam, Catal. Lett. 94 (2004) 209.

Available online at www.sciencedirect.com
SCIENCE DIRECT
Catalysis Communications 7 (2006) 192–197
CATALYSIS COMMUNICATIONS
www.elsevier.com/locate/catcom

Differences in characteristics and catalytic properties of Co catalysts supported on micron- and nano-sized zirconia

Joongjai Panpranot *, Nuttakarn Taochaiyaphum, Bunjerd Jongsomjit, Piyasan Praserthdam

Center of Excellence on Catalysis and Catalytic Reaction Engineering, Department of Chemical Engineering, Faculty of Engineering, Chulalongkorn University, Phayathai Road, Bangkok 10330, Thailand

Received 15 August 2005; received in revised form 17 October 2005; accepted 21 October 2005
Available online 27 December 2005

Abstract

Nanocrystalline zirconia was prepared by decomposition of zirconium tetra *n*-propoxide in 1,4-butanediol and was employed as a support for cobalt catalysts. The activity and the selectivity of the catalysts in CO hydrogenation were compared with cobalt supported on commercial available micron- and nano-sized zirconia. The catalytic activities were found to be in the order: Co/ZrO_2-nano-glycol $\gg$ Co/ZrO_2-nano-com > Co/ZrO_2-micron-com. Compared to the micron-sized zirconia supported one, the use of commercial nano-sized zirconia resulted in higher CO hydrogenation activity but lower selectivity for longer chain hydrocarbons (C_4–C_6), whereas the use of glycothermal-derived nanocrystalline zirconia exhibited both higher activity and selectivity for C_4–C_6. The better performance of the latter catalyst can be ascribed to not only the effect of the crystallite size but also the presence of pure tetragonal phase of zirconia.

Keywords: Nanocrystalline zirconia; CO hydrogenation; Cobalt catalyst; Glycothermal method

1. Introduction

Zirconia powder has been effectively used in different areas of chemistry such as in ceramics and catalysis. It has been found that zirconia has high catalytic activities for isomerization of olefins [1] and epoxides [2]. Use of zirconia as a catalyst support has shown promising results in many environmental catalysis reactions such as CO_2 hydrogenation [3], CO oxidation [4], and Fischer–Tropsch reaction [5–7]. Enache et al. reported that compared to conventional alumina supported Co catalysts, the ones supported on zirconia showed better reducibility and capable of hydrogen adsorption via spillover mechanism. The authors proposed that these properties resulted in a higher catalytic activity and an increase of the chain growth probability in the Fischer–Tropsch reaction. Recently, we reported the synthesis and characteristics of nanocrystalline zirconia prepared by glycothermal method using various glycols and their applications as cobalt catalyst supports [8]. Cobalt-based catalysts are known to be commercially attractive for natural gas-based Fischer–Tropsch synthesis because of their high activities, high selectivities for long chain paraffins, low water–gas shift activities, and their relatively low price compared to noble metals such as Ru [9–11].

In this work, the characteristics and catalytic properties of nanocrystalline zirconia supported Co catalysts were studied and compared to commercially available micron- and nano-sized zirconia supported ones. The physicochemical properties of the catalysts were analyzed by means of thermal gravimetric analysis (TGA), X-ray diffraction (XRD), N_2 physisorption, scanning electron microscopy (SEM), and H_2 chemisorption. The catalytic performances of the zirconia supported Co catalysts were tested in CO hydrogenation reaction at 220 °C and 1 atm.

* Corresponding author. Tel.: +66 2 218 6859/78; fax: +66 2 218 6877.
E-mail address: joongjai.p@eng.chula.ac.th (J. Panpranot).

1566-7367/$ - see front matter © 2005 Elsevier B.V. All rights reserved.
doi:10.1016/j.catcom.2005.10.007

2. Experimental

2.1. Catalyst preparation

Nanocrystalline zirconia with the average crystallite size of 4 nm was prepared by the glycothermal method according to the procedure described in [12]. Approximately 15 g of zirconium tetra *n*-propoxide, $Zr(OC_3H_7)_4$ (ZNP) with 20.5% Zr from Strem Chemicals was added to 100 ml of 1,4-butanediol (Aldrich). This mixture was placed in a 300-ml autoclave. After the atmosphere inside the autoclave was replaced with nitrogen, the mixture was heated to 300 °C at a heating rate of 2.5 °C/min and was kept at that temperature for 2 h. After cooling to room temperature, the resulting powders were collected and washed repeatedly with methanol by vigorous mixing and centrifuging. Concentrated ammonium hydroxide was added to the upper part of the mixture, if no additional particle settling was observed then washing was finished. The products were then air-dried and were used without further calcination. Commercial zirconias in micron- and nano-sized were obtained from Aldrich for comparison purposes. The zirconia supported Co catalysts were prepared by the incipient wetness impregnation of the supports with aqueous solution of Co(II) nitrate hexahydrate (Aldrich). The samples were dried at 110 °C for 1 day and then were calcined in air at 300 °C for 2 h. The final cobalt loading of the calcined catalysts were determined using atomic absorption spectroscopy (Varian Spectra A800) to be ca. 8 wt%.

2.2. Catalyst characterization

TGA was performed using a DIAMOND TG/DTA analyzer. The catalyst samples of 10–20 mg and a temperature ramping from 35 to 800 °C at 10 °C/min were used in the operation. The carrier gas was N_2 UHP. The BET surface areas were determined by N_2 physisorption using a Quantachrome Nova 1000 automated system. Each sample was degassed in the system at 150 °C for 2 h prior to N_2 physisorption. The XRD spectra of the sample powders were measured using a SIEMENS D5000 X-ray diffractometer using Cu K_α radiation with a Ni filter in the 10–80° 2θ angular regions. The particle morphology was obtained using a JEOL JSM-35CF scanning electron microscope (SEM) operated at 20 kV. Transmission electron microscopy was performed on a JEOL-TEM 200CX transmission electron microscope operated at 100 kV. The catalyst sample was first suspended in ethanol using ultrasonic agitation for 10 min. The suspension was dropped onto a thin Formvar film supported on copper grid and dried at room temperature before observation. H_2 chemisorption was carried out following the procedure described by Reuel and Bartholomew [13] using a Micromeritics Pulse Chemisorb 2700 system. Prior to chemisorption, the catalysts were reduced at 350 °C for 10 h after ramping at a rate of 1 °C/min. Static H_2 chemisorption was performed at 100 °C.

2.3. CO hydrogenation reaction

CO hydrogenation was carried out at 220 °C and 1 atm total pressure in a fixed-bed stainless steel reactor under differential conversion conditions. A flow rate of $H_2/CO/Ar = 20/2/8$ cm^3/min was used. Typically, 0.2 g of the catalyst samples were reduced in situ in flowing H_2 (50 cm^3/min) at 350 °C for 10 h prior to reaction. The data was collected every hour and analyzed by gas chromatography. The steady-state rates for all the catalysts were obtained after 5–6 h. The percentages of CO conversion and reaction rates were defined as:

$$\%\text{CO conversion} = \frac{(\text{mol of CO in feed} - \text{mol of CO in products})}{(\text{mol of CO in feed})} \times 100,$$

$$\text{Reaction rate}\,(\text{g CH}_2\,\text{g cat.}^{-1}\,\text{h}^{-1}) = \frac{\%\text{CO conversion} \times \text{flowrate of CO in feed}\,(\text{cm}^3/\text{min}) \times 60\,(\text{min}/\text{h}) \times \text{mol. wt of CH}_2\,(\text{g/mol})}{\text{catalyst weight}\,(\text{g}) \times 22{,}400\,(\text{cm}^3/\text{mol})}.$$

3. Results and discussion

Fig. 1 shows the scanning electron micrographs of micron- and nano-sized zirconia before and after cobalt loading. It was found that the commercial micron-sized zirconia have a spherical shape with an average particle size of ca. 0.2 μm. The SEM micrographs of the commercial nano-sized zirconia showed very small particle sizes that appeared to be more agglomerated. Compared to the commercial available ones, the glycothermal-derived nanocrystalline zirconia appeared as large separate spherical particles (1 μm). These particles were formed by aggregation of their primary particles. The mechanism during crystallization of zirconia in the glycols during glycothermal synthesis has been suggested in our previous study [12]. Nanocrystals were formed when starting materials were completely dissolved into the glycol. Crystallization of the glycoxide intermediates in 1,4-butanediol then proceeds via solid-state transformation. After impregnated with solutions of cobalt nitrate, dried overnight at room temperature, and calcination at 300 °C for 2 h, the morphologies of the commercial micron- and nano-sized zirconia supported catalysts were found to be more agglomerated especially the nano-sized ones. High concentration of

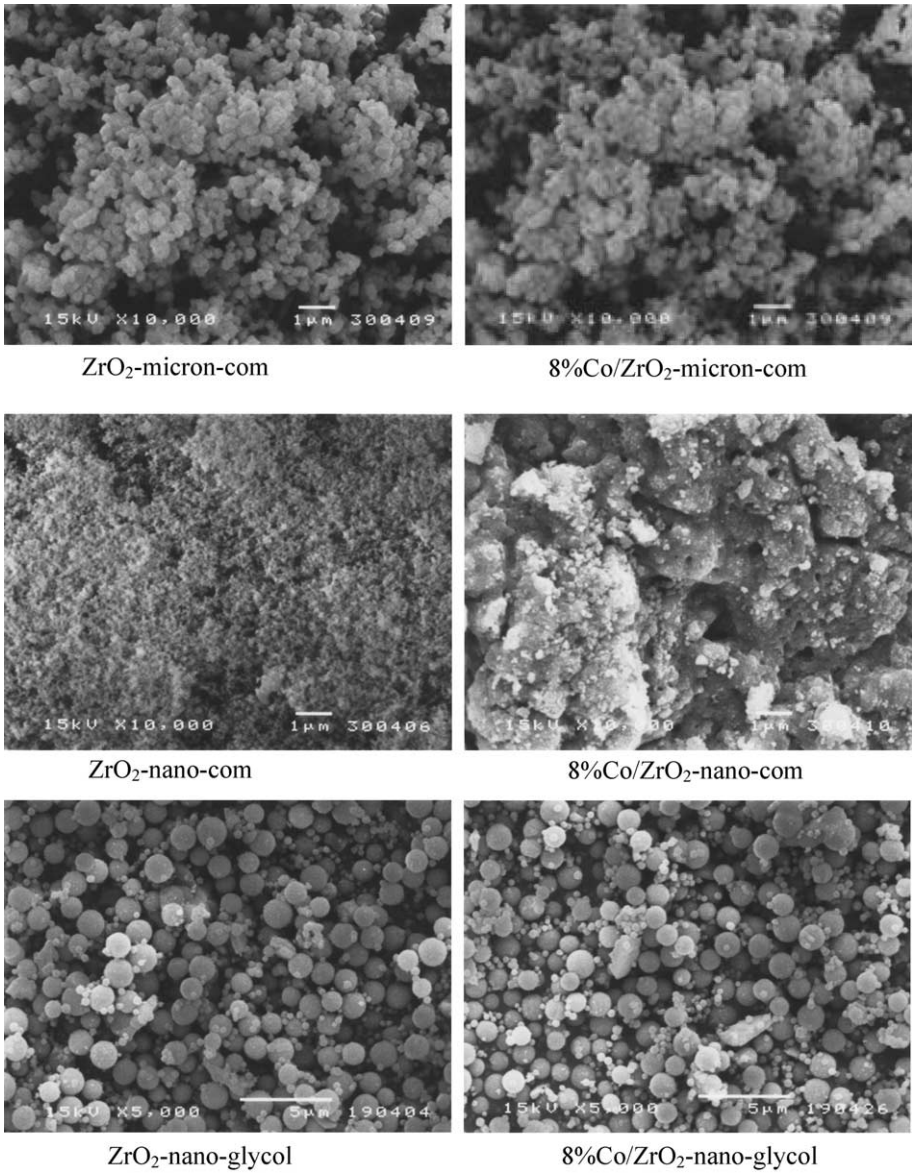

Fig. 1. SEM micrographs of various ZrO_2 and 8%Co/ZrO_2 catalysts.

cobalt appeared as light/white spots on the granules of the Co/ZrO_2-nano-com catalyst. Unlike the commercial zirconia supported Co catalysts, the morphology of the glycothermal-derived nanocrystalline zirconia supported one was not altered by cobalt impregnation and calcination even for cobalt loading as high as 8 wt%.

The X-ray diffraction patterns of the various ZrO_2 are shown in Fig. 2. Both micron- and nano-sized commercial zirconia samples exhibited the XRD patterns of both tetragonal and monoclinic zirconia while only tetragonal phase was obtained for the glycothermal-derived ones. Typically, the monoclinic phase is stable to ≈1170 °C, at which temperature it transforms into the tetragonal phase, which is stable up to 2370 °C [14]. However, at low temperature, a metastable tetragonal phase zirconia is usually observed when zirconia is prepared by certain methods such as precipitation from aqueous salt solution or thermal composition of zirconium salts as employed in this work. It is also found that there was less monoclinic phase for the commercial nano-sized zirconia compared to the micron-sized one. The transformation of the metastable tetragonal form into the monoclinic form was due probably to the lower surface energy of the tetragonal phase compared to monoclinic phase [15,16]. The average crystallite sizes of tetragonal and monoclinic zirconia determined by X-ray line broadening and BET surface areas of the zirconia samples are given in Table 1. The average crystallite size of tetragonal phase of the glycothermal-derived zirconia was calculated to be 4 nm while those of commercial ones were ca. 9–12 nm. The BET surface areas of the catalyst samples were 50–170 m^2/g in the order of Co/ZrO_2-nano-glycol ≫ Co/ZrO_2-nano-com > Co/ZrO_2-micron-com. The information on porosity of the new nanocrystalline ZrO_2 such as pore volumes and N_2 adsorption–desorption iso-

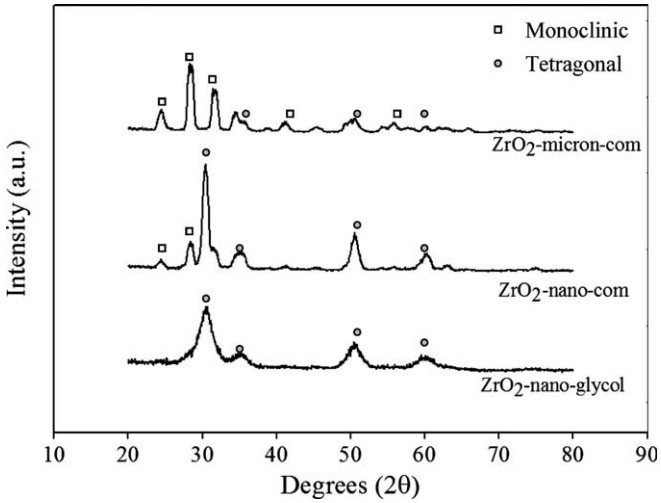

Fig. 2. XRD patterns of various ZrO_2 samples.

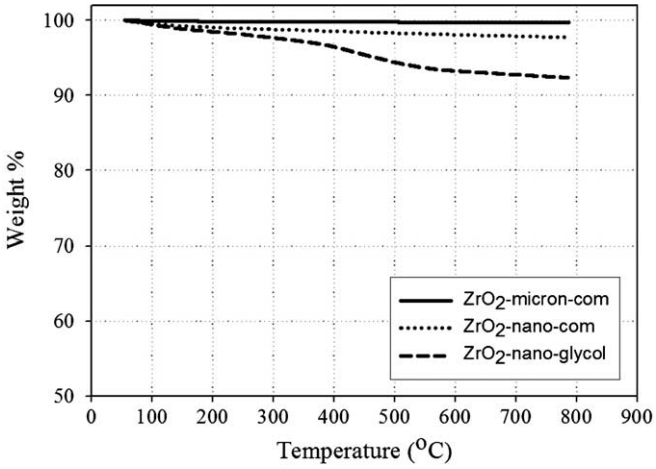

Fig. 3. TGA profiles of various ZrO_2 samples.

therms can be found in [12]. After impregnation of cobalt and calcination at 300 °C, the XRD peaks for cobalt oxides were not apparent for all the catalyst samples due probably to overlapping of Co_3O_4 peaks with those of the ZrO_2 supports. Thermal stability of the zirconia samples was investigated by thermal gravimetric analysis and the results are shown in Fig. 3. It was found that the ZrO_2-nano-glycol exhibited ≈8% and 5% more weight loss than those of ZrO_2-micron-com and ZrO_2-nano-com, respectively, during heat treatment up to 800 °C. These losses may be due to larger amount of water was adsorbed on the high surface area/pore volume ZrO_2-nano-glycol and not to the phase change as confirmed by XRD (results not shown).

The H_2 chemisorption results and the catalytic activities of zirconia supported Co catalysts are reported in Tables 1 and 2, respectively. We have performed CO hydrogenation under methanation conditions (high H_2/CO ratio) in order to minimize deactivation of the catalysts due to wax formation. It is clearly seen that the catalysts supported on nano-sized zirconia exhibited smaller Co° particle size, higher Co dispersion, and higher CO hydrogenation activities than the micron-sized supported one with the use of the glycothermal-derived nanocrystalline zirconia showed the best performances. As reported in the literature, strong metal support interaction (SMSI) between metal (i.e. Pt) and ZrO_2 occurs during high temperature reduction ⩾850 °C [17]. Under the reduction and reaction temperatures used in this study (350 and 220 °C, respectively), the SMSI effect is likely to be absent. Thus, a decrease in cobalt oxide particle size (as surface area of ZrO_2 increases) can result in faster reduction due to a greater surface area/volume ratio hence higher metal dispersion can be obtained.

It should be noted that under similar reaction conditions (methanation) relatively large portions of higher hydrocarbons (C_4–C_6) were obtained on all the Co/ZrO_2 catalysts compared to those reported in the literature for Co catalysts supported on SiO_2 [18], Al_2O_3 [19], or TiO_2 [20]. It is likely that the use of ZrO_2 support significantly enhances the polymerization reaction as also suggested by Enache et al. [7]. In this study, we report that compared to the use of micron-size ZrO_2, the nano-sized ones exhibited even higher selectivities for long chain hydrocarbons. However, for the two commercial zirconia supported Co catalysts, the product selectivities were similar in which $C_1 \gg C_4$–$C_6 > C_2$–C_3, typical for CO hydrogenation under methanation while for the glycothermal-derived nanocrystalline ZrO_2 supported catalyst, the selectivities for longer chain hydrocarbons were much higher and were found to be in the order: C_4–$C_6 \gg C_1 > C_2$–C_3. In other words, using

Table 1
The characteristics of Co/ZrO_2 catalysts

Sample	BET S.A.[a] (m^2/g)	Crystal size of ZrO_2[b] (nm)		H_2 chemisorption[d] ($\times 10^{19}$ mol g cat.$^{-1}$)	% Co dispersion[e]	d_P Co[0f] (nm)
		Tetragonal	Monoclinic			
Co/ZrO_2-micron-com	50	7.7	10.5	3.1	7.6	12.6
Co/ZrO_2-nano-com	78	11.5	10.2	10.1	24.7	3.9
Co/ZrO_2-nano-glycol	170	4.0	n.d.[c]	15.3	37.4	2.6

[a] Error of measurements = ±10%.
[b] Determined by XRD line broadening using Scherrer's equation [21].
[c] n.d. = not detected.
[d] Error of measurement = ±5%.
[e] Based on total amount of cobalt.
[f] $d_P = 5/(S_{Co} \times \rho_{Co})$, where S_{Co} is the surface area of cobalt measured by H_2 chemisorption.

Table 2
Catalytic activities of Co/ZrO_2 in CO hydrogenation

Catalysts	Reaction rate[a] ($g\ CH_2\ g\ cat^{-1}\ h^{-1}$)	Product selectivity (%)			TOFs[b] (s^{-1})
		C_1	C_2–C_3	C_4–C_6	
Co/ZrO_2-micron-com	1.7	57.8	14.4	17.8	0.66
Co/ZrO_2-nano-com	3.8	77.8	8.6	13.5	0.45
Co/ZrO_2-nano-glycol	14.5	29.5	11.4	59.1	1.13

[a] Reaction conditions were 220 °C, 1 atm and H_2/CO ratio = 10.
[b] Based on H_2 chemisorption results.

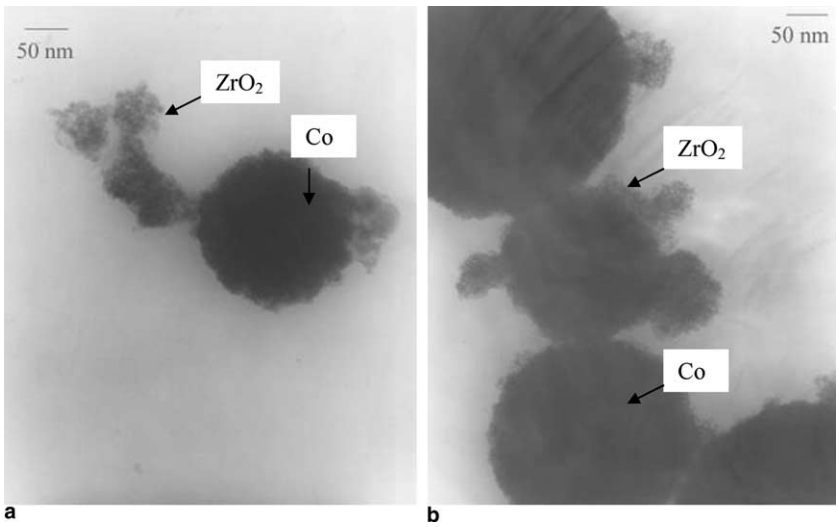

Fig. 4. TEM micrographs of Co/ZrO_2-nano-glycol: (a) before and (b) after CO hydrogenation reaction at 220 °C 1 atm for 6 h.

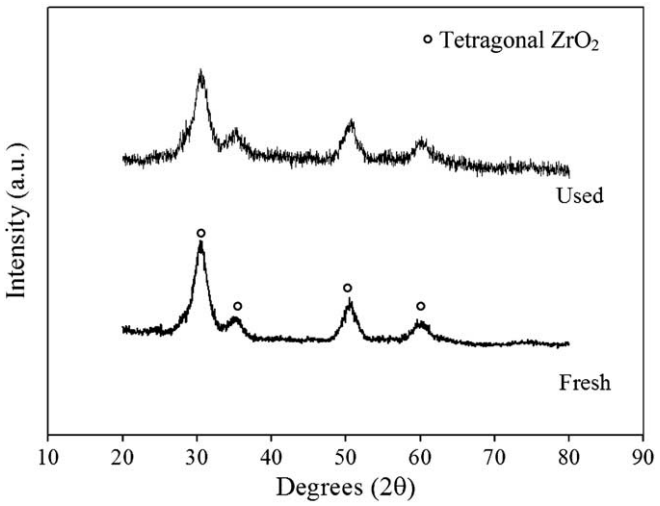

Fig. 5. XRD patterns of Co/ZrO_2-nano-glycol before and after used in CO hydrogenation reaction at 220 °C and 1 atm for 6 h.

the nano-sized zirconia resulted in higher CO hydrogenation rates but on the expense of selectivities for C_4–C_6, whereas Co catalyst supported glycothermal-derived nanocrystalline zirconia, both higher reaction rate and higher selectivities for longer chain hydrocarbons were obtained. Thus, it is not only the effect of ZrO_2 crystallite size but also the presence of pure tetragonal phase of zirconia that resulted in better catalytic performances in CO hydrogenation. Stabilization of tetragonal phase zirconia has been reported to be very important for applications as a catalyst or catalyst support [5]. The TEM micrographs and the XRD patterns of Co/ZrO_2-nano-glycol catalyst before and after CO hydrogenation reaction are shown in Figs. 4 and 5, respectively. Primary particles in nano-sized of the glycothermal-derived ZrO_2 as well as high Co dispersion can be observed for both fresh and used catalysts. There was also no change in the tetragonal phase of the ZrO_2 while the crystallite size was slightly increased from 4.0 to 4.3 nm. Overall, the results in this study suggest a marginal effect of the nanocrystalline zirconia on the catalytic activities and selectivities on CO hydrogenation reaction. Although the cost of catalyst preparation using glycothermal process is more expensive than conventional method, their unique properties such as high stability of pure tetragonal ZrO_2 offer interesting possibilities for catalyst design and for application in particular cases.

4. Conclusions

The comparison of catalytic performances in CO hydrogenation of the cobalt catalysts supported on glycothermal-derived nanocrystalline zirconia and commercial available nano- and micron-sized zirconia shows that both catalyst

activity and selectivity for long chain hydrocarbons were enhanced by the use of nanocrystalline zirconia as catalyst supports. The glycothermal-derived catalysts exhibited higher surface areas, higher Co dispersion, and highly stable pure tetragonal phase zirconia.

References

[1] Y. Nakano, T. Iizuka, H. Hattori, K. Tanabe, H. Hideshi, T. Kozo, J. Catal. 157 (1979) 1.
[2] K. Arata, K. Kato, K. Tanabe, Bull. Chem. Soc. Jpn. 49 (1976) 563.
[3] J.H. Bitter, K. Sechan, J.A. Lercher, J. Catal. 171 (1997) 279.
[4] W.P. Dow, T.J. Huang, J. Catal. 147 (1994) 322.
[5] G.K. Chuah, Catal. Today 49 (1999) 131.
[6] L. Bruce, J.F. Mathews, Appl. Catal. 4 (1982) 353.
[7] D.I. Enache, M. Roy-Auberger, R. Revel, Appl. Catal. A: General 268 (2004) 51.
[8] J. Panpranot, N. Taochaiyaphum, P. Praserthdam, Mater. Chem. Phys. 94 (2005) 207.
[9] R.B. Anderson, The Fischer–Tropsch Synthesis, Academic Press, San Diego, 1984.
[10] J.G. Goodwin Jr., Prep. ACS Div. Petr. Chem. 36 (1991) 156.
[11] E. Iglesia, Appl. Catal. A 161 (1997) 50.
[12] S. Kongwudthiti, P. Praserthdam, P.L. Silveston, M. Inoue, Ceram. Int. 29 (2003) 807.
[13] R.C. Reuel, C.H. Bartholomew, J. Catal. 85 (1984) 78.
[14] P.D.L. Mercera, J.G. van Ommen, E.B.M. Doesburg, A.J. Burggraaf, J.R.H. Ross, Appl. Catal. 71 (1991) 363.
[15] E. Tani, M. Yoshimura, S. Somiya, J. Am. Ceram. Soc. 66 (1982) 11.
[16] M.I. Osendi et al., J. Am. Ceram. Soc. 68 (1985) 135.
[17] J.H. Bitter, K. Seshan, J.A. Lercher, J. Catal. 171 (1997) 279–286.
[18] J. Panpranot, S. Kaewgun, P. Praserthdam, React. Kinet. Catal. Lett. 85 (2005) 299.
[19] B. Jongsomjit, J.G. Goodwin Jr., Catal. Today 77 (2002) 191.
[20] B. Jongsomjit, T. Wongsalee, P. Praserthdam, Catal. Commun. 6 (2005) 705.
[21] H.P. Klug, L.E. Alexander, X-ray Diffraction Procedures for Polycrystalline Amorphous Materials, second ed., Wiley, New York, 1974.

ELSEVIER

Science and Technology of Advanced Materials 6 (2005) 290–295

SCIENCE AND TECHNOLOGY OF ADVANCED MATERIALS

www.elsevier.com/locate/stam

Activity of nanosized titania synthesized from thermal decomposition of titanium (IV) *n*-butoxide for the photocatalytic degradation of diuron

Jitlada Klongdee[a], Wansiri Petchkroh[b], Kosin Phuempoonsathaporn[c], Piyasan Praserthdam[a], Alisa S. Vangnai[b,d], Varong Pavarajarn[a,*]

[a]*Department of Chemical Engineering, Faculty of Engineering, Center of Excellence on Catalysis and Catalytic Reaction Engineering, Chulalongkorn University, Bangkok 10330, Thailand*

[b]*National Research Center for Environmental and Hazardous Waste Management (NRC-EHWM), Chulalongkorn University, Bangkok 10330, Thailand*

[c]*Biotechnology Graduate Program, Faculty of Science, Chulalongkorn University, Bangkok 10330, Thailand*

[d]*Department of Biochemistry, Faculty of Science, Chulalongkorn University, Bangkok 10330, Thailand*

Received 12 January 2005; revised 15 February 2005; accepted 15 February 2005
Available online 17 June 2005

Abstract

Nanoparticles of anatase titania were synthesized by the thermal decomposition of titanium (IV) *n*-butoxide in 1,4-butanediol. The powder obtained was characterized by various characterization techniques, such as XRD, BET, SEM and TEM, to confirm that it was a collection of single crystal anatase with particle size smaller than 15 nm. The synthesized titania was employed as catalyst for the photodegradation of diuron, a herbicide belonging to the phenylurea family, which has been considered as a biologically active pollutant in soil and water. Although diuron is chemically stable, degradation of diuron by photocatalyzed oxidation was found possible. The conversions achieved by titania prepared were in the range of 70–80% within 6 h of reaction, using standard UV lamps, while over 99% conversion was achieved under solar irradiation. The photocatalytic activity was compared with that of the Japanese Reference Catalyst (JRC-TIO-1) titania from the Catalysis Society of Japan. The synthesized titania exhibited higher rate and efficiency in diuron degradation than reference catalyst. The results from the investigations by controlling various reaction parameters, such as oxygen dissolved in the solution, diuron concentration, as well as light source, suggested that the enhanced photocatalytic activity was the result from higher crystallinity of the synthesized titania.

Keywords: Titania; Thermal decomposition; Nanoparticle; Photocatalytic activity; Diuron; Degradation

1. Introduction

Titanium (IV) dioxide or titania (TiO_2) is one of the most common metal-oxides recognized in various industries. Due to its good physical and chemical properties, such as catalytic activity [1], photocatalytic activity [2], good stability toward adverse environment [3], sensitivity to humidity and gas [4], dielectric character [5], nonlinear optical characteristic [6] and photoluminescence [7], titania has been used in many fields of application including the use as catalysts, catalyst supports, electronics, cosmetics, pigments and filler coating. Nevertheless, photocatalyst is one of the most important applications of titania. Although titania is known to have three natural polymorphs, i.e. rutile, anatase, and brookite, only anatase is generally accepted to have significant photocatalytic activity [8–10].

Many factors affect the photocatalytic activity of titania. Particle size is one of the most important factors. It has been reported that photocatalytic activity is increased with the decrease in titania particle size, especially into nanometer-scale, because of high surface area and short interface migration distances for photoinduced holes and electrons [11–13]. Nanocrystalline titania can be synthesized by many methods, such as sol-gel method, hydrothermal method, vapor-phase hydrolysis, laser-induced decomposition, chemical vapor decomposition and molten salt method. In this work, nanocrystalline anatase titania was synthesized via the thermal decomposition of titanium alkoxide in organic solvent, which has been employed to synthesize various nanocrystalline metal-oxides [14–19]. It has been

* Corresponding author. Tel.: +66 2 2186 890; fax: +66 2 2186 877.
E-mail address: fchvpv@eng.chula.ac.th (V. Pavarajarn).

1468-6996/$ - see front matter © 2005 Elsevier Ltd. All rights reserved.
doi:10.1016/j.stam.2005.02.007

demonstrated that the activity of titania synthesized by this method is much higher than those of commercially available titania for photocatalytic decomposition of simple compound, such as acetic acid, in aqueous solutions [20]. However, it has never been used for the decomposition of more complex substance. In this study, photodegradation of complex substance, i.e. diuron [3-(3,4-dichlorophynyl)-1,1-dimethylurea], is employed to investigate the activity of titania prepared by this method.

Diuron has been one of the most commonly used herbicides for more than 40 years. It is bio-recalcitrant and chemically stable with half-life in soil over 300 days. Since, diuron is slightly soluble (solubility of 36.4 mg/l at 25 °C), it can slowly penetrates through soil and contaminates underground water. Photodegradation using titania as catalyst is therefore one potential option for contaminated water remediation.

2. Materials and methods

2.1. Synthesis of titania

Titanium (IV) *n*-butoxide (TNB) was used as starting material for titania synthesis. 15 g of TNB was suspended in 100 ml of 1,4-butanediol, which was used as reaction medium, in a test tube. The test tube was then placed in a 300 ml autoclave. The gap between the test tube and the autoclave wall was also filled with 1,4-butanediol. The autoclave was purged completely by nitrogen before heating up to 300 °C at a rate of 2.5 °C/min. Autogeneous pressure during the reaction gradually increased as the temperature was raised. The system was held at 300 °C for 2 h before cooling down to room temperature. The resulting powders in the test tube were repeatedly washed with methanol and dried in 110 °C oven overnight. Subsequently, the obtained product was calcined at 500 °C for 2 h in a box furnace with a heating rate of 10 °C/min.

Synthesized powders were characterized by various techniques, i.e. powder X-ray diffraction (XRD), scanning electron microscope (SEM) and transmission electron microscope (TEM). Powder X-ray diffraction (XRD) analysis was done by using a SIEMENS D5000 diffractometer with CuKα radiation. The crystallite size of the product was determined from the broadening of its main peak, using the Scherrer equation. Specific surface area of the samples was also measured by using the BET multipoint method.

2.2. Photocatalytic experiments

Photodegradation of diuron in aqueous solution was employed to investigate the photocatalytic activity of the synthesized titania. The initial concentrations of diuron used were 1 and 10 ppm, respectively. The solution was mixed with titania in the ratio of 1 mg titania to 10 ml of solution and kept in the dark for at least 15 min to allow the complete adsorption of diuron on the surface of titania. The photocatalytic reaction was initiated by exposing test tubes to light from UV lamps (Phillips Cleo 15 W). Diuron degradation was periodically monitored by using a reverse phase HPLC system. The HPLC system included Hyperclone column (150×8 mm inner diameter; 5 μm particle size) (Phenomenex, USA) with a mobile phase of 70% acetonitrile–29.5% water–0.5% phosphoric acid; a flow rate of 0.5 ml/min and a UV detector at 254 nm. The photocatalytic activity of the synthesized catalyst was compared with that of the Japanese Reference Catalyst titania, JRC-TIO-1, which is also pure nanocrystalline anatase.

3. Results and discussion

3.1. Properties of synthesized titania

The particles obtained from the decomposition of TNB in 1,4-butanediol at 300 °C was confirmed to be titania. The XRD analysis, as shown in Fig. 1, revealed that the synthesized product before calcination was already anatase phase. This result was in agreement with the results from our previous work that anatase crystals were formed by crystallization when the temperature in the autoclave reached 250 °C [21]. The crystallite size of the as-synthesized product calculated from the Scherrer equation was approximately 13 nm, while that of the calcined product was 15 nm. It should be noted that the crystallite sizes calculated were in agreement with TEM observation (Fig. 2). Therefore, it was suggested that the synthesized product synthesized was nanosized single crystal titania.

As shown in Table 1, the BET surface area measured by nitrogen adsorption (S_{BET}) of the as-synthesized products was comparable with the surface area calculated from the particle size (S_{XRD}), which was assumed that the particles were spherical and nonporous. It was therefore suggested

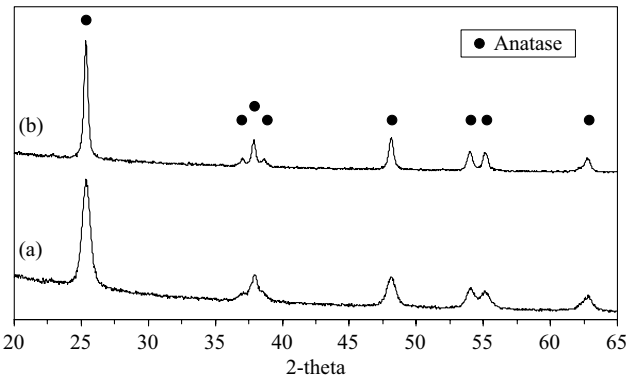

Fig. 1. XRD patterns of synthesized titania: (a) before calcination, (b) after calcination.

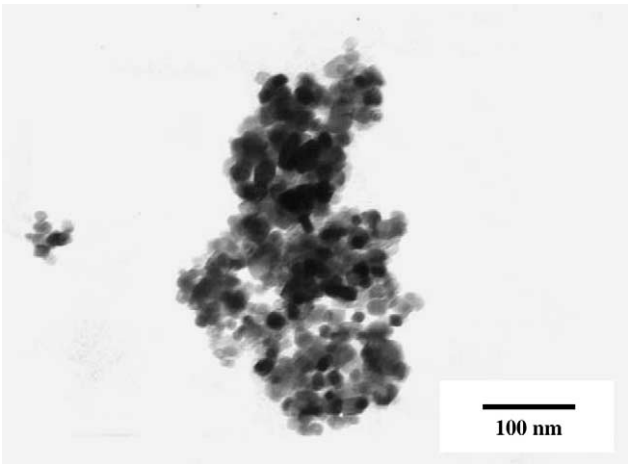

Fig. 2. TEM micrograph of as-synthesized titania.

that the primary particles were not heavily agglomerated. It was also confirmed by SEM micrographs (Fig. 3a) that the synthesized powder was an irregular aggregates of nanometer particles. According to Park et al. [22], agglomeration of the precipitates is influenced by dielectric constant of the reaction medium. The lower the dielectric constant, the higher the degree of agglomeration. Since, 1,4-butanediol has quite high dielectric constant ($\varepsilon = 32$ at 25 °C [23]), the repulsive force between anatase particles formed in this reaction medium is more pronounced than the attraction force, resulting in low degree of agglomeration.

After calcination at 500 °C, the calcined powder was still in anatase phase, as previously proved that anatase synthesized by this method is thermally stable [21]. Nevertheless, the crystallite size of titania increased due to crystal growth. Agglomeration of primary particles was also observed, according to the fact that the BET surface area was notably decreased. Despite of the smaller surface area, calcined titania has shown higher photocatalytic activity than as-synthesized titania. This is due to the fact that the crystallinity of titania was improved by calcination and the crystallinity predominantly influenced the activity rather than surface area [24].

3.2. Photodegradation of diuron

It has been reported that titania synthesized by the thermal decomposition of titanium alkoxide in organic solvent has high activity in photocatalytic decomposition of various compounds [20]. In this work, titania synthesized by this method was employed as catalyst in the photodegradation of diuron, which is chemically stable pollutant. Since, the photocatalytic activity depends upon the conditions of the reaction, such as temperature, light intensity, initial concentration of the compound to be degraded and amount of catalyst used, it is difficult to directly compare the results obtained in this work to those reported in literatures. Therefore, in order to investigate activity of the in-house synthesized catalyst, the results were compared to that of the reference catalyst (JRC-TIO-1) from the Catalysis Society of Japan. It should be noted that mass of the reference catalyst used was the same as the mass of the in-house synthesized catalyst.

Table 1
Crystallite size and surface area of the synthesized products

	Crystallite size[a], d (nm)	S_{BET} (m^2/g)	S_{XRD} (m^2/g)
Synthesized titania			
Before calcination	13	113	120
After calcination	15	68	103
Reference titania	9	53	174

[a] Crystallite size calculated from XRD peak broadening.

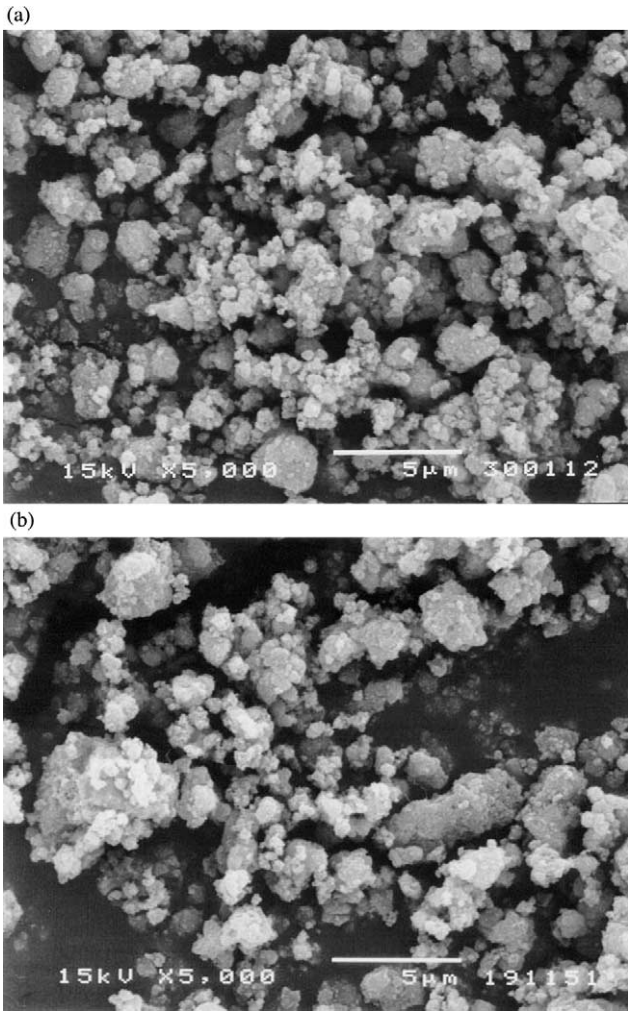

Fig. 3. SEM micrographs of synthesized titania: (a) before calcination, (b) after calcination.

Fig. 4 shows the disappearance of diuron by photocatalytic degradation using the synthesized titania or reference titania as catalyst. It should be noted that C is the concentration of diuron at time t, while C_0 is the initial diuron concentration. The results shown in Fig. 4a indicate

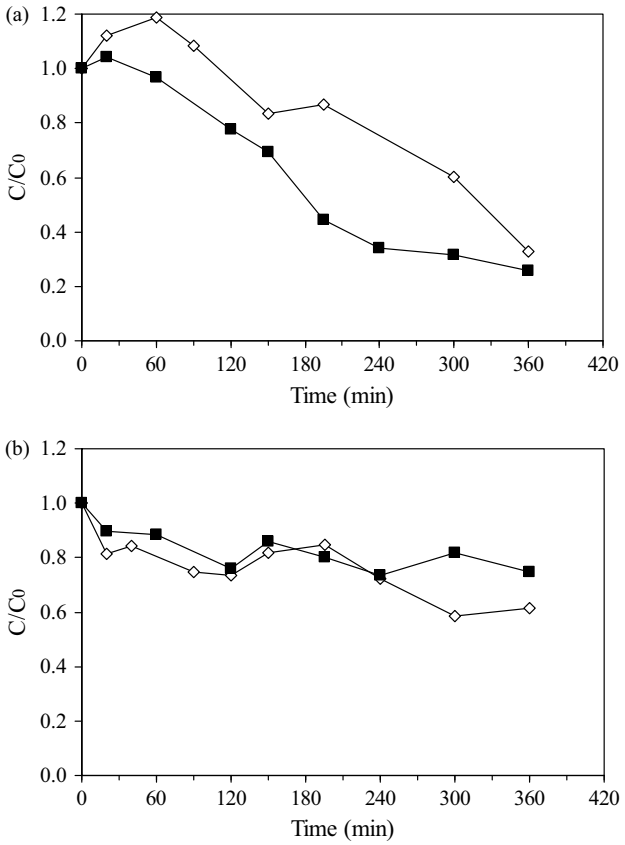

Fig. 4. Results for photocatalytic degradation of 1 ppm diuron aqueous solution: (a) in oxygen saturated solution, (b) in nitrogen-purged solution; (■) synthesized titania, (◇) reference titania.

that although both catalysts yielded approximately the same degradation after the reaction time of 6 h, the synthesized titania showed almost twice as much in the initial degradation rate than the reference catalyst. The amount of diuron was reduced to 30% of its initial value within 4 h of the reaction using the synthesized catalyst, while almost 6 h was required for the reference catalyst.

It has been recognized that the efficiency of titania in photocatalytic reaction is influenced by many factors such as crystallinity of the anatase phase [9], particle size [11] and surface area [11]. Since, the synthesized and reference titania are both anatase with roughly same particle size and surface area, the main factor accountable for the enhanced activity of the synthesized titania is its crystallinity. Although there has been no consensus on the detailed mechanism of the photocatalytic reaction on titania, it is generally agreed that the reaction involves generation of electron-hole pairs upon illumination of UV light on titania. The photogenerated holes can be subsequently scavenged by oxidizing species such as H_2O or OH^- and result in highly reactive hydroxyl radicals, which are the key for decomposition of most organic contaminants. Therefore, the separation of the photogenerated electron-hole pairs is considered to have a predominant role in photocatalytic reaction. The longer the separation period, the higher the activity. Crystallinity, including quality and quantity of both bulk and surface crystal defects, is one factor that affects the electron-hole separation [25]. It has been reported that negligible photocatalytic activity of amorphous titania is attributable to the facilitated recombination of photoexcited electrons and holes in the amorphous structure. Therefore, the result in Fig. 4a suggests that titania synthesized by thermal decomposition of TNB in 1,4-butanediol has structure with high crystallinity that prevents electron-hole recombination. This result supports the findings in our previous work that titania synthesized by this method was formed via crystallization pathway [21].

When all oxygen dissolved in the solution was purged by thoroughly bubbling with nitrogen gas, the conversion of diuron photodegradation dramatically decreased. As shown in Fig. 4(b), only about 30% of diuron was degraded within 6 h of the reaction with either the synthesized or the reference catalyst. This is in agreement with the generally accepted mechanism of the photocatalytic reaction that the presence of oxygen as an electron scavenger in the system is required for the course of the reaction [26–28]. Without electron scavenger, the electron-hole recombination spontaneously took place on the surface of titania. The enhanced effect from crystallinity of the synthesized titania was therefore compromised and the progress of the photocatalytic reactions from both catalysts were roughly the same. However, regardless of the depletion of dissolved oxygen in the solution, the reaction still slowly progressed. This was expected to be the results from chlorine radicals produced from diuron degradation. Several studies involving photocatalytic decomposition of chlorinated organic materials have proposed that chlorine radicals may be generated during photocatalysis [29] and these radicals participate in radical chain reactions [30–32].

Further, investigations on the enhanced activity of the synthesized titania were conducted by using solar irradiation, which had much higher light intensity than UV lamps. It should be noted that the concentration of

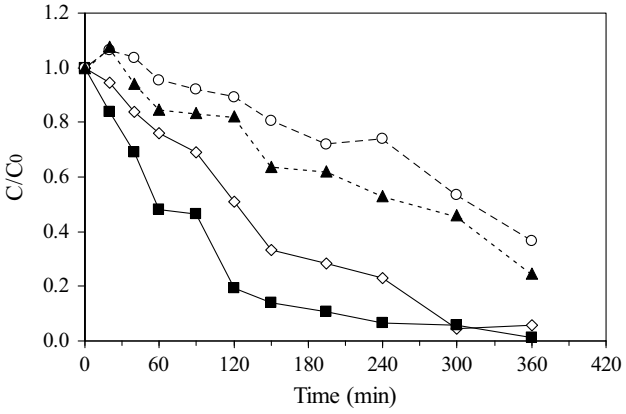

Fig. 5. Results for photocatalytic degradation of 10 ppm diuron aqueous solution: (- - -) using UV lamps, (—) using solar radiation; (■), (▲) synthesized titania, (◇), (○) reference titania.

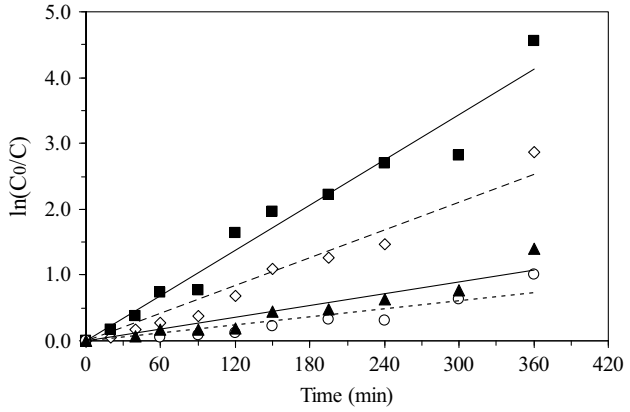

Fig. 6. First-order linear transforms of the degradation of 10 ppm diuron aqueous solution: (- - -) using UV lamps, (—) using solar radiation; (■), (▲) synthesized titania, (◇), (○) reference titania.

diuron employed was increased to 10 ppm in order to investigate the effect of the initial concentration as well. Fig. 5 shows the results comparing the photodegradation using sunlight to that using UV lamps. Furthermore, since rates of photooxidation of various organic contaminants over illuminated titania have been suggested to follow the Langmuir–Hinshelwood kinetics model [27,33,34], which can be simplified to the apparent first-order kinetics at low concentration, the plot of $\ln(C_0/C)$ versus time was expected to be a straight line with the slope equal to the apparent rate constant, k_{app}, of the degradation. The first-order linear transforms of the results shown in Fig. 5 are given in Fig. 6 and the rate constants are reported in Table 2.

Regarding the effect of diuron concentration, it was found that the degradation rate under UV light shown in Fig. 5 ($C_0 = 10$ ppm) was only slightly less than that was given in Fig. 4 ($C_0 = 1$ ppm). This is in general agreement with the pseudo first-order nature, according to the Langmuir–Hinshelwood kinetics, of the photooxidation on titania.

It can be seen from Figs. 5 and 6 that titania synthesized from thermal decomposition of titanium alkoxide has higher photocatalytic activity than the reference catalyst, especially under solar irradiation. Although it was not surprise to observe higher degradation rate under higher light intensity, it was particularly interesting to find that the enhancement in the activity from the synthesized titania increased with an increase in light intensity. According to Table 2, the reaction rate constant obtained from the synthesized titania was roughly 45% higher than that of the reference titania, when UV lamps were used. On the other hand, the rate from the synthesized titania was about 60% higher, under solar irradiation.

Table 2
Rate constants and half-life of the photocatalytic degradation reaction of diuron

	k_{app} (min^{-1})	$t_{1/2}$ (min)
Degradation using UV lamps		
Synthesized titania	3.003×10^{-3}	230.8
Reference titania	2.042×10^{-3}	339.5
Degradation using solar irradiation		
Synthesized titania	1.145×10^{-2}	60.5
Reference titania	7.027×10^{-3}	98.6

In general, under higher light intensity, more photo-electron-hole pairs are generated. However, it has been reported that a rate of the electron-hole recombination increases with increasing light intensity more progressively than the rates of charge transfer reaction [35]. Therefore, titania with high crystallinity, which prolongs the separation lifetime of the photogenerated electron-hole pairs, would utilize these greater amount of photoexcited electrons and holes with higher efficiency. Consequently, the enhancement in the photocatalytic activity under high light intensity is more pronounced than that from titania with lower crystallinity. This feature supports the aforementioned discussion that thermal decomposition of titanium alkoxide resulted in anatase titania with much higher crystallinity than the conventional preparation techniques.

Results discussed above have demonstrated that titania synthesized by thermal decomposition of TNB in 1,4-butanediol is potentially applicable for the photodegradation of diuron. However, the operating conditions for photocatalytic reaction in this work have not been optimized. Further, investigation on effects of degradation parameters on the degradation efficiency as well as the intermediates resulted from diuron degradation will be discussed in our next paper.

4. Conclusion

Nanocrystalline anatase titania can be prepared via thermal decomposition of TNB in 1,4-butanediol. The synthesized titania has shown higher photocatalytic activity comparing to the reference catalyst. It is suggested that the enhanced activity is resulted from high crystallinity of the synthesized powder, which consequently reduces the recombination of photogenerated electron-hole pairs. The synthesized titania also shows the potential for the degradation of chemically stable compound such as diuron. Nevertheless, conditions for photodecomposition need to be optimized.

Acknowledgements

The author would like to thank the Thailand Research Fund (TRF) and the Thailand-Japan Technology Transfer Project (TJTTP) for their financial support.

References

[1] K.E. Coulter, A.G. Sault, Effects of activation on the surface-properties of silica-supported cobalt catalysts, Journal of Catalysis 154 (1995) 56–64.

[2] T. Wakanabe, A. Kitamura, E. Kojima, C. Nakayama, K. Hashimoto, A. Fuijishima, in: D.E. Olis, H. Al-Ekabi (Eds.), Photocatalytic Purification and Treatment of Water and Air, Elsevier, Amsterdam, 1993, p. 747.

[3] A.M. Tonejc, M. Goti, B. Grzeta, S. Music, S. Popovi, R. Trojko, A. Turkovi, I. MuSevic, Transmission electron microscopy studies of nanophase TiO_2, Materials Science and Engineering B-Solid State Materials for Advanced Technology 40 (1996) 177–184.

[4] E. Traversa, G. Gnappi, A. Montenero, G. Gusmano, Ceramic thin films by sol–gel processing as novel materials for integrated humidity sensors, Sensors and Actuators B-Chemical 31 (1996) 59–70.

[5] B. Ohtani, S. Nishimoto, Effect of surface adsorptions of aliphatic-alcohols and silver ion on the photocatalytic activity of TiO_2 suspended in aqueous-solutions, Journal of Physical Chemistry 97 (1993) 920–926.

[6] B. O'Regan, M. Gratzel, A low-cost, high-efficiency solar cell based on dye-sensitized colloidal TiO_2 films, Nature 353 (1991) 737.

[7] Y.J. Liu, R.O. Claus, Blue light emitting nanosized TiO_2 colloids, Journal of the American Chemical Society 119 (1997) 5273–5274.

[8] S. Nishimoto, B. Ohtani, H. Kajiwara, T. Kagiya, Correlation of the crystal structure of titanium dioxide prepared from titanium tetra-2-propoxide with the photocatalytic activity for redox reactions in aqueous propan-2-ol and silver salt solutions, Journal of the Chemical Society-Faraday Transactions 1 (81) (1985) 61–68.

[9] M.A. Fox, M.T. Dulay, Heterogeneous photocatalysis, Chemical Reviews 93 (1993) 341–357.

[10] K. Tanaka, T. Hisanaga, A.P. Rivera, in: D.F. Ollis, H. Al-Ekabi (Eds.), Photocatalytic Purification and Treatment of Water and Air, Elsevier, Amsterdam, 1993, p. 169.

[11] N.P. Xu, Z.F. Shi, Y.Q. Fan, J.H. Dong, J. Shi, M.Z.C. Hu, Effects of particle size of TiO_2 on photocatalytic degradation of methylene blue in aqueous suspensions, Industrial and Engineering Chemistry Research 38 (1999) 373–379.

[12] T. Sato, Y. Yamamoto, Y. Fujishiro, S. Uchida, Intercalation of iron oxide in layered $H_2Ti_4O_9$ and $H_4Nb_6O_{17}$: visible-light induced photocatalytic properties, Journal of the Chemical Society-Faraday Transactions 92 (1996) 5089–5092.

[13] S. Uchida, Y. Yamamoto, Y. Fujishiro, A. Watanabe, O. Ito, T. Sato, Intercalation of titanium oxide in layered $H_2Ti_4O_9$ and $H_4Nb_6O_{17}$ and photocatalytic water cleavage with $H_2Ti_4O_9$/(TiO_2, Pt) and $H_4Nb_6O_{17}$/(TiO_2, Pt) nanocomposites, Journal of the Chemical Society-Faraday Transactions 93 (1997) 3229–3234.

[14] M. Inoue, Y. Kondo, T. Inui, An ethylene glycol derivative of boehmite, Inorganic Chemistry 27 (1988) 215–221.

[15] M. Inoue, H. Kominami, T. Inui, Thermal transformation of chi-alumina formed by thermal decomposition of aluminum alkoxide in organic media, Journal of the American Ceramic Society 75 (1992) 2597–2598.

[16] M. Inoue, H. Kominami, T. Inui, Novel synthetic method for the catalytic use of thermally stable zirconia—thermal decomposition of zirconium alkoxides in organic media, Applied Catalysis A-General 97 (1993) L25–L30.

[17] H. Kominami, J. Kato, S. Murakami, Y. Kera, M. Inoue, T. Inui, B. Ohtani, Synthesis of titanium (IV) oxide of ultra-high photocatalytic activity: high-temperature hydrolysis of titanium alkoxides with water liberated homogeneously from solvent alcohols, Journal of Molecular Catalysis A-Chemical 144 (1999) 165–171.

[18] S. Kongwudthiti, P. Praserthdam, P. Silveston, M. Inoue, Influence of synthesis conditions on the preparation of zirconia powder by the glycothermal method, Ceramics International 29 (2003) 807–814.

[19] O. Mekasuwandumrong, P.L. Silveston, P. Praserthdam, M. Inoue, V. Pavarajarn, W. Tanakulrungsank, Synthesis of thermally stable micro spherical chi-alumina by thermal decomposition of aluminum isopropoxide in mineral oil, Inorganic Chemistry Communications 6 (2003) 930–934.

[20] H. Kominami, J. Kato, Y. Takada, Y. Doushi, B. Ohtani, S. Nishimoto, M. Inoue, T. Inui, Y. Kera, Novel synthesis of microcrystalline titanium (IV) oxide having high thermal stability and ultra-high photocatalytic activity: thermal decomposition of titanium (IV) alkoxide in organic solvents, Catalysis Letters 46 (1997) 235–240.

[21] W. Payakgul, O. Mekasuwandumrong, V. Pavarajarn, P. Praserthdam, Effects of reaction medium on the synthesis of TiO_2 nanocrystals by thermal decomposition of titanium (IV) *n*-butoxide, Ceramics International 31 (2005) 391–397.

[22] H.K. Park, D.K. Kim, C.H. Kim, Effect of solvent on titania particle formation and morphology in thermal hydrolysis of $TiCl_4$, Journal of the American Ceramic Society 80 (1997) 743–749.

[23] J.A. Dean, Lange's Handbook of Chemistry, McGraw-Hill, New York, 1999.

[24] H. Kominami, S. Murakami, Y. Kera, B. Ohtani, Titanium (IV) oxide photocatalyst of ultra-high activity: a new preparation process allowing compatibility of high adsorptivity and low electron-hole recombination probability, Catalysis Letters 56 (1998) 125–129.

[25] S.J. Tsai, S. Cheng, Effect of TiO_2 crystalline structure in photocatalytic degradation of phenolic contaminants, Catalysis Today 33 (1997) 227–237.

[26] C. Kormann, D.W. Bahnemann, M.R. Hoffmann, Photocatalytic production of hydrogen peroxides and organic peroxides in aqueous suspensions of titanium dioxide, zinc oxide, and desert sand, Environmental Science & Technology 22 (1988) 798–806.

[27] A. Houas, H. Lachheb, M. Ksibi, E. Elaloui, C. Guillard, J.M. Herrmann, Photocatalytic degradation pathway of methylene blue in water, Applied Catalysis B-Environmental 31 (2001) 145–157.

[28] H.-S. Son, S.-J. Lee, I.-H. Cho, K.-D. Zoh, Kinetics and mechanism of TNT degradation in TiO_2 photocatalysis, Chemosphere 57 (2004) 309–317.

[29] M.R. Nimlos, W.A. Jacoby, D.M. Blake, T.A. Milne, Direct mass spectrometric studies of the destruction of hazardous wastes. 2. Gas-phase photocatalytic oxidation of trichloroethylene over TiO_2: products and mechanisms, Environmental Science & Technology 27 (1993) 732–740.

[30] Y. Luo, D.F. Ollis, Heterogeneous photocatalytic oxidation of trichloroethylene and toluene mixtures in air: kinetic promotion and inhibition, time-dependent catalyst activity, Journal of Catalysis 163 (1996) 1–11.

[31] O. dHennezel, D.F. Ollis, Trichloroethylene-promoted photocatalytic oxidation of air contaminants, Journal of Catalysis 167 (1997) 118–126.

[32] M. Lewandowski, D.F. Ollis, Halide acid pretreatments of photo-catalysts for oxidation of aromatic air contaminants: rate enhance-ment, rate inhibition, and a thermodynamic rationale, Journal of Catalysis 217 (2003) 38–46.

[33] W.Z. Tang, H. An, Photocatalytic degradation kinetics and mechan-ism of acid-blue-40 by TiO_2/UV in aqueous-solution, Chemosphere 31 (1995) 4171–4183.

[34] I.K. Konstantinou, V.A. Sakkas, T.A. Albanis, Photocatalytic degradation of propachlor in aqueous TiO_2 suspensions. Determi-nation of the reaction pathway and identification of intermediate products by various analytical methods, Water Research 36 (2002) 2733–2742.

[35] M.R. Hoffmann, S.T. Martin, W.Y. Choi, D.W. Bahnemann, Environmental applications of semiconductor photocatalysis, Chemical Reviews 95 (1995) 69–96.

Available online at www.sciencedirect.com
SCIENCE DIRECT
Materials Chemistry and Physics 97 (2006) 343–350
MATERIALS CHEMISTRY AND PHYSICS
www.elsevier.com/locate/matchemphys

Catalytic behaviors of mixed TiO_2-SiO_2-supported cobalt Fischer–Tropsch catalysts for carbon monoxide hydrogenation

Bunjerd Jongsomjit*, Tipnapa Wongsalee, Piyasan Praserthdam

Center of Excellence on Catalysis and Catalytic Reaction Engineering, Department of Chemical Engineering, Faculty of Engineering, Chulalongkorn University, Bangkok 10330, Thailand

Received 11 April 2005; received in revised form 7 July 2005; accepted 9 August 2005

Abstract

In the present study, the catalytic behaviors of mixed TiO_2-SiO_2-supported cobalt (Co) Fischer–Tropsch (FT) catalysts via carbon monoxide (CO) hydrogenation were investigated. The various weight ratios of TiO_2/SiO_2 were prepared, then consequently impregnated with the cobalt precursor. After calcination, the various samples were characterized using XRD, Raman spectroscopy, scanning electron microscopy/energy dispersive X-ray (SEM/EDX), transmission electron microscopy (TEM), temperature-programmed reduction (TPR), and H_2 chemisorption. The characteristics of various samples were further discussed in more details. Based on the reaction study, it revealed that the presence of titania in the mixed supports resulted in decreased activities dramatically. However, longer chain hydrocarbons such as C_2–C_5 can be obtained substantially with increasing the amounts of titania in the mixed supports.

Keywords: Silica; Titania; Cobalt; Catalyst; CO hydrogenation

1. Introduction

It has been known that supported cobalt (Co) catalysts are preferred for Fischer–Tropsch (FT) synthesis because of their high activities during FT synthesis based on natural gas [1], high selectivity to linear long chain hydrocarbons and also low activities for the competitive water–gas shift (WGS) reaction [2,3]. Many inorganic supports such as SiO_2 [4–8], Al_2O_3 [9–14], TiO_2 [15–17] and zeolites [18] have been extensively studied for supported Co catalysts for years. It is known that in general, the catalytic properties depend on reaction conditions, catalyst compositions, metal dispersion, and types of inorganic supports used. Thus, changes the catalyst compositions and/or even though the compositions of supports used may lead to significantly enhance the catalytic properties as well.

The TiO_2-SiO_2 mixed oxide has been considered to be very attractive as catalysts and supports, which have brought much attention in recent years. It was reported that TiO_2-SiO_2 mixed materials have been used as catalysts and supports for various reactions [19]. However, the use of this mixed oxide support here with the cobalt catalyst has not been reported yet. This TiO_2-SiO_2 mixed oxide would lead to robust catalytic supports of cobalt catalyst for carbon monoxide (CO) hydrogenation reaction.

Therefore, the main objective of this present study was to investigate the catalytic behaviors of mixed TiO_2-SiO_2-supported cobalt Fischer–Tropsch catalyst via CO hydrogenation reaction. The ratios of TiO_2/SiO_2 used were varied. The mixed oxide supports and catalyst precursors were prepared, characterized and tested for CO hydrogenation. The role of titania in the mixed oxide supports on the catalytic behaviors was also further discussed.

2. Experimental

2.1. Material preparation

2.1.1. Preparation of TiO_2-SiO_2 mixed oxide support

TiO_2-SiO_2 mixed oxide supports [surface areas of $SiO_2 = 300\,m^2\,g^{-1}$ and $TiO_2 = 70\,m^2\,g^{-1}$ (anatase form)]

* Corresponding author. Tel.: +662 2186869; fax: +662 2186877.
E-mail address: bunjerd.j@chula.ac.th (B. Jongsomjit).

0254-0584/$ – see front matter © 2005 Elsevier B.V. All rights reserved.
doi:10.1016/j.matchemphys.2005.08.016

were prepared according to the method described by Conway et al. [20]. In particular, 1 g of TiO_2-SiO_2 mixed oxide support was physically mixed by dispersing in toluene (ca. 20 ml). The mixture was stirred for 30 min, filtered, and then dried under vacuum. The TiO_2/SiO_2 weight ratios were varied from 0/1, 2/8, 4/6, 6/4, 8/2, and 1/0. The mixed supports were calcined at 500 °C for 4 h.

2.1.2. Preparation of catalyst samples

A 20 wt.% of Co/TiO_2-SiO_2 mixed support was prepared by the incipient wetness impregnation. A designed amount of cobalt nitrate [$Co(NO_3)\cdot 6H_2O$] was dissolved in deionized water and then impregnated onto the mixed oxide supports obtained from Section 2.1.1. The catalyst precursor was dried at 110 °C for 12 h and calcined in air at 500 °C for 4 h.

2.2. Catalyst nomenclature

The nomenclature used for the catalyst samples in this study is following:

- Co_*a*/*b* refers to the cobalt catalyst on the TiO_2-SiO_2 mixed oxide support, where *a* is the weight ratio of TiO_2 and *b* the weight ratio of SiO_2

2.3. Catalyst characterization

2.3.1. X-ray diffraction

XRD was performed to determine the bulk crystalline phases of catalyst. It was conducted using a SIEMENS D-5000 X-ray diffractometer with Cu Kα (λ = 1.54439 Å). The spectra were scanned at a rate of 2.4 ° min^{-1} in the range $2\theta = 20$–80°.

2.3.2. Raman spectroscopy

The Raman spectra of the samples were collected by projecting a continuous wave laser of argon ion (Ar^+) green (514.532 nm) through the samples exposed to air at room temperature. A scanning range of 100–1000 cm^{-1} with a resolution of 2 cm^{-1} was applied. The data were analyzed using the Renishaw Windows-based Raman Environment (WiRE) software, which allows Raman spectra to be captured, calibrated, and analyzed using system 2000 functionality via Galactic GRAMS interface with global imaging capacity.

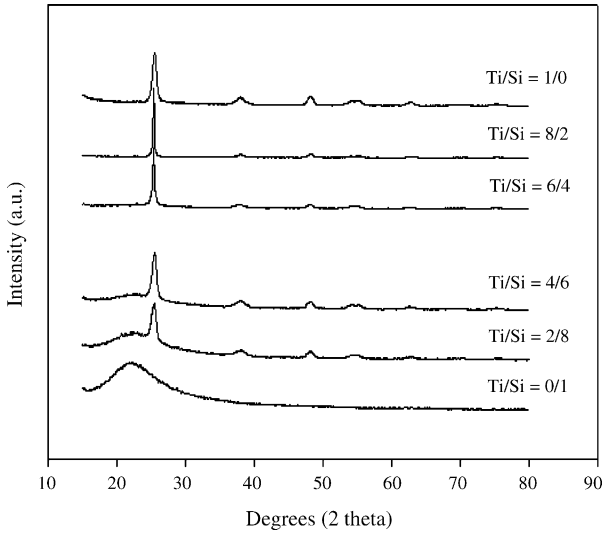

Fig. 1. XRD patterns for various ratios of TiO_2/SiO_2 mixed supports.

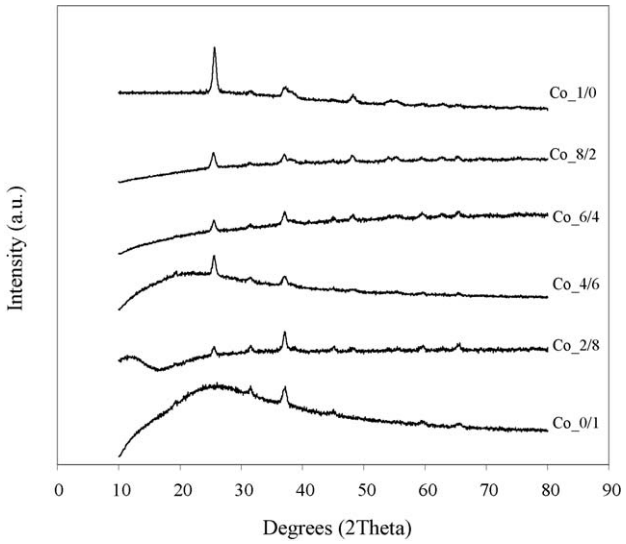

Fig. 2. XRD patterns for the various mixed TiO_2/SiO_2-supported cobalt catalysts after calcination.

2.3.3. Scanning electron microscopy (SEM) and energy dispersive X-ray (EDX) spectroscopy

SEM and EDX were used to determine the catalyst morphologies and elemental distribution throughout the catalyst granules, respectively. The SEM of JEOL mode JSM-5800LV was applied. EDX was performed using Link Isis series 300 program.

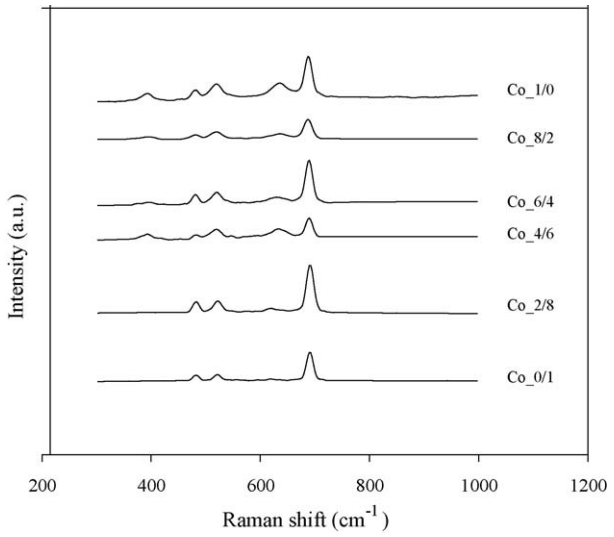

Fig. 3. Raman spectra for the various mixed TiO_2/SiO_2-supported cobalt catalysts after calcination.

2.3.4. Transmission electron microscopy (TEM)

The dispersion of cobalt oxide species on the various mixed oxide supports was determined using a JEOL-TEM 200CX transmission electron spectroscopy operated at 100 kV with 100k magnification.

2.3.5. Hydrogen chemisorption

Static H_2 chemisorption at 100 °C on the reduced cobalt catalysts was used to determine the number of reduced surface cobalt metal atoms. This is related to the overall activity of the catalysts during CO hydrogenation. Gas volumetric chemisorption at 100 °C was performed using the method described by Reuel and Bartholomew [21]. The experiment was performed in a Micromeritics ASAP 2010 using ASAP 2010C V3.00 software.

2.3.6. Temperature-programmed reduction (TPR)

TPR was used to determine the reduction behaviors and reducibilities of the samples. It was carried out using 50 mg of a sample and a temperature ramp from 35 to 800 °C at 5 °C min^{-1}. The carrier gas was 5% H_2 in Ar. A cold trap was placed before the detector to remove water produced during the reaction. A thermal conductivity detector (TCD) was used to determine the amount of H_2 consumed during TPR. The H_2 consumption was calibrated using TPR of Ag_2O at the same conditions [9,22–26].

2.4. Reaction

CO hydrogenation (H_2/CO = 10/1) was performed to determine the overall activity of the catalyst samples. Hydrogenation of CO was carried out at 220 °C and 1 atm. A flow rate of H_2/CO/He = 20/2/8 cc min^{-1} in a fixed-bed flow reactor under differential condition was used. A relatively high H_2/CO ratio was used to minimize deactivation due to carbon deposition during reaction. Typically, 20 mg of a catalyst sample was reduced in situ in flowing H_2 (30 cc min^{-1}) at 350 °C for 10 h prior to the reaction. Reactor effluent samples were taken at 1-h intervals and analyzed by GC. In all cases, steady-state was reached within 5 h.

3. Results and discussion

3.1. Characteristics of Co/TiO_2-SiO_2

The XRD patterns of mixed TiO_2-SiO_2 supports before impregnation with the cobalt precursor are shown in Fig. 1. It was observed that the pure silica exhibited a broad XRD peak assigning to the conventional amorphous silica. Similar to the pure silica, the XRD patterns of pure titania indicated only the characteristic peaks of anatase titania at 25° (major), 37°, 48°, 55°, 56°, 62°, 71°, and 75°. XRD patterns of the mixed oxide supports containing various ratios of titania and silica revealed the combination of titania and silica supports based on their contents. It can be seen that the intensity of XRD characteristic peaks for both supports was changed based on the ratios of titania and silica. After impregnation with the cobalt precursor and calcination, all samples of Co/TiO_2-SiO_2 catalyst were again identified using XRD. The XRD patterns of all calcined samples are shown in Fig. 2. After calcination, all samples exhibited XRD peaks,

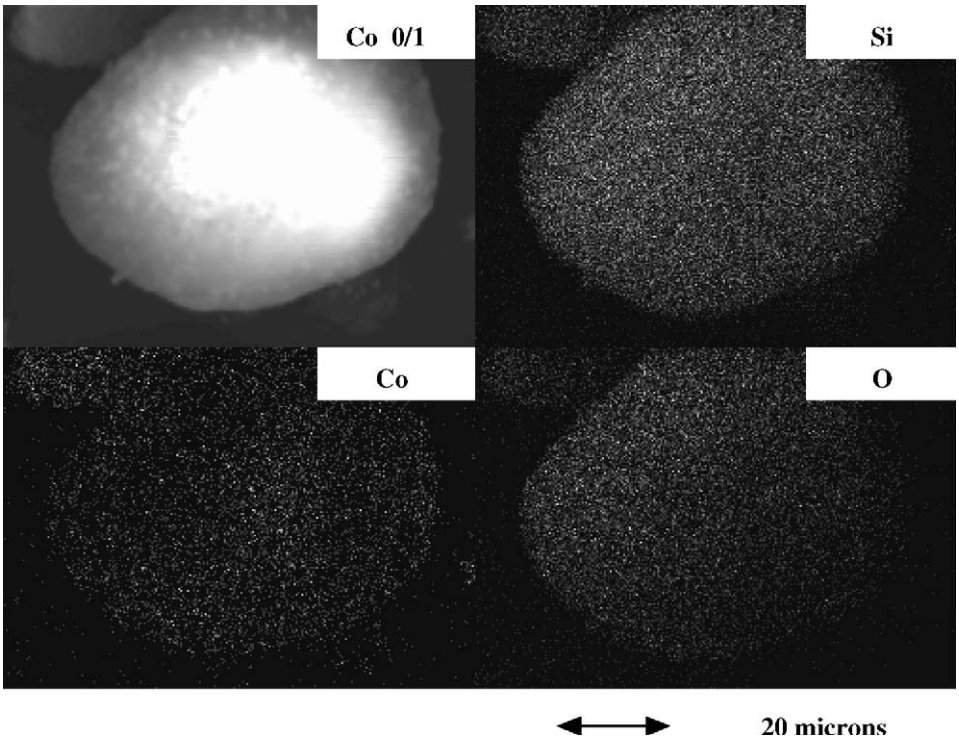

Fig. 4. SEM micrograph and EDX mapping of the calcined Co/SiO_2 catalyst.

which were identical with those for the corresponding mixed oxide supports used as seen in Fig. 1. This indicated that there was no further phase transformation from anatase to rutile occurred after calcination (at temperature ca. 500 °C for 4 h). The amorphous silica also exhibited good stability upon the same calcination process. Besides the corresponding mixed oxide supports detected, all calcined samples also exhibited weak XRD peaks at 31°, 36°, and 65°, which were assigned to the presence of Co_3O_4. Based on XRD results, it indicated that the presence of Co_3O_4 was apparently in the highly dispersed form. Raman spectroscopy is one of the most powerful techniques used to identify the metal oxide species present. It was found that the titania support exhibited the Raman bands at 640, 514 and 397 cm^{-1} for TiO_2 in its anatase form as seen from our previous work [27] whereas silica was the Raman insensitive upon the scanning range applied. The Raman spectra for all calcined samples as shown in Fig. 3 exhibited the Raman bands of the titania support as mentioned above with two shoulders at 690 and 480 cm^{-1}, assigned to Co_3O_4 [9,22,27] with corresponding to those with XRD.

SEM and EDX were also conducted in order to study the morphologies and elemental distribution of the samples, respectively. Apparently, SEM micrographs and EDX mapping exhibited similar trends of morphologies and elemental (Co, Si, Ti, and O) distributions. The typical SEM micrographs along with the EDX mapping (for Co, Si, and O) of Co/SiO_2 sample are illustrated in Fig. 4 indicating the external surface of the sample granule. It can be seen that the cobalt oxide species were well distributed (shown on EDX mapping) all over the sample granule. In order to determine the morphologies and elemental distributions of cobalt

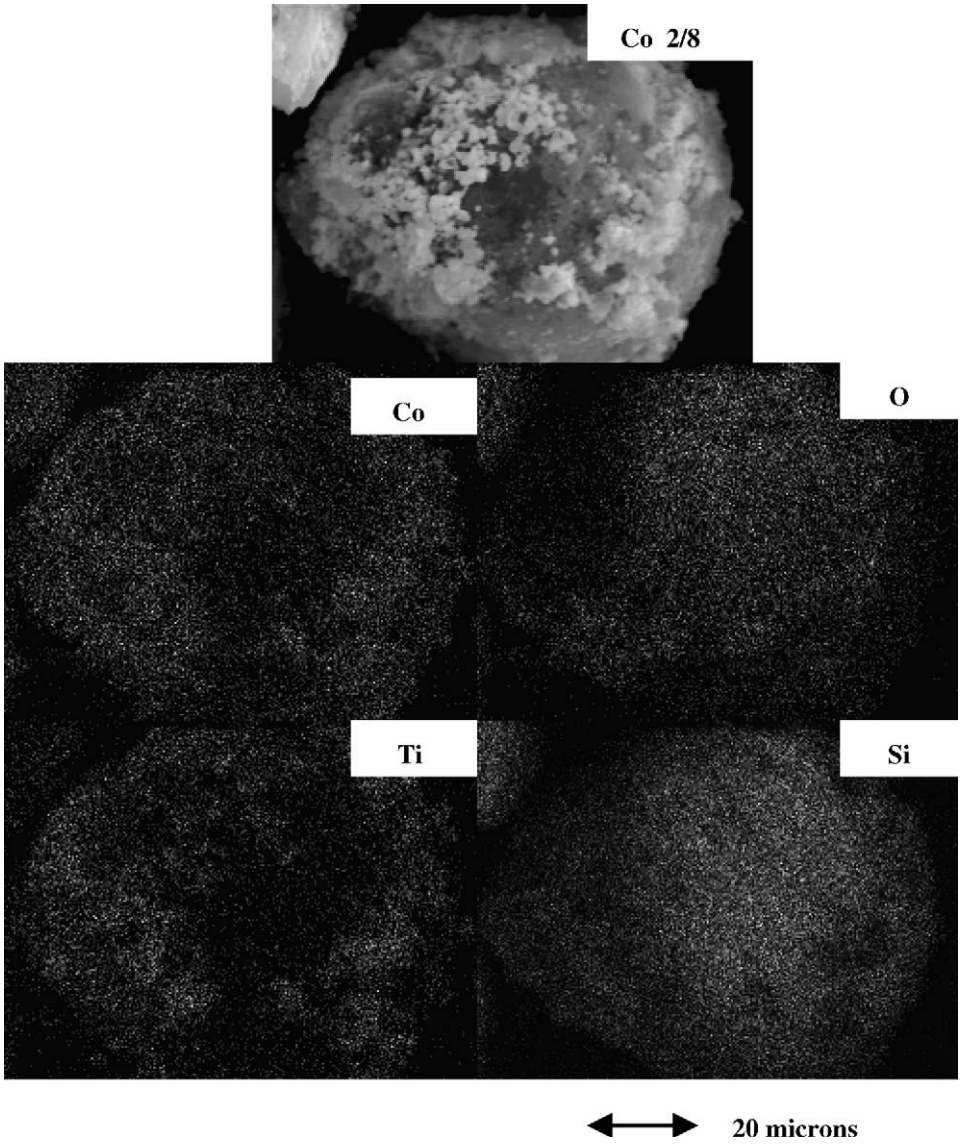

Fig. 5. SEM micrograph and EDX mapping of the calcined Co/TiO_2-SiO_2 (2/8) catalysts.

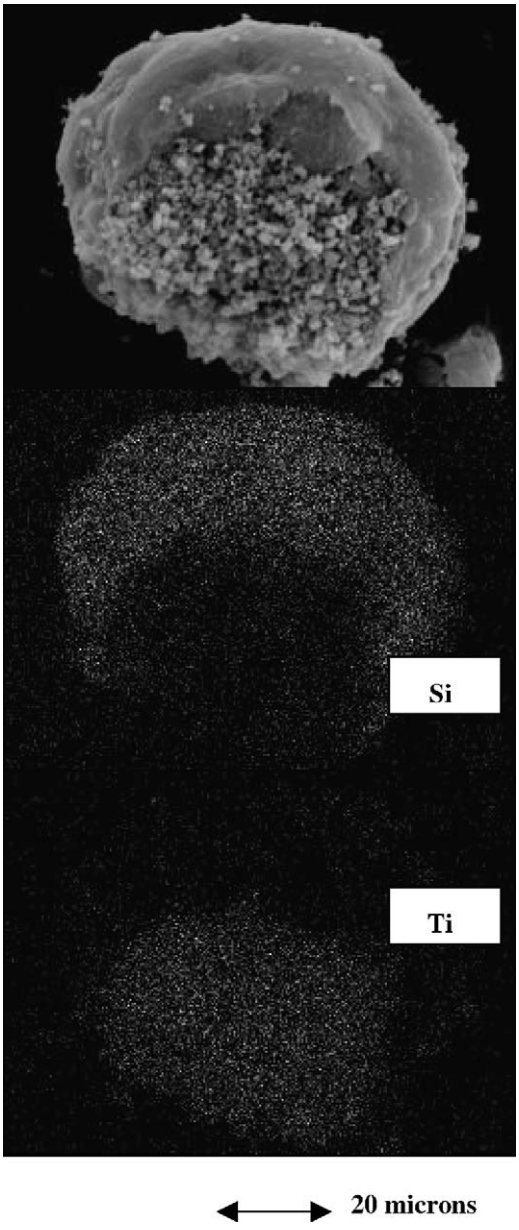

Fig. 6. A typical of SEM micrograph and EDX mapping of mixed TiO_2-SiO_2 support.

oxides on the mixed TiO_2-SiO_2 supports, the typical SEM micrographs along with the EDX mapping (for Co, Si, Ti, and O) are shown in Fig. 5, which is similar with those as seen in Fig. 4. However, an obvious charged surface under SEM electron bombarding is visible in Fig. 4. Besides the observation of well distribution for cobalt oxide species, it indicated that titania was apparently located on the outer surface of silica as shown in Fig. 6. The connectivity of Si–O–Ti can be confirmed by the IR spectroscopy indicating the IR bands at ca. 980 and 1100 cm^{-1} [28,29]. In order to determine the dispersion of cobalt oxide species on the various mixed oxide supports, a more powerful technique such as TEM was applied to all samples. The TEM micrographs for all samples are shown in Fig. 7. The dark spots represented cobalt oxide species or patches dispersing on the various mixed TiO_2-SiO_2 supports. It can be observed that a highly dispersed form of cobalt oxide species trended to be achieved with the presence of titania in the mixed oxide supports resulting in an appearance of smaller cobalt oxide patches. When combined the Raman spectroscopic results with those from TEM, it is likely that larger shoulders at 690 and 480 cm^{-1} would result in more dispersion of Co. It should be mentioned that although the more highly dispersed cobalt oxide patches with the presence of titania, their distributions seen by TEM were not as good as those seen in the pure silica support. On the other hand, the cobalt oxide patches present on the pure silica support exhibited better distribution, however, with lower degree of dispersion than any other samples. This can be attributed to higher surface areas of the silica support itself. It should be mentioned that high surface area of support could result in better distribution of Co, but somehow does not guarantee good dispersion (small Co patches). Besides, the highly dispersed form of cobalt oxide species could not guarantee the large number of reduced cobalt metal surface atoms, which is related to the overall activity of the catalyst. In addition, the highly dispersed form of cobalt oxide species, the interaction of those with the specified supports has to be essentially considered. Thus, temperature-programmed reduction on the calcined samples needs to be performed in order to give a better understanding according to such a reduction behavior. The TPR profiles for all samples are shown in Fig. 8. It was found that there was only one reduction peak, however, at different reduction temperatures for all calcined samples. The lowest reduction temperatures located at ca. 280–600 °C (maximum at 450 °C) was observed on the Co/SiO_2 sample. However, the reduction temperatures were found to dramatically shift to higher temperatures with increasing the amounts of titania present in the mixed oxide supports. Thus, the highest reduction temperatures located at ca. 370–650 °C (maximum at 550°C) can be observed for the Co/TiO_2 sample. The pronounced shift of reduction temperatures to higher ones found with the presence of titania can be attributed to the strong support interaction between the cobalt oxides and titania [30]. This was suggested that with the presence of titania it was more difficult for the cobalt oxide species to be reduced at the specified condition than those in silica itself. However, since the catalyst samples were reduced at different temperatures, it may not be useful to compare the reducibility of samples at this condition. Besides, the number of reduced Co metal surface atoms can be calculated directly from the H_2 chemisorption results, which is more acceptable since all catalyst samples are reduced at the standard reduction condition.

It is known that the active form of supported cobalt FTS catalysts is cobalt metal (Co^0). Thus, reduction of cobalt oxide species is essentially performed in order to transform cobalt oxide species obtained after calcination process into the active cobalt metal atoms for catalyzing the reac-

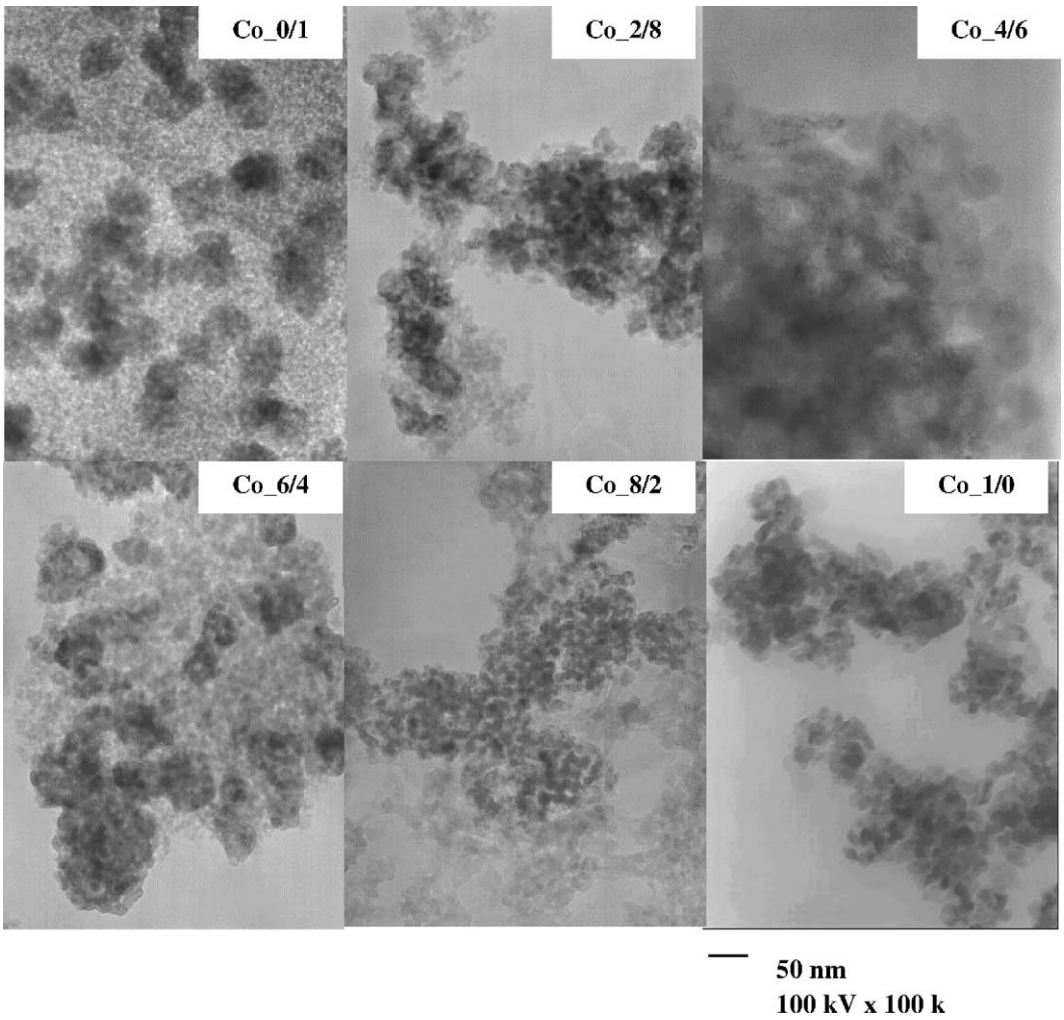

Fig. 7. TEM micrographs of the various mixed TiO_2/SiO_2-supported cobalt catalysts after calcinations.

tion. Therefore, the static H_2 chemisorption on the reduced cobalt samples was used to determine the number of reduced cobalt metal surface atoms. This is usually related to the overall activity of the catalyst during carbon monoxide hydrogenation. The resulted H_2 chemisorption for all samples are shown in Table 1. It revealed that the number of reduced cobalt metal surface atoms decreased with the amounts of titania present in the mixed oxide supports. These results were corresponding with those from the TPR as mentioned before.

3.2. Reaction study

In order to determine the catalytic behaviors of the cobalt catalyst on various mixed TiO_2-SiO_2 supports, CO hydrogenation (H_2/CO = 10/1) was performed to determine the

Table 1
Show the H_2 chemisorption, reaction rates, and product selectivity of various samples

Catalyst samples	H_2 Chemisorption (μmol g_{cat}^{-1})	Rate ($\times 10^2$ g CH_2 g_{cat}^{-1} h^{-1})[a]		Product selectivity[b] (%)	
		Initial[b]	SS[c]	CH_4	C_2–C_5
Co_0/1	11.11	38.9	34.3	99	1
Co_2/8	10.70	32.2	30.4	95	5
Co_4/6	1.85	14.2	10.0	87	13
Co_6/4	0.42	2.7	0.7	74	26
Co_1/0	0.22	1.4	0.8	68	32

[a] CO hydrogenation was carried out at 220 °C, 1 atm, and H_2/CO/He = 20/2/8.
[b] After 5 h of reaction.
[c] After 5 min of reaction.

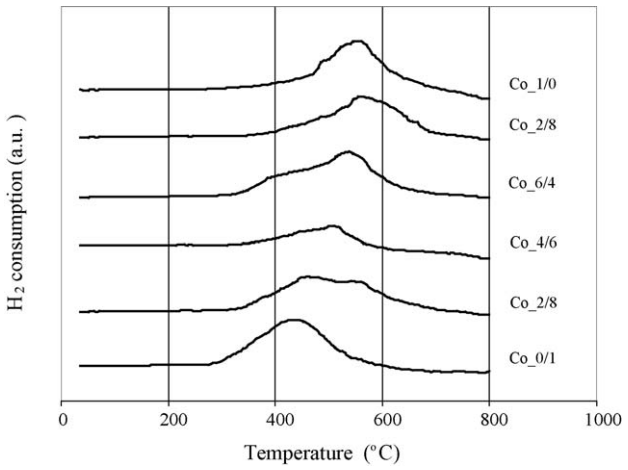

Fig. 8. TPR profiles of the various mixed TiO_2/SiO_2-supported cobalt catalysts after calcination.

overall activity and selectivity of the catalyst samples. Hydrogenation of CO was carried out at 220 °C and 1 atm. A flow rate of H_2/CO/He = 20/2/8 cc min^{-1} in a fixed-bed flow reactor under differential condition was used. In fact, a relatively high H_2/CO ratio was used to minimize deactivation due to carbon deposition during reaction. The resulted reaction study is also shown in Table 1. As expected, based on the H_2 chemisorption results, the overall activities for both initial and steady-state rates dramatically decreased with the amounts of titania present on the mixed oxide supports. This was basically due to the less number of reduced cobalt metal surface atoms with the presence of titania as seen by the H_2 chemisorption results along with higher surface area of silica as mentioned earlier. However, with some consideration on the product selectivity obtained, an interesting discovery can be observed in this present study. Considering the selectivity of product, it showed that the selectivity to methane essentially decreased with the amounts of titania in the supports. On the other hand, more amounts of longer chain hydrocarbons (C_2–C_5) can be obtained with the presence of titania in the mixed supports. It is known that CO hydrogenation is a kind of polymerization reactions where insertion of the $-CH_2-$ (methylene group) occurs through the active center. Thus, the product distribution strongly depends on the nature of active centers, rate of propagation, and rate of termination. Obviously, the termination of chain growth occurs and is recognized as the chain growth probability. Based on product selectivity found here, it can be concluded that the presence of titania in the mixed supports apparently inhibited the chain growth probability resulting in the observation of longer chain hydrocarbons even at the specified methanation condition. In order to study this effect in more details, the reaction intermediates at specified conditions must be further investigated with more powerful techniques such as the steady-state isotropic transient kinetic analysis (SSITKA) which has been successfully done by Goodwin and coworkers [5,6,8,9,31,32].

4. Summary

The present study showed impact of various mixed TiO_2-SiO_2-supported cobalt catalysts on their catalytic behaviors. It was found that both initial and steady-state rates during CO hydrogenation dramatically decreased with the amounts of titania present in the mixed supports. The decreased activities had to be attributed to the less number of reduced cobalt metal surface atoms for catalyzing the reaction. At the specified conditions, the selectivity of the longer chain hydrocarbons (C_2–C_5) was more pronounced with the presence of titania in the mixed supports. It can be concluded that the presence of titania apparently inhibited the chain growth probability during CO hydrogenation.

Acknowledgements

We gratefully acknowledge the financial support by the National Research Council of Thailand (NRCT), the Thailand Research Fund (TRF) and Thailand–Japan Technology Transfer Project (TJTTP-JBIC). We would like to thank Prof. James G. Goodwin Jr. at Clemson University for initiating this kind of project. We would like to extend our thanks to the National Metal and Materials Technology Center (MTECH) for Raman spectroscopy analysis.

References

[1] H.P. Wither Jr., K.F. Eliezer, J.W. Mechell, Ind. Eng. Chem. Res. 29 (1990) 1807.
[2] E. Iglesia, Appl. Catal. A 161 (1997) 59.
[3] R.C. Brady, R.J. Pettie, J. Am. Chem. Soc. 103 (1981) 1287.
[4] A. Martinez, C. Lopez, F. Marquez, I. Duaz, J. Catal. 220 (2003) 486.
[5] J. Panpranot, J.G. Goodwin Jr., A. Sayari, Catal. Today 77 (2002) 269.
[6] J. Panpranot, J.G. Goodwin Jr., A. Sayari, J. Catal. 211 (2002) 530.
[7] S.L. Sun, I. Isubaki, K. Fujimoto, Appl. Catal. A 202 (2000) 121.
[8] S. Ali, B. Chen, J.G. Goodwin Jr., J. Catal. 157 (1995) 35.
[9] B. Jongsomjit, J. Panpranot, J.G. Goodwin Jr., J. Catal. 215 (2003) 66.
[10] T. Das, G. Jacobs, P.M. Patterson, W.A. Conner, J.L. Li, B.H. Davis, Fuel 82 (2003) 805.
[11] G. Jacobs, P.M. Patterson, Y.Q. Zhang, T. Das, J.L. Li, B.H. Davis, Appl. Catal. A 233 (2002) 215.
[12] M. Rothaemel, K.F. Hanssen, E.A. Blekkan, D. Schanke, A. Holmen, Catal. Today 38 (1997) 79.
[13] V. Ragaini, R. Carli, C.L. Bianchi, D. Lorenzetti, G. Vergani, Appl. Catal. A 139 (1996) 17.
[14] V. Ragaini, R. Carli, C.L. Bianchi, D. Lorenzetti, G. Predieri, P. Moggi, Appl. Catal. A 139 (1996) 31.
[15] J.L. Li, G. Jacobs, T. Das, B.H. Davis, Appl. Catal. A 233 (2002) 255.
[16] G. Jacobs, T. Das, Y.Q. Zhang, J.L. Li, G. Racoillet, B.H. Davis, Appl. Catal. A 233 (2002) 263.
[17] J.L. Li, L.G. Xu, R. Keogh, B.H. Davis, Catal. Lett. 70 (2000) 127.
[18] X.H. Li, K. Asami, M.F. Luo, K. Michiki, N. Tsubaki, K. Fujimoto, Catal. Today 84 (2003) 59.

[19] X. Gao, I.E. Wachs, Catal. Today 51 (1999) 233.
[20] S.J. Conway, J.W. Falconer, C.H. Rochester, J. Chem. Soc., Faraday Trans. 185 (1989) 71.
[21] R.C. Reuel, C.H. Bartholomew, J. Catal. 85 (1984) 63.
[22] B. Jongsomjit, J. Panpranot, J.G. Goodwin Jr., J. Catal. 204 (2001) 98.
[23] B. Jongsomjit, J.G. Goodwin Jr., Catal. Today 77 (2002) 191.
[24] A. Kogelbauer, J.C. Weber, J.G. Goodwin Jr., Catal. Lett. 34 (1995) 269.
[25] Y. Zhang, D. Wei, S. Hammache, J.G. Goodwin Jr., J. Catal. 188 (1999) 281.
[26] B. Jongsomjit, C. Sakdamnuson, J.G. Goodwin Jr., P. Praserthdam, Catal. Lett. 94 (2004) 209.
[27] B. Jongsomjit, C. Sakdamnuson, P. Praserthdam, Mater. Chem. Phys. 89 (2005) 395.
[28] D.C.M. Dutoit, M. Schneider, J. Baiker, J. Catal. 153 (1995) 165.
[29] B. Jongsomjit, S. Ngamposri, P. Praserthdam, Catal. Lett. 100 (2005) 139.
[30] R. Riva, H. Miessuer, R. Vitali, G. Del Piero, Appl. Catal. A 196 (2000) 111.
[31] S. Vada, B. Chen, J.G. Goodwin Jr., J. Catal. 153 (1995) 224.
[32] S.H. Ali, J.G. Goodwin Jr., J. Catal. 176 (1998) 3.

Catalysis Letters Vol. 108, Nos. 1–2, April 2006 (© 2006)
DOI: 10.1007/s10562-006-0033-y

Effect of zirconia-modified titania consisting of different phases on characteristics and catalytic properties of Co/TiO_2 catalysts

Tipnapa Wongsalee, Bunjerd Jongsomjit*, and Piyasan Praserthdam

Center of Excellence on Catalysis and Catalytic Reaction Engineering, Department of Chemical Engineering, Faculty of Engineering, Chulalongkorn University, Bangkok 10330, Thailand

Received 8 November 2005; accepted 6 January 2006

The TiO_2 supports consisting of different phases were modified with ZrO_2 for TiO_2-supported Co catalysts. It showed that modification on the pure anatase TiO_2 resulted in decreased activities, but increased chain growth probability. In contrary, the modification on mixed phase TiO_2 resulted in increased activities without effects on selectivity.

KEY WORDS: cobalt catalyst; titania; support; zirconia modification; CO hydrogenation.

1. Introduction

In general, a supported catalyst usually consists of three components; (i) a catalytic phase, (ii) a promoter, and (iii) a support or carrier. As known, the catalytic properties apparently depend upon the components as mentioned above. The catalytic phase can be metals, metal oxides and so on. It can be used under a specified catalytic reaction. It is known that the catalytic performance is usually elevated using a promoter such as a noble metal. Besides the catalytic phase and promoter, it should be mentioned that a support could play a crucial role based on the catalytic performance. Basically, a support material acts as a carrier for the catalytic phase to be well dispersed on it. However, due to the supporting effects along with dispersion of the catalytic phase, the properties of a catalyst could be altered with the various supports used.

It is reported that many inorganic supports such as silica [1–4], alumina [5–9], titania [10–15], zirconia [16], and zeolites [17] have been extensively studied for years. During the past decades, titania-supported cobalt catalysts have been investigated by many authors, especially for the application of Fischer–Tropsch synthesis (FTS) in a continuously stirred tank reactor (CSTR) [10–12]. However, it should be noted that titania itself has different crystalline phases such as anatase, brookite and rutile phases. In our previous work, we reported that different crystalline phase compositions of titania could play important roles on the catalytic performance of titania-supported cobalt catalysts during CO hydrogenation [14,15,18]. In the present work, the modification of the titania support was extensively investigated. Since zirconia promotion appears to increase the rate of FTS on cobalt catalysts with silica support [19,20] and with alumina support [5], thus, it would be interesting to investigate the effect of zirconia modification on titania supports containing different phases.

In this study, a series of titania-supported cobalt catalysts was prepared with a range of zirconia concentrations in the titania supports. The titania supports used were in the pure anatase form and in the mixture of anatase and rutile phases. The catalysts were then characterized and tested for CO hydrogenation activity. The product selectivity was also further investigated.

*To whom correspondence should be addressed.
E-mail: bunjerd.j@chula.ac.th

2. Experimental

2.1. Materials

2.1.1. Zr-modified TiO_2 support

The Zr-modified titania supports were prepared by the impregnation method. There were two kinds of the titania supports used [(i) pure anatase phase and (ii) mixed anatase (81%) and rutile (19%) phases] from Ishihara Sangyo, Japan. First, Zr was impregnated into the support using a solution of zirconium (IV) *n*-propoxide (70 wt% in *n*-propanol, Alfa Aesar) to produce Zr-modified titania supports having 0.5, 1, and 5 wt% of ZrO_2. Second, the Zr-modified supports were calcined at 350 °C for 2 h (ramp rate 5 °C/min) prior to impregnation of cobalt.

2.1.2. Co/Zr-modified TiO_2 catalysts

Cobalt nitrate [$Co(NO_3)_2{\cdot}6H_2O$] was dissolved in deionized water and impregnated into the support as mentioned above to give a final catalyst with 20 wt% cobalt. The catalyst precursor was dried at 110 °C for 12 h and calcined in air at 500 °C for 4 h.

2.2. Catalyst nomenclature

The nomenclature used for the supports and catalyst samples in this study is as follows:

R0: TiO_2 support consisting of pure anatase phase
R19: TiO_2 support consisting of 81% anatase and 19% rutile phases
R0Z*i*: Zr-modified R0 with *i* wt% of ZrO_2
R19Z*i*: Zr-modified R19 with *i* wt% of ZrO_2
Co/support: supported cobalt catalyst on various supports as mentioned above

2.3. Characterization

2.3.1. BET surface area

BET surface area of the samples with various rutile: anatase ratios of titania was performed to determine if the total surface area changes. It was determined using N_2 adsorption at 77 K in a Micromeritics ASAP 2010.

2.3.2. X-ray diffraction

XRD was performed to determine the bulk crystalline phases of samples. It was conducted using a SIEMENS D-5000 X-ray diffractometer with CuK_α ($\lambda = 1.54439$ Å). The spectra were scanned at a rate of 2.4°/min in the range $2\theta = 20$–80°.

2.3.3. Temperature-programmed reduction

TPR was used to determine the reduction behaviors of the catalyst samples. It was carried out using 50 mg of a sample and a temperature ramp from 35 to 800 °C at 5 °C/min. The carrier gas was 5% H_2 in Ar. A cold trap was placed before the detector to remove water produced during the reaction.

2.3.4. Scanning electron microscopy and energy dispersive X-ray spectroscopy

SEM and EDX were used to determine the sample morphologies and elemental distribution throughout the sample granules, respectively. The SEM of JEOL model JSM-5800LV was applied. EDX was performed using Link Isis series 300 program.

2.3.5. Transmission electron microscopy (TEM)

The dispersion of cobalt oxide species on the titania supports were determined using a JEOL-TEM 200CX transmission electron spectroscopy operated at 200 kV with 200 k magnification.

2.3.6. Hydrogen chemisorption

Static H_2 chemisorption at 100 °C on the reduced samples was used to determine the number of reduced surface cobalt metal atoms. This is related to the overall activity of the samples during CO hydrogenation. Gas volumetric chemisorption at 100 °C was performed using the method described by Reuel and Bartholomew [21]. The experiment was performed in a Micromeritics ASAP 2010 using ASAP 2010C V3.00 software.

2.4. Reaction

CO hydrogenation (H_2/CO = 10/1) was performed to determine the overall activity and selectivity of the catalyst samples. It was carried out at 220 °C and 1 atm. A flow rate of H_2/CO/He = 20/2/8 cc/min in a fixed-bed flow reactor was used. A relatively high H_2/CO ratio was used to minimize deactivation due to carbon deposition during reaction. Typically, 20 mg of a catalyst sample was reduced in situ in flowing H_2 (30 cc/min) at 350 °C for 10 h prior to the reaction. Reactor effluent samples were taken at 1 h intervals and analyzed by GC. In all cases, steady-state was reached within 5 h. In fact, the reaction test for each sample was performed at least three times. The average point was reported.

3. Results and discussion

3.1. Characteristics

The BET surface areas of the modified supports and catalysts samples are shown in table 1. For the modified R0 (pure anatase) samples, the surface areas decreased from 70 to 47 m^2/g upon the amounts of zirconia loading. Based on the results of BET surface areas as shown in table 1, it showed that the surface area essentially slightly decreased with 0.5% Zr. The sintering was not the cause since the calcination temperature was only 350 °C. The decrease in surface area should be due to the pore blockage. The modified R19 (mixed phases) also showed decreases in surface areas from 49 to 33 m^2/g with zirconia modification. It can be observed that the surface areas of the catalyst samples on the various unmodified and modified supports slightly decreased with corresponding to the content of supports used. It should be noted that no significant changes in surface areas of samples were observed. After calcination, the various supports were characterized using XRD as shown in figure 1. For the R0 support, XRD peaks of the anatase phase of titania at 25°

Table 1
BET surface areas of various supports and catalyst samples

Supports	BET surface area (m^2/g)[a]	Catalyst samples	BET surface area (m^2/g)[a]
R0	70	Co/R0	52
R0Z0.5	55	Co/R0Z0.5	43
R0Z1	53	Co/R0Z1	42
R0Z5	47	Co/R0Z5	36
R19	49	Co/R19	34
R19Z0.5	38	Co/R19Z0.5	27
R19Z1	34	Co/R19Z1	25
R19Z5	33	Co/R19Z5	25

[a]Measurement error is ±5%.

2.2. Catalyst nomenclature

The nomenclature used for the supports and catalyst samples in this study is as follows:

R0: TiO_2 support consisting of pure anatase phase
R19: TiO_2 support consisting of 81% anatase and 19% rutile phases
R0Z*i*: Zr-modified R0 with *i* wt% of ZrO_2
R19Z*i*: Zr-modified R19 with *i* wt% of ZrO_2
Co/support: supported cobalt catalyst on various supports as mentioned above

2.3. Characterization

2.3.1. BET surface area

BET surface area of the samples with various rutile: anatase ratios of titania was performed to determine if the total surface area changes. It was determined using N_2 adsorption at 77 K in a Micromeritics ASAP 2010.

2.3.2. X-ray diffraction

XRD was performed to determine the bulk crystalline phases of samples. It was conducted using a SIEMENS D-5000 X-ray diffractometer with CuK_α ($\lambda = 1.54439$ Å). The spectra were scanned at a rate of 2.4°/min in the range $2\theta = 20$–80°.

2.3.3. Temperature-programmed reduction

TPR was used to determine the reduction behaviors of the catalyst samples. It was carried out using 50 mg of a sample and a temperature ramp from 35 to 800 °C at 5 °C/min. The carrier gas was 5% H_2 in Ar. A cold trap was placed before the detector to remove water produced during the reaction.

2.3.4. Scanning electron microscopy and energy dispersive X-ray spectroscopy

SEM and EDX were used to determine the sample morphologies and elemental distribution throughout the sample granules, respectively. The SEM of JEOL model JSM-5800LV was applied. EDX was performed using Link Isis series 300 program.

2.3.5. Transmission electron microscopy (TEM)

The dispersion of cobalt oxide species on the titania supports were determined using a JEOL-TEM 200CX transmission electron spectroscopy operated at 200 kV with 200 k magnification.

2.3.6. Hydrogen chemisorption

Static H_2 chemisorption at 100 °C on the reduced samples was used to determine the number of reduced surface cobalt metal atoms. This is related to the overall activity of the samples during CO hydrogenation. Gas volumetric chemisorption at 100 °C was performed using the method described by Reuel and Bartholomew [21]. The experiment was performed in a Micromeritics ASAP 2010 using ASAP 2010C V3.00 software.

2.4. Reaction

CO hydrogenation ($H_2/CO = 10/1$) was performed to determine the overall activity and selectivity of the catalyst samples. It was carried out at 220 °C and 1 atm. A flow rate of $H_2/CO/He = 20/2/8$ cc/min in a fixed-bed flow reactor was used. A relatively high H_2/CO ratio was used to minimize deactivation due to carbon deposition during reaction. Typically, 20 mg of a catalyst sample was reduced *in situ* in flowing H_2 (30 cc/min) at 350 °C for 10 h prior to the reaction. Reactor effluent samples were taken at 1 h intervals and analyzed by GC. In all cases, steady-state was reached within 5 h. In fact, the reaction test for each sample was performed at least three times. The average point was reported.

3. Results and discussion

3.1. Characteristics

The BET surface areas of the modified supports and catalysts samples are shown in table 1. For the modified R0 (pure anatase) samples, the surface areas decreased from 70 to 47 m^2/g upon the amounts of zirconia loading. Based on the results of BET surface areas as shown in table 1, it showed that the surface area essentially slightly decreased with 0.5% Zr. The sintering was not the cause since the calcination temperature was only 350 °C. The decrease in surface area should be due to the pore blockage. The modified R19 (mixed phases) also showed decreases in surface areas from 49 to 33 m^2/g with zirconia modification. It can be observed that the surface areas of the catalyst samples on the various unmodified and modified supports slightly decreased with corresponding to the content of supports used. It should be noted that no significant changes in surface areas of samples were observed. After calcination, the various supports were characterized using XRD as shown in figure 1. For the R0 support, XRD peaks of the anatase phase of titania at 25°

Table 1
BET surface areas of various supports and catalyst samples

Supports	BET surface area (m^2/g)[a]	Catalyst samples	BET surface area (m^2/g)[a]
R0	70	Co/R0	52
R0Z0.5	55	Co/R0Z0.5	43
R0Z1	53	Co/R0Z1	42
R0Z5	47	Co/R0Z5	36
R19	49	Co/R19	34
R19Z0.5	38	Co/R19Z0.5	27
R19Z1	34	Co/R19Z1	25
R19Z5	33	Co/R19Z5	25

[a]Measurement error is ± 5%.

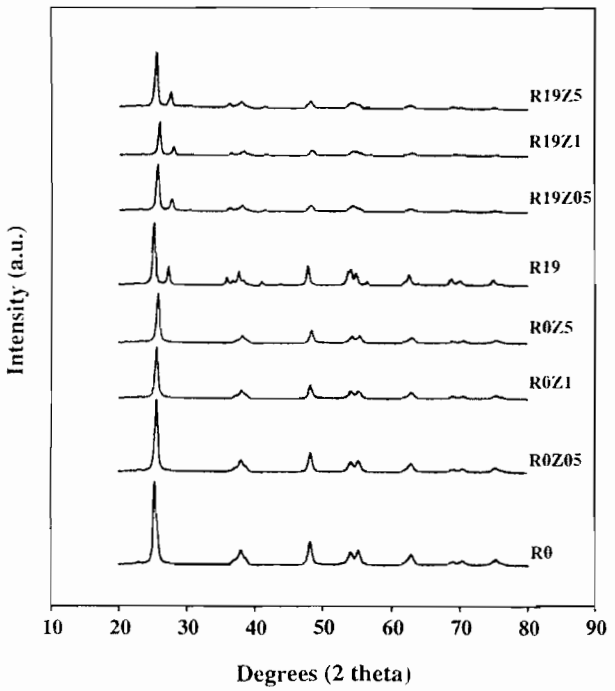

Figure 1. XRD patterns for different TiO_2 supports consisting of various amounts of ZrO_2 loading.

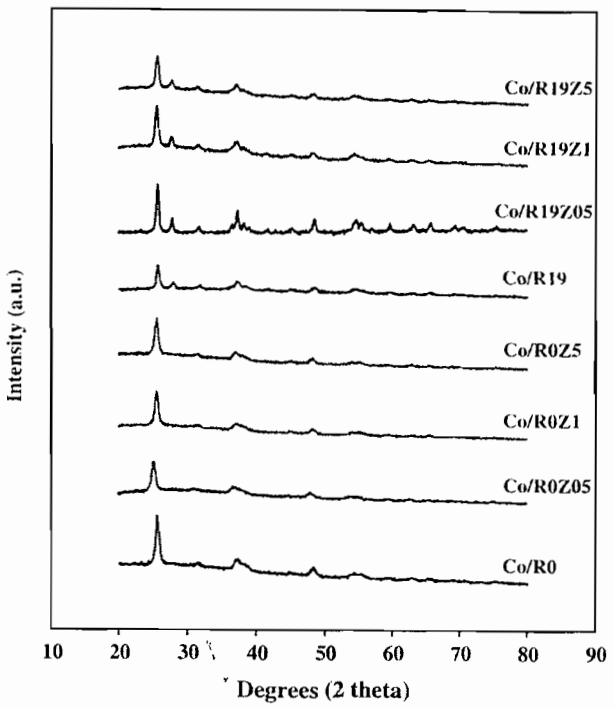

Figure 2. XRD patterns of Co/TiO_2 samples consisting of various amounts of ZrO_2 loading in TiO_2 supports.

(major), 37°, 48°, 55°, 56°, 62°, 71°, and 75° were evident. After the modification of R0 support, it was found that their characteristic peaks were still identical with those for the unmodified R0 support. This suggested that the zirconia was in the highly dispersed form. For the R19 support, it can be observed that besides the XRD peaks of pure anatase titania as mentioned before, the peaks at 28° (major), 36°, 42°, and 57° were detected. These peaks were assigned to the presence of rutile phase in the support along with the anatase phase. None of XRD peaks for zirconia was detected in the modified supports. After impregnation with the cobalt precursor and calcination, all catalyst samples were again identified using XRD. The XRD patterns of all calcined samples are shown in figure 2. It was observed that all calcined samples exhibited XRD peaks, which were identical with those for the corresponding modified supports as shown in figure 1. However, only weak intensity of XRD peak at 31° assigning to the presence of Co_3O_4 was detected. Therefore, based on the XRD results, it indicated that the presence of zirconia and cobalt oxide species were in the highly dispersed forms.

SEM and EDX were also conducted in order to study the morphologies and elemental distribution of the samples, respectively. In general, there was no significant change in morphologies and elemental distribution of all samples after calcination. The typical SEM micrograph and EDX mapping for Co/R19Z1 sample are illustrated in figure 3. Apparently, the Co oxide species exhibited well distribution on the surface of the support. In order to determine the dispersion of Co oxide species on the various modified supports, a more powerful technique such as TEM was applied to all samples. The TEM micrographs for Co/R0Z1, Co/R0Z5, Co/R19Z1, and Co/R19Z5 samples are shown in figure 4. The dark spots represented cobalt oxide species dispersing on the various modified supports after calcination of samples. The diameter of cobalt oxide particles was ca. 15, 16, 18, and 24 nm for Co/R0Z1, Co/R0Z5, Co/R19Z1, and Co/R19Z5 samples, respectively. Based on the TEM results, it indicated that the sizes of cobalt oxide species were slightly larger for those dispersing on the R19 supports than on the R0 supports as also reported in our previous work [14].

TPR was performed in order to determine the reduction behaviors of samples. The TPR profiles for all catalyst samples are shown in figure 5. The reduction temperatures for initial, final, and maximum temperatures are shown in table 2. It was found that there was only one reduction peak, however, at different reduction temperatures for all calcined samples. The one reduction peak can be assigned to the overlap of two step reduction of Co_3O_4 to CoO and then to Co metal [9,13]. Upon the TPR conditions, the two-step reduction may or may not be observed. Based on the TPR profiles, it indicated that for the zirconia-modified R0 supports, the reduction temperatures essentially shifted to the higher ones. Thus, zirconia modification of the R0 supports retarded the reduction of cobalt oxide species. Considering the zirconia modification of the R19 supports, it appeared that no effect on reduction behaviors of cobalt oxide species was found. However, it was confirmed that the

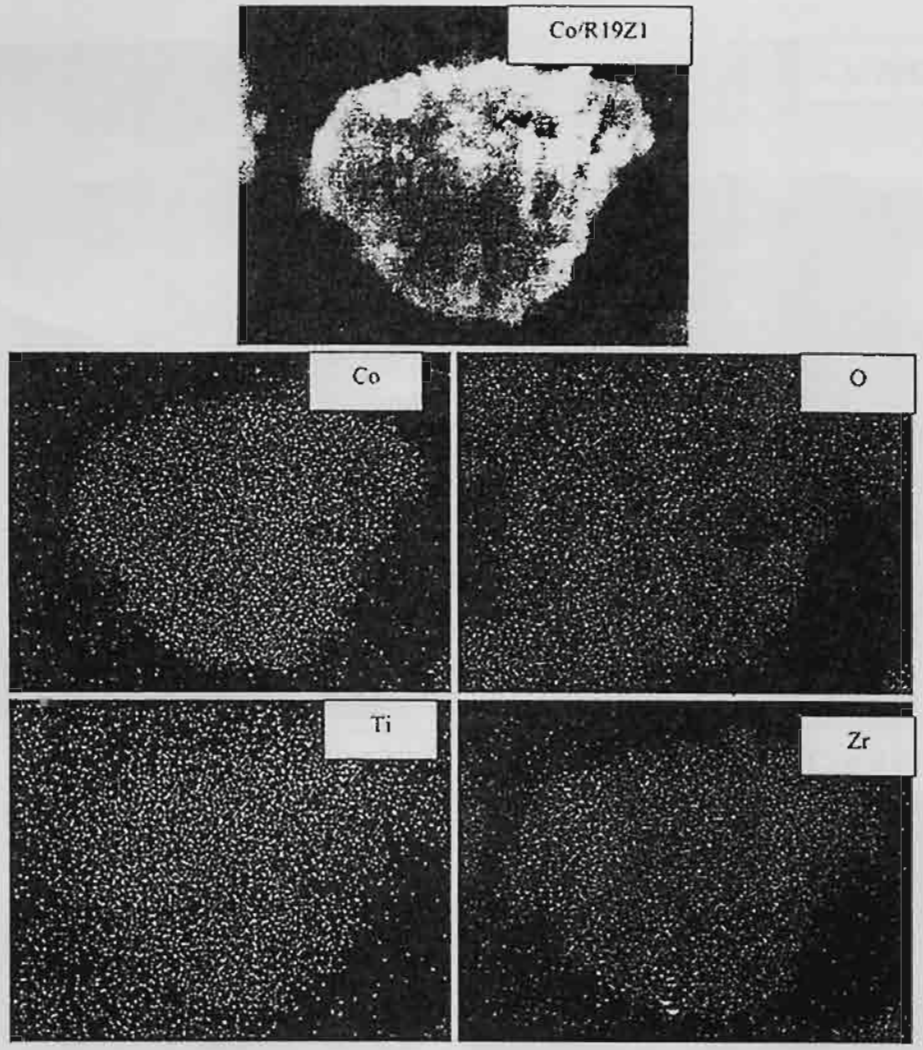

Figure 3. A typical SEM micrograph and EDX mapping for Co/R19Z1 sample.

presence of rutile phase could facilitate the reduction of Co oxide species as also reported in our previous work [14]. In order to determine the number of reduced Co metal surface atoms, which is related to the overall activity of samples during CO hydrogenation, H_2 chemisorption was performed. The results of H_2 chemisorption are shown in table 2. As seen, the amounts of H_2 chemisorption for samples with the modified R0 supports decreased consistently compared to that for samples with the unmodified ones. It should be mentioned that SMSI effect [22] is the characteristics of titania supports. However, due to the low reduction temperature (350 °C), the SMSI should not be present. Based on the results, it indicated that the catalysts (on the R0 ones) exhibited such a low H_2 chemisorption. Considering samples with the modified R19 supports, it appeared that effect of zirconia modification was observed based on the amounts of zirconia loading. On the other hand, with the low (0.5 wt% of Zr) and moderate (1 wt% of Zr) zirconia loading, the amounts of H_2 chemisorption were found to increase dramatically. However, no effect on the H_2 chemisorption was found with high (5 wt% of Zr) zirconia loading. It should be noted that the number of active sites for cobalt on the modified R19 supports increased with zirconia modification upon the low and moderate zirconia loading. The reaction study was further discussed in the next part.

3.2. Reactivity

In order to determine the catalytic behaviors of the catalyst samples dispersing on various modified titania supports, CO hydrogenation (H_2/CO = 10/1) was performed to determine the overall activity and product selectivity of the samples. Hydrogenation of CO was carried out at 220 °C and 1 atm. A flow rate of H_2/CO/He = 20/2/8 cc/min in a fixed-bed flow reactor was used. In fact, a relatively high H_2/CO ratio was used to minimize deactivation due to carbon deposition during reaction. The resulted reaction study is also shown in table 3. As expected, based on the H_2 chemisorption

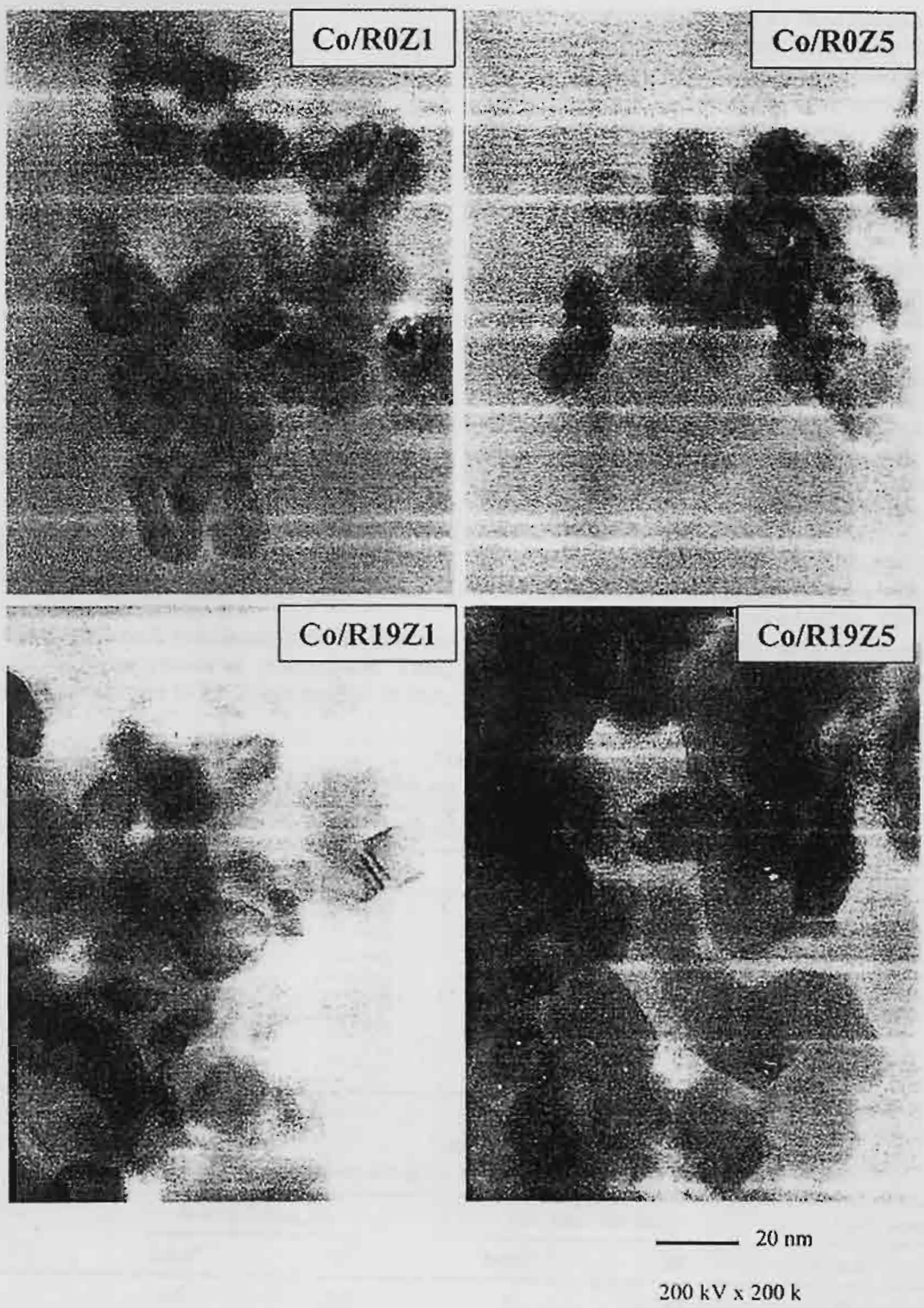

Figure 4. TEM micrographs for Co/TiO_2 samples consisting of various amounts of ZrO_2 loading in TiO_2 supports.

results, the steady-state rate of samples with low and moderate zirconia loading on R19 supports was the highest among any other samples with the R19 supports. For high zirconia loading, the modification would result in a decreased rate for the R19 support. There was no change in product selectivity upon the modification of the R19 supports. In contrary, the rate was found to decrease with zirconia modification for the R0 support with all amounts of zirconia loading used in this study. This was basically due to the less number of reduced cobalt metal surface atoms as seen from the results of H_2 chemisorption. Based on TPR results (figure 5), it was

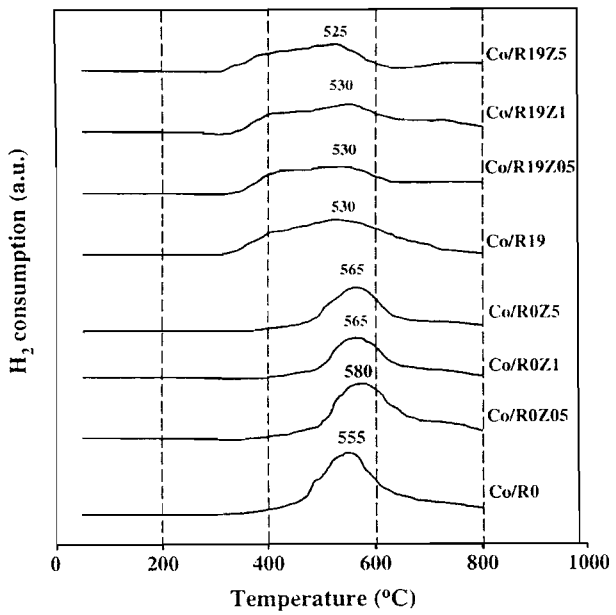

Figure 5. TPR profiles for Co/TiO_2 samples consisting of various amounts of ZrO_2 loading in TiO_2 supports.

suggested that the zirconia modification of the R0 supports resulted in higher reduction temperature. Thus, this inhibited the reduction of Co oxide species. In fact, for Co on alumina [5], the Zr modification resulted in increased activity about two times. For Co on silica [19,20], the activity also increased about two times with Zr modification. However, for both cases, the change in product selectivity was not observed. Compared to our results based on Co on titania (R19), the activity increased by 1.4 times with the Zr modification (low and moderate Zr loading) without changing the selectivity. However, with some consideration on the product selectivity obtained, an interesting discovery can be observed in this present study for the Co on R0 supports. Considering the selectivity of product for the sample with R0 support containing the low loading of zirconia, it showed that the selectivity to methane (C_1) essentially decreased. On the other hand, more amounts of longer chain hydrocarbons (C_2–C_4) can be obtained with the catalyst sample containing the low loading of zirconia on the R0 support. It is known that CO hydrogenation is a kind of polymerization reactions where insertion of the $-CH_2^-$ (methylene group) occurs through the active center. Thus, the product distribution strongly depends on the nature of active centers, rate of propagation, and rate of termination. Obviously, the termination of chain growth occurs and is recognized as the chain growth probability. Based on product selectivity found here, it was suggested that of R0 with a low

Table 2
Reduction temperatures and H_2 chemisorption of samples

Catalyst samples	Reduction temperature (°C)			H_2 chemisorption (μmol $H_2/g_{cat.}$)
	Initial	Final	Maximum	
Co/R0	370	695	550	0.93
Co/R0Z0.5	400	735	580	trace
Co/R0Z1	440	760	565	trace
Co/R0Z5	440	780	565	trace
Co/R19	320	735	530	2.44
Co/R19Z0.5	315	760	530	9.05
Co/R19Z1	315	750	530	8.54
Co/R19Z5	310	625	525	2.37

Table 3
Activity and selectivity during CO hydrogenation for various samples

Catalyst samples	Rate[a] ($gCH_2/g_{cat.}h$)		CH_4 selectivity (%)		C_2–C_4 selectivity (%)	
	Initial[b]	SS[c]	Initial[b]	SS[c]	Initial[b]	SS[c]
Co/R0	1.4	0.8	71	68	29	32
Co/R0Z0.5	1.2	0.2	32	31	68	69
Co/R0Z1	0.02	0.02	97	96	3	4
Co/R0Z5	0.01	0.01	98	90	2	10
Co/R19	3.3	2.6	98	98	2	2
Co/R19Z0.5	3.7	3.7	98	98	2	2
Co/R19Z1	3.7	3.7	97	96	3	4
Co/R19Z5	2.9	2.7	97	97	3	3

[a] CO hydrogenation was carried out at 220 °C, 1 atm, and $H_2/CO/He = 20/2/8$.
[b] After 5 min of reaction.
[c] After 5 h of reaction.

Table 4
Summarized results on the effect of zirconia modification on titania supports consisting of different phases for cobalt catalysts toward CO hydrogenation ($H_2/CO = 10$)

Samples	Activity (with zirconia modification)			Selectivity to C_2–C_4 (with zirconia modification)		
	Low Zr loading	Moderate Zr loading	High Zr loading	Low Zr loading	Moderate Zr loading	High Zr loading
Co/R0						
Co/R19						

No effect, Positive effect, Negative effect.

No effect

Positive effect

Negative effect

loading of zirconia for cobalt catalyst apparently enhanced the chain growth probability (C_2–C_4). As a matter of fact, it resulted in the observation of longer chain hydrocarbons even at the specified methanation condition where the high ratio of H_2/CO (10/1) was applied. However, at moderate and high zirconia loading of R0 supports, the selectivity to methane was majority. In order to give a better understanding the effect of zirconia modification of R0 and R19 supports on the activity and selectivity during CO hydrogenation, results are summarized in table 4.

4. Conclusions

In summary, we revealed the effect of zirconia modification in titania supports consisting of different phases on activity and selectivity of cobalt catalysts during CO hydrogenation. It was found that the modification on the R0 (pure anatase phase) supports resulted in decreased activities. However, the chain growth probability (C_2–C_4) was apparently enhanced by the low zirconia loading for the R0 support. In contrary, the increased activities were found for the catalysts consisting of R19 (mixed anatase/rutile phase) with the low and moderate zirconia loading. In addition, the product selectivity of catalysts with modified R19 supports was unchanged upon zirconia modification.

Acknowledgments

We gratefully acknowledge the Thailand Research Fund (TRF), the financial support by the National Research Council of Thailand (NRCT), and Thailand–Japan Technology Transfer Project (TJTTP–JBIC). We would like to thank Prof. James G. Goodwin, Jr. at Clemson University for initiating this kind of project.

References

[1] A. Martinez, C. Lopez, F. Marquez and I. Duaz, J. Catal. 220 (2003) 486.
[2] J. Panpranot, J.G. Goodwin Jr. and A. Sayari, Catal. Today 77 (2002) 269.
[3] J. Panpranot, J.G. Goodwin Jr. and A. Sayari, J. Catal. 211 (2002) 530.
[4] S.L. Sun, I. Isubaki and K. Fujimoto, Appl. Catal. A. 202 (2000) 121.
[5] B. Jongsomjit, J. Panpranot and J.G. Goodwin Jr., J. Catal. 215 (2003) 66.
[6] T. Das, G. Jacobs, P.M. Patterson, W.A. Conner, J.L. Li and B.H. Davis, Fuel 82 (2003) 805.
[7] G. Jacobs, P.M. Patterson, Y.Q. Zhang, T. Das, J.L. Li and B.H. Davis, Appl. Catal. A. 233 (2002) 215.
[8] B. Jongsomjit and J.G. Goodwin Jr., Catal. Today 77 (2002) 191.
[9] B. Jongsomjit, P. Panpranot and J.G. Goodwin Jr., J. Catal. 204 (2001) 98.
[10] J.L. Li, G. Jacobs, T. Das and B.H. Davis, Appl. Catal. A. 233 (2002) 255.
[11] G. Jacobs, T. Das, Y.Q. Zhang, J.L. Li, G. Racoillet and B.H. Davis, Appl. Catal. A. 233 (2002) 263.
[12] J.L. Li, L.G. Xu, R. Keogh and B.H. Davis, Catal. Lett. 70 (2000) 127.
[13] B. Jongsomjit, C. Sakdamnuson, J.G. Goodwin Jr. and P. Praserthdam, Catal. Lett. 94 (2004) 209.
[14] B. Jongsomjit, T. Wongsalee and P. Praserthdam, Mater. Chem. Phys. 92 (2005) 572.
[15] B. Jongsomjit, T. Wongsalee and P. Praserthdam, Catal. Comm. 6 (2005) 705.
[16] J. Panpranot, N. Taochaiyaphum and P. Praserthdam, Mater. Chem. Phys. 94 (2005) 207.
[17] X.H. Li, K. Asami, M.F. Luo, K. Michiki, N. Tsubaki and K. Fujimoto, Catal. Today 84 (2003) 59.
[18] B. Jongsomjit, C. Sakdamnuson and P. Praserthdam, Mater. Chem. Phys. 89 (2005) 395.
[19] S. Ali, B. Chen and J.G. Goodwin Jr., J. Catal. 157 (1995) 35.
[20] F. Rohr, O.A. Lindvag, A. Holmen and E.A. Blekkan, Catal. Today 58 (2000) 247.
[21] R.C. Reuel and C.H. Bartholomew, J. Catal. 85 (1984) 63.
[22] R. Riva, H. Miessuer, R. Vitali and G.D. Piero, Appl. Catal. A. 196 (2000) 111.

Jointly published by
Akadémiai Kiadó, Budapest
and Springer, Dordrecht

React.Kinet.Catal.Lett.
Vol. 87, No. 1, 185-190
(2006)

RKCL4851

EFFECT OF Si ADDITION ON THE PROPERTIES OF NANOCRYSTALLINE ZrO_2-SUPPORTED COBALT CATALYSTS

Joongjai Panpranot*, Nuttakarn Taochaiyaphum and Piyasan Praserthdam

Centre of Excellence on Catalysis and Catalytic Reaction Engineering, Department of Chemical Engineering, Faculty of Engineering, Chulalongkorn University, Bangkok 10330, Thailand

Received August 17, 2005
Accepted September 12, 2005

Abstract

This study shows that Si addition during the glycothermal synthesis of nanocrystalline zirconia modified the properties of the zirconia, *i.e.* particle morphology and crystallite size, resulting in an improvement in the catalytic performance of Co/ZrO_2 catalysts in CO hydrogenation.

Keywords: Nanocrystalline zirconia, Co/ZrO_2, Fischer-Tropsch synthesis

INTRODUCTION

Zirconia is an important material in the areas of ceramics and catalysis. Its catalytic properties are especially promising because zirconia has both acidic and basic properties as well as high thermal stability. For a number of reactions, *i.e.*, Fischer-Tropsch synthesis [1-3], zirconia is used as a catalyst support because high activity and selectivity can be obtained. Enache *et al.* reported that compared to conventional alumina supported Co catalysts, the ones supported on zirconia showed better reducibility and capable of hydrogen adsorption via spillover mechanism. As a catalyst support, high surface area is usually preferred in order to provide a high dispersion of metal. It has been reported that Si-modified zirconia can improve the stability of tetragonal phase zirconia upon thermal treatment and enhance their surface areas. In this study, nanocrystalline zirconia was prepared by the glycothermal technique developed by Inoue *et al.* [4-5] with various amounts of Si addition. By thermal decomposition of zirconium alkoxide in organic solvents, large surface area

*Corresponding author. Phone: 662-2186859; Fax 662-2186877
E-mail: joongjai.p@eng.chula.ac.th

0133-1736/2006/US$ 20.00.

Jointly published by
Akadémiai Kiadó, Budapest
and Springer, Dordrecht

React.Kinet.Catal.Lett.
Vol. 87, No. 1, 185-190
(2006)

RKCL4851

EFFECT OF Si ADDITION ON THE PROPERTIES OF NANOCRYSTALLINE ZrO_2-SUPPORTED COBALT CATALYSTS

Joongjai Panpranot*, Nuttakarn Taochaiyaphum and Piyasan Praserthdam

Centre of Excellence on Catalysis and Catalytic Reaction Engineering, Department of Chemical Engineering, Faculty of Engineering, Chulalongkorn University, Bangkok 10330, Thailand

Received August 17, 2005
Accepted September 12, 2005

Abstract

This study shows that Si addition during the glycothermal synthesis of nanocrystalline zirconia modified the properties of the zirconia, *i.e.* particle morphology and crystallite size, resulting in an improvement in the catalytic performance of Co/ZrO_2 catalysts in CO hydrogenation.

Keywords: Nanocrystalline zirconia, Co/ZrO_2, Fischer-Tropsch synthesis

INTRODUCTION

Zirconia is an important material in the areas of ceramics and catalysis. Its catalytic properties are especially promising because zirconia has both acidic and basic properties as well as high thermal stability. For a number of reactions, *i.e.*, Fischer-Tropsch synthesis [1-3], zirconia is used as a catalyst support because high activity and selectivity can be obtained. Enache *et al.* reported that compared to conventional alumina supported Co catalysts, the ones supported on zirconia showed better reducibility and capable of hydrogen adsorption via spillover mechanism. As a catalyst support, high surface area is usually preferred in order to provide a high dispersion of metal. It has been reported that Si-modified zirconia can improve the stability of tetragonal phase zirconia upon thermal treatment and enhance their surface areas. In this study, nanocrystalline zirconia was prepared by the glycothermal technique developed by Inoue *et al.* [4-5] with various amounts of Si addition. By thermal decomposition of zirconium alkoxide in organic solvents, large surface area

*Corresponding author. Phone: 662-2186859; Fax 662-2186877
E-mail: joongjai.p@eng.chula.ac.th

0133-1736/2006/US$ 20.00.

zirconia can be obtained directly without bothersome procedures such as purification of the reactants or handling in an inert atmosphere. Effect of Si addition in small quantities on the properties and catalytic activities of zirconia supported Co catalysts in Fischer-Tropsch synthesis were investigated.

EXPERIMENTAL

Nanocrystalline zirconia was prepared by the glycothermal method according to the procedure described in ref. [6]. Approximately 15 g of zirconium tetra *n*-propoxide (Strem Chemicals) and a desired amount of tetraethyl orthosilicate was added to 100 mL of 1,4-butanediol. This mixture was placed in a 300 mL autoclave and purged with nitrogen. The mixture was heated to 300°C at a heating rate of 2.5°C/min and held for 2 h. After cooling to room temperature, the resulting powders were collected after repeated washing with methanol. The products were then air-dried. The zirconia supported cobalt catalysts were prepared by incipient wetness impregnation method using aqueous solution of cobalt (II) nitrate hexahydrate (Aldrich). The catalysts were dried overnight at 110°C and calcined in air at 300°C for 2 h. The final cobalt loading was determined using atomic absorption spectroscopy (Varian Spectra A800) to be *ca.* 8 wt.%.

The particle morphology was obtained using a JEOL JSM-35CF scanning electron microscope (SEM) operated at 20 kV. The XRD spectra of the sample powders were measured using a SIEMENS D5000 X-ray diffractometer using Cu K_α radiation with a Ni filter in the 20-80°2θ regions. The TPR profiles of supported cobalt catalysts were obtained by temperature programmed reduction using an in-house system and a temperature ramp of 5°C/min from 30 to 800°C in a flow of 5% H_2 in argon. CO hydrogenation was carried out at 220°C and 1 atm total pressure in a fixed-bed stainless steel reactor. A flow rate of H_2/CO/Ar = 20/2/8 cm^3/min was used. Typically, 0.2 g of the catalyst samples was reduced *in situ* in flowing H_2 (50 cm^3/min) at 350°C for 3 h prior to reaction. The product samples were taken at 1-h intervals and analyzed by gas chromatography.

RESULTS AND DISCUSSION

Figure 1 shows the scanning electron micrographs of Co catalysts supported on ZrO_2 and Si-modified ZrO_2. The catalyst particles appeared as spherical particles which are typical for zirconia prepared by the glycothermal method using 1,4-butanediol as the synthesis medium. However, the Co/ZrO_2 catalyst prepared without Si addition had a narrow particle size distribution with average

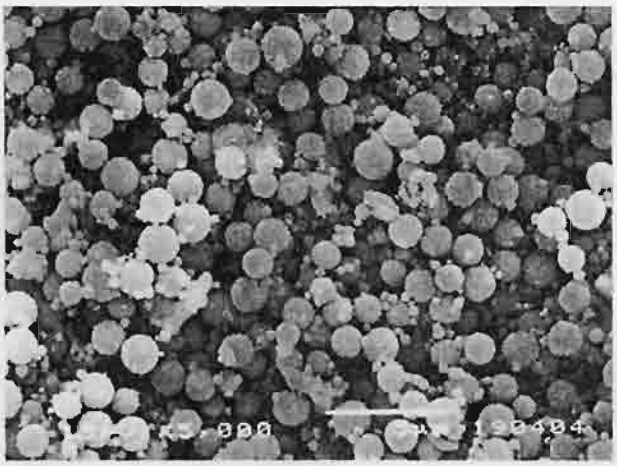

a

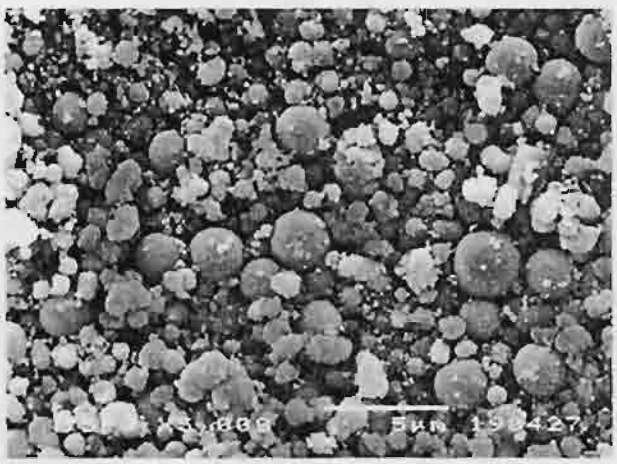

b

Fig. 1. Typical SEM micrographs of the catalyst granules of (a) Co/ZrO_2-0Si and (b) Co/ZrO_2-0.02Si

particle sizes of their primary and secondary particles of 0.4 and 1.2 micron, respectively. The particle size distribution of Co/ZrO_2 catalyst containing silica, on the other hand, was wide suggesting that Si addition altered crystallization of the zirconia. The crystallization mechanism of zirconia during glycothermal synthesis in various glycols can be found in Ref. [7]. It should be noted that the morphologies of the zirconia samples before and after impregnation with 8 wt.% Co were not significantly different due probably to high dispersion of cobalt on the zirconia particles.

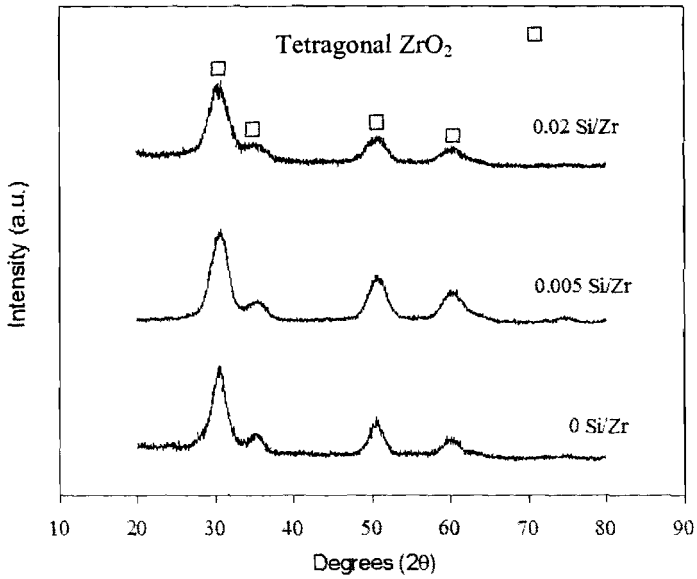

Fig. 2. XRD patterns of Co/ZrO_2 catalysts with various Si/Zr ratios

The XRD patterns of Co/ZrO_2 catalysts with various Si/Zr ratios are shown in Fig. 2. All the samples exhibited tetragonal crystalline zirconia phase. No other crystal structures were observed. The XRD diffraction peaks for cobalt oxide (Co_3O_4, Co_2O_3, or CoO) were not apparent for all the catalyst samples. The results suggest that the crystallite sizes of cobalt oxide on the glycothermal-derived zirconia were probably smaller than the lower limit of XRD detectability (3-5 nm). It is also possible that on glycothermal-derived zirconia, cobalt did not form Co_3O_4 crystallites but may have formed an amorphous cobalt oxide [8]. The average crystallite sizes of tetragonal zirconia were calculated from the X-ray line broadening using Scherrer's equation [9]. It was found that addition of small percentages of Si (0.005 and 0.02 Si/Zr) resulted in a decrease in the crystallite sizes of the tetragonal zirconia from 3.6 nm to 3.1 and 2.8 nm, respectively. It has been reported that the presence of Si-O-Zr bonds in the zirconia powders retarded the crystal growth of zirconia [10]. Modification of surface properties of the zirconia by silica can also be observed by the temperature-program and reduction (TPR) of the Co/ZrO_2 catalysts (Fig. 3). In general, the reduction behavior of supported catalyst is influenced by a wide range of variables such as metal particle size and metal-support

interaction. The TPR profiles of the Si-modified ZrO_2 supported Co catalysts were different from that of the ZrO_2 without Si addition supported one in which the reduction peaks tended to shift to lower temperatures. Therefore, cobalt oxides on the Si-modified ZrO_2 supports reduced easier to Co^0 metal which is

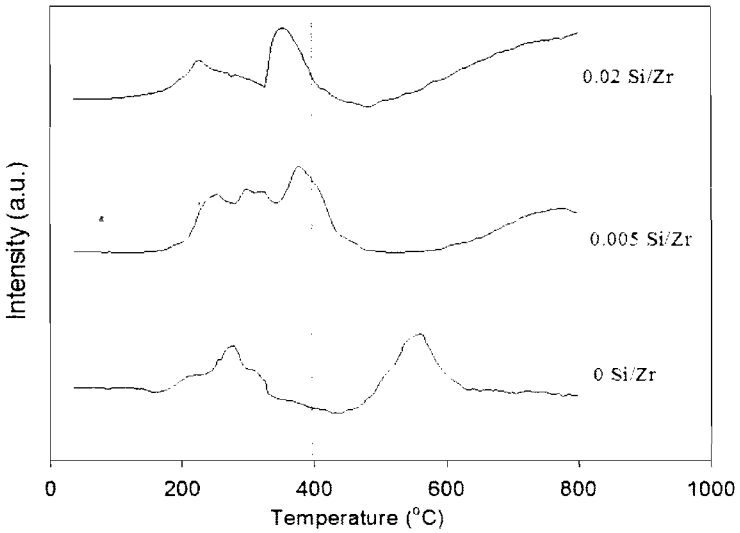

Fig. 3. TPR profiles of Co/ZrO_2 catalysts with various Si/Zr ratios

known to be the active phase for CO hydrogenation reaction. The Co/ZrO_2 catalysts were tested for catalytic activity in CO hydrogenation reaction under methanation conditions (H_2/CO = 10) in order to minimize the catalyst deactivation due to coke formation. It was found that the activities of Co/ZrO_2 catalysts increased with increasing amount of silica addition. The CO hydrogenation rates were 1.6, 2.1, and 3.0 g CH_2 g $cat^{-1}h^{-1}$ for the catalysts with 0, 0.005, and 0.02 Si/Zr, respectively. As expected, the selectivities for longer chain hydrocarbons (C_{4+}) decreased from 59.1 to 37.1% when the activities increased resulting in an increase in methane selectivities (from 29.5 to 59.4%).

Acknowledgements. The financial supports from the Thailand Japan Technology Transfer Project (TJTTP-JBIC) and the Thailand Research Fund (TRF) are gratefully acknowledged.

REFERENCES

1. G.K. Chuah: *Catal. Today*, **49**, 131 (1999).
2. L. Bruce, J. F. Mathews: *Appl. Catal.*, **4**, 353 (1982).
3. D.I. Enache, M. Roy-Auberger, R. Revel: *Appl. Catal. A.*, **268**, 51 (2004).
4. M. Inoue, H. Kominami, T. Inui: *Appl. Catal.*, **97**, 125, (1993).
5. M. Inoue, H. Kominami, T. Inui: *Catal. Lett.*, **65**, 79 (2000).
6. S. Kongwudthiti, P. Praserthdam, M. Inoue, W. Tanakulrungsank: *J. Mater. Sci. Lett.*, **21**, 1461 (2002).
7. S. Kongwudthiti, P. Praserthdam, P.L. Silveston, M. Inoue: *Ceramics International*, **29**, 807 (2003).
8. M. Kraum, M. Baerns: *App. Catal.*, **186**, 189 (1999).
9. H.P. Klug, L.E. Alexander: *X-ray diffraction procedures for polycrystalline amorphous materials*, 2nd ed. Wiley, New York 1974.
10. S. Kongwudthiti, P. Praserthdam, W. Tanakulrungsank, M. Inoue: *J. Mater. Proc. Tech.*, **136**, 186 (2003).

Available online at www.sciencedirect.com
SCIENCE DIRECT
Applied Catalysis A: General 303 (2006) 268–272
APPLIED CATALYSIS A: GENERAL
www.elsevier.com/locate/apcata

A study of alumina–zirconia mixed oxides prepared by the modified Pechini method as Co catalyst supports in CO hydrogenation

Soipatta Soisuwan [a], Joongjai Panpranot [a], David L. Trimm [b], Piyasan Praserthdam [a,*]

[a] *Centre of Excellence on Catalysis and Catalytic Reaction Engineering, Department of Chemical Engineering, Faculty of Engineering, Chulalongkorn University, Bangkok 10330, Thailand*

[b] *School of Chemical Engineering and Industrial Chemistry, University of New South Wales, Sydney NSW 2052, Australia*

Received 22 September 2005; received in revised form 1 February 2006; accepted 6 February 2006
Available online 22 March 2006

Abstract

In this study, the modified Pechini method has been used to prepare alumina–zirconia mixed oxides with 0.5, 1, 25, 40, and 75 mol% of alumina in zirconia. At low Al contents (<25%), tetragonal phase zirconia was observed, while at higher Al contents, the mixed oxide exhibited only amorphous phase. When they were employed as supports for Co catalyst for CO hydrogenation, it was found that the catalytic activities of low Al-modified zirconia supported Co catalysts increased by ca. 30% compared to the ones supported on pure zirconia or pure alumina, suggesting that the modification of zirconia by alumina has resulted in higher Co dispersion. However, when supports with high alumina contents (40–75 mol% Al) were used, low Co dispersion and poor catalytic performance were obtained despite their higher surface areas. It is likely that cobalt formed metal support compounds with the amorphous phases of these mixed oxides.

Keywords: Nano-crystalline zirconia; Alumina–zirconia mixed oxides; CO hydrogenation; Cobalt catalysts

1. Introduction

Mixed metal oxides, widely used in ceramic applications, are usually prepared by sol–gel technique, because the method requires lower temperatures compared to conventional ceramic mixing processes and it improves dispersion and homogeneity [1]. Different precursors have been used to prepare sol–gel materials, particularly metal alkoxides [2–4] and citric acid complexes [5,6]. Materials obtained from both precursors are quite similar but gel formation is approached under different conditions. Zirconia prepared by sol–gel method, however, usually possesses low surface area. Recently, it has been reported that solid powders were successfully prepared by the modified Pechini method [7,8], in which citric acid and ethylene glycol are polymerised around metal ions. Because of homogeneous starting solution, this technique leads to closer combination of mixed oxides, which may enhance strong interaction between metal ions. Moreover, high surface area of solid powders is usually obtained by this method, which could bring about high dispersion of metal loading and consequently highly active sites for catalytic reactions [8]. In this study, the modified Pechini method was used to prepare alumina, zirconia, and alumina–zirconia mixed oxides. Zirconia toughened alumina is generally employed in ceramic applications because of its well-known mechanical properties. Moreover, it has recently been introduced in medical application as a biocompatible nano-composite [9]. In catalytic reactions, alumina–zirconia mixed oxide has been used as catalyst and/or support because of its surface property, stability, and mechanical property. Modification of the mixed oxide by sulfate is also well known and has shown very good activity for isomerisation [10].

In this study, alumina–zirconia mixed oxides were prepared by the modified Pechini method with different alumina/zirconia mole ratios and the mixed oxides were employed as Co catalyst supports. The influence of the modification of surface properties of zirconia by alumina on the characteristics of the mixed oxide supported cobalt catalysts were investigated by mean of nitrogen physisorption, X-ray diffraction, H_2 chemisorption, and temperature-programmed reduction. The catalyst performances were tested in CO hydrogenation reaction at 220 °C and 1 atm.

* Corresponding author. Tel.: +66 3 8745900x3350; fax: +66 3 8745806.
E-mail address: piyasan.p@chula.ac.th (P. Praserthdam).

0926-860X/$ – see front matter © 2006 Elsevier B.V. All rights reserved.
doi:10.1016/j.apcata.2006.02.011

2. Experimental

2.1. Catalyst preparation

Alumina, zirconia, and alumina–zirconia mixed oxides were prepared using the modified Pechini method in the same manner as that of Refs. [7–11] with different amounts of alumina in zirconia at 0.5, 1, 25, 40, 75, and 100 mol%. Aluminium nitrate ($Al(NO_3)_3{\cdot}9H_2O$, Aldrich) and zirconyl nitrate ($ZrO(NO_3)_2{\cdot}xH_2O$, Aldrich) aqueous solutions were used as starting materials of alumina and zirconia. Both of the solutions were very acidic at a pH ca. 1. Citric acid (UNIVAR) and ethylene glycol (UNILAB) were employed in this method as chelating chemical and polymerizing agent, respectively. In order to obtain the alumina–zirconia mixed oxides, we introduced a desired amount of aluminium nitrate solution was introduced into zirconyl nitrate solution without precipitation. Citric acid [CA] aqueous solution was subsequently added to the solution at a molar ratio of [Al + Zr:CA] = 1:30 to form metal citrate complexes. Prior to addition of the citric acid solution and ethylene glycol [EG], 10 ml of 35% nitric acid solution was provided to adjust the pH conditions to be lowered to ca. 1 before mixing into the metal nitrate solution to avoid precipitation. The ethylene glycol was used at a molar ratio of EG/CA = 7:30. The mixed solution was heated to 70 °C and held at that temperature for 3 days until the volume of the solution was decreased by one-fourth of the starting solution volume. The nitric molecules were decomposed at the boiling conditions as observed from brownish exhausted gases when the solution was heated up to 100 °C. The solution spontaneously became a transparent gel when the temperature approached 120 °C. The gel was calcined at 600 °C for 6 h in dynamic air to remove the organic materials, resulting in a spongy white powder. The obtained powders were employed as supports for cobalt catalysts. $Co(NO_3)_2{\cdot}6H_2O$ (Aldrich) was dissolved in deionized water and impregnated into the support using the incipient wetness impregnation method to give a final catalyst with 8 wt% cobalt. The catalysts were dried at 100 °C for 12 h and calcined in air at 350 °C for 2 h in order to eliminate residual $Co(NO_3)_2$ [12].

2.2. Characterization of the catalysts

The BET surface areas were determined by N_2 physisorption using a Micromeritics ASAP 2020. Each sample was degassed in the system at 300 °C for 3 h prior to N_2 physisorption. A SIEMENS D5000 X-ray diffractometer using Cu Kα radiation with Ni filter in the 10–80° 2θ angular regions was employed to obtain XRD spectra of the sample powders. Referring to the procedures described by Reuel and Bartholomew [13], we carried out H_2 chemisorption by using a Micromeritics Pulse Chemisorb 2750 system. Approximately 0.2 g of each catalyst was reduced at 350 °C after ramping at a rate of 1 °C min^{-1} and the combination was held at that temperature for 3 h. The pulse hydrogen chemisorption was performed at 100 °C. The TPR profiles of supported cobalt catalysts were obtained by temperature programmed reduction using an in-house system and a temperature ramp of 5 °C min^{-1} from 35 to 800 °C in a flow of 3% H_2 in argon. The H_2 consumption was measured by analyzing the effluent gas with a thermal conductivity detector. The reducibility of each catalyst was estimated from the peak areas under the TPR curves, which were calculated using a PeakFit software program version 4.12 with Auto-Fit options.

2.3. Catalytic activity test

CO hydrogenation was carried out in a fixed-bed stainless steel reactor at 220 °C and 1 atm total pressure. A flow rate of $CO/H_2/Ar$ 4/40/16 cm^3 min^{-1} was used. Typically, 0.10 g of the catalyst was reduced in situ in flowing hydrogen (30 cm^3 min^{-1}) at 350 °C for 2 h prior to reaction. The effluent gases were taken at 20 min and 1 h intervals and were analyzed by GC. In all cases, the reaction approached steady state within 6 h.

3. Result and discussions

3.1. Effect of alumina content on the properties of alumina–zirconia mixed oxides

The XRD spectra of the alumina–zirconia mixed oxide powders prepared by the modified Pechini method are shown in Fig. 1. It was found that pure zirconia and Al-modified zirconia samples prepared with 0.5–1 mol% Al content exhibited pure tetragonal phase of zirconia, whereas the ones prepared with higher-in-alumina contents of 25–100 mol% were completely amorphous. Such results suggest that the orientations of alumina and zirconia structures were affected by good dispersion of alumina and zirconia mixed oxides under these preparation conditions. In general, the tetragonal phase zirconia is thermodynamically stable at a temperature above 1170 °C [14]. However, according to the work reported by Garvie [15], the energy from combustion of the polymeric material during calcination at 600 °C was probably sufficient to arrange the crystal structure in tetragonal form with crystal size less than its critical size. The crystallite sizes calculated from Scherrer's equation using 202 diffraction peaks of tetragonal peak and the BET surface areas of the same samples are reported in Table 1.

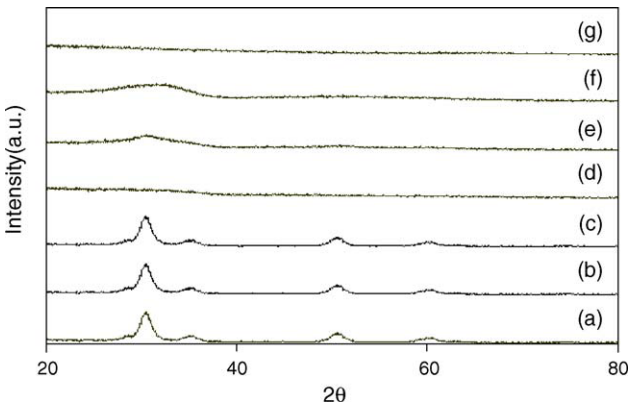

Fig. 1. The XRD patterns of the supports: (a) ZrO_2, (b) Al0.5–ZrO_2, (c) Al1–ZrO_2, (d) Al25–ZrO_2, (e) Al40–ZrO_2, (f) Al75–ZrO_2, and (g) Al_2O_3.

Table 1
Characteristics of alumina–zirconia mixed oxides

Supports	BET surface area of support ($m^2\ g^{-1}$)	Crystal size[a] (nm)	Phase Identification of Zirconia (from XRD)
ZrO_2	56	6	Tetragonal
Al0.5–ZrO_2	68	6	Tetragonal
Al1–ZrO_2	65	7	Tetragonal
Al25–ZrO_2	70	–	Amorphous
Al40–ZrO_2	182	–	Amorphous
Al75–ZrO_2	228	–	Amorphous
Al_2O_3	319	–	–

[a] Calculated from XRD broadening peak at 2θ ca. 30.8°.

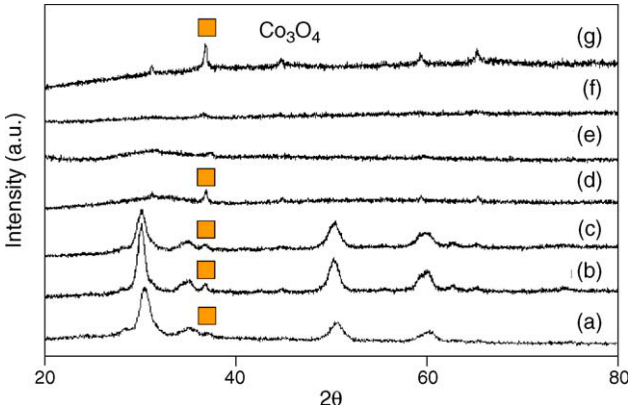

Fig. 2. The XRD patterns the catalysts: (a) 10%Co/ZrO_2, (b) 10%Co/Al0.5–ZrO_2, (c) 10%Co/Al1—ZrO_2, (d) 10%Co/Al25–ZrO_2, (e) 10%Co/Al40–ZrO_2, (f) 10%Co/Al75–ZrO_2, and (g) 10%Co/Al_2O_3.

The average crystallite sizes of the zirconia and the Al-modified zirconia were approximately 6–7 nm. The BET surface areas of support samples were found to be ca. 50–300 $m^2\ g^{-1}$. It has been reported that introducing a small amount of alumina (<5%) into zirconia can stabilize the porous structure of the zirconia [16]. A significant increase in BET surface areas was observed for the alumina–zirconia mixed oxides prepared with high alumina contents. Under these preparation conditions (40–75 mol% Al), zirconia may have been introduced into the alumina matrix; thus the powders possessed high surface areas of alumina.

3.2. The physicochemical properties and performances of alumina–zirconia mixed oxide supported cobalt catalysts

The X-ray diffraction patterns of Co/Al*x*–ZrO_2 (*x* = mol% of alumina), Co/Al_2O_3, and Co/ZrO_2 catalysts are shown in Fig. 2. The XRD characteristic peak of Co_3O_4 at 2θ of ca. 36.8° was observed for all the catalyst samples except Co/Al40–ZrO_2 and Co/Al75–ZrO_2. The crystallite size of cobalt oxide on those supports was probably below the limit of XRD detectability (3–5 nm) and/or cobalt did not form Co_3O_4 crystallites on Co/Al40–ZrO_2 and Co/Al75–ZrO_2 but existed in the amorphous form [17]. The average crystallite sizes of Co_3O_4 derived from X-ray line broadening using Scherrer's equation were 8–19 nm and the sizes increased with increasing amount of alumina content. The BET surface areas, the reducibility, the amounts of H_2 chemisorption, and %cobalt dispersion are reported in Table 2. Surface areas of the supported cobalt catalysts were found to be slightly less than that of the original supports, thus cobalt appears to have been in some the pores of the support. The impact of high surface area of alumina on the BET surface areas of the mixed oxide supported Co catalysts were observed only for Co/Al40–ZrO_2 and Co/Al75–ZrO_2 thus at low alumina contents (<25 mol%), the modification of zirconia properties was not due to the changes in BET surface areas. It was found that H_2 chemisorption and %Co dispersion of these low alumina content oxide supported Co catalysts were higher than those of Co/ZrO_2 and Co/Al_2O_3. The surface properties of zirconia were probably modified by the alumina, resulting in high amounts of active surface cobalt being measured by H_2 chemisorption. Surprisingly, for the higher alumina contents, Co/Al40–ZrO_2 and Co/Al75–ZrO_2, despite their relatively high surface areas, exhibited low H_2 chemisorption and Co dispersion. The interaction of cobalt oxide species and the supports was further investigated by means of temperature-programmed reduction (TPR).

TPR profiles of all the catalysts are shown in Fig. 3. Reduction of cobalt in the oxide form, Co_3O_4 or CoO, to Co^0 involves a two-step reduction: first reduction of Co_3O_4 to CoO and then the subsequent reduction of CoO to Co^0 [18,19]. A

Table 2
Physicochemical properties of co catalysts supported on alumina–zirconia mixed oxides

Sample	BET surface area of the catalyst ($m^2\ g^{-1}$)	Hydrogen chemisorption (molecules g^{-1} cat.$^{-1}$) $\times 10^{18}$	Reducibility[a] (%)	Crystal size of Co_3O_4 (nm)[b]	Co dispersion (%)
Co/ZrO_2	34	8.3	47	8	34
Co/Al0.5–ZrO_2	41	10.3	36	11	56
Co/Al1–ZrO_2	39	10.3	38	10	53
Co/Al25–ZrO_2	42	10.3	37	19	55
Co/Al40–ZrO_2	109	3.2	17	n.d.[c]	37
Co/Al75–ZrO_2	137	1.5	12	n.d.[c]	25
Co/Al_2O_3	191	8.5	48	19	35

[a] Calculated from reducibility (%) $= \dfrac{\text{The amount of hydrogen used to reduce 1 g of the catalyst} \times 100}{\text{The theoretical hydrogen amount needed to reduce 1 g of the catalyst}}$.

[b] Calculated from XRD broadening peak at 2θ ca. 36.8°.

[c] n.d., not detected.

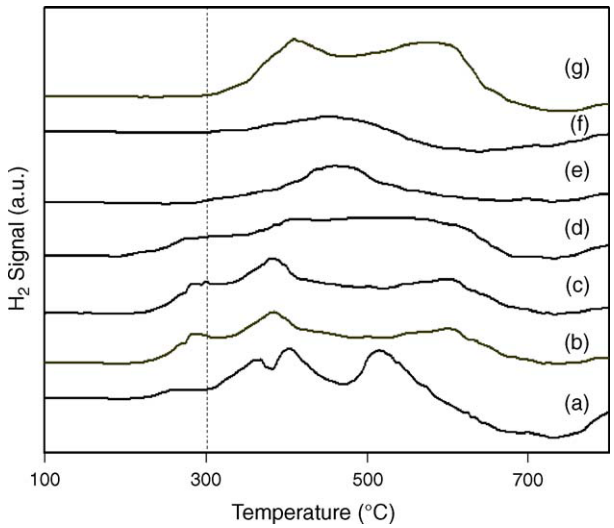

Fig. 3. Influence of alumina–zirconia support on the reduction behavior of the cobalt catalysts: (a) 10%Co/ZrO_2, (b) 10%Co/Al0.5–ZrO_2, (c) 10%Co/Al1–ZrO_2, (d) 10%Co/Al25–ZrO_2, (e) 10%Co/Al40–ZrO_2, (f) 10%Co/Al75–ZrO_2, and (g) 10%Co/Al_2O_3.

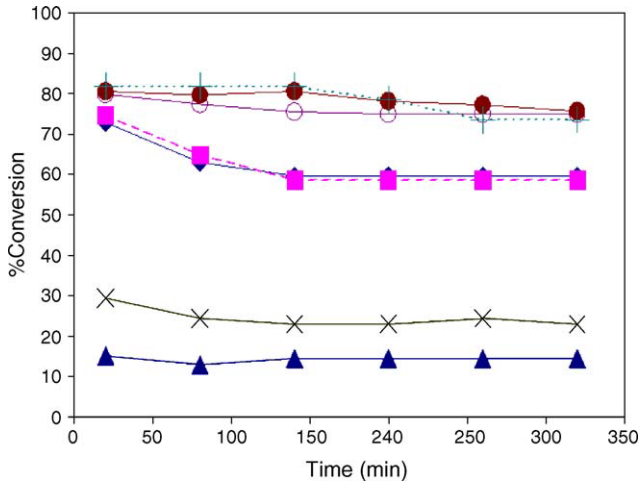

Fig. 4. Typical time-on-stream behavior of the catalyst samples in the CO-hydrogenation: (◆) Co/ZrO_2, (■) Co/Al_2O_3, (●) Co/Al0.5–ZrO_2, (+) Co/Al1–ZrO_2, (○) Co/Al25–ZrO_2, (×) Co/Al40–ZrO_2, and (▲) Co/Al75–ZrO_2.

wide range of variables, such as metal particle size and metal–support interaction, have an influence on the reduction behavior of cobalt catalysts, resulting in the observation of different locations of the TPR peaks [20,21]. It was found that, for the Co catalyst supported on the mixed oxides with low alumina content (<25%), the reduction peaks below 400 °C shifted slightly to low temperatures, whereas the Al40–ZrO_2 and Al75–ZrO_2-supported ones exhibited only a single reduction peak at temperatures higher than 400 °C. The higher reduction peak may be attributed to formation of non-reducible phases, i.e. cobalt–aluminate [20,21] and cobalt–zirconate [22,23].

The reducibilities of all the alumina–zirconia mixed oxide supported catalysts during TPR 30–800 °C were found to be lower than those of Co/ZrO_2 and Co/Al_2O_3. Such results suggest that the surface properties of the mixed oxide-supported catalysts were different from those of the pure oxide. Furthermore, it was found that Co/Al40–ZrO_2 and Co/Al75–ZrO_2 exhibited distinctly low reducibilities (12–17%). In the XRD results, only amorphous phase was observed and no XRD peaks for Co_3O_4 were found on these samples. It is likely that amorphous forms of alumina and zirconia caused formation of cobalt–aluminate and/or cobalt–zirconate by combining unreduced cobalt oxides with amorphous alumina and/or amorphous zirconia [22,23]. It should, however, be noted that the reducibility of pure amorphous alumina supported Co catalyst was similar to that of tetragonal zirconia-supported catalyst. Although cobalt aluminate compounds can be formed on the amorphous alumina surface as suggested for Al40–ZrO_2 and Al75–ZrO_2 supported catalysts, some large cobalt oxide crystallites were found on amorphous alumina so that the higher reducibility was obtained.

Fig. 4 displays the time-on-stream behaviors of the mixed oxides supported Co catalysts during CO hydrogenation. In all cases, the steady state was reached within 2 h of run. The catalytic activity and the product selectivity of all the catalysts in CO hydrogenation are given in Table 3. There was no significant difference in the product selectivities since, under the reduction conditions used, all the catalysts exhibited methane selectivities ca. 95–99%. The CO hydrogenation rates of the mixed oxide-supported cobalt catalysts prepared with low alumina contents (0.5, 1, and 25 mol%) increase by 30% at steady state compared to those of Co/ZrO_2 and Co/Al_2O_3 even though their reducibilities were slightly lower. The 0.5–25 mol% Al-modified zirconia supports may have a positive

Table 3
Results of CO hydrogenation reaction

Sample	Product selectivity (%)			Rate of CO hydrogenation (mmol of $-CH_2-$ g^{-1} s^{-1})[a]		TOF (s^{-1})	
	C_1	C_2–C_3	C_4–C_{4+}	Initial	Final	Initial	SS
Co/ZrO_2	94.4	4.8	0.7	22	18	0.79	0.65
Co/Al0.5–ZrO_2	99.3	0.7	0.0	24	23	0.79	0.71
Co/Al1–ZrO_2	98.8	1.1	0.1	24	22	0.79	0.74
Co/Al25–ZrO_2	98.9	1.1	0.0	24	22	0.70	0.65
Co/Al40–ZrO_2	95.4	4.5	0.1	9	7	0.83	0.64
Co/Al75–ZrO_2	96.7	3.3	0.0	5	4	0.92	0.87
Co/Al_2O_3	99.3	0.7	0.0	22	17	0.79	0.62

[a] Refers to the unit of CO hydrogenation rate per gram catalyst.

influence on a phase dispersion of cobalt oxide and active metallic phases derived from the Co_3O_4 particles. Enache et al. [23] proposed a relation between the degree of crystallization of Co_3O_4 particles and the types of cobalt active phase after hydrogen reduction, i.e. crystalline metallic cobalt derived from the crystalline Co_3O_4 particles and poor crystalline metallic cobalt derived from the amorphous Co_3O_4 particles. The catalyst that consisted of poorly crystalline metallic cobalt appeared to be more catalytic-active than the one with more perfect crystalline metallic cobalt. It is possible that the surface properties of zirconia modified by low amount of alumina resulted in high dispersion of active metallic cobalt phase, so that high CO hydrogenation activities were obtained.

4. Conclusions

Alumina–zirconia mixed oxide supports with various mol% of alumina prepared by the modified Pechini method exhibited interesting properties when employed as Co catalyst supports in CO hydrogenation. For the low alumina contents (i.e. 0.5–25 mol%), alumina modified the surface properties of zirconia leading to high dispersion of cobalt and high performance in CO hydrogenation reaction. However, for higher alumina contents (i.e. 40 and 75 mol%), the catalysts showed much lower Co dispersion and CO hydrogenation activities, due probably to compound formation from cobalt and amorphous alumina/zirconia.

Acknowledgements

The financial supports by the Thailand Research Fund (TRF), TJTTP-OECF, and the Graduate School of Chulalongkorn University are gratefully acknowledged. The authors also would like to thank the Cooperative Research Network of the Thai Ministry of Education for the scholarship for P.S.

References

[1] G. Ertl, H. Knözinger, J. Weitkamp, Handbook of Heterogeneous Catalysis, Wiley-VCH, 1997.
[2] J.C. Debsikdar, J. Non-Cryst. Solids 86 (1986) 231.
[3] R. Guinebretière, A. Dauger, A. Lecomte, H. Vesteghem, J. Non-Cryst. Solids 147–148 (1992) 542.
[4] J. Livage, F. Beteille, C. Roux, M. Chatry, P. Davidson, Acta Mater. 46 (1998) 743.
[5] M. Ishii, M. Kakihana, K. Ishii, Y. Ikuma, M. Yoshimura, J. Mater. Res. Soc. 11 (6) (1996) 1410.
[6] M. Kakihana, S. Kato, M. Yashima, M. Yoshimura, J. Alloys Compd. 280 (1998) 125.
[7] M.P. Pechini, Patent, 3,330,697, 11 July, 1967.
[8] C.L. Robert, F. Ansart, C. Deloget, M. Gaudon, A. Rousset, Ceram. Int. 29 (2003) 151.
[9] Y.M. Kong, C.J. Bae, S.H. Lee, H.W. Kim, H.E.A. Kim, Biomaterials 26 (2005) 509.
[10] I.I. Abu, D.D. Das, H.K. Mishra, A.K. Dalai, J. Colloid Interface Sci. 267 (2003) 382.
[11] C.L. Robert, F. Ansart, C. Deloget, M. Gaudon, A. Rousset, Ceram. Int. 29 (2003) 151.
[12] A. Lapidus, A. Krylova, V. Kazanskii, Z. Borovkov, A. Zaitsev, Appl. Catal. A 73 (1991) 65.
[13] R.C. Reuel, C.H. Bartholomew, J. Catal. 85 (1984) 78.
[14] P.D.L. Mercera, J.G. van Ommen, E.B.M. Doesburg, A.J. Burggraaf, J.R.H. Ross, Appl. Catal. 71 (1991) 363.
[15] R.C. Garvie, J. Phys. Chem. 82 (1978) 218.
[16] O. Metelkina, N. Hüsing, P. Pongrazt, U. Schubert, J. Non-Cryst. Solids 285 (2001) 64.
[17] M. Kraum, M. Baerns, Appl. Catal. 186 (1999) 189.
[18] D. Schanke, S. Vada, E.A. Blekkan, A. Hilmen, A. Hoff, A. Holmen, J. Catal. 156 (1995) 85.
[19] Y. Zhang, D. Wei, S. Hammache, J.G. Goodwin Jr., J. Catal. 188 (1999) 281.
[20] J. Panpranot, J.G. Goodwin Jr., A. Sayari, Catal. Today 77 (2002) 269.
[21] D. Potoczna-Petru, L. Kepinski, Catal. Lett. 73 (1) (2001) 43.
[22] D.I. Enache, B. Rebours, M. Roy-Auberger, R. Revel, J. Catal. 205 (2002) 346.
[23] D.I. Enache, M. Rohy-Auberger, R. Revel, Appl. Catal. A 268 (2004) 51.

Available online at www.sciencedirect.com
ScienceDirect
Catalysis Communications 7 (2006) 761–767
CATALYSIS COMMUNICATIONS
www.elsevier.com/locate/catcom

Effects of Si- and Y-modified nanocrystalline zirconia on the properties of Co/ZrO_2 catalysts

Patta Soisuwan [a], Piyasan Praserthdam [a], Joongjai Panpranot [a,*], David L. Trimm [b]

[a] *Centre of Excellence on Catalysis and Catalytic Reaction Engineering, Department of Chemical Engineering, Phayathai Road, Faculty of Engineering, Chulalongkorn University, Bangkok 10330, Thailand*
[b] *School of Chemical Engineering and Industrial Chemistry, University of New South Wales, Sydney NSW 2052, Australia*

Received 7 July 2005; received in revised form 9 November 2005; accepted 9 November 2005
Available online 17 April 2006

Abstract

Nanocrystalline zirconia and m-modified zirconia (m = Si and Y) have been prepared by the modified Pechini's method and employed as supports for cobalt catalysts. Addition of a small amount of Si or Y during the preparation of nanocrystalline zirconia did not alter the average crystallite sizes and BET surface areas of the tetragonal zirconia. However, zirconia primary particles appeared to be more agglomerated when Si/Zr and Y/Zr were greater than 0.005 and 0.01, respectively. The Si- and Y-modified zirconia supported cobalt catalysts with higher m/Zr showed higher H_2 chemisorption and CO hydrogenation activities.

Keywords: Nanocrystalline zirconia; Y-modified ZrO_2; Si-modified ZrO_2; CO hydrogenation; Cobalt catalyst

1. Introduction

During recent years zirconia has received much attention from researchers in the field of heterogeneous catalysis as a support material as well as a catalyst because it is more chemically inert than the classical supports (e.g., γ-alumina and silica) and it may possess different chemical properties such as acidity, basicity, reducing, or oxidizing ability [1]. Use of zirconia as a catalyst support has shown promising results in many environmental catalysis reactions such as CO_2 hydrogenation [2], CO oxidation [3], and the Fischer–Tropsch reaction [4–7]. Enache et al. [6] reported that the use of zirconium oxide as support in the Fischer–Tropsch synthesis leads to better reducibility of the active phase, hydrogen spillover, and higher CO conversions compared to those of γ-alumina-supported ones. In a recent work from our group, we reported that cobalt catalysts supported on nanocrystalline tetragonal zirconia prepared by solvothermal method exhibited superior CO hydrogenation activities than those of commercial zirconia supported ones [8].

It has been reported that addition of a small amount of second metals such as silicon [9,10], yttrium [11–13], lanthanum [14] and silicotungstate [15] can improve thermal stability of tetragonal phase zirconia. For examples, silica-modified zirconia obtained by the reaction of mixture of zirconium *n*-propoxide and tetraethyl orthosilicate in 1,4-butanediol at 300 °C had large surface area and high stability of tetragonal phase even after calcination at high temperatures [8]. To our knowledge, the effect of Si- or Y-modified zirconia on the properties of zirconia supported catalysts, i.e., Co/ZrO_2 has never been studied. In this article, we reported the synthesis of nanocrystalline zirconia by modified Pechini's method and their applications as cobalt catalyst supports. The modified Pechini's method is known to be a successful method for production of solid powders by polymerization of citric acid and ethylene glycol around metal ions [16]. Due to high surface areas, the obtained materials could bring about high dispersion of metal loading and consequently high active sites for

* Corresponding author. Tel.: +66 2 218 6859/6878; fax: +66 2 218 6869/6877.
E-mail address: Joongjai.p@eng.chula.a.th (J. Panpranot).

1566-7367/$ - see front matter © 2005 Elsevier B.V. All rights reserved.
doi:10.1016/j.catcom.2005.11.013

catalytic reactions. The catalysts were characterized by N_2 physisorption, XRD, H_2 chemisorption, TPR, TEM, SEM, and tested for catalytic activity in CO hydrogenation reaction.

2. Experimental

2.1. Preparation of Si- and Y-modified nanocrystalline zirconia

Nanocrystalline zirconia was prepared using the modified Pechini's method described in [16]. The Si- and Y-modified zirconia were prepared by adding a small amount of TEOS (tetraethylorthosilicate, Aldrich) and $Y(NO_3)_3 \cdot xH_2O$ (Aldrich) into the solution of $ZrO(NO_3)_2 \cdot xH_2O$ (Aldrich) 0.06 mole in 150 ml distilled water, respectively. The molar ratios of Si/Zr and Y/Zr calculated were in the range 0.001–0.02. A modified pH citric acid (UNIVAR) solution was prepared by adding 10 ml of 35% by volume nitric acid to 150 ml 2.8 M citric acid. The modified pH citric acid solution was then mixed with the precursor solution. Finally, ethylene glycol adjusted pH by 10 ml of the nitric acid was added. The mixed solution was heated to 70 °C and held at that temperature for 3 days until volume of the solution was decreased by 1/4 of the starting solutions. The solution started boiling when heated up to 100 °C. The nitrate molecules were decomposed at the boiling conditions as observed from brownish exhausted gases. When the temperature was increased to 120 °C, the solution became transparent gel. The gel was calcined at 600 °C for 6 h in dynamic air to remove the organic materials resulting in spongy white powder. The obtained powders were used as supports for cobalt catalysts. $Co(NO_3)_2 \cdot 6H_2O$ (Aldrich) was dissolved in deionized water and impregnated into the support using the incipient wetness to give a final catalyst with 10 wt% cobalt. The catalysts were dried at 100 °C for 12 h and calcined in air at 350 °C for 2 h.

2.2. Catalyst characterization

Phase identification and crystallite size of pure and modified nanocrystalline zirconia were investigated by X-ray diffraction (Siemens D5000) using Ni filter Cu Kα radiation from 20° to 80° 2θ. Crystallite size was calculated from the Scherrer's equation using 202 diffraction peak of tetragonal zirconia as follows

$$D = 0.9\lambda/\beta\cos\theta$$

where D is the crystallite size in nm, λ is the radiation wavelength, β is corrected half-width of the peak profile, and θ is the diffraction peak angle. Surface areas of the samples were measured by the single point BET method. The sample was pretreated at 200 °C in 21 cc/min Helium for 2 h and saturated with 9 cc/min Nitrogen for 30 min at temperature of liquid Nitrogen. Nitrogen desorption profile was reported by TCD signal and integrated area under the profile was used to calculate approximately surface area. Pulse hydrogen chemisorption was carried out to determine the cobalt active sties using a Micromeritic Chemisorb 2750. Prior to hydrogen chemisorption, the samples were reduced in situ at 350 °C for 3 h. The TPR profiles of supported cobalt catalysts were obtained by temperature programmed reduction using an in-house system and a temperature ramp of 5 °C/min from 35 to 800 °C in a flow of 3% H_2 in argon. Approximately 0.10 g of a calcined catalyst was placed in a quartz tube in a temperature-controlled oven and connected to a thermal conductivity detector (TCD). The H_2 consumption was measured by analyzing the effluent gas with a thermal conductivity detector.

2.3. Reaction study

CO hydrogenation was carried out in a down-flow fixed bed stainless steel reactor at 220 °C and 1 atm total pressure. A WSHV of ca. 4500 h^{-1} and a H_2/CO ratio of 10 were used. Typically, 0.10 g of the catalyst was reduced in situ in flowing hydrogen (30 cc/min) at 350 °C for 2 h prior to reaction. The effluent gases were taken at 20 min and 1 h interval and were analyzed by a GC. In all cases, the reaction approached steady state within 6 h. The percentages of CO conversion, reaction rates, and turnover frequencies were defined as:

$$\%\text{CO conversion} = \frac{\text{mole of CO in feed} - \text{mole of CO in products}}{\text{mole of CO in feed}} \times 100$$

$$\text{Reaction rate } (\text{gCH}_2\text{g cat.}^{-1}\ \text{h}^{-1}) = \frac{\%\text{CO conversion} \times \text{flowrate of CO in feed(cc/min)} \times 60(\text{min/h}) \times \text{mol. wt. of CH}_2\text{(g/mole)}}{\text{catalyst weight(g)} \times 22,400(\text{cc/mole})}$$

Turnover frequencies (TOFs) were determined based on the amount of Co^0 active site measured by H_2 chemisorption.

$$\text{TOF} = \frac{\text{rate}}{\text{site. time}}$$

3. Results and discussion

3.1. Effect of Si and Y additions on the properties of ZrO_2

The X-ray diffraction patterns of the zirconia and modified zirconia powders prepared by the modified Pechini's

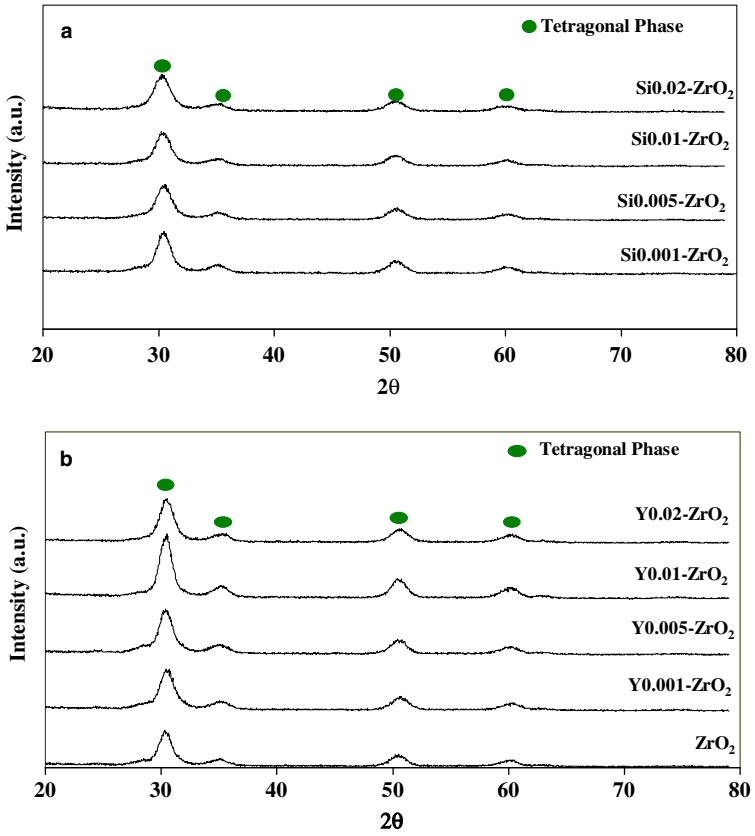

Fig. 1. X-ray diffraction results of (a) Si-doped ZrO_2 and (b) Y-doped ZrO_2.

Table 1
Crystallite sizes and BET surface areas of Si- and Y-doped zirconia

Sample	Avg. crystallite size (nm)[a]	BET surface area[b] (m^2/g)
ZrO_2	6.3	90.4
Si0.001–ZrO_2	6.2	95.2
Si0.005–ZrO_2	5.3	83.1
Si0.01–ZrO_2	5.9	86.4
Si0.02–ZrO_2	5.2	92.1
Y0.001–ZrO_2	5.9	93.1
Y0.005–ZrO_2	6.1	94.5
Y0.01–ZrO_2	6.9	92.2
Y0.02–ZrO_2	5.9	98.4

[a] Calculated from X-ray line broadening.
[b] Error of measurements = ±10%.

method are shown in Fig. 1. All the samples exhibited tetragonal crystalline zirconia phase. No other crystal structures were observed. It has been suggested that the energy from combustion of the polymeric materials during calcination at 600 °C was sufficient to arrange the crystal structure in the tetragonal form with a crystal size less than its critical size [17]. Addition of Si or Y did not have any effect on XRD patterns of the tetragonal zirconia. The crystallite sizes of tetragonal zirconia calculated from the XRD line broadening using the Scherrer's equation and the BET surface areas are reported in Table 1. The average crystallite sizes of the zirconia and the Si- or Y-modified zirconia were approximately 5–7 nm. The BET surface areas of the nanocrystalline zirconia were found to be 85–100 m^2/g. Within experimental error, there was no significant difference in BET surface areas and the crystallite sizes of the zirconia and the modified zirconia. This is in contrast to the work reported by Alvarez and Torralvo [13] that doping of 2–5% by mole of yttria to zirconia prepared by sol–gel method resulted in narrower interparticle pores and formation of denser agglomerates. However, in our study the amounts of Y and Si addition were probably low (ca. 0.10–1.96%) so that no change in BET surface areas was found. Based on SEM results (not shown here), there was also no change in the morphology of the zirconia after Si or Y doping. Both zirconia and modified-zirconia prepared by the modified Pechini's method have irregular long shapes consisting of sandwich parallel pores similar to those of sol–gel derived zirconia that appeared to form from polymeric units of hydrolysed zirconium precursors [18]. These observed pores were in a macro-range.

3.2. Characteristics and catalytic properties of Y- and Si-modified ZrO_2 supported Co catalysts

The X-ray diffraction patterns of the Co/ZrO_2 catalysts are shown in Fig. 2. After impregnation of 10 wt% cobalt, the diffraction peaks of Co_3O_4 were observed at 36.8° 2θ for all the catalyst samples. The average crystallite sizes of Co_3O_4 calculated based on X-ray line broadening using Scherrer's equation for Si-modified ZrO_2 supported cobalt

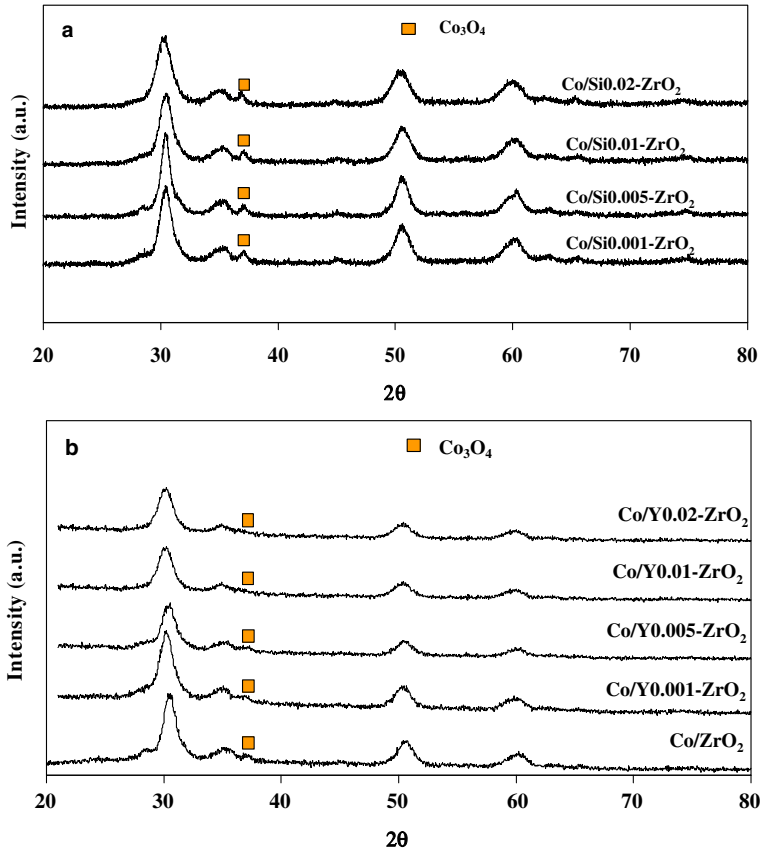

Fig. 2. X-ray diffraction results of Co catalysts supported on (a) Si-doped ZrO_2 and (b) Y-doped ZrO_2.

Table 2
Characteristics of various Co/ZrO_2 catalysts

Sample	BET surface area[a] (m^2/g)	H_2 chemisorption[b] $\times 10^{18}$ (molecule H_2/g cat.)	%Co dispersion[c]
Co/ZrO_2	52.1	5.9	14.4
$Co/Si0.001–ZrO_2$	48.7	5.1	12.5
$Co/Si0.005–ZrO_2$	51.5	5.4	13.3
$Co/Si0.01–ZrO_2$	50.8	7.0	17.0
$Co/Si0.02–ZrO_2$	52.4	9.0	21.9
$Co/Y0.001–ZrO_2$	56.2	4.5	11.0
$Co/Y0.005–ZrO_2$	54.3	4.6	11.3
$Co/Y0.01–ZrO_2$	60.1	5.5	13.5
$Co/Y0.02–ZrO_2$	53.8	6.4	15.7

[a] Error of measurements = ±10%.
[b] Error of measurements = ±5%.
[c] %Co dispersion was calculated based on the total amount of cobalt reduced at 350 °C.

catalysts were 20–40 nm. They increased with increasing Si content and were found to be larger than those of Y-modified ZrO_2 supported ones (<5 nm).

The BET surface areas of the various Co/ZrO_2 catalysts and the H_2 chemisorption results are reported in Table 2. The BET surface areas of the zirconia supported cobalt catalysts were slightly less than that of the original zirconia supports suggesting that cobalt was deposited in some of the pores of zirconia. There was no significant difference in BET surface areas of all the Co/ZrO_2 catalysts. However, it was found that at high molar ratios of Si/Zr (0.01–0.02) and Y/Zr (0.02), the amounts of H_2 chemisorption increased by ca. 10–50% with the Si-modified zirconia (Si/Zr = 0.02) exhibited the highest cobalt dispersion. The addition of lower amounts of Si or Y did not seem to have a great impact on the amount of surface cobalt measured by H_2 chemsisorption. The results of this study were found to be in agreement with the well-established trends in the literature on the influence of addition of a second metal on phase stability of zirconia. A considerably high loading of the second metals was used i.e., a commercial available 8% Y stabilized ZrO_2.

TEM micrographs were taken for all the catalysts in order to physically measure the size of cobalt oxide particles and/or cobalt clusters (Fig. 3). Darker spots represent high concentration of cobalt while lighter areas are the zirconia supports. It was found that on the Si-modified zirconia, the areas representing cobalt concentration increased with increasing Si/Zr ratios. On the other hand, on the Y-modified zirconia, small cobalt particles/clusters were observed unless for the high Y/Zr (0.02) that large cobalt clusters was apparent. TEM images were found to be in accordance with the results from XRD that small cobalt oxide particles (<5 nm) were present on Y-modified zirconia supported Co catalysts. Although TEM measurements were only done for a very small portion of each catalyst, the results are able to provide further evidence about Co

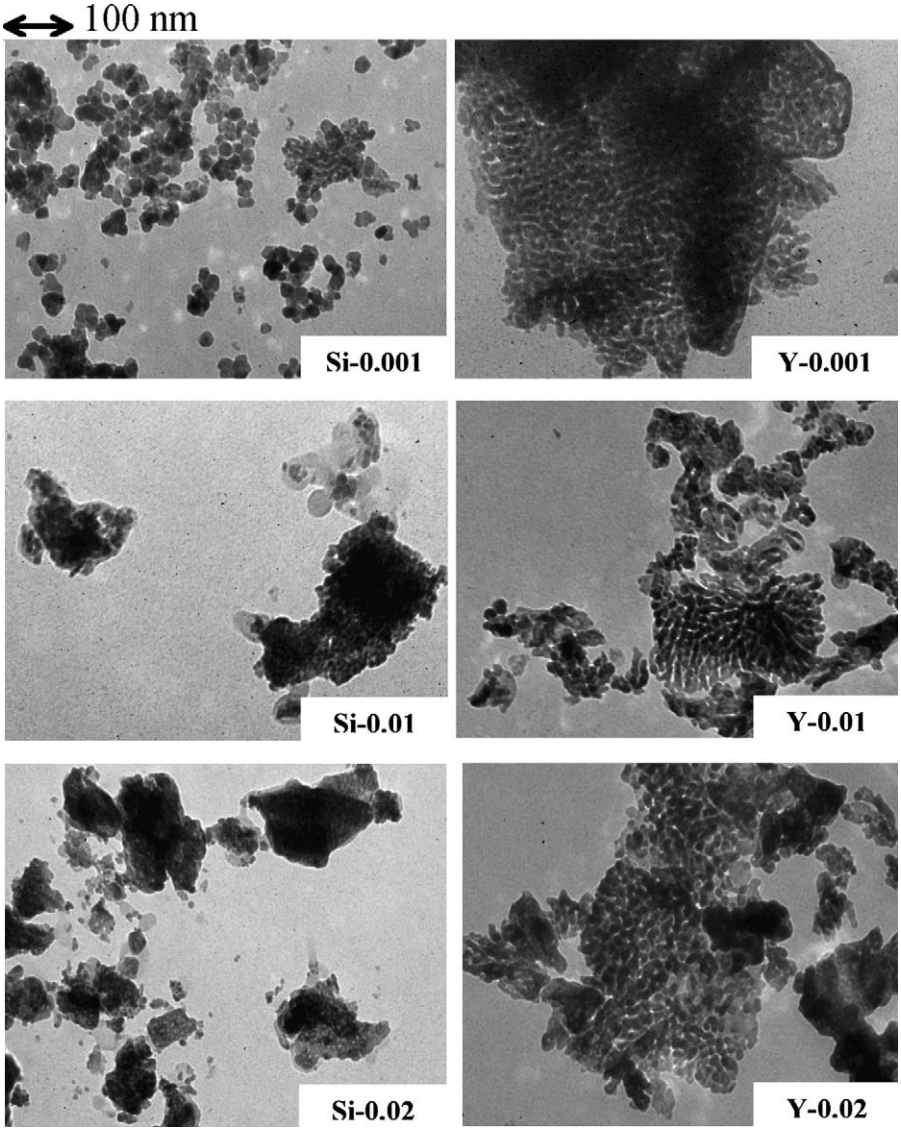

Fig. 3. TEM micrographs of various Si- and Y-modified ZrO_2 loaded with 10 wt% cobalt.

dispersion. Adding a small amount of Si and Y might alter the growth of nucleation of zirconia crystal [19]. In this study, it was found that primary particles of the nanocrystalline zirconia tend to agglomerate upon Si and Y doping. The effect was, however, more pronounced for the modification with silica than yttria as seen by agglomeration of zirconia particles for the lower Si/Zr ratios. The results were in good agreement with Alvarez and Torralvo [13] that increasing %Y addition resulted in larger and packing of primary particles.

Temperature programmed reduction (TPR) profiles of Si- and Y-modified zirconia supported Co catalysts are shown in Figs. 4 and 5, respectively. TPR is a powerful tool to study the reduction behavior of the catalysts. Reduction of cobalt in the oxide form, Co_3O_4 or Co_2O_3, to Co^0 involves a two-step reduction: first reduction of Co_3O_4 to CoO and then the subsequent reduction of CoO to Co^0 [20,21]. A wide range of variables such as, metal particle size and metal-support interaction, have an influence on the reduction behavior of cobalt catalysts resulting in the observation of different locations of the TPR peaks [22]. It was found that for the Si-modified zirconia supported cobalt catalysts reduction peaks below 400 °C tended to shift to lower temperatures, whereas those of Y-modified ones showed similar TPR profiles. The reducibilities of the catalysts calculated by integrating areas under the TPR peaks are given in Table 3. The reducibilities of all the catalysts were only 30–40%. The low reducibility of the catalysts may be due to formation of a solid solution or a zirconate phase between unreduced cobalt oxides and zirconia [6].

The catalytic activities of the Co/ZrO_2 catalysts in CO hydrogenation reaction are also reported in Table 3. As expected, the CO hydrogenation rates increased by 30–40% for the ones supported on Si- and Y-modified zirconia with $Si/Zr > 0.05$ and $Y/Zr > 0.01$ mole ratios. Since the

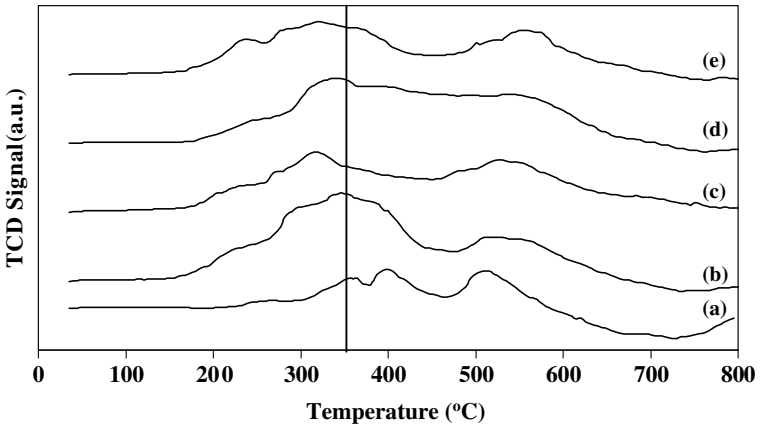

Fig. 4. Temperature-programmed reduction of the catalyst samples (a) 10%Co/ZrO_2; (b) 10%Co/Si0.001–ZrO_2; (c) 10%Co/Si0.005–ZrO_2; (d) 10%Co/Si0.01–ZrO_2 and (e) 10%Co/Si0.02–ZrO_2.

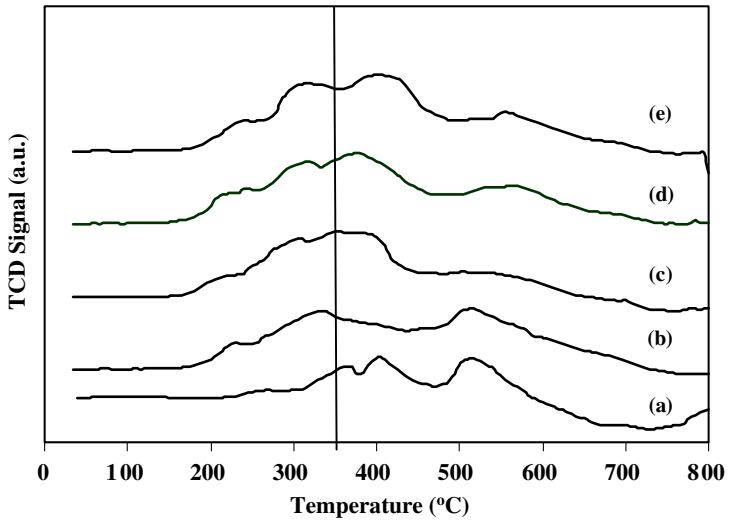

Fig. 5. Temperature-programmed reduction of the catalyst samples (a) 10%Co/ZrO_2; (b) 10%Co/Y0.001–ZrO_2; (c) 10%Co/Y0.005–ZrO_2; (d) 10%Co/Y0.01–ZrO_2 and (e) 10%Co/Y0.02–ZrO_2.

Table 3
Catalytic results in CO hydrogenation (220 °C, 1 atm, and $H_2/CO = 10$)

Catalyst	Reducibility[a] (%)	CO hydrogenation rate[b] (μmol CH_2 g cat.$^{-1}$ s^{-1})	Product selectivity (%)			TOFs[c] (s^{-1})
			C_1	C_2–C_3	C_{4+}	
Co/ZrO_2	32	15.4	88.6	9.1	2.3	0.22
Co/Si0.001–ZrO_2	39	10.7	86.0	10.8	3.2	0.27
Co/Si0.005–ZrO_2	30	10.8	98.0	2.0	0.0	0.72
Co/Si0.01–ZrO_2	34	11.9	98.6	1.4	0.0	0.66
Co/Si0.02–ZrO_2	30	18.8	97.8	2.2	0.1	0.28
Co/Y0.001–ZrO_2	31	10.4	97.6	2.3	0.1	0.28
Co/Y0.005–ZrO_2	29	16.2	89.3	8.7	2.1	0.26
Co/Y0.01–ZrO_2	29	19.6	91.7	7.1	1.3	0.23
Co/Y0.02–ZrO_2	32	24.1	97.7	2.2	0.1	0.30

[a] Based on TPR results from 35–800 °C.
[b] CO hydrogenation rate $= \frac{\%CO\ conversion \times flowrate\ of\ CO\ in\ feed(cc/min) \times 60(min/h) \times mol.\ wt.\ of\ CH_2(g/mole)}{catalyst\ weight(g) \times 22400(cc/mole)}$.
[c] Based on H_2 chemisorption results.

TOFs of Co/SiO0.005–ZrO_2 and Co/SiO0.01–ZrO_2 were almost three times higher than that of the non-modified one, there might have been some modification of the ZrO_2 surface by Si atoms resulting in higher active Co^0 surface. However, there was no such evidence for the Y-modified ones; the TOFs for all the Y-modified zirconia

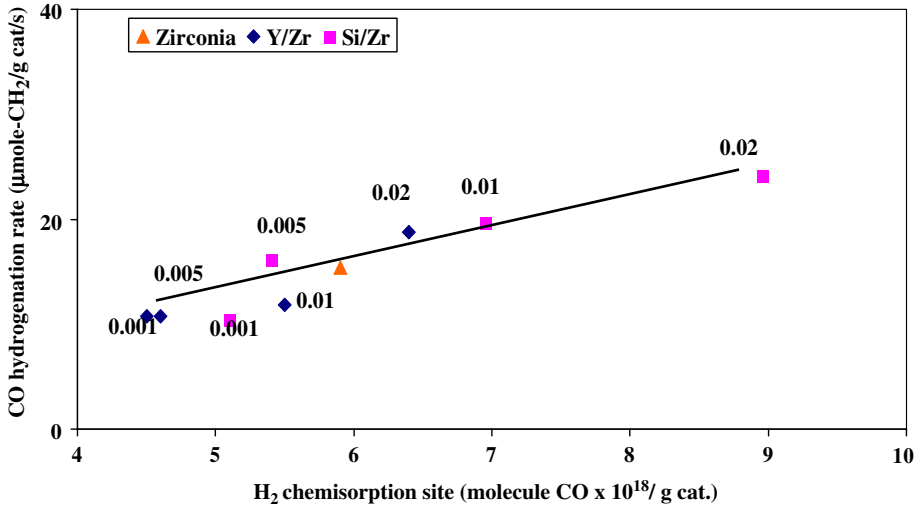

Fig. 6. Correlation of active sites measured by hydrogen chemisorption and CO hydrogenation rates.

supported Co catalysts were similar. A correlation between the amount of active sites and CO hydrogenation activities for various Co/ZrO_2 catalysts is illustrated in Fig. 6 as a straight line. The product selectivities were not significantly different since all the catalysts exhibited methane selectivities ca. 89–99% (expected product under the reaction conditions used).

4. Conclusions

Addition of a small amount of Si or Y during the preparation of nanocrystalline tetragonal zirconia accelerated the agglomeration of zirconia primary particles. However, when used as cobalt catalyst supports the Si- and Y-modified zirconia supported ones with $Si/Zr > 0.005$ and $Y/Zr > 0.01$ exhibited higher H_2 chemisorption and CO hydrogenation activities. The effect was more pronounced for Si-modified ZrO_2 than Y-modified ones as shown by higher TOF values.

Acknowledgments

The financial supports by the Thailand Research Fund (TRF), TJTTP-OECF, and the Graduate School of Chulalongkorn University for this Project are gratefully acknowledged. The authors thank the Cooperative Research Network of the Thai Ministry of Education for the scholarship for P.S.

References

[1] K. Tanabe, Mater. Chem. Phys. 13 (1985) 347.
[2] J.H. Bitter, K. Sechan, J.A. Lercher, J. Catal. 171 (1997) 279.
[3] W.P. Dow, T.J. Huang, J. Catal. 147 (1994) 322.
[4] G.K. Chuah, Catal. Today 49 (1999) 131.
[5] L. Bruce, J.F. Mathews, Appl. Catal. 4 (1982) 353.
[6] D.I. Enache, M. Roy-Auberger, R. Revel, Appl. Catal. A 268 (2004).
[7] D.I. Enache, B. Rebours, M. Roy-Auberger, R. Revel, J. Catal. 205 (2002) 346.
[8] J. Panpranot, N. Taochaiyaphum, and P. Praserthdam, Mater. Chem. Phys., in press.
[9] S. Kongwudthiti, P. Praserthdam, W. Tanakulrungsank, M. Inoue, J. Mater. Proc. Tech. 136 (2003) 186.
[10] F.D. Monte, W. Larsen, J.D. Mackenzie, J. Am. Ceram. Soc. 83 (2000) 1506.
[11] K. Yasuda, S. Arai, M. Itoh, K. Wada, J. Mater. Sci. 34 (1999) 3597.
[12] J.D. Ballard, J. Davenport, C. Lewis, W. Nelson, R.H. Doremus, L.S. Schadler, J. Thermal Spray Tech. 12 (2003) 34.
[13] M.R. Alvarez, M.J. Torralvo, Colloids Surf. A 113 (1996) 165.
[14] C.K. Loong, J.W. Richardson, M. Ozawa, M. Kimura, J. Alloys Comp. 207 (1994) 174.
[15] B.M. Devassy, G.V. Shanbhag, S.P. Mirajkar, W. Bohringer, J. Flethcher, S.B. Halligudi, J. Mol. Catal. A 233 (2005) 141.
[16] M.P. Pechini, Patent, 11 July (1967) 3,330,697.
[17] R.C. Garvie, J. Phys. Chem. 82 (1978) 218.
[18] M.A. Morris and H.M. Reidy, Ceramics Inter., in press.
[19] A.R. West, Solid State Chemistry and its Applications, Wiley, New York, 1987, p. 9.
[20] D. Schanke, S. Vada, E.A. Blekkan, A. Hilmen, A. Hoff, A. Holmen, J. Catal. 156 (1995) 85.
[21] Y. Zhang, D. Wei, S. Hammache, J.G. Goodwin Jr., J. Catal. 188 (1999) 281.
[22] J. Panpranot, J.G. Goodwin Jr., A. Sayari, Catal. Today 77 (2002) 269.

Jointly published by
Akadémiai Kiadó, Budapest
and Springer, Dordrecht

React.Kinet.Catal.Lett.
Vol. 88, No. 1, 65–71 (2006)
DOI:10.1556/RKCL.88.2006.1.9

RKCL4741

ROLE OF RUTHENIUM IN THE REDUCTION BEHAVIOR OF RUTHENIUM-PROMOTED COBALT/TITANIA FISCHER-TROPSCH CATALYSTS

Bunjerd Jongsomjit*, Chitlada Sakdamnuson, Joongjai Panpranot and Piyasan Praserthdam

Center of Excellence on Catalysis and Catalytic Reaction Engineering, Department of Chemical Engineering, Faculty of Engineering, Chulalongkorn University, Bangkok 10330 Thailand

Received February 7, 2005; in revised form August 2, 2005; accepted August 5, 2005

Abstract

Role of ruthenium in the reduction behavior of Ru-promoted Co/TiO_2 catalysts was investigated. Ru could facilitate the reduction but had no effect on water production during reduction.

Keywords: Reduction, cobalt catalyst, titania, Fischer-Tropsch

INTRODUCTION

Due to their high activities [1], high selectivity to linear hydrocarbons and low activities for the competitive water-gas shift (WGS) reaction [2,3], supported cobalt (Co) catalyst is considered to be one of the most important catalysts for Fischer-Tropsch synthesis (FTS) as well as carbon monoxide (CO) hydrogenation. During the past decade, titania-supported Co catalysts have been widely investigated by many authors, especially for the application of FTS in a continuously stirred tank reactor (CSTR) [4-6]. In general, to increase the

* Corresponding author. E-mail: bunjerd.j@chula.ac.th

0133-1736/2006/US$ 20.00.

catalytic activity of the Co catalysts, many promoters such as ruthenium (Ru), zirconium (Zr), lanthanum (La), rhodium (Rh), boron (B), and platinum (Pt) have been investigated. It has been reported that a variety of these promoters can increase the reducibility of Co, preserve the activity by preventing the formation of coke, exhibit cluster and ligand effects, act as a source of hydrogen spillover and enhance the dispersion. It should be mentioned that the active form of Co catalysts is the reduced Co metal surface atom. Although Ru promotion appears to enhance the rate of FTS, no studies have specifically addressed how Ru promotes the reaction. Understanding how Ru can modify the catalyst properties could lead to the design of more robust and active Co catalysts.

This investigation focused on giving a better understanding of the roles of Ru on reduction behavior of the Ru-promoted Co/TiO_2 catalyst. The impact of Ru promotion on the reducibility of Co in the absence and presence of water vapor was also investigated.

EXPERIMENTAL

Catalyst preparation

The unpromoted-Co/TiO_2 and Ru-promoted ($CoRu/TiO_2$) catalysts were prepared by the incipient wetness impregnation using cobalt nitrate [$Co(NO_3)\bullet 6H_2O$] and ruthenium(III) nitrosyl nitrate [$Ru(NO)(NO_3)_3$] as precursors. The TiO_2 used contained 81 mol % of anatase phase and 19 mol % of rutile phase (Ishihara Sangyo, Japan). The catalyst samples were dried at 110°C for 12 h and calcined in air at 500°C for 4 h.

Catalyst pretreatments

Standard reduction

Standard reduction of the calcined catalyst was conducted in a fixed-bed flow reactor under differential conditions (no gradient in the catalyst bed) at 1 atm using a temperature ramp from ambient to 350°C at 1°C/min and holding at 350°C for 10 h in a gas flow having a space velocity of 16,000 h^{-1} and consisting of H_2. The high space velocity of the H_2 flow was applied to insure that the partial pressure of water vapor in the catalyst bed produced by cobalt oxide reduction would be essentially zero.

Hydrothermal treatment

In order to evaluate the stability of catalysts and impacts of water vapor during reduction, hydrothermal treatment was also conducted during standard reduction above. In addition, besides using pure H_2, mixtures of H_2 and water vapor (5-10 vol.%) were also applied separately at the same reduction condition as mentioned above.

Catalyst nomenclature

The nomenclature used for the catalyst samples in this study is following:
Co/Ti : Unpromoted cobalt catalyst on the titania support,
CoRu/Ti : Ru-promoted cobalt catalyst on the titania support,
(C) : Calcined catalyst sample,
(RW0), (RW5) and (RW10): Reduced catalyst samples with no water vapor, 5 vol.% of water vapor, and 10 vol.% of water vapor added during standard reduction, respectively.

Catalyst characterization

BET surface area was determined using N_2 adsorption at 77 K in a Micromeritics ASAP 2010.

X-ray diffraction was conducted using a SIEMENS D-5000 X-ray diffractometer with CuK_α (λ = 1.54439 Å).

The Raman spectra of the samples were collected by projecting a continuous wave laser of argon ion (Ar^+) green (514.532 nm) through the samples exposed to air at room temperature.

Temperature-programmed reduction of calcined samples was carried out using 50 mg of a sample and a temperature ramp from 35 to 800°C at 5°C/min. The carrier gas was 5% H_2 in Ar.

Reaction

CO hydrogenation (H_2/CO = 10/1) was performed to determine the overall activity of the catalyst samples. Hydrogenation of CO was carried out at 220°C and 1 atm. A flow rate of H_2/CO/He = 20/2/8 cc/min in a fixed-bed flow reactor under differential conditions was used.

Table 1

Characteristics and catalytic properties of samples

Samples	BET surface area (m^2/g)[a]	Reducibility (%)[b]	Total H_2 chemisorption (μmol/g cat.)[c]	Reaction rate ($x10^2$ gCH_2 g cat. h^{-1})[d]		CH_4 Selectivity (%)	
				Initial[e]	Steady state[f]	Initial	Steady state
TiO_2	49	-	-	-	-	-	-
Co/Ti-C	34	78	4.8	25	21	94	96
Co/Ti-RW0	32	74	3.3	23	20	94	94
Co/Ti-RW5	32	72	3.2	23	20	98	98
Co/Ti-RW10	30	68	3.0	23	19	95	96
CoRu/Ti-C	37	87	7.5	37	36	99	98
CoRu/Ti-RW0	37	83	6.7	36	36	98	98
CoRu/Ti-RW5	37	77	5.9	36	35	97	97
CoRu/Ti-RW10	36	75	5.2	36	34	99	99

[a] Measurement error ± 5%

[b] Reducibility was measured during TPR at 30-800°C. The reduced samples were recalcined under the original calcination conditions prior to TPR.

[c] H_2 chemisorption was performed to determine the number of reduced Co surface atoms.

[d] CO hydrogenation was carried out at 220°C, 1 atm and $H_2/CO/Ar$ = 20/2/8 cm^3/min.

[e] After 5 min of reaction

[f] After 5 h of reaction

RESULTS AND DISCUSSION

The present study was conducted in order to investigate the roles of Ru in the reduction behavior of $CoRu/TiO_2$ catalysts. The characteristics and catalytic properties during CO hydrogenation are summarized in Table 1. It was observed that upon Co loading and Ru promotion, there was no significant change in the BET surface areas, suggesting no pore blocking or phase changes in the TiO_2 support. The XRD peaks (not shown) of all calcined samples at 26, 37,48, 55, 62, 69, 71 and 75° (TiO_2 in anatase form) and 27, 36, 42 and 57° (TiO_2 in rutile form) were observed. As expected, XRD peaks of Co_3O_4 species were also detected at 36, 46 and 65° after calcination of samples. However, after reduction with or without water vapor added, only diffraction peaks at 37 and 63° corresponding to CoO were observed. Thus, XRD revealed that Ru was well dispersed in the catalyst samples. A similar trend was also observed in Raman spectroscopy as seen for XRD results. It was found that the TiO_2 support exhibited the Raman bands at 640, 514 and 397 cm^{-1} (anatase form) and 445 cm^{-1} (rutile form). The calcined samples showed Raman bands of the TiO_2 support along with two shoulders at 690 and 480 cm^{-1}, assigned to Co_3O_4 species. Raman spectra for all reduced samples exhibited the similar Raman bands as seen for the calcined ones indicating Co_3O_4 on the surface. In order to determine the number of reduced Co metal surface atoms, H_2 chemisorption was performed as seen in Table 1. It indicated that water vapor during reduction apparently resulted in both lesser number of reduced Co metal surface atoms and reducibility due to Co-support compound formation (Co-SCF) as reported in our previous works [7, 8]. It should be noted that Ru promotion may result in enhanced activities during CO hydrogenation without changing selectivity of products due to increased number of reduced Co metal surface atoms. Roles of the Ru Ru promotion can be discussed further based on the TPR profiles as shown in Figs 1 (for the unpromoted catalysts) and 2 (for the Ru-promoted catalysts).

It can be observed that Ru can only facilitate the reduction of cobalt oxide species due to the hydrogen spillover effect resulting in lower reduction temperatures. It is known that water vapor as a byproduct of a reduction process can enhance the Co-SCF [7, 8]. Thus, water vapor was also introduced during reduction in order to investigate the roles of Ru promotion as well. As seen from Figs 1 and 2, increased amounts of water vapor during reduction had no effect on the reduction behavior of both unpromoted catalysts and Ru-promoted catalysts, indicating no shift of reduction temperatures. In summary, Ru promotion can only facilitate the reduction of cobalt oxide species but has no effect on water vapor produced during reduction.

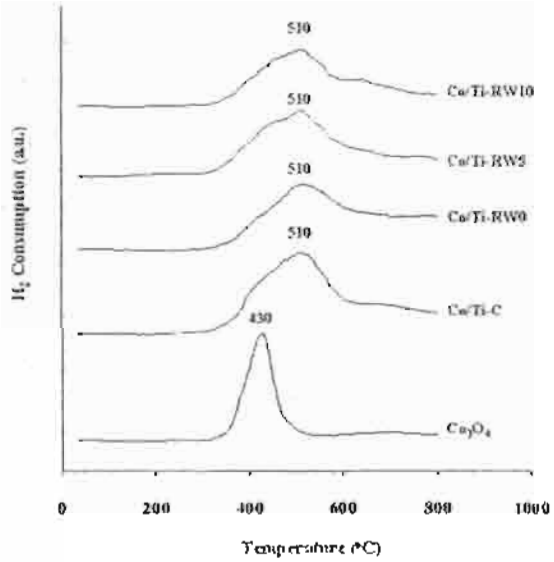

Fig. 1. TPR profiles of the unpromoted cobalt catalysts

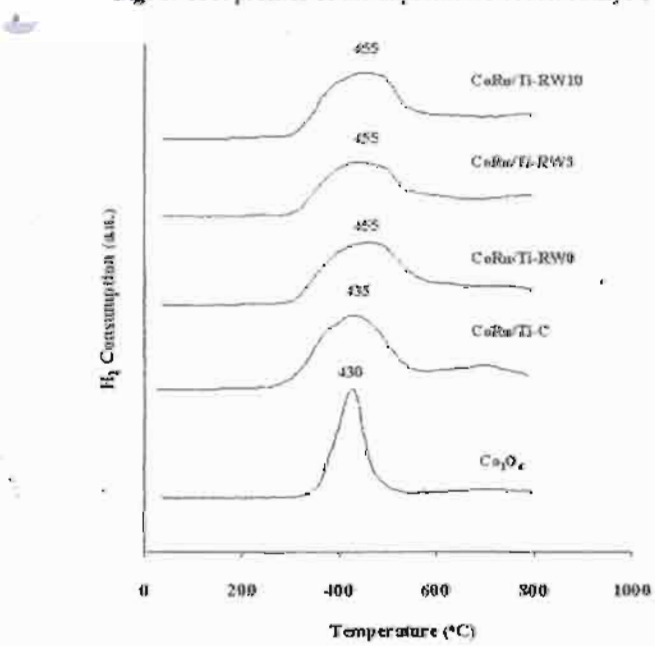

Fig. 2. TPR profiles of the Ru-promoted cobalt catalysts

Acknowledgements. We gratefully acknowledge the financial support by the National Research Council of Thailand (NRCT), the Thailand Research Fund (TRF) and Thailand-Japan Technology Transfer Project (TJTTP-JBIC). We would like to thank Prof. James G. Goodwin, Jr. at Clemson University, USA for his advice.

References

1. H.P. Wither, Jr., K.F. Eliezer, J.W. Mechell: *Ind. Eng. Chem. Res.*, **29**, 1807 (1990).
2. E. Iglesia: *Appl. Catal. A.*, **161**, 59 (1997).
3. R.C. Brady, R.J. Pettie: *J. Am. Chem. Soc.*, **103**, 1287 (1981).
4. J.L. Li, G. Jacobs, T. Das, B.H. Davis: *Appl. Catal. A.*, **233**, 255 (2002).
5. G. Jacobs, T. Das, Y.Q. Zhang, J.L. Li, G. Racoillet, B.H. Davis: *Appl. Catal. A.*, **233**, 263 (2002).
6. J.L. Li, L.G. Xu, R. Keogh, B.H. Davis: *Catal. Lett.*, **70**, 127 (2000).
7. B. Jongsomjit, J. Panpranot, J.G. Goodwin, Jr.: *J. Catal.*, **204**, 98 (2001).
8. B. Jongsomjit, C. Sakdamnuson, J.G. Goodwin, Jr.: *Catal. Lett.*, **94**, 209 (2004).

Studies in Surface Science and Catalysis, volume 159
Hyun-Ku Rhee, In-Sik Nam and Jong Moon Park (Editors)

Elucidation of reduction behaviors for Co/TiO_2 catalysts with various rutile/anatase ratios

Bunjerd Jongsomjit*, Tipnapa Wongsalee, and Piyasan Praserthdam

Center of Excellence on Catalysis and Catalytic Reaction Engineering
Department of Chemical Engineering, Chulalongkorn University
Bangkok 10330 Thailand. *corresponding author: bunjerd.j@chula.ac.th

The present study revealed effects of various rutile/anatase ratios in titania on the reduction behaviors of titania-supported cobalt catalysts. It was found that the presence of rutile phase in titania could facilitate the reduction process of the cobalt catalyst. As a matter of fact, the number of reduced cobalt metal surface atoms, which is related to the overall activity during CO hydrogenation increased.

1. INTRODUCTION

Supported cobalt (Co) catalysts are preferred for Fischer-Tropsch synthesis (FTS) based on natural gas [1] due to their high activities for FTS, high selectivity for long chain hydrocarbons and low activities for the competitive water-gas shift (WGS) reaction. Many inorganic supports such as silica, alumina, titania and Zeolites have been extensively studied for supported Co catalysts for years. It is known that in general, the catalytic properties depend on reaction conditions, catalyst compositions, types of inorganic supports and the degrees of metal dispersion as well. It is reported that during the past decades, titania-supported Co catalysts have been investigated widely by many authors, especially for the application of FTS in a continuously stirred tank reactor (CSTR) [2-4]. However, it should be noted that titania itself has different crystalline phases such as anatase, brookite and rutile phase. Thus, the differences in compositions of crystalline phases could result in changes on physical and chemical properties of titania, then consequently for the dispersion of cobalt. In order to give a better understanding of those, the focus of this present study was to investigate the cobalt dispersion on titania consisting various ratios of rutile/anatase. The Co/TiO_2 was prepared and then characterized using different characterization techniques.

2. EXPERIMENTAL

2.1 Material preparation

Preparation of titania support

The various ratios of rutile:anatase in titania support were obtained by calcination of pure anatase titania (obtained from Ishihara Sangyo, Japan) in air at temperatures between 800-1000°C for 4 h. The high space velocity of air flow (16,000 h^{-1}) insured the gradual phase transformation to avoid rapid sintering of samples. The ratios of rutile:anatase were determined by XRD according to the method described by Jung et al. [5] as follows:

$$\%\,\text{Rutile} = \frac{1}{[(A/R)0.884 + 1]} \times 100$$

Where, A and R are the peak area for major anatase ($2\theta = 25^{\circ}$) and rutile phase ($2\theta = 28^{\circ}$), respectively.

Preparation of catalyst samples

A 20 wt% of Co/TiO_2 was prepared by the incipient wetness impregnation. A designed amount of cobalt nitrate [$Co(NO_3)\bullet 6H_2O$] was dissolved in deionized water and then impregnated onto TiO_2 containing various ratios of rutile:anatase obtained from above. The catalyst precursor was dried at 110°C for 12 h and calcined in air at 500°C for 4 h.

2.2 Catalyst nomenclature

The nomenclature used for the catalyst samples in this study is following:
Rn: titania support containing **n%** of rutile phase (R)
Co/Rn: titania support containing **n%** of rutile phase (R)-supported cobalt

2.3 Catalyst characterization

X-ray diffraction: XRD was performed to determine the bulk crystalline phases of catalyst. It was conducted using a SIEMENS D-5000 X-ray diffractometer with CuK_{α} (λ = 1.54439 Å). The spectra were scanned at a rate of 2.4 degree/min in the range 2θ = 20-80 degrees.

Scanning electron microscopy and energy dispersive X-ray spectroscopy: SEM and EDX were used to determine the catalyst morphologies and elemental distribution throughout the catalyst granules, respectively. The SEM of JEOL mode JSM-5800LV was applied. EDX was performed using Link Isis series 300 program.

Transmission electron microscopy (TEM): The dispersion of cobalt oxide species on the titania supports were determined using a JEOL-TEM 200CX transmission electron spectroscopy operated at 100 kV with 100k magnification.

Hydrogen chemisorption: Static H_2 chemisorption at 100°C on the reduced cobalt catalysts was used to determine the number of reduced surface cobalt metal atoms. This is related to the overall activity of the catalysts during CO hydrogenation. Gas volumetric chemisorption at 100°C was performed using the method described by Reuel and Bartholomew [6]. The experiment was performed in a Micromeritics ASAP 2010 using ASAP 2010C V3.00 software.

Temperature-programmed reduction: TPR was used to determine the reduction behaviors of the catalyst samples. It was carried out using 50 mg of a sample and a temperature ramp from 35 to 800°C at 5°C/min. The carrier gas was 5% H_2 in Ar. A cold trap was placed before the detector to remove water produced during the reaction.

3. RESULTS AND DISCUSSION

In this present study, we basically showed dependence of the number of reduced cobalt metal surface atoms on dispersion of cobalt oxides along with the presence of rutile phase in titania. Both XRD and SEM/EDX results (not shown) revealed good distribution of cobalt oxides over the titania support. However, it can not differentiate all samples containing various ratios of rutile/anatase phase. Thus, in order to determine the dispersion of cobalt oxide species on titania, a more powerful technique such as TEM was applied with all samples. The TEM micrographs for all samples are shown in Figure 1. The dark spots represented cobalt oxides species present after calcination of samples dispersing on titania consisting various

ratios of rutile:anatase. It can be observed that cobalt oxide species were highly dispersed on the titania supports for Co/R0, Co/R3, and Co/R19 samples resulting in an appearance of smaller cobalt oxide patches present. However, the degree of dispersion for cobalt oxide species essentially decreased with increasing the rutile phase in titania from 40 to 99% as seen for Co/R40, Co/R96, and Co/R99 samples resulting in the observation of larger cobalt oxide patches. It was suggested that the presence of rutile phase in titania from 0 (pure anatase phase) to 19% exhibited the highly dispersed forms of cobalt oxide species for the calcined samples. It is known that the active form of supported cobalt catalysts is cobalt metal (Co^0). Thus, reduction of cobalt oxide species is essentially performed in order to transform cobalt oxide species obtained after calcination process into the active cobalt metal atoms for catalyzing the reaction. Therefore, the static H_2 chemisorption on the reduced cobalt samples was used to determine the number of reduced Co metal surface atoms. This is usually related to the overall activity of the catalyst during carbon monoxide (CO) hydrogenation [7].

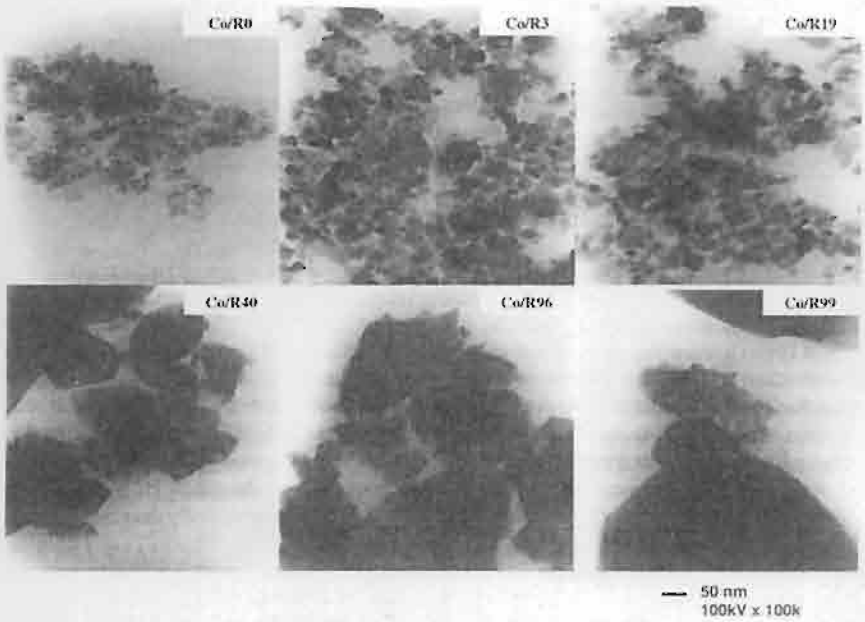

Figure 1 TEM micrographs of samples on various rutile/anatase ratios in titania

The resulted H_2 chemisorption for all samples revealed that the number of the reduced cobalt metal surface atoms increased with the presence of rutile phase in titania up to a maximum at 19% of rutile phase (Co/R19) before decreasing with the greater amounts of rultile phase as shown in **Table 1**. Considering the number of cobalt metal atoms for Co/R0 (pure anatase titania), the number was apparently low even though highly dispersed cobalt oxides species. This was suggested that highly dispersed forms of cobalt oxide species be not only the factor that insures larger number of reduced cobalt metal surface atoms in Co/TiO_2 [8]. On the other hand, it can be observed that the number of reduced cobalt metal surface atoms for Co/R40 and Co/R96 (with the low degree of dispersion of cobalt oxide species as seen by TEM) was

larger than that for Co/R0. This was due to the presence of rutile phase in Co/R40 and Co/R96. It should be mentioned that the largest number of reduced cobalt metal surface atoms for the Co/R19 sample was attributed to both highly dispersed cobalt oxide species and the presence of rutile phase in titania. In addition, the resulted TPR as also shown in Table 1 confirmed that the presence of rultie phase could facilitate the reduction of cobalt oxide species by lowering the reduction temperatures. As a result, the number of the reduced cobalt metal surface atoms increased.

Table 1 Resulted H_2 chemisorptiion and reduction temperatures for various Co/TiO_2 samples

Samples	Total H_2 Chemisorption (μmol H_2/g cat.)	Reduction Temperature ($^{\circ}$C)
Co/R0	0.93	370
Co/R3	1.55	270
Co/R19	2.44	320
Co/R40	1.66	285
Co/R96	1.71	275
Co/R99	0.69	275

4. SUMMARY

The present research showed a dependence of various ratios of rutile:anatase in titania as a catalyst support for Co/TiO_2 on characteristics, especially the reduction behaviors of this catalyst. The study revealed that the presence of 19% rutile phase in titania for Co/TiO_2 (Co/R19) exhibited the highest number of reduced Co metal surface atoms which is related the number of active sites present. It appeared that the increase in the number of active sites was due to two reasons; i) the presence of rutile phase in titania can facilitrate the reduction process of cobalt oxide species into reduced cobalt metal, and ii) the presence of rutile phase resulted in a larger number of reduced cobalt metal surface atoms. No phase transformation of the supports further occurred during calcination of catalyst samples. However, if the ratios of rutile:anatase were over 19%, the number of active sites dramatically decreased.

ACKNOWLEDGMENT

The financial support from the Thailand Research Fund (TRF) is greatly appreciated.

REFERENCES

[1] H.P. Wither, Jr., K.F. Eliezer, and J.W. Mechell, Ind. Eng. Chem. Res., 29 (1990)1807.
[2] J.L. Li, G. Jacobs, T. Das, and B.H. Davis, Appl. Catal. A., 233 (2002) 255.
[3] G. Jacobs, T. Das, Y.Q. Zhang, J.L. Li, G. Racoillet, and B.H. Davis., Appl. Catal. A., 233 (2002) 263.
[4] J.L. Li,, L.G. Xu, R. Keogh, and B.H. Davis, Catal. Lett., 70 (2000) 127.
[5] K.Y. Jung, and S.B. Park, J. Photochem. Photobio. A: Chem., 127 (1999) 117.
[6] R.C. Reuel, and C.H. Bartholomew, J. Catal., 85(1984) 63.
[7] B. Jongsomjit, C. Sakdamnuson, J.G. Goodwin, Jr., and P. Praserthdam, Catal. Lett., 94 (2004) 209.
[8] B. Jongsomjit, T. Wongsalee, and P. Praserthdam, Mater. Chem. Phys., 92 (2005) 572.

Available online at www.sciencedirect.com
ScienceDirect
Catalysis Communications 8 (2007) 548–556
CATALYSIS COMMUNICATIONS
www.elsevier.com/locate/catcom

Investigation of isosynthesis via CO hydrogenation over ZrO_2 and CeO_2 catalysts: Effects of crystallite size, phase composition and acid–base sites

Watcharapong Khaodee [a], Bunjerd Jongsomjit [a,*], Suttichai Assabumrungrat [a,*], Piyasan Praserthdam [a], Shigeo Goto [b]

[a] *Center of Excellence in Catalysis and Catalytic Reaction Engineering, Department of Chemical Engineering, Faculty of Engineering, Chulalongkorn University, Phyathai Road, Phatumwan, Bangkok 10330, Thailand*
[b] *Department of Chemical Engineering, Nagoya University, Chikusa, Nagoya 464-8603, Japan*

Received 29 March 2006; received in revised form 16 July 2006; accepted 2 August 2006
Available online 7 August 2006

Abstract

This paper investigates the isosynthesis via CO hydrogenation over zirconia and ceria catalysts. Various techniques including XRD, NH_3-TPD, CO_2-TPD and BET surface area were employed for the catalyst characterization. The results showed that not only acid–base properties, but also crystallite size and crystal phase essentially influenced the catalytic performance. It was found that the activity and the selectivity of isobutene in hydrocarbons on nanoscale catalysts were higher than those on the micronscale ones. Moreover, the acid–base properties were dependent on the fraction of tetragonal phase for zirconia, but independent on crystal phase for ceria. The synthesized nanoscale zirconias were more active than the commercial one but less than the nanoscale ceria. From the results, it was indicated that zirconia with 29% tetragonal phase exhibited the highest activity. Furthermore, the presence of tetragonal phase in zirconia played an important role on the selectivity of isobutene in hydrocarbons.

Keywords: CO hydrogenation; ZrO_2; CeO_2; Isobutene; Catalyst

1. Introduction

Isobutene, an extracted gas from C_4 stream of petroleum process, has been mainly used in the production of oxygenated compounds such as methyl *tert*-butyl ether (MTBE) and ethyl *tert*-butyl ether (ETBE). The trend of the octane enhancer demand is progressively increasing with the increased fuel consumption. Therefore the supply of isobutene from the petroleum product is possibly inadequate in the near future. It is expected that an alternative source for the production of isobutene needs to be explored. It is evident that one of the promising sources for isobutene synthesis can be achieved from a renewable resource such as biomass. It is known that fermentation of biomass produces methane and carbon dioxide. Both of these products can be used for synthesizing the syngas ($CO + H_2$), which can be subsequently converted to isobutene. Thus, advantages of this process are; (i) the chosen resource of isobutene production is renewable, then being more attractive than the conventional petroleum sources, which are about to shortage in the near future, (ii) carbon dioxide, a by-product of fermentation process, is substantially consumed to produce syngas, hence reducing the CO_2 emission to the atmosphere, and (iii) the ratio of carbon monoxide to hydrogen of 1:1 for the syngas from fermentation of biomass is suitable for the reaction of isobutene synthesis.

* Corresponding authors. Tel.: +662 218 6868; fax: +662 218 6877.
E-mail addresses: Bunjerd.J@chula.ac.th (B. Jongsomjit), Suttichai.A@chula.ac.th (S. Assabumrungrat).

1566-7367/$ - see front matter © 2006 Elsevier B.V. All rights reserved.
doi:10.1016/j.catcom.2006.08.001

It is recognized that the catalytic reaction that converts syngas to branched chain hydrocarbons, especially isobutane and isobutene, is so-called isosynthesis. As reported, the suitable catalysts for isosynthesis reaction are difficultly reducible oxides such as zirconia rather than other reduced transition metals [1]. It has been reported that zirconia was the most selective catalyst for isosynthesis [2–6]. Besides that, another oxide catalyst such as ceria (CeO_2) was also selective to isobutene in C_4 hydrocarbons [7]. Some researchers have tried to relate the characteristics of catalysts to their catalytic performance. For example, Su et al. [4] investigated the catalytic performance of various nanoscale zirconias for isosynthesis. They found that better formation of isobutene is resulted from higher ratio of base to acid sites on catalyst surface. In addition, effect of the crystal phase such as monoclinic phase in zirconia on the catalytic performance was also reported by Maruya et al. [6]. Because of the bifuntionality of zirconia, the acid–base properties could play an important role on the catalytic performance [4,8–10].

In this work, the catalytic performances of micron- and nanoscale zirconia and ceria on isosynthesis via CO hydrogenation were investigated. The synthesized nanoscale zirconia catalysts were prepared using the precipitation method with two different zirconium salt precursors. The synthesized nanoscale ceria was also prepared by the precipitation method. The catalytic performances and characteristics of the synthesized catalysts and commercial micron- and nanoscale zirconia and commercial micronscale ceria were also determined in order to eventually compare the effect of the crystallite size on the isosynthesis reaction.

2. Experimental

2.1. Catalyst preparation

The nanoscale zirconia (ZrO_2) was prepared by the precipitation method. It was carried out by slowly adding a solution of zirconium salt precursors such as zirconyl chloride ($ZrOCl_2$) or zirconyl nitrate [$ZrO(NO_3)_2$] (0.15 M) into a well-stirred precipitating solution of ammonium hydroxide (NH_4OH) (2.5 wt.%) at room temperature. The pH of the solution was carefully controlled at 10. The resulting precipitate was removed, and then washed with deionized water until Cl^- was not detected by a silver nitrate ($AgNO_3$) solution. The obtained sample was then dried overnight at 110 °C and calcined at 450 °C for 3 h with a temperature ramp of 1 °C/min. The synthesized zirconias obtained from $ZrOCl_2$ and $ZrO(NO_3)_2$ were denoted as ZrO_2–Cl (nano-syn) and ZrO_2–N (nano-syn), respectively. For a comparative study, another nanoscale zirconia was prepared by using zirconium *n*-propoxide 15 g as a starting material. The starting material was suspended in 100 ml of 1,5-pentanediol in the test tube, and then set up in 300 ml autoclave. In the gap between the test tube and autoclave wall, 30 ml of glycol was added. After the autoclave was completely purged with nitrogen, the autoclave was heated to 300 °C at the rate of 2.5 °C/min and held at that temperature for 2 h. Autogeneous pressure during the reaction gradually increased as the temperature was raised. After the reaction, the autoclave was cooled to room temperature. The resulting products were collected by repeatedly washed with methanol and centrifugation and then the products were dried in air. This synthesized zirconia was denoted as ZrO_2–PeG (nano-syn).

For the preparation of ceria (CeO_2), it was also prepared using the precipitation method as mentioned above. Cerium nitrate [$Ce(NO_3)_3$] was used as a cerium salt precursor. All conditions during preparation were the same as those for the zirconia preparation.

The commercial micron- and nanoscale zirconias named as the ZrO_2 (micron-com) and ZrO_2 (nano-com) and commercial micronscale ceria named as CeO_2 (micron-com) obtained from Aldrich were also used for the comparative study.

2.2. Catalyst characterization

2.2.1. N_2 physisorption

Measurements of BET surface area, cumulative pore volume and average pore diameter were performed by the N_2 physisorption using the Micromeritics ASAP 2020 surface area and porosity analyzer.

2.2.2. X-ray diffraction

The XRD spectra of catalysts were measured by a SIEMENS D5000 X-ray diffractometer using Cu Kα radiation with a nickel filter over the 2θ ranging from 20° to 80°. The crystal sizes of the prepared catalysts were obtained by XRD line broadening using Scherrer's equation. The characteristic peaks at $2\theta = 28.2°$ and 31.5° for (−1 1 1) and (1 1 1) reflexes, respectively, are assigned to the monoclinic phase in ZrO_2. The characteristic peak at $2\theta = 30.2°$ for the (1 1 1) reflex in the XRD patterns represents the tetragonal phase in ZrO_2. For the cubic fluorite phase in CeO_2, the XRD peaks at $2\theta = 28.6°$ and 33.1° are evident.

The percent of tetragonal and monoclinic phase in ZrO_2 was calculated by a comparison of the areas for the characteristic peaks of the monoclinic phase and the tetragonal phase. The percent of each phase was determined by means of the Gaussian areas $h \times w$, where h and w are the height and half-height width of the corresponding XRD characteristic peak as follows [4]:

$$\%\,\text{monoclinic phase} = \frac{\sum(h \times w)\text{monoclinic phase}}{\sum(h \times w)\text{monoclinic and tetragonal phase}},$$

$$\%\,\text{tetragonal phase} = \frac{\sum(h \times w)\text{tetragonal phase}}{\sum(h \times w)\text{monoclinic and tetragonal phase}}.$$

2.2.3. Transmission electron microscopy

Catalyst crystallite size and the diffraction pattern were obtained using the JEOL JEM-2010 transmission electron microscope operated at 200 kV with an optical point to point resolution of 0.23 nm at National Metal and Materials Technology Center (MTEC). The sample was dispersed in ethanol prior to the TEM measurement.

2.2.4. Temperature-programmed desorption

Temperature-programmed desorption of ammonia and carbon dioxide (NH_3- and CO_2-TPD) was used to determine the acid–base properties of catalysts. TPD experiments were carried out using a flow apparatus. The catalyst sample (0.1 g) was treated at its calcined temperature (450 °C) in helium flow for 1 h and then saturated with 15% NH_3/He mixture or pure CO_2 flow after cooling to 100 °C. After purging with helium at 100 °C for 1 h to remove weakly physisorbed NH_3 or CO_2, the sample was heated to 450 °C at a rate of 20 °C/min in a helium flow (50 cm^3/min). The amount of acid–base sites on the catalyst surface was calculated from the desorption amount of NH_3 and CO_2, respectively. It was determined by measuring the areas of the desorption profiles obtained from the Micromeritics ChemiSorb 2750 pulse chemisorption system analyzer.

2.3. Reaction procedure

CO hydrogenation was carried out at 400 °C and atmospheric pressure in a fixed-bed quartz reactor with a mixture of $CO/H_2/N_2 = 10/10/5$ cm^3/min. The catalyst sample of 2 g was used in each run. The reactor effluent samples were taken at 1.5 h interval and analyzed using the gas chromatography technique. Thermal conductivity detector (TCD) with molecular sieve 5A and Porapak-Q column was used to detect the CO and CO_2, respectively. The flame ionization detector (FID) with VZ-10 column was used to detect the light hydrocarbons such as C_1–C_4 hydrocarbons. The steady-state rate for all catalysts was obtained after 20 h.

3. Results and discussion

3.1. Physical properties

The XRD patterns of the commercial ZrO_2 and CeO_2 catalysts are shown in Fig. 1 and those of the synthesized ones are shown in Fig. 2. It showed that both commercial and synthesized CeO_2 catalysts exhibited the similar XRD peaks at $2\theta = 28.6°$ and 33.1° assigned to the typical cubic fluorite structure. However, based on the calculation, it showed that the average crystallite size for the commercial CeO_2 was in micronscale whereas the synthesized one was in nanoscale (Table 1). For the commercial micronscale ZrO_2 catalyst (Fig. 1), only the XRD peaks at $2\theta = 28.2°$ and 31.5° were observed indicating only the monoclinic phase in the micronscale ZrO_2. However, for the commercial nanoscale ZrO_2 catalyst (Fig. 1), besides the monoclinic characteristic peaks it also exhibited the XRD characteristic peaks of tetragonal at $2\theta = 30.2°$. For the synthesized ZrO_2 catalysts, ZrO_2–PeG (nano-syn) showed only tetragonal phase but ZrO_2–N (nano-syn) and ZrO_2–Cl (nano-syn) showed both of tetragonal and monoclinic phases. For all catalysts, the contents of different phases are listed in Table 1. Typically, the monoclinic phase is stable up to ca. 1170 °C and then, transforms into the tetragonal phase at higher temperature [11]. The tetragonal phase is stable up to ca. 2370 °C and finally transforms into the cubic phase at higher temperature. However, the metastable of the tetragonal phase in ZrO_2 can usually be observed when the precipitation method from an aqueous salt solution is employed as seen in this work or when the thermal decomposition of zirconium salts is used. Furthermore, the tetragonal phase appeared was attributed to size effect. Garvie [12] reported that the tetragonal phase appeared to be a critical crystallite size about 30 nm and above that point the tetragonal phase could not be stabilized at room

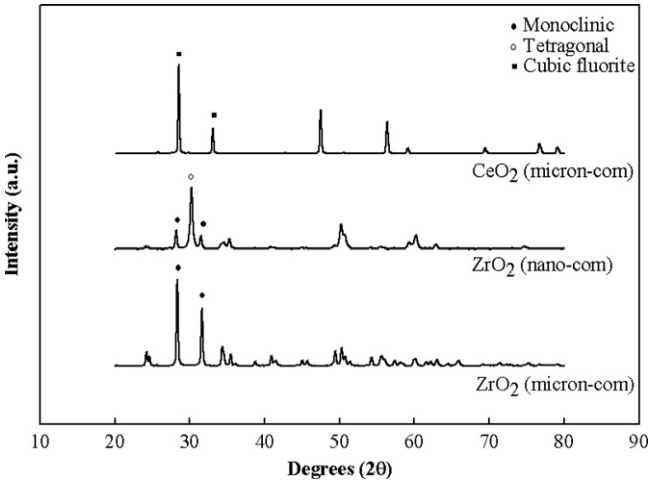

Fig. 1. XRD patterns of commercial ZrO_2 and CeO_2 catalysts.

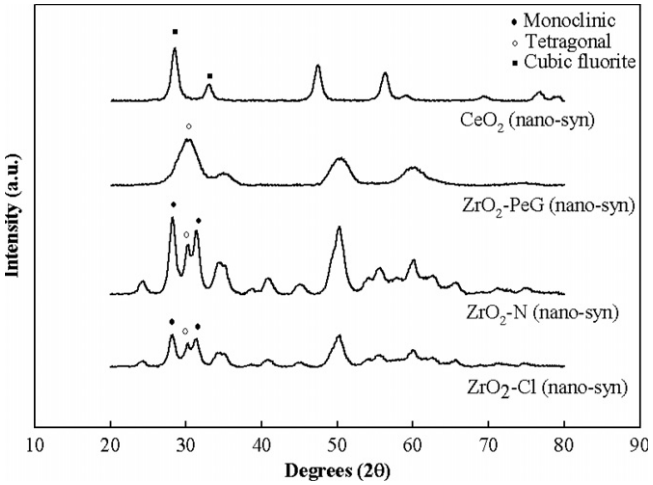

Fig. 2. XRD patterns of synthesized ZrO_2 and CeO_2 catalysts.

Table 1
Characteristics of ZrO_2 and CeO_2 catalysts

Catalysts	BET S.A.[a] (m^2/g)	Cumulative pore volume[b] (cm^3/g)	Average pore diameter[c] (nm)	Crystal size[d] (nm)			Crystal phase	Acid sites[h] (μmol/g)	Base sites[i] (μmol/g)
				M[e]	T[f]	C[g]			
ZrO_2 (micron-com)	6	0.012	9.5	65.8	–		100%M	24	15
ZrO_2 (nano-com)	41	0.115	9.9	30.3	22.2		30%M + 70%T	160	319
ZrO_2–Cl (nano-syn)	95	0.173	4.8	10.9	13.6		77%M + 23%T	361	191
ZrO_2–N (nano-syn)	92	0.169	4.9	9.8	8.3		71%M + 29%T	389	188
ZrO_2–PeG (nano-syn)	48	0.034	6.6	–	2.7	–	100%T	127	337
CeO_2 (micron-com)	4	0.008	16.6	–	–	135.9	100%C	16	9
CeO_2 (nano-syn)	91	0.149	4.7	–	–	8.1	100%C	190	161

[a] Error of measurement = ±5%.
[b] BJH desorption cumulative volume of pores between 1.7 and 300 nm diameter.
[c] BJH desorption average pore diameter.
[d] Determined by XRD line broadening using Scherrer's equation [17].
[e] Monoclinic phase in ZrO_2.
[f] Tetragonal phase in ZrO_2.
[g] Cubic phase in CeO_2.
[h] Measured by NH_3-TPD.
[i] Measured by CO_2-TPD.

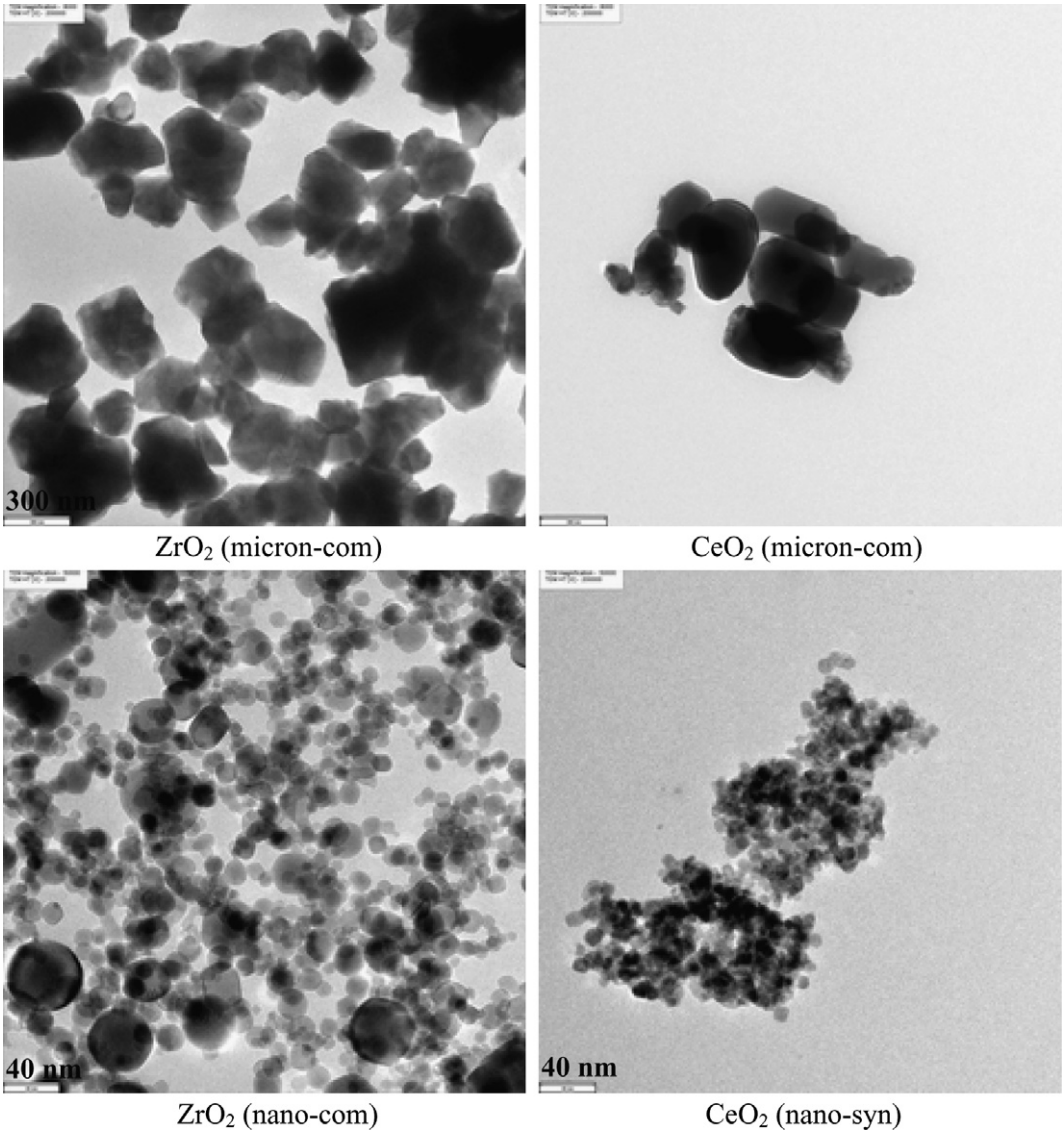

Fig. 3. TEM micrographs of ZrO_2 and CeO_2 catalysts.

temperature. The average crystallite sizes of each phase being present in all catalysts were calculated using the XRD line broadening regarding to its characteristic peaks. Thus, only the commercial micronscale ZrO_2 catalyst had no tetragonal phase because of its crystallite size was more than 30 nm. The crystallite sizes of catalysts can be determined by means of not only XRD technique, but also TEM technique. TEM provided the image of characteristics of particles indicating the crystallite size or the particle size. TEM micrographs of all catalysts are illustrated in Fig. 3. It was found that the commercial micronscale ZrO_2 and CeO_2 catalysts had the particle size more than 100 nm which absolutely indicated that these catalysts were in micron-sized. For the nanoscale catalysts, the average particle size indicated that these catalysts were in nano-sized and the values of them were similar to the values of crystallite sizes calculated by the XRD technique. Moreover, TEM with the electron diffraction mode can determine the crystallographic structure of catalyst. From the electron diffraction results (Fig. 4), it was revealed that both of the nanoscale ZrO_2 and CeO_2 catalysts were polycrystallite. The other physical properties of catalysts such as BET surface area, cumulative pore volume and average pore diameter are also summarized in Table 1. The micron- and nanoscale catalysts exhibited corresponding values based on their average crystallite sizes and BET surface areas. Compared to the micronscale catalysts, the nanoscale ones had smaller crystallite sizes which influenced not only on the increase in the cumulative pore volume, but also on the reduction of the average pore diameter. In contrast, the ZrO_2–PeG (nano-syn) had very small crystallite size, but low surface area. This was probably due to significantly less cumulative pore volume compared with other the nanoscale catalysts. For the ZrO_2 prepared by different zirconium salt precursors, the resulted crystal structure was probably changed [13]. Su et al. [5] and Wu

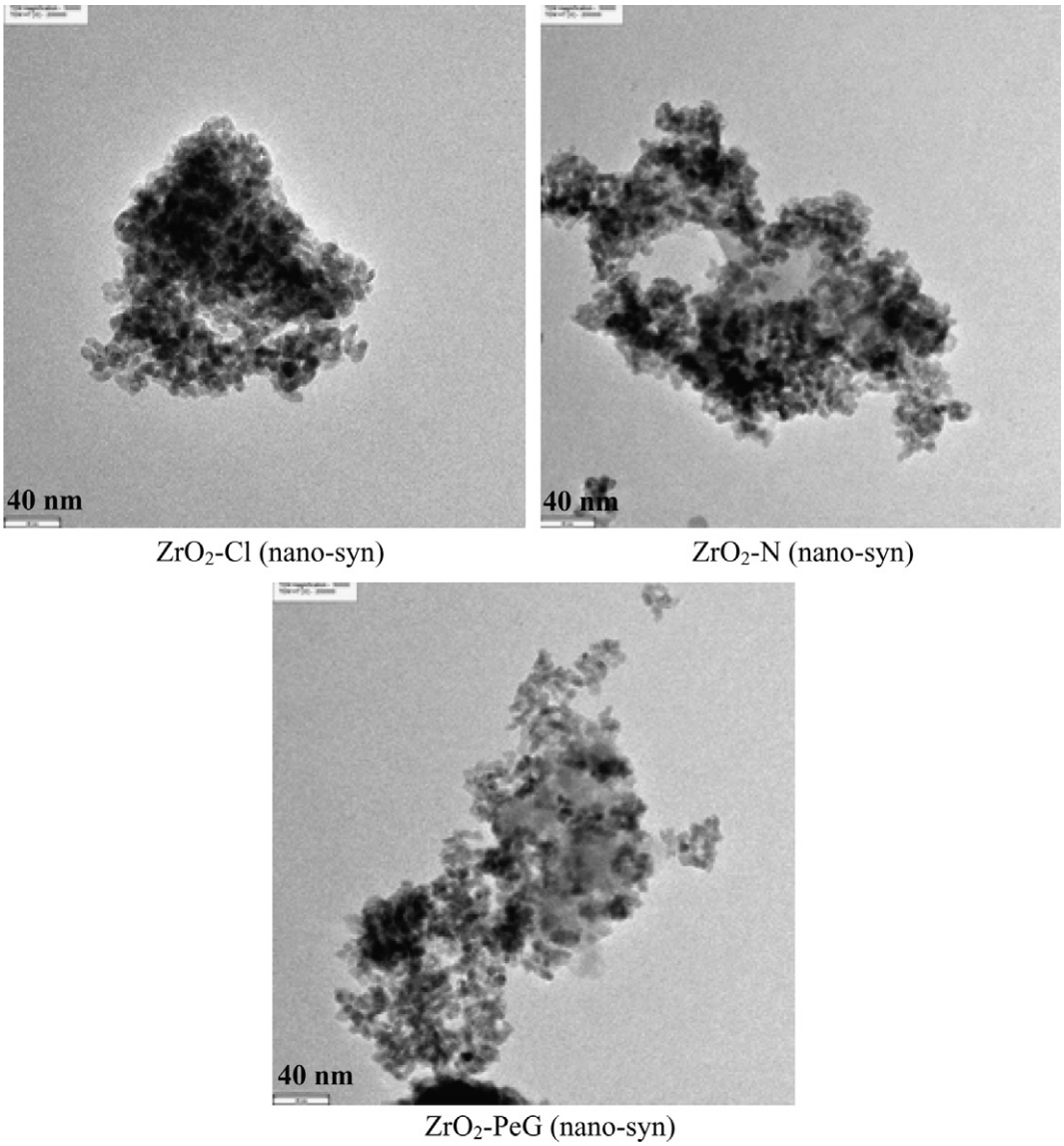

ZrO_2-Cl (nano-syn)

ZrO_2-N (nano-syn)

ZrO_2-PeG (nano-syn)

Fig. 3 (*continued*)

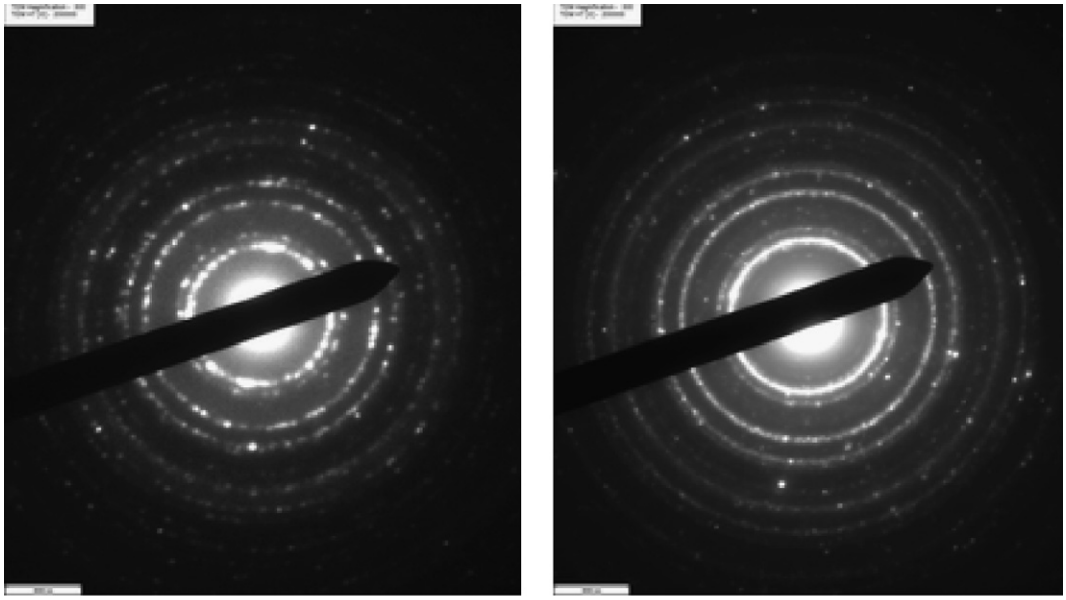

Fig. 4. TEM micrographs of nanoscale ZrO_2 and CeO_2 catalysts with electron diffraction mode.

and Yu [14] found that SO_4^{2-} from zirconium salt precursor such as $Zr(SO_4)_2$ affected crystallization and phase transformation of ZrO_2. The ZrO_2 prepared by $Zr(SO_4)_2$ showed both tetragonal phase and amorphous, but the ZrO_2 prepared by other zirconium salt precursors such as $Zr(NO_3)_4$, $ZrCl_4$ and $ZrOCl_2$ showed monoclinic and tetragonal phase. In this case, ZrO_2–Cl (nano-syn) and ZrO_2–N (nano-syn) were prepared using $ZrOCl_2$ and $ZrO(NO_3)_2$ as zirconium salt precursors, respectively. It was found that different precursors slightly affected the crystal structure in the phase composition of monoclinic/tetragonal phases over ZrO_2 and the BET surface area as well.

3.2. Acid–base properties

The acid–base properties of the catalysts were measured by NH_3- and CO_2-TPD, respectively. The NH_3- and CO_2-TPD profiles are shown in Figs. 5 and 6. From the TPD profiles, the amounts of acid and base sites which are also listed in Table 1 were calculated from the area below curve. The characteristic peaks of these profiles are assigned to their desorption temperatures indicating the strength of Lewis surface sites. From NH_3-TPD result of Ma et al. [15], it showed that NH_3 desorption peaks located at ca. 200 °C and 300 °C for ZrO_2 catalysts were corresponding to weak acid sites and moderate acid sites, respectively. Moreover, both peaks of monoclinic ZrO_2 exhibited slightly higher amount of acid sites compared to the tetragonal ZrO_2. In this work, all ZrO_2 mainly had weak acid sites whereas the moderate acid sites were evident for the ZrO_2–N (nano-syn). This was probably due to more fraction of monoclinic phase present. The other CeO_2 catalysts exhibited slightly different NH_3-TPD profiles of ZrO_2 catalysts.

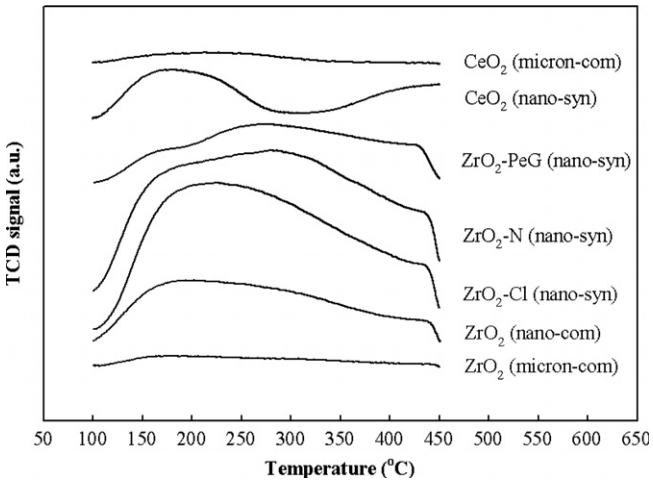

Fig. 5. NH_3-TPD profiles of catalysts.

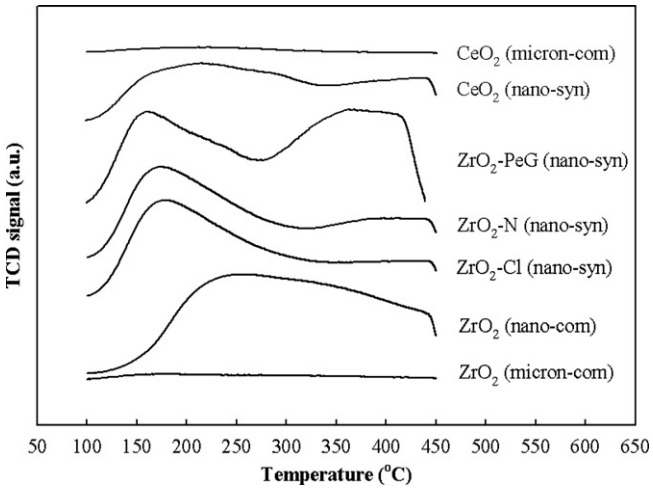

Fig. 6. CO_2-TPD profiles of catalysts.

Based on CO_2 desorption peaks, the weak base sites, moderate base sites and strong base sites can be identified [15]. It indicated that all kinds of base sites were presented in the tetragonal ZrO_2 whereas only weak and moderate base sites were observed on the monoclinic ZrO_2. For CO_2-TPD profiles of ZrO_2 (Fig. 6), the ZrO_2–PeG (nano-syn) exhibited higher desorption temperature than the other ZrO_2 catalysts due to pure tetragonal phase in ZrO_2. Furthermore, the ZrO_2–PeG (nano-syn) had the highest amount of base sites among the other ZrO_2 catalysts indicating higher basicity of tetragonal ZrO_2 than monoclinic ZrO_2. For the CeO_2 catalysts, it revealed only the weak base sites and moderate base sites. As a matter of fact, the ZrO_2 catalysts exhibited higher basicity than the CeO_2 catalysts. It should be mentioned that there were only a few acid and base sites for the micronscale catalysts (both ZrO_2 and CeO_2) compared to the nanoscale ones. It was suggested that differences in both acid and base sites can be attributed to the various fractions of crystal phases along with the crystallite sizes of catalysts. However, due to only one crystal phase in the ceria catalysts, the various acid and base sites present would be independent of crystal phase. Hence, different acid and base sites for ceria must be attributed to differences in crystallite sizes only. In fact, crystallite size also relates to BET surface area. Therefore, the amount of acid and base sites may be ascribed to effect of surface area. However, the two crystal phases of zirconia can be altered and consequently affected the acid–base properties. In order to give a better understanding, the relationship between acid–base sites and percent of tetragonal phase in ZrO_2 is illustrated in Fig. 7. It was found that the amount of acid sites increased with increased percents of tetragonal phase in ZrO_2 up to a maximum at ca. 29%, and then decreased with more tetragonal phase present. In other words, there was an optimum point at 29% of the tetragonal phase in ZrO_2, which can maximize the acid sites. Considering the base sites, the amount of base sites was apparently proportional to the percent of tetragonal phase in ZrO_2. As a result, basicity increased with increasing of tetragonal phase in ZrO_2.

3.3. Catalytic performance

The commercial ZrO_2 and CeO_2 catalysts and synthesized ones were tested for their isosynthesis activity and selectivity at 400 °C, atmospheric pressure and CO/H_2 of 1. A plot of reaction rates (based on products formed) versus the time-on-stream for all catalysts is shown in Fig. 8. Typically, time-on-stream behavior for CO hydrogenation exhibits the highest activity at initial time and gradually decreases with more reaction times until the reaction reaches the steady-state rate indicating a constant activity. Therefore, activity profiles for isosynthesis were similar to typical activity profiles CO hydrogenation. The steady-state rate was reached after 20 h and the value was shown in Table 2 along with the product selectivity. It was found that the catalytic activities of the commercial micronscale ZrO_2 and CeO_2 were low and the selectivities of isobutene in hydrocarbons were zero. No significant differences were observed regarding their physical properties. The acid–base sites for both micronscale catalysts were similar, but somehow, much lesser than those of the nanoscale ones. Therefore, the key factor that influenced the catalytic performance of the micronscale ZrO_2 and CeO_2 was essentially the amount of acid–base sites of these catalysts. From the previous works [4,8–10], it was reported that the catalytic activity and the selectivity of isobutene in hydrocarbons depended on the amount of acid and base sites of catalysts. The experimental results also revealed that the micronscale ZrO_2 was selective for C_3 in hydrocarbons, but the micronscale CeO_2 was selective for C_1 in hydrocarbons.

The synthesized nanoscale CeO_2 exhibited higher catalytic activity and selectivity of isobutene in hydrocarbons than the commercial micronscale one. It was found that the nanoscale CeO_2 had much higher BET surface area

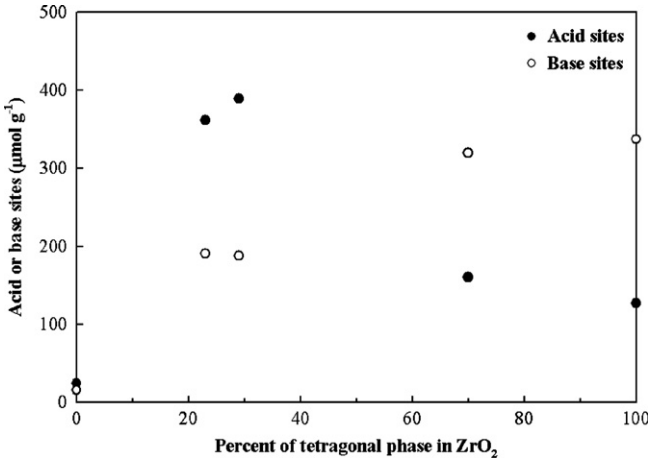

Fig. 7. Relationship between the amounts of acid–base sites and % tetragonal phase in ZrO_2.

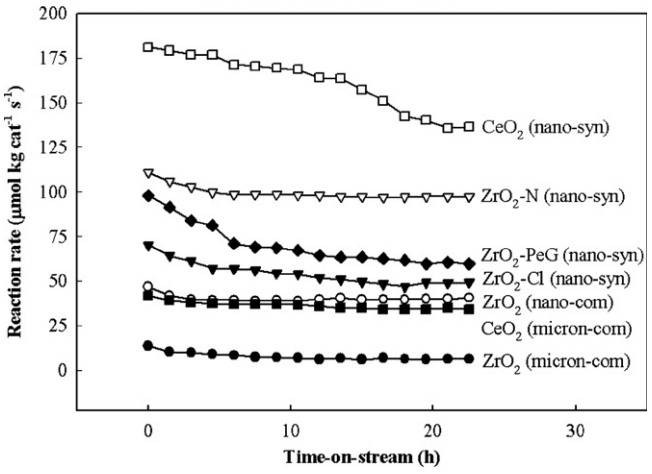

Fig. 8. Rate time profiles of catalysts on isosynthesis via CO hydrogenation.

Table 2
The catalytic performance of ZrO_2 and CeO_2 catalysts in the isosynthesis[a]

Catalysts	CO conversion (%)	Reaction rate[b] (μmol kg cat^{-1} s^{-1})	Product selectivity in hydrocarbons[c] (mol%)			
			C_1	C_2	C_3	i-C_4H_8
ZrO_2 (micron-com)	0.19	6.3	11.8	10.8 (88.4)	77.4 (100.0)	0.0
ZrO_2 (nano-com)	1.21	40.7	5.6	2.7 (59.0)	9.5 (91.6)	82.2
ZrO_2–Cl (nano-syn)	1.47	49.3	2.7	2.6 (72.6)	9.2 (96.3)	85.5
ZrO_2–N (nano-syn)	2.90	97.3	6.0	5.6 (60.4)	11.1 (87.9)	77.3
ZrO_2–PeG (nano-syn)	1.78	59.7	6.1	3.8 (67.0)	9.1 (95.9)	80.9
CeO_2 (micron-com)	1.02	34.3	69.2	8.8 (43.7)	22.0 (93.3)	0.0
CeO_2 (nano-syn)	4.07	136.4	9.4	14.4 (58.4)	18.6 (65.2)	57.6

[a] Reaction conditions were at 400 °C, 1 atm and $CO/H_2 = 1$.
[b] Steady state of reaction was reached at 20 h.
[c] Parentheses are percent of olefin being present in products.

and the amount of acid–base sites compared to the commercial micronscale one. Even though, the crystallite sizes of CeO_2 changed, the crystal phase of them was identical. Hence, it was suggested that the increase in BET surface area and/or the acid–base properties probably rendered the nanoscale CeO_2 catalyst high catalytic performance. The tendency of catalytic activity and selectivity of isobutene in hydrocarbons over the commercial micron- and nanoscale ZrO_2 was similar to those of CeO_2 according to the sizes. It was reported [2–6] that zirconia was the most selective catalyst in the isosynthesis and more effective than ceria [2,3], although it was also a selective catalyst for the formation of branched chain compounds such as isobutene in C_4 from syngas. Considering the commercial and synthesized nanoscale ZrO_2, the activity of the former exhibited less activity than the latter, but they had slightly difference in selectivity of isobutene in hydrocarbons (ca. 77–86%). The higher activity of the synthesized ZrO_2 could be due to higher amount of acid sites. The base property might slightly affect the reaction selectivity to isobutene, however, it was obscured by the higher activity. In this study, physical properties of the synthesized ZrO_2 with different zirconium salt precursor such as ZrO_2–Cl (nano-syn) and ZrO_2–N (nano-syn) did not change significantly. It was found that the ZrO_2–Cl (nano-syn) showed lower activity than the ZrO_2–N (nano-syn), which was possibly caused by lower amount of acid sites and a poison of Cl^-. The result of selectivity to isobutene decreased because of higher activity. Considering the catalytic performance reported by early researchers [5], the ZrO_2–Cl (nano-syn) showed higher activity, but lower selectivity of isobutene in hydrocarbons than the ZrO_2–N (nano-syn). This was probably due to different conditions of ZrO_2 preparation such as the precipitated pH.

It should be noted that the highest catalytic activity of ZrO_2 appeared at the highest amount of acid sites. Considering the base properties, the amount of base sites largely increased when the crystallite size was decreased from micron- to nano-sized, and then resulted in higher selectivity of isobutene in hydrocarbons. However, the nanoscale ZrO_2 at different amounts of base sites did not significantly change the selectivity of isobutene. Moreover, it was found that there was higher activity for the nanoscale CeO_2 compared to the nanoscale ZrO_2. This tendency was also similar to the case of the micronscale ZrO_2 and CeO_2 catalysts. The physical properties of both nanoscale catalysts were similar whereas the amount of acid and base sites of ZrO_2 was higher than those of CeO_2. However, the catalytic performance was changed to the opposite trend, which was perhaps due to the difference of crystal phase between ZrO_2 and CeO_2.

According to the relationship between acid–base properties and percent of tetragonal phase in ZrO_2 (Fig. 7), there was a maximum point at 29% tetragonal phase in ZrO_2 giving the highest amount of acid sites. It was the same trend as the relation of reaction rate and percent of tetragonal phase as shown in Fig. 9. It can be concluded that the catalytic activity apparently associated with acidity. Considering the relationship between selectivity of isobutene in hydrocarbons and tetragonal phase, it was proposed that the selectivities of isobutene were high and slightly changed when tetragonal phase appeared. In other words, the presence of tetragonal phase in zirconia rendered the better catalytic performance compared to with the absence of tetragonal phase.

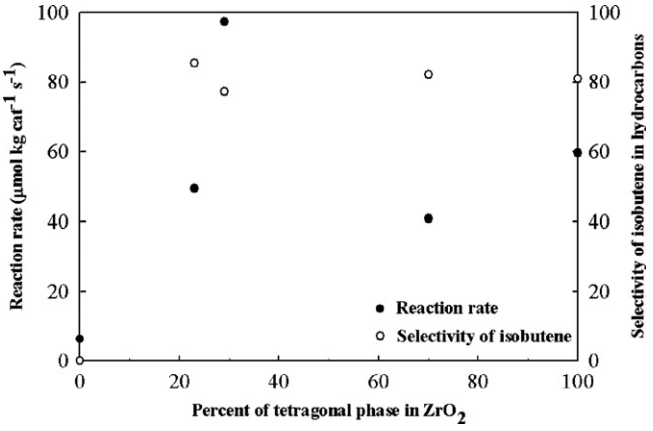

Fig. 9. Relationship between reaction rate, selectivity to isobutene in hydrocarbons and % tetragonal phase in ZrO_2.

In addition, it was reported that when compared the high reaction pressure to the low reaction pressure system, typically the latter exhibited lower catalytic activity, but higher selective of isobutene. Furthermore, lower reaction pressure may result in more selectivity of olefin, which was the same results as the previous work [6] than higher pressure system [4,5,8–10,16].

4. Conclusions

The comparison of catalytic performances in isosynthesis of various zirconia and ceria showed that nanoscale zirconia and ceria performed higher activity and selectivity of isobutene in hydrocarbons than micronscale ones. At the same crystallite size, ceria had higher activity than zirconia. The catalytic performances were dependent on crystallite sizes and amount of acid–base sites. It was indicated that the acid–base properties were dependent on the fraction of tetragonal phase for zirconia, but independent on crystal phase for ceria. The existence of tetragonal phase in zirconia rendered the high selectivity of isobutene in hydrocarbons.

Acknowledgements

The supports from the Thailand Research Fund and the Chulalongkorn University Graduate Scholarship commemoratory the 72nd Anniversary of H.M. Rama IX are greatly appreciated.

References

[1] I. Wender, Fuel Proc. Tech. 48 (1996) 189.
[2] H. Pichler, K.H. Ziesecke, Brennst. Chem. 30 (1949) 13.
[3] H. Pichler, K.H. Ziesecke, B. Traeger, Brennst. Chem. 30 (1949) 333.
[4] C. Su, J. Li, D. He, Z. Cheng, Q. Zhu, Appl. Catal. A: General 202 (2000) 81.
[5] C. Su, D. He, J. Li, Z. Chen, Q. Zhu, J. Mol. Catal. A: Chemical 153 (2000) 139.
[6] K. Maruya, T. Komiya, T. Hayakawa, L. Lu, M. Yashima, J. Mol. Catal. A: Chemical 159 (2000) 97.
[7] K. Maruya, K. Ito, K. Kushihashi, Y. Kishida, K. Domen, T. Onishi, Catal. Lett. 14 (1992) 123.
[8] Y. Li, D. He, Z. Cheng, C. Su, J. Li, Q. Zhu, J. Mol. Catal. A: Chemical 175 (2001) 267.
[9] Y. Li, D. He, Y. Yuan, Z. Cheng, Q. Zhu, Fuel 81 (2002) 1611.
[10] Y. Li, D. He, Q. Zhu, X. Zhang, B. Xu, J. Catal. 221 (2004) 584.
[11] P.D.L. Mercera, J.G. van Ommen, E.B.M. Doesburg, A.J. Burggraaf, J.R.H. Ross, Appl. Catal. 71 (1991) 363.
[12] R.C. Garvie, J. Phys. Chem. 82 (1978) 218.
[13] R. Srinivasan, B.H. Davis, Catal. Lett. 14 (1992) 165.
[14] F.C. Wu, S.C. Yu, J. Mater. Sci. 25 (1990) 970.
[15] Z.-Y. Ma, C. Yang, W. Wei, W.-H. Li, Y.-H. Sun, J. Mol Catal. A: Chemical 227 (2005) 119.
[16] Y. Li, D. He, Q. Zhang, B. Xu, Q. Zhu, Fuel Proc. Technol. 83 (2003) 39.
[17] H.P. Klug, L.E. Alexander, X-ray Diffraction Procedures for Polycrystalline Amorphous Materials, second ed., Wiley, New York, 1974.

Available online at www.sciencedirect.com
ScienceDirect
Applied Catalysis A: General 314 (2006) 128–133
APPLIED CATALYSIS A: GENERAL
www.elsevier.com/locate/apcata

Selective hydrogenation of acetylene in excess ethylene on micron-sized and nanocrystalline TiO_2 supported Pd catalysts

Joongjai Panpranot *, Kunyaluck Kontapakdee, Piyasan Praserthdam

Center of Excellence on Catalysis and Catalytic Reaction Engineering, Department of Chemical Engineering, Faculty of Engineering, Chulalongkorn University, Bangkok 10330, Thailand

Received 11 April 2006; received in revised form 22 July 2006; accepted 7 August 2006
Available online 20 September 2006

Abstract

Physicochemical properties and catalytic performances of Pd catalysts supported on commercial micron-sized and nanocrystalline TiO_2 synthesized by sol–gel and solvothermal method were studied for the selective hydrogenation of acetylene in the presence of excess ethylene. While acetylene conversions were found to be merely dependent on Pd dispersion, ethylene selectivity appeared to be strongly affected by the presence of Ti^{3+} in the TiO_2 samples. The use of pure anatase TiO_2 (either micron- or nano-sized) that contained significant amount of Ti^{3+} as supports for Pd catalysts gave high ethylene selectivities, while the use of pure rutile TiO_2 (without Ti^{3+} present) resulted in ethylene loss. The results suggest that the effect of Ti^{3+} on the TiO_2 supports was more important for high ethylene selectivity than the effect of TiO_2 crystallite size for selective acetylene hydrogenation over Pd/TiO_2 catalysts.

Keywords: Selective acetylene hydrogenation; Pd/TiO_2; Nanocrystalline TiO_2; Sol–gel; Solvothermal; Defect

1. Introduction

Removal of trace amount of acetylene in ethylene feed stream is vital for the commercial production of polyethylene since acetylene acts as a poison to the polymerization catalysts. In order to prevent ethylene loss, when acetylene is catalytically hydrogenated, it is desirable that ethylene remains intact during hydrogenation. Supported Pd-based catalyst is known to be the best catalyst so far for such reaction with good activity and selectivity. The commonly used support for palladium catalyst in selective acetylene hydrogenation is α-alumina, however, oligomer or green oil formation during reaction is inevitable over Pd/Al_2O_3 catalysts resulting in ethylene loss and shorten catalyst lifetime especially at high levels of acetylene conversion [1–6]. Several attempts to improve ethylene selectivity of the palladium catalyst have been made by many researchers, including incorporation of a second metal such as Ag [7–10], Au [11,12], Cu [13], Si [14], K [15], and Co [16], pre-treatment with oxygen-containing compounds such as CO and N_2O [17–20], and modification of the catalyst supports [21,22].

Among the various supports studied, TiO_2 is of particular interest because of its ability to manifest a strong metal–support interaction (SMSI) with group VIII metals and its low acidity compared to alumina. Moon and co-workers [21] reported an improved selectivity for ethylene production in selective acetylene hydrogenation over TiO_2-modified Pd catalysts. The authors suggest that charge transfer from Ti species to Pd weakened the adsorption strength of ethylene on the Pd surface hence higher ethylene selectivity was obtained. Moreover, the amount of green oil formation was reduced on the TiO_2-added Pd catalysts due to suppression of the multiply coordinated Pd sites resulting in an improved catalyst lifetime [23]. Fan and co-workers [24] studied selective hydrogenation of long chain alkadienes, it was shown that the presence of SMSI for Pd/TiO_2 catalysts led to higher selectivity of alkenes.

Recently, our group has reported the synthesis of nanocrystalline TiO_2 by solvothermal method and their applications as Pd catalyst supports in selective acetylene hydrogenation [25]. The solvothermal-derived TiO_2 supported Pd catalysts exhibited relatively high acetylene conversions and ethylene selectivities in the temperature range 40–90 °C in selective acetylene hydrogenation using trace amount of C_2H_2

* Corresponding author. Tel.: +66 2218 6878; fax: +66 2218 6877.
E-mail address: joongjai.p@eng.chula.ac.th (J. Panpranot).

0926-860X/$ – see front matter © 2006 Elsevier B.V. All rights reserved.
doi:10.1016/j.apcata.2006.08.024

in N_2 balance. Nevertheless, their catalytic activities and selectivities have not yet been compared to those of commercial TiO_2 supported ones under real commercial ethylene feed stocks. Thus, it is the aim of this study to investigate and compare the catalytic performances of commercial micron-sized and nanocrystalline TiO_2 supported Pd catalysts in selective acetylene hydrogenation in the presence of excess ethylene. The effects of crystallite size as well as other physicochemical properties such as the presence of Ti^{3+} defective sites of the TiO_2 on the catalytic properties of Pd/TiO_2 catalysts were investigated by means of X-ray diffraction (XRD), N_2 physisorption, X-ray photoelectron spectroscopy (XPS), CO chemisorption, scanning electron microscopy (SEM), and electron spin resonance (ESR).

2. Experimental

2.1. Preparation of TiO_2 and Pd/TiO_2 catalyst samples

The commercial anatase TiO_2 was obtained from Aldrich. By calcination in air at 1010 °C for 4 h using a space velocity of air flow 16,000 h^{-1}, the anatase TiO_2 was gradually transformed into rutile TiO_2. The commercial anatase and rutile TiO_2 were denoted as TiO_2-com-A and TiO_2-com-R, respectively.

Titanium ethoxide (Ti 20%) from Aldrich was used as Ti precursor for preparation of the nanocrystalline TiO_2 by sol–gel method [26]. A specific amount of the precursor was dissolved in ethanol and mixed with a water–ethanol solution at water to alkoxide molar ratio 165. The precursor solution was added drop wise to the aqueous solution and stirred by ultrasonic vibration at room temperature. White precipitates of hydrous oxides formed instantly and the mixture was stirred for at least two more hours. The amorphous precipitates were separated from the mother liquor by centrifugation and were re-dispersed in ethanol for five times to minimize particle agglomeration. The resulting materials were then dried and calcined at 450 °C in flowing oxygen for 2 h at the heating rate of 10 °C/min. The sol–gel derived TiO_2 was denoted hereafter as TiO_2-sol–gel.

The solvothermal-derived TiO_2 was prepared according to the method described in Ref. [27] using 25 g of titanium(IV) *n*-butoxide (TNB) 97% from Aldrich. The starting material was suspended in 100 ml of 1,4-butanediol in a test tube and then set up in an autoclave. In the gap between the test tube and autoclave wall, 30 ml of solvent was added. After the autoclave was completely purged with nitrogen, the autoclave was heated to 320 °C at 2.5 °C/min and held at that temperature for 6 h. Autogenous pressure during the reaction gradually increased as the temperature was raised. After the reaction, the autoclave was cooled to room temperature. The resulting powders were collected after repeated washing with methanol by centrifugation. They were then air-dried at room temperature. The solvothermal derived TiO_2 was denoted hereafter as TiO_2-solvothermal.

One percent Pd/TiO_2 were prepared by the incipient wetness impregnation technique using an aqueous solution of the desired amount of $Pd(NO_3)_2$ (Wako). The catalysts were dried overnight at 110 °C and then calcined in N_2 flow 60 cm^3/min with a heating rate of 10 °C/min until the temperature reached 500 °C and then in air flow 100 cm^3/min at 500 °C for 2 h.

2.2. Catalyst characterization

The BET surface areas of the samples were determined by N_2 physisorption using a Micromeritics ASAP 2000 automated system. Each sample was degassed under vacuum at <10 μm Hg in the Micromeritics ASAP 2000 at 150 °C for 4 h prior to N_2 physisorption. The XRD spectra of the catalyst samples were measured from 20–80° 2θ using a SIEMENS D5000 X-ray diffractometer and Cu Kα radiation with a Ni filter. Electron spin resonance spectra were taken at −150 °C using a JEOL JES-RE2X spectrometer. Relative percentages of palladium dispersion were determined by pulsing carbon monoxide over the reduced catalyst. Approximately 0.2 g of catalyst was placed in a quartz tube in a temperature-controlled oven. The amounts of CO chemisorbed on the catalysts were measured using a Micromeritic Chemisorb 2750 automated system attached with ChemiSoft TPx software at room temperature. Prior to chemisorption, the sample was reduced in a H_2 flow at 500 °C for 2 h then cooled down to ambient temperature in a He flow. The particle morphology was obtained using a JEOL JSM-35CF scanning electron microscope operated at 20 kV. Surface compositions of the catalysts were analyzed using an AMICUS photoelectron spectrometer equipped with a Mg Kα X-ray as a primary excitation and a KRATOS VISION2 software. XPS elemental spectra were acquired with 0.1 eV energy step at a pass energy of 75 kV. The C 1s line was taken as an internal standard at 285.0 eV.

2.3. Reaction study

Selective acetylene hydrogenation was performed in a quartz tube reactor (i.d. 9 mm). Prior to the start of each run, the catalyst was reduced in H_2 at 500 °C for 2 h. Then the reactor was purged with argon and cooled down to the reaction temperature, 40 °C. Feed gas composed of 1.46% C_2H_2, 1.71% H_2, 15.47% C_2H_6 and balanced C_2H_4 (Rayong Olefin Co., Ltd.) and a GHSV of 5400 h^{-1} were used. The composition of product and feed stream were analyzed by a Shimadzu GC 8A equipped with TCD and FID detectors (molecular sieve-5A and carbosieve S2 columns, respectively). Acetylene conversion as used herein is defined as moles of acetylene converted with respect to acetylene in feed. Ethylene selectivity is defined as the percentage of acetylene hydrogenated to ethylene over totally hydrogenated acetylene. The ethylene being hydrogenated to ethane (ethylene loss) is the difference between all the hydrogen consumed and all the acetylene which has been totally hydrogenated.

3. Results and discussion

3.1. Physicochemical properties of the TiO_2 supports

The SEM micrographs of various titania samples are shown in Fig. 1. The commercial anatase TiO_2 had a uniform particle

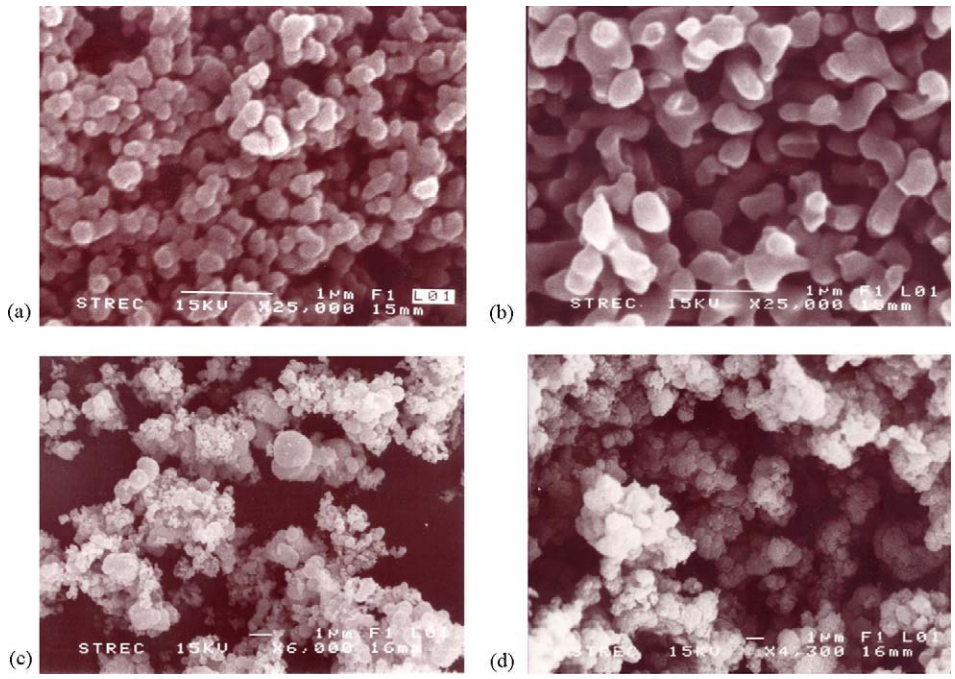

Fig. 1. SEM micrographs of: (a) TiO_2-com-A (b) TiO_2-com-R (c) TiO_2-sol–gel and (d) TiO_2-solvothermal.

size ca. 0.2 μm. After being subjected to thermal treatment (calcination) at 1010 °C for 4 h, pure anatase titania was gradually transformed into rutile titania and the particle size increased to ca. 0.4 μm. The morphology of pure anatase nanocrystalline TiO_2 prepared by sol–gel and solvothermal method was consisted of irregular shape of fine particles. However, some of the particles of those synthesized by the sol–gel method appeared to agglomerate into spherical micron-size particles. The crystallization mechanism of TiO_2 was probably different for these two methods resulting in different properties of the TiO_2 obtained. It was suggested that anatase titania synthesized by solvothermal in 1,4-butanediol was resulted from direct crystallization [27] while sol–gel method yielded a solid precipitate at relatively low temperature used and crystallization occurred during the subsequent calcination step. XRD patterns of the calcined TiO_2 samples are shown in Fig. 2. For the anatase titania (TiO_2-com-A, TiO_2-sol–gel, and TiO_2-solvothermal), XRD peaks at $2\theta = 25$ (major), 37, 48, 55, 56, 62, 71, and 75° 2θ were evident. The TiO_2-com-R exhibited XRD peaks for rutile phase at $2\theta = 28$ (major), 36, 42, and 57°. BET surface areas, average crystallite sizes, and percentages of atomic concentration (Ti/O) of the various TiO_2 samples are given in Table 1. The average crystallite sizes of the TiO_2 prepared by sol–gel and solvothermal calculated from the full width at half maximum of the XRD peak at $2\theta = 25°$ using Scherrer equation are in nanometer range (10 and 17, respectively) while those of the commercial ones could not be determined by this method due to the calculation limit of the Scherrer equation (the crystallite size may be too large). BET surface areas of the commercial anatase TiO_2 decreased essentially from 64.4 to 18.3 m^2/g after calcination in order to transform the crystalline phase to rutile phase TiO_2. It is surprising that the BET surface areas of the nano-sized TiO_2 prepared by sol–gel and solvothermal method were much lower

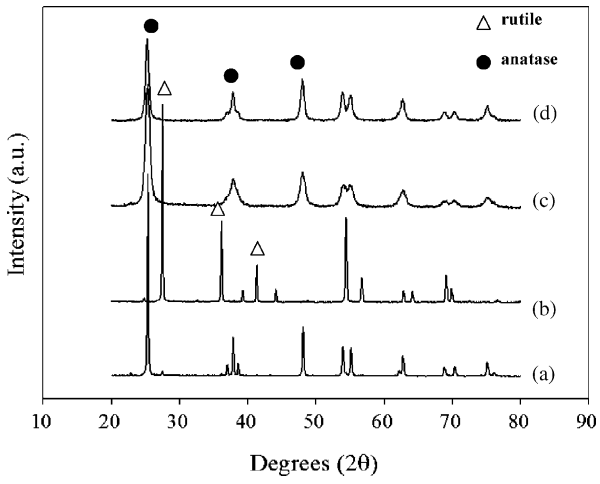

Fig. 2. XRD results of: (a) TiO_2-com-A (b) TiO_2-com-R (c) TiO_2-sol–gel and (d) TiO_2-solvothermal.

Table 1
Properties of the various TiO_2 supports

Sample	BET surface area[a] (m^2/g)	Crystallite size[b] (nm)	Atomic concentration[c] (%), Ti/O
TiO_2-com-A	64.4	n.d.	0.287
TiO_2-com-R	18.3	n.d.	0.250
TiO_2-sol–gel	39.3	10	0.232
TiO_2-solvothermal	26.8	17	0.220

[a] Error of measurement = ±10%.
[b] Determined from XRD line broadening.
[c] Determined from XPS analysis.

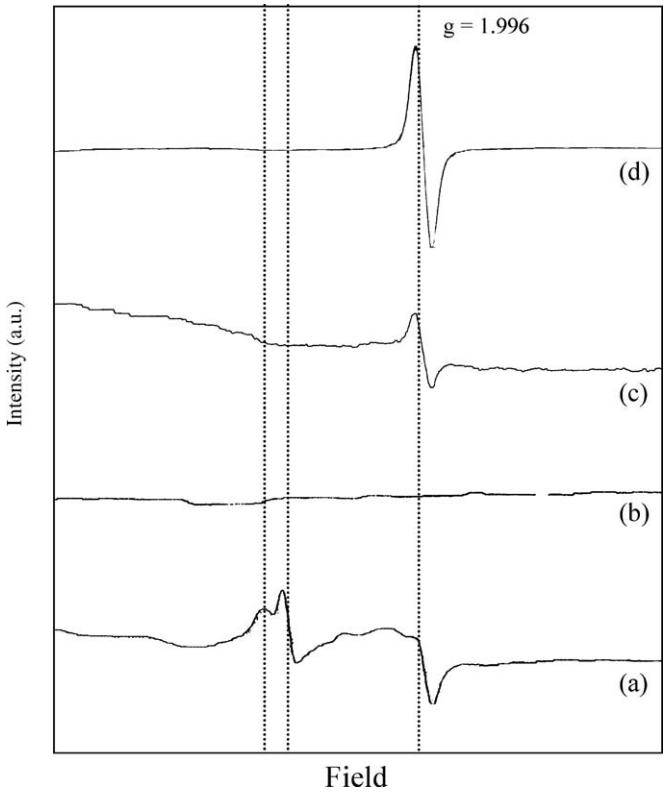

Fig. 3. ESR spectra of: (a) TiO_2-com-A (b) TiO_2-com-R (c) TiO_2-sol–gel and (d) TiO_2-solvothermal.

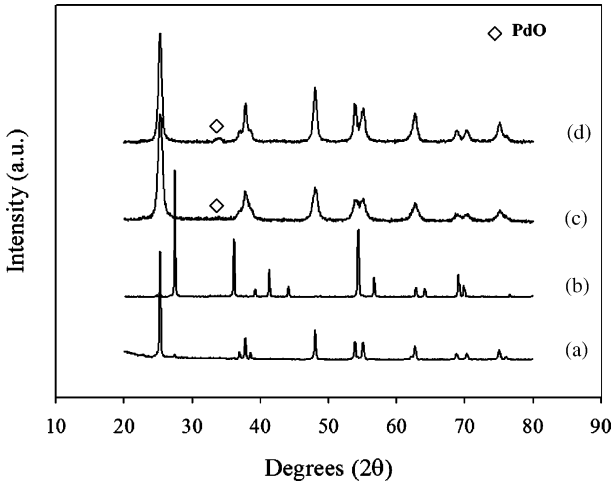

Fig. 4. XRD results of: (a) Pd/TiO_2-com-A (b) Pd/TiO_2-com-R (c) Pd/TiO_2-sol–gel and (d) Pd/TiO_2-solvothermal.

than that of the commercial anatase TiO_2. Such results suggest that the nano-crystals were closely packed resulting in low pore volume in the samples. Percentages of atomic concentrations of Ti and O on the surface of the TiO_2 were determined by the X-ray photoelectron spectroscopy. The Ti/O ratios were not significantly different among the four TiO_2 samples. There was probably an oxygen-rich layer near the surface of the TiO_2 particles, which is formed by oxygen adsorption and easy oxidation of titanium surface [28]. The ESR spectra of the TiO_2 samples are shown in Fig. 3. The signals of g values less than 2 were assigned to Ti^{3+} ($3d^1$) [29,30]. Nakaoka and Nosaka [31] reported six signals of ESR measurement occurring on the surface of titania: (i) $Ti^{4+}O^{-}Ti^{4+}OH^{-}$, (ii) surface Ti^{3+}, (iii) adsorbed oxygen (O^{2-}), (iv) $Ti^{4+}O^{2-}Ti^{4+}O^{2-}$, (v) inner Ti^{3+}, and (vi) adsorbed water. In this study, it is seen that the sol–gel and solvothermal-derived TiO_2 exhibited only one signal at g value of 1.996 which can be attributed to Ti^{3+} at the surface. Many Ti^{3+} ESR signals were observed for the commercial anatase TiO_2, it is indicated that more than one type of Ti^{3+} defects were presented in the sample, i.e. surface Ti^{3+} and inner Ti^{3+}. It should be noted that the Ti^{3+} ESR signal was observed only for the anatase TiO_2 (both micron- and nano-sized). The rutile TiO_2 did not exhibit any ESR signal. It is suggested that Ti^{4+} in the rutile TiO_2 is more difficult to be reduced to Ti^{3+}. As rutile titania is more thermodynamically and structurally stable than anatase titania so that the Ti^{3+} ions fixed in the surface lattice of anatase TiO_2 is easier to diffuse to the surface than one in the surface lattice of rutile TiO_2 [24]. The intensity of the Ti^{3+} signal was highest for the solvothermal-derived TiO_2 suggesting that this preparation method produces the highest amount of defects on the TiO_2.

3.2. Characteristics and catalytic properties of Pd/TiO_2 catalysts

The XRD patterns of the various Pd/TiO_2 catalysts are shown in Fig. 4. There were no changes in the crystalline phase of the TiO_2 after impregnation of palladium for all the catalyst samples. The major XRD characteristic peak for PdO at $2\theta = 33.8^\circ$ were

Table 2
Characteristics of the various TiO_2-supported Pd catalysts

Catalyst	BET surface area[a] (m^2/g)	CO pulse chemisorption[b] ($\times 10^{-18}$ molecule CO/g catalyst)	Pd dispersion[c] (%)	d_P[d] Pd^0 (nm)	Atomic concentration[e] (%)	
					Ti/O	Pd/Ti
Pd/TiO_2-com-A	44.5	2.23	3.93	28.5	0.253	0.084
Pd/TiO_2-com-R	17.2	1.55	2.73	41.0	0.240	0.168
TiO_2-sol–gel	33.8	1.19	2.10	53.3	0.282	0.011
Pd/TiO_2-solvothermal	26.0	0.49	0.86	130.2	0.274	0.006

[a] Error of measurement = ±10%.
[b] Error of measurement = ±5%.
[c] Based on the total amount of palladium loaded.
[d] Based on $d = 1.12/D$ (nm), where D = fractional metal dispersion [34].
[e] Determined from XPS analysis.

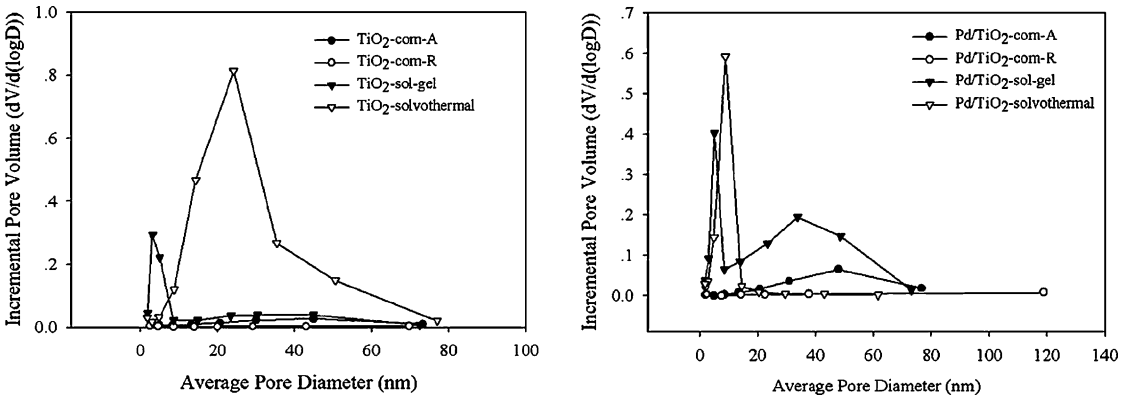

Fig. 5. Pore size distribution results of the various Pd/TiO_2 catalysts.

evident only for the catalyst prepared with the solvothermal-derived TiO_2. The BET surface areas, CO chemisorption results, and atomic concentration of surface element of the Pd/TiO_2 catalyst samples are given in Table 2. The BET surface area of the Pd catalysts were not significantly different form the original TiO_2 supports, however, changes in the pore size distribution of the catalysts due to Pd loading were observed for both sol–gel and solvothermal-derived TiO_2 supported ones suggesting that Pd was deposited in some of the pores of the TiO_2 (Fig. 5). It should also be noted that Pd/TiO_2-com-A was not heat-treated prior to the impregnation step, while the other supports were treated at 1010, 450, and 320 °C. Accordingly, it is also possible that a large decrease in the surface area of the anatase supported catalyst is caused by the calcination of the catalyst at 500 °C after the Pd loading. The percentages of Pd dispersion calculated from the CO chemisorption results were in the order Pd/TiO_2-com-A > Pd/TiO_2-com-R > Pd/TiO_2-sol–gel > Pd/TiO_2-solvothermal. The largest Pd particle size calculated from the CO chemisorption for the Pd/TiO_2-solvothermal catalyst is in a good agreement with the XRD results. It should be noted that as the anatase TiO_2 was transformed to rutile phase TiO_2, the amount of CO chemisorption decreased from 2.23×10^{18} to 1.55×10^{18} molecules CO while the calculated average particle size of Pd^0 metal increased from 28.5 to 41.0 nm. Thus, the presence of rutile phase significantly decreased dispersion of palladium on the titania supports. XPS analysis revealed an increasing Pd/Ti surface concentration from 0.084 to 0.168 when rutile TiO_2 was employed instead of anatase TiO_2. In contrast, the Pd/Ti atomic concentration ratios for those supported on sol–gel and solvothermal derived TiO_2 were much lower than those of the commercial TiO_2 supported ones.

In order to investigate the catalytic performance of the different types of TiO_2 supported Pd catalysts, selective hydrogenation of acetylene in excess ethylene was performed in a fixed bed flow reactor. Fig. 6 shows acetylene conversions and ethylene selectivities obtained from the various Pd/TiO_2 catalysts. Acetylene conversions were in the range of 20–59% and were found to be merely dependent on the Pd dispersion. The selectivities of ethylene were varied from −1.4 to 76.2% with the commercial rutile and the sol–gel derived TiO_2 supported Pd catalysts exhibited the lowest and the highest selectivities, respectively. However, it should be noted that the high ethylene selectivities of the nano-TiO_2 supported Pd catalysts may be because their conversions of acetylene were low. It is thus more appropriate to use the results from Fig. 6 only to compare the selectivities of Pd/TiO_2-com-A and Pd/TiO_2-com-R catalysts. The use of anatase TiO_2 as supports for Pd catalysts resulted in positive values of ethylene selectivity while the use of rutile TiO_2 produced ethylene loss due to over-hydrogenation of ethylene to ethane. Ethylene hydrogenation is usually believed to take place on the support by means of a hydrogen transfer mechanism [32]. Thus, the rutile phase of TiO_2 may be responsible for such reaction. Moreover, the presence of Ti^{3+} ions in anatase TiO_2 supports has a positive effect on high ethylene selectivity, i.e. increasing desorption of ethylene from the catalyst surface. It has been reported that the presence of Ti^{3+} on TiO_2 can lower the temperature to induce a strong metal–support interaction [24]. The SMSI between Pd and TiO_2 support can result in lower adsorption strength of ethylene on the catalyst surface and promotes ethylene desorption [21]. There were no such differences in ethylene selectivities for the micron- and the nano-anatase TiO_2 supported Pd catalysts. This indicates that the crystallite size of TiO_2 support did not have a significant impact on ethylene selectivity; the difference in selectivity of ethylene was due mainly to the presence/absence of Ti^{3+} defective sites on the TiO_2 support. However, in the other studies reported previously by our group [25,33], we have found that there was an optimum amount of Ti^{3+} sites to produce high ethylene selectivity since

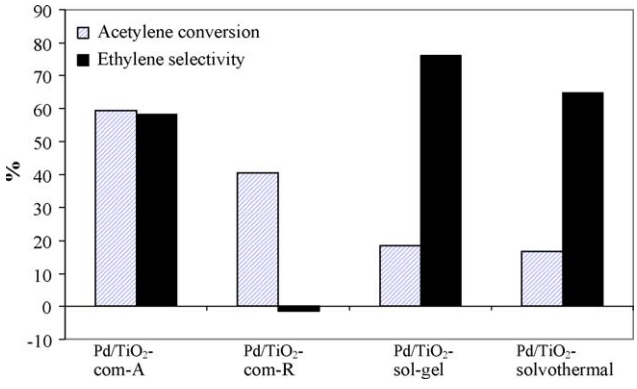

Fig. 6. Catalyst performances in selective acetylene hydrogenation.

only Ti^{3+} species that were in contact with palladium surface promoted SMSI effect and ethylene desorption [24]. Too many Ti^{3+} sites that were not in contact with Pd may result in an over-hydrogenation of ethylene to ethane. This is probably why ethylene selectivity of the Pd/TiO_2-solvothermal is not the highest among four catalysts although the ESR results of Fig. 3 indicated that the intensity of the Ti^{3+} signal was the highest for TiO_2-solvothermal.

4. Conclusions

The use of pure anatase TiO_2 (either micron- or nano-sized) as supports for Pd catalysts produced high ethylene selectivities during selective acetylene hydrogenation in excess ethylene. In contrast, the use of pure rutile TiO_2 supported ones resulted in ethylene loss due to over-hydrogenation of ethylene to ethane. The differences in ethylene selectivity of the various Pd/TiO_2 were due mainly to the presence/absence of the Ti^{3+} defective sites on the TiO_2 support, rather than the difference in the crystallite sizes of the TiO_2 support.

Acknowledgements

Financial supports from the Thailand Research Fund (TRF), Rayong Olefins Co., Ltd., and the Commission on Higher Education are gratefully acknowledged.

References

[1] M.M. Johnson, D.W. Walker, G.P. Nowack, US Patent 4,484,015 (1984).
[2] G.C. Bond, P.B. Wells, J. Catal. 5 (1965) 65.
[3] G.C. Bond, P.B. Wells, Trans. Faraday Soc. 54 (1958) 1537.
[4] M. Larsson, J. Jansson, S. Asplund, J. Catal. 162 (1996) 365.
[5] Y.-J. Huang, C.F. Shun, L.G. Daniel, E.L. Mohundro, J.E. Hartgerink, US Patent 5,332,705 (1994).
[6] K. Flick, C. Herion, H.-M. Allman, US Patent 5,856,262 (1999).
[7] J. Phillips, A. Auroux, G. Bergeret, J. Massardier, A. Renoupez, J. Phys. Chem. 97 (1993) 3565.
[8] D.C. Huang, K.H. Chang, W.F. Pong, P.K. Tseng, K.J. Hung, W.F. Huang, Catal. Lett. 53 (1998) 155.
[9] Q. Zhang, J. Li, X. Liu, Q. Zhu, Appl. Catal. A 197 (2000) 221.
[10] Y. Jin, A.K. Dayte, E. Rightor, R. Gulotty, W. Waterman, M. Smith, M. Holbrook, J. Maj, J. Blackson, J. Catal. 203 (2001) 292.
[11] C. Visser, G.P. Zuidwijk, V. Ponec, J. Catal. 35 (1974) 407.
[12] A. Sarkany, A. Horvath, A. Beck, Appl. Catal. A 229 (2002) 117.
[13] S. LeViness, V. Nair, A. Weiss, J. Mol. Catal. 25 (1984) 131.
[14] E.W. Shin, C.H. Choi, K.S. Chang, Y.H. Na, S.H. Moon, Catal. Today 44 (1998) 137.
[15] Y.H. Park, G.L. Price, Ind. Eng. Chem. Res. 31 (1992) 469.
[16] A. Sarkany, Z. Zsoldos, G. Stefler, W. Hightower, L. Guczi, J. Catal. 157 (1995) 179.
[17] L. Cider, N.-H. Schoon, Ind. Eng. Chem. Res. 30 (1991) 1437.
[18] P. Praserthdam, B. Ngamsom, N. Bogdanchikova, S. Phatanasri, M. Pramotthana, Appl. Catal. A 230 (2002) 41.
[19] B. Ngamsom, N. Bogdanchikova, M.A. Borja, P. Praserthdam, Catal. Commun. 5 (2004) 243.
[20] R.N. Lamb, B. Ngamsom, D.L. Trimm, B. Gong, P.L. Silveston, P. Praserthdam, Appl. Catal. 268 (2004) 43.
[21] J.H. Kang, E.W. Shin, W.J. Kim, J.D. Park, S.H. Moon, J. Catal. 208 (2002) 310.
[22] A. Monzón, E. Romeo, C. Royo, R. Trujillano, F.M. Labajos, V. Rives, Appl. Catal. A 185 (1999) 53.
[23] W.J. Kim, J.H. Kang, I.Y. Ahn, S.H. Moon, J. Catal. 226 (2004) 226.
[24] Y. Li, B. Xu, Y. Fan, N. Feng, A. Qiu, J. Miao, J. He, H. Yang, Y. Chen, J. Mol. Catal. A 216 (2004) 107.
[25] J. Panpranot, L. Nakkararuang, B. Ngamsom, P. Praserthdam, Catal. Lett. 103 (2005) 53.
[26] K. Suriye, P. Praserthdam, B. Jongsomjit, Ind. Eng. Chem. Res. 44 (2005) 6599.
[27] W. Payakgul, O. Mekasuwandumrong, V. Pavarajarn, P. Praserthdam, Ceram. Int. 31 (2005) 391.
[28] F. Zhang, Z. Zheng, D. Liu, Y. Mao, Y. Chen, Z. Zhou, S. Yang, X. Liu, Nucl. Instrum. Meth. B 132 (1997) 620.
[29] J.C. Conesa, P. Malet, G.M. Unuera, J. Sanz, J. Soria, J. Phys. Chem. 88 (1984) 2986.
[30] T.M. Salama, H. Hattori, H. Kita, K. Ebitani, T. Tanaka, J. Chem. Soc. Faraday Trans. 89 (1993) 2067.
[31] Y. Nakaoka, Y. Nosaka, J. Photochem. Photobiol. A 110 (1997) 299.
[32] S. Aplund, J. Catal. 158 (1996) 267.
[33] J. Panpranot, K. Kontapakdee, P. Praserthdam, J. Phys. Chem. B 110 (2006) 8019.
[34] N. Mahata, V. Vishwanathan, J. Catal. 196 (2000) 262.

Available online at www.sciencedirect.com
ScienceDirect
Journal of Crystal Growth 297 (2006) 234–238
JOURNAL OF CRYSTAL GROWTH
www.elsevier.com/locate/jcrysgro

Effect of crystallite size on the surface defect of nano-TiO_2 prepared via solvothermal synthesis

Wilasinee Kongsuebchart, Piyasan Praserthdam*, Joongjai Panpranot, Akawat Sirisuk, Piyawat Supphasrirongjaroen, Chairit Satayaprasert

Center of Excellence on Catalysis and Catalytic Reaction Engineering, Department of Chemical Engineering, Faculty of Engineering, Chulalongkorn University, Bangkok 10330, Thailand

Received 21 June 2006; received in revised form 31 August 2006; accepted 2 September 2006
Communicated by J. M. Redwing
Available online 20 November 2006

Abstract

Nano-TiO_2 powders were synthesized by the solvothermal method under various reaction conditions in order to obtain average crystallite sizes of 9–15 nm. The amounts of surface defect of TiO_2 were measured by means of temperature-programmed desorption of CO_2 and electron spin resonance spectroscopy. It was found that the ratios of surface defect/specific surface area increased significantly with increasing TiO_2 crystallite size. The TiO_2 with higher amounts of surface defects exhibited much higher photocatalytic activity for ethylene decomposition.

Keywords: A1. Crystallite size; A1. Surface defect; A1. Surface structure; B1. TiO_2; B1. Ti^{3+}

1. Introduction

Nowadays, titanium (IV) dioxide or titania (TiO_2) is one of the most popular and promising catalysts in photocatalytic applications for environmental remediation due to the strong oxidizing power of its holes, high photostability, and redox selectivity [1–7]. Titania can be synthesized by various methods such as solvothermal method [8–11], precipitation method [12], sol–gel method [13–15], and thermal decomposition of alkoxide [16]. The properties of TiO_2 synthesized by different methods vary in terms of their crystal structure, chemical composition, surface morphology, crystal defects, specific surface area, etc. While the sol–gel method is widely used to prepare nano-sized TiO_2, the precipitated powders obtained are amorphous in nature and further heat treatment is required for crystallization. The solvothermal method is an alternative route for one-step synthesis of pure anatase nano-sized TiO_2. Particle morphology, crystalline phase, and surface chemistry of the solvothermal-derived TiO_2 can be easily controlled by regulating precursor composition, reaction temperature, pressure, solvent property, and aging time [17].

There always exist structural defects on the surface and inside titania particles [18]. These structural defects are related with the density of photoexcited electrons. Surface defects are good for high photocatalytic activity because they can act as active sites for adsorption and dissociation of molecules on the TiO_2 surface [19–21]. However, the bulk defect lowers the photocatalytic activity because they provide sites for the recombination of the photogenerated electrons. According to electron spin resonance (ESR) spectroscopic study, the photoexcited electron trap at surface Ti^{3+} sites or Ti^{4+} sites within the bulk and holes trap at lattice oxygen ions [22–24]. Therefore, the bulk defect should be reduced to obtain high photocatalytic activity. The nature of defects on TiO_2 can be found in a recent review by Watson et al. [25].

In this study, nano-TiO_2 powders with average crystallite sizes in the range of 9–15 nm were synthesized by the solvothermal method. The effect of crystallite size on the

*Corresponding author. Tel.: +66 2218 6882; fax: +66 2218 6877.
E-mail address: piyasan.p@chula.ac.th (P. Praserthdam).

0022-0248/$ - see front matter © 2006 Elsevier B.V. All rights reserved.
doi:10.1016/j.jcrysgro.2006.09.018

amount of surface defects on TiO_2 was investigated by means of X-ray diffraction (XRD), N_2 physisorption, temperature-programmed desorption of CO_2, and ESR spectroscopy. Photocatalytic activities of the TiO_2 powders were determined from a gas-phase decomposition of ethylene under UV irradiation.

2. Experimental Procedure

2.1. Preparation of TiO_2

Nanocrystalline TiO_2 was prepared using the solvothermal method according to that of Ref. [26] using titanium (IV) *n*-butoxide (TNB) as starting material. In general, 15–25 g of TNB was suspended in 100 cm^3 of toluene in a test tube, which was then placed in a 300 cm^3 autoclave. The gap between the test tube and the autoclave wall was filled with 30 cm^3 of the same solvent used in the test tube. The autoclave was purged completely by nitrogen before heating up to 573 K at a rate of 2.5 K/min. Autogeneous pressure during the reaction gradually increased as the temperature was raised. Once the prescribed temperature was reached, the temperature was held constant for 0.5–8 h. After the system was cooled down, the resulting powders were repeatedly washed with methanol and dried in air. The synthesis product was then calcined in a box furnace by heating up to the desired temperature, in the range of 563–583 K, at a rate of 10 K/min and held at that temperature for 1 h in order to remove any impurity that might remain on the samples after washing with methanol.

2.2. Characterization

Powder XRD analysis was carried out using a SIEMENS D5000 diffractometer with Cu K_α radiation. The crystallite size of the product was determined from broadening of its main peak ($2\theta = 25^\circ$) using the Scherrer equation. The specific surface area was calculated using Brunauer-Emmett-Teller (BET) single-point method on the basis of nitrogen uptake measured at 77 K at a relative pressure of 0.3. Before N_2 adsorption, each sample was dried at 403 K for 30 min in a 30% N_2–helium flow. The amount of nitrogen desorbed was measured using a thermal conductivity detector. Temperature-programmed desorption using CO_2 as a probe molecule (CO_2-TPD) was performed to determine the Ti^{3+} site existing on the surface of a TiO_2 particle [27]. The CO_2-TPD was carried out using homemade equipment composed of a quartz tube in a temperature-controlled bath connecting to a gas chromatograph (GOW-MAC) with a thermal conductivity detector. Approximately 0.05 g of a TiO_2 sample was dosed by 1 vol% CO_2 in helium for 1 h and then desorbed from 143 to 273 K with a rate of 21.5 K/min. ESR spectroscopy was conducted using a JEOL JESRE2X ESR spectrometer. The intensity of ESR was calculated using a computer software program ES-PRIT ESR DATA SYSTEM (version 1.6). Transmission electron micrographs of the TiO_2 samples were obtained using a JEOL JEM 1220 electron microscope operated at 80 kVa.

2.3. Evaluation of photocatalytic activity

The decomposition of ethylene via photocatalytic reaction was employed to evaluate photocatalytic activity of the TiO_2 products obtained. Approximately 0.4 g of the synthesized TiO_2 was spread in a horizontal quartz reactor. The air containing 0.1% ethylene was continuously supplied at a constant flow rate with a gas hourly space velocity of 120 h^{-1}. The reaction temperature was set at 313 K. For each run, an air stream with 0.1% ethylene was first passed through the reactor without illumination until reaching gas–solid adsorption equilibrium (typically 120–180 min) as indicated by identical inlet/outlet ethylene concentration. Then, UV light was illuminated on the surface of the catalyst by using 500 W mercury lamps. The outlet gas was sampled and analyzed at regular intervals by using a SHIMADZU GC-14B gas chromatograph equipped with the flame-ionized detector.

3. Results and discussion

In this study, the crystallite size of the solvothermal-derived TiO_2 was varied in the range of 9–15 nm by changing the concentrations of TNB, the reaction temperatures, and the holding times. Increasing reaction temperature and holding time resulted in an increase in the average crystallite size of TiO_2. The average crystallite sizes and BET surface areas of the obtained TiO_2 from various synthesis conditions are given in Table 1. The XRD patterns of all the obtained TiO_2 powders are shown in Fig. 1. The characteristic peaks of pure anatase-phase titania were observed at 25, 38, and 48° 2θ [28] without contamination of other phases such as rutile and brookite. The average crystallite sizes of TiO_2 were calculated from the full-width at half-maximum of the XRD peak at $2\theta = 25^\circ$ using the Scherrer equation. As the average TiO_2 crystallite size increased from 9 to 15 nm, the BET surface areas decreased monotonically from 126 to 51 m^2/g. The specific surface areas of the TiO_2 samples were also calculated based on the correlation between surface area and crystallite size as follows:

$$S_2 = 6/d\rho,$$

where d is the average crystallite size and ρ is the density of TiO_2 (3.84 g cm^3) [29].

It is noticed that S_1 determined from N_2 physisorption was smaller than S_2 calculated based on the crystallite size for all the TiO_2 samples. This was probably the result of an amorphous-like phase contaminated in the TiO_2 particles [11]. Transmission electron microscope (TEM) imaging has been carried out in order to determine the shape of the particles and the existence of amorphous phase. A typical TEM micrograph of the TiO_2-9 nm sample is shown in Fig. 2. The TEM images show that the TiO_2 products

Table 1
Specific surface areas and average crystallite sizes of the TiO_2 samples obtained from various synthesis conditions

Sample	Amount of TNB in solvent (g)	Temperature (°C)	Holding time (h)	Crystallite size (nm)	Specific surface area (m^2/g)		S_1/S_2
					S_1[a]	S_2[b]	
1	15	300	0.5	9.0	126.4	170.9	0.74
2	25	300	2.0	11.0	92.3	139.9	0.66
3	25	320	6.0	12.5	78.2	123.1	0.64
4	25	350	6.0	14.5	53.1	106.1	0.50
5	25	350	8.0	15.0	51.1	102.6	0.50

[a] S_1 is specific surface area determined from N_2 physisorption results.
[b] S_2 is specific surface area calculated based on the correlation between surface area and crystallite size of TiO_2 ($S_2 = 6/d\rho$ [29]).

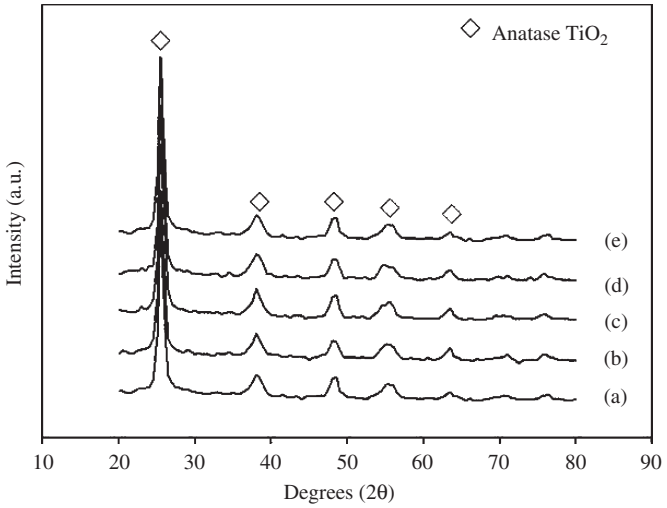

Fig. 1. XRD patterns of the TiO_2 samples with various crystallite sizes (a) 9 nm, (b) 11 nm, (c) 12.5 nm, (d) 14.5 nm, and (e) 15 nm.

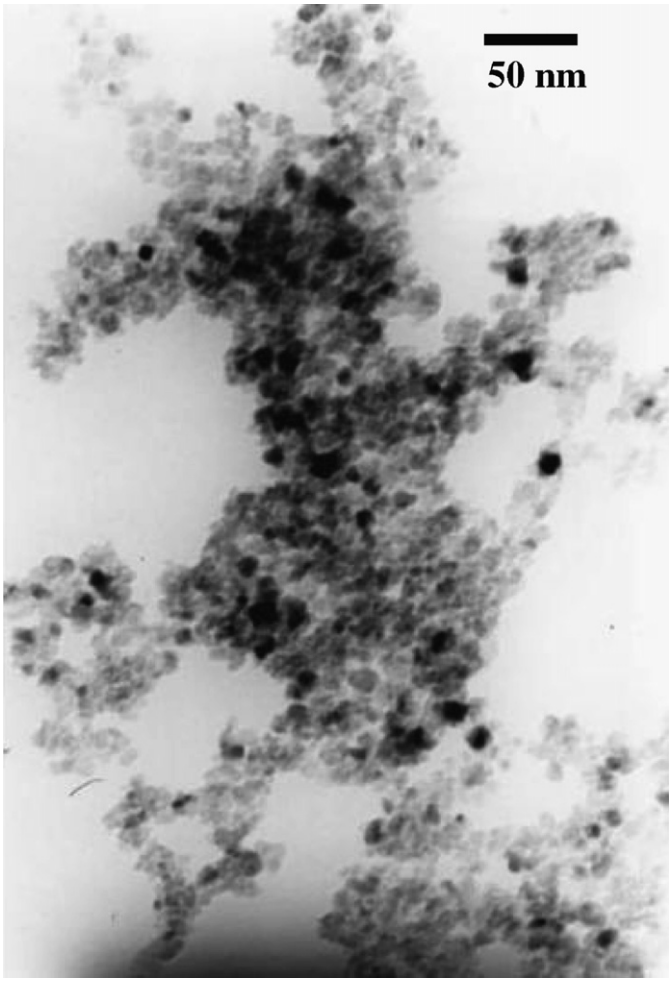

Fig. 2. A typical TEM micrograph of the TiO_2-9 nm sample.

obtained by solvothermal synthesis under the conditions used consist of spherical particles with particle sizes consistent with the calculated results. The TiO_2 samples may contain a fraction of amorphous phase since the preferential orientation of TiO_2 nanoparticles was not clearly seen; however, it is probably due to the moderate magnification used. In order to elucidate the structure of TiO_2 nanocrystallites, a high-resolution transmission electron microscope with selected area electron diffraction (SAED) may be needed.

Temperature-programmed desorption profiles of CO_2 from the titania surface are shown in Fig. 3. The titania samples exhibited two desorption peaks at temperatures ca. 183 K and 213 K, which were attributed to the two structures of TiO_2 [30]. The peak at ca. 183 K is attributed to CO_2 molecules bounding to regular five-coordinate Ti^{4+} site, which was considered as the perfect titania structure. The second peak at ca. 213 K has been considered as desorption of CO_2 molecules bounding to Ti^{3+} defect structure. It is clearly seen from the TPD results that the areas of the CO_2 desorption peak at 213 K apparently increased with increasing crystallite size. It is indicated that the larger crystallite size of TiO_2 obtained from solvothermal synthesis possessed a higher amount of Ti^{3+} surface defects. The ratios of peak areas of Ti^{3+}/Ti^{4+} were also determined by curve fitting and area calculation using a SYSTAT Peakfit program and the results are given in Table 2. It was found that the Ti^{3+} density increased with increasing TiO_2 crystallite size from 9 to 14.5 nm. The value of Ti^{3+}/Ti^{4+} for TiO_2-14.5 nm and TiO_2-15 nm was not significantly different.

An example of the ESR results of the solvothermal-derived TiO_2 powders is shown in Fig. 4. All the titania samples exhibited one major signal at a g value of 1.996,

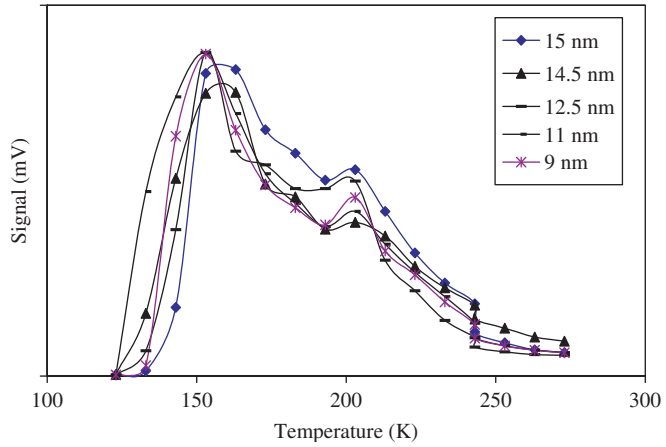

Fig. 3. Thermal desorption spectra for CO_2 adsorbed on the various TiO_2 samples.

Table 2
Ratios of peak areas of Ti^{3+}/Ti^{4+} determined from the CO_2-TPD experiments

Average crystallite size[a] (nm)	Ti^{3+}/Ti^{4+}[b]
9.0	0.923
11.0	1.046
12.5	1.299
14.5	1.580
15.0	1.474

[a]Based on XRD results.
[b]Based on CO_2-TPD results.

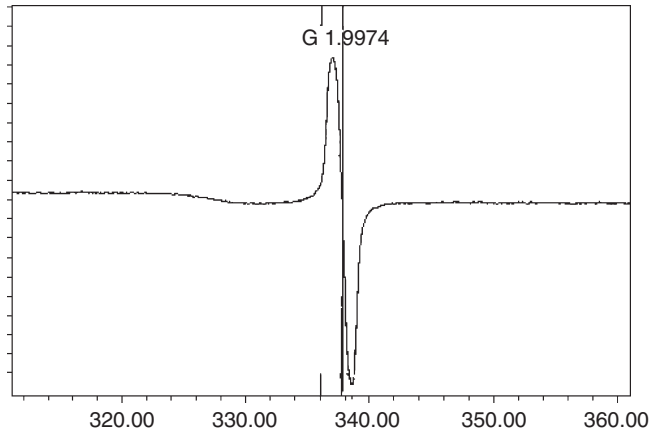

Fig. 4. ESR spectra for various TiO_2 samples.

which can be assigned to Ti^{3+} at titania surface [31–33]. According to Nakaoka and Nosaka [24], there were six ESR signals that occurred on the surface of titania: (i) $Ti^{4+}O^{-}Ti^{4+}OH^{-}$, (ii) surface Ti^{3+}, (iii) adsorbed oxygen (O^{2-}), (iv) $Ti^{4+}O^{2-}Ti^{4+}O^{2-}$, (v) inner Ti^{3+}, and (vi) adsorbed water. Fig. 5 demonstrates a relationship between the intensity of ESR spectra per surface area of the TiO_2 and the TiO_2 average crystallite size. It was found that the amount of surface defect of TiO_2 increased with increasing crystallite size.

Photocatalytic decomposition of ethylene was conducted to assess the photocatalytic activity of TiO_2 samples with various crystallite sizes. The conversion of ethylene as a function of time-on-stream for all the samples is shown in Fig. 6. In this study, 'time-on-stream' is defined as the time that surface of the catalyst was illuminated by UV light using 500 W mercury lamps. Photocatalytic activities of the various TiO_2 crystallite sizes are evidently different; ethylene conversions increased with increasing TiO_2 crystallite sizes. It can be correlated to the different amounts of Ti^{3+} defects on TiO_2 samples, in which the higher the amount of Ti^{3+} present in TiO_2, the higher photocatalytic activity obtained. In photocatalysis, light irradiation of TiO_2 powder with photon energy larger than the band-gap energy produces electrons (e^{-}) and holes (h^{+}) in the conduction band and the valence band, respectively. These electrons and holes are thought to have the respective abilities to reduce and oxidize chemical species adsorbed on the surface of TiO_2 particles. For a photocatalyst to be most efficient, different interfacial electron processes involving e^{-} and h^{+} must compete effectively

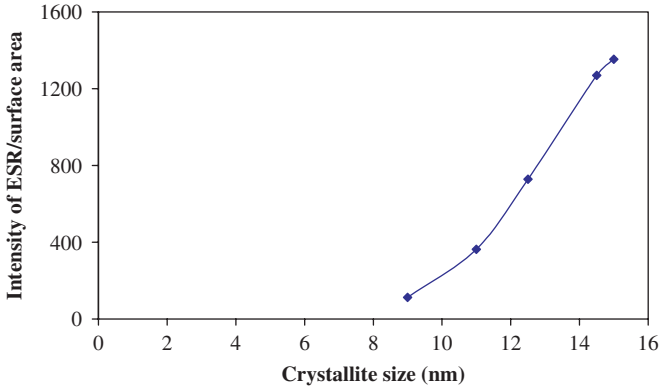

Fig. 5. The intensity of ESR spectra/surface area as a function of TiO_2 crystallite size.

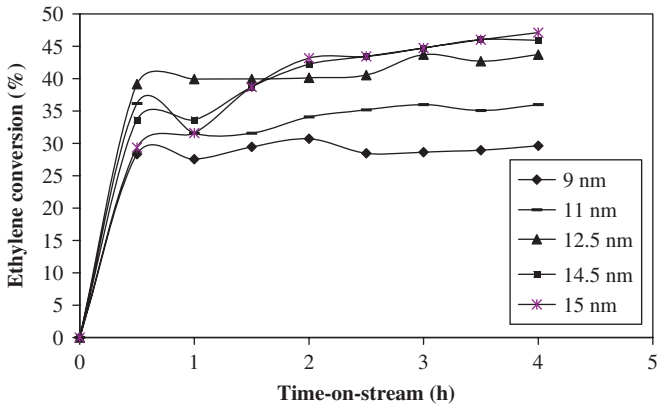

Fig. 6. Photocatalytic activity of the various TiO_2.

with the major deactivation processes involving e^-–h^+ recombination. In general, TiO_2 with higher crystallinity and higher specific surface area typically shows higher photocatalytic activity since the defect of crystal can be the recombination center of the electron–hole pair; hence the photocatalytic activity decreases [1,34,35]. However, the role of Ti^{3+} surface defects on photocatalytic activity of TiO_2 is different from that of crystal (bulk) defect. The Ti^{3+} surface defects serve as traps for photogenerated electrons and consequently prolong lifetime of holes, resulting in higher photocatalytic activity [36–38].

4. Conclusions

This work showed the impact of crystallite size of TiO_2 in the range of 9–15 nm on the Ti^{3+} surface defect present in TiO_2 powders. The amounts of Ti^{3+} defects as determined by ESR and CO_2-TPD were found to increase with increasing crystallite size of TiO_2. The photocatalytic activity of TiO_2 also increased in a similar trend due to an increase in the surface defect/specific surface area of the TiO_2 samples.

Acknowledgments

The authors would like to thank the Thailand Research Fund (TRF), the Commission on Higher Education, and the TJTTP-JBJC for the financial supports of this project.

References

[1] B. Ohtani, Y. Ogawa, S. Nishimoto, J. Phys. Chem. B 101 (1998) 3746.
[2] J.-M. Herrmann, C. Guillard, J. Disdier, C. Lehaut, S. Malato, J. Blanco, Appl. Catal. B-Environ. 35 (2002) 81.
[3] M. Bekbolet, A.S. Suphandag, C.S. Uyguner, J. Photochem. Photobiol. A: Chem. 148 (2002) 121.
[4] J. Aguado, R. Van Grieken, M.J. López-Muñoz, J. Marugán, Catal. Today 75 (2002) 95.
[5] G. Sivalingam, K. Nagaveni, M.S. Hegde, G. Madras, Appl. Catal. B-Environ. 45 (2003) 23.
[6] V.A. Sakkas, I.M. Arabatzis, I.K. Konstantinou, A.D. Dimou, T.A. Albanis, P. Falaras, Appl. Catal. B-Environ. 49 (2004) 195.
[7] D.P. Das, K. Parida, B.R. De, J. Mol. Catal. A-Chem. 240 (2005) 1.
[8] C.-S. Kim, B.K. Moon, J.-H. Park, S.T. Chung, S.-M. Son, J. Crystal Growth 254 (2003) 405.
[9] C. Wang, Z.-X. Deng, G. Zhang, S. Fan, Y. Li, Powder Technol. 125 (2002) 39.
[10] M. Kang, B.-J. Kim, S.M. Cho, C.-H. Chung, B.-W. Kim, G.Y. Han, K.J. Yoon, J. Mol. Catal. A-Chem. 180 (2002) 125.
[11] H. Kominami, M. Kohno, Y. Takada, M. Inoue, T. Inui, Y. Kera, Ind. Eng. Chem. Res. 38 (1999) 3925.
[12] H.-D. Nam, B.-H. Lee, S.-J. Kim, C.-H. Jung, J.-H. Lee, S. Park, Jpn. J. Appl. Phys. 37 (1998) 4603.
[13] C. Su, B.-Y. Hong, C.-M. Tseng, Catal. Today 96 (2004) 119.
[14] P. Yang, C. Lu, N. Hua, Y. Du, Mater. Lett. 57 (2002) 794.
[15] Y. Bessekhouad, D. Robert, J.V. Weber, J. Photochem. Photobiol. A: Chem. 157 (2003) 47.
[16] H. Kominami, J.-I. Kalo, Y. Takada, Y. Doushi, B. Ohtani, S.-I. Nishimoto, M. Inoue, Y. Kera, Catal. Lett. 46 (1997) 235.
[17] O. Carp, C.L. Huisman, A. Reller, Prog. Solid State Chem. 32 (2004) 33.
[18] T. Torimoto, R.J. Fox III, M.A. Fox, J. Electrochem. Soc. 143 (1996) 3712.
[19] V. Shklover, M.-K. Nazeeruddin, S.M. Zakeeruddin, C. Barbé, A. Kay, T. Haibach, W. Steurer, M. Grätzel, Chem. Mater. 9 (1997) 430.
[20] A.-K. Axelsson, L.J. Dunne, J. Photochem. Photobiol. A: Chem. 144 (2001) 205.
[21] G. Liu, J.A. Rodriguez, J. Hrbek, B.T. Long, D.A. Chen, J. Mol. Catal. A-Chem. 202 (2003) 215.
[22] R.F. Howe, M. Gratzel, J. Phys. Chem. 89 (1985) 4495.
[23] R.F. Howe, M. Gratzel, J. Phys. Chem. 91 (1987) 3906.
[24] Y. Nakaoka, Y. Nosaka, J. Photochem. Photobiol. A: Chem. 110 (1997) 299.
[25] U. Diebold, J. Lehman, T. Mahmoud, M. Kuhn, G. Leonardelli, W. Hebenstreit, M. Schmid, P. Varga, Surf. Sci. 411 (1998) 137.
[26] M. Inoue, H. Kominami, T. Inui, J. Chem. Soc. Dalton Trans. (1991) 3331.
[27] T.L. Thompson, O. Diwald, J.T. Yates Jr., J. Phys. Chem. B 107 (2003) 11700.
[28] S.S. Watson, D. Beydoun, J.A. Scott, R. Amal, Chem. Eng. J. 95 (2003) 213.
[29] W. Payakgul, O. Mekasuwandumrong, V. Pavarajarn, P. Praserthdam, Ceram. Inter. 31 (2005) 391.
[30] L.T. Tracy, D. Oliver, T.Y. John, J. Phys. Chem. B 107 (2003) 11700.
[31] K.-R. Park, J. Zhang, K. Ikeue, H. Yamashita, M. Anpo, J. Cataly. 185 (1999) 114.
[32] A. Watterich, A. Hofstaetter, R. Wuerz, A. Scharmann, J. Solid State Commun. 100 (1996) 513.
[33] Y. Zeng, Y. Zheng, S. Yu, K. Chen, S. Zhou, J. Electrochem. Comm. 4 (2002) 293.
[34] K.Y. Jung, S.B. Park, J. Photochem. Photobiol. A: Chem. 127 (1999) 117.
[35] M.I. Litter, Appl. Catal. B-Environ. 23 (1999) 89.
[36] G. Lu, A. Linsebigler, J.T. Yates Jr., J. Phys. Chem. 99 (1995) 7626.
[37] J. Schwitzgebel, J.G. Ekerdt, H. Gerischer, A. Heller, J. Phys. Chem. 95 (1995) 5633.
[38] D. Brinkley, T. Engel, Surf. Sci. 415 (1998) 1001.

Jointly published by
Akadémiai Kiadó, Budapest
and Springer, Dordrecht

React.Kinet.Catal.Lett.
Vol. 88, No. 1, 65–71 (2006)
DOI:10.1556/RKCL.88.2006.1.9

RKCL4741

ROLE OF RUTHENIUM IN THE REDUCTION BEHAVIOR OF RUTHENIUM-PROMOTED COBALT/TITANIA FISCHER-TROPSCH CATALYSTS

Bunjerd Jongsomjit*, Chitlada Sakdamnuson, Joongjai Panpranot and Piyasan Praserthdam

Center of Excellence on Catalysis and Catalytic Reaction Engineering, Department of Chemical Engineering, Faculty of Engineering, Chulalongkorn University, Bangkok 10330 Thailand

Received February 7, 2005; in revised form August 2, 2005; accepted August 5, 2005

Abstract

Role of ruthenium in the reduction behavior of Ru-promoted Co/TiO_2 catalysts was investigated. Ru could facilitate the reduction but had no effect on water production during reduction.

Keywords: Reduction, cobalt catalyst, titania, Fischer-Tropsch

INTRODUCTION

Due to their high activities [1], high selectivity to linear hydrocarbons and low activities for the competitive water-gas shift (WGS) reaction [2,3], supported cobalt (Co) catalyst is considered to be one of the most important catalysts for Fischer-Tropsch synthesis (FTS) as well as carbon monoxide (CO) hydrogenation. During the past decade, titania-supported Co catalysts have been widely investigated by many authors, especially for the application of FTS in a continuously stirred tank reactor (CSTR) [4-6]. In general, to increase the

* Corresponding author. E-mail: bunjerd.j@chula.ac.th

0133-1736/2006/US$ 20.00.

catalytic activity of the Co catalysts, many promoters such as ruthenium (Ru), zirconium (Zr), lanthanum (La), rhodium (Rh), boron (B), and platinum (Pt) have been investigated. It has been reported that a variety of these promoters can increase the reducibility of Co, preserve the activity by preventing the formation of coke, exhibit cluster and ligand effects, act as a source of hydrogen spillover and enhance the dispersion. It should be mentioned that the active form of Co catalysts is the reduced Co metal surface atom. Although Ru promotion appears to enhance the rate of FTS, no studies have specifically addressed how Ru promotes the reaction. Understanding how Ru can modify the catalyst properties could lead to the design of more robust and active Co catalysts.

This investigation focused on giving a better understanding of the roles of Ru on reduction behavior of the Ru-promoted Co/TiO_2 catalyst. The impact of Ru promotion on the reducibility of Co in the absence and presence of water vapor was also investigated.

EXPERIMENTAL

Catalyst preparation

The unpromoted-Co/TiO_2 and Ru-promoted ($CoRu/TiO_2$) catalysts were prepared by the incipient wetness impregnation using cobalt nitrate [$Co(NO_3)\bullet 6H_2O$] and ruthenium(III) nitrosyl nitrate [$Ru(NO)(NO_3)_3$] as precursors. The TiO_2 used contained 81 mol % of anatase phase and 19 mol % of rutile phase (Ishihara Sangyo, Japan). The catalyst samples were dried at 110°C for 12 h and calcined in air at 500°C for 4 h.

Catalyst pretreatments

Standard reduction

Standard reduction of the calcined catalyst was conducted in a fixed-bed flow reactor under differential conditions (no gradient in the catalyst bed) at 1 atm using a temperature ramp from ambient to 350°C at 1°C/min and holding at 350°C for 10 h in a gas flow having a space velocity of 16,000 h^{-1} and consisting of H_2. The high space velocity of the H_2 flow was applied to insure that the partial pressure of water vapor in the catalyst bed produced by cobalt oxide reduction would be essentially zero.

Hydrothermal treatment

In order to evaluate the stability of catalysts and impacts of water vapor during reduction, hydrothermal treatment was also conducted during standard reduction above. In addition, besides using pure H_2, mixtures of H_2 and water vapor (5-10 vol.%) were also applied separately at the same reduction condition as mentioned above.

Catalyst nomenclature

The nomenclature used for the catalyst samples in this study is following:
Co/Ti : Unpromoted cobalt catalyst on the titania support,
CoRu/Ti : Ru-promoted cobalt catalyst on the titania support,
(C) : Calcined catalyst sample,
(RW0), (RW5) and (RW10): Reduced catalyst samples with no water vapor, 5 vol.% of water vapor, and 10 vol.% of water vapor added during standard reduction, respectively.

Catalyst characterization

BET surface area was determined using N_2 adsorption at 77 K in a Micromeritics ASAP 2010.

X-ray diffraction was conducted using a SIEMENS D-5000 X-ray diffractometer with CuK_α (λ = 1.54439 Å).

The Raman spectra of the samples were collected by projecting a continuous wave laser of argon ion (Ar^+) green (514.532 nm) through the samples exposed to air at room temperature.

Temperature-programmed reduction of calcined samples was carried out using 50 mg of a sample and a temperature ramp from 35 to 800°C at 5°C/min. The carrier gas was 5% H_2 in Ar.

Reaction

CO hydrogenation (H_2/CO = 10/1) was performed to determine the overall activity of the catalyst samples. Hydrogenation of CO was carried out at 220°C and 1 atm. A flow rate of H_2/CO/He = 20/2/8 cc/min in a fixed-bed flow reactor under differential conditions was used.

Table 1

Characteristics and catalytic properties of samples

Samples	BET surface area (m^2/g)[a]	Reducibility (%)[b]	Total H_2 chemisorption (μmol/g cat.)[c]	Reaction rate ($x10^2$ gCH_2 g cat. h^{-1})[d]		CH_4 Selectivity (%)	
				Initial[e]	Steady state[f]	Initial	Steady state
TiO_2	49	-	-	-	-	-	-
Co/Ti-C	34	78	4.8	25	21	94	96
Co/Ti-RW0	32	74	3.3	23	20	94	94
Co/Ti-RW5	32	72	3.2	23	20	98	98
Co/Ti-RW10	30	68	3.0	23	19	95	96
CoRu/Ti-C	37	87	7.5	37	36	99	98
CoRu/Ti-RW0	37	83	6.7	36	36	98	98
CoRu/Ti-RW5	37	77	5.9	36	35	97	97
CoRu/Ti-RW10	36	75	5.2	36	34	99	99

[a] Measurement error ± 5%

[b] Reducibility was measured during TPR at 30-800°C. The reduced samples were recalcined under the original calcination conditions prior to TPR.

[c] H_2 chemisorption was performed to determine the number of reduced Co surface atoms.

[d] CO hydrogenation was carried out at 220°C, 1 atm and $H_2/CO/Ar$ = 20/2/8 cm^3/min.

[e] After 5 min of reaction

[f] After 5 h of reaction

RESULTS AND DISCUSSION

The present study was conducted in order to investigate the roles of Ru in the reduction behavior of $CoRu/TiO_2$ catalysts. The characteristics and catalytic properties during CO hydrogenation are summarized in Table 1. It was observed that upon Co loading and Ru promotion, there was no significant change in the BET surface areas, suggesting no pore blocking or phase changes in the TiO_2 support. The XRD peaks (not shown) of all calcined samples at 26, 37,48, 55, 62, 69, 71 and 75° (TiO_2 in anatase form) and 27, 36, 42 and 57° (TiO_2 in rutile form) were observed. As expected, XRD peaks of Co_3O_4 species were also detected at 36, 46 and 65° after calcination of samples. However, after reduction with or without water vapor added, only diffraction peaks at 37 and 63° corresponding to CoO were observed. Thus, XRD revealed that Ru was well dispersed in the catalyst samples. A similar trend was also observed in Raman spectroscopy as seen for XRD results. It was found that the TiO_2 support exhibited the Raman bands at 640, 514 and 397 cm^{-1} (anatase form) and 445 cm^{-1} (rutile form). The calcined samples showed Raman bands of the TiO_2 support along with two shoulders at 690 and 480 cm^{-1}, assigned to Co_3O_4 species. Raman spectra for all reduced samples exhibited the similar Raman bands as seen for the calcined ones indicating Co_3O_4 on the surface. In order to determine the number of reduced Co metal surface atoms, H_2 chemisorption was performed as seen in Table 1. It indicated that water vapor during reduction apparently resulted in both lesser number of reduced Co metal surface atoms and reducibility due to Co-support compound formation (Co-SCF) as reported in our previous works [7, 8]. It should be noted that Ru promotion may result in enhanced activities during CO hydrogenation without changing selectivity of products due to increased number of reduced Co metal surface atoms. Roles of the Ru Ru promotion can be discussed further based on the TPR profiles as shown in Figs 1 (for the unpromoted catalysts) and 2 (for the Ru-promoted catalysts).

It can be observed that Ru can only facilitate the reduction of cobalt oxide species due to the hydrogen spillover effect resulting in lower reduction temperatures. It is known that water vapor as a byproduct of a reduction process can enhance the Co-SCF [7, 8]. Thus, water vapor was also introduced during reduction in order to investigate the roles of Ru promotion as well. As seen from Figs 1 and 2, increased amounts of water vapor during reduction had no effect on the reduction behavior of both unpromoted catalysts and Ru-promoted catalysts, indicating no shift of reduction temperatures. In summary, Ru promotion can only facilitate the reduction of cobalt oxide species but has no effect on water vapor produced during reduction.

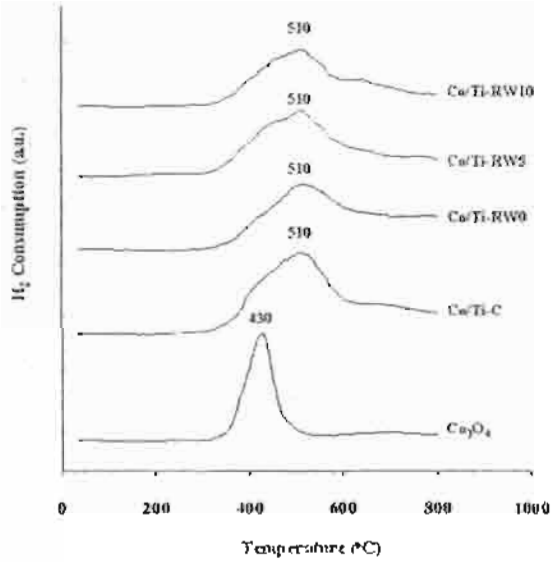

Fig. 1. TPR profiles of the unpromoted cobalt catalysts

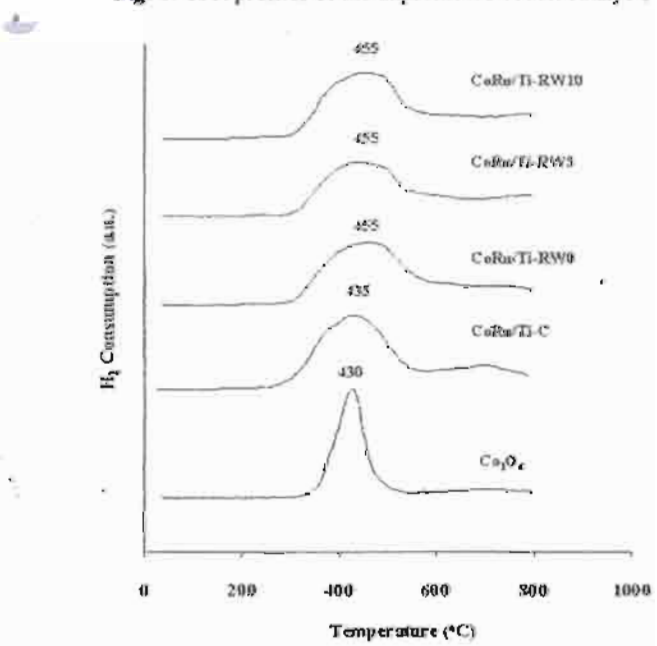

Fig. 2. TPR profiles of the Ru-promoted cobalt catalysts

Acknowledgements. We gratefully acknowledge the financial support by the National Research Council of Thailand (NRCT), the Thailand Research Fund (TRF) and Thailand-Japan Technology Transfer Project (TJTTP-JBIC). We would like to thank Prof. James G. Goodwin, Jr. at Clemson University, USA for his advice.

References

1. H.P. Wither, Jr., K.F. Eliezer, J.W. Mechell: *Ind. Eng. Chem. Res.*, **29**, 1807 (1990).
2. E. Iglesia: *Appl. Catal. A.*, **161**, 59 (1997).
3. R.C. Brady, R.J. Pettie: *J. Am. Chem. Soc.*, **103**, 1287 (1981).
4. J.L. Li, G. Jacobs, T. Das, B.H. Davis: *Appl. Catal. A.*, **233**, 255 (2002).
5. G. Jacobs, T. Das, Y.Q. Zhang, J.L. Li, G. Racoillet, B.H. Davis: *Appl. Catal. A.*, **233**, 263 (2002).
6. J.L. Li, L.G. Xu, R. Keogh, B.H. Davis: *Catal. Lett.*, **70**, 127 (2000).
7. B. Jongsomjit, J. Panpranot, J.G. Goodwin, Jr.: *J. Catal.*, **204**, 98 (2001).
8. B. Jongsomjit, C. Sakdamnuson, J.G. Goodwin, Jr.: *Catal. Lett.*, **94**, 209 (2004).

Studies in Surface Science and Catalysis, volume 159
Hyun-Ku Rhee, In-Sik Nam and Jong Moon Park (Editors)

Elucidation of reduction behaviors for Co/TiO_2 catalysts with various rutile/anatase ratios

Bunjerd Jongsomjit*, Tipnapa Wongsalee, and Piyasan Praserthdam

Center of Excellence on Catalysis and Catalytic Reaction Engineering
Department of Chemical Engineering, Chulalongkorn University
Bangkok 10330 Thailand, *corresponding author: bunjerd.j@chula.ac.th

The present study revealed effects of various rutile/anatase ratios in titania on the reduction behaviors of titania-supported cobalt catalysts. It was found that the presence of rutile phase in titania could facilitate the reduction process of the cobalt catalyst. As a matter of fact, the number of reduced cobalt metal surface atoms, which is related to the overall activity during CO hydrogenation increased.

1. INTRODUCTION

Supported cobalt (Co) catalysts are preferred for Fischer-Tropsch synthesis (FTS) based on natural gas [1] due to their high activities for FTS, high selectivity for long chain hydrocarbons and low activities for the competitive water-gas shift (WGS) reaction. Many inorganic supports such as silica, alumina, titania and Zeolites have been extensively studied for supported Co catalysts for years. It is known that in general, the catalytic properties depend on reaction conditions, catalyst compositions, types of inorganic supports and the degrees of metal dispersion as well. It is reported that during the past decades, titania-supported Co catalysts have been investigated widely by many authors, especially for the application of FTS in a continuously stirred tank reactor (CSTR) [2-4]. However, it should be noted that titania itself has different crystalline phases such as anatase, brookite and rutile phase. Thus, the differences in compositions of crystalline phases could result in changes on physical and chemical properties of titania, then consequently for the dispersion of cobalt. In order to give a better understanding of those, the focus of this present study was to investigate the cobalt dispersion on titania consisting various ratios of rutile/anatase. The Co/TiO_2 was prepared and then characterized using different characterization techniques.

2. EXPERIMENTAL

2.1 Material preparation

Preparation of titania support

The various ratios of rutile:anatase in titania support were obtained by calcination of pure anatase titania (obtained from Ishihara Sangyo, Japan) in air at temperatures between 800-1000°C for 4 h. The high space velocity of air flow (16,000 h^{-1}) insured the gradual phase transformation to avoid rapid sintering of samples. The ratios of rutile:anatase were determined by XRD according to the method described by Jung et al. [5] as follows:

$$\%\,\text{Rutile} = \frac{1}{[(A/R)0.884 + 1]} \times 100$$

Where, A and R are the peak area for major anatase ($2\theta = 25^{\circ}$) and rutile phase ($2\theta = 28^{\circ}$), respectively.

Preparation of catalyst samples
A 20 wt% of Co/TiO_2 was prepared by the incipient wetness impregnation. A designed amount of cobalt nitrate [$Co(NO_3)\bullet 6H_2O$] was dissolved in deionized water and then impregnated onto TiO_2 containing various ratios of rutile:anatase obtained from above. The catalyst precursor was dried at 110°C for 12 h and calcined in air at 500°C for 4 h.

2.2 Catalyst nomenclature

The nomenclature used for the catalyst samples in this study is following:
Rn: titania support containing **n%** of rutile phase (R)
Co/Rn: titania support containing **n%** of rutile phase (R)-supported cobalt

2.3 Catalyst characterization

X-ray diffraction: XRD was performed to determine the bulk crystalline phases of catalyst. It was conducted using a SIEMENS D-5000 X-ray diffractometer with CuK_{α} (λ = 1.54439 Å). The spectra were scanned at a rate of 2.4 degree/min in the range 2θ = 20-80 degrees.
Scanning electron microscopy and energy dispersive X-ray spectroscopy: SEM and EDX were used to determine the catalyst morphologies and elemental distribution throughout the catalyst granules, respectively. The SEM of JEOL mode JSM-5800LV was applied. EDX was performed using Link Isis series 300 program.
Transmission electron microscopy (TEM): The dispersion of cobalt oxide species on the titania supports were determined using a JEOL-TEM 200CX transmission electron spectroscopy operated at 100 kV with 100k magnification.
Hydrogen chemisorption: Static H_2 chemisorption at 100°C on the reduced cobalt catalysts was used to determine the number of reduced surface cobalt metal atoms. This is related to the overall activity of the catalysts during CO hydrogenation. Gas volumetric chemisorption at 100°C was performed using the method described by Reuel and Bartholomew [6]. The experiment was performed in a Micromeritics ASAP 2010 using ASAP 2010C V3.00 software.
Temperature-programmed reduction: TPR was used to determine the reduction behaviors of the catalyst samples. It was carried out using 50 mg of a sample and a temperature ramp from 35 to 800°C at 5°C/min. The carrier gas was 5% H_2 in Ar. A cold trap was placed before the detector to remove water produced during the reaction.

3. RESULTS AND DISCUSSION

In this present study, we basically showed dependence of the number of reduced cobalt metal surface atoms on dispersion of cobalt oxides along with the presence of rutile phase in titania. Both XRD and SEM/EDX results (not shown) revealed good distribution of cobalt oxides over the titania support. However, it can not differentiate all samples containing various ratios of rutile/anatase phase. Thus, in order to determine the dispersion of cobalt oxide species on titania, a more powerful technique such as TEM was applied with all samples. The TEM micrographs for all samples are shown in Figure 1. The dark spots represented cobalt oxides species present after calcination of samples dispersing on titania consisting various

ratios of rutile:anatase. It can be observed that cobalt oxide species were highly dispersed on the titania supports for Co/R0, Co/R3, and Co/R19 samples resulting in an appearance of smaller cobalt oxide patches present. However, the degree of dispersion for cobalt oxide species essentially decreased with increasing the rutile phase in titania from 40 to 99% as seen for Co/R40, Co/R96, and Co/R99 samples resulting in the observation of larger cobalt oxide patches. It was suggested that the presence of rutile phase in titania from 0 (pure anatase phase) to 19% exhibited the highly dispersed forms of cobalt oxide species for the calcined samples. It is known that the active form of supported cobalt catalysts is cobalt metal (Co^0). Thus, reduction of cobalt oxide species is essentially performed in order to transform cobalt oxide species obtained after calcination process into the active cobalt metal atoms for catalyzing the reaction. Therefore, the static H_2 chemisorption on the reduced cobalt samples was used to determine the number of reduced Co metal surface atoms. This is usually related to the overall activity of the catalyst during carbon monoxide (CO) hydrogenation [7].

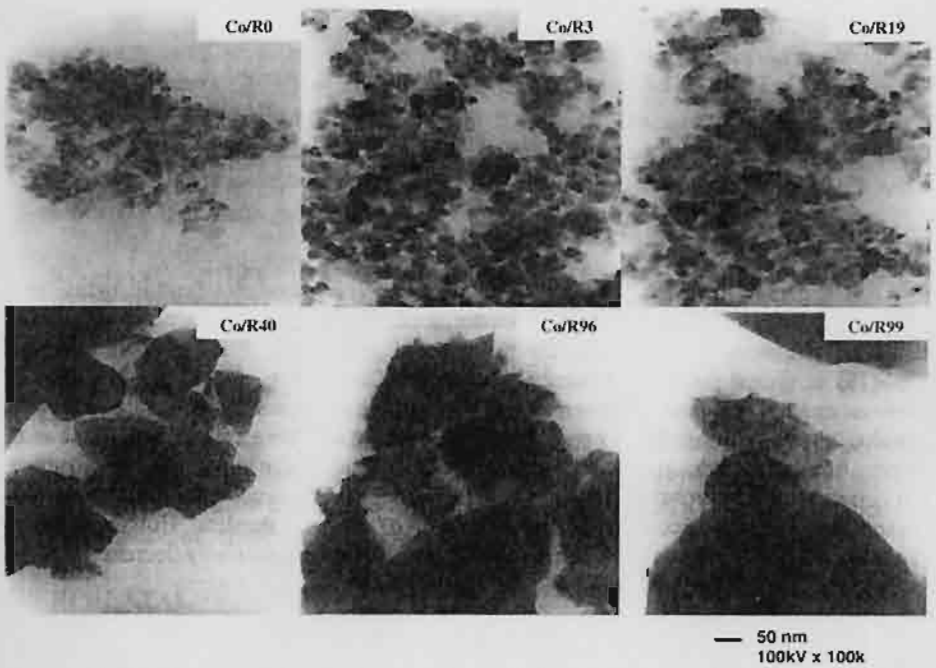

Figure 1 TEM micrographs of samples on various rutile/anatase ratios in titania

The resulted H_2 chemisorption for all samples revealed that the number of the reduced cobalt metal surface atoms increased with the presence of rutile phase in titania up to a maximum at 19% of rutile phase (Co/R19) before decreasing with the greater amounts of rultile phase as shown in **Table 1**. Considering the number of cobalt metal atoms for Co/R0 (pure anatase titania), the number was apparently low even though highly dispersed cobalt oxides species. This was suggested that highly dispersed forms of cobalt oxide species be not only the factor that insures larger number of reduced cobalt metal surface atoms in Co/TiO_2 [8]. On the other hand, it can be observed that the number of reduced cobalt metal surface atoms for Co/R40 and Co/R96 (with the low degree of dispersion of cobalt oxide species as seen by TEM) was

larger than that for Co/R0. This was due to the presence of rutile phase in Co/R40 and Co/R96. It should be mentioned that the largest number of reduced cobalt metal surface atoms for the Co/R19 sample was attributed to both highly dispersed cobalt oxide species and the presence of rutile phase in titania. In addition, the resulted TPR as also shown in Table 1 confirmed that the presence of rultie phase could facilitate the reduction of cobalt oxide species by lowering the reduction temperatures. As a result, the number of the reduced cobalt metal surface atoms increased.

Table 1 Resulted H_2 chemisorptiion and reduction temperatures for various Co/TiO_2 samples

Samples	Total H_2 Chemisorption (μmol H_2/g cat.)	Reduction Temperature (^oC)
Co/R0	0.93	370
Co/R3	1.55	270
Co/R19	2.44	320
Co/R40	1.66	285
Co/R96	1.71	275
Co/R99	0.69	275

4. SUMMARY

The present research showed a dependence of various ratios of rutile:anatase in titania as a catalyst support for Co/TiO_2 on characteristics, especially the reduction behaviors of this catalyst. The study revealed that the presence of 19% rutile phase in titania for Co/TiO_2 (Co/R19) exhibited the highest number of reduced Co metal surface atoms which is related the number of active sites present. It appeared that the increase in the number of active sites was due to two reasons; i) the presence of rutile phase in titania can facilitrate the reduction process of cobalt oxide species into reduced cobalt metal, and ii) the presence of rutile phase resulted in a larger number of reduced cobalt metal surface atoms. No phase transformation of the supports further occurred during calcination of catalyst samples. However, if the ratios of rutile:anatase were over 19%, the number of active sites dramatically decreased.

ACKNOWLEDGMENT

The financial support from the Thailand Research Fund (TRF) is greatly appreciated.

REFERENCES

[1] H.P. Wither, Jr., K.F. Eliezer, and J.W. Mechell, Ind. Eng. Chem. Res., 29 (1990)1807.
[2] J.L. Li, G. Jacobs, T. Das, and B.H. Davis, Appl. Catal. A., 233 (2002) 255.
[3] G. Jacobs, T. Das, Y.Q. Zhang, J.L. Li, G. Racoillet, and B.H. Davis., Appl. Catal. A., 233 (2002) 263.
[4] J.L. Li,, L.G. Xu, R. Keogh, and B.H. Davis, Catal. Lett., 70 (2000) 127.
[5] K.Y. Jung, and S.B. Park, J. Photochem. Photobio. A: Chem., 127 (1999) 117.
[6] R.C. Reuel, and C.H. Bartholomew, J. Catal., 85(1984) 63.
[7] B. Jongsomjit, C. Sakdamnuson, J.G. Goodwin, Jr., and P. Praserthdam, Catal. Lett., 94 (2004) 209.
[8] B. Jongsomjit, T. Wongsalee, and P. Praserthdam, Mater. Chem. Phys., 92 (2005) 572.

ELSEVIER

Chemical Engineering Science 62 (2007) 899–905

Chemical Engineering Science

www.elsevier.com/locate/ces

Shorter Communication

Effect of nano-SiO_2 particle size on the formation of LLDPE/SiO_2 nanocomposite synthesized via the in situ polymerization with metallocene catalyst

Ekrachan Chaichana, Bunjerd Jongsomjit*, Piyasan Praserthdam

Center of Excellence on Catalysis and Catalytic Reaction Engineering, Department of Chemical Engineering, Faculty of Engineering, Chulalongkorn University, Bangkok 10330, Thailand

Received 4 July 2006; received in revised form 9 October 2006; accepted 9 October 2006
Available online 17 October 2006

Abstract

Here, we revealed the effect of particle size of the nanoscale SiO_2 on catalytic and characteristic properties of LLDPE/nano-SiO_2 composites synthesized via the in situ polymerization with a zirconocene/MAO catalyst. In the experiment, SiO_2 (10 and 15 nm) was first impregnated with MAO. Then, copolymerization of ethylene/1-hexene was performed in the presence of nano-SiO_2/MAO to produce LLDPE/nano-SiO_2 composites. It was found that the larger particle exhibited higher polymerization activity due to fewer interactions between SiO_2 and MAO. The larger particle also rendered higher insertion of 1-hexene leading to decreased melting temperature (T_m). There was no significant change in the LLDPE molecular structure by means of ^{13}C NMR.

Keywords: Nanoscale SiO_2; LLDPE; Polymerization; Metallocene; Polymer composite

1. Introduction

It is known that the copolymerization of ethylene with higher 1-olefins is a commercial importance for production of elastomer and linear low-density polyethylene (LLDPE). LLDPE (density 0.920–0.940) is one of the most widely used polyolefins in many applications, especially, for plastic films. However, in some cases, the use of polyolefins and LLDPE is limited by their drawbacks such as low mechanical strength, low thermal resistance, poor optical properties and so on. Hence, in order to improve the specific properties of these polymers, some additives are used to blend with them.

It has been reported that blending polymer with inorganic materials is considered a powerful method to produce new materials called polymer composites or filled polymers. However, due to the significant development in nanotechnologies in the recent years, nanoscale inorganic materials such as SiO_2, Al_2O_3 and TiO_2 have brought much attention to this research field. Therefore, the polymer composites filled with nanoscale fillers are well recognized as polymer nanocomposites. Essentially, the addition of nanoscale fillers into polymers may lead to overcome the drawbacks and produce new materials, which are robust. Basically, there are three methods used to produce the filled polymer: (i) melt mixing; (ii) solution blending; and (iii) in situ polymerization. Due to the direct synthesis via polymerization along with the presence of nanoscale fillers, the in situ polymerization is perhaps considered the most powerful technique to produce polymer nanocomposites with good distribution and dispersion of the fillers inside polymer matrix. Although LLDPE composites have been studied by many authors (Danjaji et al., 2001, 2002; Huang and Zhang, 2003; Nawang et al., 2001; Verbeek, 2002a,b), those polymer samples were only synthesized by the melt mixing and solution blending. Only few research articles have been reported on the LLDPE nanocomposites synthesized via the in situ polymerization with metallocene catalysts (Jongsomjit et al., 2005a).

In the present study, we developed a new technique to synthesize the LLDPE/nano-SiO_2 via the in situ polymerization with zirconocene/MAO catalyst. The effect of nano-SiO_2

* Corresponding author. Tel.: +662 2186869; fax: +662 2186877.
E-mail address: bunjerd.j@chula.ac.th (B. Jongsomjit).

0009-2509/$ - see front matter © 2006 Elsevier Ltd. All rights reserved.
doi:10.1016/j.ces.2006.10.005

particle size on characteristics and catalytic properties was investigated.

2. Experimental section

The preparation of LLDPE/nano-SiO_2 composites via in situ polymerization was performed as follows; all chemicals [nano-SiO_2 (10 and 15 nm) from Aldrich, toluene, *rac*-ethylenebis (indenyl) zirconium dichloride [*rac*-Et(Ind)$_2$ZrCl_2] from Aldrich, methylaluminoxane (MAO) donated by Tosoh Akzo, Japan, trimethylaluminum (TMA), ethylene (National Petrochemical, Thailand) and 1-hexene (Fluka Chemie)] were manipulated under an inert atmosphere using a vacuum glove box and/or Schlenk techniques.

The nano-SiO_2 filler was heated under vacuum at 400 °C for 6 h prior to impregnation with MAO. In order to impregnate MAO onto the nano-SiO_2, the method as follows was described. One gram of the nano-SiO_2 was reacted with the desired amount of MAO at room temperature and stirred for 30 min. The solvent was then removed from the mixture. About 20 ml of toluene was added into the obtained precipitate, stirred the mixture for 5 min, and then removed the solvent. This procedure was done for five times to ensure the removal of impurities. Then, the solid part was dried under vacuum at room temperature to obtain white powder of the nano-SiO_2/ MAO. The amount of $[Al]_{MAO}$ in the nano-SiO_2 particles was determined by the energy dispersive X-ray spectroscopy (EDX) as shown in Fig. 1.

The ethylene/1-hexene copolymerization reaction was carried out in a 100 ml semi-batch stainless steel autoclave reactor equipped with a magnetic stirrer. At first, 0.1, 0.2, and 0.3 g of the nano-SiO_2/MAO ($[Al]_{MAO}/[Zr]_{cat} = 1135$, 2270, and 3405, respectively) and 0.018 mol of 1-hexene along with toluene (to make the total volume of 30 ml) were put into the reactor. The desired amount of Et(Ind)$_2$ZrCl_2 and TMA ($[Al]_{TMA}/[Zr]_{cat} = 2500$) was mixed and stirred for 5-min aging at room temperature, separately, then was injected into the reactor. The reactor was frozen in liquid nitrogen to stop reaction for 15 min and then the reactor was evacuated to remove argon. The reactor was heated up to polymerization temperature (70 °C). To start reaction, 0.018 mol of ethylene was fed into the reactor containing the comonomer and catalyst mixtures. After all ethylene was consumed, the reaction was terminated by addition of acidic methanol (0.1% HCl in methanol) and stirred for 30 min. After filtration, the obtained copolymer (white powder) was washed with methanol and dried at room temperature. In order to give a better understanding for the preparation of the LLDPE/SiO_2nanocomposites.

The LLDPE/nano-SiO_2 composites obtained were characterized by means of scanning electron microscopy (SEM) and energy dispersive X-ray spectroscopy (EDX) to identify morphologies and elemental distribution, respectively. Transmission electron microscopy (TEM) was also used to investigate the dispersion of nano-SiO_2 in LLDPE. The molecular structure of LLDPE/nano-SiO_2 composite was obtained using ^{13}C NMR. The melting temperature (T_m) was determined using differential scanning calorimetry (DSC). The molecular weight (MW) and molecular weight distribution (MWD) of the LLDPE fraction were measured using gel permeation chromatography (GPC).

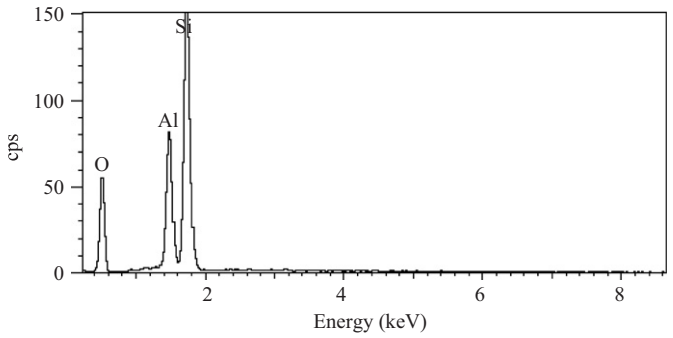

SiO_2	Average wt% of $[Al]_{MAO}$ in SiO_2
10 nm	10.75
15 nm	6.55

Fig. 1. Average amount of $[Al]_{MAO}$ in SiO_2 determined by EDX.

3. Results and discussion

Prier to XRD measurement, the sample was mounted on an adhesive carbon tape as pellets. They were prepared in a glove box and transferred under inert atmosphere. The XRD patterns for the nano-SiO_2 before and after impregnation with MAO (not shown) exhibited the similar XRD patterns indicating only broad XRD band of the amorphous SiO_2. After impregnation of MAO onto the SiO_2, no XRD peaks of $[Al]_{MAO}$ were detected indicating highly dispersed form of it being present. By means of EDX as shown in Fig. 1, it was found that the average amounts of $[Al]_{MAO}$ on 10 and 15 nm-SiO_2 were 10.75 and 6.55 wt%, respectively. Thus, in order to keep the similar ratios of $[Al]_{MAO}/[Zr]_{cat}$ for each nano-SiO_2, the amounts of catalyst used needed to be adjusted. After the in situ polymerization was done, the polymerization time and yield were recorded. They are listed in Table 1 along with some other characteristics of polymers. It can be observed that the total polymer yield for two of the runs was considerably less than 0.5 g. Besides, the ethylene content of all the products, except for one, made with the 15 nm silica particles was < 0.4 g (calculated from the yield and the 1-hexene content of product). The low yields found in two of the runs should be due to two possible factors according to the effect of SiO_2 size: (1) the deactivation of catalyst occurred at a certain time after polymerization, and (2) the chain transfer was prevailed resulting in only oligomers obtained, then they were washed out during filtration. To better illustrate the effect of particle size of nano-SiO_2 on the activities at the same amounts of it, a plot of activity versus the weight of nano-SiO_2 used corresponding to different ratios of $[Al]_{MAO}/[Zr]_{cat}$ is shown in Fig. 2. It can be observed that increased amounts of nano-SiO_2 resulted in increased activities during polymerization for both 10 and 15 nm-SiO_2. This can be attributed to an increase in the $[Al]_{MAO}/[Zr]_{cat}$ ratios from 1135 to 2270 and, then to 3405 corresponding to 0.1, 0.2, and

Table 1
Activity and characteristics of LLDPE-SiO_2 nanocomposites

Filler	Weight (g)	Polymerization Yield (g)	Time (s)	Activity[a]	%SiO_2[b]	T_m[c] (°C)	1-Hexene insertion[d] (%)
Nano-SiO_2 (10 nm)	0.1	0.1355	1714	811	37.9	102.3	25.7
	0.2	0.9164	326	28,827	16.0	70.4	47.7
	0.3	0.8633	330	26,827	23.0	86.3	38.7
Nano-SiO_2 (15 nm)	0.1	0.5505	400	23,163	14.4	99.6	29.7
	0.2	0.9555	149	107,930	16.2	89.7	54.5
	0.3	1.002	134	125,853	21.6	87.7	65.0

[a]Activities (kg of polym/mol of Zr h) were measured at polymerization temperature of 70 °C, [ethylene] = 0.018 mol, [1-hexene] = 0.018 mol, $[Al]_{MAO}/[Zr]$ = 1135 to 3405, $[Al]_{TMA}/[Zr] = 2500$, in toluene with total volume = 30 ml and $[Zr]_{cat} = 0.71 \times 10^{-5}$ M (for 15 nm SiO_2) and 1.17×10^{-5} M (for 10 nm SiO_2).
[b]The amount of SiO_2 present in the LLDPE composites based on yield.
[c]Melting temperature (T_m) was obtained from the DSC measurement.
[d]1-hexene insertion or incorporation was calculated based on ^{13}C NMR.

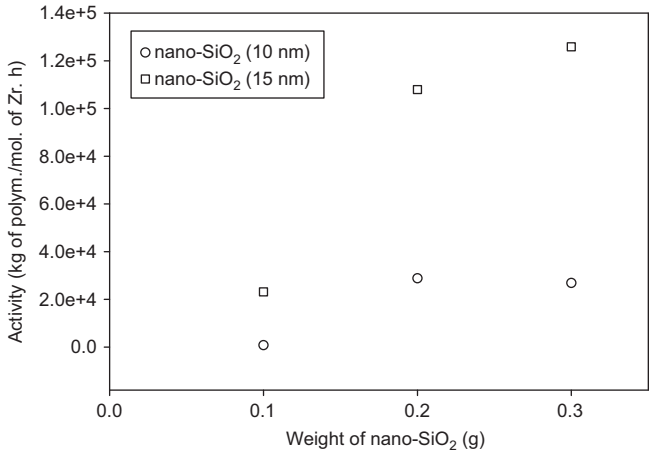

Fig. 2. Activities regarding different particle size and amount added of nano-SiO_2.

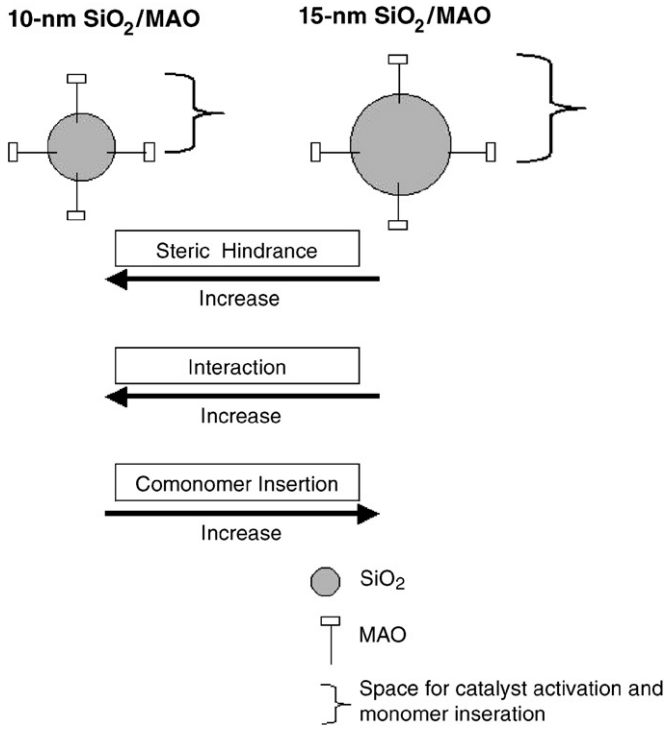

Scheme 1. Conceptual model for impact of nano-SiO_2 particle size on steric hindrance, interaction, and comonomer insertion.

0.3 g of the nano-SiO_2, respectively. It was reported that the greater amounts of MAO resulted in more active species being present during polymerization (Jongsomjit et al., 2004a,b). It was proposed that MAO possibly had many functions, such as an alkylating agent, a stabilizer for a cationic metallocene alkyl and/or counterion, an ionizing and/or reducing agent for the transition element, and a scavenger for the metallocene catalytic system. However, one of the most important roles of MAO is apparently to prevent the formation of $ZrCH_2CH_2Zr$ species, which is formed via a bimolecular process (Chao et al., 2003).

Considering, activities for both 10 and 15 nm-SiO_2, it was found that the 15 nm-SiO_2 exhibited higher activities with the same ratios of $[Al]_{MAO}/[Zr]_{cat}$ as seen in Fig. 2. The higher activities can be attributed to fewer interactions between SiO_2 and MAO arising from the larger particles. It should be noted that SiO_2 is one of the materials having strong interaction with species being present on its surface (Kogelbauer et al., 1995). A wide range of variables including particle size, types of material, and pretreatment condition can affect the particle interaction (Jongsomjit et al., 2001). The smaller particles may interact more with MAO resulting in decreased activities because it is more difficult for metallocene to react with the strongly interacted MAO on SiO_2 surface. Besides, the strong interaction between SiO_2 and MAO, it should be mentioned that the smaller particles also render more steric hindrance. In fact, steric hindrance means more bulky (less space). Considering the small and large particles with the same amounts of MAO on them, the gap between the MAO should be larger on the larger particles due to higher external surface areas. Thus, smaller particles should have more steric hindrance than the larger ones. As the result, the insertion of 1-hexene is more difficult due to the steric hindrance (more bulky). It is known that SiO_2 is one of many supports having a strong interaction with species

being present on it. A wide range of variables including particle size, nature of adsorbed species, preparation methods and pretreatment conditions can affect the interaction. The effects of particle size and nature of adsorbed species i.e., MAO can be superimposed on each other. Based on the results, it was suggested that the smaller SiO_2 particles may interact more with MAO resulting in lower activity. In order to give a better understanding, a conceptual model for impact of nano-SiO_2 particle size on the steric hindrance, interaction, and comonomer insertion is illustrated as shown in Scheme 1.

The characteristics of LLDPE/nano-SiO_2 were also further investigated. The typical morphologies of LLDPE/nano-SiO_2 composites obtained by SEM and the elemental distribution for Si and O are shown in Fig. 3 . There was no significant change in polymer morphologies for LLDPE nanocomposites containing 10 and 15 nm-SiO_2 with the same amounts of SiO_2. It can be observed that SiO_2 was well distributed in polymer. As known, images from high resolution TEM is an essential component of nanoscience, therefore TEM was performed to identify the dispersion of nano-SiO_2 in LLDPE. The TEM micrographs of LLDPE/nano-SiO_2 are shown in Fig. 4 . Fig. 4a–c represented LLDPE with 10 nm-SiO_2 at 0.1–0.3 g of SiO_2, respectively. Fig. 4d–f showed LLDPE containing 15 nm-SiO_2 at 0.1, 0.2, and 0.3 g of SiO_2, respectively. As seen from both 10 and 15 nm-SiO_2, they appeared as a bunch of spherical-like particles indicating the agglomeration of the primary particles. This was suggested that the poor dispersion being observed. The poor dispersion was due to interaction between particles leading to agglomeration. In addition, there was no pronounced difference among each LLDPE/nano-SiO_2 sample. Thus, in order to obtain well dispersion, the modification of the nano-SiO_2 needs to be further investigated for future work. It has been known that ^{13}C NMR is one of the most powerful techniques to identify the polymer microstructure, especially polyolefins. The resulted ^{13}C NMR spectra (not shown) for all samples were assigned typically to the LLDPE obtained from copolymerization of ethylene/1-hexene. The triad distribution was identified based on the method described by Randall (1989). It can be observed that the LLDPE consisting of 10 and 15 nm-SiO_2 exhibited similar ^{13}C NMR patterns indicating similar molecular structure of polymer. Based on calculations described by Galland et al. (1996), the triad distribution of monomer is listed in Table 2. It indicated that all LLDPE samples were random copolymer with the difference in 1-hexene insertion. This result was also similar with what we found in our previous works without the addition of nano-SiO_2 (Jongsomjit et al., 2004a–c, 2005a–d). According to the triad distribution shown in Table 2, the insertion of 1-hexene can be calculated based on the reference (Galland et al., 1996). The 1-hexene insertion in LLDPE/nano-SiO_2 is shown in Table 1. It can be observed that larger particle resulted in increased 1-hexene insertion due to less steric hindrance. Hence, with larger particles, the large molecule of 1-hexene can insert more. The melting temperature (T_m) as also shown in Table 1 trended to decrease with more insertion of 1-hexene due to decreased crystallinity. However, it can be observed that the T_m of the nanocomposites of 15 nm-SiO_2 (weight 0.2 and 0.3 g) with higher 1-hexene insertion were higher than those of 10 nm-SiO_2 (weight 0.2 and 0.3 g) with lower 1-hexene insertion as shown in Table 1. This should be addressed that besides the effect of 1-hexene insertion on the T_m, the SiO_2 particles added also affect the T_m of polymer as well. Apparently, while higher 1-hexene insertion resulted in

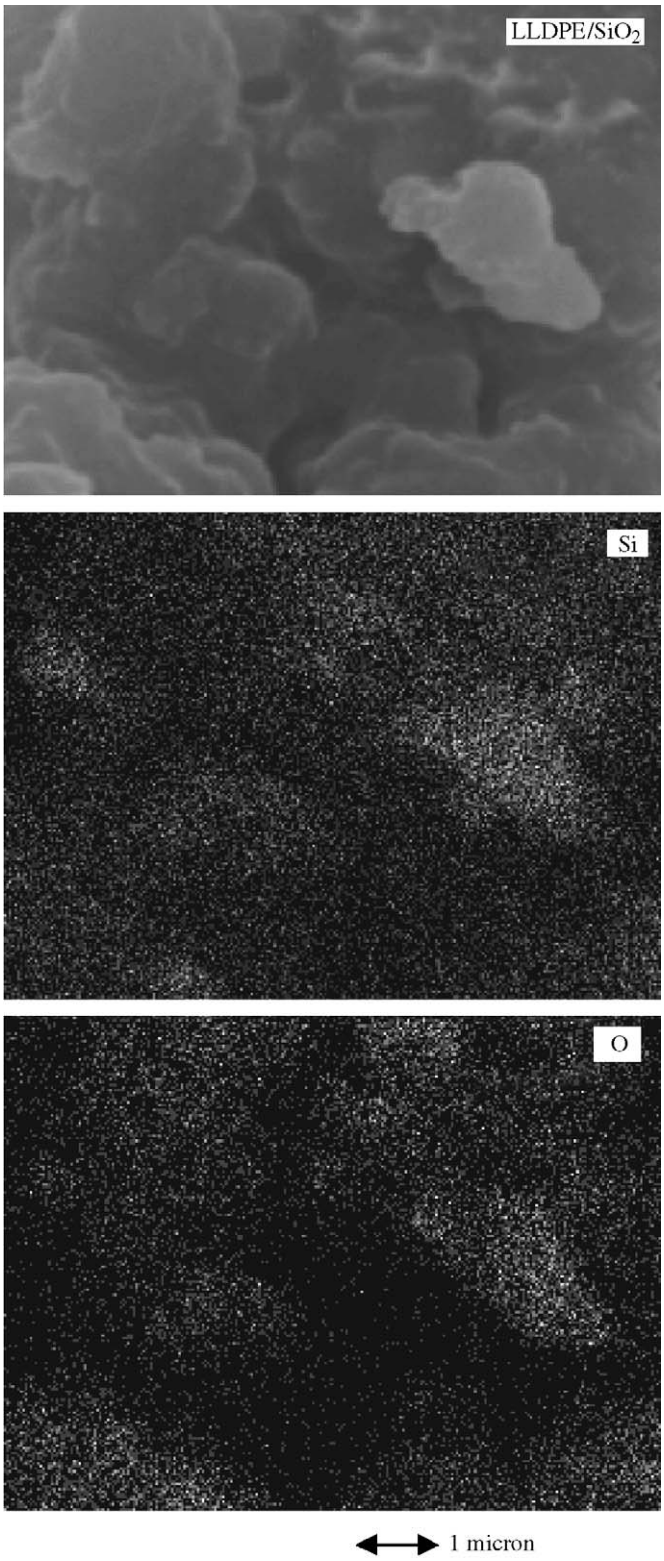

Fig. 3. A typical SEM and EDX images for LLDPE/nano-SiO_2 composites.

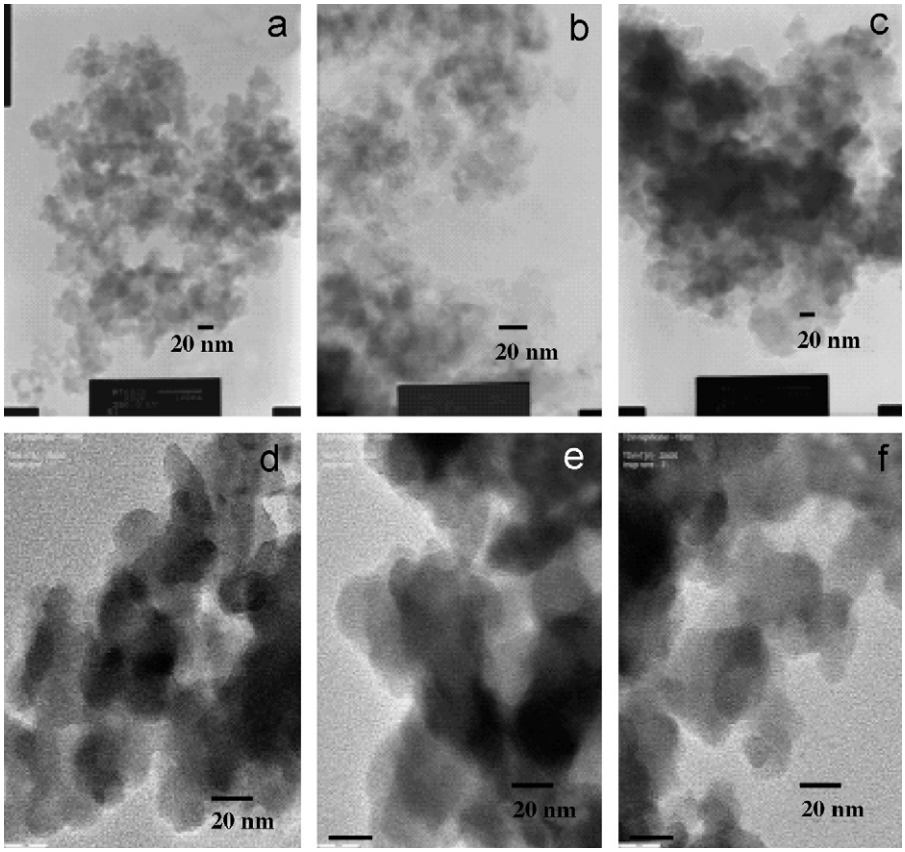

Fig. 4. TEM micrographs of: (a) SiO_2-10 nm, 0.1 g; (b) SiO_2-10 nm, 0.2 g; (c) SiO_2-10 nm, 0.3 g; (d) SiO_2-15 nm, 0.1 g; (e) SiO_2-15 nm, 0.2 g and (f) SiO_2-15 nm, 0.3 g.

Table 2
Triad distribution[a] obtained from ^{13}C NMR of LLDPE-SiO_2 nanocomposites

Filler	Weight (g)	EEE	EEH + HEE	HEH	EHE	EHH + HHE	HHH
Nano-SiO_2 (10 nm)	0.1	0.66	0.09	0	0.04	0.21	0
	0.2	0.39	0.12	0.02	0.06	0.41	0
	0.3	0.47	0.13	0.02	0.07	0.31	0
Nano-SiO_2 (15 nm)	0.1	0.61	0.09	0	0.05	0.25	0
	0.2	0.31	0.12	0.03	0.07	0.47	0
	0.3	0.19	0.12	0.04	0.08	0.57	0

[a]E refers to ethylene and H refers to 1-hexene.

lower T_m, higher content of SiO_2 in polymer rendered higher T_m. It was reported that the particles in polymer matrix can act as nucleating agents (Luyt et al., 2006). Consequently, they increase the crystallinity of polymer. When the particles are too small (i.e., 10 nm-SiO_2), they may locate themselves in the interlamellar spaces, which leave little room for additional crystallization. So, the presence of these particles may even inhibit crystallization. In the case, higher T_m for LLDPE nanocomposites of 15 nm-SiO_2 having higher 1-hexene insertion compared to those of the 10 nm-SiO_2 was essentially observed.

The additional study was conducted by keeping the $[Al]_{MAO}/[Zr]$ ratio (at 2270) constant with changing the catalyst concentrations, [Zr]. Thus, the amounts of nano-SiO_2 can be varied without changing the $[Al]_{MAO}/[Zr]$ ratio. In fact, only 15 nm-SiO_2 was chosen to study the effect of amounts of nano-SiO_2 added. Using the similar ways as mentioned above, the activities and characteristics of LLDPE/15 nm-SiO_2 composite were obtained as shown in Table 3. It was found that at the specified condition the activity went to a maximum with the certain amount of nano-SiO_2 (0.2 g), then went down with increased amount of nano-SiO_2 (0.3 g). Increased activity with increasing the amount of nano-SiO_2 at the beginning can be attributed to increased distribution of MAO. Consequently, this also resulted in increased 1-hexene insertion as seen in Table 3. However, increased more amounts of nano-SiO_2 apparently resulted in decreased activity. This was probably due

Table 3
Activity and characteristics of LLDPE-SiO_2 nanocomposites at $[Al]_{MAO}/[Zr] = 2270$

Filler	Weight (g)	Polymerization Yield (g)	Time (s)	Activity[a]	$\%SiO_2$[b]	T_m [c] (°C)	1-Hexene insertion[d] (%)
Nano-SiO_2 (15 nm)	0.1	0.1000	717	4695	46.7	107.6	19.86
	0.2	0.9555	149	107,930	16.2	89.7	54.5
	0.3	0.7545	248	34,136	26.6	101.2	67.5

[a]Activities (kg of polym/mol of Zr h) were measured at polymerization temperature of 70 °C, [ethylene] = 0.018 mol, [1-hexene] = 0.018 mol, $[Al]_{MAO}/[Zr] = 2270$, $[Al]_{TMA}/[Zr] = 2500$, in toluene with total volume = 30 ml and $[Zr]_{cat} = 0.36$ to 1.07×10^{-5} M.
[b]The amount of SiO_2 present in the LLDPE composites based on yield.
[c]Melting temperature (T_m) was obtained from the DSC measurement.
[d]1-hexene insertion or incorporation was calculated based on ^{13}C NMR.

Table 4
Triad distribution[a] obtained from ^{13}C NMR of LLDPE-SiO_2 nanocomposites

Filler	Weight (g)	EEE	EEH + HEE	HEH	EHE	EHH + HHE	HHH
Nano-SiO_2 (15 nm)	0.1	0.61	0.09	0	0.05	0.25	0
	0.2	0.31	0.12	0.03	0.07	0.47	0
	0.3	0.19	0.12	0.04	0.08	0.57	0

[a]E refers to ethylene and H refers to 1-hexene.

Table 5
MW and MWD of LLDPE fraction in the composites

Filler	Weight (g)	MW ($gmol^{-1}$)	M_n ($gmol^{-1}$)	MWD[a]
Nano-SiO_2 (10 nm)	0.1	38,200	6900	5.5
	0.3	27,200	3400	8.0
Nano-SiO_2 (15 nm)	0.1	41,900	4800	8.7
	0.3	31,700	4000	7.9

[a]MWD was calculated from MW/M_n.

to stronger interaction between the particles. In addition, T_m (Table 3), triad distribution (Table 4) are also present. The effect of nano-SiO_2 particle size on MW and MWD was also investigated as shown in Table 5. In fact, no significant change was observed regarding to the particle size of the nano-SiO_2. Only slight increase in MW with the larger particles was evident. It can be observed that increased amounts of SiO_2 resulted in decreased MW. In addition, a slightly broad MWD was seen for all samples.

4. Summary

Based on this study, it was found that the larger particle (15 nm-SiO_2) exhibited higher activity due to fewer interactions between SiO_2 and MAO. The larger particle also rendered higher insertion of 1-hexene. In particular, higher 1-hexene insertion resulted in decreased melting temperature due to decreased crystallinity. No change in molecular structure of LLDPE was observed. However, the agglomeration of SiO_2 in polymer was seen by TEM. In order to overcome the poor dispersion of particles, the nano-SiO_2 needs to be modified prior to use. Thus, the modification of SiO_2 should be further investigated in the near future.

Acknolwedgments

The authors thank the Thailand Research Fund (TRF), Thailand-Japan Technology Transfer Project (TJTTP-OECF), and the National Science and Technology Development Agency (NSTDA) for the financial support of this project.

References

Chao, C., Praserthdam, P., Khorbunsongserm, S., Rempel, G.L., 2003. Effect of TMA and MAO on ethyelene-propene copolymer using supported zirconocene catalysts. Journal of Macromolecular Science Part A: Pure and Applied Chemistry 40, 181.

Danjaji, I.D., Nawang, R., Ishiaku, U.S., Ismail, H., Mohd Ishak, Z.A., 2001. Sago starch-filled linear low-density polyethylene (LLDPE) films: their mechanical properties and water absorption. Journal of Applied Polymer Science 79, 29.

Danjaji, I.D., Nawang, R., Ishiaku, U.S., Ismail, H., Mohd Ishak, Z.A., 2002. Degradation studies and moisture uptake of sago-starch filled linear low-density polyethylene composites. Polymer Testing 21, 75.

Galland, G.B., Quijada, P., Mauler, R.S., de Menezes, S.C., 1996. Determination of reactivity ratios for ethylene/1-olefin copolymerization catalyzed by the $C_2H_4[Ind]_2ZrCl_2$/methylaluminoxane system. Macromolecular Rapid Communications 17, 607.

Huang, Y.Q., Zhang, Y.Q., 2003. Studies on dynamic mechanical and rheological properties of LLDPE/nano-SiO_2 composites. Journal of Material Science Letters 22, 997.

Jongsomjit, B., Panpranot, J., Goodwin Jr., J.G., 2001. Co-support compound formation in alumina-supported cobalt catalysts. Journal of Catalysis 204, 98.

Jongsomjit, B., Praserthdam, P., Kaewkrajang, P., 2004a. A comparative study of supporting effect during copolymerization of ethylene/1-olefins with silica-supported zirconocene/MAO catalyst. Materials Chemistry and Physics 86, 243.

Jongsomjit, B., Kaewkrajang, P., Shiono, T., Praserthdam, P., 2004b. Supporting effects of silica-supported methylaluminoxane (MAO) with zirconocene catalyst on ethylene/1-olefin copolymerization behaviors for linear low-density polyethylene (LLDPE) production. Industrial & Engineering Chemistry Research 43, 7959.

Jongsomjit, B., Kaewkrajang, P., Wanke, S.E., Praserthdam, P., 2004c. A comparative study of ethylene/1-olefin copolymerization with silane-modified silica-supported MAO using zirconocene catalysts. Catalysis Letters 94, 205.

Jongsomjit, B., Chaichana, E., Praserthdam, P., 2005a. LLDPE/nano-silica composites synthesized via in situ polymerization of ethylene/1-hexene with MAO/metallocene catalyst. Journal of Material Science 40, 2043.

Jongsomjit, B., Ngamposri, S., Praserthdam, P., 2005b. Catalytic activity during copolymerization of ethylene and 1-hexene via mixed TiO_2/SiO_2-supported MAO with rac-Et[Ind]$_2ZrCl_2$ metallocene catalyst. Molecules 10, 672.

Jongsomjit, B., Ngamposri, S., Praserthdam, P., 2005c. Role of titania in TiO_2-SiO_2 mixed oxides-supported metallocene catalyst during ethylene/1-octene copolymerization. Catalysis Letters 100, 139.

Jongsomjit, B., Ngamposri, S., Praserthdam, P., 2005d. Application of silica/titania mixed oxide supported zirconocene catalyst for synthesis of linear low-density polyethylene. Industrial & Engineering Chemistry Research 44, 9059.

Kogelbauer, A., Weber, J.C., Goodwin Jr., J.G., 1995. The formation of cobalt silicates on Co/SiO_2 under hydrothermal conditions. Catalysis Letters 34, 259.

Luyt, A.S., Molefi, J.A., Krump, H., 2006. Thermal, mechanical and electrical properties of copper powder filled low-density polyethylene composites. Polymer Degradation and Stability 91, 1629.

Nawang, R., Danjaji, I.D., Ishiaku, U.S., Ismail, H., Mohd Ishak, Z.A., 2001. Mechanical properties of sago starch-filled linear low-density polyethylene (LLDPE) composites. Polymer Testing 20, 167.

Randall, J.C., 1989. A review of high-resolution liquid ^{13}carbon nuclear magnetic resonance characterizations of ethylene-based polymer. Journal of Macromolecular Science Reviews in Macromolecular Chemistry and Physics C29, 201.

Verbeek, C.J.R., 2002a. Verbeek, C.J.R. Highly filled polyethylene/phlgopite composites. Materials Letters 52, 453.

Verbeek, C.J.R., 2002b. Effect of preparation variables on the mechanical properties of compression-molded phlogopite/LLDPE composites. Materials Letters 56, 226.

Available online at www.sciencedirect.com
ScienceDirect
Materials Chemistry and Physics 100 (2006) 445–450
MATERIALS CHEMISTRY AND PHYSICS
www.elsevier.com/locate/matchemphys

Preparation and phase transformation behavior of χ-alumina via solvothermal synthesis

Okorn Mekasuwandumrong [a,*], Varong Pavarajarn [b], Masashi Inoue [c], Piyasan Praserthdam [b,*]

[a] *Department of Chemical Engineering, Faculty of Engineering and Industrial Technology, Silpakorn University, Nakorn Pathom 73000, Thailand*
[b] *Research Center on Catalysis and Catalytic Reaction Engineering, Department of Chemical Engineering, Faculty of Engineering, Chulalongkorn University, Bangkok 10330, Thailand*
[c] *Department of Energy and Hydrocarbon Chemistry, Graduate School of Engineering, Kyoto University, Kyoto 606-8077, Japan*

Received 9 August 2005; received in revised form 21 November 2005; accepted 23 January 2006

Abstract

Solvothermal reaction of aluminum isopropoxide (AIP) in mineral oil at 250–300 °C over 2 h duration provides χ-alumina powder, which transforms directly to α-alumina after calcination at high temperature. The mechanism of the crystallization process appears to be the initial formation of a spherical complex which subsequently decomposes further to precipitate a solid. This mechanism is suggested by XRD, IR, TG/DTA, SEM and TEM characterization of the powder formed. χ-Alumina attains a critical crystallite size around 15 nm through accretion on calcination and then transforms directly to α-alumina through nucleation and growth process. Direct α-phase transformation of χ-alumina powders rather than passage through κ-alumina can be explained by the absence of the cation contamination and the higher crystallinity of χ-alumina in the AIP decomposition process.

Keywords: Solvothermal; Direct transformation; χ-Alumina

1. Introduction

Alumina is one of the most common crystalline materials used in many applications such as adsorbents, coatings, soft abrasives, catalyst and catalyst support [1–3] due to its fine particle size, high surface area and catalytic activity. The structural stability of alumina also makes it an important constituent of many protective oxides formed on the surface of high temperature metals and alloys.

There are many metastable polymorphs of transition alumina, including χ-alumina. χ-Alumina is normally prepared by the dehydration of gibbsite (<200 nm) [3–5]. It transforms to κ-alumina at temperature around 650–750 °C before final transformation to α-alumina at 1000–1100 °C. Both transformations lead to loss in the surface area and changes in surface properties. Three different unit cells have been proposed for χ-alumina. Stumpf et al. [6] suggested that χ-alumina has a cubic unit cell with lattice parameter of 7.95 Å, whereas other researchers [4] proposed hexagonal unit cells with either $a = 5.56$ Å and $c = 13.44$ Å or $a = 5.57$ Å and $c = 8.64$ Å. Hexagonal χ-alumina possess a layered structure, in which the hexagonal arrangement of oxygen is inherited from the structure of gibbsite and aluminum occupies octahedral sites within the hexagonal structure.

Recently, Inoue et al. [7–10] have examined the thermal decomposition of metal alkoxides in inert organic solvents, e.g. glycols, and demonstrated that various kinds of novel crystalline product, including χ-alumina, can be directly obtained without bothersome procedures such as purification of the reactants or handling in inert atmosphere.

Nanocrystalline χ-alumina prepared from the thermal decomposition of AIP in inert organic solvent has high thermal stability. It transforms directly to α-alumina at the temperature around 1150 °C, without passing into the κ-phase [7,11,12], resulting in neither the loss in surface area nor the change in surface properties. Moreover, the abrupt crystal growth

* Corresponding authors. Tel.: +66 63116537; fax: +66 34219368.
E-mail address: okornm@yahoo.com (O. Mekasuwandumrong).

0254-0584/$ – see front matter © 2006 Elsevier B.V. All rights reserved.
doi:10.1016/j.matchemphys.2006.01.040

Table 1
The physical properties of as-synthesized products obtained by the thermal decomposition of AIP in mineral oil in various reaction conditions

Reaction conditions		Phase	Crystallite size (nm)	S_{BET} ($m^2\ g^{-1}$)	S_t ($m^2\ g^{-1}$)[a]	Pore volume ($cm^3\ g^{-1}$)[b]	Mode pore diameter (nm)[c]
Temperature (°C)	Time (h)						
250	0	Amorphous	–	7	7	0.03	11.8
250	2	χ-Alumina	9	192	186	0.64	13.3
250	6	χ-Alumina	10.8	149	189	0.43	11.5
270	2	χ-Alumina	10.2	180	210	0.52	11.5
300	2	χ-Alumina	9.4	124	138	0.45	14.2

[a] Calculated from the initial slope of the *t*-plot.
[b] Total nitrogen uptake at relative pressure of 0.98.
[c] Calculated from the desorption branch of the isotherm using the BJH method.

occurring during phase transformation can be effectively controlled. Therefore, nanocrystalline α-alumina can be simply obtained via the direct transformation from nanocrystalline χ-alumina. In this paper, we provide results for the reaction of AIP in mineral oil, including morphology of the synthesized particles and the phase transformation behavior.

2. Experiment

2.1. Sample preparation

Twenty-five grams of aluminum isopropoxide (AIP; Aldrich; >97%) was suspended in 100 ml of mineral oil (liquid paraffin; Ajax; specific gravity 0.830–0.890; CAS No. 8012-95-1) in a test tube, which was then set in a 300 ml autoclave. In the gap between the test tube and the autoclave wall, 30 ml of mineral oil was added. The autoclave was purged completely by nitrogen and heated up to the desired temperature, in the range of 250–300 °C, at a rate of 2.5 °C min^{-1}, and held at that temperature for the desired period of time (0–2 h). After the mixture was cooled down, the resulting powders were repeatedly washed with acetone and dried in air.

Parts of the product obtained was calcined in a box furnace by heating-up to the desired temperature (1000–1200 °C) at a rate of 10 °C min^{-1}. The calcination process was held at that temperature for 1 h.

2.2. Characterization

Powder X-ray diffraction (XRD) was measured on a SIEMENS XRD D5000 using Cu Kα radiation. The crystallite size was calculated from the Scherrer equation. The value of the shape factor, *K*, was taken to be 0.9 and α-alumina was used as an external standard. Infrared (IR) Spectra were recorded on a NICOLET FT-IR Impact 400 spectroscopy using an ex situ IR technique. The thermal behavior of the samples were analyzed on a Perkin-Elmer Diamond TG/DTA thermal analyzer at a heating rate of 10 °C min^{-1} in a 40 ml min^{-1} flow of dried air. Nitrogen adsorption isotherm and BET surface area of the samples were measured by a micromeritics medel ASAP 2000 using nitrogen as the adsorbate. The primary particles of alumina samples were observed by a JEOL TEM-200cx transmission electron microscope operated at 100 kV. Morphologies of alumina products were observed on JEOL scanning electron microscope.

3. Results and discussions

Table 1 summarizes the physical properties of obtained products before calcination. The products synthesized from the decomposition of AIP in mineral oil at 250, 270 and 300 °C with a holding time exceeding 2 h are χ-alumina, while the product obtained from heating the system up to 250 °C without holding time is amorphous. The amorphous product has much lower BET surface area and pore volume than all crystalline products. χ-Alumina obtained by the reaction at 250 °C for 2 h has the highest BET surface area and pore volume. When the reaction temperature is increased or the holding time is prolonged, BET surface area and pore volume of the obtained product is decreased by the coagulation of primary particles due to thermal effect.

The IR spectra of the products are shown in Fig. 1. All as-obtained powders show two adsorption bands attributed to water of crystallization at 3500–3200 cm^{-1} (υ(OH)) and 1640 cm^{-1} (δ(OH)) [13]. The amorphous powder obtained by quenching from 250 °C shows a strong adsorption bands at 1340–1470 cm^{-1} due to the isopropyl hydrocarbon groups [13]. As the holding time or reaction temperature is increased, the adsorption bands due to the organic group decrease and eventually disappear. The characteristic bands of boehmite were detected at 773 and 615 cm^{-1} [10] in the products obtained from 2 h reaction at 250 and 300 °C. This observation can be explained by the formation of boehmite by hydrolysis of AIP with water produced during the reaction.

Fig. 2 shows the results from the thermogravimetric analysis, i.e. TGA and DTA plots, of all powders prepared in mineral oil using various reaction conditions. Two weight decrease processes were detected from the amorphous powder corresponding on one endothermic and exothermic process. The first decrease in mass at around 80–200 °C, accompanied by the endothermic peak in DTA signal, is attributed to the desorption of physisorbed water. The second sharp mass decrease in TGA plot with sharp exothermic peak in DTA plot at around 300 °C is attributed to the combustion of organic moiety. The overall mass loss of this

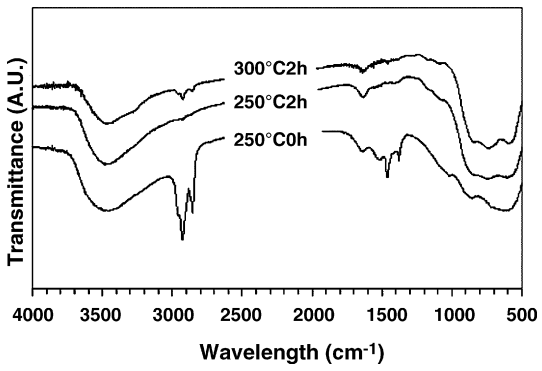

Fig. 1. IR spectra of as-synthesized products at various reaction conditions.

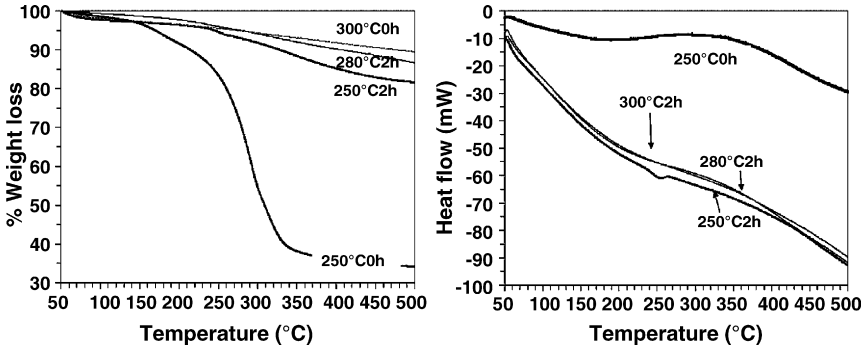

Fig. 2. TG and DTA data of the as-synthesized products.

amorphous sample is around 45%, which is lower than theoretically loss for AIP decomposition (75%). It is indicated that the starting AIP partially decomposes in mineral oil during the heating-up process. The remaining organic moieties from the partial decomposition of AIP reside in the amorphous product.

The nitrogen adsorption isotherms of as-synthesized products are shown in Fig. 3. All the crystalline samples exhibit the hysteresis loop with type-A adsorption characteristic, which is corresponding to the presence of two-ended tabular pore structure. On the other hand, the amorphous product shows the type-E hysteresis loop, which is an indication for the presence of tabular, through short pores with winded parts of various widths [14,15]. These pores are formed among the primary particles of alumina. Fig. 4 presents the pore size distribution of as-synthesized. All crystalline products exhibited the typical characteristic of mesopore system with pore size around 10 nm. It is shown that all products have narrow size distribution.

Fig. 5 shows the morphologies of as-synthesized and calcined samples observed by SEM. Spherical particles with average diameter around 1.8 μm were observed in the amorphous products prepared by quenching the reaction after the temperature had reached 250 °C (Fig. 5a). For the reaction with the holding

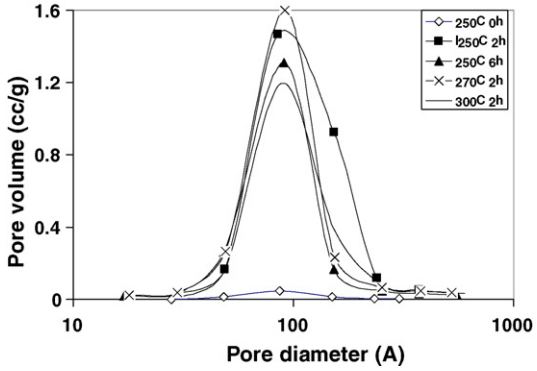

Fig. 4. Pore size distribution of as-synthesized product.

time prolonged to 2 h, similar spherical particles in the products can still be observed. However, the average size of the particles decreases to 1.2 μm (Fig. 5b). These particles are secondary aggregates of nanocrystalline χ-alumina. With the increase of reaction temperature to 300 °C, size of the secondary particles further decreases to 1 μm (Fig. 5c). The results suggest that AIP decomposes stepwise in the inert solvent during heating-up

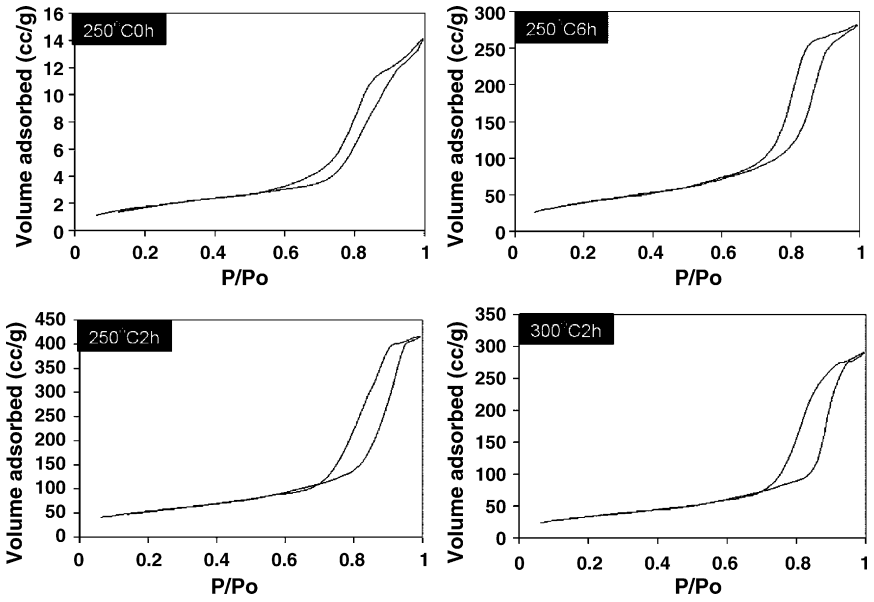

Fig. 3. The nitrogen adsorption isotherms of as-synthesized products.

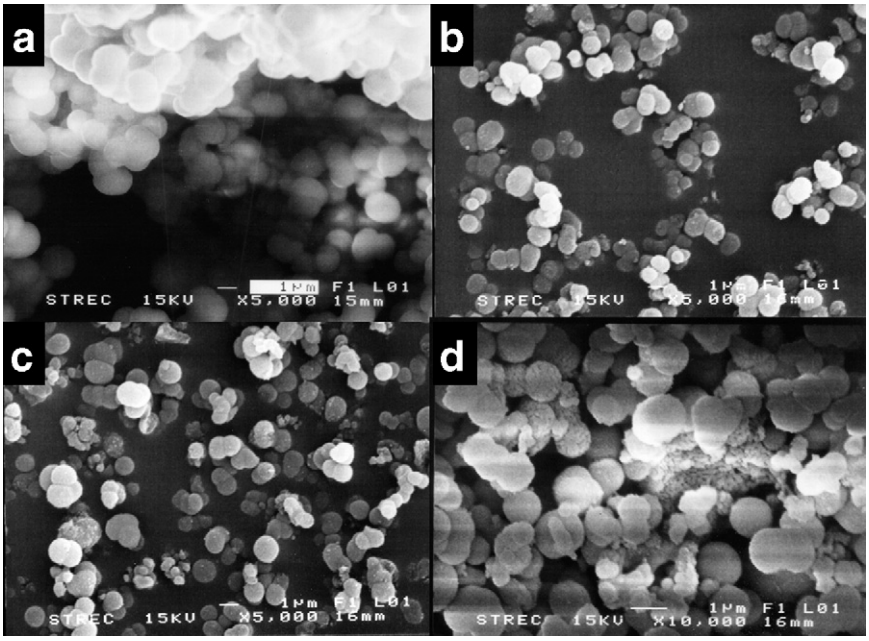

Fig. 5. SEM images: (a) as-synthesized product prepared by quenching reaction in mineral oil at 250 °C, (b) as-synthesized product prepared in mineral oil at 250 °C for 2 h, (c) as-synthesized product prepared in mineral oil at 300 °C for 2 h and (d) product (b) calcined at 1150 °C.

process, which results in an intermediate complex suspending in mineral oil. SEM micrographs confirms that this complex assumes a spherical shape. During the holding period, the complex further decomposes giving the nanocrystalline χ-alumina aggregated in form of spherical particles. The decrease in particle size with the increase in holding time and reaction temperature is due to the loss of the organic moiety in the complex by further decomposition. In this case, there are two nucleation processes. The first nucleation process is the formation of tiny droplets of the intermediate complex. This process is related to the salting out phenomena. During the partial decomposition of organic moieties, the decomposed intermediate is supersaturated in the solution and it is salted out forming the glassy droplets. Because the number of droplets formed in mineral oil is small, the droplets grow and large spherical particles are obtained. The second nucleation step is the formation tiny crystallites of χ-alumina. The morphology of products obtained in this work is different from χ-alumina obtained from the reaction in toluene [12]. This result will be further discussed.

According to Derjaguin–Landua–Verwey–Overbeek (DLVO) theory, the energy barrier between two particles, which inhibit agglomeration, is expressed as follow:

$$V_b = \left(\frac{A\kappa\alpha}{12}\right) + 2\pi\varepsilon_0\varepsilon_r\kappa\alpha\phi^2$$

where A is the effective Hamaker constant, κ the Debye–Huckel parameter, α the particle diameter, ε_0 the permittivity in the free space, ε_r the dielectric constant of the continuous phase and ϕ is the particle surface potential. Because of the constant ionic strength of the solvent, ε_0 and κ is constant, the maximum repulsive force estimated from the second term of the right hand side of the equation ($2\pi\varepsilon_0\varepsilon_r\kappa\alpha\phi^2$) is determined by the dielectric constant, particle size and repulsive force. Mineral oil (liquid paraffin) is the mixtures of long straight chain hydrocarbon produced as the bottom product from distillation. The dielectric constant of long chain hydrocarbon is around 1.9–2 ($C_{13}H_{28} = 2.02$, $C_{14}H_{30} = 2.05$, $C_{19}H_{40} = 2.09$), which lower than toluene (2.379). According to the quite low dielectric constant of mineral oil, the particles become discrete and form spherical particles. Fang and Chen [16] reported that, for the synthesis of TiO_2 by the reaction of $TiCl_4$ in a mixed solvent of *n*-propanol and water, the spherical particles were

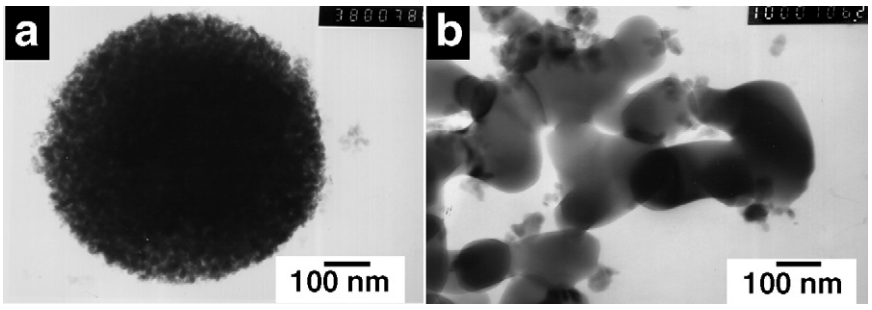

Fig. 6. TEM images: (a) as-synthesized product prepared in mineral oil at 250 °C for 2 h and (b) product (a) calcined at 1150 °C.

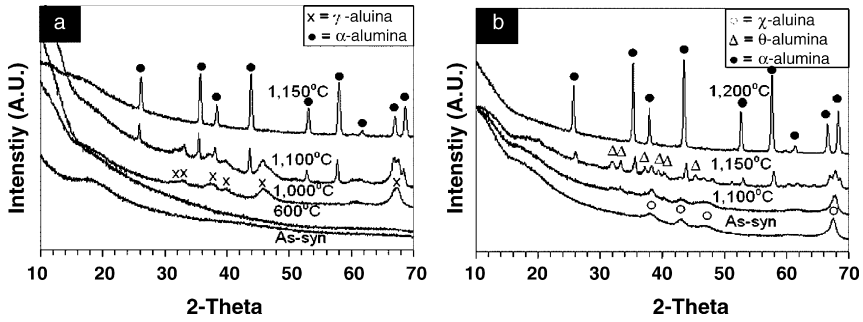

Fig. 7. The XRD patterns of powder synthesized by the reaction of AIP in mineral oil calcined at various reaction conditions: (a) 250 °C for 0 h and (b) 300 °C for 2 h.

formed in the solvent with *n*-propanol/water ratio resulting in the lowest value of dielectric constant.

Transmission electron micrographs of the as-obtained powder and calcined powder are shown in Fig. 6. The as-synthesized χ-alumina products are comprised of agglomerated primary particles having average diameter around 10 nm. As shown in Table 1, the crystallite size calculated by XRD peak broadening, using the Scherrer equation, is 9 nm. Good agreement between both values indicates that each primary particle observed by TEM is a single crystal of χ-alumina.

The XRD patterns of calcined product are shown in Fig. 7. The amorphous product remains amorphous even after calcination at 600 °C (Fig. 7a). However, after calcination at 1000 °C, γ-alumina is observed. The α-phase transformation takes place at temperature around 1150 °C and completes at 1200 °C. It should be noted that the peak at 42.5°, which is corresponding to χ-alumina, is not detected. This indicates that χ-alumina is not formed by calcination of the amorphous product. Therefore, the formation of χ-alumina occurs only in the inert organic solvent. For the calcination of χ-alumina obtained from thermal decomposition of AIP at 300 °C for 2 h (Fig. 7b), χ-alumina transforms to α-alumina directly at temperature around 1100 °C. No κ-alumina was detected. The χ-to-α phase transformation is completed at temperature around 1200 °C. Phase transformation sequences of products obtained from other reaction conditions are summarized in Table 2.

After calcination, the secondary particles still remain spherical with unchanged average particle size, regardless of the crystalline phase (see Fig. 5d). Some finger-like primary particles aggregating on the spherical secondary particles were also observed after the calcination at 1200 °C. TEM micrographs of calcined samples clearly show two groups of primary particles after the phase transformation. The first group is the spherical χ-alumina particles, which do not transform to α-alumina. These particles have crystallite size calculated from the Scherrer equation that is the same as particle size observed by using TEM. The second group of primary particles is the finger-like α-alumina transformed from the low-temperature transition alumina nanocrystals via the nucleation and growth mechanism (see Fig. 6b).

The direct phase transformation of χ- to α-alumina is a specific property for powders prepared by the decomposition of AIP in an inert organic solvent. In our previous work, it has been proposed that the direct phase transformation is the result from the absence of contaminating cations in crystals, as well as high crystallinity of the synthesized product due to the small amount of water adsorbed on the surface. Chou and Nieh [17] have reported that the nucleation of α-alumina occurs along (2 2 0) crystallographic plane of γ-alumina in nanocrystalline oxide synthesized by radio frequency reactive sputtering deposition. Johnston et al. [18] have reported that γ-alumina prepared by laser ablation synthesis directly transforms into α-phase and they have attributed that the particle size of the product is well below the grain size limit for super plastic alumina (500 nm). Bahlawane and Watanabe [19] prepared anhydrous alumina which transformed directly to α-alumina by sol–gel method. Shek et al. [20] have reported that amorphous powders prepared by oxidation of pure aluminum metal crystallize to γ-alumina, which directly transforms to α-alumina at 1370 K. They have attributed this result to the facilitation of nucleation of α-alumina by the strain relaxation of the transition alumina lattice. However, relaxation of the γ-alumina structure should decrease the energy level of γ-alumina and disturb the nucleation of more stable phases. Simpson et al. [21] have reported that samples prepared via electron-beam evaporation of alumina onto a sapphire substrate held at room temperature crystallize to γ-alumina, which transforms into α-alumina without formation

Table 2
The crystallite size calculated by the Scherrer equation and phase of the as-synthesized and calcined products

Reaction condition		Crystallite size and phase of alumina after treat at various temperatures (°C)				
Temperature (°C)	Time (h)	As-synthesized	1000	1100	1150	1200
250	0	– (Amorphous)	6.2 (γ)	16.5 (γ), 31.1 (α)	33.7 (α)	– (α)
250	2	9 (χ)	9.2 (χ)	9.6 (χ)	12.3 (χ), 36.4 (α)	68 (α)
250	6	10.8 (χ)	11.2 (χ)	12.5 (χ)	15.2 (χ), 39.2 (α)	77.2 (α)
270	2	10.2 (χ)	9.4 (χ)	10.3 (χ)	15.6 (χ), 33.5 (α)	97.5 (α)
300	2	9.4 (χ)	10.8 (χ)	14.2 (χ), 39.5 (α)	14.6 (χ), 41.3 (α)	44.7 (α)

of other intermediate phases. They have attributed this result to the epitaxial growth of α-alumina on the sapphire substrate. Ogihara et al. [22] have prepared monodispersed, spherical alumina by the controlled hydrolysis of aluminum alkoxide in a dilute solution containing octanol and acetonitrile. They have found that the amorphous product crystallizes to γ-alumina at 1000 °C which converted to α-alumina at 1150 °C without intermediate phase. However, they did not give any explanation for this result. It has also reported that γ-alumina formed by thermal decomposition of aluminum sulfate transforms into α-alumina directly [23–25].

The crystallite sizes of calcined products are summarized in Table 2. The crystallite size of is initially about 9–10 nm. χ-Alumina grows to 16 nm upon calcination but the growth stop at this size even after the calcination at high temperature. At higher calcination temperature, only α-alumina was observed. It is suggested that χ-alumina grows to the critical size and then abruptly transforms into α-alumina. The result suggests that the critical size of χ-alumina, beyond which it is unstable and undergoes phase transformation into α-alumina, is around 16 nm. Once the phase transformation takes place, the primary particles grow drastically and then become sluggish. The α-phase transformation is considered to occur through a nucleation and growth mechanism [26,27]. Investigations on the phase transformation after the crystallite size has reach the critical size have been reported by many researchers [28–30]. Yen et al. [28,29] have found that, during the phase transformation, there is a critical size for θ-alumina (around 22 nm) at the nucleation stage, which initiates the formation of α-alumina nucleus.

4. Conclusion

Thermal decomposition of AIP in mineral oil at temperature between 250 and 300 °C with holding time of 2 h results in the micro-spherical particles formed by agglomeration of nanocrystalline χ-alumina. On the contrary, the powder obtained during the heating-up process to 250 °C is amorphous. The fact that χ-alumina is not formed by the calcination of the amorphous intermediate confirms that χ-alumina is formed only by AIP decomposition in the inert organic solvent. It is suggested that a spherical particle of complex moieties forms through stepwise decomposition of AIP in the solvent. With the prolonged holding time or increased reaction temperature, this complex sheds organic moieties and solid-state phase of χ-alumina is formed. After calcination at high temperature, χ-alumina transformed to α-alumina directly. The crystallite size of χ-alumina is initially around 9–10 nm and grows upon the calcination to the critical size of 16 nm, beyond which χ-alumina transforms to α-alumina. This direct transformation behavior of nanocrystalline χ-alumina is attributed to the absence of cations and the less defect structure.

Acknowledgement

The author would like to thank the Thailand Research Fund (TRF) for their financial support.

References

[1] W.H. Gitzen, Alumina as a Ceramics Material, American Ceramic Society, Columbus, OH, 1970.
[2] G.M. Pajonk, Appl. Catal. A: Gen. 72 (2) (1991) 217–266.
[3] K. Wefers, G.M. Bell, Oxides and Hydroxides of Alumina, Alcoa, Bauxite, AR, 1972.
[4] H. Saalfeld, Structure Phases of Dehydrated Gibbsite, Elsevier, The Netherlands, 1961.
[5] G.W. Brindley, J.O.T. Choe, Am. Miner. 46 (7–8) (1961) 771785.
[6] H.C. Stumpf, A.S. Russell, J.W. Newsome, C.M. Tucker, Ind. Eng. Chem. 42 (7) (1950) 1398–1403.
[7] M. Inoue, H. Kominami, T. Inui, J. Am. Ceram. Soc. 75 (9) (1992) 2597–2598.
[8] M. Inoue, H. Kominami, T. Inui, Appl. Catal. A: Gen. 121 (1) (1995) L1–L5.
[9] S. Iwamoto, K. Saito, M. Inoue, K. Kagawa, Nano Lett. 1 (8) (2001) 417–421.
[10] P. Pratherthdam, M. Inoue, O. Medkasuvandumrong, W. Thanakulrangsan, S. Phatanasri, Inorg. Chem. Commun. 3 (11) (2000) 671–676.
[11] O. Mekasuwandumrong, P.L. Silveston, P. Praserthdam, M. Inoue, V. Pavarajarn, W. Tanakulrungsank, Inorg. Chem. Commun. 6 (7) (2003) 930–934.
[12] O. Mekasuwandumrong, H. Kominami, M. Inoue, P. Praserthdam, J. Am. Ceram. Soc. 87 (8) (2004) 1543–1549.
[13] D.A. Skoog, J.J. Leary, Principles of Instrumental Analysis, Saundres College Publishing, Philadelphia, San Diego, 1992.
[14] B.C. Lippens, J.H. de Boer, J. Catal. 4 (3) (1965) 319–323.
[15] B.C. Lippens, J.H. de Boer, J. Catal. 3 (1) (1964) 32–37.
[16] C. Fang, Y. Chen, Mater. Chem. Phys. 78 (3) (2003) 739–745.
[17] T.C. Chou, T.G. Nieh, J. Am. Ceram. Soc. 74 (9) (1991) 2270–2279.
[18] G.P. Johnston, R. Muenchausen, D.M. Smith, W. Fahrenholtz, S. Foltyn, J. Am. Ceram. Soc. 75 (12) (1992) 3293–3298.
[19] N. Bahlawane, T. Watanabe, J. Am. Ceram. Soc. 83 (9) (2000) 2324–2326.
[20] C.H. Shek, J.K.L. Lai, T.S. Gu, G.M. Lin, Nanostruct. Mater. 8 (5) (1997) 605–610.
[21] T.W. Simpson, Q. Wen, N. Yu, D.R. Clarke, J. Am. Ceram. Soc. 81 (1) (1998) 61–66.
[22] T. Ogihara, H. Nakagawa, T. Yanagawa, N. Ogata, K. Yoshida, J. Am. Ceram. Soc. 74 (9) (1991) 2263–2269.
[23] D.W. Johnson, F.J. Schnettler, J. Am. Ceram. Soc. 53 (8) (1970) 440–444.
[24] E. Kato, K. Daimon, M. Nanbu, J. Am. Ceram. Soc. 64 (8) (1981) 436–445.
[25] M.D. Sacks, T.-Y. Tseng, S.Y. Lee, Ceram. Bull. 63 (2) (1984) 301–310.
[26] D.S. Tucker, J. Am. Ceram. Soc. 68 (7) (1985) C163–C164.
[27] F.W. Dynys, J.W. Halloran, J. Am. Ceram. Soc. 65 (9) (1982) 442–448.
[28] F.S. Yen, H.L. Wen, Y.T. Hsu, J. Crystal Growth 233 (4) (2001) 761–773.
[29] F.S. Yen, H.S. Lo, H.L. Wen, R.J. Yang, in press.
[30] R.B. Bagwell, G.L. Messing, P.R. Howell, J. Mater. Sci. 36 (7) (2001) 1833–1841.

Available online at www.sciencedirect.com
ScienceDirect
Ceramics International xxx (2006) xxx–xxx
CERAMICS INTERNATIONAL
www.elsevier.com/locate/ceramint

Preparation of ZnO nanorod by solvothermal reaction of zinc acetate in various alcohols

Parawee Tonto [a], Okorn Mekasuwandumrong [b,*], Suphot Phatanasri [a,*], Varong Pavarajarn [a], Piyasan Praserthdam [a]

[a] Center of Excellence on Catalysis and Catalytic Reaction Engineering, Department of Chemical Engineering, Faculty of Engineering, Chulalongkorn University, Bangkok 10330, Thailand
[b] Department of Chemical Engineering, Faculty of Engineering and Industrial Technology, Silpakorn University, Nakorn Pathom 73000, Thailand

Received 26 April 2006; received in revised form 10 May 2006; accepted 22 August 2006

Abstract

Solvothermal reaction of zinc acetate in various alcohols resulted in the formation of zinc oxide (ZnO) nanorods. The effects of reaction conditions on the product morphology as well as crystallization mechanism were investigated by using X-ray diffraction (XRD), infrared spectroscopy (IR), scanning electron microscopy (SEM), energy dispersive X-ray spectroscopy (EDS) and transmission electron microscopy (TEM) techniques. It was found that average diameter and length of the nanorods increased with an increase in reaction temperature or the initial concentration of zinc acetate. On the contrary, the aspect ratio of the product depended upon type of alcohol used as the reaction medium. The aspect ratio of ZnO nanorods increased from 1.7 to 5.6 when the alcohol was changed from 1-butanol to 1-decanol. An investigation of the reaction mechanism suggested that the formation of ZnO nanorods was initiated from the esterification reaction between zinc acetate precursor and alcohol to form ZnO seeds.

Keywords: D. ZnO; Nanorod; Alcohol; Solvothermal

1. Introduction

Nanostructured materials have received increasing attention due to their potential uses as active components or interconnects in nanoscaled electronic, optical, optoelectronic, electrochemical, and electromechanical devices [1]. One material that has been in great interest from wide range of technological field associated with nanotechnology is zinc oxide (ZnO) [2]. ZnO is a material with large direct band gap (3.3 eV) and excellent chemical and thermal stability. It has unique optical and acoustic properties, as well as electronic properties of the II–VI semiconductor with large exciton binding energy (60 meV) [3]. Therefore, zinc oxide has been used in various applications, e.g. as varistor, gas-sensor, catalyst and pigment. According to great function of zinc oxide, several techniques have been proposed for zinc oxide synthesis, e.g. hydrothermal synthesis [4,5], thermal decomposition method [6,7], sol–gel synthesis [8], flame spray pyrolysis [9], and precipitation method [10].

Control of the particle shape is another concern for nanostructured material synthesis because electrical and optical properties of nanomaterials depend sensitively on both size and shape of the particles. Therefore, it is desired to synthesize nanomaterial in a controllable shape and size by simple approach. For zinc oxide particles, various shapes including nanorods [11–13], whiskers [14,15] and nanowires [16] have been successfully prepared. However, it was the result from different synthesis methods under different preparation conditions [17].

In this study, the solvothermal method was employed to synthesize ZnO nanorods. This technique is based on thermal decomposition of organometallic compound in organic solvent and has been successfully applied for the synthesis of various types of nanosized metal oxide with large surface area, high crystallinity and high thermal stability [18–20]. The influences of reaction conditions, i.e. type of solvent, concentration and

* Corresponding authors. Tel.: +66 63116537; fax: +66 34219368.
E-mail addresses: okornm@yahoo.com (O. Mekasuwandumrong), Suphot@thaipeginner.com (S. Phatanasri).

0272-8842/$30.00
doi:10.1016/j.ceramint.2006.08.003

Please cite this article in press as: P. Tonto et al., Preparation of ZnO nanorod by solvothermal reaction of zinc acetate in various alcohols, Ceram. Int. (2006), doi:10.1016/j.ceramint.2006.08.003

reaction temperature, on physical properties of the synthesized nanorods as well as the mechanism were investigated. An interesting correlation between aspect ratio of the ZnO products and physical properties of the solvent was observed and presented in this work.

2. Experiment

2.1. Preparation of ZnO

Zinc acetate ($Zn(CH_3CO_2)_2$) in a predetermined amount in the range of 10–25 g was suspended in 100 ml of alcohol in a glass vessel, which was then placed in a 300 ml autoclave. Alcohols used in this work were 1-butanol, 1-hexanol, 1-octanol and 1-decanol, respectively. The gap between autoclave wall and the glass vessel was filled with 30 ml of the same alcohol. The autoclave was completely sealed and purged with nitrogen. The mixture was heated to desired temperature, in the range of 250–300 °C, at a constant heating rate of 2.5 °C/min, and held at that temperature for 2 h. Subsequently, after the autoclave was cooled, the product obtained in the vessel was collected by centrifugation, washed with methanol and dried in air at room temperature.

2.2. Characterization

The prepared samples were examined by X-ray diffraction (XRD) analysis using a SIEMENS XRD D500 diffractometer with Cu Kα radiation. The morphology and crystallite size of the nanoparticles were observed on a JEOL JSM6400 Scanning Electron Microscope (SEM) and a JEOL JEM1220 Transmission Electron Microscope (TEM). Infrared spectra of the products were also obtained using Nicolet FT-IR spectrophometer model Impact 400. Each sample was mixed with KBr in the ratio of 1:100 and then pressed into a thin pellet. Infrared spectra were recorded at wave number in the range of 400 and 4000 cm^{-1}.

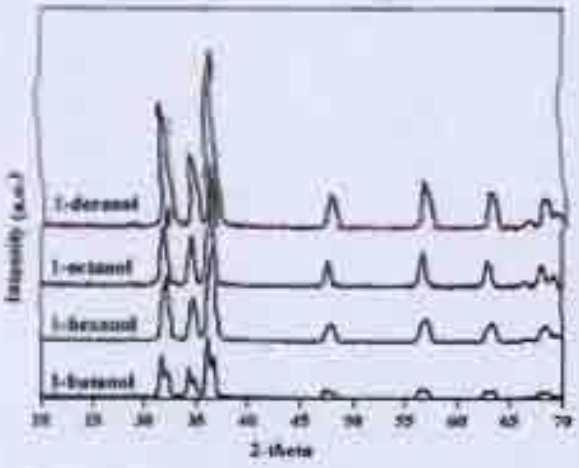

Fig. 1. The X-ray diffraction patterns of ZnO powder prepared by solvothermal reaction at 250 °C for 2 h in various alcohols.

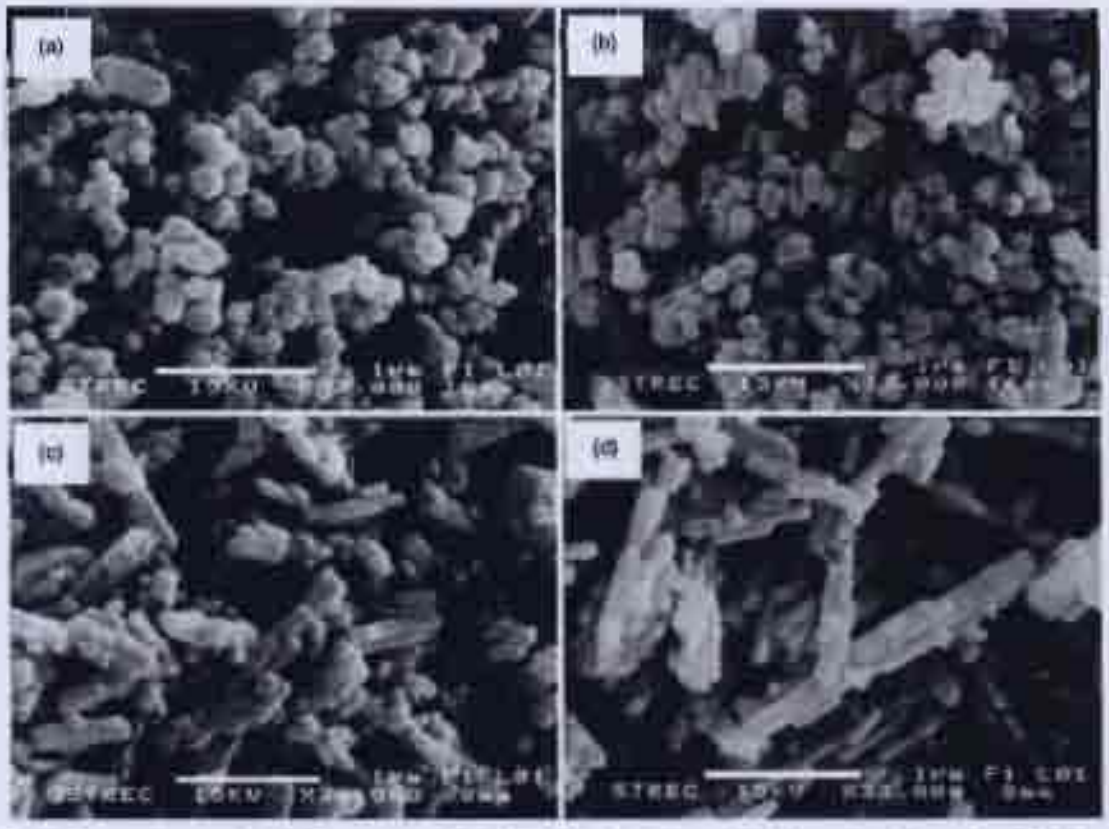

Fig. 2. SEM images of as-synthesized ZnO synthesized at 250 °C for 2 h in: (a) 1-butanol, (b) 1-hexanol, (c) 1-octanol and (d) 1-decanol.

Please cite this article in press as: P. Tartaj et al., Preparation of ZnO nanorod by solvothermal reaction of zinc acetate in various alcohols, Ceram. Int. (2006), doi:10.1016/j.ceramint.2006.05.003

3. Results and discussion

3.1. Effect of various reaction conditions

XRD patterns of powders synthesized by the solvothermal reaction in various alcohols at 250 °C are shown in Fig. 1. All peaks of the obtained product were corresponding to the hexagonal wurtzite structure of ZnO with lattice parameters a and c of 3.24 and 5.19 Å, respectively. No peak from either ZnO in other phases or impurities was observed. This result confirmed that ZnO was successfully synthesized by the solvothermal reaction in all alcohols investigated. Nevertheless, it should be noted that the XRD pattern of the product synthesized in 1-butanol showed slight split for all XRD peaks, which suggested non-homogeneity in the crystal structure of the ZnO product.

Fig. 2a–d show SEM images of the products synthesized in 1-butanol, 1-hexanol, 1-octanol and 1-decanol, respectively. It was clearly illustrated that morphology of particles synthesized in these alcohols were significantly different. Nearly spherical particles were obtained when 1-butanol was used as the reaction medium, while smooth solid hexagonal rods were observed in the product prepared in 1-decanol. Therefore, it could be taken that the product from the solvothermal synthesis in alcohol was ZnO nanorods and the length of the rods increased when alcohol with longer molecule was employed.

Morphology of the primary ZnO particle was examined from TEM images, as shown in Fig. 3. The results confirmed with SEM observation that nanorods synthesized were straight and non-porous. The selected area electron diffraction (SAED) patterns shown as the inset in Fig. 3 suggested that each primary particle was a rod-shaped single crystal of ZnO. The observed morphology was consistent with the hexagonal nanorods grown in 0 0 1 direction. It was also found that all synthesized ZnO nanorods were quite uniform in size. The distributions of diameter of the rods measured from TEM micrographs are shown in Fig. 4. According to Fig. 4, it was shown that the synthesized ZnO nanorods had narrow size distribution, regardless of the type of alcohol employed. The average diameter and length as well as the calculated aspect ratio of the particles are summarized in Table 1.

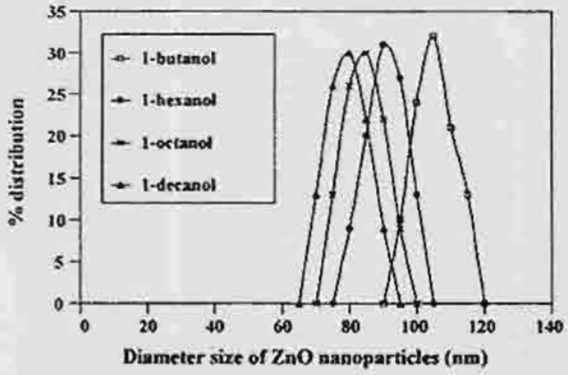

Fig. 4. The size distributions for diameter of ZnO nanorods synthesized in: (a) 1-butanol, (b) 1-hexanol, (c) 1-octanol and (d) 1-decanol.

According to Table 1, ZnO synthesized in alcohol having long carbon chain tended to be nanorods that were longer and had

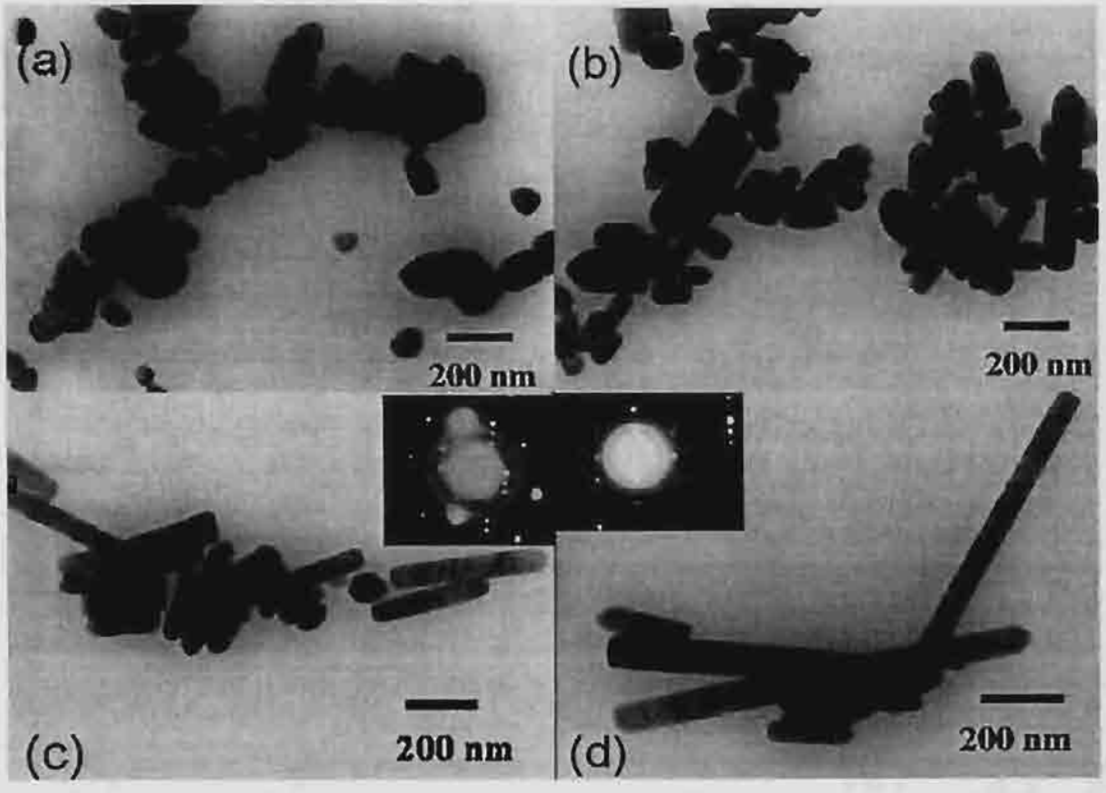

Fig. 3. TEM images of as-synthesized ZnO synthesized in: (a) 1-butanol, (b) 1-hexanol, (c) 1-octanol and (d) 1-decanol.

Please cite this article in press as: P. Tonto et al., Preparation of ZnO nanorod by solvothermal reaction of zinc acetate in various alcohols, Ceram. Int. (2006), doi:10.1016/j.ceramint.2006.08.003

Table 1
The crystallite size and aspect ratio of ZnO nanorods

Solvent	Synthesis emperature (°C)	Amount of zinc acetate used (g)	Average diameter of product (nm)	Average length (nm)	Aspect ratio
1-Butanol	250	15	107	184	1.7
1-Hexanol	250	15	91	264	2.9
1-Octanol	200	15	67	284	4.2
1-Octanol	230	15	75	308	4.1
1-Octanol	250	10	79	316	4.0
1-Octanol	250	15	84	343	4.1
1-Octanol	250	20	97	385	4.0
1-Octanol	300	15	110	472	4.3
1-Decanol	200	15	69	392	5.7
1-Decanol	230	15	74	419	5.7
1-Decanol	250	10	76	423	5.6
1-Decanol	250	15	81	455	5.6
1-Decanol	250	20	91	506	5.6

diameter smaller than those synthesized in short-chain alcohol. The aspect ratio of the obtained nanorods increased corresponding to an increase in length of the carbon chain of the reaction medium. When 1-decanol was used instead of 1-butanol, the length of nanorods increased from 184 to 455 nm, while the average diameter decreased from 107 to 81 nm. Consequently, the aspect ratio increased approximately three-fold.

Table 1 also summarizes dimension of ZnO particles synthesized under various reaction conditions. It was found that both average diameter and length of the ZnO nanorods increased with an increase in either initial concentration of the precursor (i.e. zinc acetate) or reaction temperature. This observation suggested the increase in crystal growth with number of nuclei sites as well as the energy of the system. However, it should be noted that the aspect ratio of ZnO particles was not affected by either the temperature or amount of precursor. In the other words, the change in the reaction conditions did not alter the growth of ZnO nanoparticles into preferential orientation. Type of alcohol employed as the reaction medium was the only major factor affecting the aspect ratio of the synthesized particles.

The aspect ratio of ZnO nanorod was determined from relative growth rates from various faces of the crystal. The rate of crystal

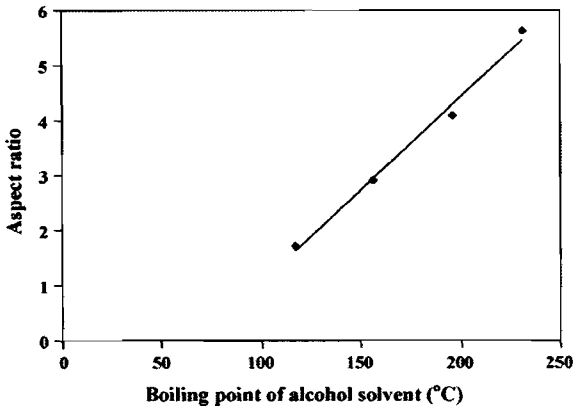

Fig. 5. The correlation between boiling points of the employed solvent and aspect ratio of ZnO products.

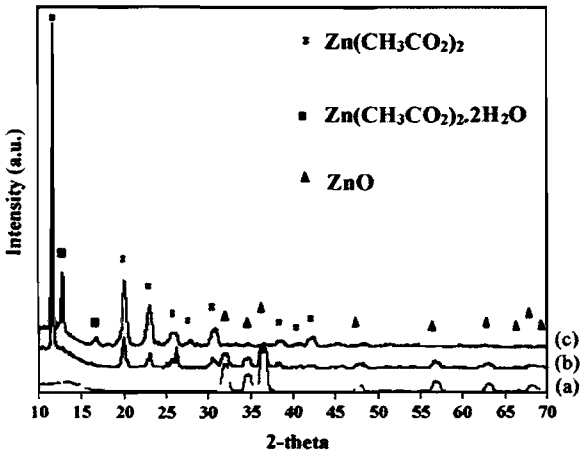

Fig. 6. The X-ray diffraction patterns of: (a) the reaction precursor, i.e. zinc acetate, (b) ZnO synthesized in 1-octanol at 150 °C and (c) ZnO synthesized in 1-octanol at 200 °C.

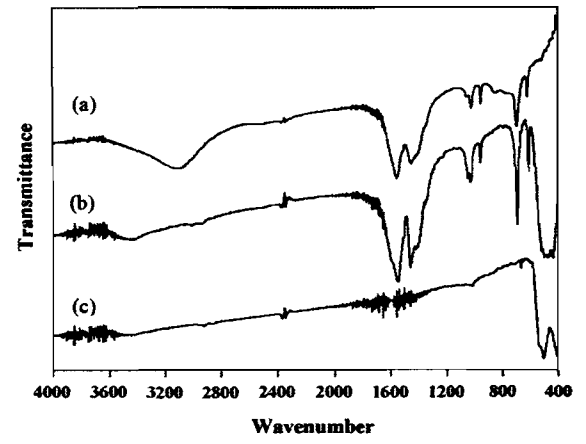

Fig. 7. IR spectra of: (a) the reaction precursor, i.e. zinc acetate, (b) ZnO synthesized in 1-octanol at 150 °C and (c) ZnO synthesized in 1-octanol at 200 °C.

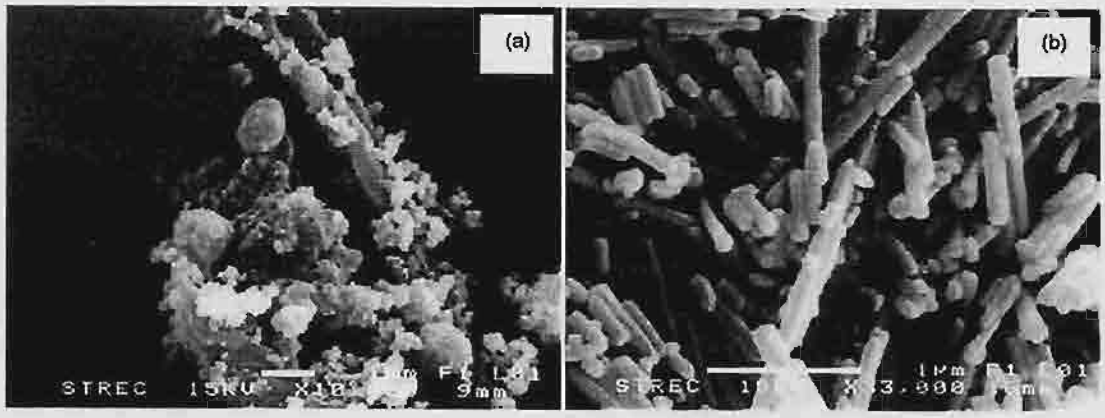

Fig. 8. SEM images of ZnO synthesized in 1-octanol for 2 h at (a) 150 °C and (b) 250 °C.

growth from any particular face was controlled by a combination of internal factors (e.g. intermolecular bonding preference or dislocation in crystal) and external factors (e.g. supersaturation condition, reaction temperature and type of solvent) [21]. ZnO in wurtzite structure is a polar crystal with (0 0 1) facet having higher-symmetry (C6v) than the other faces. Therefore, crystal growth along *c*-axis, or (0 0 1) direction, is a typical behavior observed from wurtzite ZnO. Nevertheless, Cheng and Samulski [4] have reported that the growth rate from each face of ZnO under the condition of hydrothermal synthesis is also controlled by properties of solvent that affected the interface–solvent interactions. The results in this work supported this report. It was found that the aspect ratio of the ZnO product was correlated with physical properties of the solvent. Fig. 5 shows a plot between boiling points of solvent and aspect ratio of the ZnO product. Interestingly, a linear relationship was observed. Although direct relationship between the boiling point of solvent and the preferential crystal growth may not have scientifically significance, the boiling point of alcohol could be used as an index for "non-polar" nature of alcohol molecule. For all alcohols investigated, the hydrogen bonding and the dipole–dipole interactions among molecules are roughly the same, but the van der Waals dispersion forces are stronger in alcohol with longer hydrocarbon chain and it results in an increase in boiling point of alcohol. As the long-chain alcohol was employed as the reaction medium, the interaction between the alcohol molecules and the (0 0 1) facet of the ZnO crystal, which was the slight positively charged Zn surface, was weak, allowing ZnO crystal to grow along the preferential *c*-axis.

Although the crystallization phenomenon of ZnO nanorod is unambiguously demonstrated by the presented correlation shown in Fig. 5, the detailed mechanism of the crystal growth is still under investigation. However, the behavior shown in Fig. 5 should prove useful in practical application, since the correlation allows and estimation of the aspect ratio of ZnO nanorod from type of alcohol used.

3.2. *Investigation of reaction mechanism*

To understand the reaction mechanism, the reaction temperature in octanol was decreased to 200 and 150 °C, respectively. Fig. 6 shows the XRD patterns of thus-obtained products. It was found that the powder prepared at 150 °C was a mixture of zinc acetate and zinc oxide. No shift in XRD pattern was observed. IR spectra of the product as shown in Fig. 7 also confirmed the existence of zinc acetate in the product synthesized at 150 °C without the presence of functional groups corresponding to alcohol. These results indicated that no intermediate was formed from the reaction between zinc acetate and alcohol.

Fig. 8 shows SEM images of the as-synthesized products prepared at various temperatures. The product prepared at 150 °C was composed of two types of particles, i.e. the particles with irregular shape, which was assigned to be zinc acetate and rod-shaped particles of ZnO. The elemental mapping showed that carbon atoms were distributed only on the irregular-shaped particles. The content of carbon decreased dramatically at the boundary between the irregular-shaped particles and rod-like particles. This SEM observation, together with XRD and FTIR results, indicated that ZnO rods grew from the ZnO seeds formed via the direct decomposition of zinc acetate.

To further investigate the reaction mechanism, the solvent recovered after the reaction was collected and analyzed by gas chromatography. Ester and water were detected in the remaining solvent. Therefore, it was proposed that the interaction between zinc acetate and alcohol under the solvothermal conditions resulted in esterifaction reaction, which proceeded to form ZnO, ester and water, according to the following reaction:

$$Zn(CH_3COO)_2 + 2R\text{-}OH \rightarrow ZnO + 2CH_3\text{-}CO\text{-}R + H_2O$$

Once the ZnO seeds were formed, further reaction resulted in crystal growth of ZnO nanoparticles. The size and shape of the particles were controlled by the reaction condition, as discussed previously.

4. Conclusion

Zinc oxide nanorods were successfully prepared by one-step solvothermal reaction of zinc acetate in alcohols. The as-synthesized ZnO was found to be an aggregation of nanorods having aspect ratios of 1.7, 3, 4 and 5.6 when 1-butanol, 1-

Please cite this article in press as: P. Tonto et al., Preparation of ZnO nanorod by solvothermal reaction of zinc acetate in various alcohols, Ceram. Int. (2006), doi:10.1016/j.ceramint.2006.08.003

hexanol, 1-octanol and 1-decanol, respectively, was used as the reaction medium. The interesting linear relationship between boiling point of the solvent used and aspect ratio of the product obtained was observed. This plot can be used to select the appropriate solvent for the preparation of zinc oxide nanorod with desired aspect ratio.

Acknowledgement

Authors would like to thank Thailand Research Fund and Commissions on Higher Education, Ministry of Education, Thailand for financial support.

Reference

[1] Z.W. Pan, Z.R. Dai, Z.L. Wang, Nanobelts of semiconducting oxides, Science 291 (2001) 1947–1949.
[2] L. Guo, Y.L. Ji, H. Xu, Regularly shaped, single-crystalline ZnO nanorods with wurtzite structure, J. Am. Chem. Soc. Commun. 124 (2002) 14864–14865.
[3] Q. Li, V. Kumar, Y. Li, H. Zhang, T.J. Marks, R.P.H. Chang, Fabrication of ZnO nanorods and nanotubes in aqueous solutions, J. Am. Chem. Soc. 17 (5) (2005) 1001–1006.
[4] B. Cheng, E.T. Samulski, Hydrothermal synthesis of one-dimensional ZnO nanostructures with different aspect ratios, Chem. Commun. (2004) 986–987.
[5] H. Wei, Y. Wu, N. Lun, C. Hu, Hydrothermal synthesis and characterization of ZnO nanorods, Mater. Sci. Eng. A 393 (2005) 80–82.
[6] Y Yang, H. Chen, Size control of ZnO nanoparticles via thermal decomposition of zinc acetate coated on organic additives, J. Cryst. Growth 263 (2004) 447–453.
[7] P. Saravanan, S. Alam, G.N. Mathur, Synthesis of ZnO and ZnS nanocrystals by thermal decomposition of zinc (II) cupferron complex, Mater. Lett. 58 (2004) 3528–3531.
[8] M.N. Kamalasanan, S. Chandra, Sol–gel synthesis of ZnO thin films, Thin Solid Films 288 (1996) 112–115.
[9] R. Mueller, L. Mädler, S.E. Pratsinis, Nanoparticle synthesis at high production rates by flame spray pyrolysis, Chem. Eng. Sci. 58 (2003) 1969–1976.
[10] J.E. Rodriguez, A.C. Caballero, Controlled precipitation methods: formation mechanism of ZnO nanoparticles, J. Eur. Ceram. Soc. 21 (2001) 925–930.
[11] Y. Zhang, Y. Dai, Y. Huang, C. Zhou, Shape controlled synthesis and growth mechanism of one-dimensional zinc oxide nanomaterials, J. Univ. Sci. Technol. Beijing 11 (2004) 23–29.
[12] J.Y. Li, X.L. Chen, H. Li, M. He, Z.Y. Qiao, Fabrication of zinc oxide nanorods, J. Cryst. Growth 233 (2001) 5–7.
[13] K. Sue, K. Kimura, M. Yamamoto, K. Arai, Rapid hydrothermal synthesis of ZnO nanorods without organics, Mater. Lett. 58 (2004) 3350–3352.
[14] J.Q. Hu, X.L. Ma, Z.Y. Xie, N.B. Wong, C.S. Lee, S.T. Lee, Characterization of zinc oxide crystal whiskers grown by thermal evaporation, Chem. Phys. Lett. 344 (2001) 97–100.
[15] Y. Liu, Z. Liu, G. Wang, Synthesis and characterization of ZnO nanorods, J. Cryst. Growth 252 (2003) 213–218.
[16] S.C. Lyu, Y. Zhang, H. Ruh, H.J. Lee, H.W. Shim, E.K. Suh, C.J. Lee, Low temperature growth and photoluminescence of well-aligned zinc oxide nanowires, Chem. Phys. Lett. 363 (2002) 134–138.
[17] X. HaiYan, W. Hao, Hydrothermal synthesis of zinc oxide powders with controllable morphology, Ceram. Int. 30 (2004) 93–97.
[18] O. Mekasuwandumrong, H. Kominami, P. Praserthdam, M. Inoue, Synthesis of thermally stable x-alumina by thermal decomposition of aluminum isopropoxide in toluene, J. Am. Ceram. Soc. 87 (2004) 1543–1549.
[19] S. Iwamoto, K. Saito, M. Inoue, K. Kagawa, Preparation of the xerogels of nanocrystalline titanias by the removal of the glycol at the reaction temperature after the glycothermal method and their enhanced photocatalytic activities, Nano Lett. 1 (2001) 417–421.
[20] M. Inoue, H. Kominami, T. Inui, Novel synthesis method for thermally stable monoclinic zirconia. Hydrolysis of zirconium alkoxides at high temperatures with a limited amount of water dissolved in inert organic solvent from the gas phase, App. Catal. A Gen. 121 (1995) L1–L5.
[21] N. Kubota, Effect of impurities on the growth kinetics of crystals, Cryst. Res. Technol. 36 (2001) 749–769.

Effect of Aging on Synthesis of Graft Copolymer of EPDM and Styrene (EPDM-*g*-PS)

Chalermpol Wonglert, Supakanok Thongyai, Piyasan Praserthdam

Center of Excellence on Catalysis and Catalytic Reaction Engineering, Department of Chemical Engineering, Chulalongkorn University, Bangkok 10330 Thailand

Received 30 September 2004; accepted 14 March 2006
DOI 10.1002/app.24673
Published online in Wiley InterScience (www.interscience.wiley.com).

ABSTRACT: The effect of aging on synthesis by the graft copolymerization of styrene onto random ethylene–propylene–diene monomer with benzoyl peroxide (BPO) as the initiator is described. Results showed that yields of graft copolymer are increased in the first 10 min. After 10 min, the total polymer produced has a maximum at about 25 min. However, the portion of the graft copolymer is decreased and the portion of the pure polystyrene is increased. In addition, the influence factors, such as reaction time, temperature, BPO concentrations and styrene concentrations, effect of solvents on the extent of graft copolymerization were discussed. The extent of grafted copolymerization was verified by hexane and acetone Soxhlet (solvent extraction). © 2006 Wiley Periodicals, Inc. J Appl Polym Sci 102: 4809–4813, 2006

Key words: EPDM/styrene graft copolymer; benzoyl peroxide; aging effect

INTRODUCTION

Graft copolymer of styrene (St) with ethylene–propylene–diene monomer (EPDM) has been widely studied in recent years. Among the several attempts to improve the weak points of high impact polystyrene (HIPS), the substitution of EPDM for butadiene has been widely investigated.[1,2] The usual method is to replace the butadiene with EPDM because it has long been known that EPDM has outstanding resistance[3] to heat, light, oxygen, and ozone because of its nonconjugated diene component.[4] In this study, St monomers were grafted onto EPDM under argon atmosphere in the presence of benzoyl peroxide (BPO) as an initiator. Various variables were observed to maximize the yield of product copolymer, such as aging of the solution, the concentration of St and others. The previous BPO reaction on EPDM and St monomer has been preliminary studied.[5] However, effects of aging the solution before mixing with St has not been mentioned earlier, which could further increase the yield of the copolymer. The excellent properties of the copolymer are that the EPDM-*g*-PS has a good miscibility between blends with PS[6] than the normal EPDM and can be distributed in small domain size.[7]

The effects of the reaction time, temperature, initiator concentration, solvents, and aging time on the graft reaction were investigated. The yields of graft copolymer were analyzed by hexane Soxhlet and acetone Soxhlet. The hexane will dissolve EPDM or the short branch chain of EPDM-*g*-PS, while acetone will dissolve the polystyrene formed.[7]

Correspondence to: S. Thongyai (tsupakan@chula.ac.th).
Contract grant sponsors: Thailand Research Fund (TRF); TJTTP-J.

EXPERIMENTAL

Materials

The Dupont EPDM 4640 rubber used was donated by S.K. Polymer Co., Thailand. The St monomer used to prepare the copolymer was manufactured by Fluka Chemie A.G., Switzerland, and purified with NaOH and distilled under vacuum before use. The BPO, as a free radical initiator, was manufactured by Merck, Muchen, Germany, and recrystallined in ethanol before use. The solvents such as *n*-hexane, heptane, THF, and toluene were of analytical purity and used as received.

Preparation

EPDM (~ 5 g) was dissolved in 50 mL of toluene and heated at 80°C. The solution was stirred until the EPDM was completely dissolved. Free radical initiator used was BPO, which was recrystallined in ethanol to remove the impurities. St monomer was extracted with NaOH solution (5% w/w) in distillated water, and then was further purified by distilling over sodium under vacuum atmosphere before use.

Graft copolymer polymerization

The copolymerization was conducted in a 250-mL three-neck flask equipped with stirrer, under argon

atmosphere. The graft reaction was carried out in toluene solvent at 60 or 90°C. To stop the polymerization reaction, excess acidic methanol was added to the reaction solution. The precipitated polymer was washed with methanol and dried under vacuum. The unreacted EPDM was extracted in hexane Soxhlet extractor and the produced polystyrene was further extracted in acetone Soxhlet extractor[8] for 12 h and the remaining graft copolymer of EPDM and St (EPDM-*g*-St) was obtained after drying.

RESULTS AND DISCUSSION

The purpose of this work is to limit the optimum condition in the synthesis of graft copolymer of EPDM and polystyrene to improve the properties of the obtained polymer blends. Therefore, this section provides information about some preliminary results concerning the reaction conditions such as polymerization time, polymerization temperature, concentration of initiator, condition of synthesis, effect of solvent as a synthesis medium, and effect of aging for initializing the synthesis. The characterizations of graft copolymer were conducted by NMR and DSC.[7] Moreover, the tensile strength tests have been used to investigate the mechanical properties reported elsewhere.[7]

Effect of time on synthesis of graft copolymer of EPDM and St

The effect of reaction time was investigated by varying the time for polymerization of EPDM and St in the range of 1–4 h while using BPO as the initiator. The copolymerization was performed in toluene at 90°C using ~ 5 g of EPDM, 1.50×10^{-3} to 2.08×10^{-3} mol/L BPO concentration, with total St concentration of 2.49 mol/L. The influence of time on the synthesis of graft copolymer is shown in Figure 1.

From the previous data of Sheng,[5] the yield of the copolymer will increase as time goes by and slightly increase after 1 h of polymerization. In a trend similar to that in Sheng's work, the copolymer formed (after extracting with acetone) has the tendency to saturate at certain yield. However, when the polymerization time reaches 4 h, the portion that did not dissolve in acetone (the moderate branch EDPM-*g*-PS) starts to increase abruptly, which indicated that the growth of the side chains exceeds the solubility limit in hexane (EDPM and short branch EDPM-*g*-PS will dissolve in hexane), while the quantity of PS formed (that dissolved in acetone) is quite constant. The experiments ceased after 4 h because the activity of the catalytic process are not worth to perform. The difference between Sheng's data and our data is the properties of the EDPM and reaction conditions used, which might lead to different results; but, however the tendency of the graph is very similar.

Effect of BPO initiator concentration on the synthesis of graft copolymer of EPDM and St

The effects of the initiator concentration were investigated under 3 h polymerization times. The concentration of BPO initiator was varied in the range of 2.08×10^{-3} to 6.25×10^{-3} mol/L. The polymerizations were performed in toluene at 90°C using ~ 5 g of EPDM, with St concentration of 2.49 mol/L. The influence of BPO concentration on synthesis of graft copolymer is shown in Figure 2.

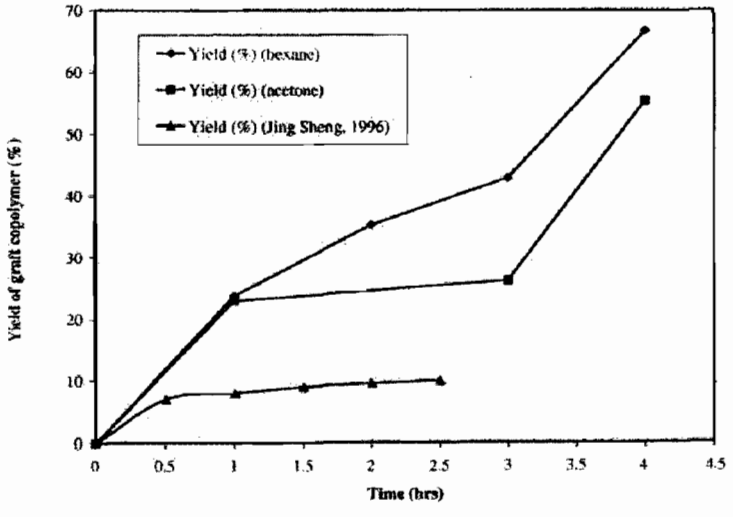

Figure 1 Yield of graft copolymer at different times. Polymerization conditions: EPDM, 3–5 g; [St], 2.49 mol/L (20 mL); BPO, 1.50×10^{-3} to 2.08×10^{-3} mol/L; solvent, toluene; polymerization temperature, 90°C.

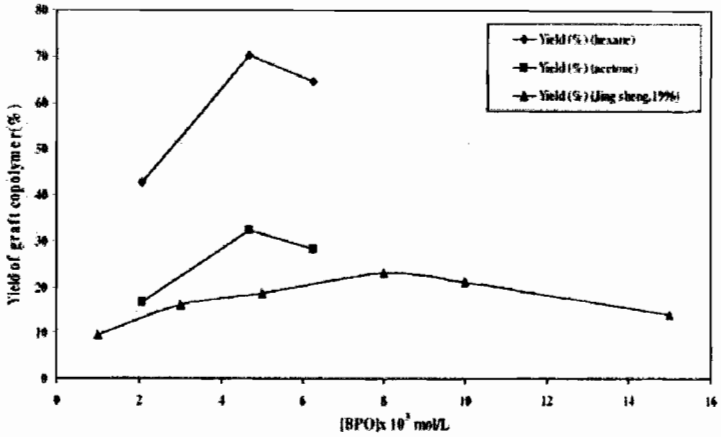

Figure 2 Yield of graft copolymer at different BPO concentrations. Polymerization conditions: EPDM, 5.687 g; [St], 2.49 mol/L (20 mL); time, 3 h; solvent, toluene; polymerization temperature, 90°C.

As shown in Figure 2, the yield of the synthesized graft copolymer increased with increasing concentrations of BPO, leading to a maximum value at about 4.67×10^{-3} mol/L. When the percent of BPO was less than the maximum value, the amounts of monomer radical, polymer radical, and graft copolymer radical increased with increasing concentrations of BPO, which increased the probability of interaction of radicals. When the percent of BPO was in excess, the grafting percent of St onto EPDM was decreased because the reaction of BPO by itself gradually increases. The viscosity of polymerization was increased with synthesis time, and because of the increasing concentration of BPO, which was evident, the movement of radicals was more difficult.[5] The trend of the results can be compared with Sheng's, but the differences arise due to the dissimilar reaction conditions. (In Sheng's work, concentration of EPDM was 60 g/L, St concentration was 0.3 mol/L, and time of reaction was 2 h.)

Effect of solvents on synthesis of graft copolymer of EPDM and St

The effects of solvents were investigated by using polymerization time of 1 h. The temperature for polymerization of EPDM and St was 60 and 90°C. The polymerizations were performed using ~ 5 g of EPDM, 1.507×10^{-3} to 2.039×10^{-3} mol/L BPO concentrations, with total St concentration of 1.24 mol/L. The influences of solvent on synthesis of graft copolymer are shown in Table I for the reaction at 60°C and in Table II for the reaction at 90°C.

As shown in Table I, at 60°C, yields of graft copolymer were increasing from THF, hexane, toluene, and heptane respectively. However, at the temperature of 90°C, toluene gave more yield than heptane and eight times higher yield from the same solvent at 60°C (Table I). The nature of solvent may also affect k_d (rate of thermal decomposition).[9] Therefore, rate of thermal decomposition of BPO to give free radical depends on various solvents and temperature, as can be seen. Therefore, at temperature of 90°C, cyclic solvent gives higher initiator radical than linear solvent in the process of high grafting polymer.

TABLE I
Yield of Graft Copolymer of Each Solvent at 60°C

Solvent	Yield (%) (hexane)	Activity (g of polymer/(mol of BPO) h
Toluene	1.65	147.83
Hexane	0.24	21.357
Heptane	2.71	203.25
THF	0.03	2.72

Polymerization conditions: EPDM, 4–5 g, [St], 1.24 mol/L (10 ml); BPO, 1.507×10^{-3} to 2.039×10^{-3} mol/L; polymerization temperature, 60°C.

Effect of temperatures on the synthesis of graft copolymer of EPDM and St in toluene solvent

The effect of temperature was investigated by using BPO concentrations of 1.507×10^{-3} and 2.039×10^{-3} mol/L at 1 h for polymerization of EPDM and St. The polymerizations were performed in toluene and using ~ 5 g of EPDM and 1.24 mol/L concentration

TABLE II
Yield of Graft Copolymer of Each Solvent at 90°C

Solvent	Yield (%) (hexane)	Activity (g of polymer/(mol of BPO) h)
Heptane	25.57	1915.76
Toluene	29.30	2192.96

Polymerization conditions: EPDM, 4–5 g, [St], 1.24 mol/L (10 ml); BPO, 1.507×10^{-3} to 2.039×10^{-3} mol/L; polymerization temperature, 90°C.

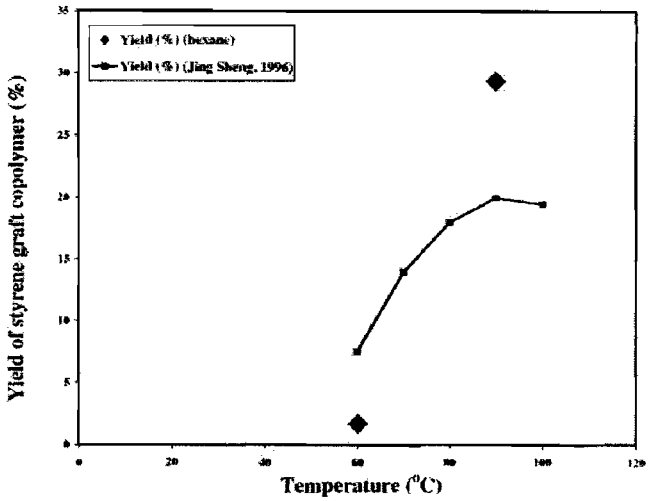

Figure 3 Yield of graft copolymer at different temperatures. Polymerization conditions: EPDM, 4–5 g; [St], 1.24 mol/L (10 mL), BPO, 1.507×10^{-3} to 2.039×10^{-3} mol/L; solvent, toluene.

of St. The influence of temperature on synthesis of graft copolymer is shown in Figure 3.

As shown in Figure 3, yield of graft copolymer increased with increasing temperature, yielding a maximum value at 90°C and then decreased at the same time, presumably because of the reduction of the half-life of BPO with rising temperature,[10] which would increase the number of BPO radicals. When the temperature of the reaction was more than 90°C, the extent of grafting decreased because the number of radicals was decreased while increasing velocity of decomposition of BPO.[5] Thus, most of the reactions are commenced at 90°C.

Effect of aging time on synthesis of graft copolymer of EPDM and St

The effect of aging time was investigated by using BPO as the initiator. The time for polymerization of EPDM and St was set at 2 h. The copolymerization was performed in toluene at 90°C using ~ 5 g of EPDM, BPO concentration about 1.50×10^{-3} to 2.08×10^{-3} mol/L,

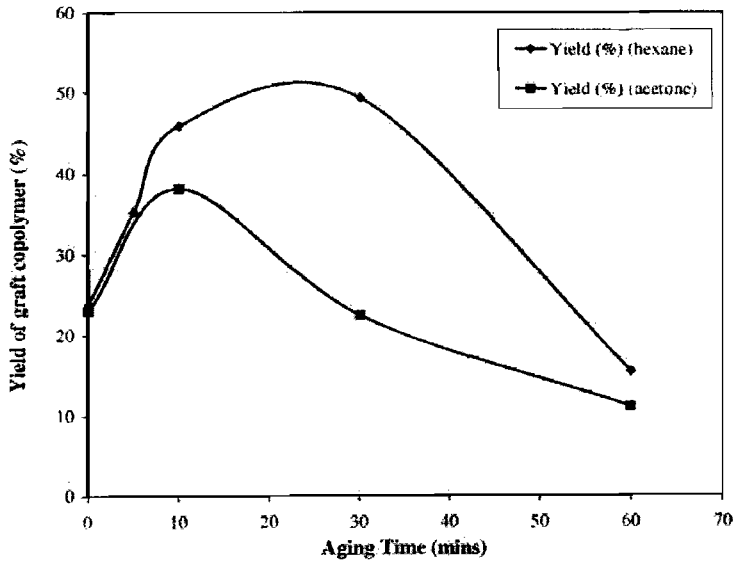

Figure 4 Yield of graft copolymer at different aging times. Polymerization conditions: EPDM, 3–5 g; BPO, 1.5×10^{-3} to 2.08×10^{-3} mol/L; solvent, toluene; polymerization temperature, 90°C; polymerization time, 2 h.

with total St concentration of 2.49 mol/L. The influence of aging time on synthesis of graft copolymer is shown in Figure 4.

As shown in Figure 4, yield of graft copolymer increased with increasing aging time, yielding a maximum value at 10 min (acetone) and 30 min (hexane). After 10 min, the portion that can be dissolved in acetone is increased, which indicates that more polystyrene is formed and can be detected by the portion that dissolved in acetone. However, the aging time is important for the reaction because the initial reaction solutions were very viscous and the reaction of the free radical is impeded by the viscosity of the solution. However, the BPO free radical can be decomposed by as many processes[7] and too long aging may cause adverse effects on the reactions, which can be clearly seen in Figure 4.

CONCLUSIONS

This research revealed the importance of aging time besides all the process parameters. The increase of the aging time to an appropriate amount will increase the yield of EPDM-g-PS to a larger extent. However, too much aging time will cause adverse effect on the polymerization reaction. All the process parameters were elucidated, which also comply with the results of Sheng.[5] Effect of solvents at different temperatures were stated, and in this reaction, toluene is the best solvent.

References

1. Meredith, C. L.; Von Bodungen, G. A. U.S. Pat. 3,657,395 (1972).
2. Shimokawa, S.; Yamamoto, Y. U.S. Pat. 4,314,041 (1982).
3. Crevecoeur, J. J.; Nelissen, L.; van der Sanden, M. C. M.; Leinstra, P. J. Polymer 1995, 36, 753.
4. Qu, X.; Shang, S.; Lin, C.; Zhang, L. J Appl Polym Sci 2002, 86, 428.
5. Sheng, J.; Hu, J. J Appl Polym Sci 1996, 60, 1499.
6. Sheng, J.; Hu, J.; Yuan, X.-B.; Han, Y.-P.; Li, F.-K.; Bian, D.-C. J Appl Polym Sci 1998, 70, 805.
7. Wonglert, C. M.S. Thesis, Chulalongkorn University, Thailand, 2003.
8. Chung, T. C.; Janvikul, W.; Bernard, R.; Jaing, G. J. Macromolecules 1994, 27, 26.
9. Matyjazewski, K.; Thomas, D. P. Handbook of Radical Polymerization; Wiley: New York, 1998.
10. Stevens, M. P. Polymer Chemistry: An Introduction, 3rd ed.; Oxford University Press: New York, 1999.

New Synthesis Methods for Polypropylene-*co*-Ethylene-Propylene Rubber

Satit Thanyaprueksanon, Supakanok Thongyai, Piyasan Praserthdam

Department of Chemical Engineering, Center of Excellence on Catalysis and Catalytic Reaction Engineering, Faculty of Engineering, Chulalongkorn University, Bangkok 10330 Thailand

Received 8 May 2006; accepted 13 August 2006
DOI 10.1002/app.25392
Published online in Wiley InterScience (www.interscience.wiley.com).

ABSTRACT: In this research, the reinforcement of polypropylene (PP) was studied using a new method that is more practical for synthesizing polypropylene-*block*-poly(ethylene-propylene) copolymer (PP-*co*-EP), which can be used as a rubber toughening agent. This copolymer (PP-*co*-EP) could be synthesized by varying the feed condition and changing the feed gas in the batch reactor system using Ziegler–Natta catalysts system at a copolymerization temperature of 10°C. The ^{13}C-NMR tested by a 21.61-ppm resonance peak indicated the incorporation of ethylene to propylene chains that could build up the microstructure of the block copolymer chain. Differential scanning calorimetry (DSC), scanning electron microscopy (SEM), and dynamic mechanical analysis (DMA) results also confirmed these conclusions. Under these conditions, the morphology of copolymer trapped i PP matrix could be observed and the copolymer T_g woul decrease when the amount of PP-*co*-EP was increased. DM study also showed that PP-*co*-EP is good for the polypropy ene reinforcement at low temperature. Moreover, the PP-*c* EP content has an effect on the crystallinity and morpholog of polymer blend, i.e., the crystallinity of polymer decrease when the PP-*co*-EP content increased, but tougher mechan cal properties at low temperature were observed. © 200 Wiley Periodicals, Inc. J Appl Polym Sci 103: 3609–3616, 2007

Key words: polypropylene-*co*-poly(ethylene-propylene copolymer; synthesis; rubber toughening; Ziegler–Natt polypropylene

INTRODUCTION

Isotactic polypropylene (iPP) is a typical semi-crystalline polymer that has been used to produce various products. However, it has a mechanical properties limit. It is well known that iPP has poor mechanical properties in the low-temperature range (0°C in the normal refrigerator) under its glass transition temperature (T_g). The general method to improve the mechanical properties of iPP is to blend iPP with a rubbery material such as poly(ethylene-propylene), copolymer (EPR), ethylene-propylene-diene terpolymer (EPDM), or any other copolymer.[1–3] The iPP/EPR blends, called toughened polypropylene, have been widely used in consumer products and automotive industry. However, the strong incompatibility of EPR and iPP has presented a considerable problem in the modification of mechanical properties of iPP/EPR blending systems/methods.[4]

Copolymers are interesting alternatives as important materials to improve mechanical properties of iPP. The propylene-*co*-poly(ethylene-propylene) copolymer is one of the polymers that can be used for the rubber toughening of PP. Examples of the syntheses and characterization of PP-*co*-EP have bee reported.[5–11]

Coates and colleagues[5] reported the synthesis of syndiotactic polypropylene-*block*-poly(ethylene-pro pylene) with a metallocene catalyst system. Fukui an Murata[6] also reported the synthesis of polypropylene *block*-poly(ethylene-*co*-propylene), using metallocen catalyst systems. However, these catalysts are n only expensive but are also rapidly deactivated b moisture and oxygen. Until now, the metallocen catalysts have remained difficult to operate and us practically.

Nitta et al.[7] reported that the PP/EPR blends an polypropylene-*block*-poly(ethylene-*co*-propylene) ca be synthesized by a short-period polymerizatio method. Mori et al.[8] reported the synthesis of a poly propylene-*block*-poly(ethylene-propylene) by high pressure-type and stopped-flow polymerization meth ods using the Ziegler–Natta catalyst.

However, the short-period polymerization an stopped-flow polymerization methods are not practi cal and are too complicated in polymer synthesis fields as they must be controlled by a computer to generat sudden changes in gas feed conditions in 0.2 s.

Fan et al.[9] reported that fraction of structure an properties of iPP/EPR in situ blend was synthesize by spherical Ziegler–Natta catalyst in two stages: th liquid phase propylene homopolymerization, and the the gas phase ethylene-propylene copolymerization.

Correspondence to: S. Thongyai (tsupakan@chula.ac.th).

However, all the above-mentioned methods are not practical to use in the industrial applications. To overcome the problem, this work presents a new and simple method for the synthesis of polypropylene-*co*-poly (ethylene-propylene) (PP-*co*-EP) copolymer, using the Ziegler–Natta catalyst for industrial production. The nuclear magnetic resonance (NMR) results confirmed the corporation of ethylene (E) in the molecule of propylene (P). The results of differential scanning calorimetry (DSC) and dynamic mechanical analysis (DMA) show that less pure P and pure E are produced in the PP-*co*-EP polymers. The copolymer obtained can be used for the rubber toughening of polypropylene. The DMA results show the advantage in the low temperature range below T_g of the pure PP in the blending of PP with PP-*co*-EP polymers.

EXPERIMENTAL

Materials

Ethylene and propylene (polymerization grade) and triethylaluminum ($AlEt_3$; TEA) were obtained from Bangkok Polyethylene Company (Bangkok, Thailand). $TiCl_4$ was purchased from Merck. Anhydrous $MgCl_2$ was supplied by Sigma-Aldrich; phthalic anhydride, diethylphthalate (DEP, used as an internal donor) and *n*-decane were purchased from Fluka Chemie A.G. (St. Gallen, Switzerland). Hexane was donated by Exxon Chemical Thailand (Bangkok, Thailand).

The solvents were distilled over sodium/benzophenone under argon atmosphere before use. Ultra-high-purity (UHP) argon (99.999%) was obtained from Thai Industrial Gas Company (Bangkok, Thailand) and was further purified by molecular sieves –3 Å, BASF catalyst R3-11G, NaOH, and phosphorus pentoxide (P_2O_5), to remove traces of oxygen and moisture. Commercial-grade polypropylene was donated by the Thai Polyplastic Industry Public Company (Bangkok, Thailand).

All chemicals were manipulated under purified argon. All operations were carried out under an inert atmosphere of argon, using a vacuum atmosphere glove box and/or standard Schlenk techniques.

Preparation of catalyst

Anhydrous magnesium chloride ($MgCl_2$), *n*-decane, and 2-ethyl-1-hexanol were put into a Schlenk tube and heated to 130°C for 2 h under magnetic stirring and argon atmosphere. Then phthalic anhydride was introduced into the solution and stirred until $MgCl_2$ was completely dissolved. The resulting uniform solution was cooled to room temperature, and wholly dropped wise of titanium tetrachloride ($TiCl_4$), kept stirring at –20°C. The temperature was then raised to 110°C, and diethylphthalate was injected in. The mixture was maintained at this temperature for 2 h. After the 2-h reaction, the solid portion was collected from the reaction mixture and again suspended in 20 mL of titanium tetrachloride and reacted at 120°C for another 2 h. It was then collected and later washed with *n*-decane and *n*-hexane for 2 and 3 times, respectively. The resulting solid was next vacuum dry to form a powder in gray color which must to be stored under argon atmosphere.

Synthesis of polypropylene-*co*-poly (ethylene-propylene) copolymer

Polymerization was carried out in a 100-mL stainless steel autoclave reactor with magnetic stirrer in hexane, using a $MgCl_2$/DEP/$TiCl_4$–TEA catalytic system. The polymer was synthesized in a two-stage reaction process. First, the solvent, co-catalyst, and catalyst

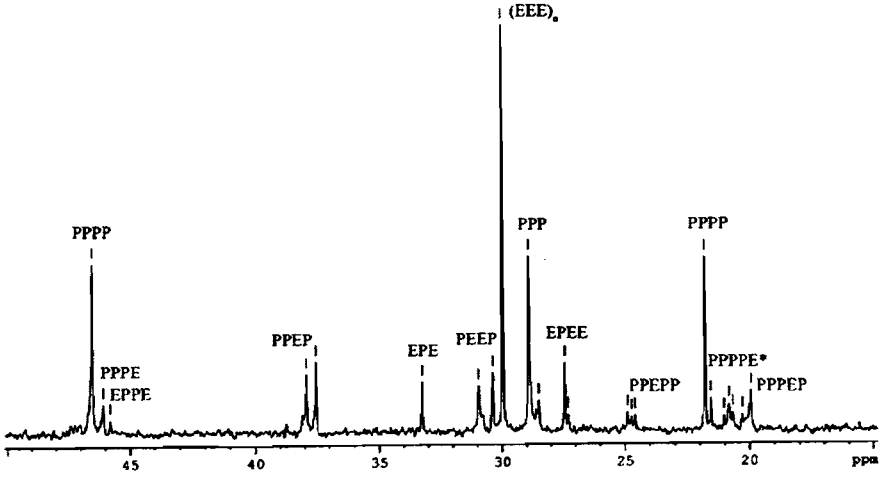

Figure 1 ^{13}C-NMR spectrum of PP-*co*-EP copolymer (polymer 5).

TABLE I
Characterization of Polymers by DSC

Polymer[a]	Temp (°C)	P_E (psi)	Mn	MWD	Heat 1[b]			Heat 2[b]			
					T_g	T_{m1}	T_{m2}	T_g	T_{m1}	T_{m2}	T_c
Polymer 1	60	50	—	—	−21.34	nd	nd	−22.51	113.80	147.10	92.04
Polymer 2	40	50	—	—	−17.41	123.67	152.35	−17.64	124.97	150.45	99.34
Polymer 3	10	50	—	—	−15.88	117.84	147.19	−14.72	118.67	145.70	91.47
Polymer 4	10	60	—	—	−16.96	124.99	148.67	−16.25	116.11	146.82	94.83
Polymer 5	10	70	141,528	12.24	−21.72	126.10	145.34	−22.41	117.22	143.13	95.93
Polymer 6	10	—	65,658	9.08	−9.86	nd	151.27	−10.85	nd	149.40	102.25

nd, not detected.
[a] Synthesis by $TiCl_4/MgCl_2$/DEP-TEA, Al/Ti = 167; propylene pressure feeding constant = 30 psi.
[b] Ramp rate = 40°C/min both heating and cooling; heating 1 – cooling – heating 2 from −60° to 200°C.

were added into the reactor, and subsequently placed in some liquid nitrogen to control the reaction between the catalyst and co-catalyst. After that, the reactor was evacuated to remove both the argon and the liquid nitrogen, and then heated up to polymerization temperature. The first stage of polymerization is the propylene homopolymerization, to feed only propylene gas into the reactor for 10 min. The reactor was then heated under the controlled temperature to start the polymerization reaction. The second stage is to copolymerize the ethylene into the PP structure by successively feeding the pure ethylene gas into a stirred reactor for a duration of 30 min. The mixture was then quenched in the HCl/methanol solution after the completion of the reaction. The polymer obtained that precipitates out is to be washed thoroughly in methanol and finally dried at room temperature.

Blending and molding of polymer

Polypropylene (PP) and the PP-co-EP were combined by the melt-mixing method on a digital hot plate at 220°C with 5%, 10%, 15%, and 20% of PP-co-EP. The polymer blend was then was molded with LAB TECH Automatic Hydraulic Hotpress LP-50 M/C 9701 in an aluminum mold at 200°C 1500 psi. Then, the polymer blend was cooled down at room temperature. The sample size for tensile testing is 30 × 100 × 0.5 mm and 10 × 40 × 0.5 for DMA.

Characterization

DSC analyses of polymers were carried out using Perkin-Elmer Diamond DSC, calibrated for temperature and melting enthalpy, with indium as the standard. Each sample, ~ 10 mg in weight, was sealed in an aluminum pan for further measurement before being heated from −60 to 200°C at a scanning rate of 40°C/min under N_2 atmosphere.

^{13}C-NMR spectra of the polymers were measured on an Avance DPX400 NMR spectrometer at 120°C, while *o*-dichlorobenzene and benzene-d_6 were used as solvents to prepare the polymer solution.

The morphologies of all polymer fracture surfaces were investigated with a JSM-5410LV scanning electron microscope (SEM). The samples for SEM analysis

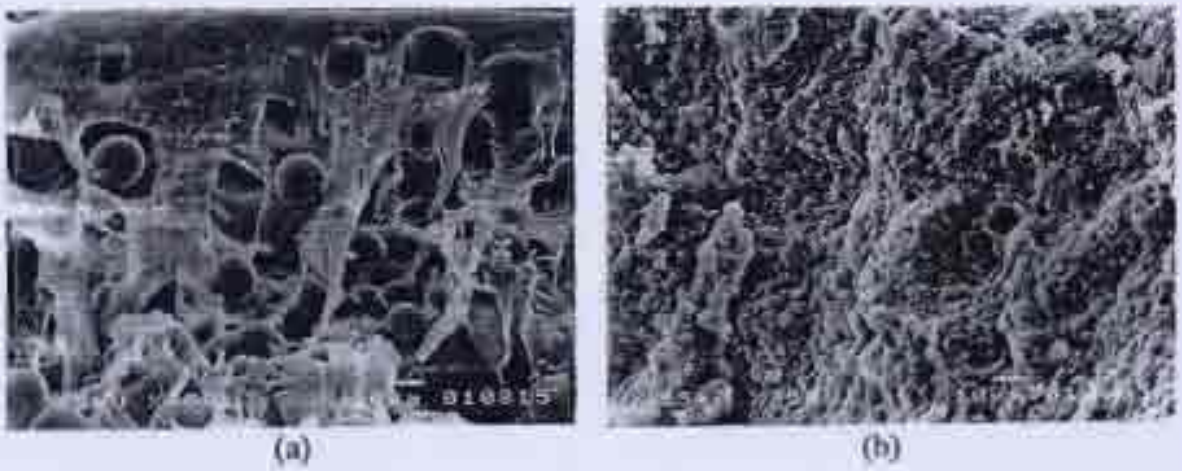

(a) (b)

Figure 2 SEMs of cryogenic polymer fracture surface. (a) Polymer fracture of PP-block-EP copolymer 5; (b) polymer fracture of PP (polymer 6). ×750.

TABLE II
Characteristics of Polymer Blend and Polypropylene

			Heat 1[b]			Heat 2[b]			Cool[b]	
Polymer[a]	Mn	MWD	T_g	T_m	ΔH	T_g	T_m	ΔH	T_c	ΔH
EP00	35,283	10.47	−0.22	165.96	97.18	−1.45	165.96	96.59	106.92	96.54
EP05	—	—	−7.48	167.07	95.76	−8.42	165.21	94.03	109.08	95.61
EP10	56,474	4.09	−10.54	167.82	91.91	−11.13	167.79	91.68	108.70	91.64
EP15	—	—	−13.98	166.31	89.13	−14.82	165.21	88.69	109.75	88.88
EP20	70,676	4.96	−16.14	164.18	83.53	−16.34	162.13	83.33	110.17	83.38

[a] EP00, EP05, EP10, EP15, and EP20, referring to PP, were added PP-*b*-EP 0%, 5%, 10%, 15%, and 20%, respectively.
[b] Ramp rate = 40°C/min both heating and cooling; heating 1 – cooling – heating 2 from −60° to 200°C, ΔH = kJ/g.

were coated with gold particles by ion sputtering device to provide electrical contact for the specimens.

Dynamic mechanical properties of blending polymers were characterized, using Perkin-Elmer DMA-Pyris Diamond. The entire experiment was operated at 1 Hz in tension mode over a temperature range of −140°C to 150°C with 1.5°C/min; sample sizes were 10 × 50 × 0.5 mm, using liquid nitrogen as the cryogenic medium.

The molecular weight and molecular weight distribution were finally determined using gel permeation chromatography (GPC, Waters 2000) with Styragel HT6E column at 135°C with 1,2,4-trichlorobenzene as the solvent.

RESULTS AND DISCUSSION

Synthesis of copolymer

Figure 1 shows a typical ^{13}C-NMR spectrum of the synthesized PP-*co*-EP (polymer 5). The chemical shift assignments for ^{13}C resonances are similar to those reported by Fukui et al.[6] The mole fractions of propylene/ethylene unit (P/E unit) in the block copolymer were determined as 37/63 mole% from the peak areas of methylene and methyl carbons.[12–15] From the ^{13}C-NMR spectrum, the peak at 21.61 ppm showed the characteristic of propylene (P) that has the ethylene (E) laid in the adjacent of PPPPE, indicating the cooperation of E in the P chain. Because only the pure propylene was allowed in the reactor at the beginning, the first polymerization product in the reactor was the propylene pure chains only (for a duration of 10 min) The second step of polymerization allowed E to react in the reactor for a duration of 30 min, so that the discovered E incorporated in the P chain would support the formation of the block copolymer of PP and EP in the second stage. This shows that at least some of the PP chain will survive through the second stage of the reaction, with E incorporation as the consequence. Unfortunately, because of the batch reactions, the variation in the partial pressure of propylene and ethylene changed with time during the synthesis prevailed against the exact quantitative calculations of the cooperation of E in the P chain.

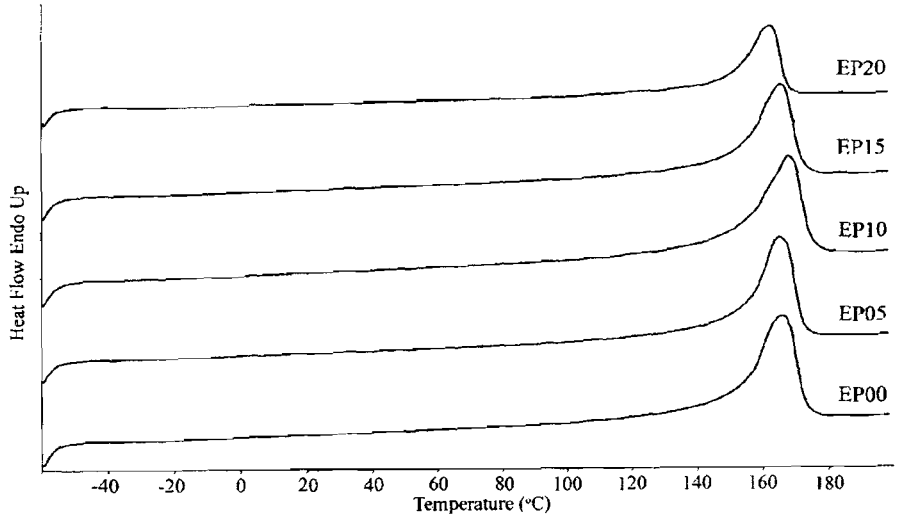

Figure 3 DSC curves of EP00, EP05, EP10, EP15, and EP20.

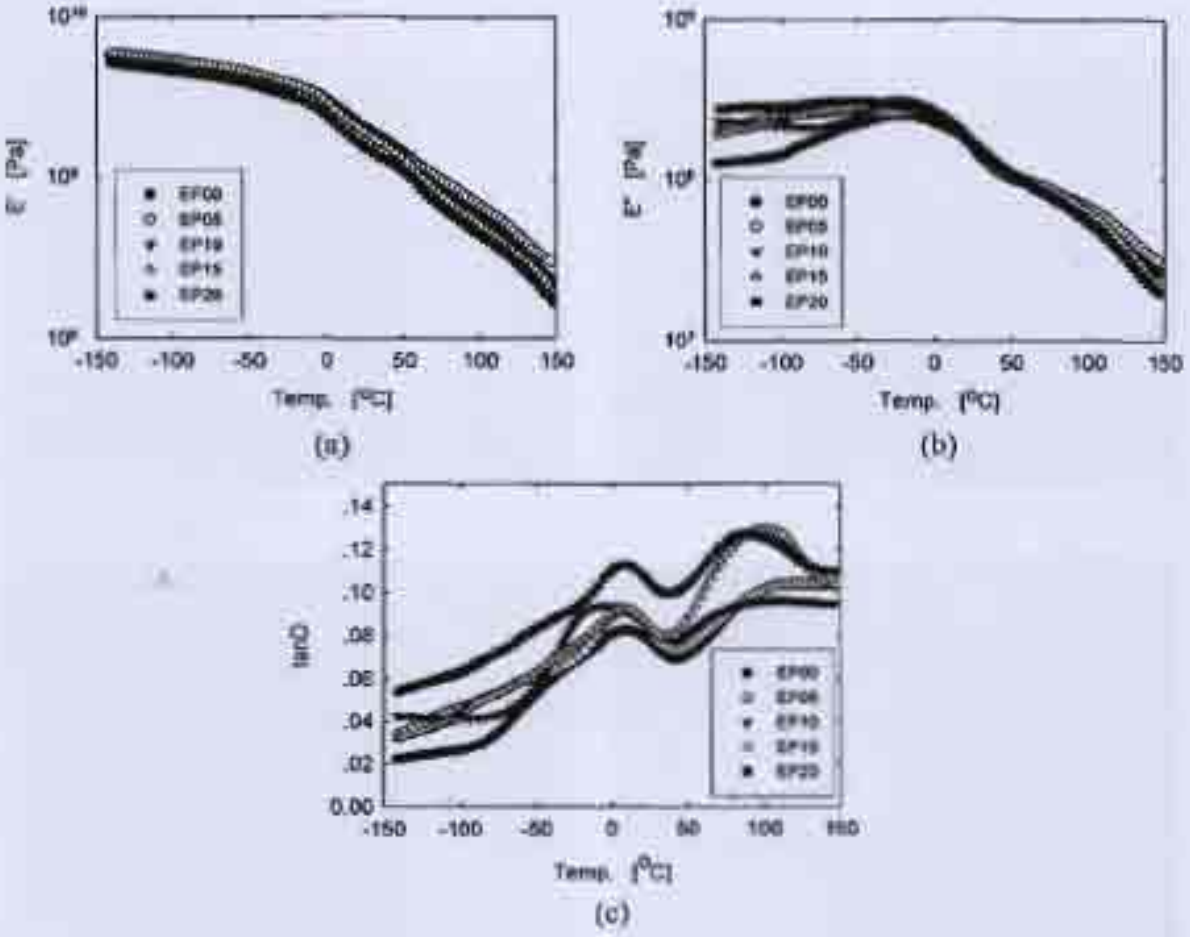

Figure 4 Temperature dependence of dynamic mechanical properties at 1 Hz. (a) Storage modulus; (b) loss modulus; (c) tanδ.

Table I shows the effects of polymerization temperature and pressure of corporate ethylene gas when added into the reactor at the glass transition temperature (T_g), melting temperature (T_m), and temperature of crystallization of PP-co-EP products from DSC results. In addition to the NMR result, the DSC graphs of T_g of copolymer show that there are two phases in the PP-b-EP block copolymer, as the DSC results clearly show two T_ms in the synthesized polymers. In the first phase, PP is dominant and the other phase appears to have the E contribution.

From Table I we can conclude that a higher polymerization temperature gives the lower T_g of the products. This might be because there is more incorporation of E in the P chain at the higher polymerization rate. Usually, the lower T_g in the block copolymer will result from the incorporation of the low T_g component (E) in the higher T_g matrix (P). The lower T_g also confirms the NMR results that E has cooperation in the PP chain without serious segregation of pure PP because no clear pure component T_g of PP (−10–0°C) was detected. Moreover, synthesized polymers have the dispersed phase of the ethylene-propylene rubber even at the rector temperature of 60°C. Usually at higher temperature, polymerization will give results in the higher chain transfer rate (polymer 1, polymer 2, and polymer 3), which shorten the progressive chains of PP; it is most likely that the E cannot totally incorporate on the PP chain.

As a consequence, the higher feeding ethylene pressure gives the lower T_g temperature (polymer 3, polymer 4, and polymer 5) at the same reaction temperatures. These may result from the higher incorporation of E, because the concentration of E is increased along with the pressure of the system. The higher concentration of E presented in the reactions shows the higher incorporation of E onto the PP chain and the samples. Unfortunately, with the limit of the DSC scanning temperature (from −60°C to 200°C), the T_g of the pure E at −100°C was not confirmed. However, the lower

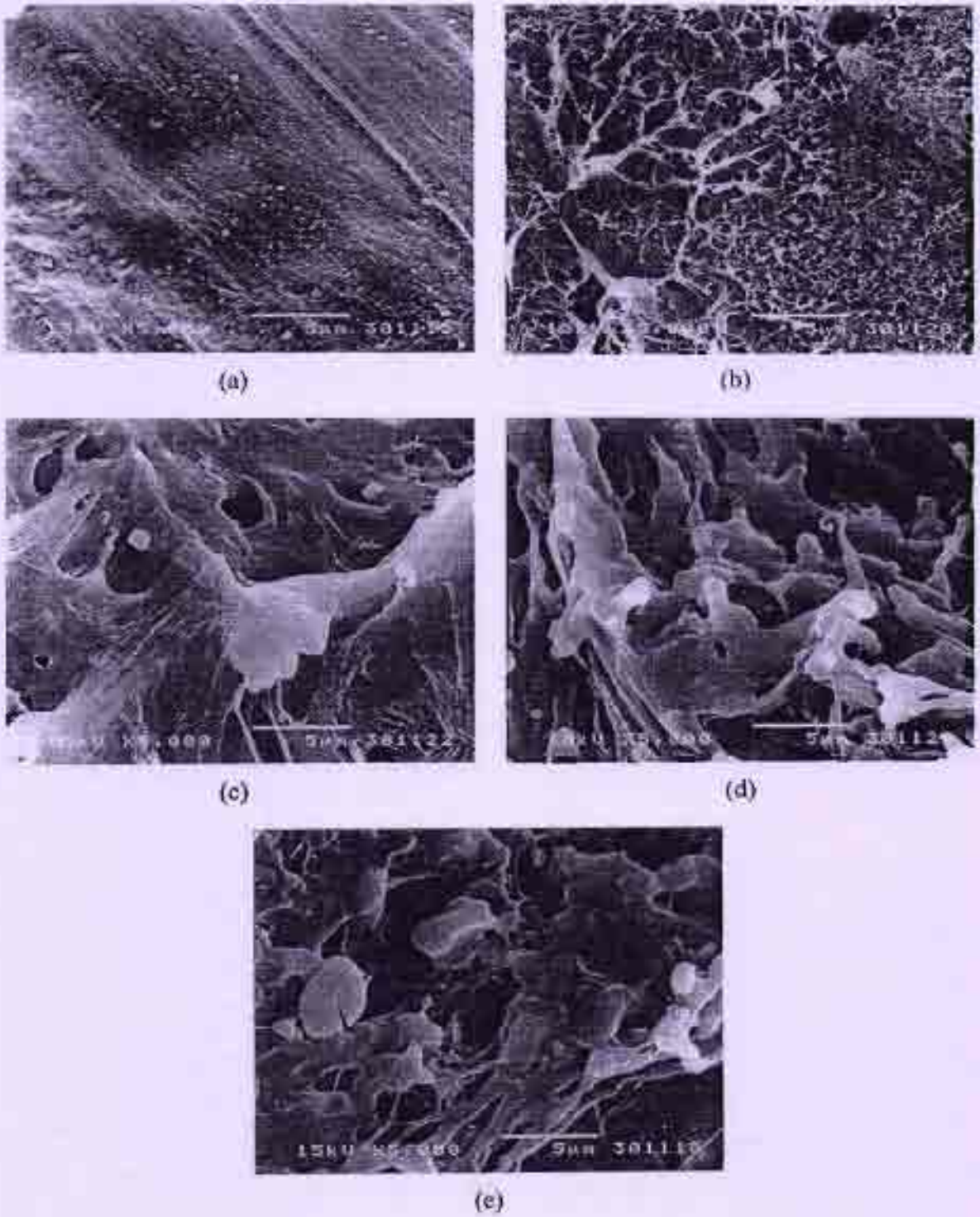

Figure 5 SEMs of room temperature specimen fracture. (a) EP00; (b) EP05; (c) EP10; (d) EP15; (e) EP20. ×5000.

T_g of PP according to the incorporation of E in these systems also supports the incorporation of E onto PP chains without substantial termination of the active site of PP.

In polymer 6, only the P was allowed in the reactor, and the polymer formed is the PP only. Because the time for PP to react is the same as other samples before the supply of E to the reactor, the polymer formed will represent the PP chains before the cooperation of E. The clear T_g of PP was observed at -9°C, which was clearly higher than the T_g of the corporate polymer with E. The molecular weight of PP6 and the T_m confirm the high quality of PP produced. If we further corporate E onto this PP, the polymer formed will have substantial characteristics of PP. Moreover, the higher T_m of pure PP in polymer 6 than in the other cooperation of E samples shows that the crystals of pure PP were affected by the cooperation of E, and no clear separated peak T_m for pure PP was observed again after cooperation with E.

According to the DSC results, the appearance of the rubbery phase of the block copolymer can be seen in SEMs of polymer fracture [Fig. 2(a)]) The minor phase of EP can be seen as the phase separated droplets in the fracture surface picture. In the pure PP micrographs [polymer 6, Fig. 2(b)], the droplet characteristics cannot be observed. These appearances support the DSC results that represent the two phase characteristics.

Polymer blend

The influence of PP-*b*-EP incorporated in commercial-grade polypropylene on T_g, T_m, and T_c of polymer blend is shown in Table II. The suffix number at the name of the blend stands for the weight percentage of the PP-*co*-EP added to the blend. As can be seen, T_g value decreases with an increase of the PP-*b*-EP content (from 0% to 20%), while T_m and T_c values are not clearly affected. Generally, T_g represents an amorphous part of polymer. The T_g value of pure polypropylene is approximately 0°C (EP00) and the T_g of the blend with PP-*co*-EP decreases with the increase of the PP-*b*-EP copolymer content.[7] The T_g of polymer blend ranges from that of PP and synthesized PP-*b*-EP. The T_m and T_c results suggest that EP molecule does not substantially affect the crystallinity of polypropylene.[16] Moreover, ΔH indicated the crystallinity of polypropylene. It was found that ΔH decreased with an increase of PP-*b*-EP content. Thus, the addition of PP-*b*-EP can reduce the crystallinity of polypropylene.[17] Our results confirm the previous work on the blend of PP and EP;[7,16,17] thus, our PP-*co*-EP can affect the properties of the PP like other references but is better in that it has an easier preparation. Figure 3 shows heat 2 DSC curve of PP (EP00) and polymer blend in which the T_m of the polymer blend was similar to PP.

Figure 4 shows the effect of PP-*b*-EP on the dynamic mechanical properties of the polymer blend. The result indicates that both PP and polymer blend have similar values of E within the range of -140–150°C [Fig. 4(a)]. As shown in Figure 3(b), the E of polymer blend is higher than PP at a temperature of < 0°C. This means that the polymer blend can dissipate more energy than pure polypropylene (EP00) at low temperature (< 0°C). Figure 4(c) shows the value of tanδ, which is determined by E''/E'. The tanδ of polymer blend is higher than that of the pure polypropylene. It can be said that the toughness of the polymer blend increases within the range of low temperature, while PP-*co*-EP only presents in the polypropylene blend. In addition, the T_β peak, ascribed to glass transition in amorphous part, is present in polymer blend [Fig. 4(c)]. The broader T_β peak resulted from the incorporation of EP molecule in the amorphous PP region.[16] Moreover, the T_g of E at ~ -100°C was not observed. This may suggest that the samples have too small an amount of PE molecules generated in amorphous phases to be detected by DMA.

As shown in Figure 5, SEM confirmed that the polymer blend has greater toughness than PP. From the room temperature fracture surface of polymer blends, these pictures show a rubbery morphology in addition to the PP matrix. The blends have an additional rubbery phase that stretches and binds the PP together. The more PP-*co*-EP added, the more the stretched rubbery phase can be observed. This rubbery phase might be responsible for the low-temperature toughness of the blends.

CONCLUSION

The results presented show that the PP-*co*-EP can be synthesized by a simple method. The ethylene content in the copolymer chain increased while increasing the ethylene fed pressure. The ^{13}C-NMR result indicated incorporation of ethylene in the propylene chain. DSC and SEM showed the rubbery material of the copolymer resulting from lowering the T_g of the blends further than the T_g of pure PP in the copolymers. The convenient condition shown in the present work for the synthesis PP-*co*-EP is 30 psi of propylene feeding and 70 psi of ethylene feeding pressure at a 10°C copolymerization temperature. The results of PP/PP-*b*-EP blends show a relationship among the PP-*b*-EP content with toughness, T_g, and crystallinity. DSC, DMA, and SEM indicated that the PP-*b*-EP included in the amorphous region of PP and the polymer blends have lower T_g and crystallinity, but higher toughness, than commercial-grade PP within the low-temperature range. We can conclude that PP-*b*-EP is a

good rubber toughening agent for polypropylene reinforcement at low temperature that can be simply prepared, using the method described.

The authors thank the Bangkok Polyethylene Co. for supplying the ethylene and propylene gas, as well as the TEA and GPC characterization. We also thank the Thai Polyplastic Industry Public Co., Ltd., for its donation of the commercial-grade polypropylene. Furthermore, great appreciation is due to the MEKTEC Manufacturing Corporation (Thailand) Ltd., for its support of the equipment.

References

1. Yokoyama, Y.; Ricco, T. Polymer 1998, 36, 3675.
2. Michler, G. H. In Polypropylene. An A–Z Reference; Karger-Kocsis, J., Ed.; Kluwer Academic: Dordrecht, the Netherlands, 1999; p 194.
3. Wang, Z. J Appl Polym Sci 1996, 60, 2239.
4. Teh, J. W.; Rudin, A.; Keung, J. C. Polym Technol 1994, 13, 1.
5. Tian, J.; Hustad, P. D.; Coates, G. W. J Am Chem Soc 2001, 123, 5134.
6. Fukui, Y.; Murata, M. Appl Catal A: Gen 2002, 237, 1.
7. Nitta, K.; Kawada, T.; Yamahiro, M.; Mori, H.; Terano, M Polymer 2001, 41, 6765.
8. Mori, H.; Yamahiro, M.; Prokhorov, V. V.; Nitta, K.; Terano, M Macromolecules 1999, 32, 6008.
9. Fan, Z.; Zhang, Y.; Xu, J.; Wang, H.; Feng, L. Polymer 2001, 42 5559.
10. Yamahiro, M.; Mori, H.; Nitta, K.; Terano, M. Polymer 1999 40, 5265.
11. Nitta, K.; Kawada, T.; Prokhorov, V. V.; Yamahiro, M.; Mori H. J Appl Polym Sci 1999, 74, 958.
12. Randall, J. C. Macromolecules 1978, 11, 33.
13. Randall, J. C. Macromol Chem Phys 1982, 29, 20.
14. Carman, C. J.; Harrington, R. A.; Wilkes, C. E. Macromolecules 1977, 10, 536.
15. Wang, W.; Zhu, S. Macromolecules 2000, 33, 1157.
16. Nitta, K.; Shin, Y.; Hashiguchi, H.; Tanimoto, S.; Terano, M Polymer 2005, 46, 965.
17. D'Orazio, L.; Mancarella, C.; Martuscelli, E.; Cecchin, G.; Corrieri, R. Polymer 1999, 40, 2745.
18. Liang, J. Z.; Li, R. K. Y. J Appl Polym Sci 2000, 77, 409.
19. Jang, B. Z.; Uhlmann, D. R.; Vander Sande, J. B. J Appl Polym Sci 1985, 30, 2485.
20. Tam, W. Y.; Cheung, T.; Li, R. K. Y. Polym Test 1996, 15, 363.

Interfacial Adhesion Enhancement of Polyethylene–Polypropylene Mixtures by Adding Synthesized Diisocyanate Compatibilizers

Lerdlaksana Ubonnut, Supakanok Thongyai, Piyasan Praserthdam

Faculty of Engineering, Department of Chemical Engineering, Center of Excellence on Catalysis and Catalytic Reaction Engineering, Chulalongkorn University, Bangkok 10330, Thailand

Received 5 May 2006; accepted 30 November 2006
DOI 10.1002/app.25945
Published online in Wiley InterScience (www.interscience.wiley.com).

ABSTRACT: Immiscible and incompatible binary blends of commercial polypropylene (PP)/polyethylene (PE) display poor mechanical properties. The addition of compatibilizer to reinforce and enhance an adhesion at the interfaces between PE–PP mixtures has been conducted. The compatibilizer chosen was in the group of Ziegler–Natta's PE–PP block copolymer with diisocyanate linkage. The effects of adding the compatibilizers were assessed by morphology studies, thermal analysis, and mechanical testing. DSC curves of crystallization and FTIR provided evidences to support the formation of PP/PE block copolymer. Significant improvements in the mechanical properties of 50/50 PE/PP blends containing compatibilizer have been noted. © 2007 Wiley Periodicals, Inc. J Appl Polym Sci 000: 000–000, 2007

Key words: PE/PP blend; polyethylene-polypropylene block copolymer; compatibilizer

INTRODUCTION

AQ2 Polyethylene (PE) and polypropylene(PP) are among the most common plastic wastes, because they are among the most frequently used commercial plastics in our daily lives as well as in industries.[1] It is impossible and not appropriate to identify and totally separate the waste mixtures of these two polymers. Usually, their waste mixture can recycle as mixed waste plastics in the form of blends. This reuse approach is attractive, because it avoids the difficult task of separation. As a consequence, academic and industrial interest in virgin and recycled polymer blends is rapidly expanding.

Unfortunately, the incompatibility between PE and PP has already been reported by various authors.[2] The strong phase separation leading to a coarse-phase structure and the low interfacial adhesion between the phases is responsible for a decrease in mechanical properties especially related to its morphology, including impact strength, strain at break, and ductile to brittle transition. According to Shanks,[3] the immiscibility between the phases makes the rule of mixtures ineffective in predicting some properties of interest.

To overcome this difficulty, the usages of various coupling agents have been reported. Incorporating a compatibilizer into a multiphase system generally leads to a fine phase structure and results in the enhanced interfacial adhesion. Among others,[4–6] Yang[7] showed that the addition of a commercial ethylene/propylene block copolymer improved the ductility of LDPE/PP blends, particularly for PP-rich blends. Bertin and Robin[8] studied and characterized virgin and recycled LDPE/PP blends and the usage of compatibilizing agents, such as ethylene–propylene–diene monomer (EPDM) copolymer or PE-*g* (2-methyl-1,3-butadiene) graft copolymer, to enhance their impact strength and elongation at break. Claudia and Agnes showed the partial compatibility of the PP/HDPE reflected in the improvement of tensile strength and elongation by the addition of extracted recycled PP.[9] Although this may solve the compatibility problem, the use of compatibilizers adds cost to the recycled product, usually resulting in loss of interest from the recycling sector.

In this work, we try to synthesize the cost-effective compatibilizer in simple system that can improve the mechanical properties of PE/PP mixtures. Thus, we applied the rapid reaction between a polyfunctional isocyanate and a hydroxyl-terminated oligomer leads to urethane linkage. Consequently, the addition of Ziegler–Natta PE/PP-block copolymer synthesized by diisocyanate has the ability to reinforce the PE–PP mixtures as it is expected. Thermodynamically, the PP-*b*-PE will sit at the interface between the two components. In this work, the morphology, thermal

Correspondence to: S. Thongyai (supakanok.t@chula.ac.th).

Contract grant sponsor: Graduate school of Chulalongkorn University.

properties, and tensile properties of PP/PE blends were evaluated.

EXPERIMENTAL

Chemicals

Commercially graded PP and PE were donated from Thai Polyplastic Industry. Polymerization-grade propylene and ethylene were donated from National Petrochemical, Thailand. The $AlEt_3$ (TEA) and MDI were donated from Bangkok Polyethylene, Thailand. The $TiCl_4$ were purchased from Merck. Anhydrous $MgCl_2$ was supplied from Sigma-Aldrich, phthalic anhydride, diethylphthalate (DEP, used as an internal donor), and *n*-decane were purchased from Fluka Chemie A.G., Switzerland. Hexane was donated from Exxon Chemical, Thailand. It was purified by refluxing over sodium/benzophenone under argon atmosphere prior to use. Ultra high purity (UHP) argon (99.999%) and oxygen (UHP) was obtained from Thai Industrial Gas and was further purified by passing through molecular sieves 3Å, BASF catalyst R3-11G, NaOH, and phosphorus pentoxide (P_2O_5) to remove traces of oxygen and moisture.

All operations were carried out under an inert atmosphere of argon using a vacuum atmosphere glove box and/or standard Schlenk techniques.

Catalyst preparation

A catalyst of type $TiCl_4$/DEP/$MgCl_2$ was synthesized in the following manner. About 0.476 g of anhydrous $MgCl_2$ was added to 2.5 mL of *n*-decane. This suspension was treated with 2.34 mL of 2-ethylhexanol and 0.1089 g of phathalic anhydride at 130°C. It was stirred until the $MgCl_2$ was dissolved. $TiCl_4$ (20 mL) was added dropwise at −20°C, with subsequent treatment of the solution in the presence of 0.26 mL of DEP at 110°C for 2 h. The resulting solid product was separated by filtration and the addition of 20 mL of $TiCl_4$ was repeated at room temperature. After keeping the solution at 120°C for 2 h, this slurry was siphoned-off and washed twice with 10 mL of *n*-decane and thrice with 10 mL of hexane, respectively. The catalyst was dried under vacuum for 30 min at 40°C and contained 3% Ti.

Polymerization reaction

PE and PP terminal hydroxyl group

The propylene polymerization and ethylene polymerization reactions were carried out in a 100-mL semi-batch stainless steel reactor equipped with magnetic stirrer. About 26.55-mL hexane, 0.01 g catalyst (Al/Ti molar ratio = 167), and 3.45-mL TEA were introduced into the reactor and stirred for 5 min at room temperature in the atmospheric glove boxes. Followed by that, the reactor was put in liquid nitrogen immediately to stop the reaction between the catalyst and cocatalyst. After the solution was frozen for 15 min, the reactor was evacuated for 3 min to remove argon. The reactions were conducted at 60°C and the polymerization was started by continuous feeding of ethylene (propylene) at constant pressure of 50 psi for 1 h. Then the polymerization was stopped by directly bringing into contact with oxygen gas at room temperature followed by precipitation in hydrochloric acid solution in methanol and dried at room temperature.

PE block PP copolymerization

Copolymerization was carried out in a glass reactor equipped with magnetic stirrer. PE and PP-containing hydroxyl group 50/50 wt % were added and dissolved in *o*-dichlorobenzene at 120°C. Followed by that excess MDI was dropped in the solution that remained stir for 1 h. The solution was washed with excess methanol and polymer was filtered and dried.

Blend and molding preparation

The melt mixing method was performed in digital hot plate stirrer at 220°C, further kept for 5 min at 300°C, and annealed at 200°C for 20 min before the experiments[20] to allow the equilibrium and ensure the migration of the PE-*b*-PP to the interfaces. All blends were prepared with 50 wt % of commercial grade PE and 50 wt % of commercial grade PP (PE/PP), because PE/PP will become the easiest phase-separated and large amount of interfaces obtained. When the block copolymer was used, 3 wt % of the block copolymer was added base on the total weight of the 50/50 blend. And then, the block copolymer was added in PE/PP blend for 3, 6, 12, and 20 wt %. All polymer blends were molded with the LAB TECH hydraulic hot press LP-50M/C 9701.

Measurements and characterization of block copolymers and blends

Infrared survey spectra were recorded with FTIR (IFS28). The scanning ranged from 400 to 4000 cm^{-1} on the pallet sample of KBr powder (to hold the powder samples as a blank) with scanning 32 times.

The molecular weight and its distribution were determined by using GPC Model: Waters 2000 Column: Styragel HT6E with 1,2,4-trichlorobenzene as a solvent at 135°C.

The melting temperatures of the block copolymer-added polymer blends were determined with a PerkinElmer DSC-Pyris Diamond over the range −60 to

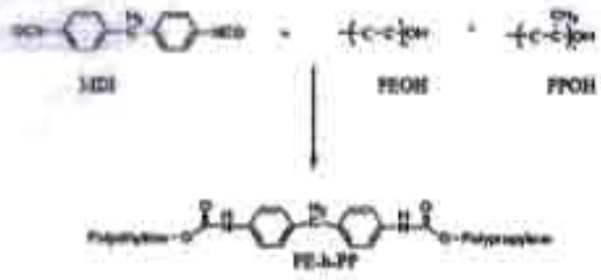

Scheme 1

200°C of scanning rate 40°C/min under nitrogen atmosphere.

Tensile properties were characterized using an Instron universal testing machine with a test speed of 12.5 mm/min. The tests were conducted according to ASTM D 882-02.

The morphologies of all block copolymers were investigated by JSM-5410LV Scanning Microscope. The samples for SEM analysis were coated with gold particles by ion-sputtering device to provide electrical contact to the specimens.

RESULTS AND DISCUSSION

Chain structure of PE/PP block copolymer diisocyanate linkage

On the basis of this result, a plausible products of the block copolymerization are proposed as shown in Scheme 1. S1

In addition, besides PE-*b*-PP, there have others two byproducts of the reaction, which are PE-*b*-PE and PP-*b*-PP. Moreover, there are other two products (urea end chain with hydrogen (not hydroxyl and OH) are PE, PP, and the small amount of remaining reactant, that is, PEOH and PPOH. The fractions of these byproducts are hardly to be quantified and it cannot be completely fractionated by solvent extraction. Thus, unidentified fraction distribution of the block copolymers will be along with what is identified as PE-*b*-PP throughout this study. However, the mixture identify as PE-*b*-PP had good phase binding with the melted blend of PP/PE that can be seen in SEM photo (Figs. 3 and 4). Consequently, the mixture of PE-*b*-PP copolymer in this study (PE-*b*-PP, and various sizes of PP and PE) comprised the phases that will dissolve in the melted blend of PP/PE without any difficulty. F3 F4 AQ3

Characterization of PE-*b*-PP and their blends

From GPC results, the PE-*b*-PP has a wide molecular weight distribution resulted from the reaction of wide MWD of PPOH and PEOH with diisocyanate. To confirm the reaction that contribute to the block copolymer of PE-*b*-PP in this system, the IR spectrum of block copolymer obtained at 25°C is illustrated in Figure 1. The peak of isocyanate (NCO) transmittance is 1530 cm^{-1}, $\nu_{C=O}$ MDI = 1711 cm^{-1}, ν_{NH} = 3404, 1599, and 814 cm^{-1}. Thus, IR spectrum has identified the diisocyanate linkage in PE-*b*-PP copolymer structure. Moreover, the binding properties of PE-*b*-PP can be confirmed in SEM photo (Figs. 3 and 4) to ensure the abilities of our compatibilizer. F1

As shown in Table I, the effects of adding isocyanate compatibilizer can be clearly assured by their blends' properties. The PEOH has larger molecular weight compared to PPOH. Consequently, the molecular weights of PE-*b*-PP are higher than PPOH and change according to the isocyanate reaction. The *MI* T1

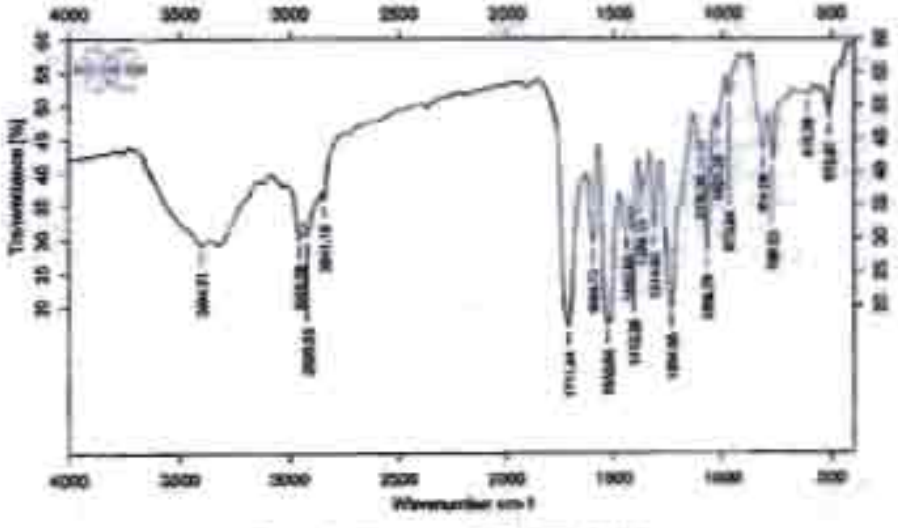

Figure 1 IR spectra of PE-*b*-PP at 25°C.

TABLE I
Characterization of Polymer

Polymer	Mw[a] ($\times 10^{-4}$)	MWD[a]	Heating 1 (°C)[b]				Cooling (°C)[b]			Heating 2 (°C)[b]			
			T_{m1}	T_{m2}	T_g	ΔH_1	T_{c1}	T_{c2}	ΔH_2	T_{m1}	T_{m2}	T_g	ΔH_3
PEOH	117.3	7.5	145	Nd	Nd	181.4	110	Nd	123.6	137	Nd	Nd	118.9
PPOH	39.5	8.7	Nd	156	−5	40.7	100	Nd	58.8	Nd	154	−5	51.4
PE-*b*-PE	Na	Na	135	Nd	Nd	255.4	108	Nd	83.2	132	Nd	Nd	84.1
PP-*b*-PP	Na	Na	93	158	−7	32.5	102	Nd	28.7	Nd	153	−8	29.7
PE-*b*-PP	58.3	12.5	130	153	−6	71.7	113	120	96.7	129	152	−7	59.3
PE/PP	32.4	6.1	135	151	−6	68.3	98	110	67.1	135	151	−6	64.7
3%PEbPP	Na	Na	136	163	Nd	131.6	111	Nd	133.7	134	164	Nd	137.3
6%PEbPP	Na	Na	138	166	Nd	137.9	109	Nd	134.7	138	164	Nd	137.8
12%PEbPP	Na	Na	138	165	Nd	122.9	109	Nd	122.3	136	163	Nd	122.3
20%PEbPP	Na	Na	137	164	Nd	119.9	109	Nd	120.9	136	164	Nd	113.9

Na, not available.
Nd, not detected.
[a] Determined by gel permeation chromatography, PS standard.
[b] Determined by DSC, ΔH = (J/g).

of the melted blend of pure PE/PP is lower than all of the PE-*b*-PP addition samples, and this implied that the cystallinity of melted blend of pure PE/PP is increased when added with PE-*b*-PP. In other words, the copolymer enhanced the crystallization of both PE and PP in the melted blend of PE/PP. From the highest ΔH, the largest percent of crystallinity is at 6% PE-*b*-PP in PE/PP. This may result in the best mechanical properties because of the formed crystal and contribute to the highest tensile strength. In addition, portion of T_m that represented the PP crystal in PE/PP were increased from pure PE/PP in all the composition of added PE-*b*-PP. Usually, T_m describing the quality of crystallinity in polymer blend form crystalline and decrease the entanglement in polymer blend). This can be concluded that the addition of our PE-*b*-PP alter both the quality and quantity of the crystallinity of PE/PP.

The chain structure of polymer blend and block copolymer was studied by DSC analysis of crystalline-segregated samples. After stepwise annealing of the samples at different temperatures, the long PP and PE segments can form crystalline lamellae of different thickness according to their sequential lengths, and these lamellae will melt at different temperatures.[11] By recording the endothermic curves of the polymer blend and block copolymer in a DSC scan, we are able to identify the sequential contribution of PE/PP blend and effects of the synthesized PE-*b*-PP in crystallinity of PE/PP.

The T_g of the block copolymer should exhibit the glass transition of each of the respective homopolymer component as same as polymer blends.[12,13] According to Table I, the T_g of PP[14] around −5°C indicate the cooperation of PP in the compatibilizer. Unfortunately, because of the low T_g of PE at −110°C,[15] it cannot be detected in these DSC experiments. However, the crystalline melting characteristic of PE-*b*-PP shows the combination characteristics of both PE and PP. The melting peak at about 130–140°C corresponds to the melting temperature of PE crystal and the peak above 140°C corresponds to the melting temperature originate from PP crystal. The appearance of the curves of PE/PP blend and PE-*b*-PP is similar. In the cases of adding PE-*b*-PP to PE/PP blend, the melting temperatures of PP in PE/PP increase about 10°C (as shown in Table I). This may confirm the appearance of the synthesized PE-*b*-PP and the consequence of the addition of block copolymer.

Morphology

According to SEM picture, it clearly shows the differences of the rough surface particles and the bridge formation with PP matrix of PE/PP blend, which continuously changed according to the concentration of PE-*b*-PP. The addition of PE-*b*-PP to PE/PP blend vividly shows the smaller phase particles size as increased concentrations. Many studies[16–19] on polymer alloys have shown that for multiphase polymer systems, the toughening effect is determined by two factors. First, the smaller the particles and the narrower the particles size distributions are, the better impact the strength is. Second, the stronger the adhesion between particle and the matrix, the better is the impact properties.

The SEM micrographs of compatibilized PE/PP blends (3, 6, 12, and 20% PE-*b*-PP) are shown in Figures 2 and 3. Figure 2 shows the tensile fracture of PE/PP and compatibilized PE/PP, while indicated that the interfacial adhesions, and therefore the compatibility of the PE and PP phases is better than the uncompatibilized PE/PP. In room temperature fracture experiments, the PE is in the form of tough rubbery polymer compared to PP. These might be shown as the stretch rubbery structure in the blends. The cryogenic fracture of the similar blends in Figure 3 will result in the clear domain size because at the

F2

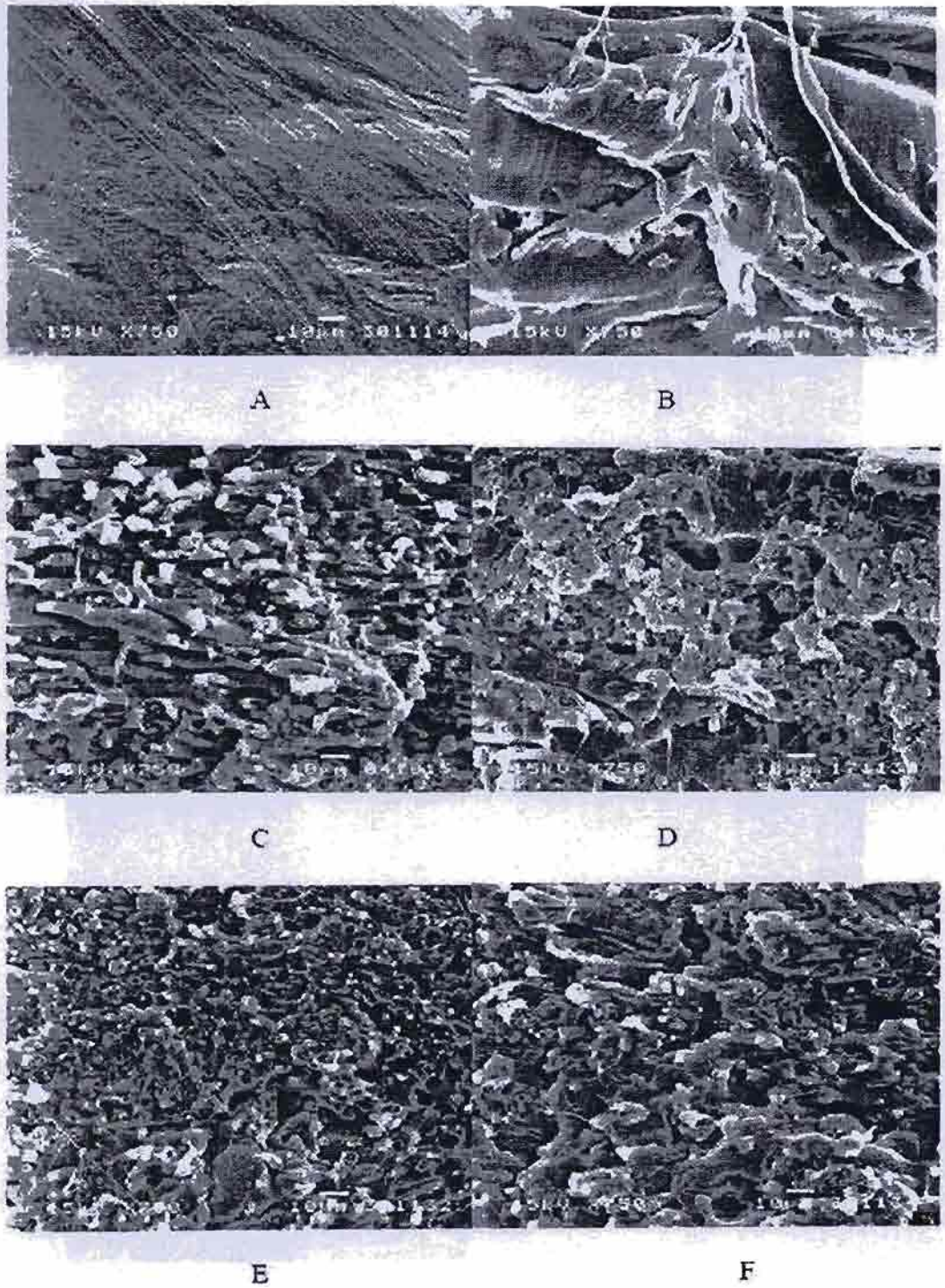

Figure 2 SEM of tensile fracture surface of (a) PP, (b) PE/PP blend, (c) PE/PP+ PEbPP3%, (d) PE/PP+ PEbPP6%, (e) PE/PP+ PEbPP12%, and (f) PE/PP+ PEbPP20%.

cryogenic temperature both PE/PP are in the glassy states and the fractures cut directly to the cross sections of the segregation size in the blends.

In Figure 3, the cryogenic fracture of PE/PP and compatibilized PE/PP indicated clearly decrease in domain sizes (dispersion of PE in PP) and finer parti-

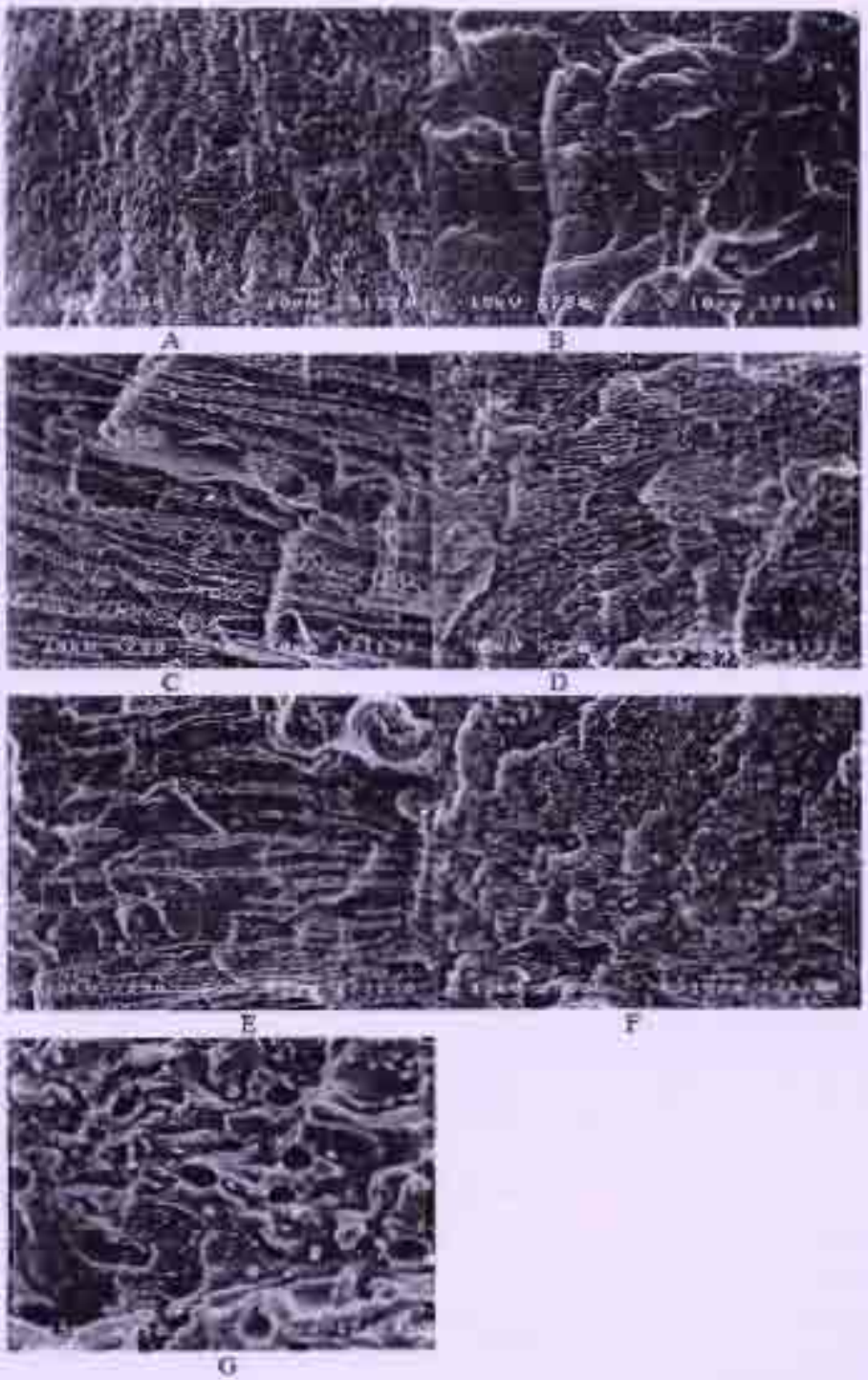

Figure 3 SEM of cryogenic fracture surface of (a) PE, (b) PP, (c) PE/PP blend, (d) PE/PP+ PEbPP3%, (e) PE/PP+ PEbPP6%, (f) PE/PP+ PEbPP12%, and (g) PE/PP+ PEbPP20%.

cle size distributions when adding more PE-b-PP in the blends. As might be confirmed by the SEM, the phase segregation decrease deliberately but the clear second dots of PE/PP are captured in the 12% and 20 wt % PE-b-PP, which might be the reason for the weaker interfacial ability than the 6 wt % PE-b-PP.

J. ID: ZSE Customer A. ID: 25945 Date: 15-FEBRUARY-07 Stage: 1 Page: 7

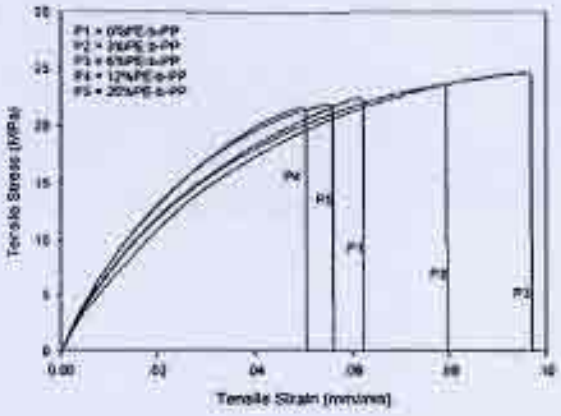

Figure 4 Additive effect of PE-*b*-PP to PE/PP blend on stress–strain behavior at 25°C.

Those samples have lower tensile properties than the 6 wt % PE-*b*-PP. These phenomena can confirm mechanical properties results.

Mechanical properties

The results of tensile stress tests are shown in Figure 4 and Table II. As the concentration of PE-*b*-PP in melted blend of pure PE/PP increased, both the tensile strength and the elongation at break increased. These show that the addition of PE-*b*-PP to PE/PP can improve the reinforcement of polymer by increasing the interfacial adhesion between PE and PP. At 6% PE-*b*-PP in PE/PP, the highest tensile stress of the blend occurred, which resulted from more stiffness and toughness of the samples. Thus, the tensile properties of PE-*b*-PP in PE/PP were in agreement with DSC results as we discussed earlier that the 6 wt % PE-*b*-PP has the most reinforcement characteristics. The reasons of decreasing tensile strength and elongation at break at 12 and 20% PE-*b*-PP contents might be because of the lower percent crystal in the samples together with the increase of PE, PP pure from PE-*b*-PP that have the higher molecular weight than the commercial PE/PP. The amount of high molecular weight might result in the more incompatible of PE/PP. As usual, the portion of high molecular weight in the blend will result in phase separation of the high molecular weight species easier than the low molecular weight portions.[20] The SEM results supported what can be found in tensile testing. As the consequence, this can be concluded that the addition of our PE-*b*-PP will have the optimum at 6 wt % PE-*b*-PP.

TE2

TABLE II
Summary of Mechanical Properties

Sample	Modulus (MPa)	Tensile strength (MPa)	Elongation (%)
PE/PP	879.89	22.46	6.2
3%PE-*b*-PP	782.19	23.63	8.0
6%PE-*b*-PP	763.14	24.67	9.7
12%PE-*b*-PP	927.01	21.59	8.1
20%PE-*b*-PP	854.27	21.88	5.6

CONCLUSIONS

A new synthesis method of PE-*b*-PP copolymer by converting the H-terminated chain ends to hydroxyl-terminated ones and blocking with diisocyanate is performed by the effective compatibilizer for immiscible blend of PE/PP. The diisocyanate linkages of PE-*b*-PP copolymers were confirmed by IR, which indicated that PE-*b*-PP copolymers occurred in the blocking reaction. The effects of PE-*b*-PP copolymers on the morphology of PE/PP blends were investigated by SEM with image analysis. The presence of the block copolymer dramatically reduced the phase size. Furthermore, the mechanical properties, such as tensile strength, elongation at break, and crystallinity, have been improved because of PE-*b*-PP copolymers. The phase-binding phenomena happened because the PE-*b*-PP contained PE and PP segments, which attached and bound the PE/PP segregate phase blend, leading to superior properties via changing morphology than the normal mixing blend without PE-*b*-PP. As confirmed by DSC, the compatibilized blends showed the increase of cystallinity percentage. The optimum content of compatibilizer is 6 wt % PE-*b*-PP, which shows the best optimal values from DSC, tensile tests, and SEM results.

The author thanks the Bangkok Polyethylene for the GPC characterizations and thank the Natural Petrochemical for supplying the ethylene and propylene gas. Furthermore, we like to thank MEKTEC manufacturing (Thailand) for supporting the characterize equipments and Ms. Nongnaphat for IR analysis.

References

1. Patel, D. R.; Vinson, C. E.; Locke, C. E. Polym Eng Sci 1973, 13, 202.
2. Tse, J. W.; Rudin, A.; Kwong, J. C. Adv Polym Tech 1994, 13, 1.
3. Shanks, R. A.; Li, J.; Chen, F.; Amarasinghe, G. Chin J Polym Sci 2000, 18, 263.
4. Radonjic, G.; Cubeljak, N. Macromol Mater Eng 2002, 287, 122.
5. Androeopoulos, A. G.; et al. J Macromol Sci Pure 1999, 36, 1113. AQ4
6. Vaccaro, L.; Dibenedetto, A. T.; Huang, S. J. J Appl Polym Sci 1997, 63, 275.
7. Yang, M. B.; Wang, K.; Ye, L.; Mai, Y. W.; Wu, J. S. Plast Rubber Compos 2003, 32, 27.
8. Bertin, S.; Robin, J. J. Eur Polym J 2002, 38, 2255.
9. Claudia, M. C.; Agnes, F. J App Polym Sci 2001, 80, 1305.

ID: 40456 Date: 15/2/07 Time: 00:34 Path: J:/Production/APP#/VOL00000/070132/3B2/C2APP#070132

10. Ubonnut, L. Masters' Thesis, Chulalongkorn University, Bangkok, Thailand, 2005.
11. Starck, P. Polym Int 1996, 40, 111.
12. Allport, D. C.; Janes, W. H., Eds. Block Copolymers; Applied Science Publishers: London; 1973; Chapter 4.
13. Noshay, A.; McGrath, J. E. Block Copolymers, Overview and Critical Survey; Academic Press: New York, 1977: Chapter 5c.
14. Frank, H. P. Polypropylene; Gardon and Breach: New York, 1968.
15. Baldwin, E. P.; Ver Strate, G. Rubber Chem Technol 1972, 45, 709.
16. Jiang, B. Z.; Uhlmann, D. R.; Sande, J. B. V. J Appl Polym Sci 1985, 30, 2485.
17. Yang, D. C.; Zhang, B. L.; Yang, Y. K.; Fang, Z.; Sun, G. F. Polym Eng Sci 1984, 24, 612.
18. Van Gisbergen, J. G. M.; Hoeben, W. F. L. M.; Meijer, H. E. H. Polymer 1991, 31, 1539.
19. Jiang, M. Physical Chemistry in Polymer Alloys; Chengdu, China: Sichuan Educational Press, 1988.
20. McMaster, L. P. Macromolecules 1973, 6, 760.

Korean J. Chem. Eng., 24(3), 397-402 (2007)

Synthesis of nanocrystalline alumina by thermal decomposition of aluminum isopropoxide in 1-butanol and their applications as cobalt catalyst support

Kamonchanok Pansanga, Okorn Mekasuwandumrong*, Joongjai Panpranot and Piyasan Praserthdam†

Center of Excellence on Catalysis and Catalytic Reaction Engineering, Department of Chemical Engineering, Faculty of Engineering, Chulalongkorn University, Bangkok 10330, Thailand
*Department of Chemical Engineering, Faculty of Engineering and Industrial Technology, Silpakorn University, Nakorn Pathom 73000, Thailand
(*Received 21 August 2006 • accepted 13 November 2006*)

Abstract–Nanocrystalline alumina powders were prepared by thermal decomposition of aluminum isopropoxide (AIP) in 1-butanol at 300 °C for 2 h and employed as cobalt catalyst supports. The crystallization of alumina was found to be influenced by the concentration of AIP in the solution. At low AIP content, wrinkled sheets-like structure of γ-Al_2O_3 was formed, while at high AIP concentrations, fine spherical particles of χ-Al_2O_3 were obtained. It was found that using these fine particles alumina as cobalt catalyst supports resulted in much higher amounts of cobalt active sites measured by H_2 chemisorption and higher CO hydrogenation activities.

Key words: Nanocrystalline Alumina, Thermal Decomposition, Cobalt Catalyst, Solvothermal Method, CO Hydrogenation

INTRODUCTION

Alumina powders are very interesting crystalline materials with broad applicability as adsorbents, coatings, soft abrasives, ceramic tools, fillers, wear-resistant ceramics, catalysts, and catalyst supports [1,2]. Because of their fine particle size, high surface area, high melting point (above 2,000 °C), high purity, good adsorbent, and high catalytic activity, they have been employed in a wide range of large-scale technological processes [3,4].

Various transition aluminas (α, γ, χ, δ, η and θ) have been prepared by different methods, such as sol-gel synthesis [5,6], hydrothermal synthesis [7], microwave synthesis [8], emulsion evaporation [9], plasma technique [10], and solvothermal synthesis [11-18]. Among these methods, solvothermal synthesis attracts the most attention because it gives the products with small uniform morphology, well-controlled chemical composition, and narrow size distribution. Furthermore, the desired shape and size of particles can be produced by controlling process conditions such as solute concentration, reaction temperature, reaction time, and the type of solvent [19,20]. For example, Berntsen et al. [21] described a simple route to high surface area nanostructured MoS_2 based on the decomposition of cluster-based precursor $(NH_4)_2Mo_3S_{13}{\cdot}xH_2O$ in toluene at 380 °C. It was found that solvothermal decomposition resulted in nanostructured material distinct from that obtained by decomposition of the precursor in sealed quartz tubes at the same temperature. Wang et al. [22] prepared nanocrystalline titania in alcohols under solvothermal conditions at 100 °C for 24 h. The selection of crystal structures, grain sizes, and morphologies was achieved by simply varying the alcohols and other reaction conditions.

Alumina prepared by the solvothermal method is considered high thermal stability. In our recent works [23-26], nanocrystalline transition alumina with micro spherical particles and high thermal stability has been synthesized by decomposition of aluminum isopropoxide (AIP) under solvothermal conditions. The mechanism of the process involves the formation of amorphous complexes before further decomposition takes place. Inoue et al. [27] prepared silica-modified alumina by the reaction of AIP and tetraethyl orthosilicate (TEOS) in 1,4-butanediol at 300 °C. The products were found to maintain large surface areas after calcination at high temperature.

In this study, the influence of concentration of aluminum isopropoxide in 1-butanol used in the preparation of nanocrystalline alumina by solvothermal method on the properties of alumina powders and alumina supported cobalt catalysts was investigated by using various characterization techniques such as XRD, BET analysis, TEM, SEM, EDX, H_2 chemisorption, and temperature-programmed reduction. The catalytic activity of the catalysts was tested in carbon monoxide hydrogenation at 220 °C and atmospheric pressure.

EXPERIMENTAL

1. Catalyst Preparation

1-1. Preparation of Nanocrystalline Al_2O_3

A selected amount of aluminum isopropoxide (Aldrich) (10-35 g) was suspended in 100 ml of 1-butanol (Ajax Finechem) in a test tube, which was then placed in a 300 ml autoclave. In the gap between the test tube and the autoclave wall, 30 ml of 1-butanol was added. The atmosphere inside the autoclave was purged completely with nitrogen. The mixture was heated to 300 °C at a heating rate of 2.5 °C/min and was kept at that temperature for 2 h. After cooling to room temperature, the resulting powders were collected after repeated washing with acetone by centrifugation. They were then air-dried. The calcination of the products was carried out in a box furnace by heating up to 600 °C at a rate of 10 °C/min and held at that temperature for 1 h.

1-2. Preparation of Al_2O_3-Supported Co Catalysts

The Co/Al_2O_3 catalysts were prepared by incipient wetness impregnation of Al_2O_3 with a desired amount of an aqueous solution

†To whom correspondence should be addressed.
E-mail: piyasan.p@chula.ac.th

of cobalt nitrate [$Co(NO_3)_2 \cdot 6H_2O$] (Aldrich). The final loading of the catalysts was determined by atomic absorption spectroscopy (Varian Spectra A800) to be ca. 10 wt% cobalt. The catalysts were dried at 110 °C for 24 h and calcined in air at 300 °C for 2 h using a ramp rate of 1 °C/min.

2. Catalyst Nomenclature

In this study, alumina and alumina-supported cobalt catalysts are referred to as Al-x and Co/Al-x, where x is the amount (g) of AIP used in the preparation of alumina powders. For example, Al-10 and Co/Al-10 refer to Al_2O_3 and Co/Al_2O_3 catalyst prepared with 10 g AIP.

3. Catalyst Characterization

XRD patterns of the samples were collected with a SIEMENS D-5000 X-ray diffractometer with Cu K_α radiation (λ=1.54439 Å). The spectra were scanned at a rate of 0.04°/step from 2θ=15° to 80°. BET surface areas were calculated by using the BET-single point method at liquid N_2 temperature. Transmission electron microscopy (TEM) was performed with a JEOL JEM1220. SEM and EDX were performed with a JEOL JSM-35CF scanning electron microscope in the back scattering electron (BSE) mode at 20 kV. EDX was performed by using Link Isis 300 software. Static H_2 chemisorption was carried out on the reduced cobalt catalyst samples at 100 °C according to the method described by Reuel and Bartholomew [28] by using a Micromeritics Pulse Chemisorb 2700 system. Prior to H_2 chemisorption, the catalyst samples were reduced at 350 °C in flowing H_2 for 3 h. Temperature-programmed reduction (TPR) was performed by using an in-house system. Approximately 0.1 g of the catalyst was placed in the middle of a stainless steel reactor. A temperature ramp from 35 to 600 °C at a ramp rate 5 °C/min and the reduction gas 5% H_2 in Ar were used. A thermal conductivity detector (TCD) was used to determine the amount of hydrogen consumed. A cold trap was placed before the detector to remove water produced during the reduction. The hydrogen consumption was calibrated by using TPR of silver oxide (Ag_2O) at the same conditions.

4. Reaction

CO hydrogenation was carried out in a fixed-bed quartz reactor under differential reaction conditions (<10% conversion) at 220 °C, 1 atm total pressure, and H_2/CO=10/1. The total flow rate of H_2/CO/Ar was 80/8/32 cc/min. Typically, 0.1 g of the catalyst sample was reduced *in situ* in flowing H_2 (50 cc/min) at 350 °C for 3 h prior to CO hydrogenation. After the startup, samples were taken in 1-h interval and analyzed by gas chromatography. Steady state was reached within 6 h in all cases.

RESULTS AND DISCUSSION

1. Effect of AIP Concentration on the Properties of Al_2O_3

Fig. 1 shows the XRD patterns of various alumina powders obtained from thermal decomposition of AIP in 1-butanol after calcination at 600 °C for 1 h. XRD patterns of Al_2O_3 show strong diffraction peaks at 31°, 33°, 38°, 43°, 47.5°, and 68° (according to the JCPDSs database). It was found that when lower amounts of AIP were used, only γ-alumina was formed as seen by the XRD characteristic peaks at 2θ=33° according to the JCPDSs database. The XRD characteristic peaks of χ-alumina were observed at 2θ=42.5° for the ones prepared with AIP 25 and 35 g. The intensity of χ-alumina peaks became stronger with increasing amount of AIP content. It is indicated that increasing AIP content during the synthesis resulted in formation of mixed phase between γ-alumina and χ-alumina. The crystallization process of alumina was probably affected by the amounts of AIP in 1-butanol.

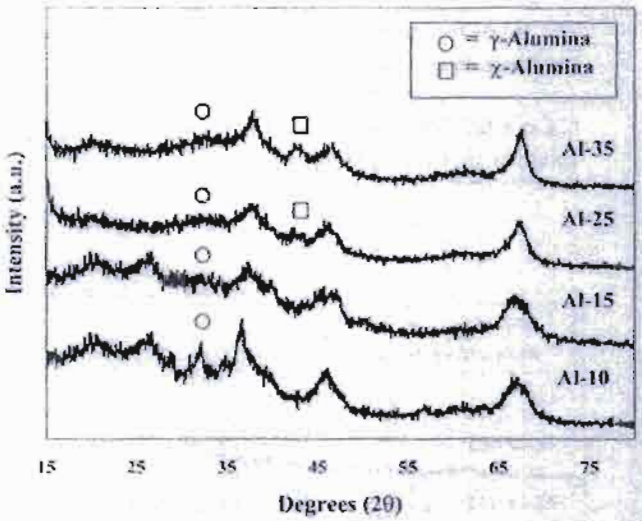

Fig. 1. XRD patterns of various nanocrystalline alumina prepared by the reaction of AIP in 1-butanol at 300 °C for 2 h (after calcinations at 600 °C for 1 h).

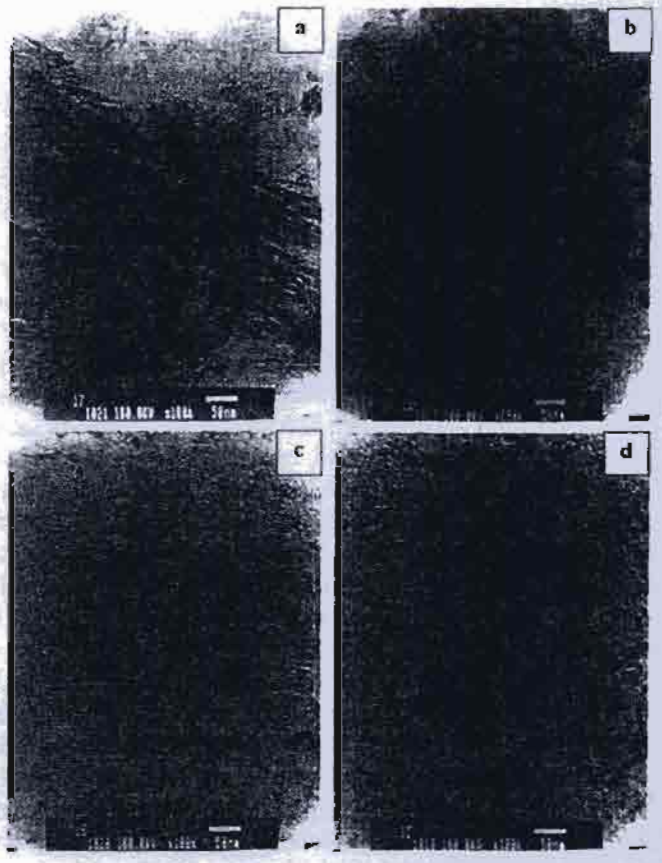

Fig. 2. TEM images of alumina obtained by the reaction of AIP in 1-butanol at 300 °C for 2 h with different amounts of AIP (a) Al-10 (b) Al-15 (c) Al-25 (d) Al-35.

Table 1. The physical and chemical properties of Al_2O_3 supports

Samples	Amounts of AIP (g)	Surface area (m^2/g)*	Bulk density (g/cm^3)*	Morphology
Al-10	10	70	0.3824	Wrinkled sheets
Al-15	15	120	0.3858	High amount of wrinkled sheets
Al-25	25	139	0.3928	Wrinkled sheets and small amount of spherical particles
Al-35	35	145	0.5358	Small amount of wrinkled sheets and high amount of spherical particles

*Error of measurement=±5%

TEM images of alumina powders prepared with different amounts of AIP are shown in Fig. 2. For the ones prepared with lower amounts of AIP, Al-10 and Al-15, the wrinkled sheets morphology was observed. They were found to be similar to those obtained from the formation of γ-alumina by decomposition of glycol or alkyl derivatives on boehmite [26,27]. As the amounts of AIP increased, the wrinkled sheets morphology became less apparent and spherical particles were observed. The presence of spherical particles was probably due to the formation of χ-alumina, which is normally formed by thermal decomposition reaction of AIP in inert organic solvents at 300 °C [23-26]. TEM results were in good agreement with the XRD patterns that a mixture of γ-alumina and χ-alumina was observed when AIP concentration increased.

The physical properties of the alumina products are summarized in Table 1. The BET surface areas increased with increasing AIP concentration as a result of morphology changing from wrinkled sheets structure to small spherical particles. BET surface area of the Al-35 (145 m^2/g) was found to be twice of that of Al-10 (70 m^2/g). Similar trend was observed for the bulk density of the alumina powders. The bulk density increased with increasing AIP contents.

Mechanism of thermal decomposition of AIP in alcohol has been proposed in our previous works [23,26] involving three competitive reactions. First, AIP reacted with 1-butanol yielding aluminum butoxide, which decomposed further to give the alkyl (butyl) derivative of boehmite. Second, 1-butanol can be dehydrated to give water which then hydrolyzes aluminum isopropoxide or butoxide yielding pseudoboehmite. Finally, the direct decomposition of aluminum alkoxide in organic solvent, which proceeded slowest, gave χ-alumina. In the present work, at low AIP content, boehmite was probably the main product and γ-alumina was obtained after calcination at 600 °C for 1 h. The morphology of the boehmite products obtained via solvothermal reaction was wrinkled sheets [23,26], which was also similar to those of γ-alumina decomposed from. However, when the amounts of AIP in 1-butanol increased, formation of χ-alumina from direct decomposition of AIP in the solvent occurred as the main reaction.

2. Characteristics of Co/Al_2O_3 Catalysts

The XRD patterns of cobalt catalysts supported on alumina prepared with various amounts of AIP are shown in Fig. 3. The XRD patterns of the Co/Al_2O_3 catalysts were not significantly different from those of alumina supports. No XRD peaks of Co_3O_4 or other Co compounds were detected. This indicates that cobalt was present in a highly dispersed form on alumina even for cobalt loading as high as 10 wt% [29].

SEM and EDX were performed in order to study the morphology and elemental distribution of the catalyst samples, respectively. Typical SEM micrographs of Co/Al_2O_3 catalysts are shown in Fig. 4. There was no significant change in morphology of the catalyst samples due to the effect of AIP concentrations in 1-butanol used in the preparation process. The white or light spots observed in all figures can be attributed to the cobalt patches distributed on the external surface of catalyst granules. Fig. 5 shows the SEM micrographs and the EDX mapping of the cross-sectioned Co/Al-35 catalyst granule. The distribution of cobalt was found to be well dispersed throughout the catalyst granule.

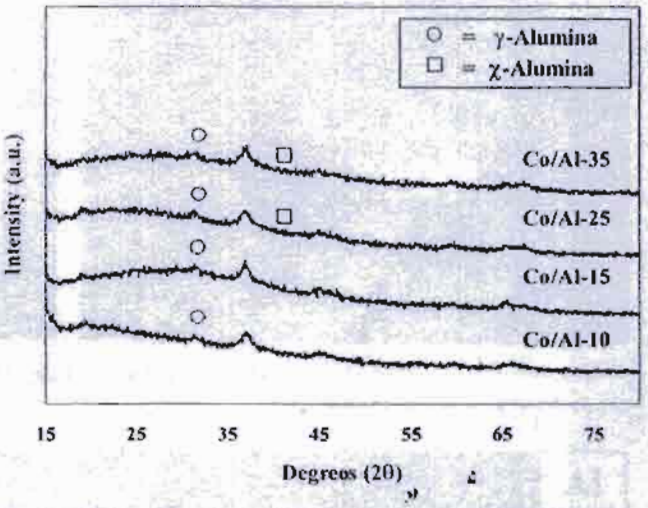

Fig. 3. XRD patterns of Co/Al_2O_3 catalysts with different amounts of AIP.

The relative amounts of active surface cobalt on the catalyst samples were calculated from H_2 chemisorption experiments at 100 °C according to Reuel and Bartholomew [28]. It is known that only surface cobalt metal atoms are active for CO hydrogenation, not its oxide or carbide [30]. The H_2 chemisorption results are reported in Table 2. The amounts of H_2 chemisorption increased from 0.90 to 20.65 μmol/g cat., with increasing amount of AIP in 1-butanol used in the preparation of the alumina supports from 10 to 35 g. It is likely that the increase in the relative amounts of active cobalt metals was due to the formation of the small spherical particles of χ-alumina. As also seen in the Table 2, the amount of H_2 chemisorption of Co/Com-Al (13.38 μmol/g cat.), prepared from the commercial γ-alumina which the crystal shape of alumina was spherical (the results was not shown), was better than solvothermal-made Co/γ-alumina (0.90 μmol/g cat.) but lower than Co/χ-alumina (20.65 μmol/g cat.).

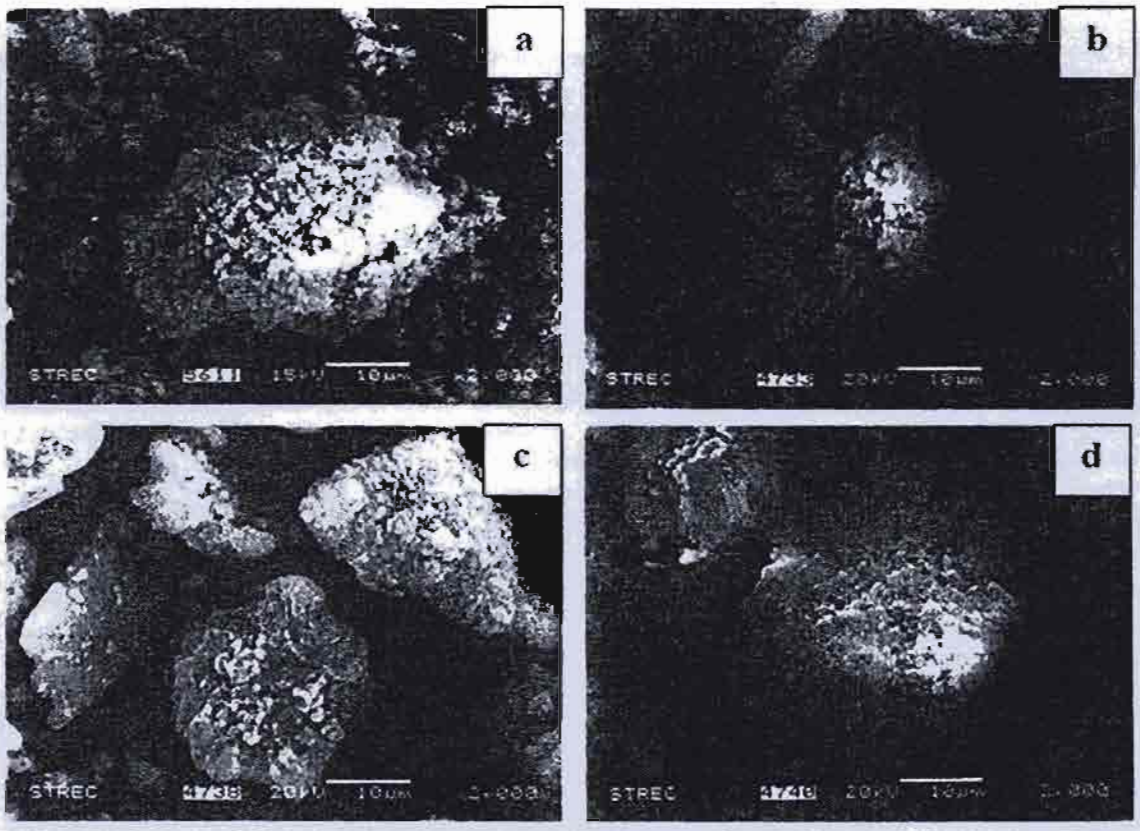

Fig. 4. SEM micrographs of (a) Co/Al-10, (b) Co/Al-15, (c) Co/Al-25, and (d) Co/Al-35.

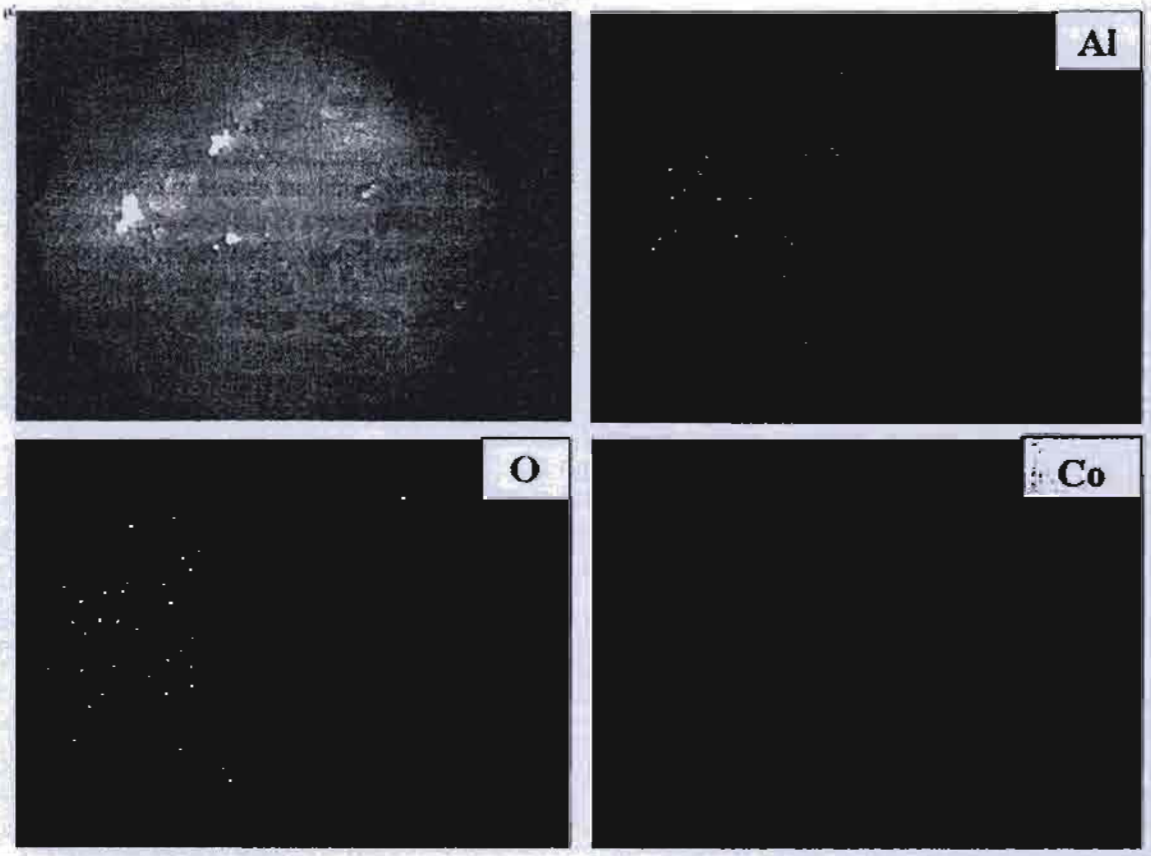

Fig. 5. SEM micrograph and EDX mapping of cross-sectioned Co/Al-35 catalyst granule.

It was again confirmed that the spherical morphology of the alumina support is important in achieving a higher amount of active cobalt metal.

3. Reduction and Catalytic Behaviors of Co/Al_2O_3 Catalysts

Temperature program reduction (TPR) is a powerful tool for studying the reduction behavior of the catalysts. The TPR profiles of various nanocrystalline alumina supported cobalt catalysts are shown in Fig. 6. All the catalyst samples exhibited two main reduction peaks which could be assigned to the two-step reduction of Co_3O_4: first reduction of Co_3O_4 to CoO and then the subsequent reduction of CoO to Co^0 [31]. The two reduction steps may not always be observed as separate peaks in TPR profile [32], as seen in the Co/Al-35 sample. A wide range of variables such as metal particle size and metal-support interaction have an influence on the reduction behavior of cobalt catalysts resulting in the observation of different locations of the TPR peaks. The TPR profiles for all the catalysts except Co/Al-35 appeared to be not significantly different, suggesting that the AIP content had little impact on the interaction of cobalt and alumina supports. Thus, high dispersion of cobalt obtained on Co/Al-35 was rather to be due to the formation of small spherical particles alumina and not to the change in reducibility of the catalysts.

Table 2. The characteristics and H_2 chemisorption of cobalt catalyst

Catalyst samples	Surface area (m^2/g)[a]	Amount of H_2 chemisorption ($\mu mol/g$ cat.)[a]
Co/Al-10	61	0.90
Co/Al-15	87	2.29
Co/Al-25	108	7.58
Co/Al-35	114	20.65
Co/Com-Al*	145	13.38

[a]Error=±5%, as determined directly.
*Commercial γ-alumina, BET surface area of alumina 230 m^2/g.

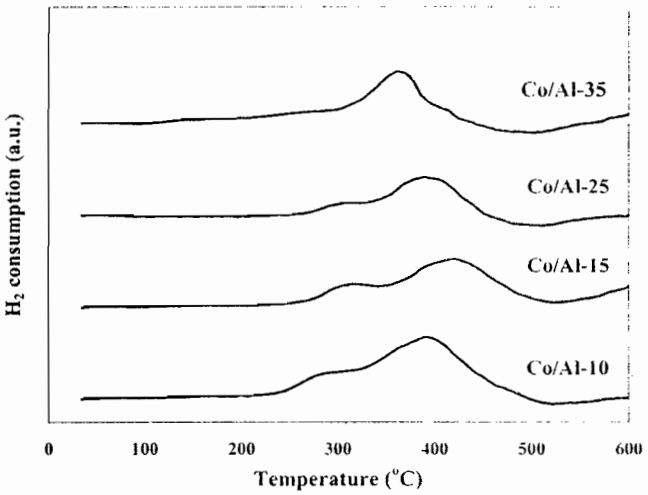

Fig. 6. TPR profiles of the catalyst samples.

CO hydrogenation reaction was carried out as a test reaction to determine the catalytic activity of the catalyst samples. The results are shown in Table 3. It is clearly seen that alumina prepared with higher amounts of AIP in 1-butanol resulted in much higher CO hydrogenation activities and CH_4 selectivities. The reaction results confirm the amount of surface cobalt metals measured by H_2 chemisorption.

CONCLUSIONS

Nanocrystalline alumina powders were prepared by thermal decomposition of AIP in 1-butanol with various AIP contents. The concentration of AIP in 1-butanol had a significant impact on the properties of alumina and alumina supported cobalt catalysts. Increasing amounts of AIP in the solution resulted in the transformation of wrinkled sheet γ-alumina to fine spherical particles of χ-alumina. It also gave rise to the cobalt active sites and CO hydrogenation activities when employed as supports for preparation of Co/Al_2O_3 catalysts.

ACKNOWLEDGMENTS

The authors would like to thank the Thailand Research Fund (TRF) for the financial support of this project.

REFERENCES

1. J. S. Church, N. W. Cant and D. L. Trimm, *Appl. Catal. A*, **101**(1), 105 (1993).
2. G. Pajonk and S. Teichner, *Aerogels*, Spinger, Berlin (1986).
3. C. Misra, *Industrial alumina chemicals*, ACS Monograph 184, Washington (1986).

Table 3. Reaction rate and selectivity for CO hydrogenation on catalyst samples

Catalyst samples	CO conversion (%)[a]		Rate ($\times 10^2$ gCH_2 $gcat^{-1}h^{-1}$)[b]		CH_4 selectivity (%)	
	Initial[c]	SS[d]	Initial	SS	Initial	SS
Co/Al-10	1.92	0.54	5.76	1.62	13	11
Co/Al-15	2.63	0.75	7.89	2.25	49	47
Co/Al-25	5.45	3.02	16.35	9.06	56	54
Co/Al-35	8.49	4.03	25.47	12.09	70	67

[a]CO hydrogenation was carried out at 220 °C, 1 atm, and H_2/CO/Ar=80/8/32.
[b]Error±5%, as determined directly.
[c]After 20 min of reaction.
[d]After 6 h of reaction.

4. H. Topsoe, B. S. Clausen and F. E. Massoth, *Hydrotreating catalysis*, Springer, Berlin (1996).
5. C. J. Brinker and G. W. Scherrer, *Sol-gel science*, Academic Press, San Diego (1990).
6. K.-C. Song, K.-J. Woo and Y. Kang, *Korean J. Chem. Eng.*, **16**, 75 (1999).
7. W. H. Dawson, *Am. Ceram. Soc. Bull.*, **67**, 1673 (1988).
8 S. G. Deng and Y. S. Lin, *Sci. Lett.*, **16**, 1291 (1997).
9. Y. Sarikaya, I. Sevinc and M. Akinc, *Powder Technol.*, **116**(1), 109 (2001).
10. S.-M. Oh and D.-W. Park, *Korean J. Chem. Eng.*, **17**, 299 (2000).
11. M. Inoue, H. Kominami and T. Inui, *J. Am. Ceram. Soc.*, **73**, 1100 (1990).
12. M. Inoue, H. Kominami and T. Inui, *J. Chem. Soc. Dalton Trans.*, 3331 (1991).
13. M. Inoue, H. Kominami and T. Inui, T. *J. Am. Ceram. Soc.*, **75**, 2597 (1992).
14. M. Inoue, H. Kominami and T. Inui, *Appl. Catal. A*, **97**, L25 (1993).
15. M. Inoue, H. Kominami and T. Inui, *Appl. Catal. A*, **121**, L1 (1995).
16. M. Inoue, H. Kominami and T. Inui, *J. Am. Ceram. Soc.*, **75**, 2597 (1996a).
17. M. Inoue, Y. Kondo and T. Inui, *Inorg. Chem.*, **27**, 215 (1988).
18. M. Inoue, H. Otsu, H. Kominami and T. Inui, *Ind. Eng. Chem. Res.*, **35**, 295 (1996b).
19. Y. Deng, G-D. Wei and C.-W. Nan, *Chem. Phys. Lett.*, **368**(5-6), 639 (2003).
20. Y. Deng, X.-S. Zhou, G-D. Wei, J. Liu, C.-W. Nan and S.-J. Zhao, *J. Phys. Chem. Solids*, **63**(11), 2119 (2002).
21. N. Berntsen, T. Gutjahr, L. Loeffler, J. R. Gomm, R. Seshadri and W. Tremel, *Chem. Mater.*, **15**(23), 4498 (2003).
22. C. Wang, Z.-X. Deng, G. Zhang, S. Fan and Y. Li, *Powder Technol.*, **125**(1), 39 (2002.
23. O. Mekasuwandumrong, H. Kominami, P. Praserthdam and M. Inoue, *J. Am. Ceram. Soc.*, **87**(8), 1543 (2004a).
24. O. Mekasuwandumrong, P. Praserthdam, M. Inoue, V. Pavarajarn and W. Tanakulrungsank, *J. Mater. Sci.*, **39**, 2417 (2004b).
25. O. Mekasuwandumrong, P. L. Silveston, P. Praserthdam, M. Inoue, V. Pavarajarn and W. Tanakulrungsank, *Inorg. Chem. Commu.*, **6**(7), 930 (2003).
26. P. Praserthdam, M. Inoue, O. Mekasuvandumrong, W. Tanakulrungsank and S. Phatanasri, *Inorg. Chem. Commu.*, **3**(11), 671 (2000).
27. M. Inoue, H. Otsu, H. Kominami and T. Inui, *Ind. Eng. Chem. Res.*, **35**, 295 (1996c).
28. R. C. Reuel and C. H. Bartholomew, *J. Catal.*, **85**, 63 (1984).
29. B. Jongsomjit, J. Panpranot and J. G. Goodwin Jr., *J. Catal.*, **215**(1), 66 (2003).
30. R. B. Anderson, *The Fischer-Tropsch synthesis*, Academic Press, San Diego (1984).
31. Y. Zhang, D. Wei, S. Hammache and J. G. Goodwin Jr., *J. Catal.*, **188**(2), 281 (1999).
32. B. Ernst, S. Libs, P. Chaumette and A. Kiennemann, *Appl. Catal. A*, **186**(1-2), 145 (1999).

4. H. Topsoe, B. S. Clausen and F. E. Massoth, *Hydrotreating catalysis*, Springer, Berlin (1996).
5. C. J. Brinker and G. W. Scherrer, *Sol-gel science*, Academic Press, San Diego (1990).
6. K.-C. Song, K.-J. Woo and Y. Kang, *Korean J. Chem. Eng.*, **16**, 75 (1999).
7. W. H. Dawson, *Am. Ceram. Soc. Bull.*, **67**, 1673 (1988).
8 S. G. Deng and Y. S. Lin, *Sci. Lett.*, **16**, 1291 (1997).
9. Y. Sarikaya, I. Sevinc and M. Akinc, *Powder Technol.*, **116**(1), 109 (2001).
10. S.-M. Oh and D.-W. Park, *Korean J. Chem. Eng.*, **17**, 299 (2000).
11. M. Inoue, H. Kominami and T. Inui, *J. Am. Ceram. Soc.*, **73**, 1100 (1990).
12. M. Inoue, H. Kominami and T. Inui, *J. Chem. Soc. Dalton Trans.*, 3331 (1991).
13. M. Inoue, H. Kominami and T. Inui, T. *J. Am. Ceram. Soc.*, **75**, 2597 (1992).
14. M. Inoue, H. Kominami and T. Inui, *Appl. Catal. A*, **97**, L25 (1993).
15. M. Inoue, H. Kominami and T. Inui, *Appl. Catal. A*, **121**, L1 (1995).
16. M. Inoue, H. Kominami and T. Inui, *J. Am. Ceram. Soc.*, **75**, 2597 (1996a).
17. M. Inoue, Y. Kondo and T. Inui, *Inorg. Chem.*, **27**, 215 (1988).
18. M. Inoue, H. Otsu, H. Kominami and T. Inui, *Ind. Eng. Chem. Res.*, **35**, 295 (1996b).
19. Y. Deng, G-D. Wei and C.-W. Nan, *Chem. Phys. Lett.*, **368**(5-6), 639 (2003).
20. Y. Deng, X.-S. Zhou, G-D. Wei, J. Liu, C.-W. Nan and S.-J. Zhao, *J. Phys. Chem. Solids*, **63**(11), 2119 (2002).
21. N. Berntsen, T. Gutjahr, L. Loeffler, J. R. Gomm, R. Seshadri and W. Tremel, *Chem. Mater.*, **15**(23), 4498 (2003).
22. C. Wang, Z.-X. Deng, G. Zhang, S. Fan and Y. Li, *Powder Technol.*, **125**(1), 39 (2002.
23. O. Mekasuwandumrong, H. Kominami, P. Praserthdam and M. Inoue, *J. Am. Ceram. Soc.*, **87**(8), 1543 (2004a).
24. O. Mekasuwandumrong, P. Praserthdam, M. Inoue, V. Pavarajarn and W. Tanakulrungsank, *J. Mater. Sci.*, **39**, 2417 (2004b).
25. O. Mekasuwandumrong, P. L. Silveston, P. Praserthdam, M. Inoue, V. Pavarajarn and W. Tanakulrungsank, *Inorg. Chem. Commu.*, **6**(7), 930 (2003).
26. P. Praserthdam, M. Inoue, O. Mekasuvandumrong, W. Tanakulrungsank and S. Phatanasri, *Inorg. Chem. Commu.*, **3**(11), 671 (2000).
27. M. Inoue, H. Otsu, H. Kominami and T. Inui, *Ind. Eng. Chem. Res.*, **35**, 295 (1996c).
28. R. C. Reuel and C. H. Bartholomew, *J. Catal.*, **85**, 63 (1984).
29. B. Jongsomjit, J. Panpranot and J. G. Goodwin Jr., *J. Catal.*, **215**(1), 66 (2003).
30. R. B. Anderson, *The Fischer-Tropsch synthesis*, Academic Press, San Diego (1984).
31. Y. Zhang, D. Wei, S. Hammache and J. G. Goodwin Jr., *J. Catal.*, **188**(2), 281 (1999).
32. B. Ernst, S. Libs, P. Chaumette and A. Kiennemann, *Appl. Catal. A*, **186**(1-2), 145 (1999).

Available online at www.sciencedirect.com
ScienceDirect
Materials Letters 61 (2007) 1376–1379
materials letters
www.elsevier.com/locate/matlet

Effect of nanoscale SiO_2 and ZrO_2 as the fillers on the microstructure of LLDPE nanocomposites synthesized via *in situ* polymerization with zirconocene

Bunjerd Jongsomjit *, Joongjai Panpranot, Piyasan Praserthdam

Center of Excellence on Catalysis and Catalytic Reaction Engineering, Department of Chemical Engineering, Faculty of Engineering, Chulalongkorn University, Bangkok 10330, Thailand

Received 7 February 2006; accepted 13 July 2006
Available online 1 August 2006

Abstract

In the present study, the nanoSiO_2 and nanoZrO_2 were used as the fillers for linear low-density polyethylene (LLDPE) nanocomposites. In fact, the LLDPE nanocomposites were synthesized via the *in situ* polymerization of ethylene/1-octene with a zirconocene/MAO catalyst in the presence of the fillers. The LLDPE–nanocomposites were further characterized by means of TEM, DSC, ^{13}C NMR and XPS. It was found that productivity increased more when the nanoZrO_2 filler was applied. The similar distribution for both fillers was observed by TEM. Based on the ^{13}C NMR results, it appeared that the LLDPE nanocomposites obtained from both fillers were random copolymer. In particular, the resulted binding energy and elemental concentration at surface obtained from XPS measurement were further discussed in more details.

Keywords: Polymer nanocomposite; Nanofillers; Metallocene; LLDPE; XPS

1. Introduction

Polymer composites are important commercial materials with various applications. It is known that materials or fillers with synergistic properties can be selected to create the polymer composites with desired properties. However, upon the significant development of nanoscience and nanotechnology in the recent years, nanoscale fillers have brought attraction to research in polymer composite. As known, polymers filled with nanoscale fillers are recognized as polymer nanocomposites. Apparently, with addition of nanoscale fillers into polymers, robust materials can potentially be produced due to the synergistic effects (cooperating for enhanced effects) arising from the blending process. In general, there are technically three methods used to produce a polymer composite; (i) a melt mixing [1–5], (ii) a solution blending [6] and (iii) *in situ* polymerization [7]. Due to the direct synthesis via polymerization along with the presence of fillers, the *in situ* polymerization is perhaps considered the most promising technique to produce polymer nanocomposites with homogeneous dispersion of nanoscale fillers inside the polymer matrix. Based on the commercial interest of using metallocene catalysts for olefin polymerization, it has led to an extensive effort for utilizing metallocene catalysts efficiently [8–11]. With a combination of knowledge in nanotechnology, polymerization, and metallocene catalysis, a promising way to synthesize the polymer nanocomposites using a metallocene catalyst is captivating.

In our previous work [12], we revealed that LLDPE nanocomposites could be synthesized via the *in situ* polymerization with a zirconocene/MAO catalyst. However, our present study focussed on further development in order to give a better understanding on how different nanoscale fillers could interact inside the polymer matrix. Obviously, this can result in different properties of polymer nanocomposites obtained.

2. Experimental

All chemicals [ethylene (99.96%) donated by the National Petrochemical of Thailand, toluene (Exxon), *rac*-ethylenebis (indenyl) zirconium dichloride [*rac*-Et$(Ind)_2ZrCl_2$] from Aldrich, methylaluminoxane (MAO, 2.67 M in toluene) donated by the

* Corresponding author. Tel.: +66 2 2186869; fax: +66 2 2186877.
E-mail address: bunjerd.j@chula.ac.th (B. Jongsomjit).

0167-577X/$ - see front matter © 2006 Elsevier B.V. All rights reserved.
doi:10.1016/j.matlet.2006.07.034

Table 1
Characteristics of LLDPE nanocomposites

Characteristics	LLDPE–$nanoSiO_2$	LLDPE–$nanoZrO_2$
1) Productivity (kg polymer/mol cat. h)	1319	6924
2) Melting temperature, T_m (°C)	90	94
3) Copolymer type (obtained from ^{13}C NMR)	Random	Random
4) C 1s binding energy (eV)	286.5	285.7

Tosoh Akso, Japan, trimethylaluminum (TMA, 2.0 M in toluene) from Nippon Alkyls, Japan, 1-octene (98%, Aldrich), $nanoSiO_2$ (Aldrich) and $nanoZrO_2$ fillers] were manipulated under an inert atmosphere using a vacuum glove box and/or the Schlenk techniques. 1-Octene was purified by distilling over sodium under argon atmosphere. Toluene was dried over dehydrated $CaCl_2$ and distilled over sodium benzophenone under argon atmosphere prior to use.

The $nanoZrO_2$ filler was synthesized by flame spray pyrolysis (FSP) as described by Mueller et al. [13]. The primary particle size of ZrO_2 was in the range of 6–35 nm. The crystal structure consisted of the tetragonal/monoclinic phase (95/5 by mol%). The $nanoSiO_2$ filler was obtained from Aldrich (30–40 nm). First, 1 g of the filler reacted with a desired amount of MAO in toluene at room temperature and was stirred for 30 min. The solvent was then removed from the mixture. About 20 ml of toluene was added into the obtained precipitate, the mixture was stirred for 5 min, and then the solvent was removed. This procedure was done for 5 times to ensure the removal of impurities. The white powder of nanoscale filler-impregnated MAO was obtained.

The ethylene/1-octene copolymerization reaction on the filler-impregnated MAO was carried out in a 100-ml semi-batch stainless steel autoclave reactor equipped with a magnetic stirrer. At first, 0.3 g of the nanoscale filler-impregnated MAO ($[Al]_{MAO}/[Zr]=3405$) and 0.018 mol of 1-octene along with toluene (to make a total volume of 30 ml) were put into the reactor. The desired amount of *rac*-$Et(Ind)_2ZrCl_2$ (5×10^{-5} M) and TMA ($[Al]_{TMA}/[Zr]=2500$) was mixed and stirred for 5 min aging at room temperature, separately, then was injected into the reactor. The reactor was heated up to polymerization temperature at 70 °C. To start reaction, 0.018 mol of ethylene was fed into the reactor. After, all ethylene was consumed, the reaction was terminated by addition of acidic methanol. After filtration, washing with methanol and drying at room temperature, white powder of $nanoZrO_2$ (SiO_2)-filled polymer was obtained.

The polymer sample was then characterized using the differential scanning calorimetry; DSC (NETZSCH DSC 200), transmission electron microscopy; TEM (JEOL-TEM 200CX), X-ray photoelectron spectroscopy; XPS (Shimadzu AMICUS with VISION 2 control software), and ^{13}carbon nuclear magnetic resonance; ^{13}C NMR (JEOL JMR-A500).

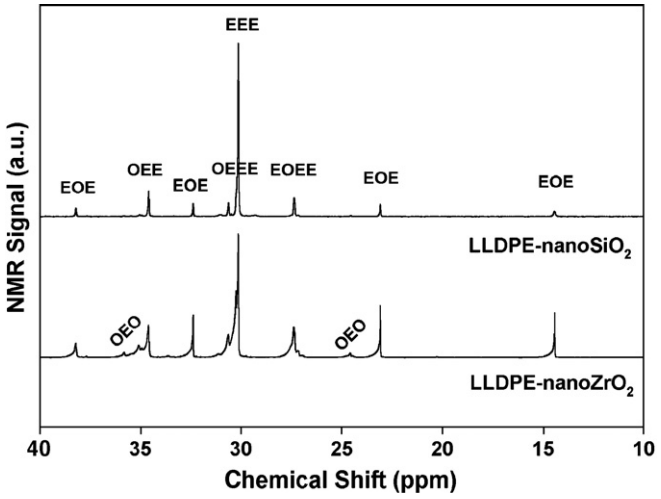

Fig. 2. ^{13}C NMR spectra of the LLDPE–$nanoSiO_2$ and LLDPE–$nanoZrO_2$ and their triad distribution identification (**E** refers to the ethylene sequence and **O** refers to the 1-octene sequence).

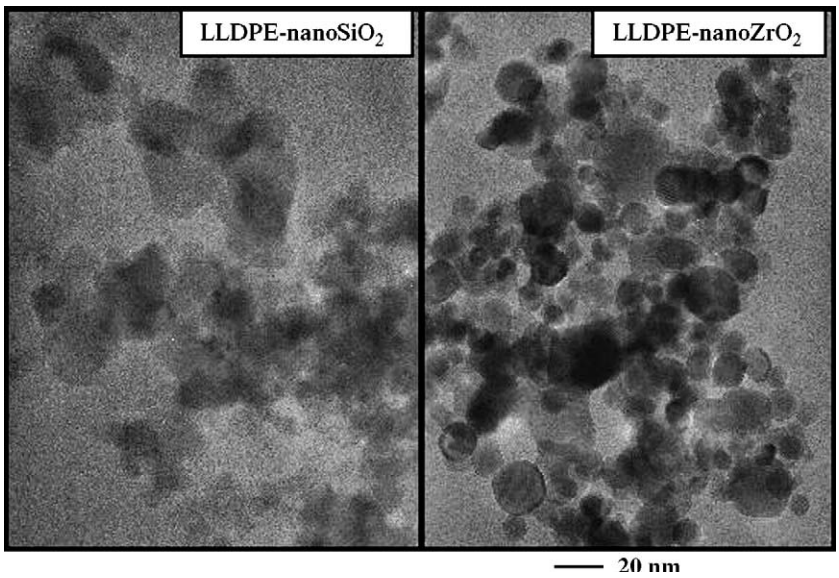

Fig. 1. TEM micrographs of the LLDPE–$nanoSiO_2$ and LLDPE–$nanoZrO_2$.

3. Results and discussion

In the present study, we synthesized the LLDPE–nanoSiO_2 and LLDPE–nanoZrO_2 composites via the *in situ* polymerization with a zirconocene/MAO catalyst. At low amounts of the MAO impregnated-fillers, the activities of catalyst were very low. Hence, the amount of filler at 0.3 g which was corresponding to the ratio of $[Al]_{MAO}/[Zr]=3405$ was applied. After polymerization, the white powder of LLDPE nanocomposites was obtained. The characteristics of LLDPE nanocomposites are shown in Table 1. It was found that the productivity of LLDPE–nanoZrO_2 synthesized via this specified condition was much higher than that of the LLDPE–nanoSiO_2 about 5 times. This was probably due to the strong interaction between MAO and the nano-SiO_2. The melting temperature (T_m) obtained by DSC showed only slight difference in T_m of the two samples. As known, images from high resolution transmission electron microscopy (TEM) are an essential component of nanoscience and nanotechnology, therefore, TEM was performed in order to determine the distribution and dispersion of fillers. The TEM images of the LLDPE–SiO_2 and LLDPE–ZrO_2 are shown in Fig. 1. As seen from both two images, the nanoscale fillers appeared as a group of spherical-like particles indicating the agglomeration of the primary particles. It only indicated that the nanoscale fillers were well distributed inside the polymer matrix, but somehow were poorly dispersed due to the agglomeration. There was no significant difference based on the TEM images for the LLDPE–nanoSiO_2 and LLDPE–nanoZrO_2.

Among a number of important aspects for making a polymer composite, one has to mention how the microstructure of polymer is altered with the addition of nanoscale fillers. Technically, the nanoscale fillers added should not affect the polymer microstructure, but only change the physical properties based on the macroscopic point of view. It has been known that up to now ^{13}C NMR is one of the most powerful techniques used to identify the microstructure of polymer, especially polyolefins. The ^{13}C NMR spectra obtained from LLDPE–nanoSiO_2 and LLDPE–nanoZrO_2 are shown in Fig. 2. The resulted ^{13}C NMR spectra were assigned typically to the LLDPE obtained from the copolymerization of ethylene/1-octene. The triad distribution was identified based on the method reported by Randall [14] where **E** refers to the ethylene sequence and **O** refers to the 1-octene sequence. It can be observed that both samples exhibited the similar ^{13}C NMR patterns indicating the similar molecular structure. Upon the calculation described by Galland et al. [15], the distribution of comonomer was random as also shown in Table 1. This was similar to what we have found in our previous work when no filler was added [10]. However, as seen from Fig. 2, it showed that the degree of 1-octene incorporation for LLDPE–nanoZrO_2 was slightly higher.

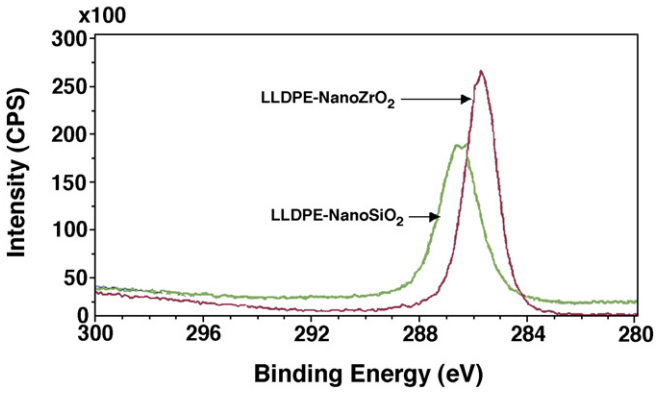

Fig. 3. A plot of binding energy for C 1s obtained from XPS of LLDPE–nanoSiO_2 and LLDPE–nanoZrO_2.

Table 2
Elemental distribution on the surface of LLDPE nanocomposite and the binding energy measured by XPS

Polymer nanocomposite	Peak	B.E. (eV)	FWHM (eV)	Atomic conc. (%)	Mass conc. (%)
LLDPE–nanoZrO_2	O 1s	533.3	1.386	1.79	2.37
	C 1s	285.7	1.419	98.19	97.47
	Zr 3d	185.7	0.756	0.02	0.16
LLDPE–nanoSiO_2	O 1s	534.3	2.368	29.99	32.35
	C 1s	286.5	1.740	59.90	48.50
	Si 2p	104.6	1.944	10.11	19.15

Although ^{13}C NMR showed that the molecular structure of polymer did not change upon the addition of the nanoscale fillers, it cannot differentiate interaction arising from different fillers inside the polymer matrix. Hence, a more powerful characterization technique was necessary for such a purpose. Here, we used the X-ray photoelectron spectroscopy (XPS) to identify different interactions inside the polymer matrix. Since XPS is one of the most powerful techniques used for many applications in surface analysis, so it is also interesting to extend the use of XPS in order to probe the different interactions of the polymer nanocomposites. A plot of the binding energy (BE) for C 1s obtained from XPS for both LLDPE–nanoSiO_2 and LLDPE–nano-ZrO_2 is shown in Fig. 3. BE for the LLDPE–nanoSiO_2 was found to be 286.5 eV whereas the BE for LLDPE–nanoZrO_2 was 285.7 eV (Table 1). Obviously, as seen from Fig. 3, the shift of BE was observed with different nanoscale fillers due to perhaps a different interaction between the fillers and polymer matrix. In fact, the binding energy between 285.7 and 286.5 eV was assigned to the C–C bond in the polymer chain under a different environment. It must be noted that the samples used in this study are insulators. The insulators are always a problem in XPS due to the sample charging. The problem can be partially alleviated, but shifts in BE of several eV can still occur in the presence of charging. To overcome the charging problem, the samples must be coated with a very thin layer of gold by sputtering. It is common practice in XPS to refer the BE to the C 1s electrons that are to be measured. Hence, the energy reference for Ag metal (368.0 eV for $3d_{5/2}$) was used in this study. Besides the BE obtained from XPS, the amounts of Si and Zr atomic and mass concentrations at surface (the depth for XPS is ca. 5 nm) were also determined as shown in Table 2. Surprisingly, with the same amount (0.3 g) of the nanoscale fillers added to the polymer, the penetration of them was totally different. As seen in Table 2 for the mass concentrations, it can be observed that only 0.16% of Zr was found at the surface. This indicated that the ZrO_2 filler penetrated more deeply into the polymer matrix. In contrast, it was found that 19.15% of Si was present at the surface. It was suggested that the SiO_2 filler preferred to be located on the surface more. Therefore, a different location of fillers in the polymer matrix would result in a different interaction indicating the slight shift of BE of the C–C bond in the polymer chain as seen by XPS.

4. Summary

In summary, the LLDPE–nanoSiO_2 and LLDPE–nanoZrO_2 were synthesized via *in situ* polymerization using a zirconocene/MAO catalyst. With the use of nanoZrO_2, the productivity increased more pronouncedly about 5 times. The distribution of both nanoscale fillers obtained from TEM was similar. It also

showed that both LLDPE–nanocomposites exhibited the similar ^{13}C NMR spectra indicating that only random copolymer was obtained. In particular, the XPS measurement indicated only a slightly different interaction for those LLDPE–nanocomposites. It was found that the different location of the nanoscale fillers rendered the BE shift of the C–C bond in the polymer chain.

Acknowledgments

We thank the National Science and Technology Development Agency (NSTDA), the Thailand–Japan Technology Transfer Project (TJTTP-OECF), and the Thailand Research Fund (TRF) for the financial support of this project. We also thank Dr. Okorn Mekasuwandumrong for providing the nanoZrO_2 filler used in this study.

References

[1] C.J.R. Verbeek, Mater. Lett. 56 (2002) 226–231.
[2] R. Nawang, I.D. Danjaji, U.S. Ishiaku, H. Ismail, Z.A.M. Ishak, Polym. Test. 20 (2001) 167–172.
[3] Y. Haung, Y.Q. Zhang, Y.Q. Hua, J. Mater. Sci. Lett. 22 (2003) 997–998.
[4] I.D. Danjaji, R. Nawang, U.S. Ishiaku, H. Ismail, Z.A.M. Ishak, Polym. Test. 21 (2002) 75–81.
[5] C.J.R. Verbeek, Mater. Lett. 52 (2002) 453–457.
[6] G.B. Rossi, G. Beaucage, T.D. Dang, R.A. Vaia, Nano Lett. 2 (4) (2002) 319–323.
[7] T.K. Mandal, M.S. Fleming, D.R. Walt, Nano Lett. 2 (1) (2002) 3–7.
[8] C.L.P. Shan, J.B.P. Soares, A. Penlidis, Polym. Chem. 40 (2002) 4426–4451.
[9] K.L. Chu, C.L.P. Shan, J.B.P. Soares, A. Penlidis, Macromol. Chem. Phys. 200 (1999) 2372–2376.
[10] B. Jongsomjit, P. Kaewkrajang, P. Praserthdham, Mater. Chem. Phys. 86 (2004) 243–246.
[11] B. Jongsomjit, S. Ngamposri, P. Praserthdam, Catal. Letters 100 (2005) 139–146.
[12] B. Jongsomjit, E. Chaichana, P. Praserthdam, J. Mater. Sci. 40 (2005) 2043–2045.
[13] R. Mueller, R. Jossen, S.E. Pratsinis, M. Watson, M.K. Akhtar, J. Am. Ceram. Soc. 87 (2004) 197–202.
[14] J.C. Randall, J. Macromol. Sci., Rev. Macromol. Chem. Phys. C29 (1989) 201–315.
[15] G.B. Galland, P. Quijada, R.S. Mauler, S.C. deMenzes, Macromol. Rapid Commun. 17 (1996) 607–613.

Available online at www.sciencedirect.com
ScienceDirect
Materials Chemistry and Physics 100 (2006) 445–450
MATERIALS CHEMISTRY AND PHYSICS
www.elsevier.com/locate/matchemphys

Preparation and phase transformation behavior of χ-alumina via solvothermal synthesis

Okorn Mekasuwandumrong [a,*], Varong Pavarajarn [b], Masashi Inoue [c], Piyasan Praserthdam [b,*]

[a] *Department of Chemical Engineering, Faculty of Engineering and Industrial Technology, Silpakorn University, Nakorn Pathom 73000, Thailand*
[b] *Research Center on Catalysis and Catalytic Reaction Engineering, Department of Chemical Engineering, Faculty of Engineering, Chulalongkorn University, Bangkok 10330, Thailand*
[c] *Department of Energy and Hydrocarbon Chemistry, Graduate School of Engineering, Kyoto University, Kyoto 606-8077, Japan*

Received 9 August 2005; received in revised form 21 November 2005; accepted 23 January 2006

Abstract

Solvothermal reaction of aluminum isopropoxide (AIP) in mineral oil at 250–300 °C over 2 h duration provides χ-alumina powder, which transforms directly to α-alumina after calcination at high temperature. The mechanism of the crystallization process appears to be the initial formation of a spherical complex which subsequently decomposes further to precipitate a solid. This mechanism is suggested by XRD, IR, TG/DTA, SEM and TEM characterization of the powder formed. χ-Alumina attains a critical crystallite size around 15 nm through accretion on calcination and then transforms directly to α-alumina through nucleation and growth process. Direct α-phase transformation of χ-alumina powders rather than passage through κ-alumina can be explained by the absence of the cation contamination and the higher crystallinity of χ-alumina in the AIP decomposition process.

Keywords: Solvothermal; Direct transformation; χ-Alumina

1. Introduction

Alumina is one of the most common crystalline materials used in many applications such as adsorbents, coatings, soft abrasives, catalyst and catalyst support [1–3] due to its fine particle size, high surface area and catalytic activity. The structural stability of alumina also makes it an important constituent of many protective oxides formed on the surface of high temperature metals and alloys.

There are many metastable polymorphs of transition alumina, including χ-alumina. χ-Alumina is normally prepared by the dehydration of gibbsite (<200 nm) [3–5]. It transforms to κ-alumina at temperature around 650–750 °C before final transformation to α-alumina at 1000–1100 °C. Both transformations lead to loss in the surface area and changes in surface properties. Three different unit cells have been proposed for χ-alumina. Stumpf et al. [6] suggested that χ-alumina has a cubic unit cell with lattice parameter of 7.95 Å, whereas other researchers [4] proposed hexagonal unit cells with either $a = 5.56$ Å and $c = 13.44$ Å or $a = 5.57$ Å and $c = 8.64$ Å. Hexagonal χ-alumina possess a layered structure, in which the hexagonal arrangement of oxygen is inherited from the structure of gibbsite and aluminum occupies octahedral sites within the hexagonal structure.

Recently, Inoue et al. [7–10] have examined the thermal decomposition of metal alkoxides in inert organic solvents, e.g. glycols, and demonstrated that various kinds of novel crystalline product, including χ-alumina, can be directly obtained without bothersome procedures such as purification of the reactants or handling in inert atmosphere.

Nanocrystalline χ-alumina prepared from the thermal decomposition of AIP in inert organic solvent has high thermal stability. It transforms directly to α-alumina at the temperature around 1150 °C, without passing into the κ-phase [7,11,12], resulting in neither the loss in surface area nor the change in surface properties. Moreover, the abrupt crystal growth

* Corresponding authors. Tel.: +66 63116537; fax: +66 34219368.
E-mail address: okornm@yahoo.com (O. Mekasuwandumrong).

0254-0584/$ – see front matter © 2006 Elsevier B.V. All rights reserved.
doi:10.1016/j.matchemphys.2006.01.040

Table 1
The physical properties of as-synthesized products obtained by the thermal decomposition of AIP in mineral oil in various reaction conditions

Reaction conditions		Phase	Crystallite size (nm)	S_{BET} ($m^2\ g^{-1}$)	S_t ($m^2\ g^{-1}$)[a]	Pore volume ($cm^3\ g^{-1}$)[b]	Mode pore diameter (nm)[c]
Temperature (°C)	Time (h)						
250	0	Amorphous	–	7	7	0.03	11.8
250	2	χ-Alumina	9	192	186	0.64	13.3
250	6	χ-Alumina	10.8	149	189	0.43	11.5
270	2	χ-Alumina	10.2	180	210	0.52	11.5
300	2	χ-Alumina	9.4	124	138	0.45	14.2

[a] Calculated from the initial slope of the *t*-plot.
[b] Total nitrogen uptake at relative pressure of 0.98.
[c] Calculated from the desorption branch of the isotherm using the BJH method.

occurring during phase transformation can be effectively controlled. Therefore, nanocrystalline α-alumina can be simply obtained via the direct transformation from nanocrystalline χ-alumina. In this paper, we provide results for the reaction of AIP in mineral oil, including morphology of the synthesized particles and the phase transformation behavior.

2. Experiment

2.1. Sample preparation

Twenty-five grams of aluminum isopropoxide (AIP; Aldrich; >97%) was suspended in 100 ml of mineral oil (liquid paraffin; Ajax; specific gravity 0.830–0.890; CAS No. 8012-95-1) in a test tube, which was then set in a 300 ml autoclave. In the gap between the test tube and the autoclave wall, 30 ml of mineral oil was added. The autoclave was purged completely by nitrogen and heated up to the desired temperature, in the range of 250–300 °C, at a rate of 2.5 °C min^{-1}, and held at that temperature for the desired period of time (0–2 h). After the mixture was cooled down, the resulting powders were repeatedly washed with acetone and dried in air.

Parts of the product obtained was calcined in a box furnace by heating-up to the desired temperature (1000–1200 °C) at a rate of 10 °C min^{-1}. The calcination process was held at that temperature for 1 h.

2.2. Characterization

Powder X-ray diffraction (XRD) was measured on a SIEMENS XRD D5000 using Cu Kα radiation. The crystallite size was calculated from the Scherrer equation. The value of the shape factor, *K*, was taken to be 0.9 and α-alumina was used as an external standard. Infrared (IR) Spectra were recorded on a NICOLET FT-IR Impact 400 spectroscopy using an ex situ IR technique. The thermal behavior of the samples were analyzed on a Perkin-Elmer Diamond TG/DTA thermal analyzer at a heating rate of 10 °C min^{-1} in a 40 ml min^{-1} flow of dried air. Nitrogen adsorption isotherm and BET surface area of the samples were measured by a micromeritics medel ASAP 2000 using nitrogen as the adsorbate. The primary particles of alumina samples were observed by a JEOL TEM-200cx transmission electron microscope operated at 100 kV. Morphologies of alumina products were observed on JEOL scanning electron microscope.

3. Results and discussions

Table 1 summarizes the physical properties of obtained products before calcination. The products synthesized from the decomposition of AIP in mineral oil at 250, 270 and 300 °C with a holding time exceeding 2 h are χ-alumina, while the product obtained from heating the system up to 250 °C without holding time is amorphous. The amorphous product has much lower BET surface area and pore volume than all crystalline products. χ-Alumina obtained by the reaction at 250 °C for 2 h has the highest BET surface area and pore volume. When the reaction temperature is increased or the holding time is prolonged, BET surface area and pore volume of the obtained product is decreased by the coagulation of primary particles due to thermal effect.

The IR spectra of the products are shown in Fig. 1. All as-obtained powders show two adsorption bands attributed to water of crystallization at 3500–3200 cm^{-1} (υ(OH)) and 1640 cm^{-1} (δ(OH)) [13]. The amorphous powder obtained by quenching from 250 °C shows a strong adsorption bands at 1340–1470 cm^{-1} due to the isopropyl hydrocarbon groups [13]. As the holding time or reaction temperature is increased, the adsorption bands due to the organic group decrease and eventually disappear. The characteristic bands of boehmite were detected at 773 and 615 cm^{-1} [10] in the products obtained from 2 h reaction at 250 and 300 °C. This observation can be explained by the formation of boehmite by hydrolysis of AIP with water produced during the reaction.

Fig. 2 shows the results from the thermogravimetric analysis, i.e. TGA and DTA plots, of all powders prepared in mineral oil using various reaction conditions. Two weight decrease processes were detected from the amorphous powder corresponding on one endothermic and exothermic process. The first decrease in mass at around 80–200 °C, accompanied by the endothermic peak in DTA signal, is attributed to the desorption of physisorbed water. The second sharp mass decrease in TGA plot with sharp exothermic peak in DTA plot at around 300 °C is attributed to the combustion of organic moiety. The overall mass loss of this

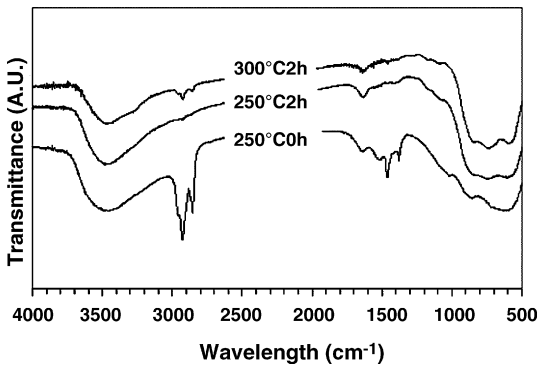

Fig. 1. IR spectra of as-synthesized products at various reaction conditions.

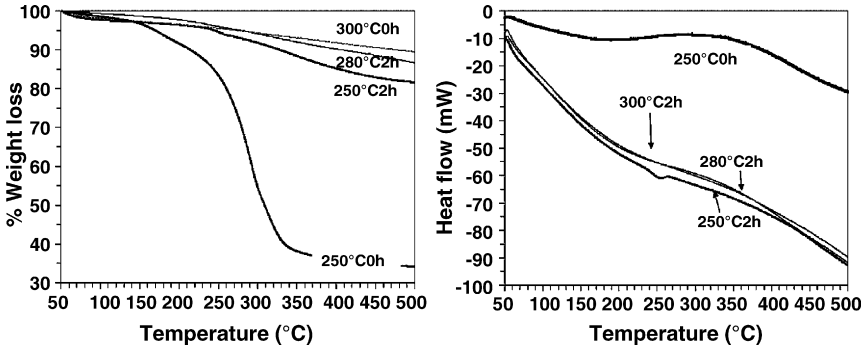

Fig. 2. TG and DTA data of the as-synthesized products.

amorphous sample is around 45%, which is lower than theoretically loss for AIP decomposition (75%). It is indicated that the starting AIP partially decomposes in mineral oil during the heating-up process. The remaining organic moieties from the partial decomposition of AIP reside in the amorphous product.

The nitrogen adsorption isotherms of as-synthesized products are shown in Fig. 3. All the crystalline samples exhibit the hysteresis loop with type-A adsorption characteristic, which is corresponding to the presence of two-ended tabular pore structure. On the other hand, the amorphous product shows the type-E hysteresis loop, which is an indication for the presence of tabular, through short pores with winded parts of various widths [14,15]. These pores are formed among the primary particles of alumina. Fig. 4 presents the pore size distribution of as-synthesized. All crystalline products exhibited the typical characteristic of mesopore system with pore size around 10 nm. It is shown that all products have narrow size distribution.

Fig. 5 shows the morphologies of as-synthesized and calcined samples observed by SEM. Spherical particles with average diameter around 1.8 μm were observed in the amorphous products prepared by quenching the reaction after the temperature had reached 250 °C (Fig. 5a). For the reaction with the holding

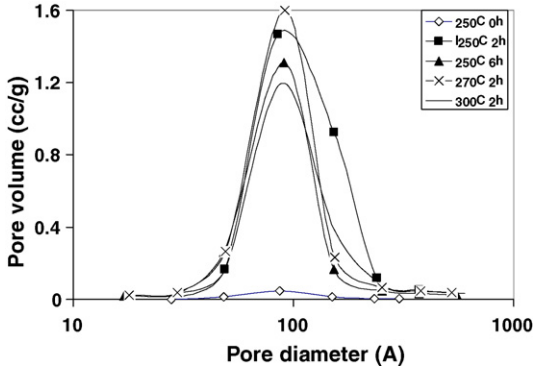

Fig. 4. Pore size distribution of as-synthesized product.

time prolonged to 2 h, similar spherical particles in the products can still be observed. However, the average size of the particles decreases to 1.2 μm (Fig. 5b). These particles are secondary aggregates of nanocrystalline χ-alumina. With the increase of reaction temperature to 300 °C, size of the secondary particles further decreases to 1 μm (Fig. 5c). The results suggest that AIP decomposes stepwise in the inert solvent during heating-up

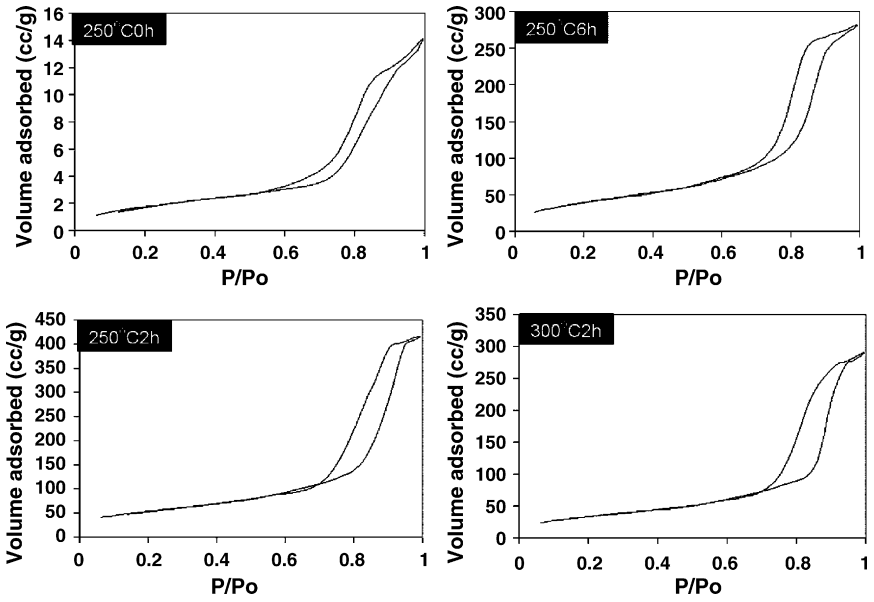

Fig. 3. The nitrogen adsorption isotherms of as-synthesized products.

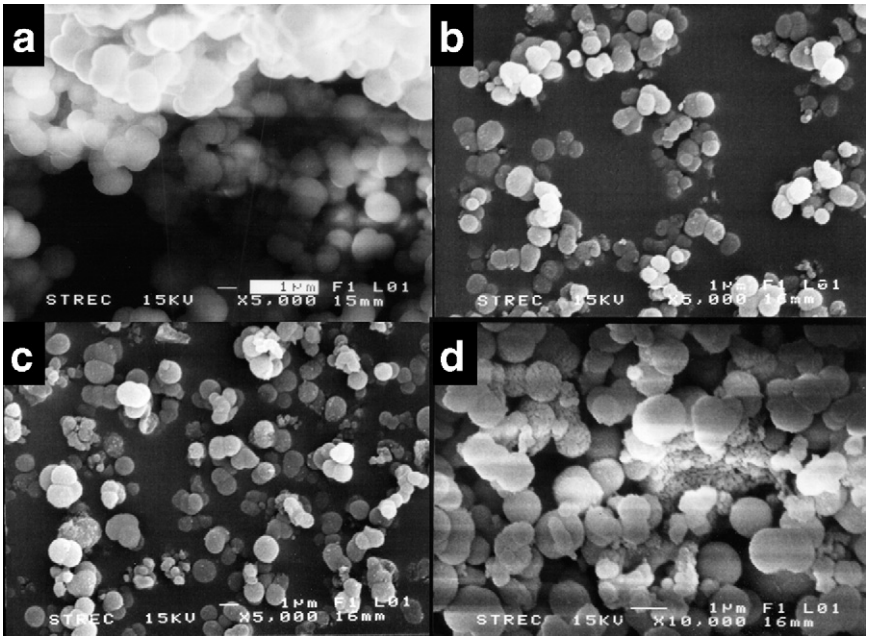

Fig. 5. SEM images: (a) as-synthesized product prepared by quenching reaction in mineral oil at 250 °C, (b) as-synthesized product prepared in mineral oil at 250 °C for 2 h, (c) as-synthesized product prepared in mineral oil at 300 °C for 2 h and (d) product (b) calcined at 1150 °C.

process, which results in an intermediate complex suspending in mineral oil. SEM micrographs confirms that this complex assumes a spherical shape. During the holding period, the complex further decomposes giving the nanocrystalline χ-alumina aggregated in form of spherical particles. The decrease in particle size with the increase in holding time and reaction temperature is due to the loss of the organic moiety in the complex by further decomposition. In this case, there are two nucleation processes. The first nucleation process is the formation of tiny droplets of the intermediate complex. This process is related to the salting out phenomena. During the partial decomposition of organic moieties, the decomposed intermediate is supersaturated in the solution and it is salted out forming the glassy droplets. Because the number of droplets formed in mineral oil is small, the droplets grow and large spherical particles are obtained. The second nucleation step is the formation tiny crystallites of χ-alumina. The morphology of products obtained in this work is different from χ-alumina obtained from the reaction in toluene [12]. This result will be further discussed.

According to Derjaguin–Landua–Verwey–Overbeek (DLVO) theory, the energy barrier between two particles, which inhibit agglomeration, is expressed as follow:

$$V_b = \left(\frac{A\kappa\alpha}{12}\right) + 2\pi\varepsilon_0\varepsilon_r\kappa\alpha\phi^2$$

where A is the effective Hamaker constant, κ the Debye–Huckel parameter, α the particle diameter, ε_0 the permittivity in the free space, ε_r the dielectric constant of the continuous phase and ϕ is the particle surface potential. Because of the constant ionic strength of the solvent, ε_0 and κ is constant, the maximum repulsive force estimated from the second term of the right hand side of the equation ($2\pi\varepsilon_0\varepsilon_r\kappa\alpha\phi^2$) is determined by the dielectric constant, particle size and repulsive force. Mineral oil (liquid paraffin) is the mixtures of long straight chain hydrocarbon produced as the bottom product from distillation. The dielectric constant of long chain hydrocarbon is around 1.9–2 ($C_{13}H_{28} = 2.02$, $C_{14}H_{30} = 2.05$, $C_{19}H_{40} = 2.09$), which lower than toluene (2.379). According to the quite low dielectric constant of mineral oil, the particles become discrete and form spherical particles. Fang and Chen [16] reported that, for the synthesis of TiO_2 by the reaction of $TiCl_4$ in a mixed solvent of *n*-propanol and water, the spherical particles were

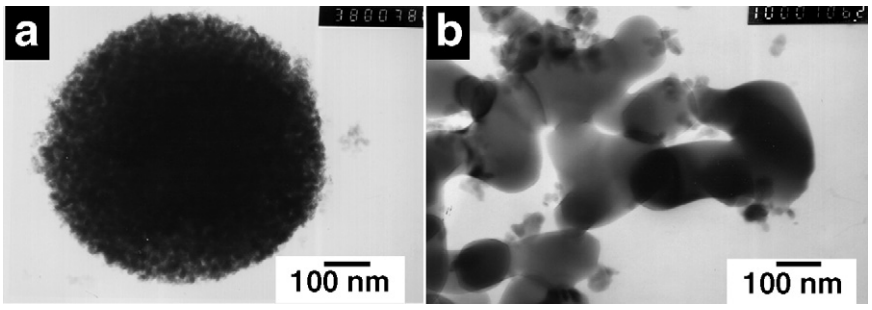

Fig. 6. TEM images: (a) as-synthesized product prepared in mineral oil at 250 °C for 2 h and (b) product (a) calcined at 1150 °C.

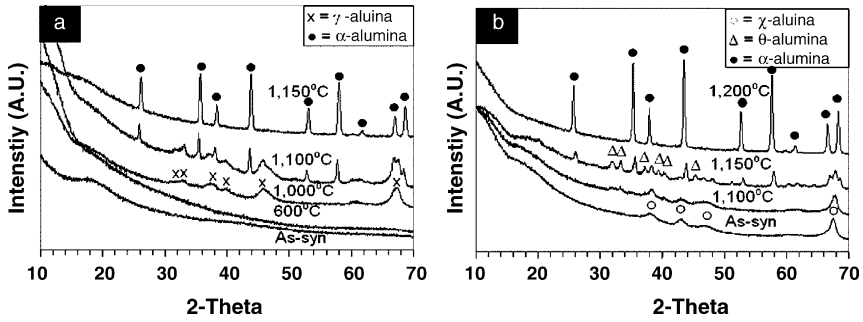

Fig. 7. The XRD patterns of powder synthesized by the reaction of AIP in mineral oil calcined at various reaction conditions: (a) 250 °C for 0 h and (b) 300 °C for 2 h.

formed in the solvent with *n*-propanol/water ratio resulting in the lowest value of dielectric constant.

Transmission electron micrographs of the as-obtained powder and calcined powder are shown in Fig. 6. The as-synthesized χ-alumina products are comprised of agglomerated primary particles having average diameter around 10 nm. As shown in Table 1, the crystallite size calculated by XRD peak broadening, using the Scherrer equation, is 9 nm. Good agreement between both values indicates that each primary particle observed by TEM is a single crystal of χ-alumina.

The XRD patterns of calcined product are shown in Fig. 7. The amorphous product remains amorphous even after calcination at 600 °C (Fig. 7a). However, after calcination at 1000 °C, γ-alumina is observed. The α-phase transformation takes place at temperature around 1150 °C and completes at 1200 °C. It should be noted that the peak at 42.5°, which is corresponding to χ-alumina, is not detected. This indicates that χ-alumina is not formed by calcination of the amorphous product. Therefore, the formation of χ-alumina occurs only in the inert organic solvent. For the calcination of χ-alumina obtained from thermal decomposition of AIP at 300 °C for 2 h (Fig. 7b), χ-alumina transforms to α-alumina directly at temperature around 1100 °C. No κ-alumina was detected. The χ-to-α phase transformation is completed at temperature around 1200 °C. Phase transformation sequences of products obtained from other reaction conditions are summarized in Table 2.

After calcination, the secondary particles still remain spherical with unchanged average particle size, regardless of the crystalline phase (see Fig. 5d). Some finger-like primary particles aggregating on the spherical secondary particles were also observed after the calcination at 1200 °C. TEM micrographs of calcined samples clearly show two groups of primary particles after the phase transformation. The first group is the spherical χ-alumina particles, which do not transform to α-alumina. These particles have crystallite size calculated from the Scherrer equation that is the same as particle size observed by using TEM. The second group of primary particles is the finger-like α-alumina transformed from the low-temperature transition alumina nanocrystals via the nucleation and growth mechanism (see Fig. 6b).

The direct phase transformation of χ- to α-alumina is a specific property for powders prepared by the decomposition of AIP in an inert organic solvent. In our previous work, it has been proposed that the direct phase transformation is the result from the absence of contaminating cations in crystals, as well as high crystallinity of the synthesized product due to the small amount of water adsorbed on the surface. Chou and Nieh [17] have reported that the nucleation of α-alumina occurs along (2 2 0) crystallographic plane of γ-alumina in nanocrystalline oxide synthesized by radio frequency reactive sputtering deposition. Johnston et al. [18] have reported that γ-alumina prepared by laser ablation synthesis directly transforms into α-phase and they have attributed that the particle size of the product is well below the grain size limit for super plastic alumina (500 nm). Bahlawane and Watanabe [19] prepared anhydrous alumina which transformed directly to α-alumina by sol–gel method. Shek et al. [20] have reported that amorphous powders prepared by oxidation of pure aluminum metal crystallize to γ-alumina, which directly transforms to α-alumina at 1370 K. They have attributed this result to the facilitation of nucleation of α-alumina by the strain relaxation of the transition alumina lattice. However, relaxation of the γ-alumina structure should decrease the energy level of γ-alumina and disturb the nucleation of more stable phases. Simpson et al. [21] have reported that samples prepared via electron-beam evaporation of alumina onto a sapphire substrate held at room temperature crystallize to γ-alumina, which transforms into α-alumina without formation

Table 2
The crystallite size calculated by the Scherrer equation and phase of the as-synthesized and calcined products

Reaction condition		Crystallite size and phase of alumina after treat at various temperatures (°C)				
Temperature (°C)	Time (h)	As-synthesized	1000	1100	1150	1200
250	0	– (Amorphous)	6.2 (γ)	16.5 (γ), 31.1 (α)	33.7 (α)	– (α)
250	2	9 (χ)	9.2 (χ)	9.6 (χ)	12.3 (χ), 36.4 (α)	68 (α)
250	6	10.8 (χ)	11.2 (χ)	12.5 (χ)	15.2 (χ), 39.2 (α)	77.2 (α)
270	2	10.2 (χ)	9.4 (χ)	10.3 (χ)	15.6 (χ), 33.5 (α)	97.5 (α)
300	2	9.4 (χ)	10.8 (χ)	14.2 (χ), 39.5 (α)	14.6 (χ), 41.3 (α)	44.7 (α)

of other intermediate phases. They have attributed this result to the epitaxial growth of α-alumina on the sapphire substrate. Ogihara et al. [22] have prepared monodispersed, spherical alumina by the controlled hydrolysis of aluminum alkoxide in a dilute solution containing octanol and acetonitrile. They have found that the amorphous product crystallizes to γ-alumina at 1000 °C which converted to α-alumina at 1150 °C without intermediate phase. However, they did not give any explanation for this result. It has also reported that γ-alumina formed by thermal decomposition of aluminum sulfate transforms into α-alumina directly [23–25].

The crystallite sizes of calcined products are summarized in Table 2. The crystallite size of is initially about 9–10 nm. χ-Alumina grows to 16 nm upon calcination but the growth stop at this size even after the calcination at high temperature. At higher calcination temperature, only α-alumina was observed. It is suggested that χ-alumina grows to the critical size and then abruptly transforms into α-alumina. The result suggests that the critical size of χ-alumina, beyond which it is unstable and undergoes phase transformation into α-alumina, is around 16 nm. Once the phase transformation takes place, the primary particles grow drastically and then become sluggish. The α-phase transformation is considered to occur through a nucleation and growth mechanism [26,27]. Investigations on the phase transformation after the crystallite size has reach the critical size have been reported by many researchers [28–30]. Yen et al. [28,29] have found that, during the phase transformation, there is a critical size for θ-alumina (around 22 nm) at the nucleation stage, which initiates the formation of α-alumina nucleus.

4. Conclusion

Thermal decomposition of AIP in mineral oil at temperature between 250 and 300 °C with holding time of 2 h results in the micro-spherical particles formed by agglomeration of nanocrystalline χ-alumina. On the contrary, the powder obtained during the heating-up process to 250 °C is amorphous. The fact that χ-alumina is not formed by the calcination of the amorphous intermediate confirms that χ-alumina is formed only by AIP decomposition in the inert organic solvent. It is suggested that a spherical particle of complex moieties forms through stepwise decomposition of AIP in the solvent. With the prolonged holding time or increased reaction temperature, this complex sheds organic moieties and solid-state phase of χ-alumina is formed. After calcination at high temperature, χ-alumina transformed to α-alumina directly. The crystallite size of χ-alumina is initially around 9–10 nm and grows upon the calcination to the critical size of 16 nm, beyond which χ-alumina transforms to α-alumina. This direct transformation behavior of nanocrystalline χ-alumina is attributed to the absence of cations and the less defect structure.

Acknowledgement

The author would like to thank the Thailand Research Fund (TRF) for their financial support.

References

[1] W.H. Gitzen, Alumina as a Ceramics Material, American Ceramic Society, Columbus, OH, 1970.
[2] G.M. Pajonk, Appl. Catal. A: Gen. 72 (2) (1991) 217–266.
[3] K. Wefers, G.M. Bell, Oxides and Hydroxides of Alumina, Alcoa, Bauxite, AR, 1972.
[4] H. Saalfeld, Structure Phases of Dehydrated Gibbsite, Elsevier, The Netherlands, 1961.
[5] G.W. Brindley, J.O.T. Choe, Am. Miner. 46 (7–8) (1961) 771785.
[6] H.C. Stumpf, A.S. Russell, J.W. Newsome, C.M. Tucker, Ind. Eng. Chem. 42 (7) (1950) 1398–1403.
[7] M. Inoue, H. Kominami, T. Inui, J. Am. Ceram. Soc. 75 (9) (1992) 2597–2598.
[8] M. Inoue, H. Kominami, T. Inui, Appl. Catal. A: Gen. 121 (1) (1995) L1–L5.
[9] S. Iwamoto, K. Saito, M. Inoue, K. Kagawa, Nano Lett. 1 (8) (2001) 417–421.
[10] P. Pratherthdam, M. Inoue, O. Medkasuvandumrong, W. Thanakulrangsan, S. Phatanasri, Inorg. Chem. Commun. 3 (11) (2000) 671–676.
[11] O. Mekasuwandumrong, P.L. Silveston, P. Praserthdam, M. Inoue, V. Pavarajarn, W. Tanakulrungsank, Inorg. Chem. Commun. 6 (7) (2003) 930–934.
[12] O. Mekasuwandumrong, H. Kominami, M. Inoue, P. Praserthdam, J. Am. Ceram. Soc. 87 (8) (2004) 1543–1549.
[13] D.A. Skoog, J.J. Leary, Principles of Instrumental Analysis, Saundres College Publishing, Philadelphia, San Diego, 1992.
[14] B.C. Lippens, J.H. de Boer, J. Catal. 4 (3) (1965) 319–323.
[15] B.C. Lippens, J.H. de Boer, J. Catal. 3 (1) (1964) 32–37.
[16] C. Fang, Y. Chen, Mater. Chem. Phys. 78 (3) (2003) 739–745.
[17] T.C. Chou, T.G. Nieh, J. Am. Ceram. Soc. 74 (9) (1991) 2270–2279.
[18] G.P. Johnston, R. Muenchausen, D.M. Smith, W. Fahrenholtz, S. Foltyn, J. Am. Ceram. Soc. 75 (12) (1992) 3293–3298.
[19] N. Bahlawane, T. Watanabe, J. Am. Ceram. Soc. 83 (9) (2000) 2324–2326.
[20] C.H. Shek, J.K.L. Lai, T.S. Gu, G.M. Lin, Nanostruct. Mater. 8 (5) (1997) 605–610.
[21] T.W. Simpson, Q. Wen, N. Yu, D.R. Clarke, J. Am. Ceram. Soc. 81 (1) (1998) 61–66.
[22] T. Ogihara, H. Nakagawa, T. Yanagawa, N. Ogata, K. Yoshida, J. Am. Ceram. Soc. 74 (9) (1991) 2263–2269.
[23] D.W. Johnson, F.J. Schnettler, J. Am. Ceram. Soc. 53 (8) (1970) 440–444.
[24] E. Kato, K. Daimon, M. Nanbu, J. Am. Ceram. Soc. 64 (8) (1981) 436–445.
[25] M.D. Sacks, T.-Y. Tseng, S.Y. Lee, Ceram. Bull. 63 (2) (1984) 301–310.
[26] D.S. Tucker, J. Am. Ceram. Soc. 68 (7) (1985) C163–C164.
[27] F.W. Dynys, J.W. Halloran, J. Am. Ceram. Soc. 65 (9) (1982) 442–448.
[28] F.S. Yen, H.L. Wen, Y.T. Hsu, J. Crystal Growth 233 (4) (2001) 761–773.
[29] F.S. Yen, H.S. Lo, H.L. Wen, R.J. Yang, in press.
[30] R.B. Bagwell, G.L. Messing, P.R. Howell, J. Mater. Sci. 36 (7) (2001) 1833–1841.

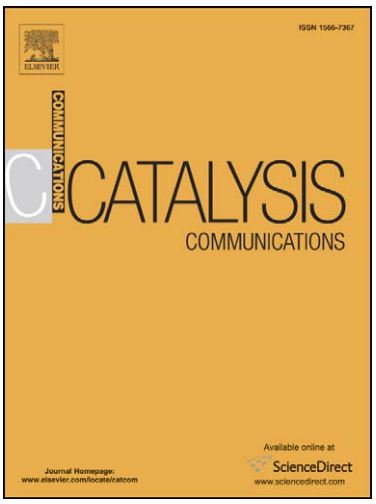

Effect of Mixed γ and χ Crystalline Phases in Nanocrystalline Al_2O_3 on the Dispersion of Cobalt on Al_2O_3

Kamonchanok Pansanga, Joongjai Panpranot, Okorn Mekasuwandumrong, Chairit Satayaprasert, James G. Goodwin, Jr., Piyasan Praserthdam

PII: S1566-7367(07)00244-0
DOI: 10.1016/j.catcom.2007.05.042
Reference: CATCOM 1276

To appear in: *Catalysis Communications*

Received Date: 10 January 2007
Revised Date: 22 May 2007
Accepted Date: 22 May 2007

Please cite this article as: K. Pansanga, J. Panpranot, O. Mekasuwandumrong, C. Satayaprasert, J.G. Goodwin, Jr., P. Praserthdam, Effect of Mixed γ and χ Crystalline Phases in Nanocrystalline Al_2O_3 on the Dispersion of Cobalt on Al_2O_3, *Catalysis Communications* (2007), doi: 10.1016/j.catcom.2007.05.042

"REVISED II"

Effect of Mixed γand χ Crystalline Phases in Nanocrystalline Al_2O_3 on the Dispersion of Cobalt on Al_2O_3

Kamonchanok Pansanga[a], Joongjai Panpranot[a], Okorn Mekasuwandumrong[b], Chairit Satayaprasert[a], James G. Goodwin, Jr.[c], and Piyasan Praserthdam[*,a]

[a] Center of Excellence on Catalysis and Catalytic Reaction Engineering, Department of Chemical Engineering, Faculty of Engineering, Chulalongkorn University, Bangkok 10330, Thailand

[b] Department of Chemical Engineering, Faculty of Engineering and Industrial Technology, Silpakorn University, Nakorn Pathom 73000, Thailand

[c] Department of Chemical and Biomolecular Engineering, Clemson University, Clemson, South Carolina, 29634, USA

Keywords: nanocrystalline alumina; crystalline phase; cobalt catalyst; CO hydrogenation; χ alumina; γalumina

Submitted to: *Catalysis Communications*

Date: May 22, 2007

[*] All correspondence should be addressed.

"REVISED II"

Effect of Mixed γand χ Crystalline Phases in Nanocrystalline Al_2O_3 on the Dispersion of Cobalt on Al_2O_3

Kamonchanok Pansanga[a], Joongjai Panpranot[a], Okorn Mekasuwandumrong[b], Chairit Satayaprasert[a], James G. Goodwin, Jr.[c], and Piyasan Praserthdam[*,a]

[a] Center of Excellence on Catalysis and Catalytic Reaction Engineering, Department of Chemical Engineering, Faculty of Engineering, Chulalongkorn University, Bangkok 10330, Thailand

[b] Department of Chemical Engineering, Faculty of Engineering and Industrial Technology, Silpakorn University, Nakorn Pathom 73000, Thailand

[c] Department of Chemical and Biomolecular Engineering, Clemson University, Clemson, South Carolina, 29634, USA

Keywords: nanocrystalline alumina; crystalline phase; cobalt catalyst; CO hydrogenation; χ alumina; γalumina

Submitted to: *Catalysis Communications*

Date: May 22, 2007

[*] All correspondence should be addressed.

Tel: 66-2218-2882 Fax: 66-2218-6877 E-mail: piyasan.p@chula.ac.th

Abstract

This paper reports the results of a study into the effect of mixed γ and χ crystalline phases in Al_2O_3 on the characteristics and catalytic activities for CO hydrogenation of Co/Al_2O_3 catalysts. The catalysts were characterized by X-ray diffraction, N_2 physisorption, transmission electron microscopy, and H_2 chemisorption. Increasing Co loading from 5 to 20 wt% for the mixed phase Al_2O_3-supported Co catalysts resulted in a constant increase in both the number of cobalt metal active sites and the hydrogenation activities. However, for those supported on γ-Al_2O_3, Co dispersion increased up to 15 wt% Co and declined at 20 wt% Co loading. It is suggested that the spherical-shape like morphology of the χphase Al_2O_3 prevented agglomeration of Co particles, especially at high Co loadings.

1. Introduction

Alumina is one of the most common commercial carriers used to disperse catalytic materials because of its excellent thermal stability, high mechanical resistance, and wide range of chemical, physical, and catalytic properties. In general, acidic, high surface area alumina hydrates are produced at relatively low temperatures by precipitation from either acidic or basic solutions and then are transformed to "transition" β, γ, η, χ, κ, δ, θ, and αAl_2O_3 by dehydration and treatment at high temperatures [1].

Despite a wide range of crystalline structures, only γ- and αAl_2O_3 have been studied often as catalyst supports. Typically, γ-Al_2O_3 provides a better dispersion of catalytically active metals than αAl_2O_3 due to its higher surface area. Only a few publications have reported the effect of other crystalline phases of alumina on the properties of alumina-supported catalysts. For example, Chary et al. [2] reported that dispersion of vanadium oxide on alumina as well as its catalytic activities in partial oxidation decreased with increasing calcination temperature due to the transformation of γ-alumina into θ-alumina, δ-alumina, and α-alumina phases. Recently, Moya et al. [3] studied silver nanoparticles supported on α, η, and δ-Al_2O_3 prepared by a colloidal processing route. It was found that silver particle sizes varied between 1-100 nm depending on the alumina phase. To our knowledge, the effect of mixed γ- and χ-Al_2O_3 phases on the properties of Al_2O_3 as a catalyst support has never been reported.

In this study, nanocrystalline transition Al_2O_3 (γ-Al_2O_3 and mixed γ- and χ-Al_2O_3) were synthesized by decomposition of aluminum isopropoxide (AIP) under solvothermal conditions. The advantages of the solvothermal method are that it gives products with uniform morphology, well-controlled chemical composition, and

narrow particle size distribution [4-8]. Furthermore, desired shapes and sizes of particles can be tailored by controlling process conditions such as solute concentration, reaction temperature, reaction time, and the type of solvent [9-10]. The effects of mixed crystalline phases of Al_2O_3 on the dispersion of cobalt on Al_2O_3 and the resulting catalytic activity for CO hydrogenation were investigated.

2. Experimental

2.1. Preparation of alumina

Nanocrystalline transition Al_2O_3 was prepared by the solvothermal method according to the procedure described in Ref. [11]. The desired amount of aluminum isopropoxide (AIP) (Aldrich) (10, 15, 25, or 35 g) was suspended in 100 ml of 1-butanol (Ajax Finechem) in a beaker, which was then placed in a 300 ml autoclave. In the gap between the beaker and the autoclave wall, 30 ml of 1-butanol was added. After the atmosphere inside the autoclave was purged completely with nitrogen, the mixture was heated to 300°C at a heating rate of 2.5°C/min and was kept at that temperature for 2 h. After cooling to room temperature, the resulting powders were collected after repeated washing with acetone and were then air-dried. The calcination of the products was carried out in a box furnace by heating up to 600°C at a rate of 10°C/min and held at that temperature for 1 h.

2.2. Catalyst preparation

The Al_2O_3-supported cobalt catalysts with different Co loadings (5, 10, 15, and 20 wt%) cobalt were prepared by incipient wetness impregnation of alumina with a desired amount of an aqueous solution of cobalt nitrate [$Co(NO_3)_2 \cdot 6H_2O$] (Aldrich).

After impregnation, the catalysts were dried at 110°C for 24 h and calcined in air at 300°C for 2 h using a ramp rate of 1°C/min.

2.3 Catalyst characterization

X-ray diffraction patterns of the samples were collected using a SIEMENS D-5000 X-ray diffractometer with Cu K_α radiation (λ = 1.54439 Å). The spectra were scanned at a rate of 0.04°/step from 2θ = 15° to 80°. The composition of each crystalline phase has been calculated from the calibration of X-ray diffraction peak areas of the mixtures between each pure phase (physically mixed). BET surface areas of the sample were calculated using the BET-single point method at liquid N_2 temperature. Transmission electron microscopy was performed to study the morphologies of the catalyst samples and the dispersion of cobalt oxide species on the alumina supports using a JEOL JEM 1230. The number of surface cobalt metal atoms was determined by pulse H_2 chemisorption at 100°C on the reduced cobalt catalysts based on the static method described by Reuel and Bartholomew [12] using a Micromeritics Pulse Chemisorb 2750 system. Prior to H_2 chemisorption, the catalyst samples were reduced at 350°C in flowing H_2 for 3 h. The X-ray photoelectron spectroscopy (XPS) analysis was performed using an AMICUS photoelectron spectrometer equipped with a Mg K_α X-ray as a primary excitation and a KRATOS VISION2 software. XPS elemental spectra were acquired with 0.1 eV energy step at a pass energy of 75 kV. The C 1s line was taken as an internal standard at 285.0 eV.

2.4 Reaction study

CO hydrogenation was carried out at 220°C and 1 atm total pressure in a fixed-bed quartz reactor under differential reaction conditions. The H_2/CO ratio used was 10/1. Typically, 0.1 g of the catalyst sample was reduced *in situ* in flowing H_2 (50 cc/min) at 350°C for 3 h prior to reaction. After the start up, samples were taken at 1-h intervals and analyzed by gas chromatography. Steady state was reached within 6 h in all cases.

3. Results and Discussion

In this study, nanocrystalline alumina powders were prepared by thermal decomposition of AIP in 1-butanol with various AIP content. XRD patterns of these alumina samples after calcination at 600°C for 1 h are shown in **Figure 1**. The XRD patterns of transition Al_2O_3 were observed at degree 2θ= 31°, 33°, 38°, 43°, 47.5°, and 68°. It was found that when lower amounts of AIP were used (10 and 15 g in 100 cm^3 of 1-butanol), only γ-Al_2O_3 was formed by calcination, as seen by the XRD characteristic peaks at 2θ = 33° according to the JCPDSs database. These γ-Al_2O_3 samples are denoted hereafter as Al-G1 and Al-G2, respectively. The XRD characteristic peak of χ-alumina was observed at 2θ = 42.5° for the supports prepared with higher amounts of AIP (25 and 35 g in 100 cm^3 1-butanol). The mixed γ- and χ-crystalline phase samples containing χ-phase of ca. 33% and 57% were denoted as Al-GC1 and Al-GC2, respectively. Pure χ-alumina prepared by reaction of AIP in toluene was used as the reference sample and denoted as Al-C. The intensity of χ-Al_2O_3 peaks became stronger with increasing amount of AIP content during

preparation, indicating that increasing AIP content during the solvothermal synthesis resulted in formation of alumina giving rise to mixed phases of γ-Al_2O_3 and χ-Al_2O_3 after calcination. The physical properties of the various Al_2O_3 samples are shown in **Table 1**. The BET surface area of the Al-GC2 (145 m^2/g) was found to be twice of that of Al-G1 (70 m^2/g). A similar trend was observed for the bulk density of the Al_2O_3 powders. The bulk density increased with increasing amount of AIP used during preparation (from 0.38 g/cm^3 to 0.54 g/cm^3). The BET surface areas also increased with increasing AIP concentration, probably as a result of morphology changing from a wrinkled sheet structure to small spherical particles (see **Figure 3)**. These results were confirmed by Al-C with highest BET surface area (180 m^2/g), highest bulk density (0.56 g/cm^3) and complete spherical particle morphologies. From results such as these, it has been proposed that for preparation with low AIP contents, boehmite is the main product resulting in γ-alumina after calcination at 600°C for 1 h. The morphology of the boehmite products obtained via the solvothermal reaction has been shown to be wrinkled sheets [13-14]. The precursor to spherical-shaped χ-Al_2O_3 was formed by direct decomposition of AIP in the solvent and appeared to increase with increasing AIP concentration.

Figure 2 shows the IR spectra of alumina supports after calcination at 600°C for 1 h. The IR peaks assigned to OH stretching were observed at around 3730 and broad peak between 3200 to 3600 cm^{-1}. According to Peri's model [15], the features at 3791, 3730, and 3678 cm^{-1} are assigned to surface isolated hydroxyl groups. The broader peak at 3589 cm^{-1} is due to the vibration of associated hydroxyl groups of aluminum oxide. The spectra which assigned to OH groups of all samples were nearly identical. Therefore, the amounts and nature of OH groups of all supports were essentially same.

The nanocrystalline γ-Al_2O_3 and mixed γ- and χ-Al_2O_3 were then employed as catalyst supports for Co catalysts. The Co/Al_2O_3 catalysts were prepared using the incipient wetness impregnation method with cobalt loadings of 5, 10, 15, and 20 wt% in order to investigate the effect of mixed crystalline phases of Al_2O_3 on the dispersion of Co and its catalytic activity for CO hydrogenation. The XRD patterns of the various Co/Al_2O_3 catalysts after calcination at 300°C were not significantly different from those of the Al_2O_3 supports (results not shown). No XRD characteristic peaks of Co_3O_4 and/or other Co compounds were detected for all the catalyst samples. This suggests that the crystallite size of cobalt oxide on Al_2O_3 was probably below the lower limit for XRD detectability (3-5 nm). Such results also indicate that cobalt oxide species were present in a highly dispersed form on these nanocrystalline Al_2O_3 even for cobalt loadings as high as 20 wt%.

The morphology and distribution of cobalt oxide particles on the Al_2O_3 supports were investigated by transmission electron microscopy (TEM). The typical TEM micrographs of 20 wt% of cobalt on alumina supports containing different compositions of γ and χ phases are shown in **Figure 3**. In all the TEM figures, the darker spots on the catalyst granules represent a high concentration of cobalt and its compounds while the lighter areas indicate the support with minimal or no cobalt present. It was found that the wrinkled sheets-like structure of γ-Al_2O_3 was maintained after impregnation and calcination for both 20Co/Al-G1 and 20Co/Al-G2 catalysts (Figure 2a and 2b). The mixed structure between spherical particles of χ-Al_2O_3 and wrinkled sheets of γ-Al_2O_3 were also observed for 20Co/Al-GC1 and 20Co/Al-GC2 samples (Figure 2c and 2d). However, cobalt oxide species appeared to be more

agglomerated on the γ-Al_2O_3 supports than on the mixed γ- and χ-ones as shown by the appearance of larger cobalt oxide particles/granules.

Static H_2 chemisorption on the reduced cobalt catalyst was used to determine the number of active surface cobalt metal atoms [16]. The H_2 chemisorption results for all the catalyst samples are reported in **Table 2**. The overall dispersion of reduced Co and crystal size of Co^0 in the catalyst samples based on the H_2 chemisorption results is also given. In order to distinguish the effect of mixed γ and χ crystalline phases of Al_2O_3 and the effect of BET surface area, we also report the H_2 chemisorption results in terms of the amount of H_2 chemisorption per total specific surface area of the catalyst (see **Figure 4**). For the Co/Al-G1 and Co/Al-G2 catalysts in which the Al_2O_3 contained only the γ phase, the number of active surface cobalt metal atoms per unit surface area increased with increasing Co loading up to 15 wt%. Further increase of the amount of Co loading to 20 wt% resulted in both a lower cobalt dispersion and fewer exposed surface cobalt metal atoms (**Table 2**), even taking into account BET surface area (**Figure 4**). This is typical for supported Co Fischer-Tropsch catalysts. Dispersion usually decreases with increasing Co loading beyond a certain point [17-21]. On the contrary, the amounts of H_2 chemisorption per unit surface area of the mixed γ and χ crystalline phases Al_2O_3 supported Co catalysts (Co/Al-GC1 and Co/Al-GC2) constantly increased with increasing Co loading from 5 to 20 wt% (**Table 2, Figure 4**). To study the effect of phase composition on active sites of Co catalyst, 15%Co/pure χ-alumina catalyst was characterized to compare with 15%Co deposited on pure γ-Al_2O_3 and mix phase supports. The amounts of H_2 chemisorption increased from 9.2 to 21.4 μmol/g catalyst as the χ phase contents increased from 0 to 57%. While the amounts of H_2 chemisorption of Co/pure χ-

alumina catalyst ranged around 16.8 μmol/g catalyst. It is suggested that the presence of χ phase in γ-Al_2O_3 may prevent agglomeration of Co particles especially at high Co loadings, resulting in the maintenance of high Co dispersion. Because of its surface sensitivity, XPS is used to identify the surface compositions of the catalysts as well as the interaction between Co and the alumina supports. The results are given in Table 3. It was found that the ratio of Al/O atomic concentration was slightly increased while that of Co/Al decreased with the presence of χphase in γ-Al_2O_3 suggesting higher dispersion of Co on the mixed phase Al_2O_3 supports. There was also a slight shift of Co 2p binding energy to higher values for the 15Co/Al-GC1 and 15Co/Al-GC2 catalysts compared to those supported on γ-Al_2O_3 (Al-G1 and Al-G2). Such results suggest stronger interaction between Co and the mixed phases γ- and χ-Al_2O_3.

CO hydrogenation was carried out in a fixed-bed quartz reactor under differential reaction conditions in order to determine the catalytic activity of the catalyst samples. The reaction results in terms of CO conversion, hydrogenation rate, and the turnover frequency (TOF) per exposed Co atom calculated using the hydrogen chemisorption data are given in **Table 4**. The catalytic activities increased with increasing Co loading in general (at least to 15 wt% Co). For a similar Co loading, Co catalysts supported on the mixed crystalline phases Al_2O_3 exhibited higher CO hydrogenation activities compared to those supported on the ones containing only γ phase Al_2O_3. The TOFs of the cobalt catalysts in which the Al_2O_3 support contained only the γ phase decreased with increasing Co loading, suggesting perhaps an underestimation of exposed Co metal atoms by H_2 chemisorption. However, the TOFs for the mixed crystalline phases Al_2O_3 did not significantly change regardless of cobalt loading percentage. The reaction results are in a good agreement with the

H_2 chemisorption results since CO hydrogenation is usually considered to be a structure insensitive reaction [22-26]. Thus, higher dispersion of Co yields higher hydrogenation activity.

4. Conclusions

Nanocrystalline γ-Al_2O_3 and mixed γ and χ-Al_2O_3 were obtained by decomposition of AIP in 1-butanol by varying the amounts of AIP used under the solvothermal conditions. For a similar Co loading, the presence of χphase in γ-Al_2O_3 support resulted in higher dispersion of Co as well as higher CO hydrogenation activities of the Co/Al_2O_3 catalysts. It is suggested that the spherical-shape like morphology of the χphase Al_2O_3 provide better stability of the Co particles, especially for those with high Co loadings.

Acknowledgments

The authors would like to thank the Thailand Research Fund (TRF) for the financial support of this project.

Table 1 Properties of the various nanocrystalline Al_2O_3 samples prepared by the reaction of AIP in 1-butanol at 300°C for 2 h.

Samples	Amounts of AIP (g)	Amounts of χ phase (%)	Surface area (m^2/g)[a]	Bulk density (g/cm^3)[a]	Morphology [27]
Al-G1	10	-	70	0.38	Wrinkled sheets
Al-G2	15	-	120	0.38	High amount of wrinkled sheets
Al-GC1	25	33	139	0.39	Wrinkled sheets and small amount of spherical particles
Al-GC2	35	57	145	0.53	Small amount of wrinkled sheets and high amount of spherical particles
*Al-C	25	100	180	0.56	Spherical particles

[a] Error of measurement = ±5%

* Pure χAl_2O_3

Table 2 H_2 chemisorption results

Catalyst samples	Amounts of H_2 chemisorption (μmol/g cat.)[a]				% Co dispersion[b]				dp Co^0 (nm) (96.2/D%)			
	5%Co	10%Co	15%Co	20%Co	5%Co	10%Co	15%Co	20%Co	5%Co	10%Co	15%Co	20%Co
Co/Al-G1	0	0.9	9.2	3.3	0	0.1	0.7	0.2	0	962	137	481
Co/Al-G2	0.9	2.3	14.9	10.9	0.2	0.3	1.2	0.6	481	321	80	160
Co/Al-GC1	5.6	7.6	18.9	19.5	1.1	1.1	1.5	1.5	87	87	64	64
Co/Al-GC2	5.8	20.7	21.4	24.6	1.3	1.7	1.7	1.8	74	57	57	53
*Co/Al-C	-	-	16.8	-	-	-	1.3	-	-	-	74	-

[a] Error = ±5 %, as determined directly.

[b] % Co dispersion = [2 ×(total H_2 chemisorption/g cat.) / (no. of μmol of Co total/g cat.)] ×100 %

* Co/Al_2O_3 prepared from pure χAl_2O_3 support.

Table 3 Surface compositions based on XPS results for 15 wt% Co/Al_2O_3 catalysts

Sample	Binding Energy (eV)			Atomic Concentration (%)	
	Co 2p	O 1s	Al 2s	Al/O	Co/Al
15Co/Al-G1	782.4	533.1	120.9	0.29	0.026
15Co/Al-G2	782.4	533.1	120.6	0.33	0.027
15Co/Al-GC1	782.8	533.1	121.0	0.34	0.015
15Co/Al-GC2	782.9	532.9	120.3	0.40	0.019

Table 4 Reaction rate for CO hydrogenation on Co/Al_2O_3 catalysts.

Catalyst samples	CO conversion (%)[a]				Rate (μmol $gcat^{-1}s^{-1}$)[b]				TOF (s^{-1})[b,c]			
	5%Co	10%Co	15%Co	20%Co	5%Co	10%Co	15%Co	20%Co	5%Co	10%Co	15%Co	20%Co
Co/Al-G1	0.5	1.9	8.8	2.1	0.3	1.1	5.2	1.3	-	0.6	0.3	0.2
Co/Al-G2	1.1	2.6	10.0	4.0	0.7	1.6	6.0	2.4	0.4	0.3	0.2	0.1
Co/Al-GC1	2.9	5.5	10.2	7.3	1.7	3.3	6.1	4.3	0.2	0.2	0.2	0.1
Co/Al-GC2	4.0	8.5	10.6	10.7	2.4	5.1	6.3	6.3	0.2	0.1	0.1	0.2

[a] CO hydrogenation was carried out at 220°C, 1 atm, and $H_2/CO/Ar$ = 80/8/32.

[b] Error of measurement = ±5% as determined directly.

[c] Based on H_2 chemisorption.

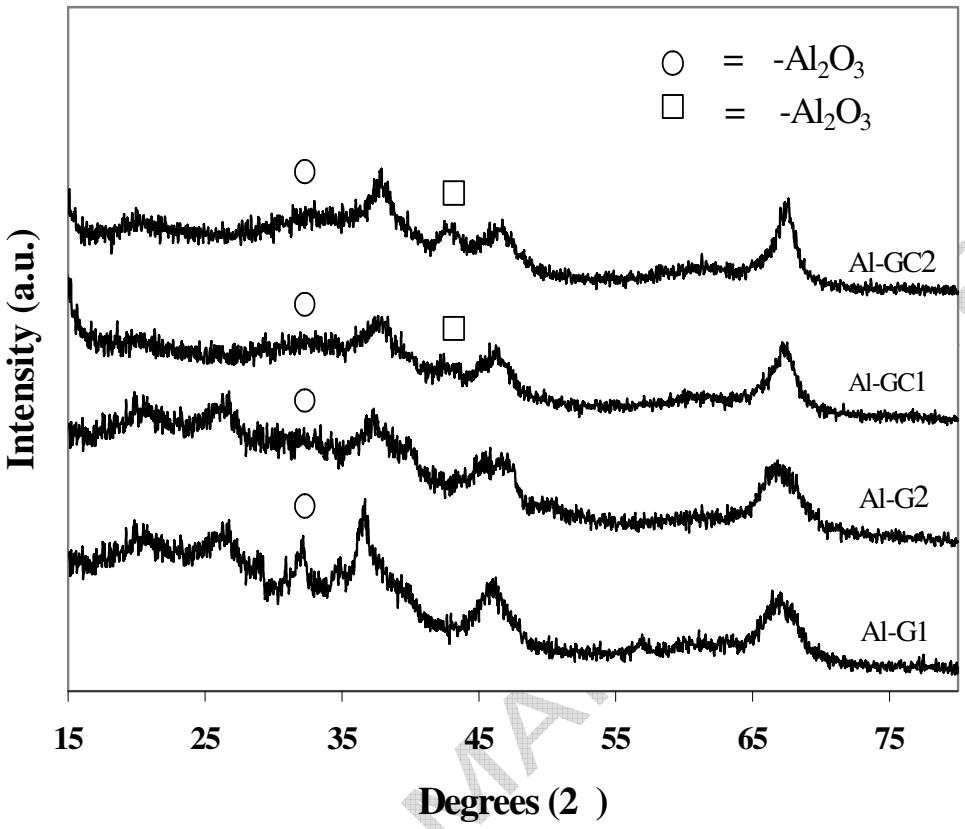

Figure 1 XRD patterns of the various nanocrystalline alumina prepared by the reaction of AIP in 1-butanol at 300°C for 2 h (after calcination at 600°C for 1 h).

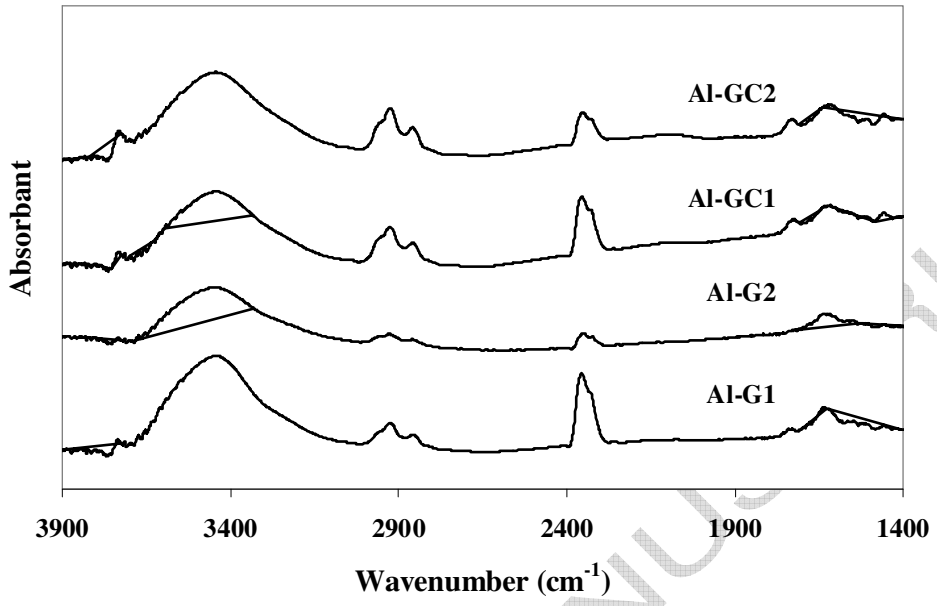

Figure 2 IR spectra of various alumina supports.

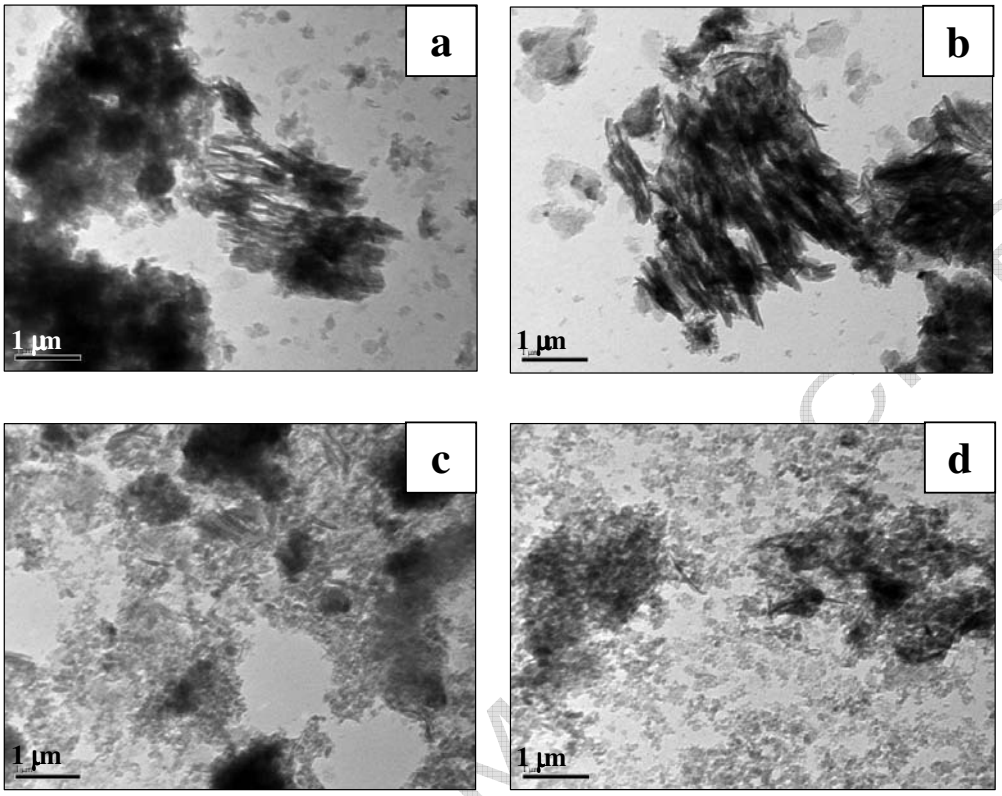

Figure 3 TEM micrographs of the various 20 wt% Co/Al_2O_3 catalysts

(a) 20Co/Al-G1 (b) 20Co/Al-G2 (c) 20Co/Al-GC1 (d) 20Co/Al-GC2.

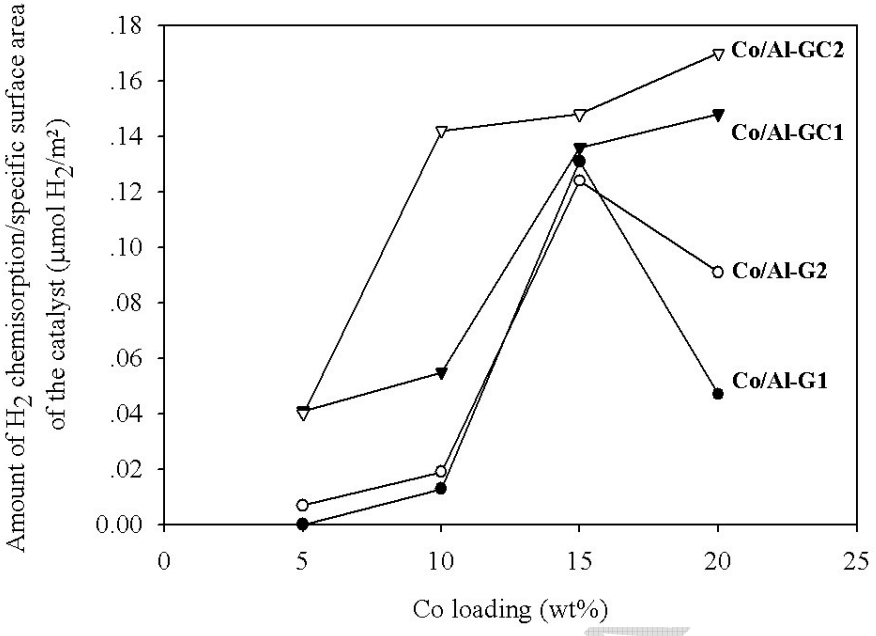

Figure 4 The amount of H_2 chemisorption/specific surface area of the Co/Al_2O_3 catalysts as a function of cobalt loading.

References

[1] R. J. Farrauto, C. H. Bartholomew, Fundamentals of Industrial Catalytic Processes, (Blackie Academic & Professional, London, 1997).

[2] K. V. R. Chary, G. Kishan, C. P. Kumar, G. V. Sagar, Appl. Catal. A 246 (2003) 335.

[3] A. Esteban-Cubillo, C. Diaz, A. Fernandez, L. A. Diaz, C. Pecharroman, R. Torrcillas, J. S. Moya, J. European Ceramic Soc. 26 (2006) 1-7

[4] M. Inoue, H. Kominami, T. Inui, J. Am. Ceram. Soc. 73 (1990) 1100.

[5] M. Inoue, H. Kominami, T. Inui, J. Chem. Soc. Dalton Trans. (1991) 3331.

[6] M. Inoue, H. Kominami, T. Inui, J. Am. Ceram. Soc. 75 (1992) 2597.

[7] M. Inoue, H. Kominami, T. Inui, Appl. Catal. A 77 (1993) L25.

[8] M. Inoue, Y. Kondo, T. Inui, Inorg. Chem. 27 (1988) 215.

[9] Y. Deng, X. Zhou, G. Wei, J. Liu, C.W. Nan, S. Zhao, J. Phys. Chem. Solids 63 (2002) 2119.

[10] Y. Deng, G.D. Wei, C.W. Nan, Chem. Phys. Lett. 368 (2003) 639.

[11] O. Mekasuwandumrong, P. L. Silveston, P. Praserthdam, M. Inoue, V. Pavarajarn, W. Tanakulrungsank, Inorg. Chem. Commun. 6 (2003) 930.

[12] R. C. Reuel, C. H. Bartholomew, J. Catal. 85 (1984) 63.

[13] M. Inoue, H. Otsu, H. Kominami, T. Inui, Ind. Eng. Chem. Res. 35 (1995) 295.

[14] P. Praserthdam, M. Inoue, O. Mekasuvandumrong, W. Tanakulrungsank, S. Phatanasri, Inorg. Chem. Commun. 3 (2000) 671.

[15] J.B. Peri, J. Phys. Chem. 69 (1965) 211.

[16] B. Jongsomjit, T. Wongsalee, P. Praserthdam, Mater. Chem. Phys. 92 (2005) 572.

[17] L. B. Backman, A. Rautiainen, A. O. I. Krause, M. Lindblad, Catal. Today 43

(1998) 11.

[18] L. B. Backman, A. Rautiainen, M. Lindblad, A. O. I. Krause, Appl. Catal. A 191 (2000) 55.

[19] G. Jacobs, T. K. Das, Y. Zhang, J. Li, G. Racoillet, B. H. Davis, Appl. Catal. A 223 (2002) 263.

[20] A. Martinez, C. Lopez, F. Marquez, I. Diaz, J. Catal. 220 (2003) 486.

[21] S. A. Hosseini, A. Taeb, F. Feyzi, Catal. Commun. 6 (2005) 233.

[22] V. Ragaini, R. Carli, C. L. Bianchi, D. Lorenzetti, G. Predieri, P. Moggi, Appl. Catal. A 139 (1996) 31.

[23] J. Panpranot, J. G. Goodwin, Jr., and A. Sayari, Catal. Today 77 (2002) 269.

[24] B. G. Johnson, C. H. Bartholomew, D. W. Goodman, J. Catal. 128 (1991) 231.

[25] E. Iglesia, Appl. Catal. A 161 (1997) 59.

[26] N. Tsubaki, S. Sun, K. Fujimoto, J. Catal. 199 (2001) 236.

[27] K. Pansanga, O. Mekasuwandumrong, J. Panpranot, P. Praserthdam, Korean J. Chem. Eng., In Press, Corrected Proof.